

876544846444684151654225454

# FCRAR 2017

30th Florida Conference on  
Recent Advances in Robotics

Proceedings May 11 - 12 @ the FAU Boca Raton Campus

## KEYNOTE SPEAKERS

Andrew Goldenberg, Ph.D.

Professor Emeritus, Mechanical Engineering, University of Toronto, Department of Mechanical and Industrial Engineering. "Evolution of Robotics: Technology & Related Business, Past, Present & Future"

Deborah Nagle, M.D.

Medical Director, Endomechanical Franchise and Surgical Oncology, Johnson & Johnson  
"The Evolution of Robotic Surgery"

## TOPICS

- Robot Kinematics, Dynamics and Controls
- Design and Modeling of Robotic Mechanical Systems
- Robot Applications and Software Development
- Serial and Parallel Manipulators
- Mobile and Humanoid Robots
- Autonomous and Unmanned Vehicles
- Micro and Nano Scale Robotics
- Automation and Teleoperation
- Biomedical and Assistive Robotics
- Control Theory and Applications
- Mechatronics
- Machine Vision
- Education issues related to Robotics, Automation and Mechatronics

## SPONSORED BY



DEPARTMENT OF COMPUTER &  
ELECTRICAL ENGINEERING  
AND COMPUTER SCIENCE  
College of Engineering & Computer Science  
Florida Atlantic University



COLLEGE OF ENGINEERING  
& COMPUTER SCIENCE  
Florida Atlantic University



DEPARTMENT OF OCEAN &  
MECHANICAL ENGINEERING  
College of Engineering & Computer Science  
Florida Atlantic University

# Active Thermal Control System for CubeSat

Pradeep Shinde, Anthony Fernandez, Ibrahim Tansel, Sabri Tosunoglu

Department of Mechanical and Materials Engineering  
Florida International University  
10555 West Flagler Street  
Miami, Florida 33174

pshin001@fiu.edu, afern401@fiu.edu, tanseli@fiu.edu, tosun@fiu.edu

## ABSTRACT

The use of CubeSat systems for low-orbit data collection has increased due to their low cost development and light weight designs. For efficient data collection to occur, it is imperative that the satellite's internal components remain fully functional throughout its mission life. To ensure the components remain in their operational range, an internal thermal control subsystem must be developed to effectively combat the transfer of heat. The standard size and payload of a CubeSat eliminates the possibility of designing a conventional fluid flow piping system. Through the development of a phase change material (PCM) thermal control system, the internal components will experience smaller temperature variations, while remaining within their operational limits. The melting temperature for optimal PCM performance, with a component operational range from 0-40°C, is currently desired to be 45°C, and the selection between Organic and Inorganic materials can be found below. The calculations developed in this report assume that the outside radiation and ultraviolet heat sources will minimally impact the temperature of the interior structure, allowing for further focus on the component heat generation. This paper presents preliminary designs and calculations towards the development of a low cost and replicable active thermal control system for the interior of CubeSats and is originally intended for implementation on Florida International Universities' NEESAT.

## Keywords

Heat transfer, Conduction, Radiation, Phase change material (PCM), Thermal control system, CubeSat, 3U, FUNSAT, NEESAT

## NOMENCLATURE

$Q$	Thermal Energy, $W$
$k$	Thermal Conductivity, $W/m \cdot K$
$A$	Cross-Sectional Area, $m^2$
$l$	Section Length, $m$
$D$	Diameter, $m$
$T_h$	Hot Temperature, $^{\circ}C$
$T_c$	Cold Temperature, $^{\circ}C$
$\rho$	Density, $kg/m^3$

## 1. INTRODUCTION

The increase in popularity of CubeSat systems has allowed for large scale research towards the development of low cost, low weight and effective in-orbit data collection. The Florida International University's Near Earth Explorer Club is currently manufacturing a 3U picosatellite for use in the NASA FUNSAT competition, with the goal of further developing existing CubeSat research. To minimize the systems payload while remaining in the satellite's internal boundaries (10 x 10 x 30 cm), the overall weight and size of the thermal control system must be minimized. To achieve this goal, the current system design integrates the use of a PCM to provide the necessary thermal control to allow the multiple internal components (seen in 3.1 – Components) to operate efficiently throughout the intended twenty-year mission life.

A PCM, or phase change material, is a description given to any substance that has a sharp melting point and a large heat of fusion [1]. This combination of properties allows PCMs to have vast applications in the thermal control of space equipment and vehicles. Through the use of chemical bonds, PCMs are able to store and release large amounts of latent heat energy while consistently having a low temperature difference [1]. The latent heat storage method developed through PCMs has 5-14 times more heat capacity per unit volume when compared to materials used in sensible heat storage systems, further increasing their effective usage in a CubeSat cooling subsystem. The most common and effective PCM transformation is the solid-liquid because of the small volume change necessary for implementation, when compared to vaporization and sublimation [2]. Due to the complexity of the design, the large volume changes that occur during the vaporization and sublimation phase transition rules out their potential utility in a thermal storage system [3].

A PCM material needs a high latent heat of fusion per unit mass to be able to store a large amount of latent heat energy in a small volume of material. A high thermal conductivity is necessary to increase the temperature gradient required for charging the storage material so the material could absorb large quantities of heat in a short period of time. With a large density value, a smaller volume of material will provide an ease for encapsulation method designs, while maintaining proper absorption and rejection parameters. To ensure a stable system life, the phase change material must have minimal chemical decomposition, as well as an increased thermal stability [1]. PCMs are categorized into three main material groups:

organics, inorganics and eutectic (combination of organic and inorganic materials), as seen in Figure 1 – ‘Classification of PCMs’ below.

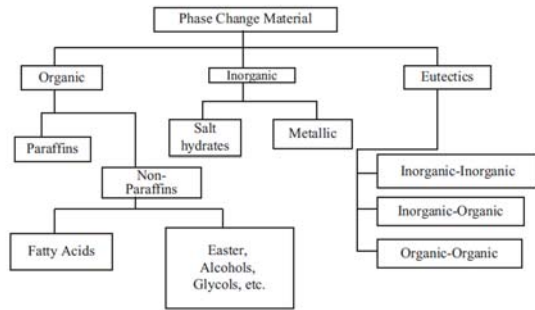


Figure 1 – Classification of PCMs [3]

## 2. THERMAL CONTROL SYSTEM FOR INTERNAL HEAT GENERATION

The thermal control system serves the main function of maintaining the internal components within their operational temperatures throughout the proposed mission life. The NEESat system is composed of multiple heat generating subsystems, each with their own components, as follows: optical, attitude determination and control, communication and computing, as seen in 3.1 – Components, below. A major challenge in the development of the PCM thermal control system lies in the configuration of the separate subsystem components within the overall CubeSat structure. Multiple phases of thermal calculations were performed to gather a fundamental understanding of the effects of parameter variations within the preliminary design. An example of a PCM thermal control system can be seen in Figure 2 – PCM ‘Thermal-Control System for Short-Duty-Cycle Electronic Components’, below.

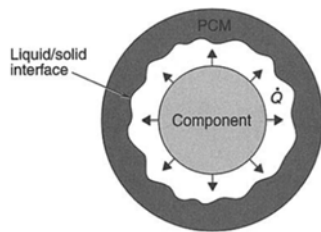


Figure 2 - PCM Thermal-Control System for Short-Duty-Cycle Electronic Components [2]

In this thermal control system, the PCM is component dependent, meaning that each component requires its own thermal control system. A CubeSat system containing many heat generating internal components would not benefit from such a system due to the strict payload and space parameters. A design containing a centralized PCM thermal control system would have the greatest advantage for a CubeSat system because it will centralize the heat and transfer it equally throughout the system.

### 2.1 Components

As previously mentioned, the proposed components for the NEESat are separated into the following subsystems: optical, attitude determination and control, communication and computing, with a more detailed list shown in Table 1 – ‘NEESat Components per Subsystem’, below.

Table 1 – List of Components per System [4]

Subsystem	Component	Max Power Req. (W)
Optical	CMOS	0.38
	OV14810 CMOS	0.64
	SeekThermal	0.28
	TMP36 (x10)	0.00
	IR Temp Sensor (x6)	0.08
Attitude Determination and Control	LSM9DS0	0.04
	Sun Sensor (x6)	1.5
Communication	USRP + GPS + Antenna	3.0
	Power Amplifier	7.0
Computing	Arduino Mega	5.0
	BeagleBone Black (x2)	22.01
Total		39.93

For the mission of the NEESat system to be fully achievable, the thermal control system must be designed to combat the maximum power output achievable by the internal components. The components require the temperature to be maintained between 0-40°C because of the lower operational temperature range of the onboard lithium polymer batteries, as seen in Table 2 – ‘Internal Component Operating Temperatures.’

Table 2 – Internal Component Operating Temperatures [4]

Internal Components	Operating Temperatures [°C]	
	$T_{min}$	$T_{max}$
CMOS	-40	+85
OV14810 CMOS	-30	+70
SeekThermal	-30	+70
TMP36	-40	+125
IR Temp Sensor	-40	+125
Arduino Mega	-40	+85
BeagleBone Black	-40	+90
Lithium Polymer Battery	0	+45

An example of some of the components used in the optical system can be seen in Figure 3 – ‘Sensor Components used in Optical Subsystem’ below. The sizes of the individual components and computing chips vary, but each poses a challenge for the design of a centralized heat exchange system.

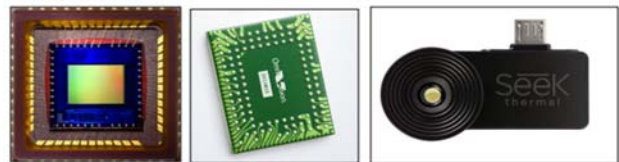


Figure 3 – Sensor Components used in Optical Subsystem [4]

The NEESat system is composed of multiple subsystems, each with its own set of components, example seen in Figure 3 above and Figure 4 below. Figure 3 shows an example of the SeekThermal and CMOS chips, both located in the optical system. Figure 4, below, shows an example of the LSM9DS0 sensor which is used in

the attitude and orbital control system, developed by a previous FIU FUNSAT team, to orient the CubeSat towards the sun [5].

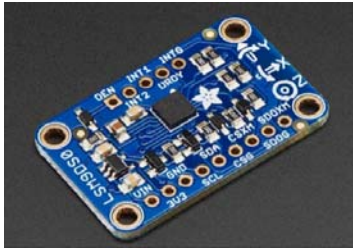


Figure 4 – LSM9DS0 Sensor used in Attitude and Orbital Control [5]

For the development of preliminary thermal calculations, the overall power consumption for each NEESat subsystem was determined through past experiences, as well as literature research, and is populated in Table 1, above. The overall component power consumption of ~40 Watts will be used to aid in the determination of the various centralized PCM parameters, as seen in section 3.2 – *Thermal Calculations*.

## 2.2 Thermal Calculations

The preliminary calculations developed in the following phase sections were determined using the heat transfer equations and fixed parameters, shown below. The development of the thermal control system required that the maximum power consumption of the electronic components be equal to the maximum heat generated, as seen in Table 4 below. Designing in terms of the worst possible scenario will ensure that the components will remain in their operational range. The first equation (1), as seen below, was used to determine the average conduction temperature of the PCM in the centralized heat pipe system design with the following fixed parameters:

Table 3. Fixed Parameters in Phase 1

Parameter	Value	Units
Thermal Conductivity [ $k$ ]	401	$W/m * K$
Cross-Sectional Area [ $A$ ]	0.053	$cm^2$
Heat Pipe Length [ $L$ ]	1	$cm$
Component Temperature [ $T_h$ ]	35	$^{\circ}C$

The thermal conductivity value of  $401 W/m * K$  stated above is taken from the copper heat pipe material, while the heat pipe length was fixed for preliminary calculations. The cross sectional area value was determined from the diameter value of  $2.59 mm$  in 10 gauge copper wire. The temperature of the component was set to  $35^{\circ}C$  because of the maximum operational temperature of  $40^{\circ}C$  for the internal components.

$$Q = \frac{kA}{L} * (T_h - T_c) \quad (1)$$

$$T_c = T_h - \frac{QL}{kA} \quad (2)$$

Equation (1) was then manipulated to determine the temperature at the end of the heat pipe secured to the central PCM encasement, as seen in Equation (2) above.

With the use of Equation (2), the PCM temperature for each of the components, with the parameters detailed above, were determined and noted in Table 4 – ‘*Determined PCM Temperature per Component*’.

Table 4. Determined PCM Temperature per Component

Component	Total Heat Output [W]	Determined PCM Temperature [ $^{\circ}C$ ]
CMOS	0.38	33.22
OV14810 CMOS	0.64	31.95
SeekThermal	0.28	33.67
IR Temp Sensor	0.08	34.61
LSM9DS0	0.04	34.83
Sun Sensor	1.50	27.89
USRP + GPS + Antenna	3.00	20.77
Power Amplifier	7.00	1.81
Arduino Mega	5.00	11.29
BeagleBone Black	22.01	-69.37

### 2.2.1 Phase 1 – Average Temperature of PCM

The first phase of calculations will determine the average temperature of the centralized PCM encasement by utilizing the component data provided in Table 4, as well as the fixed parameters detailed in Table 3. With the total heat output being ~40 Watts, it was determined that the average temperature of the PCM with all the components generating heat is  $16.07^{\circ}C$ .

### 2.2.2 Phase 2 – Heat Pipe Length Variations

The three components with the largest heat generation were selected to determine the thermal effect when changing the heat pipe length. The parameters selected for the second phase of preliminary calculations can be found in Table 5 below.

Table 5. Fixed Parameters in Phase 2

Parameter	Value	Units
Thermal Conductivity [ $k$ ]	401	$W/m * K$
Cross-Sectional Area [ $A$ ]	0.053	$cm^2$
Heat Pipe Length [ $L$ ]	2	$cm$
Component Temperature [ $T_h$ ]	35	$^{\circ}C$

The effect of doubling the heat pipe length for the BeagleBone Black, power amplifier and Arduino Mega can be found in Table 6 below.

Table 6. Length Variation Effect on Component Temperature

Component	Total Heat Output [W]	Determined PCM Temperature [ $^{\circ}C$ ]
Arduino Mega	5.00	-12.42
Power Amplifier	7.00	-31.39
BeagleBone Black	22.01	-173.75

As seen in Table 6, it was determined that doubling the length of the heat pipe resulted in a lower average temperature for the central PCM system. To be able to properly design a centralized PCM thermal control system, the final design will have varying heat pipe lengths for each component, which will be determined in a future calculation phase.

### 2.3 PCM Selection

To effectively combat the ~40 Watt heat output of the internal components, it was determined that a material with a ~45°C phase change temperature is effective at regulating the large temperature variations. The PCM types being considered for use in the NEESat internal thermal control subsystem are Organic and Inorganic, as seen in Figure 1 above. The NEESat internal thermal control research conducted will focus on organic PCMs due to their environmental and financial benefits, but will also include inorganics because of their high heat of fusion and availability [3].

PCMs contain many important physical and chemical properties that allow them to be useful and efficient in thermal energy storage environments. A PCM requires a high latent heat of fusion per unit mass to be able to store large amounts of latent heat energy in a small amount of material [1]. A high thermal conductivity is necessary to increase the temperature gradient required for charging the material to a phase change temperature to aid in the capturing of latent heat [1]. With a larger density value, a small volume of material will reduce necessary space requirements for the method of centralized PCM encapsulation. In comparison to inorganics, organic materials have a moderate thermal energy storage density, which requires a larger surface area to combat the effect of the lower conductivity. Besides having a melting point in the desired temperature parameters for the application, a PCM should be non-poisonous, non-flammable and non-explosive to minimize the health and safety requirements needed to develop and operate such a system, as well as minimizing the ecological and environmental impacts of its production and use. To ensure a stable system life, the phase change material must have minimal chemical decomposition, as well as an increased thermal stability [1].

Research was conducted to determine commercially available and cost effective PCM materials ~45°C melting, or phase change, temperature. The organic and inorganic PCMs proposed for possible use in the NEESat internal thermal cooling subsystem can be found in Tables 7 – ‘Organic PCMs Proposed for NEESat Application’ and 8 – ‘Inorganic PCMs Proposed for NEESat Application’ seen on the following page..

**Table 7. Organic PCMs Proposed for NEESat Application**

Material	Phase Change Temperature [°C]	Density [kg/m <sup>3</sup> ]	Latent Heat Capacity [kJ/kg]
PureTemp 42*	42	940	218
PureTemp 48*	48	900	230
A43**	43	780	165
A44**	44	805	242
A46**	46	910	155
A48**	48	810	234

\* Material and technical information gathered from Entropy Solutions, LLC

\*\* Material and technical information gathered from PCM Products.

**Table 8. Inorganic PCMs Proposed for NEESat Application**

Material	Phase Change Temperature [°C]	Density [kg/m <sup>3</sup> ]	Latent Heat Capacity [kJ/kg]
S44**	44	1584	100
S46**	46	1587	210

\*\* Material and technical information gathered from PCM Products.

Tables 7 and 8 show a direct comparison between the latent heat capacities of organic and inorganic PCMs. Although the latent heat per mass values vary by ~100 kJ/kg, the value that contributes to the large thermal capacity of inorganic PCMs is the density. The lower material densities of organic materials will require a larger volume, which could be inhibited by the NEESat internal space parameters.

Although extremely beneficial to space and component limited thermal energy storage systems, PCMs experience degradations such as phase segregation and super cooling. Organic phase change materials constantly operate in a melting and freezing cycle without any phase segregation, or congruent melting, they crystallize with little super cooling and they usually share non-corrosive properties [3]. Salt hydrate inorganic PCMs succumb to the problem of phase separation and super cooling, which decreases the temperature at which the material solidifies. [6]. When salt hydrates are melted, multiple other hydrates form. These newly developed hydrates settle out over time and reduce the overall volume available for the storage of latent heat [6]. With the addition of multiple different chemicals and materials to PCMs, such as conductive particles into organic paraffins or nucleating agents in inorganic salt hydrates, these problems could be effectively countered [6].

### 2.4 Proposed Design

The thermal control system for the internal heat generating components of the NEESat will consist of a centralized PCM heat exchange design. The proposed PCM thermal energy storage (TES) design will thermoregulate the electrical components by direct conduction through a heat pipe alternative, as seen in Figure 5 – ‘Central PCM TES System’ below. In this thermal energy storage system, the energy lost from the electronic components during its hot atmospheric orbit is transferred directly into the central PCM, through heat pipes, with the indirect intention of heating the system during its cold atmospheric orbit [2].

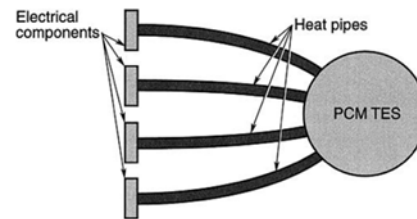


**Figure 5 – Central PCM TES System [2]**

The proposed system design will be composed of PCM encapsulated in a metallic, chemically compatible, container with a direct and secure connection to one end of the heat pipe. The other end of the heat pipe will be securely fastened to the surface of the electrical component, to ensure that connections remain fixed through the vibrations experienced during the CubeSat’s journey to

orbit. The heat pipe will be developed through use of commercially available copper wire, as seen in Figure 6 – ‘NEESat Proposed Copper Wire Heat Pipe’ below, with the final gauge size to be determined for each component through further simulation and testing. Copper was chosen as the heat transfer medium due to its high thermal conductivity of  $\sim 401 \text{ W/m} \cdot \text{K}$ , its low cost and commercial availability.



**Figure 6 – NEESat Proposed Copper Wire Heat Pipe**

Through a series of precise solders, the heat pipe could be securely fastened to the proposed encapsulation sphere of the PCM. One challenge of thermal regulation in space is the limitation to conductive methods of heating and cooling, which increases the difficulty of securing the remaining end of the heat pipe to the components surface. A component friendly method of securing the heat pipe to its respective surface will ensure efficient operation throughout the systems desired mission life.

The preliminary phase calculations seen in section 3.2, above, use the average temperature value of the PCM to determine the average heat pipe length for the system. It is important to note that this phase of calculations does not reflect the heat pipe length of each individual component in the system.

### 3. DISCUSSION

This paper presents an active thermal control system for the internal regulation of CubeSat systems, with specific implementation on the FIU NEESat. The proposed design incorporates a centralized phase change material encasement, previously discussed in section 3.4, which will thermoregulate the 40 Watts of internal heat generated by the components through a series of conductive heat pipes. Section 3.2 details the preliminary phase thermal calculations conducted to begin the determination of the final PCM as well as the parameters necessary to design an efficient system. The PCMs average temperature through the hot atmospheric orbit was determined to be  $16.07 \text{ }^\circ\text{C}$  with the initial parameters set in section 3.2.1. The initial heat pipe length of 1.0 cm was varied in section 3.2.2 to determine the relationship between temperature variations with the length values. It was determined that doubling the heat pipe length from 1.0 to 2.0 cm resulted in a large decrease in the PCMs average temperature. Further research, analysis and development will be conducted towards the final design of the centralized PCM internal thermal control system through use of two simulation software, SolidWorks and ANSYS, as well as laboratory vacuum chamber testing at FIU’s Advanced Materials Engineering Research Institute (AMERI).

### 4. CONCLUSION

The proposed internal thermal control subsystem design offers a cost effective, commercially available and easily adaptable method of thermoregulating a wide range of CubeSat applications. This

report outlines the research, calculations and analysis performed towards the development of an interior cooling system for the FIU NEESat, which will be competing in the 2016-2017 NASA FUNSAT competition. The active thermal control system offers payload and space advantages while thermoregulating the  $\sim 40$  Watts of maximum component heat generated into the system.

The proposed subsystem was designed using the parameters on the existing NEESat structure, the FUNSAT competition standards, the CubeSat standards, as well as the multiple parameters listed in section 3.2. Along with the finalization of the proposed thermal control system design, the individual components must be simulated and tested for their conductive heat generation as well as the determination of the PCM thermal regulating rates.

### 5. ACKNOWLEDGMENTS

The development of the NEESat system is being performed as part of the 2016-2017 FUNSAT competition, which is organized by NASA’s Florida Space Grant Consortium (FSGC). The FSGC provided the financial funding necessary for the NEESat subsystem research to be conducted, as well as the project motivation and competition parameters. The authors also acknowledge the support received from Florida International University’s (FIU) Department of Mechanical and Materials Engineering (MME), as well as the reviewers for their comments. The authors would also like to extended their thanks to the members of FIU’s Near Earth Explorer (NEE) student chapter for the continuation of aerospace research towards competition success and the future development of an aerospace academic program.

### 6. REFERENCES

- [1] A., Sekar, Siddhartha Jain D.N., Govinda K.V., and Arun Kumar S. "Phase Change Materials (PCM) for Thermal Control During Spacecraft Transportation." *International Journal of Mechanical and Industrial Engineering* 3.1 (2013): 1-5. Web.
- [2] Bledjian, L., M.J. Hoover, and M.J. O'Neill. "Phase-Change Materials." (n.d.): 373-403. Web.
- [3] Rathod, Manish K, and Jyotirmay Banerjee. "Thermal Stability of Phase Change Materials Used in Latent Heat Energy Storage Systems: A Review," *Renewable and Sustainable Energy Reviews* 18 (2013): 246-58. Web.
- [4] Hernandez, Sergio, Walter Salas, Cruz Philippe, Elijah Newman, Paul Frosik, and Jonathan De Groot. RoarSAT. Thesis. Florida International University, 2016. N.p.: n.p., n.d. Print.
- [5] Shinde Pradeep, Newman Elijah, Tansel Ibrahim, Tosunoglu Sabri. Design of FIU FUNSAT System: Attitude Control for the 3U CubeSat. FCRAR 2016.
- [6] Lane GA. Solar heat storage: latent heat material, vol. 1, Background and scientific principles. Florida: CRC Press; 1983.

# Autonomous Surface Marker Buoy

Hailey Armstrong, Justin Bryan, Kyle Muir, Juan Rothe

Florida Atlantic University  
777 Glades Rd  
Boca Raton, FL 33431

hsteven9@fau.edu, jbryan2013@fau.edu, kmuir4@fau.edu, jrothe2012@fau.edu

## ABSTRACT

The main objective of this engineering design project is to replace the traditional diving surface marker buoy (SMB) which alerts nearby boaters that a diver is in the area. The traditional surface marker buoy has a tether that can get caught in reefs or other objects which can be dangerous. The design presented in this paper eliminates the use of the traditional tether making it safer for the free-diver. The autonomous surface marker communicates with a diver device wirelessly through radio, travels close to the diver's last known surface location, and keeps this location until a new one is received. A dive-band determines the diver's GPS coordinates when the diver is on the surface and transmits them to the autonomous surface vehicle (ASV). The ASV determines its GPS location and compares it to the diver's location. It then determines its instantaneous heading and compares it to the desired heading to calculate the most efficient way to travel to the diver. The ASV is controlled by sending individual duty cycles to two motor drivers. These motor drivers then send RC signals to their respective thrusters which controls the rotational speed of each thruster individually. This creates varying thrusts which causes forward, backward, and turning movements. After multiple tests, the optimal thruster algorithm was created and the autonomous surface vehicle successfully traveled to the diver's location. The accuracy of the system could be improved upon by purchasing more accurate sensors if given a larger budget.

## Keywords

Surface marker Buoy (SMB), Autonomous surface vehicle (ASV), Electronic speed controllers (ESCs)

## 1. INTRODUCTION

Freediving is a sport/hobby practiced all around the world and is very similar to scuba diving. The difference is that in scuba diving, there is an oxygen tank that allows the diver to breathe underwater which eliminates the need for frequent resurfacing. When free diving, the diver relies on their own skill and physical abilities to hold their breath until they resurface. One additional possibility is that the diver uses a snorkel which eliminates the need for complete resurfacing.

Free diving has become very popular recently, and the industry continues to grow each year due to its connection with many activities such as spearfishing, photography, snorkeling, etc. The ocean covers most the earth's surface and free divers are not the only ones in the ocean, which is a reason why it can be a dangerous sport/hobby to practice. Today, free divers utilize a diving buoy that

is known as a surface marker buoy (SMB). On this buoy, there is a flag or sign that indicates to others that divers are in the area and in some cases a flashing battery powered light [1]. The problem with this type of surface marker is that the buoy is tethered to the diver, meaning that the diver is constantly dragging the marker around, which is not only tedious but dangerous. This tether can become entangled or caught by underwater features which can lead to injury or death. An example of the traditional SMB can be seen below in Figure 1.



Figure 1: Basic Design of Dive Buoy [2]

Recently, there has been a lot of interest in autonomous vehicles for research and recreational purposes. These vehicles are driverless and are capable of maneuvering along a surface or a body of water. This peaked interest is shown in an influx of recent patents and journal articles relating to the subject. These patents include devices capable of utilizing GPS [3] [4] [5] [6] [7] [8] [9] [10] [11] [12], wireless communication devices [13] [14] [15] [16] [5] [7] [11] [17], and position sensors [18] [19] [6] [7] [9] [10] [12]. One useful application for an autonomous vehicle is to combine these components to create an autonomous surface vehicle (ASV) which can track a free diver's movements. This eliminates the need for the dangerous tether while increasing the possible applications.

A simple way to control an ASV with two thrusters is through electric propulsion. This is the norm in small, remotely controlled boats [20]. This allows the motors revolutions per minute (rpm) to be easily adjusted through a pulse width modulated (PWM) signal and a speed controller. This speed controller converts the PWM signal into a pulse width control signal (PWC) that controls the speed and direction of the rotation. With being able to control the

speed and direction of each thruster independently, it allows for the direction of travel to be altered without the use of a rudder.

This report will detail a design that will protect all recreational free divers from the hazards of using the traditional SMB. This new idea, besides providing protection to the diver just like the existing SMB, can maintain two-way communication between the buoy and diver without a physical presence of an attachment, such as a tether, as well as providing the possibility for useful devices to be attached to the platform. This device looks more like a mini pontoon boat than a traditional dive buoy. It can follow the diver around autonomously. The basic breakdown of the system is as follows. The diver will wear a device that will send GPS coordinates through radio frequencies to the buoy every time the diver resurfaces. After the GPS coordinates have been received, the buoy will send a confirmation signal back to the diver's device which will alert the diver it is safe to submerge again. As soon as the buoy receives the diver's position, it will immediately determine the most efficient path to get to the location and begin moving.

### 1.1 Problem Conceptualization and Definition

The traditional SMB is tethered to the diver, and this creates a problem with safety. The diver can easily become entangled on an object such as a reef or a boat propeller. This could cause devastating results such as serious injury or death. The design presented in this report is to be operated under minimal wind, wave, and cloud cover. This will prevent tipping of the ASV as well as quick and accurate GPS location reception.

The problem is to replace the traditional SMB with an autonomous surface marker that can efficiently travel to a free diver's surface locations and maintain the most recent position while the diver is submerged. This diver-buoy system will not be physically connected which will increase the safety of the system.

### 1.2 Project Objectives and Goals

The overall goal of this design project is to move a diver's flag safely and efficiently to a diver's most recent surface location and hold this position until the diver resurfaces.

The objectives of this project are: The device should sense its own GPS location and be able to distinguish its relative heading when compared to another GPS coordinate. The device should be able to efficiently move from its original position to an established GPS coordinate (with an error of 15 feet). The device should be able to maintain the last known diver surface position while the diver is underwater as well as obtain and move to the diver's newest surface location once the diver surfaces.

## 2. SYSTEMS ENGINEERING

### 2.1 Concept of Operations

#### 2.1.1 Level 1

For the first level of success, the ASV can rotate and face a preprogrammed GPS location. This is done by the ASV sensing its own location and determining its bearing by comparing its location against the preprogrammed location. This bearing is then compared to its instantaneous heading to determine its relative heading. This relative heading is the error associated with the system. The desired error is a range between  $-15^\circ$  and  $15^\circ$ . If the relative heading is greater than  $15^\circ$ , the ASV must rotate counter-clockwise to right itself. This is done by putting the left thruster in reverse and the right thruster in forward. If the error is less than  $-15^\circ$ , the ASV must rotate clock-wise to right itself. This is done by putting the left

thruster in forward and the right thruster in reverse. The visual representation of this program flow is shown in Figure 2 below.

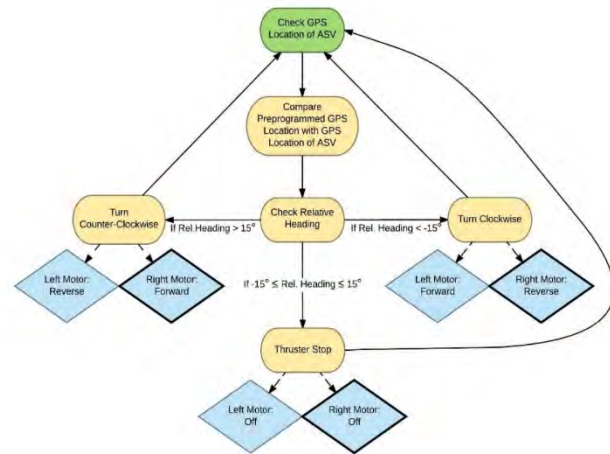
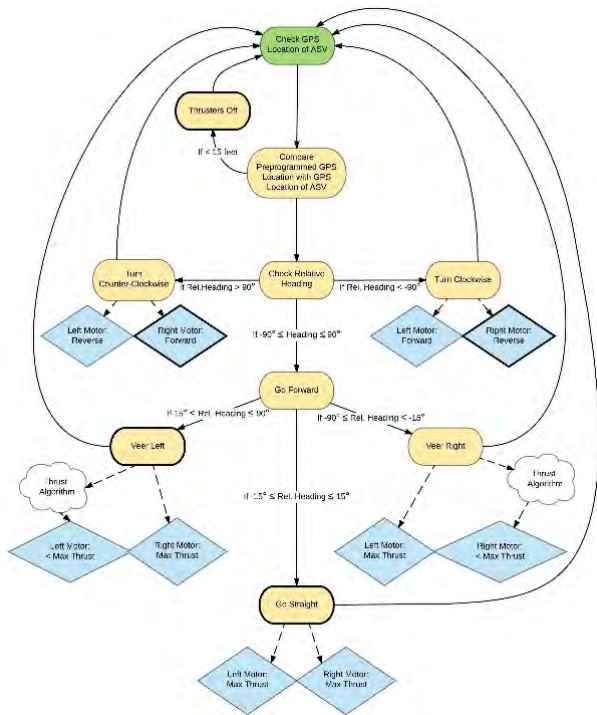


Figure 2: Level 1 Pseudocode

#### 2.1.2 Level 2

In the second level of success, the ASV must perform level 1 if the relative heading is greater than  $90^\circ$  or less than  $-90^\circ$ , but also must move towards the preprogrammed GPS location if the error does not fall within this range. If the error is within the range of  $-90^\circ$  and  $90^\circ$ , the ASV begins to move forward. This is done by turning the primary thruster, the most lateral thruster to the center of desired rotation, up to max forward thrust and turning the secondary thruster, the most medial thruster to the center of desired rotation, to a lesser forward thrust. The water drag on the secondary thruster causes the ASV to veer in that direction. The way that the secondary thruster's speed changes to cause the proper turning is explained later in this report. If the error is within the range of  $-15^\circ$  to  $15^\circ$ , the secondary thruster's speed matches the speed of the primary thruster which causes the boat to follow a straight path. When the ASV comes within 15 feet of the desired location, the thrusters will shut off. A visual representation of these processes is shown in Figure 3 below.



**Figure 3: Level 2 Pseudocode**

### 2.1.3 Level 3 - ASV

In level 3, the ASV follows the same mode of travel, but the system does not utilize a preprogrammed GPS coordinate. A diver device is used to send GPS coordinates to the ASV. Each time the ASV receives the diver's new GPS coordinates, they replace the old diver coordinates and the ASV sends a confirmation to the diver device. A visual representation of the level 3 program flow is shown in Figure 4 below.

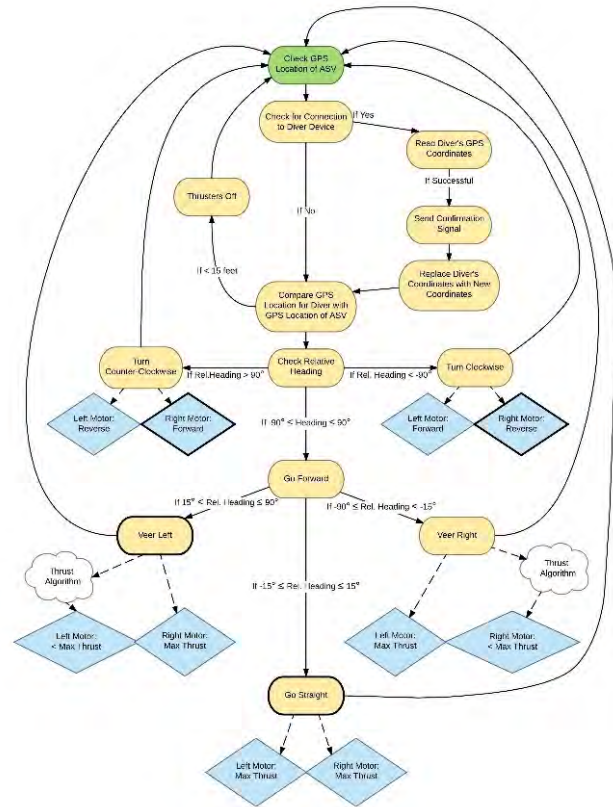


**Figure 4: Level 3 ASV Pseudocode**

### 2.1.4 Level 3 – Dive-band

In level 3, the dive-band is used to tell the ASV the diver's location. The dive-band's program flow is shown in Figure 5 below. The dive-band will sense the diver's depth using a barometer. If the depth is greater than six inches, the critical depth for receiving GPS coordinates, the dive-band will notify the diver through 4 short pulses. Once the diver resurfaces, the dive-band will collect the diver's GPS coordinates and send them to the ASV through radio. If the confirmation signal, described in section 2.1.3 above, is received, the dive-band will notify the diver using 2 short pulses. But if the confirmation is not received within 8 seconds, signifying a malfunction, the dive-band will get the diver's attention by vibrating for 3 seconds.

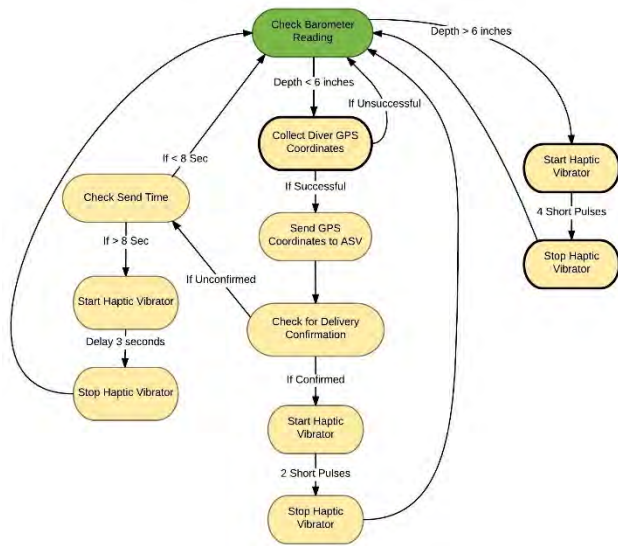


**Figure 5: Level 3 Dive-Band Pseudocode**

## 2.2 Functional Analysis

This design will use GPS, a compass, and radio in order supply the information necessary for an ASV to effectively follow a free diver around. This will be done by the diver wearing a device with a GPS sensor, barometer, and radio to transmit the collected GPS coordinates for the diver's location. These received coordinates will then be compared to the ASV's coordinates to determine a relative heading. The programming within the ASV will then determine the most efficient way to travel to the desired end location. Once the vehicle comes within 15 feet of the diver's most recent location, it will maintain this position until the diver resurfaces.

The barometer on the diver's device will keep the GPS and radio from trying to transmit and collect data while the diver is submerged. It will also notify the diver with a haptic vibrator when the diver has reached a depth where the GPS and radio will be disabled

## 2.3 Detailed Final Design Description

### 2.3.1 Autonomous Surface Vehicle (ASV)

The chosen design for the ASV, seen below in Figure 6, was modeled off a pontoon boat. This decision was made so that when traveling through the water, the ASV would be able to keep its heading. The two pontoons are made of PVC pipe, 3D printed nose cones, and plastic end caps. The plate is made of 6061 aluminum and held on by 3D printed brackets and stainless steel bolts. The waterproof box is made of plastic with a rubber ring. This box houses the batteries, ESCs, the electronics, and the waterproof switch. The electronics are held in place by a 3D printed plate that the PCB clips into and include an Arduino Mega, compass, GPS module, XBEE radio, and two 11.1 volt 6200 mAh batteries. The thrusters, used for propulsion, are attached to the rear end of the pontoons by 3D printed brackets that form fit the pontoon curvature.

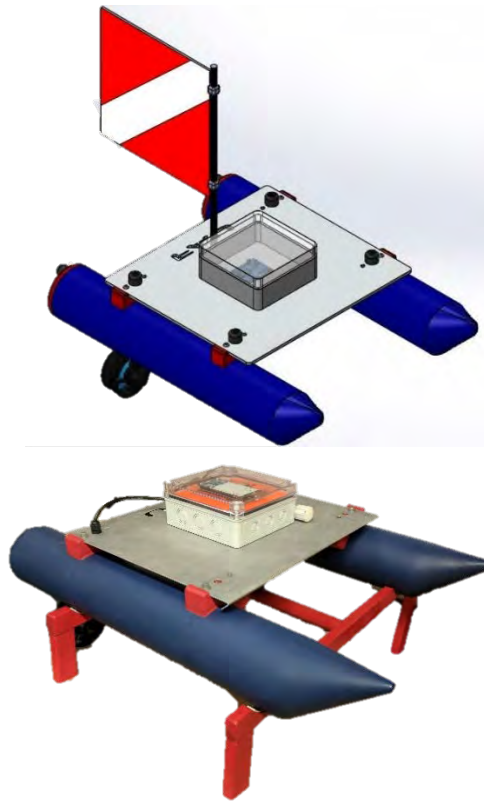


**Figure 6: Final ASV Design**

### 2.3.2 Dive-band

The chosen design for the dive-band includes a waterproof box, a 3D printed mount compatible with GoPro accessories, an Arduino Mega, GPS module, XBEE radio, barometer, haptic vibrator, and two 3.7 volt 500 mAh batteries. These electronics are held in place by a 3D printed mount designed to fit snugly into the waterproof container. This final design is shown in Figure 7 below.



**Figure 7: Final Dive-band Assembly**

The waterproof box protects all the electronics from water damage, but is also clear so the GPS module can easily gather the dive-band's location. The batteries are connected in series to make a nominal voltage of 7.4 volts which supplies the components with the necessary power for operation. The barometer senses the internal pressure of the container which relates to the depth of the armband. This allows the armband to alert the diver when they reach a critical depth by activating the haptic vibrator. The XBEE radio is used to send the dive-band's location to the ASV and receive a confirmation signal.

## 2.4 Requirements and Constraints

### 2.4.1 Requirements

The requirements for the Engineering Design course are that the senior design projects have at least two actuators and at least two sensors. This project has three actuators (the two thrusters, and the haptic vibrator) and six sensors (the two Radio XBee sensors, the two GPS sensors, the digital compass, the barometer).

#### 2.4.1.1 Level 1

The ASV can sense its own GPS location and rotate itself clockwise or counter-clockwise to face a preprogrammed GPS coordinate by comparing its compass heading with the desired heading.

#### 2.4.1.2 Level 2

In addition to the level 1 requirements, the ASV will can travel from its original location to the preprogrammed GPS coordinate efficiently. Once at this position, the ASV can adequately compensate for external forces (wind, current, etc.) to maintain this position.

#### 2.4.1.3 Level 3

In addition to the level 2 requirements, the ASV's desired GPS coordinates will be updated with the diver's new position while the diver is on the surface of the water.

### 2.4.2 Constraints

#### 2.4.2.1 Weather, Wind and Current

The operation of this project will occur in winds under 4 mph and in seas with minimal waves/current as well as on a clear day where the GPS coordinates are easily collected.

#### 2.4.2.2 Budget

The total cost paid for by the school will not exceed \$500.

#### 2.4.2.3 Operation Time between Charges

The design will not be used for periods lasting more than 1 hour without recharging fully. The dive-band will die before the ASV.

### 2.4.3 Assumptions

#### 2.4.3.1 Underwater Travel Distance

Diver will not travel a distance that exceeds the radio's range before resurfacing.

#### 2.4.3.2 Resurfacing Procedure

Diver will follow safety protocols when resurfacing (i.e. Rising out of water with arm pointed at the sky.) which will help with collecting new GPS coordinates as well as reestablishing connection with the ASV.

#### 2.4.3.3 Line of Sight and Obstructions

There will be no other objects in the water that could impact the ASV or obstruct the line of sight between the ASV and diver.

#### 2.4.3.4 Water depth

The water depth that the ASV is operating in is deep enough to where it will not run aground.

## 2.5 Management Plan

### 2.5.1 Machining and Assembly

Both the ASV and dive-band were initially designed in Solidworks. They are both made of parts that were manufactured as well as 3D

printed. All machining and assembly was completed by Kyle Muir and Juan Rothe.

#### 2.5.1.1 ASV Overall Assembly

The overall assembly started with a simple PVC pipe that was shortened to the desired length of twenty-four inches. An aluminum metal sheet was used as the base of the ASV. Nose cones, thruster mounts, plate brackets, and a PCB mount were all 3D printed to precisely fit the unique design dimensions. The thruster mounts, plate brackets, and nose cones were attached to the PVC pipe with plastic epoxy glue in the interior and on the exterior. This process was done carefully to prevent any possible leaks. The epoxy was later sanded various times with different grades of sand paper to achieve a smooth finish that makes the pontoon look like a single piece. These sealed pontoons were then painted and protected with multiple matte finish coats.

#### 2.5.1.2 Dive-Band Overall Assembly

The overall assembly of the dive-band was done using a 3D printed GoPro mount and acquired waterproof box. Using the supplied head strap GoPro mount, the printed mount easily attached to it using a screw. The printed GoPro mount was attached to the waterproof box using epoxy. The overall dive-band assembly is light and is easily worn on the divers head.

### 2.5.2 Electrical Design

Hailey Armstrong and Justin Bryan did the electrical design of the system. Juan Rothe designed the printed circuit board. Help was received from the electronics lab personnel, John Kielbasa, Ed Henderson and Adam Prey, whenever questions about problems that could not be solved arose.

#### 2.5.2.1 Wiring Diagrams

##### 2.5.2.1.1 ASV

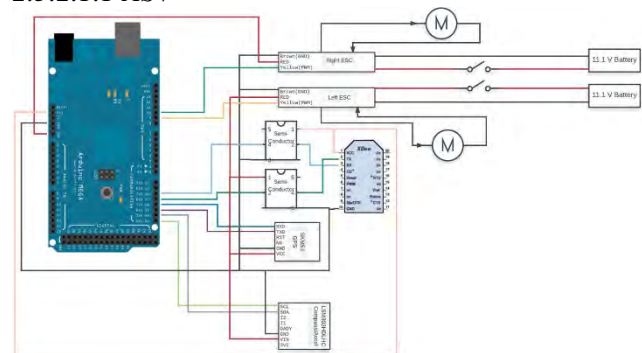
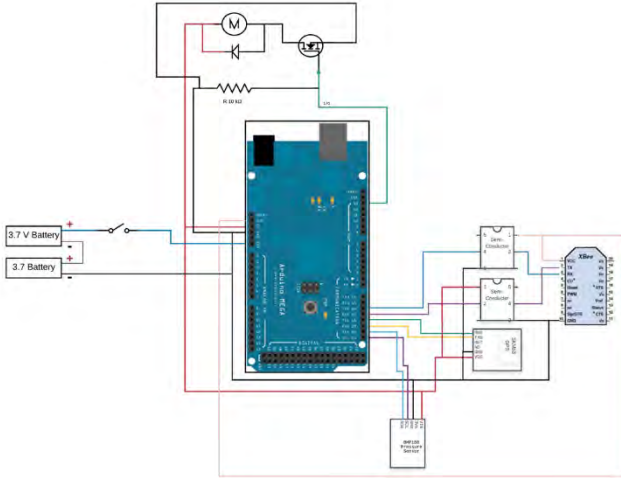


Figure 8: ASV Wiring Diagram

##### 2.5.2.1.2 Dive-Band



**Figure 9: Dive-band Wiring Diagram**

### 2.5.2.2 Printed Circuit Board (PCB)

Once the final wiring diagram was completed and several tests were performed in the engineering west pool, the board schematics were initiated. Both the ASV and dive-band PCBs were created using the EAGLE CAD software. The boards were milled out of a copper plate in FAU's Engineering East lab. Both PCBs are single layer boards. In the PCB layout, every component has its designated position and solder points. With the printed circuit board, the team obtained a fully functional and professional looking product.

## 3. Design and Engineering

### 3.1 Calculation of Bearing and Distance Between Two GPS Coordinates

#### 3.1.1 Bearing

The bearing is the angle relating to the direction of travel relative to north

$$\theta = \text{atan2}(\sin(\Delta\beta)\cos(\varphi_2), \cos(\varphi_1)\sin(\varphi_2) - \sin(\varphi_1)\cos(\varphi_2)\cos(\Delta\beta))$$

Where:

$\theta$  = the bearing angle between start and end  
 $\varphi_1$  and  $\varphi_2$  = the start and end latitudes, respectively  
 $\Delta\beta$  = the difference in longitude

#### 3.1.2 Distance

$$a = \sin^2\left(\frac{\Delta\varphi}{2}\right) + \cos(\varphi_1)\cos(\varphi_2)\sin^2\left(\frac{\Delta\beta}{2}\right)$$

$$c = 2 * \text{atan2}(\sqrt{a}, \sqrt{1-a})$$

$$d = Rc$$

Where:

$\Delta\varphi$  = the difference in latitudes  
 $R$  = the radius of the earth (6,371 km)  
 $d$  = the distance between the start and end

## 3.2 Gain Calculations

### 3.2.1 Stationary Gain

The stationary gain is the difference between the maximum desired duty cycle and the duty cycle necessary for no thruster activity divided by the maximum error possible. This is used to control the forward and reverse thrust of the primary and secondary thrusters, respectively.

$$K_s = \frac{\text{ThrusterFull} - \text{ThrusterStop}}{180}$$

Where:

$K_s$  = the stationary gain

ThrusterFull = the maximum desired duty cycle for the ASV (optimal 1650 microsec)

ThrusterStop = the duty cycle for no thruster activation (1500 microsec)

### 3.2.2 Moving Gain

The moving is the proportion between the difference in the duty cycles listed above and the angle at which the secondary thruster should begin assisting in the forward travel of the ASV. This is used to control the forward thrust of the secondary thruster.

$$K_m = \frac{\text{ThrusterFull} - \text{ThrusterStop}}{\text{minAngle}}$$

Where:

$K_m$  = the moving gain

minAngle = the angle at which secondary thruster is desired to activate

### 3.2.3 Distance Gain

The distance gain is used for controlling the thrusts of the primary and secondary thrusters as they approach the end location. This also assists with "feathering the clutch" if the ASV begins to drift away from the desired location. It will slowly increase the thrusts until the ASV no longer moves away from the desired position. This helps the ASV oppose the effect of currents and steady winds.

$$K_d = 1 - \left( \frac{1}{1 + (100000e^{-0.9d})} \right)$$

Where:

$K_d$  = the distance gain

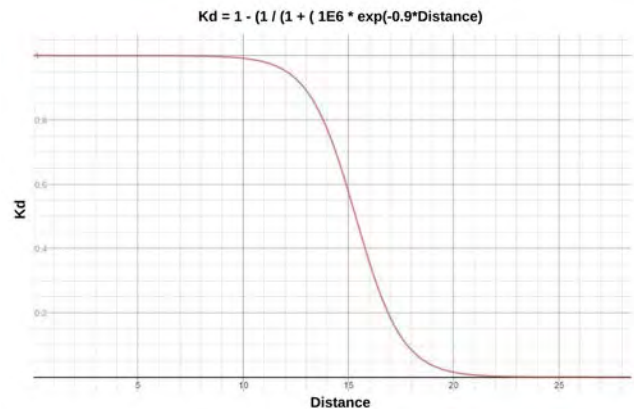


**Figure 10: Distance Gain**

### 3.3 Thruster Control

The autonomous movement of the ASV is obtained through a proportional gain error based controller. The calculations to obtain the gains are listed in section 3.2 above. In this controller design, the thruster that provides the most forward thrust is known as the primary thruster and the other thruster is known as the secondary thruster. These labels switch between thrusters based on the heading and bearing as the ASV travels through the water. If clockwise rotation is needed to reduce the error, the left thruster is the primary and the right is secondary. The opposite is true if counter-clockwise rotation is necessary.

As the ASV approaches the desired end location, the distance gain lowers the duty cycles until the thrusters are turned off. This prevents the ASV from colliding with the diver and assists in opposing outside forces such as currents and winds when trying to maintain its location.

#### 3.3.1 Error

$$error = |bearing - heading|$$

$$\text{if } error > 180 \text{ then } error = error - 180$$

Where:

error = the error associated with the system

#### 3.3.2 Stationary Rotation ( $error > maxAngle$ )

The maxAngle is the angle at which the ASV is to switch between stationary rotation and turning while moving forward. While the error is greater than this maxAngle, the ASV will rotate in place by having one thruster, the primary, provide forward thrust and the other, the secondary thruster, provide a reverse thrust.

##### 3.3.2.1 Primary Thruster

$$Signal = ThrusterStop + (1 - Kd)(Ks)(error)$$

Where:

Signal = the duty cycle sent to the electronic speed controller (ESC)

##### 3.3.2.2 Secondary Thruster

$$Signal = ThrusterStop - (1 - Kd)(Ks)(error)$$

#### 3.3.3 Moving ( $error < maxAngle$ )

Once the error is less than the maxAngle, the ASV will continue turning but will begin moving forward.

##### 3.3.3.1 Error $> minAngle$

The minAngle is the angle at which the secondary thruster will begin providing forward thrust. While the error is greater than this minAngle, the secondary thruster will be turned off and all forward movement and rotation will be provided by the primary thruster and the drag on the secondary thruster.

##### 3.3.3.1.1 Primary Thruster

$$Signal = ThrusterFull - Kd(ThrusterFull - ThrusterStop)$$

##### 3.3.3.1.2 Secondary Thruster

$$Signal = ThrusterStop$$

##### 3.3.3.2 Error $< minAngle$

When the error becomes less than the min Angle, the secondary thruster will begin providing a forward thrust. This will slow the ASV's turning which will prevent overshoot and oscillation during travel. As the error approaches zero, the secondary thruster's thrust will approach that of the primary thruster. This way, the ASV will travel straight.

##### 3.3.3.2.1 Primary Thruster

$$Signal = ThrusterFull - Kd(ThrusterFull - ThrusterStop)$$

##### 3.3.3.2.2 Secondary Thruster

$$Signal = Signal_{primary} + (1 - Kd)(Km)(error)$$

Where:

Signal<sub>primary</sub> = the duty cycle sent to the primary thruster's ESC

### 3.4 Primary and Secondary Thruster Selection

#### 3.4.1 Heading $>$ Bearing

##### 3.4.1.1 Error $> 0$

If the heading is greater than the bearing and the error is greater than zero, then the ASV must move counter-clockwise to reduce the error. This makes the right thruster the primary thruster and the left the secondary.

##### 3.4.1.2 Error $< 0$

If the heading is greater than the bearing and the error is less than zero, the ASV must move clockwise to reduce the error. This means that the left thruster must be the primary thruster and the right must be the secondary.

#### 3.4.2 Heading $<$ Bearing

##### 3.4.2.1 Error $> 0$

If the heading is less than the bearing and the error is positive, the ASV must move clockwise to reduce the error, this means that the left thruster needs to be the primary thruster and the right thruster must be the secondary

##### 3.4.2.2 Error $< 0$

If the heading is less than the bearing and the error is negative, the ASV must move counter-clockwise to reduce the error. To achieve this the right thruster must be the primary, and the left thruster must be the secondary.

## 4. Testing and Evaluation

### 4.1 Individual System, Subsystem, Component Testing

Each individual component, such as each sensor, was tested individually before integrating multiple components together. All systems passed in this level of testing for both the ASV and dive-band.

### 4.2 Systems Integration Testing

After individual testing stages passed, multiple combinations of components were made and tested as integrated systems. All system integrations for both the ASV and dive-band passed its testing.

### 4.3 System Evaluation

#### 4.3.1 Flotation Without Movement

Weight testing was done on the ASV to determine the critical payload while the ASV is not moving. The waterline was measured with different weights and the results can be seen below in Figure 11. The critical weight was found to be 10 lbs. At this weight, the waterline was right at the watertight connectors that the thruster wires run through.

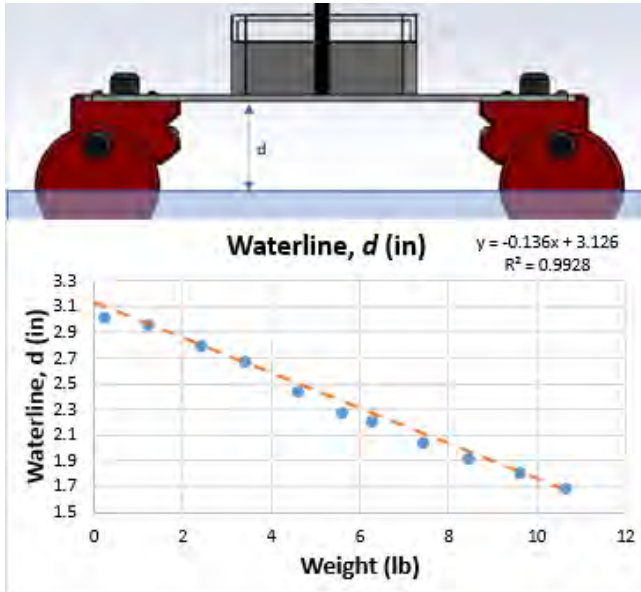


Figure 11: Waterline Weight Test

#### 4.3.2 Level 1

##### 4.3.2.1 Overshoot

The overshoot was measured with different weights and different release angles to determine the optimal speed. The overshoot is represented by  $\Phi$  in Figure 12 below and the desired turn angle is represented as  $\theta$ . The results from the overshoot tests are shown in Figure 13, Figure 14, and Figure 15.

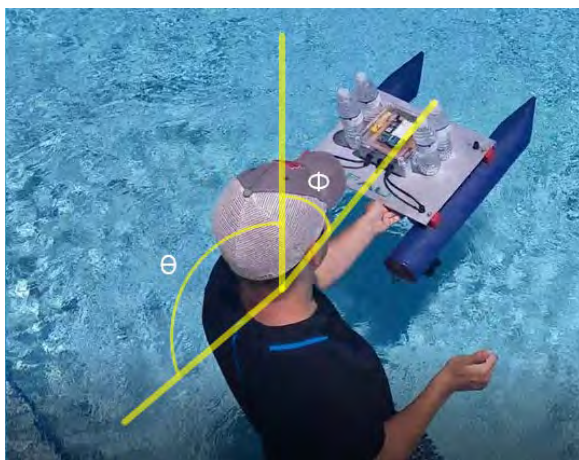


Figure 12: Overshoot Example

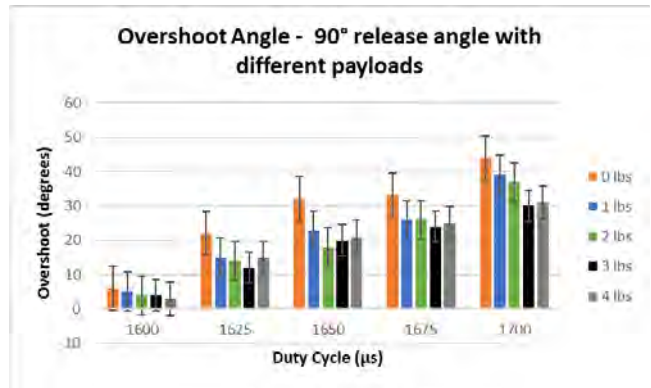


Figure 13: Overshoot with 90° Release Angle

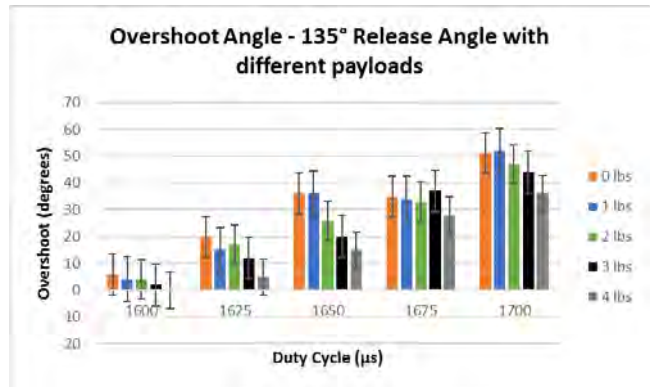


Figure 14: Overshoot with 135° Release Angle

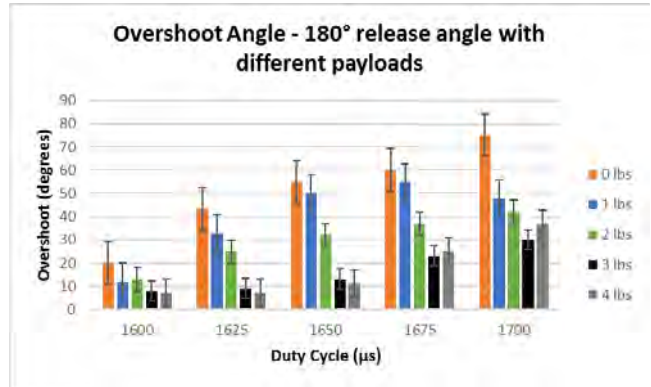


Figure 15: Overshoot with 180° Release Angle

##### 4.3.2.2 Correction time

The time to correct the error (in degrees) was also measured at different weights and different release angles. Those results are in the figures below.

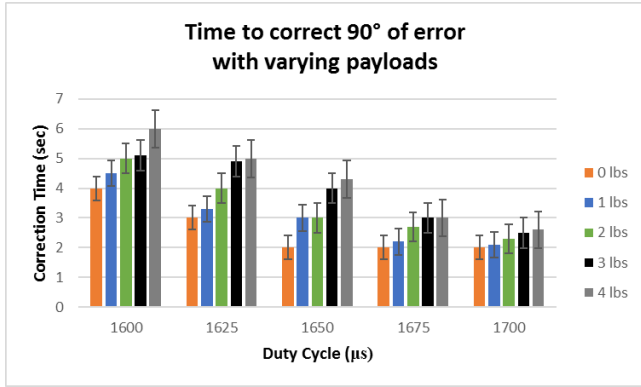


Figure 16: Correction Time - 90° Error

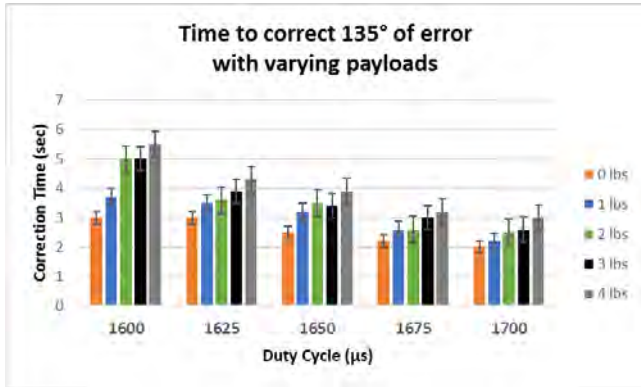


Figure 17: Correction Time - 135° Error

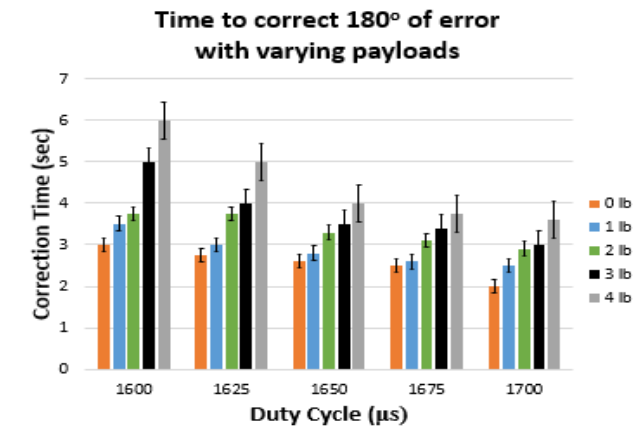


Figure 18: Correction Time - 180° Error

### 4.3.3 Level 2

#### 4.3.3.1 Desired Position vs. Actual Position



Figure 19: Position Example

To measure the accuracy in the ASV's end location, the average distance between the preprogrammed GPS location and the end location of the ASV was found. The ASV on average ended within 9 feet of the desired GPS location. This is due to the GPS inaccuracies that cause the ASV to think it's further away from the diver than it actually is. An example can be seen above in Figure 19 above.

#### 4.3.3.2 Maximum Speed with Different Payloads

The maximum speed was found with different payloads by dividing the distance traveled, in this case 25 ft, by the time (sec). Below in Figure 20 are the results.

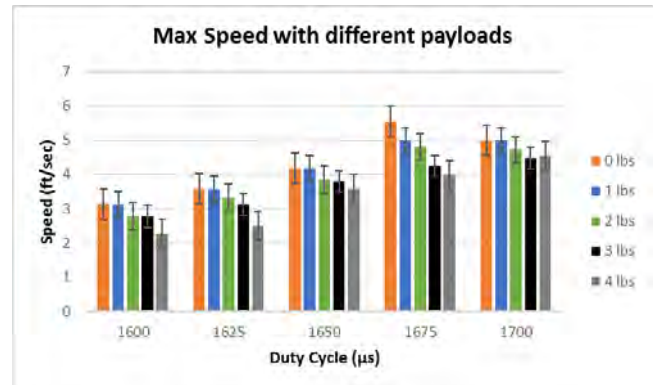


Figure 20: Maximum Speed with Different Payloads

### 4.3.4 Level 3

#### 4.3.4.1 Confirmation Time

To determine how long it took to send and receive a message between the two devices, an Arduino code was written. It was determined that the time ranged from 12 to 56 milliseconds but averaged at 44 seconds.

#### 4.3.4.2 User Survey

A survey was created to determine user satisfaction. The survey is displayed in Figure 21.

**Bob-N-Around Survey**

On a scale of 1 to 10:

How comfortable is the dive band?  
1 2 3 4 5 6 7 8 9 10

How strong is the vibration intensity?  
1 2 3 4 5 6 7 8 9 10

How likely are you to use this product?  
1 2 3 4 5 6 7 8 9 10

How satisfied were you with the outcome?  
1 2 3 4 5 6 7 8 9 10

**Figure 21: User Survey**

Twelve people were given the survey and here are the following averages:

How comfortable is the dive band? – 8.2

How strong is the vibration intensity? – 7

How likely are you to use this product? – 9.5

How satisfied were you with the outcome? - 9

## 5. REFERENCES

- [1] J. F. Hudson, "Lighted Dive Buoy". United States Patent US2011006534A1, 17 March 2011.
- [2] "Dolphin Scuba," [Online]. Available: <http://media.dolphinscuba.com/images/category/FL.jpg>. [Accessed 29 November 2016].
- [3] M. A. Cardoza, W. A. Adamez, D. M. Tomlinson, S. A. Benedict and M. H. Wolf, "Water drift compensation method and device". United States Patent US12151397, 16 April 2009.
- [4] S. Takashima and Y. Kojima, "Small craft with G.P.S.". United States Patent US6125782A, 3 October 2000.
- [5] N. Mišković and đ. Nad, "Guidance and control of an overactuated autonomous surface platform for diver tracking," *Control & Automation (MED)*, vol. 21st Mediterranean Conference, pp. 1280 - 1285, 2013.
- [6] M. B. Shahid, M. U. Shahzad, S. M. Rameez Bukhari and M. A. Abasi, "Autonomous vehicle using GPS and magnetometer with HMI on LabVIEW," *Intelligent Robot Systems (ACIRS)*, Vols. Asia-Pacific Conference, pp. 163 - 167, 2016.
- [7] P. Prempraneerach, M. Janthong, T. Klanthip, S. Boonyarak, C. Choosui, K. Phothongkum, S. Timpitak and P. Kuvanit, "Autonomous way-point tracking navigation of surveying surface vessel with real-time positioning system," *Computer Science and Engineering Conference (ICSEC)*, 2015.
- [8] "ERON: A flexible autonomous surface vessel," *Control and Automation (MED)*, vol. 24th Mediterranean Conference, pp. 71 - 76, 2016.
- [9] E. Iscar and M. Johnson-Roberson, "Autonomous surface vehicle 3D seafloor reconstruction from monocular images and sonar data," *OCEANS'15 MTS/IEEE Washington*, 2015.
- [10] Z. Yu, X. Bao and K. Nonami, "Journal of System Design and Dynamics," *Special Issue on The Twelfth Asia Pacific Vibration*, vol. 2, no. 1, pp. 389-400, 2008.
- [11] R. Bachnak, C. Steidley, M. Mendez, J. Esparza and D. Davis, "Real-Time Control of a Remotely Operated Vessel," *5th WSEAS Int. Conf. on Signal Processing, Robotics and Automation*, pp. 188-194, 2006.
- [12] N. Sakagami and Y. Terao, "Development of a measurement and autonomous control system for wave-powered boats," *OCEANS*, 2012.
- [13] G. W. Buckley, V. V. Divljakovic, P. K. Gaynor, J. C. Ehlers and D. E. Clarkson, "Control system for a marine vessel". United States Patent US09528144, 14 August 2001.
- [14] K. H. Wilcoxon, "Self-propelled remotely controlled buoy". United States Patent US2941492A, 21 June 1960.
- [15] M. Imran, "Self-propelled buoy for monitoring underwater objects". United States Patent US20120063262A1, 15 March 2012.
- [16] P. Kilbourn and R. Dane, "Unmanned ocean vehicle". United States Patent US20070051292A1, 30 July 2007.
- [17] K. J. DeMarco, M. E. West and A. M. Howard, "Sonar-Based Detection and Tracking of a Diver for Underwater Human-Robot Interaction Scenarios," *Systems, Man, and Cybernetics (SMC)*, pp. 2378 - 2383, 2013.
- [18] M. Suemori and H. Kaji, "Marine vessel maneuvering supporting apparatus, marine vessel including the marine vessel maneuvering supporting apparatus, and marine vessel maneuvering supporting method". United States Patent US11013567, 25 January 2007.
- [19] P. G. Trepagnier, J. E. Nagel, M. T. Dooner, M. T. Dewenter, N. M. Traft, S. Drakunov, P. Kinney and A. Lee, "Control and systems for autonomously driven vehicles". United States Patent US8126642B2, 28 February 2012.
- [20] 和.原.久.森.茂.中.美.寺.尚.西.純.松浦, "Electric propulsion system for small vessels". Japan Patent JP 5518383B2, 11 June 2014.

# BudE: Assistant to Parent a Child

Erick Bu Pons, Mario Aranega, Melissa Morris, Sabri Tosunoglu

Department of Mechanical and Materials Engineering  
Florida International University  
Miami, Florida 33174

ebupo001@fiu.edu, maran052@fiu.edu, mmorr009@fiu.edu, tosun@fiu.edu

## ABSTRACT

This paper proposes a robot to assist in the care of young children. Although a very challenging task, it is anticipated that the initial work presented here may be developed further to offer a viable and practical solution in the future. In the current presentation, the concept is introduced and the development and construction of the first prototype is reviewed.

## 1. INTRODUCTION

At some point, every family has members that cannot care for themselves. In an ever faster-paced society, caregivers and family members can often find themselves caught between keeping up with the world or caring for their loved ones. This work outlines the creation of an interactive robotic device that will not replace the caregiver, but will assist in the caring. The platform will be able to monitor the care recipient and alert the caregiver of an immediate hazard. Although the application of this platform can be suitable for the care of the elderly, the convalescent, and the physically/mentally challenged, we will concentrate our attention into care of very young children.

The robot is to be designed with three goals in mind:

1. Complete a minute-long song and dance. The song is to be played through the speaker attached and have motion components in order to look as though it was dancing.
2. Program the robot to detect and avoid obstacles with the on-board sensors.
3. Monitor a care recipient.

## 2. GOALS AND MOTIVATION

BudE will be a mobile interactive platform with the objective of assisting new generation parents to keep up with their parenting in times when other things demand attention.

In order to keep BudE moving and responsive to what it will be programmed, the design will have to keep track of a child while the caregiver may be distracted taking a call or preparing food. BudE has to be able to detect smoke, high/low temperatures, or if the child

leaves a designated area. It must alert the caregiver if any of these occur.

### 2.1 Target Market

In the age of cellphones, Youtube and Instagram, parents can't help but to find themselves busier and busier, and babysitting can be expensive. Therefore, let the same technology be of assistance to care for those who matter most. It is very clear that technology is only going to continue to progress and become more efficient and effective in the way that it is used in the daily life, so having technology help parents will benefit them greatly.

### 2.2 Current Market

In the market, there are various products available that can help new parents, however these products have very high costs. Two of these products are Avatar by Ipal and Pepper by Softbank. Currently, the price range for either of this unit varies from 2500 to 3000 dollars depending on the selected features. With all of that money invested, there is still a few things that it will not do nor will detect for the busy parents.



Figure 1. Current Market Robot Child Monitor

Even though Ipal and Pepper seem to have it all, the truth is that the price for such a unit is not something most families could afford. Therefore, we are aiming to create a platform that will have the most important capabilities present in a platform like Ipal or Pepper, but at a fraction of their price. This will be accomplished by making it simpler to develop, manufacture, and easy to transport.

### 3. SYSTEM DESIGN

#### 3.1 Design Concept

Shown in Figure 2, an overall idea was in mind from the very beginning. This was to produce a low cost and effective solution to the problem at hand, all while providing a very densely packaged and robust package. This meant that the robot will meet all of the requirements that are needed and have a long life in the use at home with the child. At the same time, it needed to have an appealing appearance so that a child would not mind having it around or following them.

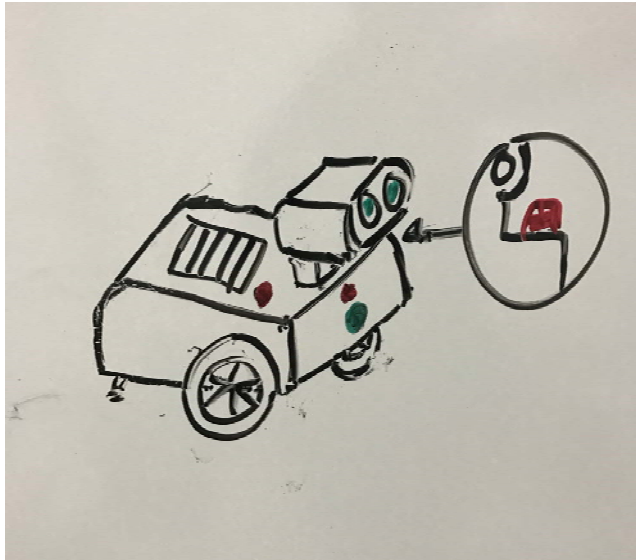


Figure 2. Hand Sketched BudE Concept

#### 3.2 Proposed Solution

Due to time constraints, we chose to concentrate on the most common and dangerous hazards that can occur in a home as well as make sure that the platform is out of the way. Therefore, a selection of sensors for use were considered. This project used a temperature sensor, flame sensor, gas sensor, sonar, and IR sensor.

However, a truly do-it-all platform should also have face recognition, speech recognition/capable, and have the ability to interact with the user. The Pixie Cam could be implemented user tracking and following as a step toward these additional goals. Also, it would need to detect numerous gas/vapor hazards, extreme temperatures, unstable/dangerous objects, and it would need to alert the caretakers if any threat is detected.

Finally, the platform itself should not be a threat. Therefore, it must be capable of detecting objects in its path not to knock them down nor to roll under someone's foot and become itself a trip hazard.

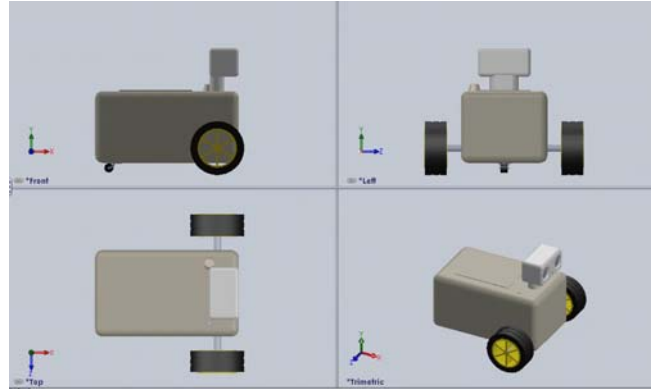


Figure 3. CAD Model of BudE Concept Design

### 4. MANUFACTURING

#### 4.1 Component Selection

There are many different options when considering how to build a prototype robot ranging from a fully custom built frame and individually-selected components or utilizing available kits. Table 1 shows a sampling of kits that offer a distinct variety of products. For this particular application, the Thames and Kosmos Robotic Kit was selected due to the fact that many of the sensors that would have needed to be purchased individually were already included.

Table 1. Various Component Kit Description

	Thames and Kosmos Robotics Kit	Keyestudio Bluetooth Mini Tank Robot	SunFounder Robotics Model Arduino Car Kit
Prototyping Flexibility	Modular building blocks(similar to LEGOS), suitable for any size board	Ample spaces for extra sensors, suitable for Arduino UNO and Mega(w/ Modifications)	Tight in space, suitable for Arduino UNO board
Arduino Compatibility	Not compatible	Compatible	Compatible
Team Cost	Already owned (Christmas Gift)/\$140	\$99.00	\$89.00

Even though this kit contained a programmable board, it was decided to incorporate a fully functioning Arduino board in order to have the full control to modify the robot as needed. This opened up the sensor options as shown in Figure 4.

Most of the names of the sensors shown below were used to make BudE be a fully capable robot that is there to truly take care of a child. These sensors include a HC-SR04 sonar sensor, flame detector, IR obstacle module, MQ-2 gas detector, DS18B20 temperature sensor and a speech recognition module. Combined with the proper calibration and programming, these sensors means that no matter the environment that the child is placed in at home, there will be a monitor for the situation.



Figure 4. Potential Sensors to Be Implemented In Bude

## 4.2 Prototyping

The prototyping stage was divided into three stages. The first stage was to assemble a frame sufficiently large to hold a battery pack, an Arduino Mega 2560, an L293D Motor Shield V1 board, and all the onboard sensors. The final structure had dimensions of 19.1 cm long, 13.3 cm wide, and 10.1 cm tall (not including height due to wheels).

The second stage consisted of preparing the Mega and L293D boards to accept all the wiring from the sensors and the servo motors as well as mating the boards with the structure and finding optimal locations for placing the sensors on the structure. One key aspect of this stage was the modification of the servo motors to allow use of the L293D Motor shield. This had to be done to remove the proprietary control boards included with the Thames and Kosmos kit shown in Figure 5. Another key aspect was the modification of the battery pack to produce an output voltage of 9 volts to meet the recommended operation voltage for an Arduino board of 7 – 12 volts. This is shown in Figure 6.

The third and final stage was to develop, test, and debug Bude's software. This stage was divided into two smaller stages. One sub-stage was to develop and test the program for the individual sensors and later stage was to test the program using the full collection of sensors working together. The sensors are shown in Figure 7. Code from sub-stage one was reused and implemented in the final program.



Figure 5. Servo Motor Controller Modification (Proprietary Control Boards Shown)

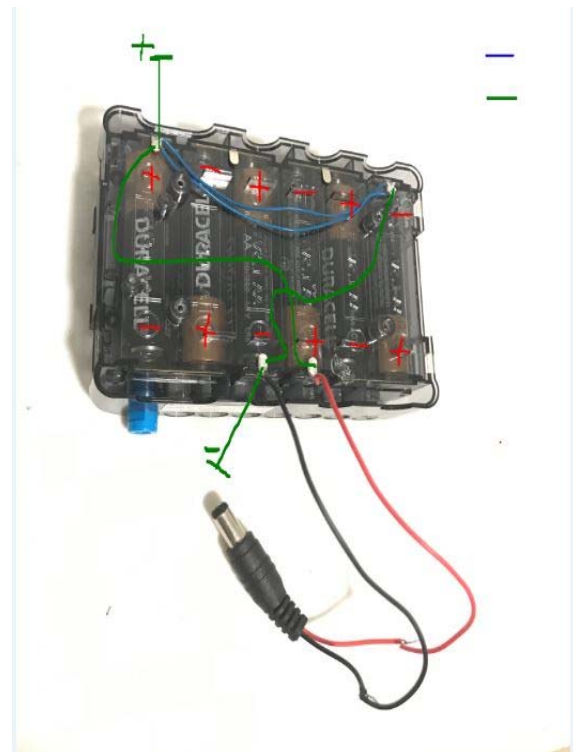
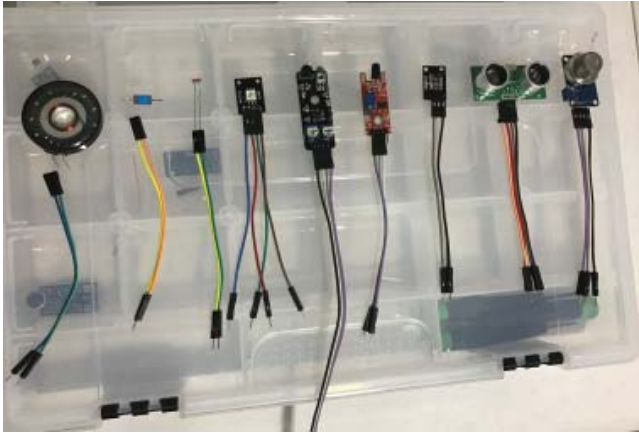


Figure 6. Battery Pack Modification (Old connection shown in Green)



**Figure 7. Array of Sensors for BudE (Left to right: Speaker, tilt switch [not used], Photoresistor, RGB LED, IR Obstacle detection module, Flame Module, DS18B20 Temperature Module, HC-SR04 Sonar, MQ-2 Gas Module)**

### 4.3 Final Product

After research and trial and error, a working robot was produced. BudE sprung to life and met the criteria outlined early in this paper. The camera was not implemented due to time constraints, but all other sensors were fully functional. This made BudE a very capable robot able to provide the protection and surveillance that the child needs when adult eyes are not constantly on them. Figures 8-12 show the completed robot in multiple views showing all aspects.

When tested, BudE was able to turn on an LED light as well as an alarm that can alert the parents if a combustible gas/vapor is detected, if there is a visible fire, if the lighting in a room becomes poor, if temperatures fall below 15 degrees Celsius, or if temperatures rise above 35 degrees Celsius.

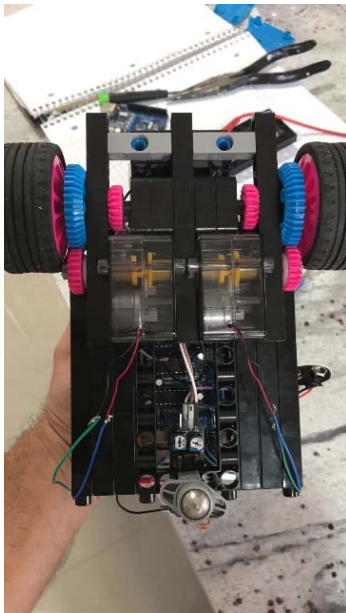


**Figure 8. Underside Showing the Drive-train**

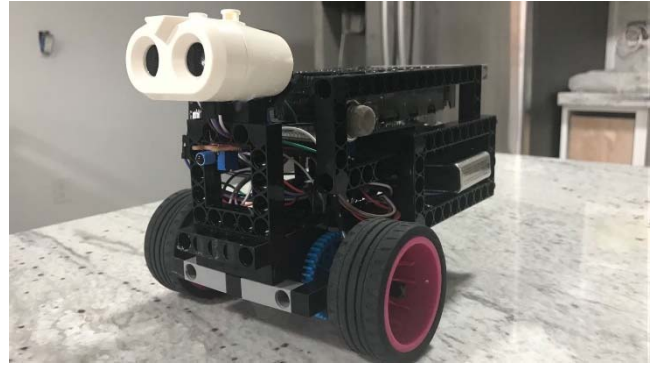


**Figure 9. Right Isometric View of BudE Showing Front Sonar Sensor**



**Figure 10. Right Side View of BudE**

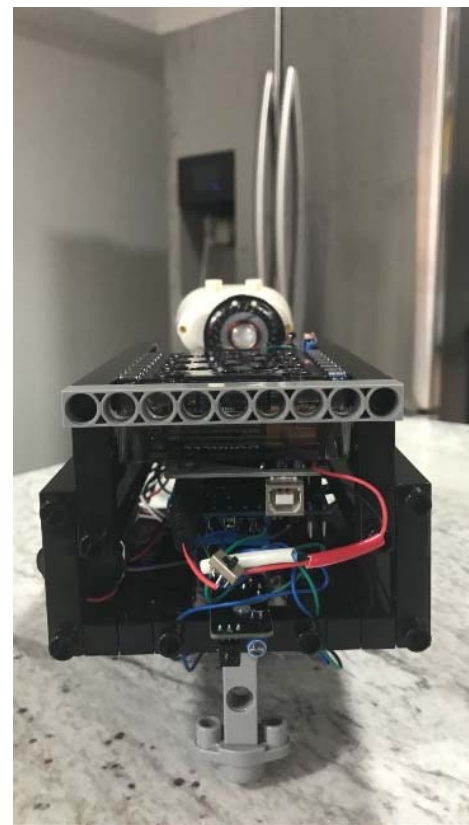


**Figure 11. Rear View of BudE**

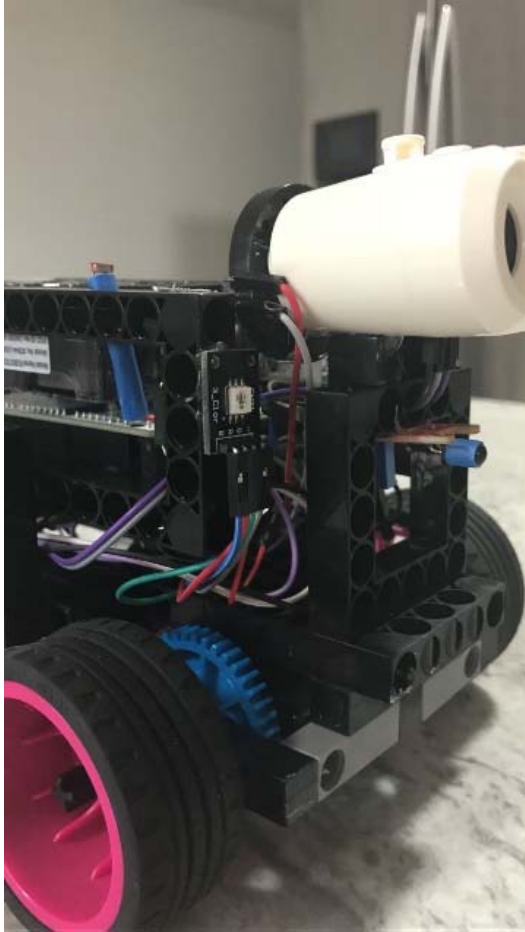


Figure 12. Left Isometric View of BudE

## 5. LESSONS LEARNED

As seen in most new projects, we have experienced several challenges as summarized below.

### 5.1 Coding Issues

As mentioned earlier, the programming of this robot was something that needed to be performed from the very beginning. Arduino tutorials [4] helped assist in this process. This was not a straightforward task since the robot is heavily covered by sensors – as each sensor requires its own specific verbiage and its own dedicated coding for proper use.

From the robot not moving at first to the robot starting to lounge forward and every small milestone in-between, coding ultimately proved to be the greatest challenge of this project.

### 5.2 Debugging

With every serious problem faced in the project, there was a resolution that allowed the project to succeed. For example, the motors would start BudE moving only to stop working in mid-operation. The cause was that the current drawn by the motors was too high, despite the voltage being within range. This caused the L293D Motor Shield V1 board to overheat and shutdown. The solution was to either obtain another L293D chip and solder it on

top of the existing L293D to double the current capacity of the motor shield, or to use motors rated at a lower current. Since the board was not working properly for a motor within the specified voltage range by the manufacturer, our team decided to go with the second option and changed the drive-train to two geared servos rated at 2 volts with a resistance of 10.1 ohms; therefore, requiring only 198 mA. According to the motor shield's manufacturers website [5] the board could provide up to a constant 600 mA and a peak of 1200 mA. BudE was mobile again with torque to spare.

## 6. CONCLUSION AND DISCUSSION

Being able to use new knowledge and implement it into a functioning program did not occur the first time. It took the team several weeks of coding and testing to reach the proper code. There were points that the robot would not respond, other times that it would get stuck in a certain subroutine, and at times that it detected nothing and seemingly did not know how to behave. However, perseverance helped us to develop better code that made the robot perform substantially better.

This project also has benefits that extend outside of the learning experience. At some point, many families will have children and become overwhelmed by the responsibilities. It will only be fair to allow the same technology that keeps us so busy to help with the caring for our loved ones.

This project aimed at the creation of an interactive robotic device (BudE) that would not replace the caregiver, but can assist in the caring. The platform developed in this paper is able to monitor the care recipient's environment and alert the caregiver of an immediate hazard or when the child needs assistance. BudE will be easy to manufacture, easy to transport, and will be accessible to most families.

## 7.1 Future Work and Improvements

Moving forward, it is necessary to work out some of the problems that the current setup has in order to create a more consistent product. There is also the need for further development of the use of the sensors to trigger their full potential. As it stands, some of the sensors are being used for very basic functions and can be put to better use by better analyzing and interpreting the collected data. A different model of smoke detector, the MQ-5 for example, can be used to detect other harmful chemicals in the air.

Not only do the sensors need to be tapped into for better use, but the overall mobility of the robot can be improved. Currently, the drive-train of BudE consist of motors nearly directly driving the individual wheels through limited gears. This decreases efficiency and increases the amount of code. Implementing a better and more refined gear box will allow BudE to move about better and have less of an issue with surrounding obstacles.

## 7. ACKNOWLEDGMENTS

A very big thank you goes out to the wife and child of Erick Bu Pons since the family and the child initially inspired this project. The entire project is formatted and geared towards making families' daily routines simpler and safer. Having a child at a young age today is no easy task and having them be the driving factor in a project is just as labor intensive.

The authors thank the access provided and the resources offered by the Robotics and Automation Laboratory located in the Department of Mechanical and Materials Engineering at Florida International University in Miami. Special thanks are also extended to Scott Jagolinzer who helped the team in every stage of the project in the Robotics and Automation Laboratory.

## 8. REFERENCES

[1] Softbank: Pepper for Biz [Online]. Available:  
<http://www.softbank.jp/en/robot/>

[2] Avatar Mind: iPal A Full Time Companion [Online]. Available: <http://www.avatar-mind.com/partner.action>

[3] Arduino: Arduino MEGA 2560 & Genuino MEGA 2560 [Online]. Available:  
<https://www.arduino.cc/en/Main/arduinoBoardMega2560>

[4] Arduino: Arduino Learning Tree [Online]. Available:  
<https://playground.arduino.cc/Main/AdafruitMotorShield>

[5] AdaFruit: Arduino Motor Shield Manual [Online]. Available: <https://cdn-learn.adafruit.com/downloads/pdf/adafruit-motor-shield.pdf>

# Color Tracking Load Bearing Wheeled Rover

Erim Gokce, Alfonso Jarquin, Johnny Louis, Neha Chawla, Sabri Tosunoglu

Department of Mechanical and Materials Engineering  
Florida International University  
Miami, Florida 33174

egokc001@fiu.edu, ajraq004@fiu.edu, jloui034@fiu.edu, nchaw002@fiu.edu, tosun@fiu.edu

## ABSTRACT

This paper entails the mechanisms of operation, prospective market desire and consumer benefit of a motorized autonomous rover with adaptable tracking and following capabilities.

## Keywords

Wheeled rover, tracking, color tracking, load carrying.

## 1. INTRODUCTION

### 1.1. Problem Statement

As society continues to strive towards automation of repetitive or laborious tasks, it becomes necessary to locate the areas where simple implementation and energy-saving potential coincide. Manual labor is one such area, where significant scale of humans still perform physically demanding tasks that have the potential of being completely automated.

### 1.2. Motivation

There exists a multitude of benefits, both on the corporate and individual levels, in having the ability of an intelligent rover to follow a user-controlled moving target. The primary feature of such a device would be in towing of items from one location to the other. This rover can be used at industry for transporting tools or scrap materials or at home for grocery shopping. The main aim of this robot is to reduce the human effort in carrying heavy loads thus preventing any injury from lifting. It can also be used for the disbursement of pesticides across a pre-set grid or the chlorination of a swimming pool. In the interest of preserving the versatility of this rover, the concept build outlined herein will not contain a load-bearing or load-towing feature.

### 1.3. Literature Survey

Automated robots are currently used in several industrial applications. They are used in warehouses, factory, and to transport products or items from one point to another. These robots are normally traditional 4 wheeled moving platforms rovers. They are low to the ground with a very high load capacity. They can carry weight several times that of themselves. The research conducted prior to the design of the robot was carried out with the intent to learn not only about vehicle automation and

drivability, but also the current uses, applications and models available to the public with similar uses.



**Figure 1. Amazon warehouse automated guided vehicles (AGV)**

The primary type of guided robot discovered in the research phase was an AGV, or automated guided vehicle. AGVs are platform like robots which follow predetermined paths from point to point and move cargo across busy warehouse floors. The AGVs use different markers to define their paths like laser triangulation, magnetic strips, colored lines, wire markers, magnetic grids, and natural feature recognition. Each type of technology has its own advantages and can be used according to the application of the robot.

## 2. DESIGN CRITERIA

We have used the colored line recognition and the natural feature recognition in our robot design. The colored line tracking will allow the robot to drive via an “eye” which is located on the front bottom side. The “eye” detects the colors on the floor and drives the robot while maintaining the colored line in sight at all times. Our design will be able to track users based on color and will also be programmed to maintain a certain distance between the robot and the user.

### 2.1. Selecting the Camera

An important feature of the rover would be its adaptability and versatility when it comes to following an objective. Since it is

necessary for the rover to stay locked onto a target, the need for the rover to feature a camera as its main tracking tool became apparent. Research was conducted into the use of pre-prepared libraries such as OpenCV, which when married with a camera, can perform as desired. We used PixyCam, an 80x80 pixel camera since it features the foundation of the data acquisition and relaying feedback mechanism that was required of this tracking system. The PixyCam can be programmed to track a specific hue of color, or a pattern of up to seven hues in proximity of each other. It is also capable of relaying coordinates of height, width, distance back to a microcontroller. This set of features would be integral in having the robot working properly



Figure 2. PixyCam, a crowd-funded tracking camera

## 2.2. Powering the System

The tracking rover would require a simple system of power that is long-lasting and low in weight. There are multiple components on the rover that require power, such as the camera, the microcontroller, and the motors. Since minimizing the weight is of the utmost importance, We chose to power the robot with a 9V dry cell battery and a 12V set of 8 AA batteries connected in-series. This method would prove to be optimal against other ideas such as a rechargeable battery pack, which could not supply the voltage required to drive the motors, as well as be the necessary fit and weight.

## 2.3. Driving the System

A set of DC motors that are used in various DIY RC home kits was selected for our prototype since it had a gear-ratio of 1:48 and a no-load speed of 200 RPM. While they are rated at 6V, we found that supplying twice the amount of voltage yielded no issues and with the inclusion of a motor shield on the microcontroller, which would be an Arduino Uno, the rover would be capable of being speed-controlled consistently with the included encoders.

For the small scale of this project, it was deemed best to favor DC motors over servomotors, for their power output. The Arduino Uno is incapable of supplying the sufficient wattage needed to drive both DC motors, so it became necessary to attach a separate motor shield, which would be independently powered by the 12V source. The 9V battery would power the Arduino, which connects

through a ribbon cable to the PixyCam, powering it as well. This method supplies everything sufficiently and is low in weight and cost.



Figure 3. A DC motor with encoder and wheel attached

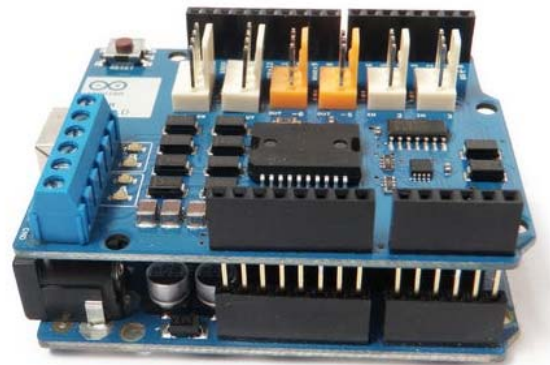


Figure 4. Motor shield mounted onto an Arduino Uno

For the included DC motor, there was also included a pair of encoders. These encoders can track the revolutions of the wheel in real time, and pre-setting a desired max RPM. Therefore, the supplied battery that is double the voltage that the motors are rated for should not be an issue. The encoders will keep the wheels spinning at the rate needed to keep up with the walking pace of an adult human, and this limitation of output will preserve battery life, effectively doubling the rate of runtime without needing to replace the batteries.

## 2.4. Rover Chassis

The chassis of the rover should be comprised of both metal and acrylic. The bottom base is metal, for stability and support, and the top level is acrylic, to house the electrical components since it will not conduct electricity.

## 2.5. 180° Rotation of View

The implementation of visuals in the robot must be capable of viewing angle of at least 180° to minimize power draw by preventing unnecessary rotation of the robot when possible, as

well as provide more rapid and sophisticated tracking method. For this reason, a dual-servomotor setup was implemented into the base of the PixyCam, which would allow for both panning left to right and tilting up and down of the camera. The programming will notify the servos the correct time to rotate or tilt the PixyCam, per which motor is required to engage to keep the centroid of the object centered.



**Figure 5. A pan/tilt servomotor setup, compatible with PixyCam**

### 2.6. Communication and Instruction

For instruction of the PixyCam for when to pan and tilt, as well as for the communication to the motors of when and how rapidly to turn, the base hub of the system was chosen to be the Arduino Uno. The Arduino will be programmed with the instructions of how close to travel to the stimulus, obstacle avoidance, reversing, full rotation of the body, and full relaying of the coordinates provided from the PixyCam to the motor shield.

The methodology of tracking will be handled by the accompanying software, PixyMon. The software is intuitive to use and relays the necessary data. PixyMon allows tracking of up to seven different items, each item with the option of being comprised of just one tracked hue, or up to a pattern of seven. The tracked objects can be tracked to a much beyond needed distance, provided the object is of sufficient size. The PixyMon software separates each object into a “block” for which it assigns a signature. This block signature can be relayed back to the Arduino with important information, such as the height, width, and distance of the block. These parameters can be taken as X, Y, and Z coordinate data, and put to good use in telling the DC motors to operate. A computer is needed to tag blocks.

PixyMon is taught a block by holding up the item in front of the PixyCam, and selecting the “Set Signature” option. This allows the user to select in a rectangular box of desired size, the item shown on screen. PixyMon then highlights the entire object of the selected hue, and assigns it a signature. This is stored inside the PixyCam after disconnected from the computer.

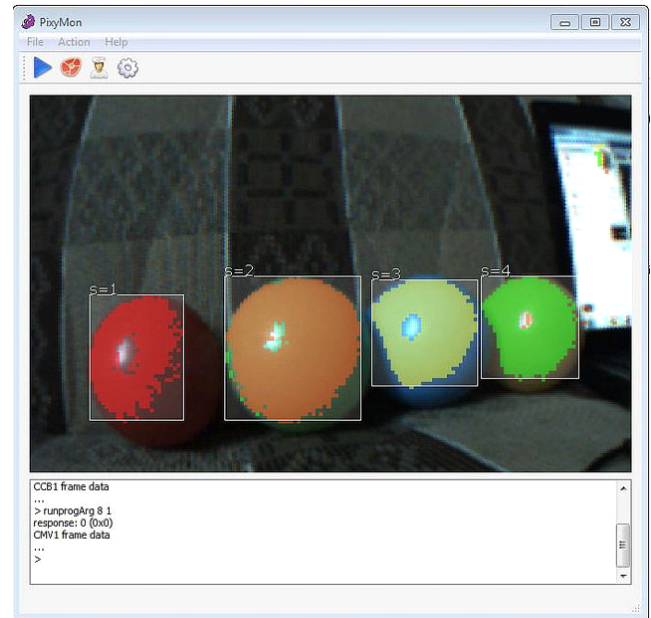


**Figure 6. The PixyMon tracking software interface**

## 3. CONCEPTUAL PROTOTYPE DESIGN

The initial, conceptual design of the robot was brainstormed to be constructed out of 3D printed ABS plastic. The base would be a printed piece in the shape of a skateboard, and attached to stacked platforms inside which electronics and batteries could be stored. The design features a small compartment on the back to carry items, and the propulsion would be through front-wheel drive. A rear idler wheel would keep the platform stable.

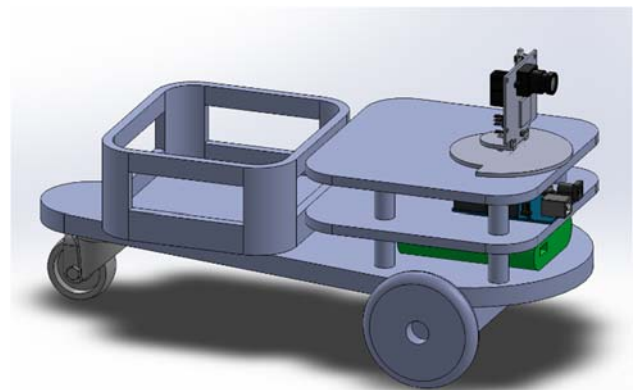


**Figure 7. A conceptual design of the robot, with storage crate**

We discovered that the method of 3D printing was more cost-prohibitive than purchasing multiple pre-made platforms which could be adjusted to affix to one another. Also, a design choice was made to remove the storage crate from the final prototype, to preserve versatility. It was decided to instead run a side production of a towing crate which could be affixed to the final robot, and could be reliant on its power output to be carried around.

An additional feature of the conceptual design was that it would be run off a rechargeable battery pack (See Fig. 7, battery pack in green). This was removed in the final product to minimize weight.

#### 4. FINAL PROTOTYPE DESIGN

The completed prototype is constructed from an aluminum base which houses the wheels, batteries, and DC motors. The base connects to an acrylic roof, on top of which the electrical components are mounted. The Arduino Uno, motor shield, and PixyCam are secured to the top through holes drilled into the acrylic. These components connect through wiring to the bottom metal base. The wheels attach to the DC motors, those of which are secured to the metallic bottom through hot glue. The front idler wheel was screwed in to the slots in the front of the chassis.

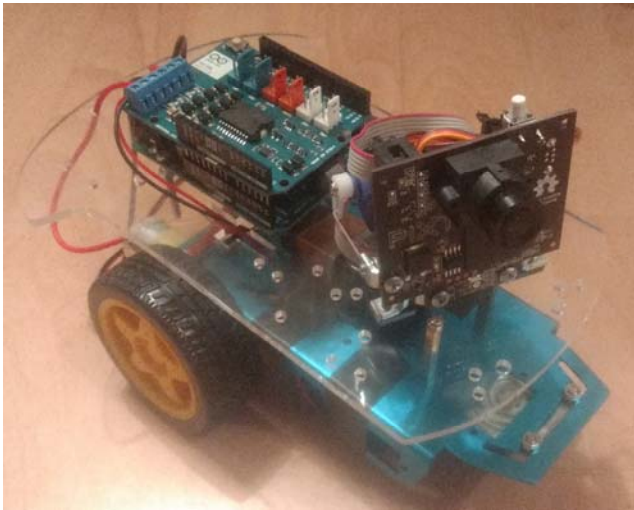


Figure 8. The completed prototype

As mentioned prior, the prototype does not feature a load bearing capacity. However, the prototype can withstand towing a load of 1-2 lbs, which can be stowed on a platform that can be easily attachable to a hitch on the rear of the robot. A detriment of including a hitched tow would be in the reversing of the robot, so it is of our's interest to gauge the demand for this product and, if sufficiently significant, modify the design to include the load crate.

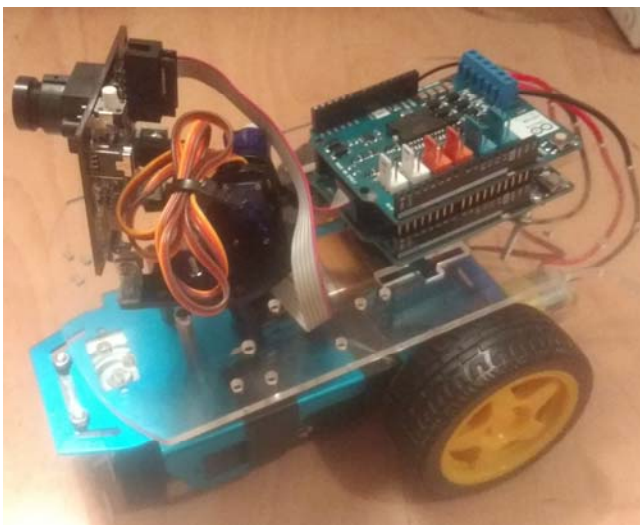


Figure 9. A side view of the robot

Certain design choices were made that vary from the original concept. The final robot is now rear-wheel driven, as opposed to front wheel driven. The multi-level platforms were removed in favor of one singular platform, which would improve stability. The batteries are mounted on both the top and bottom of the metal portion, with the bottom battery pack secured with Velcro. The wheels are wider than in the original concept. There is sufficient clearance between the batteries and the ground.

#### 4.1. Size and Weight Specifications

The robot weighs just over eighteen ounces. It is eight-and-a-half inches long and six inches wide. The height is six inches. The robot was designed to be scalable, so a consumer-ready product would scale to two feet and ten inches long, two feet wide, and two feet high. The final product would be much denser, approximately 20 pounds due to the batteries, all-metallic infrastructure, and powerful motors.

#### 4.2. Cost Breakdown Analysis

Much of the expenditure was towards the PixyCam. However, it is of important note that this price will remain stagnant and will not become costlier with the full scaled model. Many of the components were already on-hand, however we felt it necessary to identify the true cost of this project.

Table 1. Total Cost Breakdown of Color Tracker Robot

Component	Quantity	Price
Arduino Uno	1	\$19
Metallic Platform	1	\$16
Motor Shield	1	\$25
Acrylic Platform	1	\$12
Wheels	2	\$4
9V Battery	1	\$2
AA Battery	8	\$5
PixyCam	1	\$79
Servos for Pixy	2	\$20
DC Motors	2	\$10
Cables/Connectors	Various	\$10
<b>FINAL</b>		<b>\$202</b>

#### 4.3. Methodology of Connection

The 12V battery pack supplies its energy through a positive and negative cable, which secures into the motor shield in the SUPPLY and GND terminals. This motor shield has two output nodes which route the voltage into the two DC motors through positive and negative wire which are soldered onto the motor terminals. The motor shield rests directly on top of the Arduino, and is secured through the numerous pins which are custom-matched to fit into the Arduino's analog, digital, and power inputs. The Arduino itself is powered through the 9V cable. The PixyCam shares power draw with the Arduino, and is connected to it through a custom ribbon cable attached to an in-circuit serial programmer node. Finally, the PixyCam is secured to a base which we constructed with two 180° servomotors, which control the pan and tilt functions of the PixyCam.

## 5. CONTROL THEORY

The bulk of the control theory is through the relaying of information from PixyCam to the motors. It was necessary to program the Arduino to be the middleman in this interaction.

### 5.1. Language and Method

The language used was C++. The code required an object-oriented programming language, and C++ is native to the Arduino environment. The code relies heavily on object calls and if statements. The idea is to teach PixyCam an object, and scrape the data it relays into Arduino, which is taught to react to that information accordingly.

### 5.2. Code Breakdown

The code begins by establishing a servo loop class, a proportional/derivative feedback loop for the pan and tilt servo tracking of the “block”. This ensures that the robot remains stationary if the angle is changing, but the proximity of block to robot is unchanged.

```
class ServoLoop
{
public:
  ServoLoop(int32_t proportionalGain, int32_t
  derivativeGain);
  void update(int32_t error);
  int32_t m_pos;
  int32_t m_prevError;
  int32_t m_proportionalGain;
  int32_t m_derivativeGain;};
// ServoLoop Constructor
ServoLoop::ServoLoop(int32_t proportionalGain,
int32_t derivativeGain)
{
  m_pos = RCS_CENTER_POS;
  m_proportionalGain = proportionalGain;
  m_derivativeGain = derivativeGain;
  m_prevError = 0x8000000L;}
```

The servo loop then updates, by calculating a new output based on the measured error and the current state.

```
void ServoLoop::update(int32_t error)
{
  long int velocity;
  char buff[32];
  if (m_prevError!=0x80000000)
  {
    velocity = (error*m_proportionalGain + (error -
    m_prevError)*m_derivativeGain)>>10;
    m_pos += velocity;
    if (m_pos>RCS_MAX_POS)
    {
      m_pos = RCS_MAX_POS;
    }
    else if (m_pos<RCS_MIN_POS)
    {
      m_pos = RCS_MIN_POS;
    }
  }
  m_prevError = error;}
```

Next was the creation of a simple motor class. This would communicate to the motor driver, which utilizes timer 1 on the Arduino, to control the DC motors using a 20-kilohertz pulse-width modulation.

```
class SimpleMotors
{
public:
  // constructor (doesn't do anything)
  SimpleMotors();
  // enable/disable flipping of motors
  static void flipLeftMotor(boolean flip);
  static void flipRightMotor(boolean flip);
  // set speed for left, right, or both motors
  static void setLeftSpeed(int speed);
  static void setRightSpeed(int speed);
  static void setSpeeds(int leftSpeed, int rightSpeed);
private:
  static inline void init()
  { static boolean initialized = false;
  if (!initialized)
  { initialized = true;
  init2();
  }
  }
  // initializes timer1 for proper PWM generation
  static void init2();
};
#define PWM_L 10
#define PWM_R 9
#define DIR_L 13
#define DIR_R 12
#ifdef defined(__AVR_ATmega168__) //
defined(__AVR_ATmega328P__) || defined
(__AVR_ATmega32U4__)
#define USE_20KHZ_PWM
#endif
static boolean flipLeft = false;
static boolean flipRight = false;
```

After the simple motor class was established, it was important to create the reaction of the robot car to orient itself to face the tracked block one PixyCam is normalized. This occurs once the block begins changing proximity to the robot. Size is the area of the object, and a running average of eight sizes are kept.

```
int32_t size = 400;
void FollowBlock(int trackedBlock)
{
  int32_t followError = RCS_CENTER_POS -
  panLoop.m_pos;
  size += pixy.blocks[trackedBlock].width *
  pixy.blocks[trackedBlock].height;
  size -= size >> 3;
  int forwardSpeed = constrain(400 - (size/256), -100,
  400);
  int32_t differential = (followError + (followError *
  forwardSpeed))>>8;
  int leftSpeed = constrain(forwardSpeed + differential,
  -400, 400);
  int rightSpeed = constrain(forwardSpeed - differential,
  -400, 400);}
```

Forward speed will decrease as the robot approaches the object. The steering differential is proportional to the error times the forward speed, and this adjusts the left and right speeds.

```

if (k%50 == 0 ) {
  Serial.println("Speeds in follow");
  Serial.println(rightSpeed);
  Serial.println(leftSpeed);
}
motors.setLeftSpeed(leftSpeed);
motors.setRightSpeed(rightSpeed);
}

```

Another important prompt was to instruct the PixyCam to search for blocks, by panning back and forth at random until a block with the "correct" hue is detected, after which the following begins.

```

int scanIncrement = (RCS_MAX_POS -
RCS_MIN_POS) / 150;
uint32_t lastMove = 0;
void ScanForBlocks()
{
  if (millis() - lastMove > 20)
  {
    lastMove = millis();
    panLoop.m_pos += scanIncrement;
    if ((panLoop.m_pos >=
RCS_MAX_POS) || (panLoop.m_pos <=
RCS_MIN_POS))
    {
      tiltLoop.m_pos = random(RCS_MAX_POS * 0.6,
RCS_MAX_POS);
      scanIncrement = -scanIncrement;
      if (scanIncrement < 0)
      {
        motors.setLeftSpeed(-250);
        motors.setRightSpeed(250);
      }
      else
      {
        motors.setLeftSpeed(+180);
        motors.setRightSpeed(-180);
      }
      delay(random(250, 500));
    }
    pixy.setServos(panLoop.m_pos, tiltLoop.m_pos);
  }
}

```

The robot is intelligent enough to reverse when it is being approached by the tracked object, and to not begin movement until the tracked item changes in proximity to the robot. The distance is measured by multiplying the height and width variables that the PixyCam can measure.

```

void setup()
{Serial.begin(9600);
Serial.print("Starting...\n");
motors.setSpeeds(0, 0);
pixy.init(); }
uint32_t lastBlockTime = 0;

```

The main loop is included below. This runs continuously after setup, which precedes the main loop and runs at startup.

```

void loop()
{
  if (k%50 == 0 )
  Serial.println("Loop Started");
  k++;
  uint16_t blocks;
  blocks = pixy.getBlocks();
  // If we have blocks in sight, track and follow them
  if (blocks)
  {
    if (k%50 == 0 )
    Serial.println("blocks in sight");
    int trackedBlock = TrackBlock(blocks);
    FollowBlock(trackedBlock);
    lastBlockTime = millis();
  }
  else if (millis() - lastBlockTime > 100)
  {
    motors.setLeftSpeed(0);
    motors.setRightSpeed(0);
    ScanForBlocks();
  }
}
int oldX, oldY, oldSignature;

```

## 6. EXPERIMENTATION

The robot was tested by setting it to track a red hat that the tester would hold in front of it. The lighting conditions of the room were optimal, with no natural daylight interference. The PixyCam is not as functional when daylight is factored in, and as such, has poorer outdoor performance. Nonetheless, the robot was tested both inside at nighttime and outside with daylight.

## 7. RESULTS

Testing was successful in the indoor test, and the robot tracked and followed the object for five minutes. The robot lost visual sight of the hat once, due to the lighting conditions of the testing room, but the panning back-and-forth code block restored the visual sight to the hat, and the robot could continue following the tester. The robot is calculated and expected to last up to thirty minutes of continuous motion following. It was able to achieve a maximum speed of four miles per hour.

The outdoor test proved difficult, with the red hat reflecting much of the light and causing PixyCam to behave erratically. We were able to remedy this issue, by programming the PixyCam with a custom-made color signature, which comprised of a piece of paper with three different unique and bright colors. The robot functioned normally until subjected to direct contact with sunlight, which interfered in the tracking. PixyCam should be avoided from direct sunlight.

PixyCam's lens is focused through screwing in/out, and as such it is recommended to users to secure the lens in place once it is set. We encountered multiple scenarios of the camera losing focus due to a loose lens that was turning on its own due to the motion of the moving robot.

## 8. CONCLUSION

The concept of tracking a pattern by a platform has been demonstrated in terms of a first prototype and encouraging results have been observed. Application of this concept in industrial as well as personal robotics offers a potentially wide spectrum of new designs for robotic platforms and even manipulators.

In conclusion, we successfully built the color tracking rover which would identify the programmed color and then follow the path taken by the color. Further research can be carried out on programming the rover to move irrespective of the light conditions.

## 9. ACKNOWLEDGEMENTS

We would like to acknowledge Gene Yllanes for her assistance in construction of the programming code.

## 10. REFERENCES

- [1] Bhasin, Kim, and Patrick Clark. "How Amazon Triggered a Robot Arms Race." *Bloomberg Technology*. Bloomberg, 16 June 2016. Web. 27 Apr. 2017.
- [2] "CMUcam5 Pixy." *Wiki - CMUcam5 Pixy - CMUcam: Open Source Programmable Embedded Color Vision Sensors*, 2017.
- [3] "Arduino UNO Rev3." Arduino Store USA. N.p., n.d. Web. 27 Feb. 2017.
- [4] Cade, D. L. "Pixy: A Low Cost Camera that Recognizes and Follows Objects by Color." *PetaPixel*. N.p., 01 Sept. 2013. Web. 27 Apr. 2017.
- [5] Knight, Will. "An Italian scooter maker invents a robot that follows you around carrying your stuff." *MIT Technology Review*. MIT Technology Review, 07 Feb. 2017. Web. 27 Apr. 2017.
- [6] "Adafruit Motor Shield V2 for Arduino." *Using DC Motors / Adafruit Motor Shield V2 for Arduino, Adafruit Learning System*. N.p., n.d. Web. 27 Apr. 2017.
- [7] *Product Details and Description*. N.p.: n.p., n.d. *Mantech*. Feetech, 2013. Web. 27 Apr. 2017.
- [8] Team, Editorial. "Control a DC Motor with an Arduino." *All About Circuits*. N.p., 07 July 2015. Web. 27 Apr. 2017.
- [9] "Tutorial: Pixy (CMUcam5)." *Physical Computing*. IDEate, n.d. Web. 27 Apr. 2017.

# Comments on ASTM F2508 – 13

Oren Masory

Department of Ocean and Mechanical Engineering

Florida Atlantic University

Boca Raton, FL 33431

masoryo@fau.edu

## ABSTRACT

In 2013 the American Society of Testing and Materials (ASTM) F13 committee on Pedestrian/Walkway Safety and Footwear, adapted a new standard F2508-13 “Standard Practice for Validation, Calibration, and Certification of Walkway Tribometers Using Reference Surfaces”. The purpose of the standard is to provide a procedure for validation and calibration of tribometers so that their readings of the Coefficient of Friction (COF) in wet conditions will be more reliable and consistent. The drive behind for this standard is a well-known problem where there are large deviations between the readings obtained by different tribometers when measuring the COF between the same surfaces under wet conditions. The standard is based on a study in which four different reference surfaces were ranked according to their slipperiness measured by the number of slips detected while subjects were walking across them. A validated tribometer, according to this standard, is required to correctly rank the slipperiness of reference tiles with statistically significant differentiation between the COF readings. It should emphasize that the standard does not dictate any particular COFs’ values for these reference surfaces.

The purpose of this paper is to point out some of the difficulties in applying this standard: 1) Different validated tribometers produce different values for the Coefficient of Friction (COF) of the same ranked surface. Or, vice versa, for the same value of the COF different tribometers will rank the surface’s slipperiness differently; 2) Reference surfaces are not the same; and 3) The COF of the higher friction surfaces depends on the direction of the test which is not necessarily in the direction that a person slipped during the accident. These issues will present confusion in case of litigation and the test results are subjected to subjective interpretations.

**Keywords:** Coefficient of friction, Friction Measurements, Slipmeters, Tribometers,

## I. INTRODUCTION

Slips and falls accidents are the leading cause of workers’ compensation claims and the leading cause of occupational injury for people aged 55 years and older. Compensation & medical costs associated with employee slip/fall accidents is approximately \$70 billion annually [1]. A report by The Bureau of Labor Statistics [2] states “Together, falls, slips, or trips accounted for 35 percent of the injuries and illnesses to heavy and tractor-trailer truck drivers in 2014.” In [3] it is reported “falls on

the same level is the second highest category of compensable loss and cost \$6.7 billion, according to the 2006 Liberty Mutual Workplace Safety Index. Further, the cost for these injuries grew more than 30 percent from 1998 to 2004.” There are numerous reports on the subject but one that demonstrate the severity of this problem is given in a report of a study performed by the National Floor Safety Institute (NFSI) that found that more than 3 million food service employees and over 1 million guests are injured annually as a result of restaurant Slips and Falls accidents. These injuries are increasing at a rate of about 10% annually [4].

The slipperiness of a surface depends on many factors including: presence of moisture or contaminants, slope and cross slope, surface texture, wear, surface finish and the Coefficient of Friction (COF) between the sliding surfaces. However, the measurement of COF, which is the dominant factor effecting slipperiness, is commonly used to qualify a walking surface as a safe one.

The COF is defined by the ratio of the shear force that acts tangent to the contact surfaces between two bodies and the normal force between the two bodies. Thus, in order to find out the value of the COF both forces have to be measured while the bodies are impending motion for the Static COF or in motion for Dynamic COF. In case of Slip and Fall accident the static COF is of interest since it represents the maximum available friction. Once slip occurs, the value of the COF assumes its dynamic value which is lower than the static one. Thus, the static COF represents a threshold between slipping and non-slipping conditions.

Although it might be perceived as a very simple measurement process, test results, of the same surface, might be substantially different due to: 1) Inconsistency of COF readings from one operator to another; 2) Inconsistency of COF readings from one tribometer to another; 3) Inconsistency between reference surfaces; 4) Inconsistency with the same reference surface; and 5) Inconsistency in COF reading of the same model tribometers.

To address difficulties in measuring COF, different organizations, such as ASTM and ANSI, developed numerous standards (a partial list is given in Appendix I). In addition, experts and researcher do not agree on a COF value which ensures a safe floor. However, the value of 0.5 is commonly agreed as the threshold between slippery and non-slippery condition. Many codes adapted this value and a good survey can be found in [5].

In 2013 the American Society of Measurements and Materials (ASTM) established a new standard - ASTM 2508 “Standard Practice for validation, calibration, and certification of walkway

slip meters using reference surface” [6]. The standard provides the following:

1. Provides a walkway tribometer supplier (and other entities) with procedures and suit of reference surfaces to validate their walkway tribometer.
2. Provides the user of such tribometers with a procedure and suit of reference surfaces to test whether or not his tribometer is calibrated to the manufacturer’s specifications.
3. Describes the necessary materials, specification, foot treatment and the cleaning process of the reference surfaces.

The standard is not addressing the issue of the interpretation of the readings obtained by these tribometers and leaves it to the user.

The validation by the supplier consists of a series of 40 tests, in wet conditions, on each reference surface (10 tests for each of the four perpendicular direction). These surfaces, provided by ASTM, are Black Granite, VCT (Vinyl Composition Tile), Porcelain and Ceramics which are ranked as Very Slippery, Moderately Slippery, Acceptable Slippery and Not Slippery respectively. The tribometer is considered valid if:

1. It ranks the four reference surfaces slipperiness in the proper order. For this purpose the mean value of the (COF), of each tile, is used.
2. There is significant differentiation between the results obtained for each surface. This is determined by the following:

$$t = \frac{d_m}{SD/\sqrt{N}} \quad (1)$$

Where  $d_m$  is the mean of the differences between of all data point of consecutively ranked surfaces, divided by the number of pairs (40):

$$d_m = \frac{\sum_{i=1}^{40} (A_{j+1} - A_j)}{40} \quad j = 1,2,3 \quad (2)$$

where the index  $j$  increases from “Very Slippery” to “Not Slippery” etc.

$SD$  is the standard deviation of the differences between all pairs and  $N$  is the number of pairs (40)

3. If  $t$  is larger than 1.694 than a statistically significance exists between the COFs of the two surfaces. Otherwise, no statistically significance exists between the two surfaces. This statistical treatment assumes that the data in normally distributed which is not necessarily the case.

The user has to check and determine if his tribometer is calibrated by conducting 16 tests on the same reference surfaces. If the means of the COFs that were found falls within the 95% confidence level that was provided by the manufacturer his tribometer is considered to be calibrated.

The standard is based on a research performed at USC [7] on 84 health young human subjects (42 males, 42 females) between the ages of 22 and 38 (mean  $25,9 \pm 3.8$  years). The subjects were walking at the speed of  $2.18 \pm 0.13$  m/s across the above mentioned

4 tiles, in wet conditions, and slip occurrence was detected by cameras. The slipperiness of the tiles was ranked according to the numbers of detected slips (heel or toe) and the coefficient of friction of these tiles was measured by variety of commercial slip meters. The above two criteria were applied to the readings of each tribometer for its validation.

The use of young healthy subjects for this research implies that if a healthy young person is in risk of slipping than an older persons or persons who are not in good health are exposed to higher risk of slipping. Also, walking speed of 2.18 m/s (4.876 mph) is a very high walking speed which requires a very large steps (displacement) increasing the probability of slip [8, 9]. Average walking speed is 2.8 mph (for young people 3.37 mph and for older people 2.65 mph).

## II. ANALYSIS OF TESTS’ RESULTS PERFORMED IN [7]

Out of the 12 tribometers that were tested in [7] only 4 passed the two criteria mentioned above. The mean values of the COF, for the 4 reference surfaces, measured by these tribometers, are shown in Figure 1.

Similar tests were reported in [10] in which 9 tribometers were tested on 3 different surfaces (HPL, Derlin and Teflon) in dry and wet conditions. These cases were ranked, using three slipperiness categories: Not Slippery, Slippery and Very Slippery, according to the number of slips detected on each surface. Out of the 9 tribometers only 2 passed the criteria specified above. The values of COF obtained by theses two tribometers are shown in Figure 2.

Observing the results shown in Figures 1 and 2, which were obtained by validated tribometers, raises the following concerns:

- 1) There are large differences in the values of the COF obtained by these tribometers for the surface (see Figures 1 and 2). For example, on a surface ranked as Not Slippery tribometer C reads a COF value of 0.69 while tribometer B reads a value of 0.42. This is a difference of almost 40%.
- 2) Due to the particular ranking it is difficult to determine the risk in an intermediate reading. For example, a reading of 0.21 by tribometer A ranks the surface between Moderately Slippery and Acceptable Slipper. Thus, the interpretation of the COF’s value with regard to the risk of slipping is subjective (see dash line in Figure 1).
- 3) The dotted line in Figure 1 demonstrates another problem: The user of tribometer A will rank the surface as Moderately Slippery; the user of tribometer B will rank the surface as Acceptable Slippery and the user of tribometer D will rank the surface as Very Slippery. In case of litigation these three different classification of the surface will cause a major confusion.
- 4) It is interesting to note that for Slippery and Very Slippery conditions (wet or dry conditions), shown in Figure 2, the value of the COF is below 0.5 which is used in many codes as the threshold between slippery and not slippery conditions.

### III. ANALYSIS OF TESTS' RESULTS PERFORMED BY TRIBOMETERS' SUPPLIERS

Once the new standard was published, tribometers' suppliers had to validate their tribometers accordingly. Some suppliers published the results of their validation's tests [11, 12, 13]. The tests' results on dry surfaces, for three tribometers, are shown in Figure 3.

It should be noted that tribometers E, and G did not pass the validation tests performed in [4]. Figure 4 illustrates the difference between the suppliers' tests' results and the ones published in [4]. As shown, there are large, above 60% in one case, differences between the measurements. It should be emphasized that the tests were performed on the same reference surfaces. These discrepancies are not likely due to operator's skill since the tests were performed by trained and experienced operators. It is probably due to differences between same model tribometers, differences between the reference surfaces and other factors.

### IV. VARIABILITY BETWEEN SLIP METERS OF THE SAME MODEL AND SUPPLIER

A study performed by "Zurich Services" [14] compares the performance (COF readings) of the same model tribometers supplied by two suppliers (A & B), each provided 3 same model devices (will be referred as A-1, A-2, A-3, B-1, B-2 and B-3). The experiments were performed under wet and dry conditions. All the tests' feet were calibrated using a Tile Council of North America TCNA C-1028 calibration tile which was included with each individual tribometer kit. The TCNA C-1028 calibration tile is made of ceramic material and have a matte finish. Each test was repeated 12 times and the mean was used for comparison.

Figure 5 illustrated the deviations in the readings of the COF obtained by each tribometer relative to the mean of all measurement obtained by the same three tribometers on the same surface. The graphs, for dry conditions, indicate that in some cases the deviation value exceeds 10% which might classify the slipperiness of the surface wrong. On wet surfaces, the problem that this standard is addressing, the deviations are larger and in some cases they exceed 50% which has high probability to rank the slipperiness of the surface wrong.

It should be emphasized that the differences between same model same supplier tribometers is being addressed by the new standard since each individual tribometer has to be validated by the supplier and its particular characteristics (mean COF as well as the 95% confidence interval for each reference surface) are provided to the user for the purpose of calibration of his own tribometer. However, such large variations might lead to false classification of actual tested tile.

### V. VARIABILITY BETWEEN REFERENCE SURFACES

The standard is based on the assumption that the characteristics of the reference surfaces, being used by the suppliers and the users, are the same within 95% confidence interval. This assumption has not been verified in particular since the tiles are manufactured by a process which has its own variabilities. As

results, it is expected to observe variations in the value of COF from one tile to another. Thus, variations between different sets of reference surfaces are expected. The problem becomes an issue where there are differences between the reference surfaces used by the manufacturer and the one being used by the user for calibration of his tribometer.

The following is a court case where an English XL tribometer, validated by the supplier using ASTM F-2508 standard, was used to measure SCOF in wet conditions [15]. The details of the opinion are not of interest here. The expert calibrated his tribometer according to ASTM F-2508 standard using the 4 reference surfaces that were provided by ASTM. His opinion was rejected since the values of the COF he obtained during calibration did not fall within the 95% confidence interval provided by the supplier (see row 1 and 2 in Table 4). After the trial the expert's tribometer was sent back to the supplier for testing. The results of the expert's calibration tests and the ones conducted by the supplier are shown Table 1.

The first row in Table 1 shows the 95% confidence intervals for each reference surface given by the tribometer's supplier. The second row provides the values of the COF measured by the expert during the calibration process using his reference surfaces. **Notice that none of the calibration values fall within the 95% confidence intervals.** The third row shows the results, obtained by the supplier tests, when using the expert's tribometer and the supplier's reference surfaces. **Again, none of these values fall within the 95% confidence intervals provided by the supplier.** Lastly, the supplier measured the COF of the expert's reference surfaces using its own tribometer. The results of these tests are given in the fourth row of Table 4. **In this case only one value (Granite Tile) falls within the interval provided by the supplier.**

The tests' results shown in Table 4 raise two questions:

1. It is expected that measurements (see 2<sup>nd</sup> and 4<sup>th</sup> rows) obtained by both tribometers, using the same reference surfaces, will be the same (within the 95% confidence interval). Here, the results are different and three out of four readings, obtained by using the supplier's tribometer, are not within the 95% confidence interval.
2. It is expected that the measured values of the COF using of the same tribometer and two sets of reference surfaces (see 2<sup>nd</sup> and 3<sup>rd</sup> rows) would be the same. In this case none of the COFs' values fall within the 95% confidence interval (1<sup>st</sup> row).

The only conclusion that will explain the above results is that the COFs is different from one set of reference surfaces to another. This conclusion was arrived to in [15] "the tile-to-tile variations in friction in the same areas of the restaurant were also statistically significant

### VI. VARIABILITY WITHIN THE SAME REFERENCE SURFACE

ASTM procedure requires 40 tests on each tile 10 in each direction (North, East, South and West). The validation tests' results provided in [11, 12, 13] include the information including the measured COF values as well as the test' direction. If the tile's surface is uniform it expected that the mean value of the COF will be the same in any direction.

**Table 1: Tests' results using the expert's tribometer.**

	Granite	Porcelain	Vinyl	Ceramic
95th Percentile Confidence Interval	0.078-0.082	0.132-0.137	0.173-0.180	0.605-0.616
Gill's calibration using her tribometer and tiles	0.0700	0.1013	0.1727	0.8505
Excel's calibration using Gill's tribometer and its own tiles	0.066	0.116	0.165	0.576
Excel's calibration using its own tribometer and Gill's tiles	0.080	0.100	0.149	0.641

To test this hypothesis a one way ANOVA test was performed for each tile where the data for each direction is considered as a sample (see results are shown in Table 2). If the surface passed the test it means that the deviations in the mean values of the COF, in all four directions, are insignificant and all readings belong to the same population. In other words the surface's COF is uniform and undependable of the measurements' direction.

The results in Table 2 indicate that, when tribometers I and II are being used, the high friction tiles, C - Acceptable Slippery or D – Not Slippery, are “failing” the test. The tests performed by tribometer III passed the test because the measurements were performed under wet conditions where COF's values are reduce. This means that the COF property of the failed tiles is not consistent

**Table 2: One way ANOVA results**  
( $F_{critical} = 2.86626$  for for all cases)

Tribometer	Tile	<i>F</i>	<i>P-value</i>	Criteria
I	A	0.77665	0.51473	PASS
	B	0.642857	0.59249	PASS
	C	5.92053	0.00216	FAIL
	D	2.535354	0.07210	FAIL
II	A	0.545455	0.65437	PASS
	B	0.861592	0.46984	PASS
	C	0.861592	0.46984	PASS
	D	3.950367	0.01558	FAIL
III	A	0.17321	0.91381	PASS
	B	3.41658	0.02747	PASS
	C	26.91388	2.61E-0	PASS
	D	6.060302	0.00189	PASS

.In order to determine if the test direction has any effect on the value of the COF, the same data was arrange in pairs of opposite testing directions (e.g. North – South). Each pair was tested as follows:

<sup>1</sup> ASTM C-1028 was withdrawn in 2014. However, the test is still valid since the reason for withdrawal is not due to technical deficiencies: “**This standard is being withdrawn without replacement due to its limited use by industry**”.

1. First, f-Test was performed to determine if the variances of each pair are the same.
2. According to the f-Test results, t-Test, either for pairs of the same variance or pairs with different variance, was performed in order to determine if the two samples belong to the same population (in other words if their means are the same within 95% confidence interval). The results of these tests are given in Table 3.

The results in Table 3 indicate that all high friction surfaces (C and D) have one particular direction where the value of the COF is being effected by the test direction. This is a clear indication that the manufacturing process affecting the surface in such a way that it is “rough” in one direction and “rougher” in the opposing one.

A series of tests, in which the COF of a TCNA standard tile was measured 10 times in 8 different directions in increments of 45° (North-South, North East- South West etc.), was conducted according to ASTM C1028 standard<sup>1</sup>. The tests were conducted in dry conditions and the results are given in Table 4.

A one way ANOVA test, on the 8 samples, revealed that there is no significant difference between the means indicating that all 8 samples belong to the same population ( $F = 2.010117$ ,  $P_{Value} = 0.065407$ ,  $F_{critical} = 2.139656$ ). However, t-Test of pairs of samples of opposite directions show that in one particular case, North-South, there is significant difference between the means (see t-Test results in Table 5) indicating that there is a difference in the COF values when testing in opposing directions). Worthwhile to note that this direction was parallel to the edge of the tile, indicating that the manufacturing process might affect the surface.

## VII. CONCLUSIONS

The new standard for validation of tribometers assumes that the reference surfaces, used by the suppliers and the users, have the same (within 95% confidence level) COF. This assumption has to be checked out in light of the results shown above.

Tribometers, which were validated by the standard, provide different COF, in some cases with large deviation, for the same reference surfaces. Thus, either the reference surfaces are not the same or the measurements are incorrect. This differences present a major issue when it comes to litigation since two validated tribometer might indicate different level of slipperiness.

Also, most safety and building codes specify a minimum value for the COF in order to certify a walking surface, e.g. 0.5, the test result which will identify the surface as “Not Slippery”, might have a COF smaller than the required one by the codes. Also, a COF reading that fall between two slipperiness ranking, e.g. between “Moderate Slipperiness and “Acceptable Slipperiness” is open for subjective interpretation.

Deviations in COF within the same tile, measured in opposite directions, is another issue that has to be address since in cases of

Slip and Fall a person might slip in the direction of the low COF while the measurements for validation were taken in the opposite direction.

All this issues can be solved if a reference surface can be produced with very high repeatability resulting the same COF. Thus, it will be expected that all tribometers will measure the same value COF, eliminated the confusion discussed above.

**Table 3: f-Test and t-Test results.**

(P – Pass the test, F – Failed the test)

(P for f-Test means variances are the same within 95% confidence interval)

(P for t-Test means averages are the same within 95% confidence interval)

( $F_{Critical}(1\ tail)=3.178$  and  $T_{Critical}(2\ tails)=2.1$  for all cases)

Tribo-meter	Tile	Dire-ction	F	Crit-eria	T <sub>stat</sub>	Crit-eria
I	A	N-S	1.35	P	1.386	P
		E-W	1.81	P	0	P
	B	N-S	1.98	P	0	P
		E-W	1	P	1.325	P
	C	N-S	2.75	P	3.113	F
		E-W	1.24	P	0.547	P
	D	N-S	1.29	P	0	P
		E-W	1.14	P	2.750	F
II	A	N-S	1.19	P	1.394	P
		E-W	2.44	P	0	P
	B	N-S	1.33	P	1.463	P
		E-W	1.23	P	0.884	P
	C	N-S	1.8	P	3.515	F
		E-W	1.6	P	0	P
	D	N-S	1.11	P	0	P
		E-W	1.02	P	3.398	F
III	A	N-S	1.31	P	0.144	P
		E-W	2.01	P	0.610	P
	B	N-S	9.85	F	1.279	P
		E-W	1.20	P	2.368	F
	C	N-S	2.11	P	8.504	F
		E-W	1.36	P	1.523	P
	D	N-S	15.6	F	0.979	P
		E-W	1.95	P	2.286	F

**Table 4: COF values obtained by the 8-directions tests.**

Test	Direction							
	N	S	E	W	NE	SE	SW	NW
1	0.412	0.417	0.441	0.446	0.451	0.475	0.422	0.422
2	0.470	0.417	0.436	0.451	0.523	0.456	0.427	0.489
3	0.484	0.412	0.412	0.417	0.508	0.436	0.508	0.480
4	0.417	0.412	0.393	0.408	0.432	0.403	0.547	0.508
5	0.446	0.398	0.422	0.451	0.393	0.393	0.432	0.508
6	0.446	0.388	0.384	0.398	0.427	0.384	0.384	0.432
7	0.451	0.393	0.398	0.412	0.480	0.432	0.384	0.441
8	0.451	0.441	0.432	0.427	0.499	0.542	0.393	0.441
9	0.412	0.432	0.456	0.436	0.465	0.528	0.369	0.374
10	0.441	0.422	0.465	0.412	0.451	0.499	0.451	0.417
Mean	0.443	0.413	0.424	0.426	0.463	0.455	0.432	0.451
Variance	0.000568	0.000275	0.000732	0.000367	0.001627	0.003071	0.003287	0.001924

**Table 5: t-Test results.**

	Direction			
	N-S	E-W	NE-SW	SE-NW
F	2.066	1.994	1.890	1.110
F <sub>Critical</sub>	3.178	3.178	3.178	3.178
T <sub>Stat</sub>	<b>3.237</b>	0.182	1.467	0.359
T <sub>Critical</sub>	2.100	2.100	2.100	2.100

## VIII. REFERENCES

- [1] National Floor Safety Institute, <https://nfsi.org/>
- [2] BLS News Letter USDL 15-2205, November 19, 2015
- [3] Liberty Mutual Research Institute for Safety, Vol. 10, No. 3,
- [4] Slips and Falls Study: Objective Auditing Techniques to Control Slips and Falls in Restaurants, CNA June 2007. Autumn 2007
- [5] Steven Di Pilla, Slip and Fall Prevention – A practical Handbook, CRC Press, 2<sup>nd</sup> Edition, ISBN-13:978-1420082340, 2010.
- [6] ASTM 2508-13 “Standard Practice for validation, calibration, and certification of walkway slip meters using reference surfaces.”
- [7] C.M. Powers, et. al. “Validation of Walkway Slip meters: Establishing a Reference Standard”, J. of Forensic Sciences, Vol. 55, No. 2, March 2010.
- [8] Yakeshi Yamaguchi, et. al., “Effect of Step Length and Walking Speed on Traction Coefficient and Slip between Shoe Sole and Walkway”, Tribology Online, vol. 3 no. 2, 2008.
- [9] Rachel A. Brady, et. al, “Foot Displacement but not velocity predicts the outcome of a slip induced in young subjects while walking”, J. of Biomechanics, vol. 33, 2000.
- [10] C.M. Powers, et. al. “Assessment of Walkway Slip meter Reading in Evaluating Slip Resistance: A Gait-Based Approach”, J. of Forensic Sciences, Vol. 52, No. 2, March 2007.
- [11] Report of ASTM F2508 validation of the ENGLISH XL VIT Base-Model variable incidence/articulated strut slip meter with standard XL VIT non-treaded test foot and standardized test foot preparation device  
<http://www.excelslipmeters.com/uploads/download/XL%20VIT%20Base-Model%20F2508%20Std%20Foot%20Validation%20Report.pdf>  
<http://www.excelslipmeters.com/uploads/download/XL%20VIT%20with%20Sequencer%20F2508%20Std%20Foot%20Validation%20Report.pdf>
- [12] Slip meter Certification (Mark IIIB)  
[http://www.slip-test.com/Slip-Test\\_MarkIIIB\\_F2508\\_Certification.pdf](http://www.slip-test.com/Slip-Test_MarkIIIB_F2508_Certification.pdf)
- [13] Copy of ASTM F2508-11 RESULTS DATA COLLECTION TABLE. DATE: SEPT. 6-7, 2011. METHOD: WET DCOF/SBR\*/8 INCH. TEMP: 75.3 F. RH: 29%. TILE A. TILE B. TILE C. TILE D.  
<http://s159433513.onlinehome.us/ASTM%20F2508%20Results%20BOT-3000.pdf>
- [14] Zurich “A Comparison of two slip meters”, Risktopic 4-3.010 October 2012
- [15] Kill v. City of Seattle  
<http://www.zurichservices.com/ZSC/REEL.nsf/e7d01e983421df7fc125710e00503352/940489e7eefcfabc1257a910061185e!OpenDocument&ExpandSection=1>

## APPENDIX I – LIST OF STANDARDS

### ASTM Standards

1. F609-05(2013)- “Standard Test Method for Using a Horizontal Pull Slipmeter (HPS)”
2. F462 - 79(2007) - “Standard Consumer Safety Specification for Slip-Resistant Bathing Facilities”
3. F695 - 01(2009) - “Standard Practice for Ranking of Test Data Obtained for Measurement of Slip Resistance of Footwear Sole, Heel, and Related Materials”
4. F1240 - 01(2009) - “Standard Guide for Ranking Footwear Bottom Materials on Contaminated Walkway Surfaces According to Slip Resistance Test Results”
5. F1637 - 13 - “Standard Practice for Safe Walking Surfaces”
6. F1646 – 13 - “Standard Terminology Relating to Safety and Traction for Footwear”
7. F1694 - 14 - “Standard Guide for Composing Walkway Surface Investigation, Evaluation and Incident Report Forms for Slips, Stumbles, Trips, and Falls”
8. D2047 – 11 - “Standard Test Method for Static Coefficient of Friction of Polish-Coated Flooring Surfaces as Measured by the James Machine (lab use) “
9. F2048-00(2009) - “Standard Practice for Reporting Slip Resistance Test Results”
10. F2913 - “ Standard Test Method for Measuring the COF for Evaluation of Slip Performance of Footwear and Test Surface/Flooring Using a Whole Shoe Tester”
11. D5859 - “Standard Test Method for Determining the Traction of Footwear on Painted Surfaces Using the Variable Incident Tester (Withdrawn 2005) “
12. F2508-13 - “Standard Practice for Validation, Calibration, and Certification of Walkway Tribometers Using Reference Surfaces”
13. E303-93(2013) - “ Standard Test Method for Measuring Surface Frictional Properties Using the British Pendulum Tester”

### ANSI standards

1. A137.1 - “Tile Slip Test”
2. A1264.1 - “Safety Requirements for Workplace Walking/Working Surfaces and their Access; Workplace, Floor, Wall and Roof Openings; Stairs and Guardrails System”
3. A1264.2 - “Standard for the Provision of Slip Resistance on Walking/Working Surfaces”
4. A1264.2 - “Provision of Slip Resistance on Walking/Working Surfaces”
5. B101.1 - “Test Method for Measuring Wet SCOF of Common Hard-Surface Floor Materials”
6. B101.3 - “Test Method for Measuring Wet DCOF of Common Hard-Surface Floor Materials”

### ASTM withdrawn Standards

1. F489-96e1 - “Standard Test Method for Using a James Machine (Withdrawn 2005) “
2. F1677-05 - “Standard Test Method for Using a Portable Inclineable Articulated Strut Slip Tester (PIAST) (Withdrawn 2006) “
3. F1678-96 - “Standard Test Method for Using a Portable Articulated Strut Slip Tester (PAST) (Withdrawn 2005) “
4. F1679-04e1 - “Standard Test Method for Using a Variable Incidence Tribometer (VIT) (Withdrawn 2006) “
5. D5859-96e1 - “Standard Test Method for Determining the Traction of Footwear on Painted Surfaces Using the Variable Incidence Tester (Withdrawn 2005) “
6. C1028-07e1 - “ Standard Test Method for Determining the Static Coefficient of Friction of Ceramic Tile and Other Like Surfaces by the Horizontal Dynamometer Pull-Meter Method (Withdrawn 2014) “
7. F802-83(2003) – “Standard Guide for Selection of Certain Walkway Surfaces When Considering Footwear Traction (Withdrawn 2012) “

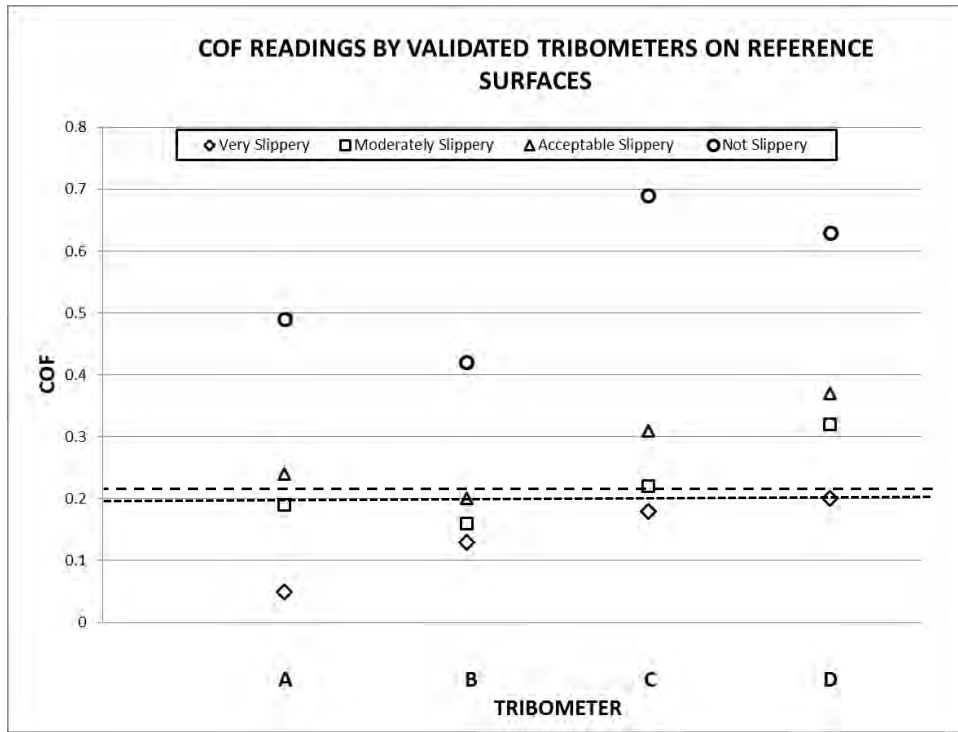


Figure 1: COF measurements of the reference surfaces by the 4 validated tribometers.

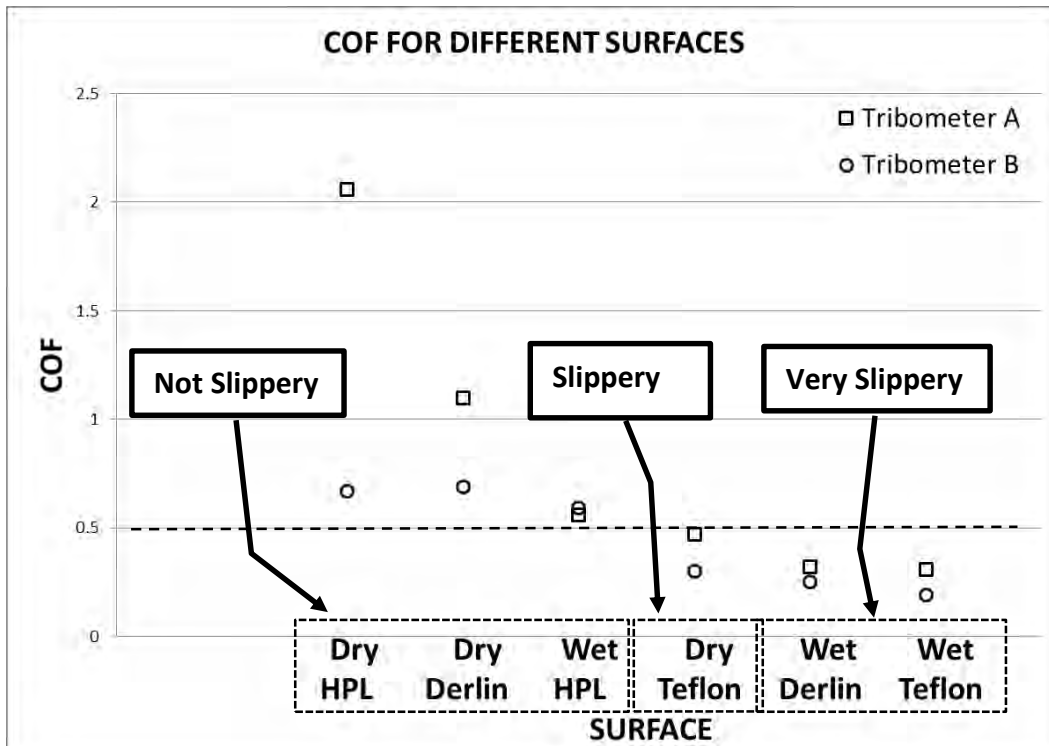
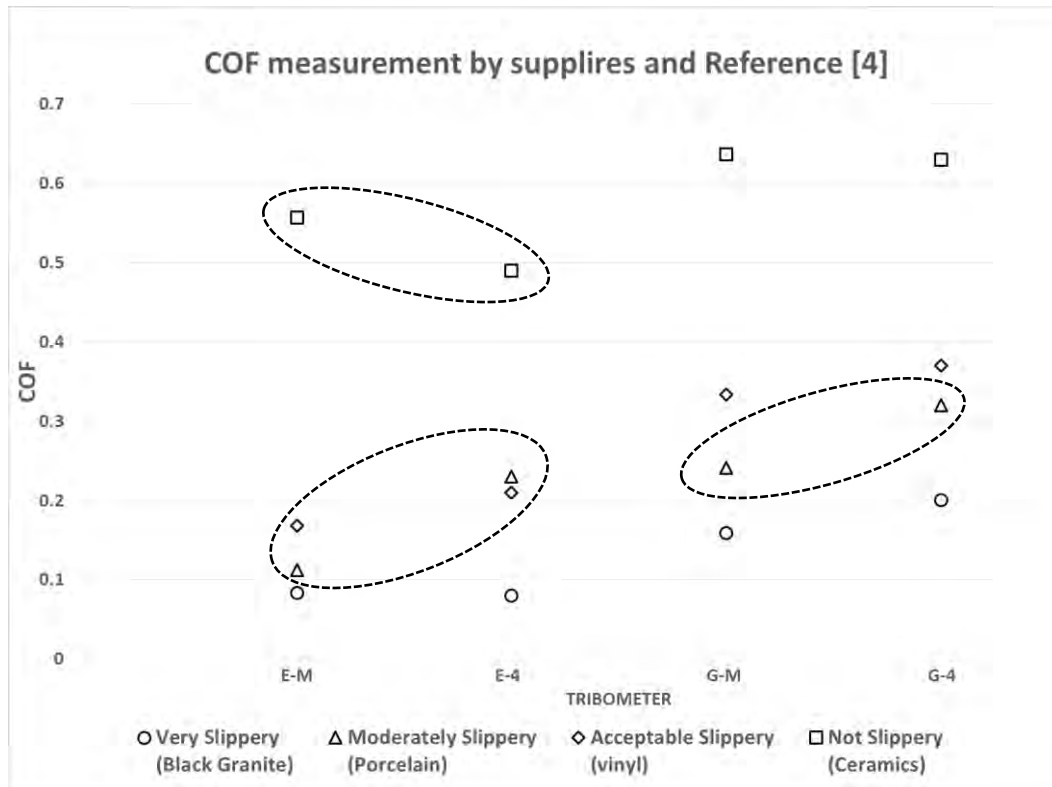


Figure 2: COF measurements of the reference surfaces by the 2 validated tribometers.



Figure 3: Tests' results performed by the suppliers in order to validate their tribometers.



**Figure 4: Manufacturers' tests results compared to the results in [4].**

(E-M – Tribometer E - supplier's results

E-4 - Tribometer E - Ref. 4 results

G-M – Tribometer G - supplier's results

G-4 - Tribometer G - Ref. 4 results)

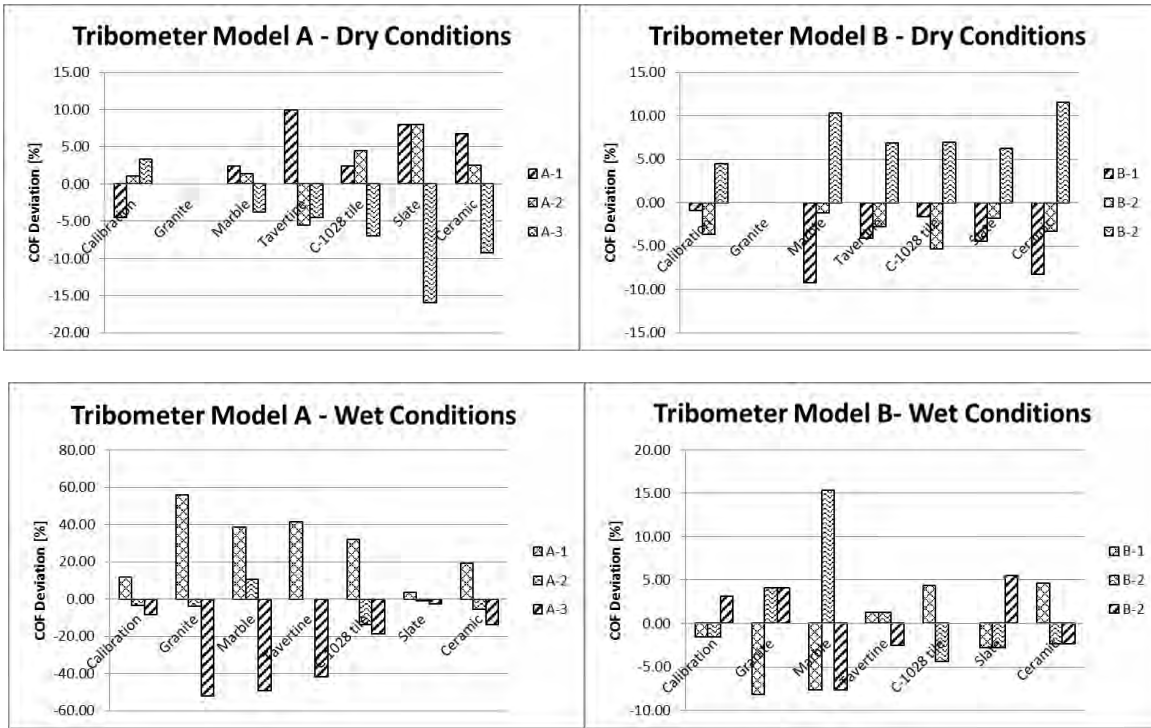


Figure 5: Deviation of the tribometers reading relative to the mean value of COF obtain by the total readings of the three tribometers of the same model.

# CubeSat Thermal Analysis

Pradeep Shinde, Alvaro Quintero, Ibrahim Tansel, Sabri Tosunoglu

Department of Mechanical and Materials Engineering  
Florida International University  
10555 West Flagler Street  
Miami, Florida 33174

pshinde@fiu.edu, aquin061@fiu.edu, tanseli@fiu.edu, tosun@fiu.edu

## ABSTRACT

A complete thermal analysis on picosatellites is of most importance because it helps in the development of thermal control system that can protect the satellite's internal systems from the extreme condition of outer space. Lack of a properly designed thermal control system could potentially mean the failure of the mission. Budget constraints in the design of the NEESAT-1U picosatellite, lead the team to implement passive thermal control systems on their CubeSat. In this paper, various materials have been considered for implementation as a thermal insulator. These materials have been evaluated by numerical methods. Best performing material was then evaluated using one-dimensional heat conduction to find the appropriate thickness needed to maintain the internal components at a safe operating temperature.

## Keywords

Passive thermal control, Thermal insulation, CubeSat.

## NOMENCLATURE

$q_s$	Solar Radiation, $W/m^2$
$q_e$	Earth's IR Radiation, $W/m^2$
$q_a$	Albedo Radiation, $W/m^2$
$G_s$	Solar Constant, $W/m^2$
$\alpha_s$	Absorbance of material, Dimensionless
$\phi$	Angle between surface normal vector and direction of solar rays, Degrees
$\theta$	Angle between surface normal vector and direction of solar rays, Degrees
$q_e$	Earth's IR Radiation, $W/m^2$
$\sigma$	Stefan Boltzmann Constant, $5.67e8, W/(m^2*K^4)$
$T_e$	Effective Black Body Temperature, $K$
$F_e$	View Factor
$R$	Resistance of the Material, $(m^2*K)/W$
$L$	Thickness of the Material, $m$
$K$	Thermal Conductivity of the Material $W/(m*K)$
$A$	Area, $m^2$
$Q_{in}$	Heat Flux into the System, $w/m^2$
$T_{out}$	Temperature on the Outer Surface, $K, C$
$T_{in}$	Temperature on the Inner Surface, $K, C$

## 1. INTRODUCTION

A 1U CubeSat is a small satellite measuring 10cm x 10cm x 10cm with a maximum weight of 1.33kg, these satellites have gained popularity among the researchers, universities, and schools across the world due to their short development time and low cost [1]. The CubeSat project began as a collaborative effort between Prof. Jordi Puig-Suari at California Polytechnic State University (Cal Poly), San Luis Obispo, and Prof. Bob Twiggs at Stanford University and it was intended to standardize the development and construction of microsattellites [2]. There are many different sub sections involved in the development of a CubeSat. The RoarSat team at Florida International University (FIU), have already completed a study on the development of an attitude control system used in their microsattelite [3]. Following their steps and aiming to assist future teams in the development of CubeSat, the NEESAT-1U team conducted this study on the thermal control system of a CubeSat. Micro and Nano-satellites with their low thermal capacitance are vulnerable to rapid temperature fluctuations [4], which creates the need for a thermal control system that can protect the internal components of the satellite from the extreme conditions of the Lower Earth Orbit (LEO). This issue has been approached by many researchers in the past from different angles [5,6,7], for instance, by development of numerical methods capable of analyzing the thermal behavior of a nanosatellite in LEO [5], or by creating new panel configuration capable of managing the radiation energy coming into the CubeSat Systems [7]

## 2. THERMAL CONTROL SYSTEM

A thermal analysis on our CubeSat is of most importance because it helps in the development of thermal insulation that can protect the satellite's internal systems from the extreme condition of outer space. The lack of a property designed thermal layer, could potentially mean the failure of the mission since there is an elevated risk of damaging the internal components. Due to the budget constraint, it was decided to come up with a passive thermal control that can satisfy the mission requirements. In this section, various materials will be considered using analytical methods and simulations.

### 2.1 Environment

For analytical thermal insulation calculations, it is important to state the operation conditions of a CubeSat. One of the most common orbits where nanosatellites are being launched is at a reference altitude of 600km, 97.8° inclination Sun Synchronous

Low Earth Orbit [8], for simplification of these calculations in this study, an angle of 0° inclination is assumed.

Thermal control is a process of energy management in which environmental heating plays a key role [1]. The first step in obtaining a proper thermal layer was to compute the different fluxes coming into the systems. Due to the lack of a medium, the primary mode of heat transfer in LEO is radiation. Equations 1 to 3 were used to obtain the heat flux value for the primary sources of radiation.

Equation 1 represents, direct solar radiation flux absorbed by a spacecraft surface [9].

$$q_s = G_s \alpha_s \cos \varphi \quad (1)$$

Equation 2 represents the direct Earth IR radiation,  $T_e$  is the effective blackbody temperature of the Earth (255 K on average) [9], and  $F_e$  is the view Factor from the Space craft Surface to the Earth's disk. Due to the huge size difference between the NEESAT-1U and Earth, the View factors was assumed to be 1.

$$q_e = \sigma T_e^4 \alpha_{IR} F_e \quad (2)$$

Finally, Equation 3 details the radiation flux absorbed by the spacecraft surface due to albedo [9].

$$q_a = G_s (AF) \alpha_s F_e * \cos \theta \quad (3)$$

Using the previous equations following heat flux values were obtained.

**Table 1. Sources of heat flux**

Source	Heat Flux (W/m)
Solar Radiation	1366
Albedo	237
Earth's IR Radiation	368

## 2.2 Analytical Design

After researching multiple possible materials that could be used as thermal insulators, Cryogel insulating blankets were selected as a possible insulation for current work. This product is made from Aerogel, a material which has a thermal conductivity of .014 W/m\*k and an extremely low density of 13 g/m<sup>3</sup>. Cryogel has an operating temperature of -200 °C to 200 °C [10] making it a very light and affordable selection.

The next step was to use the concept of one-dimensional conduction through a wall to calculate the appropriate insulation layer thickness.

Equation 4 is used to calculate the thermal resistance (R) of each one of the walls using the thickness of the material (L). The thermal conductivity of the material (K), and area (A), Equation 5 is the heat transfer between the wall form point  $T_{s,1}$  to  $T_{s,4}$ .

$$R = \frac{L}{KA} \quad (4)$$

$$q_x = \frac{T_{s1} - T_{s4}}{\Sigma R_t} \quad (5)$$

$$Q_{in} = \frac{T_{out} - T_{in}}{\frac{L_{in}}{K_{in} * A_a}} \quad (6)$$

Using equation 6 an appropriate thickness of Aerogel was found for each one of the three radiation sources.

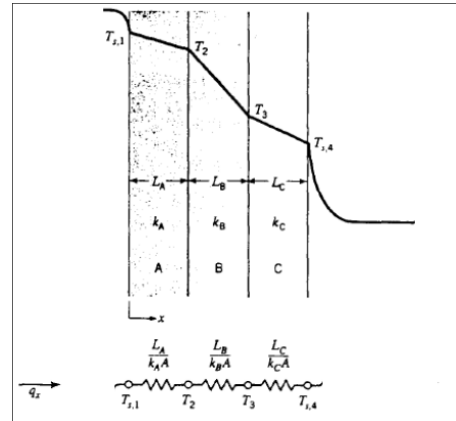


**Figure 1. Thermal Resistance Across Multiple Layers**

## 3. NUMERICAL APPROACH

### 3.1 Simulation Scenarios

To select a suitable insulation material that could satisfy the thermal requirement of mission at LEO, a selection of three materials was compiled for a finite element analysis. Table 1 displays the materials selected and their properties.

**Table 2. Material Properties**

Material	K (W/mk)	$\rho$ (kg/m <sup>3</sup> )	Cp (J/kg.K)	Max service temp (C)	Source
Aerogel	0.014	1100	Not Available	200	buyaerogel.com
Polyurethane	0.19	130	1760	100	Matweb.com
Polyimide	0.0657	596	Not Available	300	Matweb.com

To simplify the analysis and with the requirement that a thermal control system should be able to maintain an appropriate temperature inside a CubeSat, even when exposed to a large heat flux, a single insulation panel was modeled. Such panel, simulates the surface of a 1U CubeSat wall, an arbitrary thickness of 2 mm was used for this model. Next, a material from table 1 was added to the model, and an initial temperature of 20°C was applied to inner surface. Finally, a heat flux of 1366 W/m was applied to the outside surface simulating a 100% exposure to solar radiation.

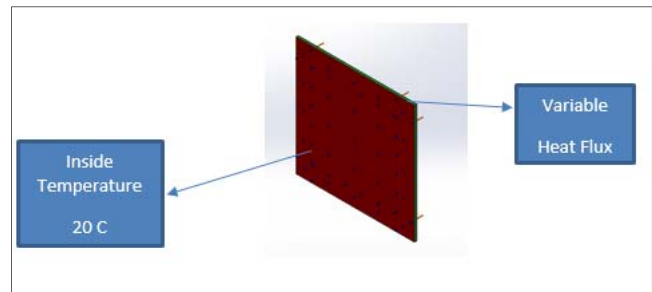


**Figure 2. General Set Up for Steady State Simulation**

The best performing material was then, put through a different study, where the thickness obtained using analytical methods for

the highest heat flux, was compared to a larger and a smaller thickness, to analyze their response to an incoming heat flux.

### 3.2 Computational Details

SolidWorks 2016 software was used to complete the thermal study for the materials and appropriate thickness for insulation layer. To increase the result's accuracy from the study, the following mesh controls were applied to the simulation. A solid fine mesh was used with an element size of 2.44 mm with a tolerance of 1.44 mm. The under-relaxation factor was set as automatic and the convergence tolerance was set to  $10 \times 10^{-6}$ . Other parameter used in this simulation are listed in figure 3.

Mesh Details	
Study name	Hot Case [-Default-]
Mesh type	Solid Mesh
Mesher Used	Standard mesh
Automatic Transition	Off
Include Mesh Auto Loops	Off
Jacobian points	4 points
Mesh Control	Defined
Element size	2.88444 mm
Tolerance	0.144222 mm
Mesh quality	High
Total nodes	519024
Total elements	331691
Maximum Aspect Ratio	3.496
Percentage of elements with Aspect Ratio < 3	100
Percentage of elements with Aspect Ratio > 10	0
% of distorted elements (Jacobian)	0
Time to complete mesh(hh:mm:ss)	00:01:20
Computer name	ALVAROLT

Figure 3. Mesh Details

## 4. RESULTS AND DISCUSSION

After completing all analytical calculation for the different scenarios, the values obtained are shown in Table 3, they represent the appropriate thermal insulation thickness for a 1U CubeSat at various heat fluxes. Since the primary concern is an elevated temperature damaging the inside components inside the satellite, the insulation for the largest heat flux solar radiation has been chosen because it protects the satellite at the worst-case scenario.

Table 3. Calculated Insulation Thicknesses

Source (W/m)	Insulation Thickness(mm)
Solar Radiation	1.84
Albedo	10.6
Earth's IR	6.85

The results from the steady state simulation demonstrated that Aerogel material was a suitable candidate as the thermal insulator, it was evident that it dissipated energy better than any the other three materials as shown in Table 4 and Figure 3.

Table 4. Numerical Solutions Results

Material	$T_{in}$ (K)	Flux ( $W/m^2$ )	Thickness (mm)	$T_{out}$ (K)	$T_{out}$ (C)
Aerogel	293	1366	2.0	488.1	214.95
Polyurethane	293	1366	2.0	307.4	34.25
Polyimide	293	1366	2.0	334.6	61.45

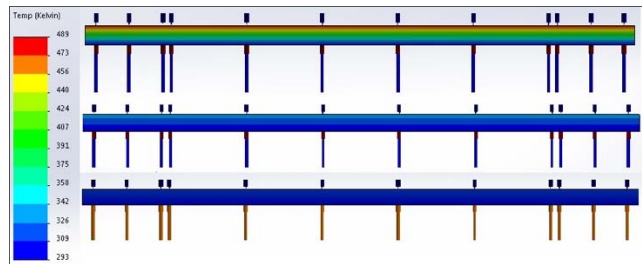


Figure 4. Thermal Dissipation Across Insulation Material: Top – Aerogel, Middle – Polyimide, Bottom – Polyurethane

Finally, the thicknesses found by analytical solution and the best performing material form the simulation were combined to verify how the different thicknesses responded to an incoming flux. Table 5 shows how larger thickness increases the outside temperature to a value greater than the maximum operation temperature of an Aerogel material. This table also shows how a smaller thickness has a lower outside temperature meaning that it does not provide thermal barrier better than the analytical thickness and therefore allowing the external radiative flux to raise the internal temperature of the satellite.

Table 5. Aerogel Thickness Performance

Flux ( $w/m^2$ )	Thickness (mm)	$T_{in}$ (K)	$T_{out}$ (K)	$T_{out}$ (C)
1366	5	293	781	507.85
1366	1.84	293	472.7	199.55
1366	1	293	390.7	117.55

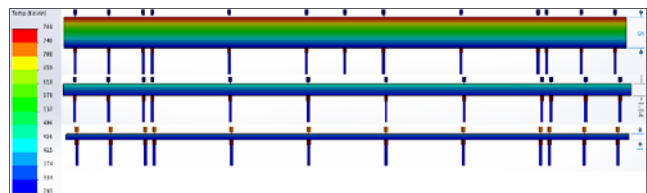


Figure 5. Thermal Dissipation across Different Thicknesses: Top – 5mm, Middle – 1.84 mm, Bottom – 1 mm

It is recommended to further validate these results through a vacuum chamber test, where a 1U CubeSat prototype can be exposed to the conditions prescribed in this paper and the results for such test should be compared to those presented in this study.

## 5. CONCLUSION

In this study, a thermal analysis was conducted for the development of a passive thermal control system that could satisfy the requirement for a CubeSat mission in the LEO. To accomplish this, the study first, establishes the environmental conditions to which a CubeSat might be exposed to. Next, one-dimensional thermal resistance equation was solved to find an appropriate thermal insulation layer thickness.

Different materials were analyzed using finite element methods, and the best candidate as an insulator for a 1U CubeSat was selected. Later, the thickness of the best performing material was optimized using the results obtained from the analytical calculations. It was demonstrated that a thickness larger than the 1.84 mm, would provide better thermal resistance raising the temperature of the outside surface of the insulation. Whereas, a smaller thickness than the optimum, could not provide the required thermal barrier and allow to raise the internal satellite temperature resulting in the mission failure.

It is also important to study the effect of the infiltrating external radiation on the satellites internal component to ensure the mission success for the satellite lifetime. Vacuum thermal bake studies will be suggested to study the outgassing of the components.

## 6. ACKNOWLEDGMENTS

The authors of this study, intend that the results obtained and presented in this paper can be used for the development of CubeSats at FIU. The authors would like to acknowledge the support of the Department of Mechanical Engineering at FIU and to the reviewers who assisted with the improvement of this paper with their timely remarks. Finally, the authors would like to extend their thanks to the Near Earth Explorer (NEE) Club and the students involved in the club, who will continue the work by testing the thermal control system proposed in this paper.

## 7. REFERENCES

- [1] Bulut, M., & Sozbir, N. (2014). *Analytical investigation of a nanosatellite Panel surface temperatures for different altitudes and panel combination*. Elsevier B.v.
- [2] Home. (n.d.). Retrieved April 23, 2017, from <http://www.cubesat.org/>
- [3] Shinde, P., Newman, E., Tansel, I., & Tosunoglu, S. (2016). Design of FIU FUNSAT System: Attitude Control for the 3U CubeSat.
- [4] Cao, S., Chen, X., Wu, G., Yang, J., Wang, R., Shang, K., & Wang, L. (2011). *Variable Emissivity Surfaces for Micro and Nano-Satellites*. Elsevier B.V.
- [5] Corpino, S., Caldera, M., Niclele, F., Masoero, M., & Viola, N. (2015). *Thermal Design and Analysis of a Nanosatellite in Low Earth Orbit*. Elsevier B.V.
- [6] Escobar, E., Diaz, M., & Zagal, J. (2016). *Evolutionary Design of a Satellite Thermal Control system: Real Experiments for a Cubesat Mission*. Elsevier B.V.
- [7] Sugawara, Y., Nakasuka, S., Higashi, K., Kobayashi, C., Koyama, K., & Okada, T. (2009). *Structure and Thermal Control of Panel Extension Satellite (PESAT)*. Elsevier B.V.
- [8] Selcan, D., Kirbis, G., & Kramberger, I. (2016). *Nanosatellites in LEO and beyond: advanced radiation protection techniques for COTS-based Sapecraft*. Elsevier B.v.
- [9] VanOutryve, C. (2008). *A Thermal Analysis and Design Tool for Small Spacecraft*. ProQuest LLC
- [10] Cryogel@ Z Blanket. (n.d.). Retrieved April 23, 2017, from <http://www.buyaerogel.com/product/cryogel-z/>

# Design of a 3D Printable Time Simulating Solar System Model

Mark B. Moffett, Pierre Larochelle

Robotics and Spatial Systems Laboratory  
Florida Institute of Technology  
150 W University Blvd  
Melbourne, FL 32901

mmoffett2015@my.fit.edu, pierrel@fit.edu

## ABSTRACT

The previous paper presented at the 2016 FCRAR discussed the research topic of creating time simulating solar system models. This paper is an overview of the work done over the passed year in solar system model creation and the potential future work in STEM education. The use of designed tools to assist with relating abstract ideas to reality is now a possibility with the use of the modern manufacturing method of 3D printing. A 3D printed solar system model was designed and printed. Research was conducted to relate the history of mechanical engineering and the solar system to STEM education through the use of the solar system model. The inner four planets' natural orbital periods with respect to Earth were modeled in SolidWorks and then fabricated using 3D printing. A 3D printable mechanical time simulating solar system model used in science, technology, engineering, and mathematics (STEM) could assist with the user's understanding of the history of science, planetary orbital mechanics, gearing ratios, 3D printing, and systematically constructing a project using instructions. This paper describes the design of a 3D printable time simulating solar system model and how its construction could be used to teach the history of mechanical engineering and the abstract idea of the solar system. The combination of these two ideas could inspire users to learn, pursue coursework and, eventually, a career in a STEM field.

**Keywords:** STEM Education, Solar System, 3D printing

## 1. INTRODUCTION

The development of the solar system model started with the idea of a project around space science, mechanical systems, 3D printing, and a possibility to make something original on the subject of solar system models. This proposal was published at the FCRAR in 2016 [1] and a master's thesis was completed on the topic [2]. Researching the history and functions of mechanical clocks was a significant area of focus which allowed the project to work as designed. The project had two main research focus points, the first being designing a functional solar system model, the second being how 3D printable systems can be built and function as designed. Tolerances played a large role in the parts meshing properly; more work can be done on the trends and charting of 3D printed tolerances. By expanding the goals of the project to include more than building the solar system, a STEM education

focus with the history of science became a large area that allowed for significant research. Beyond the completion of the project build, a background of where the solar system model came from allowed for a STEM education application. Looking into the background of where a heliocentric system originated led to a journey of the birth of mechanical engineering through the study of the night sky and Sir Isaac Newton's laws of motion. The impact of the work could be seen as a view of where the field of mechanical engineering originated, the study of the planets, and how continuing that study is relevant to current engineers and scientists as well as for STEM education as space programs are planning to send humans to Mars and beyond.

## 2. THE SOLAR SYSTEM

The development of a solar system model required research into mechanical systems that were developed to teach the solar system from the past. There were three main mechanical teaching systems that dominated the science of astronomy until the invention of the telescope in the early 17th century [3]. These three tools allowed for predicting the orbits of moon and planets, telling the time by using the Sun and the date, and teaching visually how the dates are based on the equinoxes, perihelion, and aphelion of the Earth's orbit.

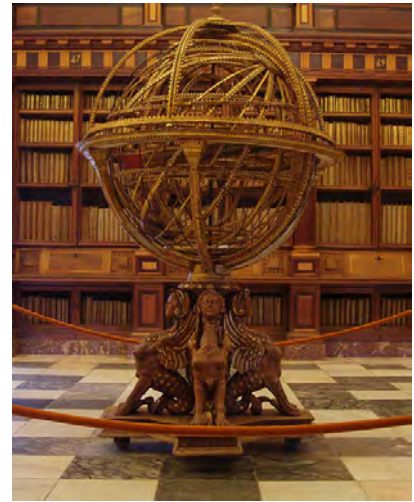
1. **Celestial Globes:** Ptolemy, an authority on the solar system during the 2nd century AD Alexandria, created a celestial globe to teach astronomy [3]. The device can be seen in Figure 1a. This mechanical system was the first proposed mechanical calculator for astronomy capable of making complex spherical triangle calculations of the stars by using physical representation rather than 2D drawn or painted images of the night sky[3].
2. **Astrolabes:** The astrolabe is a mechanical calculator that is similar to a celestial globe in its calculations, but different physically as it uses numbers and dials to display the results as shown in Figure 1b. Astrolabes were used by astronomers and navigators to determine local time using latitude and Sun or planetary positions [3]. The written theories and uses of the astrolabe are accredited to Hipparchus. Although he did not invent the astrolabe, his work in astronomy contributed



(a) Celestial Globe [4]



(b) Astrolabe [5]



(c) Armillary Sphere [6]

Figure 1: Three typical astronomical devices used before mechanical clocks were developed [3]

greatly to understanding the calculations made possible by using the device.

3. **Armillary Spheres:** Armillary spheres were popular among medieval scholars from the 13th century to the 17th century [3]. They are similar to celestial spheres in appearance but focus on the Earth as the center body rather than on the surrounding outer sphere of stars, like that of the celestial sphere. The armillary sphere shows the ecliptic, the tropics of capricorn and cancer, the axial tilt, and many other complications depending on the armillary sphere creator. There are two type of spheres: the Ptolemaic armillary sphere and the Copernican armillary sphere, the former being geocentric and the latter being heliocentric.

These mechanisms track the motion of the planets relative to Earth. They accurately describe the predictable motion of the planets no matter if they are geocentric or heliocentric systems. Figure 2 shows the contrasting views of the solar system models. Since the view of the planets from Earth could interpret the planetary motions as shown in Figures 2a and 2b, it should not be a trivial task to understand the abstract idea of planetary motion. The construction of the solar system model could potentially allow for this idea to bring curiosity and conversation around the history associated with the abstract idea of a heliocentric system.

### 3. THE SOLAR SYSTEM MODEL

The design of the solar system model was driven by the study of mechanical solar system models from *Geared to the Stars* [3] as well as from mechanical devices as shown in Figure 1.

There were three design questions being asked:

1. Can gear ratios similar to the orbital ratios of the planets be determined within resolution restraints of the 3D printer?
2. Once discovered, can a large, functioning gear train system be 3D printed based on the results?
3. Can features be added to the gear train system once it is functioning?

Table 1: Orbital periods from the NASA website [7]

	Mercury	Venus	Earth	Mars
Orbital Period	0.241	0.615	1	1.88

Table 3: The gear ratio error

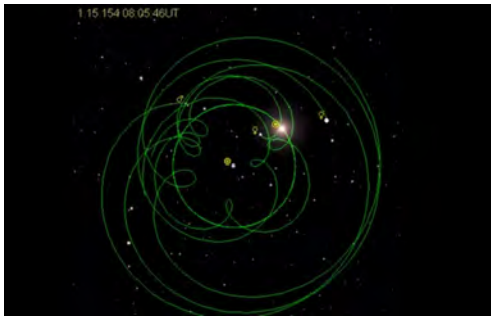
	Goal Ratio	Actual Ratio	Error (%)
Mercury	0.241	0.24064	0.1494
Venus	0.615	0.61497	0.0043
Earth	1	1	0
Mars	1.88	1.88888	0.4723

### 3.1 Planetary Ratios

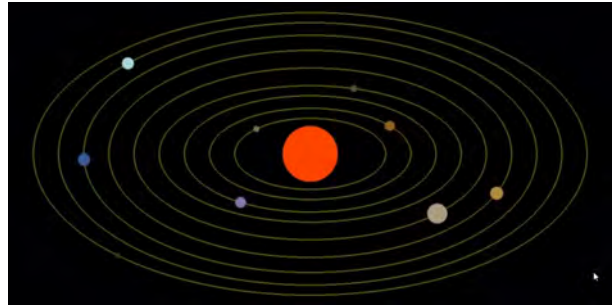
The first design question relies on the naturally occurring planetary ratios for the inner four planets. In order to create an accurate representation of the inner four planets, the designed gear ratios between them must be accurate to their actual rotational ratios. Table 1 shows the planetary ratios from NASA's website [7]. These ratios were the basis of synthesizing a 3D printable series of gears to achieve similar numbers. Table 2 shows the developed algorithm to arrive at the desired gear ratio. The driving number of 22 teeth for the Earth stayed consistent as the systematic path was followed to achieve the desired NASA planetary gear ratios as shown in Table 2 and to complete the first design question.

The mathematics behind determining an effective gear ratio uses the principle of working from the goal and finding a suitable gear ratio near an integer. Since there are limitations when working with integer gear teeth, this approach allowed for a minimal amount of error despite the additive manufacturing method used. The following equation describes how the gear ratio is calculated.

$$\prod_{i=1}^n \frac{\text{driven}}{\text{driver}_i} \dots \frac{\text{driven}}{\text{driver}_n} = \text{ratio} \quad (1)$$



(a) The geocentric model



(b) The heliocentric model

Figure 2: The geocentric and heliocentric models of the solar system

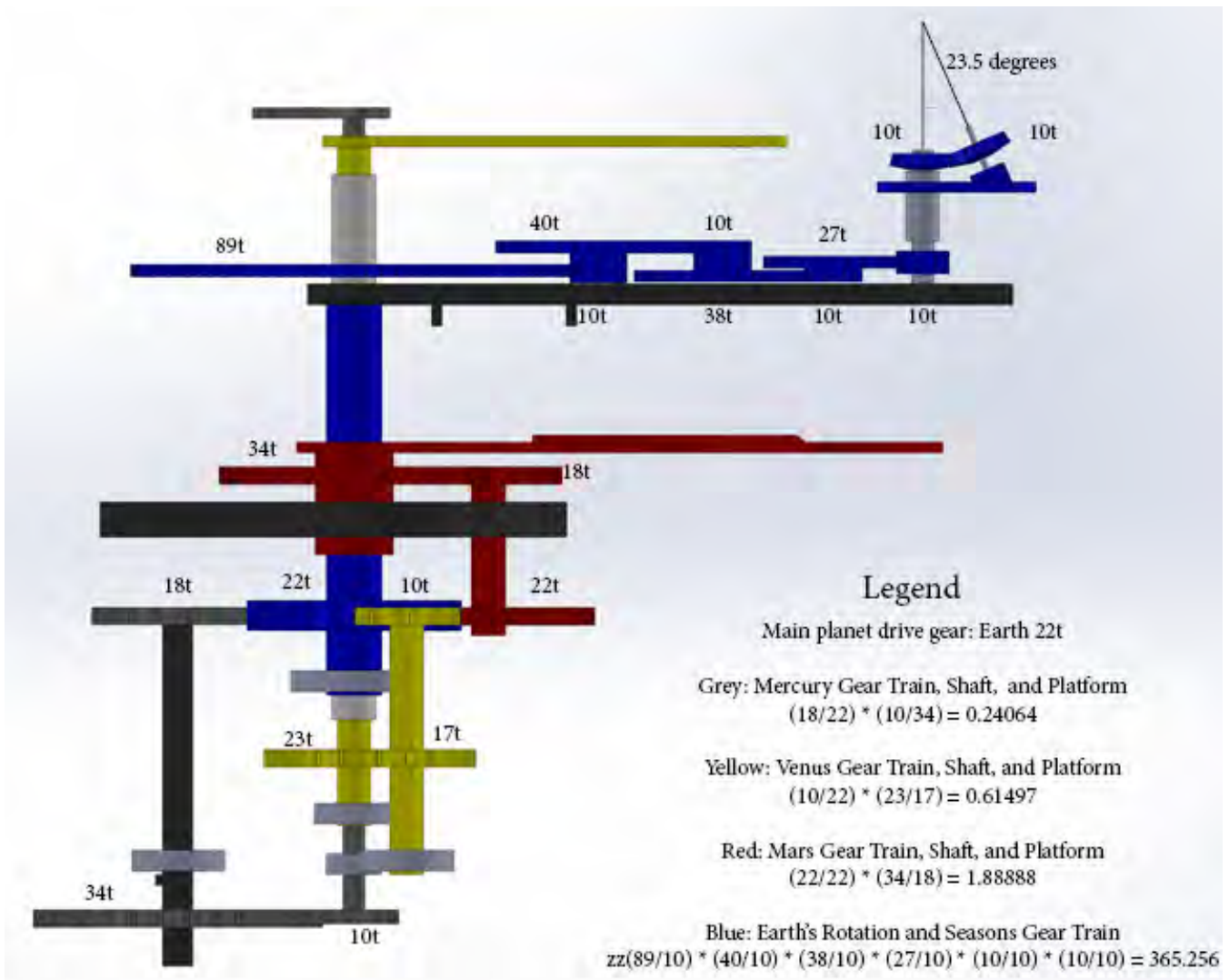


Figure 3: The gears, their teeth numbers, and how the gear train system is connected



Figure 4: The parts used to create a full build are shown

Table 2: The method of calculating the gear teeth numbers in the gear trains

Gear Ratio Solution				Formula				
Goal: 1.88	Mechanical Period			Goal: 1.88				
Driver	Driven	Driver	Driven					
Earth	Mars	Pinion	Gear	Earth	Mars	Pinion	pinion	
22	22	18.0851063829787	34	1.888888888888889	22	22	$=(22*34)/(1.88*22)$	34
	Final: 18				Final: 18			
Goal: 0.615	0.614973262032086			Goal: 0.615				
Earth	Venus	Pinion	Gear	Earth	Venus	Pinion	gear	
22	10	16.99926	23	0.614973262032086	22	10	$=(10*23)/(0.615*22)$	23
	Final: 17				Final: 17			
Goal: 0.241	0.240641711229947			Goal: 0.241				
Earth	Mercury	Pinion	Gear	Earth	Mercury	Pinion	gear	
22	18	33.949	10	0.240641711229947	22	18	$=(18*10)/(0.241*22)$	10
	Final: 34				Final: 34			

The Venus gear train calculation will be shown as an example. The velocity ratio of the planets with respect to Earth is the goal of the gear train. By keeping the error to a minimum, the gear trains will closely mimic the actual movement of the planets with respect to Earth.

### Example

Ratio of Earth to Venus's orbital period: 0.615  
 Goal = find driver gear teeth number on second gear/pinion portion as shown in Equation 1:

$$\frac{10}{22} * \frac{24}{goal} = 0.615 \quad (2)$$

Rearranging the above equation leads to a solution to the goal:

$$\frac{10}{22} * \frac{24}{0.615} = goal = 17.738 \quad (3)$$

As can be seen, the determined number is near not near an integer solution. Rounding up to 18 would produce a significant error in the goal period ratio of 0.615. The driven gear tooth amount is changed from 24 to 23:

$$\frac{10}{22} * \frac{23}{0.615} = goal = 16.999 \quad (4)$$

The value found is near an integer value, albeit not perfect, but near for the purposes of this integer based solar system model. This iterative process of finding a near integer was used to create the gear trains for all of the planets as shown in Table 2. The error created from the Venus gear train ratio is shown below:

$$\frac{NASA \text{ period value} - approximate \text{ value}}{NASA \text{ period value}} * 100 = error$$

$$\frac{0.615 - 0.614973}{0.615} * 100 = 0.0043 \% \text{ error} \quad (5)$$

A summary of the error of each of the ratios can be found in Table 3.

### 3.2 Gear Trains

To answer the second research question, more than a 3D CAD model was required to test the functionality of the gear trains.

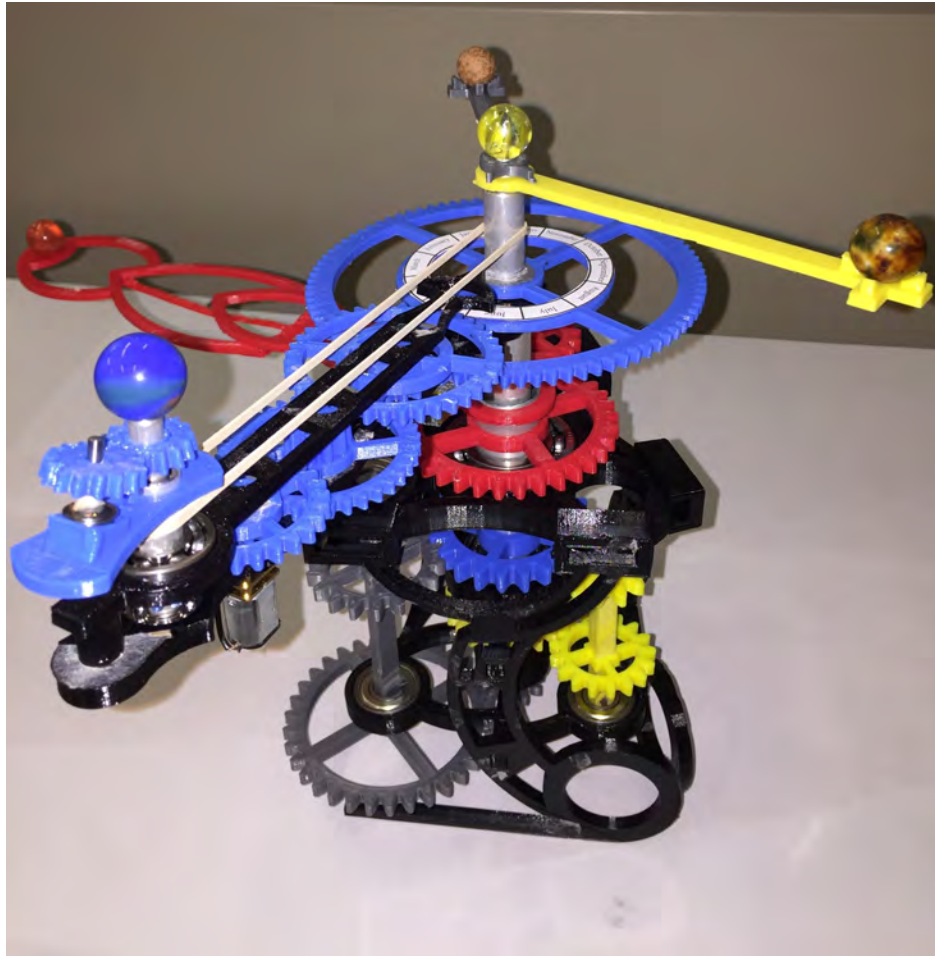


Figure 5: The fully built 3D printed solar system model

Figure 3 shows the layout of the gear trains. The system consists of four gear trains working together to move the planets around the Sun. There is one primary driving gear called Earth\_22t. This gear simultaneously drives the three other planetary gear trains: Mercury, Venus, and Mars. This method of supporting the gears through 3D printed shafts and bearings allowed for the second research about 3D printing a functioning system question to be answered.

### 3.3 Features

The solar system model has two features that allow it to give additional planetary data. A feature is an added subsystem to the gear trains that gives additional meaning to the overall output. The main output of the system is the orbital rotations of the inner four planets. The two additional subsystems are the day rotation and the seasonal tilt of the Earth. The Earth rotation can be seen in the upper right corner of Figure 3. In order to achieve the 365.25 gear ratio of the Earth rotation per year, a similar technique shown in Table 2 was used to determine the gear train teeth values.

The second feature was the addition of the season tilt of the Earth. Earth is tilted 23.5 degrees as it orbits about the Sun. This tilt is always facing the same direction; it does not always face the Sun. The feature necessary to achieve this required a one to one ratio between the Earth's rotation and the center shaft. This would

allow the tilt to maintain its position as it orbits about the Sun. The top right section of Figure 3 shows the platform and the concentric tubes which are then connected via belt. The implementation of these two features solved the final design question about adding features to the solar system model.

### 3.4 Printing and Assembly

The solar system model was printed using PLA filament and standardized settings across all parts on a Wanhao Duplicator 4 3D printer. The purpose was to make the parts printable on any hobby level 3D printer. No tools are required for assembly as all of the parts are pressure fitted. Assembly instructions have been created but are too long to be included in the context of this paper.

## 4. USE IN STEM EDUCATION

The solar system model has been developed and is able to be 3D printed and pieced together into a functioning model. The next step is to develop a curriculum combining the history of engineering and science along with the fabrication of the solar system model. Connecting the planetary orbital periods, history, and a modern manufacturing technique into one curriculum could give students an interest in building and learning as the course offers hands on experience which is a notable technique to stimulate curiosity [8].

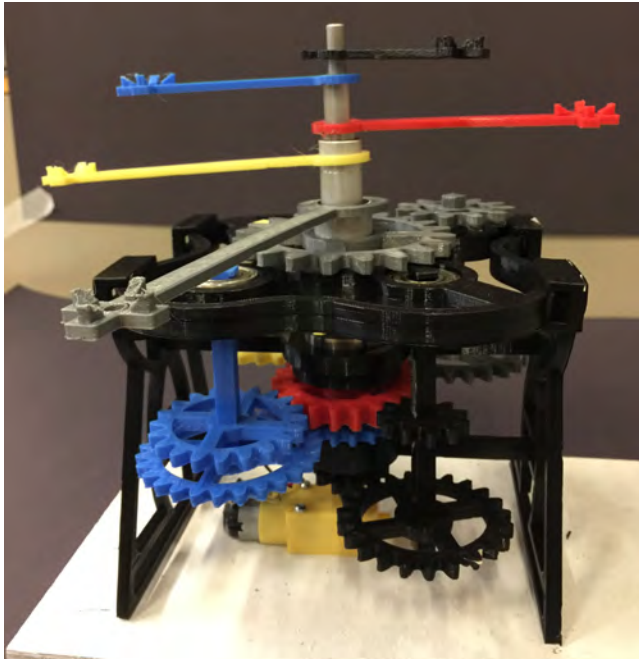


Figure 6: The KOI-500 solar system

Using 3D printing to develop historic experiments for students to handle and learn from could be an effective method of developing and holding interest in STEM fields [8].

## 5. OTHER SOLAR SYSTEMS

### 5.1 KOI-500

The solar system KOI-500 was designed, modeled, and fabricated for the use of a physics student to describe the motion of the planets as shown in Figure 6. Figure 7 shows the ratios that were used to derive the gear trains necessary to design the solar system model.

### 5.2 TRAPPIST-1

TRAPPIST-1 is a solar system discovered by NASA that has 7 earth-like planets. These seven planets are all in the habitable zone about its sun. Figure 8 shows the ratios of the planetary orbits. The model is currently being designed. The status is shown in Figure 9.

## 6. FUTURE WORK

This paper discussed the development techniques required to make a 3D printable solar system model. Techniques to create gear trains that move relative to one another at a specified rate were developed and proven to work effectively. Future work could be to develop even more solar systems using this same technique to give physicists the ability to showcase their work with respect to the orbital mechanics of their solar system of study. The systematic process could be repeated to create the desired solar system as shown in the three examples.

The technique to determine a gear teeth number for the specified ratio is not optimized. A program could be developed to determine the most optimal integer value to achieve the goal ratio. This work is currently being developed.

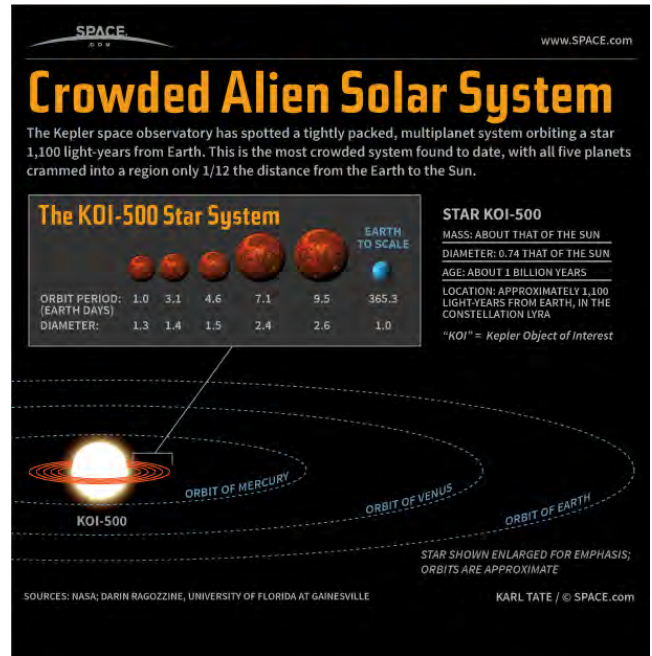


Figure 7: Facts and ratios of the KOI-500 solar system  
 Source: <http://www.space.com/18075-tiny-alien-solar-system-koi-500-planets-infographic.html>



Figure 8: Facts and ratios of the TRAPPIST-1 solar system.  
 Source: <https://en.wikipedia.org/wiki/TRAPPIST-1>



Figure 9: The current status of the TRAPPIST-1 model design

A tolerance table for additive manufacturing could be developed specifically for radial tubing in 3D printed parts. This would be useful for creating pressure fitted gearing on radial tubing. Specifically for this project, it would be useful for fitting the gears onto the tubing as well as for fitting the bearings into their holders. The heating and cooling of the PLA material used in 3D printing causes variances from the designed part based on the thickness, diameter, and width of the outer diameter of the structure. A graph of tolerances reference sheet could lead to a strategic method to prototyping pressure fitted radial parts.

The future work for STEM education would be to test teaching and presentation methods of the solar system model. As this paper discussed the development and background of the solar system model, the next step is to present the model to groups of students and teachers and record their understanding and interest. Systematically discovering the strong and weak points of the presentation would allow for a concise, interactive, and interesting presentation to be developed and performed to promote STEM education.

## 7. CONCLUSION

This paper discussed the background of solar system models, heliocentric and geocentric systems, and the development of a 3D printed solar system model with features. As mentioned previously, there is work to be done to further develop the design process for gear ratio systems. The background of the solar system is linked to the history of mechanical engineering through Newton's laws of motion and gravity which were developed through planetary studies. This STEM education focused work gives an opportunity for students and teachers to learn about 3D printing, the solar system, and the history of engineering and science. To find videos and updates to the 3D printable time simulating solar system model visit the RASSL website at: <http://research.fit.edu/rassl/>

## References

- [1] Moffett M, Laroche P, *Time Simulating Solar System Models* FCRAR Conference 2016 May 12-13, 2016, Florida International University, Miami, FL, USA
- [2] Mark B. Moffett, "*Design of a 3D Printable Mechanical Time Simulating Solar System Model For Use in STEM Education*", master's thesis, Florida Institute of Technology, 2017
- [3] *Geared to the Stars*, Henry C. King 1979. Toronto Press
- [4] Mechanical celestial globe made by Eberhard Baldewein in 1574 in Kassel, Germany. Photograph: Istituto e Museo di Storia della Scienza
- [5] Astrolabe of Jean Fusoris (fr), made in Paris, 1400
- [6] Armillary sphere in monastery of "El Escorial", San Lorenzo del Escorial, Madrid, Spain. Constructed by Antonio Santucci; date of construction circa 1582
- [7] NASA, Dr. David R. Williams [http://nssdc.gsfc.nasa.gov/planetary/factsheet/planet\\_table\\_ratio.html](http://nssdc.gsfc.nasa.gov/planetary/factsheet/planet_table_ratio.html) [Online; accessed: 20-January-2017]
- [8] Michaelis, J.E., & Nathan, M.J. (2015, June). *The four-phase interest development in engineering survey*. American Society of Engineering Education (ASEE 2015) Education Research Methods (ERM) Division. Seattle, WA.

# Design of a Drone with a Robotic End-Effector

Suhas Varadaramanujan, Sawan Sreenivasa, Praveen Pasupathy, Sukeerth Calastawad,  
Melissa Morris, Sabri Tosunoglu

Department of Mechanical and Materials Engineering  
Florida International University  
Miami, Florida 33174

svara008@fiu.edu, ssree005@fiu.edu , ppasu001@fiu.edu, scala007@fiu.edu,  
mmorr009@fiu.edu, tosun@fiu.edu

## ABSTRACT

The concept presented involves a combination of a quadcopter drone and an end-effector arm, which is designed with the capability of lifting and picking fruits from an elevated position. The inspiration for this concept was obtained from the swarm robots which have an effector arm to pick small cubes, cans to even collecting experimental samples as in case of space exploration. The system as per preliminary analysis would contain two physically separate components, but linked with a common algorithm which includes controlling of the drone's positions along with the movement of the arm.

## Keywords

Drone, end effector, autonomous, payload.

## 1. INTRODUCTION

A robot is a machine that is programmable and capable of carrying out a series of complex actions automatically. Robots can be guided by an external control device or the control may be embedded within. Robots may be constructed to take on a human form, but most robots are machines designed to perform a task with little regard to how they look. Robots can be autonomous or semi-autonomous such as Honda's Advanced Step in Innovative Mobility, also known as ASIMO, and TOSY's Ping Pong Playing Robot (TOPIO) which are marvels in the field of robotics. In addition to this there is considerable progress seen in area of industrial robots, medical robots, patient assisting robots, human rehabilitation, athletic training robots, and a whole set of more applications. In addition to land-based robots there is also developments in the bots used for aerospace and marine applications. By mimicking a lifelike appearance or automating movements, a robot may convey a sense of intelligence or thought of its own.

An unmanned aerial vehicle (UAV), commonly known as a drone, is an aircraft without a human pilot aboard. UAVs are a component of an unmanned aircraft system (UAS) which include a UAV, a ground-based controller, and a system of communications between the two. The flight of UAVs may operate with various degrees of autonomy either under remote control by a human operator, or fully or intermittently autonomously by on-board computers. For

example, the widely-used predator drone for military purposes is the MQ-1 by General Atomics which is remote controlled, UAVs typically fall into one of six functional categories (i.e. target and decoy, reconnaissance, combat, logistics, R&D, civil and commercial).

With the advent of aerial robotics technology, UAVs became more sophisticated and led to development of quadcopters which gained popularity as mini-helicopters. A quadcopter, also known as a quadrotor helicopter, is lifted by means of four rotors. In operation, the quadcopters generally use two pairs of identical fixed pitched propellers; two clockwise (CW) and two counterclockwise (CCW). They use independent variation of the speed of each rotor to achieve control. By varying the speed of each rotor, it is possible to specifically generate a desired total thrust, to locate for the center of thrust both laterally and longitudinally, and to create a desired total torque or turning force. In addition to this development, quadcopters were designed to adopt an end effector. In robotics, an end effector is the device at the end of a robotic arm designed to interact with the environment. The exact nature of this device depends on the application of the robot.

In the strictest definition, which originates from serial robotic manipulators, the end effector is the last link (end) of the robot. At this endpoint, the tools are attached. In a wider sense, an end effector is the part of a robot that interacts with the work environment. This does not refer to the wheels of a mobile robot nor the feet of a humanoid robot which are not end-effectors because they are part of the robot's mobility.

End effectors may consist of a gripper or a tool. When referring to robotic end-effectors, there are four broad categories of robot grippers. These are (a) Impactive – jaws or claws which physically grasp by direct impact upon the object, (b) Ingressive – pins, needles or hackles which physically penetrate the surface of the object (used in textile, carbon and glass fiber handling), (c) Astrictive – suction forces applied to the objects surface (whether by vacuum, magneto- or electro adhesion) and (d) Contigutive – requiring direct contact for adhesion to take place (such as glue, surface tension or freezing) [10].

## 2. LITERATURE SURVEY

Mendoza et al. [1] introduced a conceptual design which involved using multiple quadrotors programmed to make use of the yaw movement, linked to each other using a bar containing end effectors as seen in Figure 1. This paper aimed to introduce and spread an extensive mathematical formality that is used to build a new kind of UAV manipulator. The main contribution of this paper was to introduce the possibility of linkages that could be created between two systems.

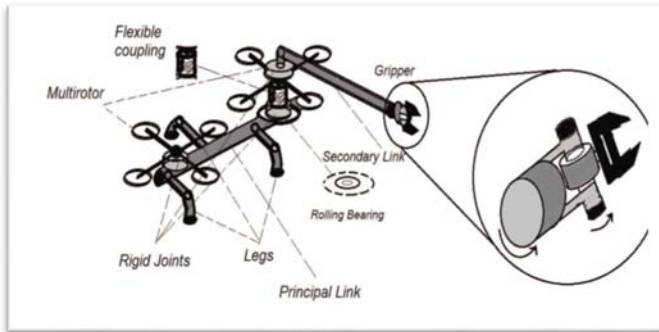


**Figure 1. Air-arm and end-effector**

A parallel manipulator with robustly maintained precise end effector position stowed below a quadrotor UAV used for lifting of light weight mass was developed by Danko et al. [2] They also proposed, constructing a six degree of freedom parallel manipulator which is used to robustly maintain precise end effector positions despite post-UAV perturbations. The parallel manipulator allows for very little moving mass and is easily stored below a quad rotor UAV as can be visualized from Figures 2 and 3.

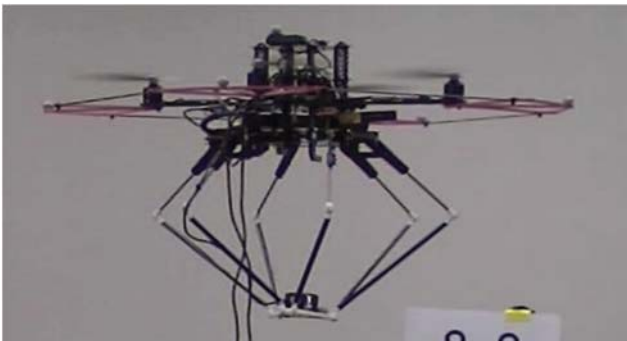


**Figure 2. Parallel manipulator extended**

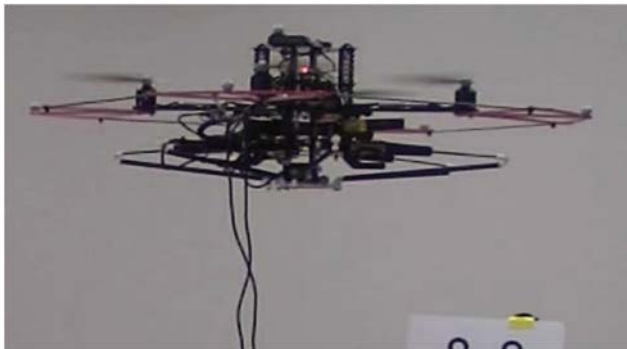


**Figure 3. Parallel manipulator stowed**

Paul et al. [3] introduced the concept of a hyper-redundant manipulator as seen in Figure 4 to be used for the mobile manipulating UAVs. The flexibility of the links was observed by authors when the arm was programmed in MATLAB for moving in the shape of eight as seen in Figure 5 for testing the controllers.

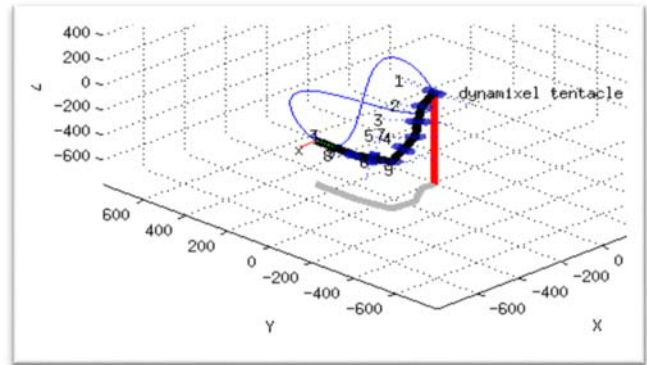


**Figure 4. Hyper redundant arm**

It can be controlled in such a way that links is moved within the arm's free space to help reduce negative impacts on the host platform's stability and the end effector to track environmental objects smoothly despite host platform motions. The hyper redundant manipulator does not include a spherical wrist, even though through preliminary reachability analysis, the manipulator had an improved reachable arm volume by over 20 %.



**Figure 5. Hyper-redundant arm sweeping in the shape of "8"**

Maier et al. [4] discussed about an approach allowing independent control of position and orientation of a UAV, whereby an arbitrary stable attitude controller could be used. The main contribution of this literature was to propose a new control approach for the entire system composed of Vertical Take and Landing (VTOL) UAV and a manipulator. The advantage of the presented approach is that the interaction forces between robots and UAV were considered explicitly and that a Lyapunov stability proof for the UAV subsystem could be derived directly. This approach extends the classical Cartesian impedance controller to account for the UAV's rigid body dynamics.

Zisimatos et al. [5] proposed a robotic hand which is efficient in grasping a series of everyday life objects, is general purpose, and is

validated using series of experimental paradigms. This approach further improves the design of conventional grippers that are commonly used for grasping, both in industry and research due to its low complexity and relatively low cost. The authors introduced a new end effector system capable of lifting heavy weights and with grippers varying from two fingers to four fingers with a weight of 0.088 lb. to 0.53 lb. respectively as seen in Figure 6.



**Figure 6. Different robot hands created using identical modular fingers and the modular fingers basis**

Brown et al. [6] studied the kinematic and dynamic behavior of humans lifting heavy weights and applied it to a robotic arm which was made to lift heavy weights as a part of dynamic task. The authors discussed the kinematic and dynamic behavior of the robot with experimental results.

The results showed that the arm could lift 20 kg mass with the links having kinematics like that of human muscle. This approach uses a new methodology that is dynamic motion control. This technology is applicable not only for lifting but for pulling, peeling and destroying tasks.

Bhope et al. [7] gives an overall review of robot application employed over a period. The paper also provides information on the type of end effector used for fruit picking with pictorial representation as shown in Figure 7.

The robot mentioned in this paper deals with applications such as spraying and motorized weed control, fruit selection and inspecting the farms day and night for an efficient result which in turn reduces the farmer's effort. One of the advantages of the smaller machines employed in agriculture is that they are more satisfactory to the non-farm population.



**Figure 7. Fruit picking robot**

Sarig [8] discusses the technological improvements over the past decade related to fruit picking and the way robots have been programmed to locate the fruit in specified area without any damage to the fruit. The author developed an end effector with six degrees of freedom, having three rotational joints connecting neighboring links to cover the defined workspace. The author has made use of the Puma 560 robot arm which has forward and reverse kinematics whose controls are programmed through MATLAB Robotic Tool Box. The joint angles, velocities and torques of the robot arm were studied during example pick cycles which span the work space of representative peach and orange trees.

In addition to fruit picking robot as specified previously further developments was done by Henten et al. [9] who discussed the specific application of cucumber picking robots and the efficiency of the end effector. The manipulator was designed with seven degrees of freedom. The robot is equipped with computer vision system which could detect more than 95% of cucumbers in a green house. The ripeness of the cucumbers was determined based on the geometric models.



**Figure 8. Vegetable harvest robot in the greenhouse**

### 3. OBJECTIVES OF PROPOSED WORK

The objectives of the proposed drone model are:

1. To help the physically handicapped person pick an object of necessity (Water bottle, food items, fruits etc.) from a far-off distance and bring it to his/her vicinity.

2. To help farmers in harvesting the fruits and vegetables thereby reducing the distance of travel in long fields and on a minor scale help develop automated farming.
3. Along with this the drone can be used to spray fertilizers and pesticides over the crops, thereby reducing health hazards of farmers.

#### 4. MODEL SPECIFICATION

Based on the literature survey conducted, it was found that developing the prototype to suit the purpose of agriculture and domestic application is more effective in this situation as it would reduce the complexity of modeling and would be a significant innovation in the field of automated farming. Modeling of a drone for applications such as military and industrial would be complex.

##### Drone Parameters

1. Number of rotors: 4
2. Wings span: 23.22 in
3. Weight: 1.890 Kg (2.84 lbs.)
4. Electronic Speed controller: 20A
5. Arm material: Acrylonitrile Butadiene Styrene BS – A (ABS)
6. Propeller Material: ABS
7. Payload Capacity: 450 g (0.99 lbs.)
8. Length of arm: 11.81 in
9. Effector radius: 2.36 in

##### Camera Parameters

1. Height in pixels: 3000
2. Width in pixels: 4000
3. Lens focal length in mm: 3.61
4. Lens field of view: 94°

##### Controller

1. Control System: Remote
2. Operating Range: 2000m
3. Controller Frequency: 2.4Hz
4. Controller Voltage: 7.4V

##### Battery

1. Battery Capacity: 7000 mAh
2. Battery type: Lithium Polymer 4S
3. Battery Power: 14.8V

Figure 9 represents the isometric view of the drone that has been modeled considering the specifications as given above. A clear picture of the placement of components has been shown in Figure 10, which shows that the drone has been designed carefully with each component being reserved with spaces meant for them. Figure 11 shows the assembled view of the drone with the end effector arm. The arm is enabled with a 2- DOF link with the effector having a rotational DOF which is equipped with suction cups to hold the payload firmly. Figures 12-17 represent the stress analyses that was performed when the drone was made to carry loads varying in mass and major concentration in the arms. Both displacement and Von-Mises simulation results have been presented with figures indicating that as the load increases, the displacement in the drone's arm increases and hence leading to the conclusion that a restricted amount of load can be carried. The arm could be manufactured using 3D printing technology and could be time-consuming and

costlier than the conventional method wherein the arms are built using traditional manufacturing methods which is even more time consuming but less costly when compared to former. It is important to note that most of the products that will be used for prototyping the proposed model are 3D printed.

#### 4.1. Prototype Modeling



Figure 9. Isometric view of the drone

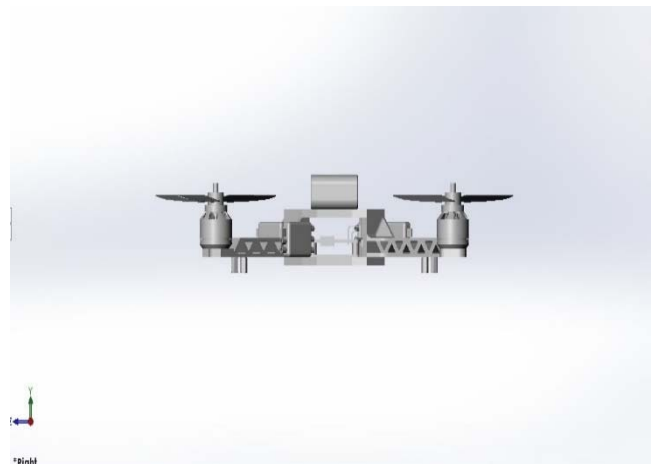


Figure 10. Right view of the drone

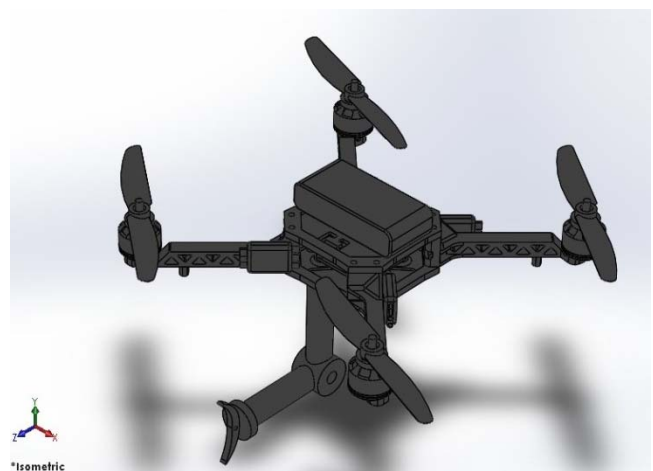


Figure 11. Assembled view of the drone

### 4.2.1 Displacement simulation results

The figures shown below indicate the displacement of the drone arm with increase in the mass of the payload lifted. The payload masses range from 0.75 N to 3N with intervals of 0.75 N.

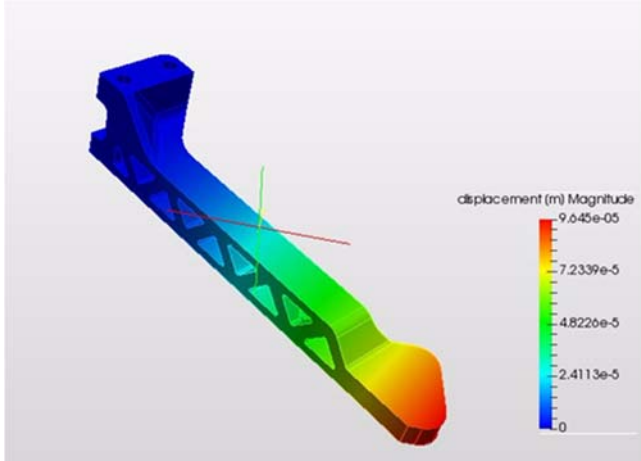


Figure 12. Displace results for 0.75 N

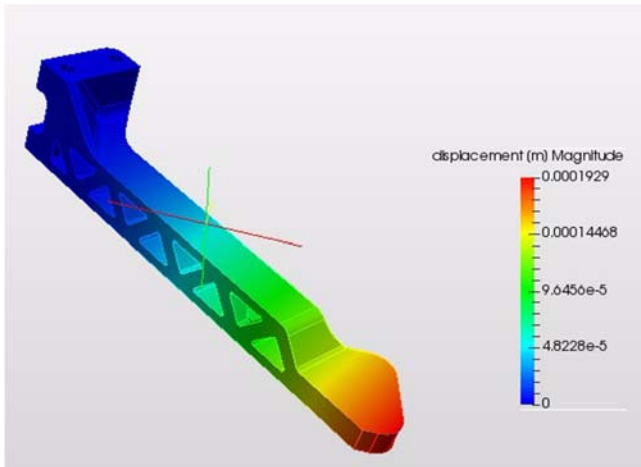


Figure 13. Displacement for 1.5 N

Figure 12 and 13 show the displacement for 0.1686 lbs. and 0.3372 lbs. respectively. Figure 12 shows that the load factor near the propeller region is critical. As the motor provides downward thrust, the beam must withstand the thrust near the propeller. When the analysis was carried out for 0.1686 lbs., the value of displacement obtained was about  $9.645 \times 10^{-5}$  m. The factor of safety of the ABS material is about 2.5. Similarly, for 0.3372 lbs. the displacement obtained was about 0.001929 m.

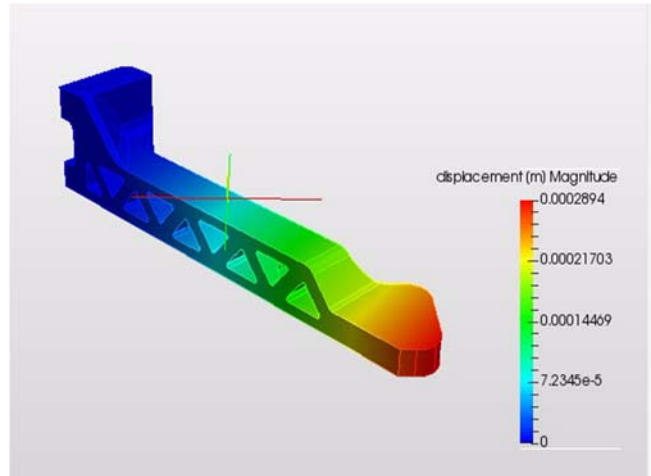


Figure 14. Displacement results for 2.25 N

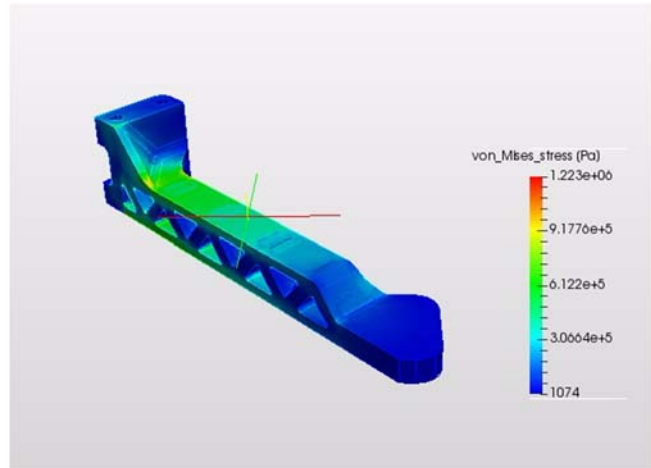


Figure 15. Displacement results for 3 N

Figure 14 and 15 show the displacement for 0.50 lbs. and 0.67 lbs. for a factor of safety of 2.5.

### 4.2.2 Von-Mises simulation results

This section illustrates the results of Von-Mises stresses that occur in the drone arm which increase with the increase in load that is carried.

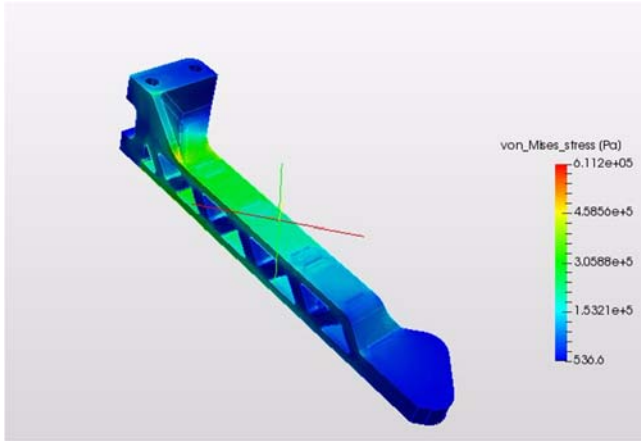


Figure 15. Von-Mises results for 0.75 N

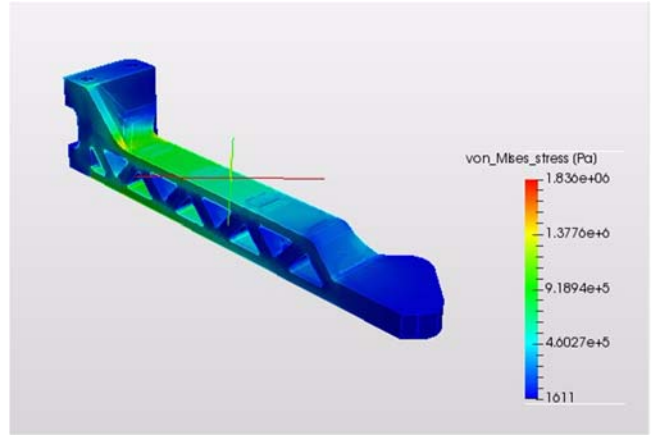


Figure 17. Von-Mises results for 3 N

Figures 16 and 17 show the stress analysis for varying loads. From the analyses conducted, it was concluded that the Von-Mises stresses increase with increase in the load applied on the arm. The arm is being designed to carry light weight loads and the results of analyses show that loading the arm with furthermore load results in a structural damage or failure. For higher loads, we obtained  $1.8636 \times 10^6$  Pa which was an ideal value for our proposed design.

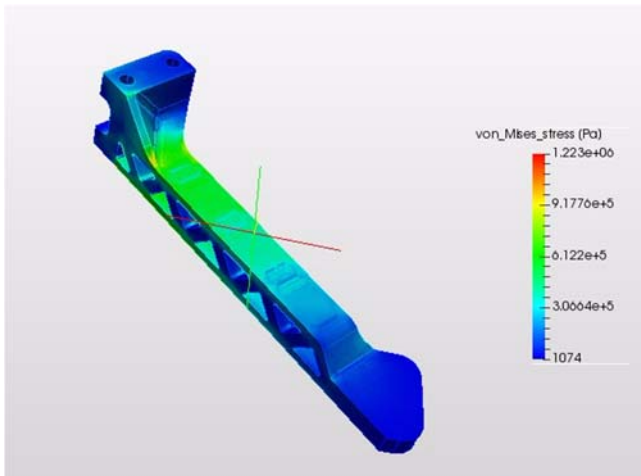


Figure 16. Von-Mises results for 1.5 N

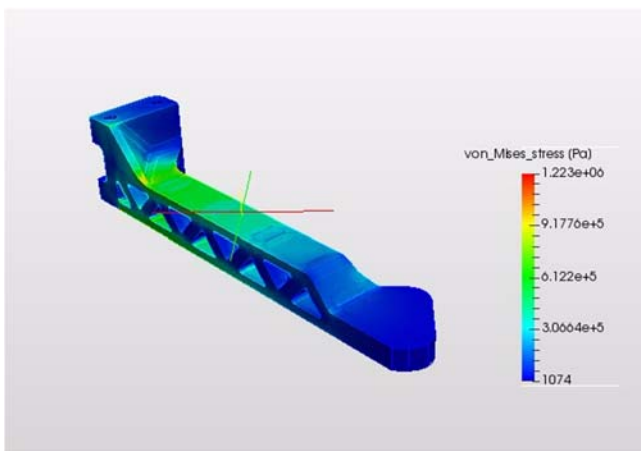


Figure 17. Von-Mises results for 2.25 N

## 5. COST OF MANUFACTURING

The estimated costs of each parts that are used to build the drone model are shown in Table 1. The value of each part presented here has been carefully chosen to avoid compromises with the working of drone. As Table 1 succinctly summarizes, 3D printing of the parts takes up the largest percentage of the overall cost. Hence, as the cost of 3D printing comes down, so will the overall cost of the system. The second most expensive item is observed to be the LiPo battery. Other costly items in descending order are the motor and the remote-control unit.

Table 1. Estimated cost of Manufacturing

COMPONENT	QUANTITY (UNITS)	COST (US \$)
3D Printing (Arms, baseplate, motor mount, drone arm)	14	272.47
Motors	4	72.22
Propeller	4	15.00
LiPo Battery	1	90.00
Electronic Speed controller (ESC)	1	21.30
Camera	1	42.00
Arduino-Uno Microcontroller	1	24.99
Remote control	1	49.99
Miscellaneous (Fasteners, connectors)	-	15.00
Total		\$602.97

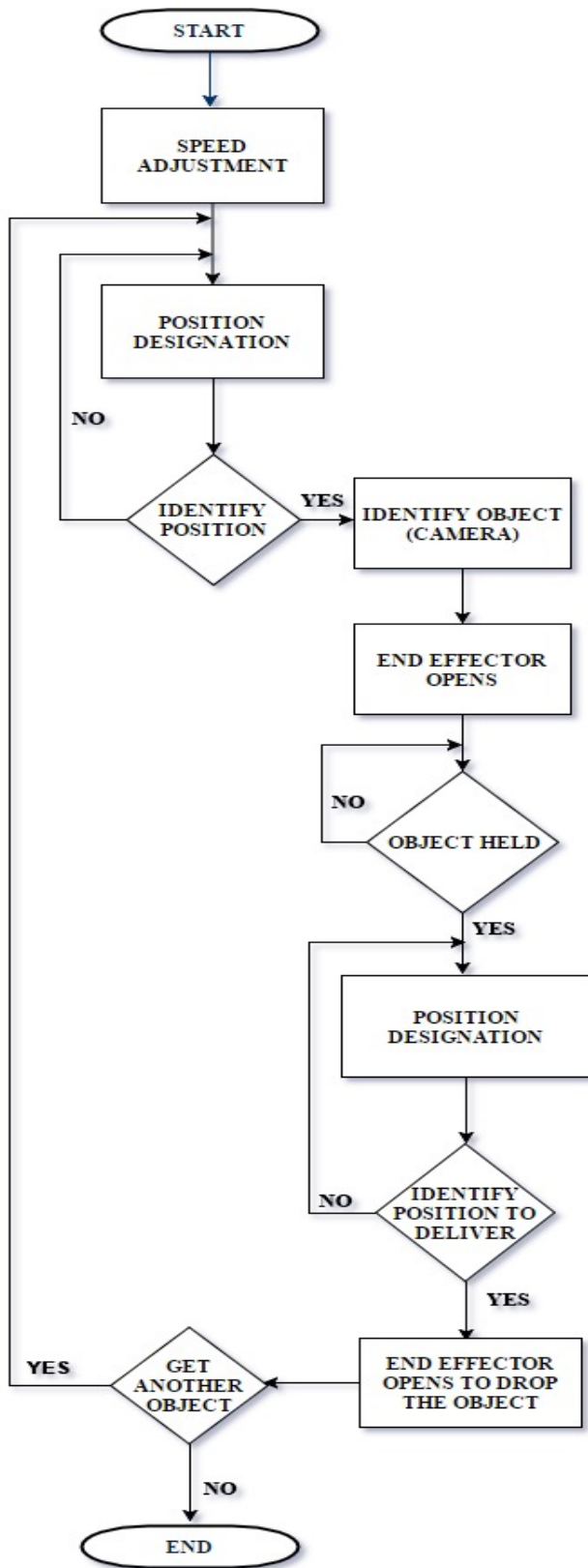


Figure 18. Flowchart for drone and end-effector control

## 6. DRONE WORKING ALGORITHM

Figure 18 represents the algorithm of the proposed drone. The process of lifting the payload initially begins with switching on the power supply from batteries to other electronic components such as the motor and the electronic speed controller. As soon as the systems and the microcontroller powers up the rotors, the speed is adjusted for vertical take-off. The drone is now in air with the arm preset to grab the required object.

The drone is designated with the position, which is monitored by the controller (human) through the camera attached to it. Once the location of the drone is set as per the instructions provided by the controller, the drone's speed is decreased and the end effector opens and grabs the required object firmly with the help of suction cups attached along the internal lining of the effector. This process is repeated until the required object is obtained through series of trials by the controller.

This problem can be eliminated in the future by the development of autonomous self-guided system. The drone after grabbing the object hovers towards the controller based on the instruction specified by the operator. The drone is kept away at a safe distance and the end effector based on designated position of the operator drops the object in his/her vicinity. This process is repeated continuously and the estimated endurance for the current proposed drone model is about 15-20 min.

## 7. CONCLUSION

The function of the robot is defined in the simplest of way which enables the UAV to perform a specific task. The materials and parts selection have been considered based on detailed evaluation of drones available in the market along with the mass of payload to be carried. The end-effector is modeled such that it is equipped with suction cups which give a better grip to the object help by the arm also the arm is stationary with the links being adjusted manually. The drone model presented here is controlled by means of a remote, where further developments can be pursued to have a complete autonomous system with capabilities of self-positioning, tracking and voice control of the drone.

## 8. ACKNOWLEDGMENT

Our sincere thanks are extended to the Robotics and Automation Laboratory in the Department of Mechanical and Materials Engineering for providing access to the equipment and resources.

## 9. REFERENCES

1. Mendoza-Mendoza, Julio, et al. "Air-arm: A new kind of flying manipulator." *Research, Education and Development of Unmanned Aerial Systems (RED-UAS), 2015 Workshop on*. IEEE, 2015.
2. Danko, Todd W., Kenneth P. Chaney, and Aul Y. Oh. "A parallel manipulator for mobile manipulating UAVs." *Technologies for Practical Robot Applications (TePRA), 2015 IEEE International Conference on*. IEEE, 2015.
3. Danko, Todd W., and Paul Y. Oh. "A hyper-redundant manipulator for mobile manipulating unmanned aerial vehicles." *Unmanned Aircraft Systems (ICUAS), 2013 International Conference on*. IEEE, 2013.

4. Maier, Moritz, and Konstantin Kondak. "Landing of VTOL UAVs using a stationary robot manipulator: An innovative approach for coordinated control." *Decision and Control (CDC), 2015 IEEE 54th Annual Conference on*. IEEE, 2015.
5. Zisimatos, Agisilaos G., et al. "Open-source, affordable, modular, light-weight, underactuated robot hands." *Intelligent Robots and Systems (IROS 2014), 2014 IEEE/RSJ International Conference on*. IEEE, 2014.
6. T. Ueno, N. Sunaga, K. Brown and H. Asada., "Mechanism and Control of a Dynamic Lifting Robot. " *International Association for Automation and Robotics in Construction (ISARC 1996), 1996 ISARC International Conference*.
7. Gund, Miss Shwetal Ramesh, and V. P. Bhope. "A Review on Agricultural Robots." *International Journal of Advanced Research in Computer Engineering & Technology (IJARCET 2015)*.
8. Sarig, Y. Robotics of fruit harvesting: A state-of-the-art review. *Journal of agricultural engineering research*, 54(4), 265-280, 1993.
9. Van Henten, E. J., Van Tuijl, B. V., Hemming, J., Kornet, J. G., Bontsema, J., & Van Os, E. A. Field test of an autonomous cucumber picking robot. *Biosystems engineering*, 86(3), 305-313, 2003.
10. Monkman, Gareth J., Stefan Hesse, Ralf Steinmann, and Henrik Schunk. "Robot grippers". *John Wiley & Sons*, 2007.

# Development and Control of a Robotic Attendant Wheelchair

Oscar Chuy Jr.

Department of Electrical and Computer Engineering  
University of West Florida  
ochuy@uwf.edu

Asma Al Selwadi

Department of Electrical and Computer Engineering  
University West Florida  
ama74@students.uwf.edu

Jonathan Herrero

Department of Electrical and Computer Engineering  
University of West Florida  
jah119@uwf.edu

## ABSTRACT

Attendant Wheelchairs(AWs) provide mobility to patients who cannot control wheelchairs. They are either manual, which have excellent maneuverability but offer no power assistance, or electric powered with joystick control interface, which provide power assist but have poor maneuverability in confined spaces. Hence, with the objective of combining the merits of manual and electric powered AWs, this paper presents the development and control of a robotic AW. The AW provides power assistance by using a motorized mobile base while excellent maneuverability is achieved by employing a motion control strategy that emulates the behavior of a manual AW. The motion control employs a desired dynamics that takes user's intention in the form of applied force/torque and generates desired velocities, which are tracked by low-level controllers. Experimental results show the efficacy of the control approach.

**Keywords:** Motion Control, Wheelchair

## 1. Introduction

Improving quality of life of people with disability requires the aid of intelligent assistive devices and one of them is an attendant wheelchair(AW). AWs aid not only patients, but also caregivers/attendants. They are used to transport patients who do not have the ability to control wheelchairs and commonly employed in airports, hospitals, and healthcare facilities. Manual AWs have excellent maneuverability, but do not provide power assist to the attendant while electric powered AWs with joystick control interface provide power assist but have poor maneuverability in confined spaces. Hence, it will be ideal to have an AW that combine the positive characteristics of manual and electric powered AWs.

Robotic wheelchairs have been studied in [1],[4], however, the focus is generally on control interfaces and assistance to patients and not toward attendants/caregivers. For example in [1], a slip mitigation approach for electric powered wheelchair has been proposed to improve safety of the user. Excellent maneuverability of motorized assistive devices specifically walking support systems has been demonstrated in [2],[3],[5], where force/torque sensors are used as control interface and basis for the assistive device motion behavior.

This paper presents the development and control of a robotic AW with the object of assisting attendants through power assist and excellent maneuverability functionalities. To achieve the aforementioned objectives, this study uses an electric powered wheelchair modified to have a custom built control system and uses a force/torque interface for excellent attendant-wheelchair physical interaction and manipulation. A desired dynamics, which emulates a passive system specifically a manual pushed wheelchair, uses the force/torque information and generates desired velocities of the AW. Figure 1. shows the general control diagram of the robotic AW. A force/torque sensor reads the attendant's intention, which is fed to the desired dynamics and used as a basis to determine the desired linear and angular velocities of the wheelchair. The inverse kinematics transforms robot velocities to left and right wheel velocities. The desired wheel velocities are tracked by low-level controllers. The above hardware configuration and control approach should enable the robotic AW to provide power assistance and have excellent maneuverability.

The remaining sections are described as follows. Section II discusses the high-level control, which addresses the attendant-wheelchair interaction. The high level control emulates the behavior of a manual attendant wheelchair.

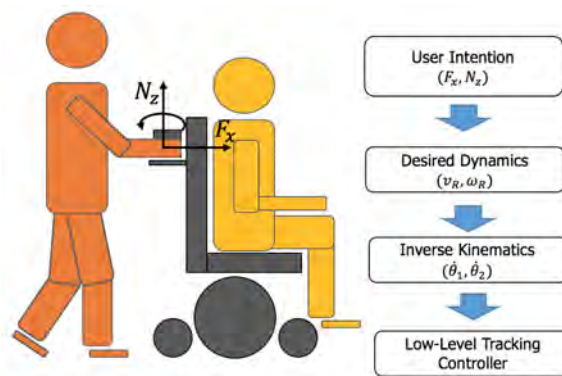


**Figure 1.** General control diagram of the robotic attendant wheelchair

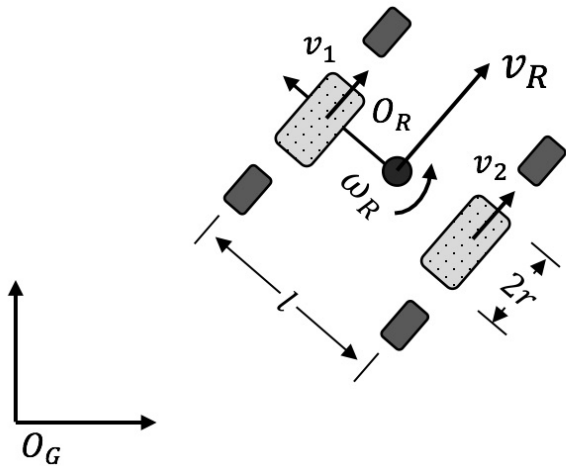


**Figure 2.** Kinematic diagram of the attendant wheelchair, where  $v_R$  is linear velocity,  $\omega_R$  is the angular velocity,  $v_1$  left wheel linear velocity, and  $v_2$  is the right wheel linear velocity

Section III discusses the electronic hardware used by the robotic AW. Section IV presents the evaluation and followed by the summary.

## 2. High Level Control

The high level control emulates the behavior of a manual wheelchair, which is described by a desired dynamics. A force/torque sensor reads the attendant's intention, which is fed to the desired dynamics and used as basis to determine the desired linear and angular velocities of the wheelchair.

The equation of the desired dynamics is described below

$$\mathbf{M}_d \ddot{\mathbf{x}}_d + \mathbf{D}_d \dot{\mathbf{x}}_d = \mathbf{F}_a, \quad (1)$$

where  $\mathbf{M}_d$  and  $\mathbf{D}_d \in R^{2 \times 2}$  are the inertia and damping and are respectively given below

$$\mathbf{M}_d = \begin{bmatrix} M_{dx} & 0 \\ 0 & M_{d\theta} \end{bmatrix}, \mathbf{D}_d = \begin{bmatrix} D_{dx} & 0 \\ 0 & D_{d\theta} \end{bmatrix}.$$

$\mathbf{F}_a$  is the attendant intention given as

$$\mathbf{F}_a = \begin{bmatrix} F_x \\ F_\theta \end{bmatrix}.$$

Note that the variables with a subscript of  $x$  are for the linear motion while variables with a subscript of  $\theta$  are for the angular motion.

The output is  $\dot{\mathbf{x}}_d$ , where the components are the desired linear and angular velocities of the robotic AW and is given below

$$\dot{\mathbf{x}}_d = \begin{bmatrix} v_R \\ \omega_R \end{bmatrix}.$$

Based Fig. 2, the forward kinematics of the AW is given below

$$\begin{bmatrix} v_R \\ \omega_R \end{bmatrix} = \begin{bmatrix} 1/2 & 1/2 \\ -1/l & 1/l \end{bmatrix} \begin{bmatrix} v_1 \\ v_2 \end{bmatrix} \quad (2)$$

where  $v_R$  is the linear velocity of the wheelchair,  $\omega_R$  is the angular velocity,  $v_1$  is the linear wheel velocity of the left

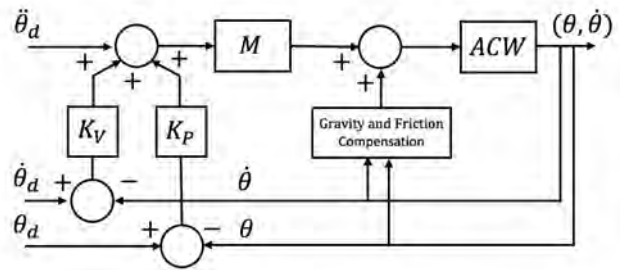


**Figure 3.** Low-Level controller of the robotic attendant wheelchair

wheel, and  $v_2$  is the linear wheel velocity of the right wheel. For control purposes, the inverse kinematics will be used that is  $v_1$  and  $v_2$  will be expressed in terms of  $v_R$  and  $\omega_R$  and is given below

$$\begin{bmatrix} v_1 \\ v_2 \end{bmatrix} = \begin{bmatrix} 1 & -l/2 \\ 1 & l/2 \end{bmatrix} \begin{bmatrix} v_R \\ \omega_R \end{bmatrix}. \quad (3)$$

The left and right desired wheel angular velocities can be expressed as  $\dot{\theta}_1 = v_1/r$  and  $\dot{\theta}_2 = v_2/r$ , respectively. Hence, (3) can be written as

$$\begin{bmatrix} \dot{\theta}_1 \\ \dot{\theta}_2 \end{bmatrix} = \begin{bmatrix} 1/r & -l/2r \\ 1/r & l/2r \end{bmatrix} \begin{bmatrix} v_R \\ \omega_R \end{bmatrix}. \quad (4)$$

The result of (4) will be assigned as desired wheel velocities and represented as  $\{\dot{\theta}_{d1}, \dot{\theta}_{d2}\}$ . The desired wheel positions and accelerations are respectively represented as  $\{\theta_{d1}, \theta_{d2}\}$  and  $\{\ddot{\theta}_{d1}, \ddot{\theta}_{d2}\}$ , which are numerically determined for the use of the low-level controller as shown in Fig. 3.

## 3. Experimental Setup

Figure 4 shows the experimental setup. It based on a commercially available electric powered wheelchair that is



**Figure 4.** Experimental setup based on an electric powered wheelchair with force/torque sensor as control interface

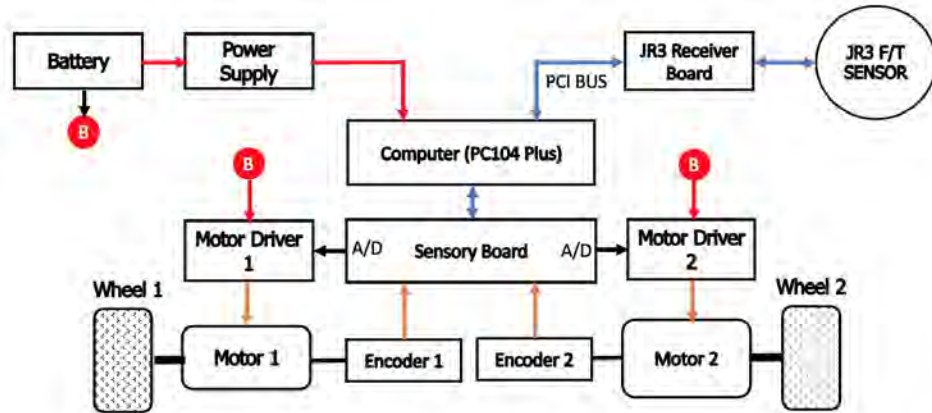


Figure 5. Hardware diagram the robotic AW.

modified to handle the high level control as discussed in Sec 2. Fig. 5 shows the hardware diagram of the robotic AW. A PC104 plus computer system with pentium III 900 MHz processor runs the realtime QNX operating system. It also handles the low-level control and high level motion control algorithm and both are running at 1 kHz control rate. It is stacked with a Sensoray 526 data acquisition board as shown in Fig. 6 and JR3 receiver board as shown in Fig. 7. The Sensoray 526 reads the incremental encoders, which are directly coupled to the motor shafts. In addition, the 526 communicates to the motor drivers through its analog to digital channels. The force/torque sensor captures user's intention and transmits the data to the receiver board.

Figure 8 shows the left wheel, motor, and encoder assembly. The motors are coupled with gearboxes with gear ratio of 32:1. To read the wheel angular positions, incremental encoders with resolutions of 1000 counts per revolution are installed at the back of the motors. This approach gives a finer angular wheel resolution and requires less hardware modification/installation in contrast to attaching the encoders to the wheels.

## 4. Evaluation

This section discusses the initial evaluation of the high level control of the robotic AW. A predefined path as shown in Fig. 9 is given and the user needs to track it with different desired dynamics parameters, i.e.,  $M_x$  and  $D_x$ , for generating

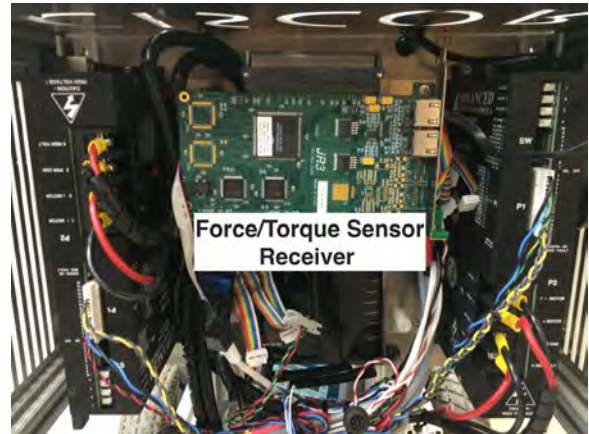


Figure 7. This figure shows the receiver board of the JR3 sensor

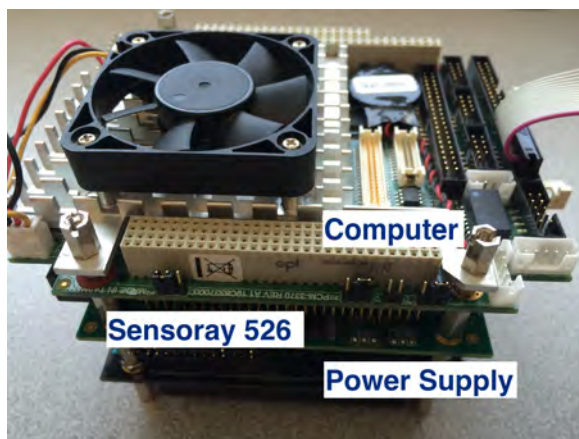


Figure 6. PC104 computer system (PIII 900 MHz) with Sensoray data acquisition board. The computer system runs the QNX realtime operating system.

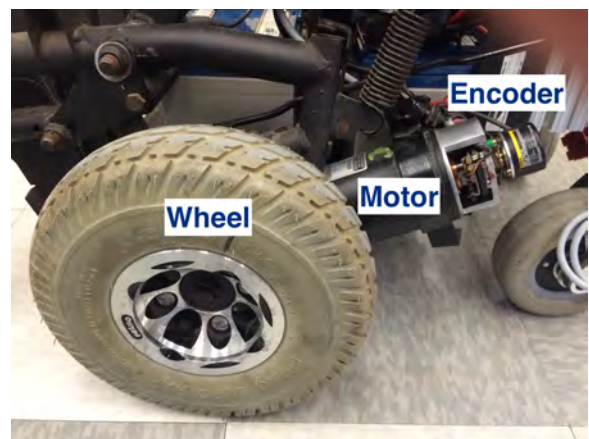


Figure 8. This figure shows the wheel, motor, and encoder assembly. The encoder is attached at the back of the motor to measure wheel angular position

translational velocities while fixing  $M_\theta$  and  $D_\theta$ . The user moves from the starting point to A, B, C, and returns to start.

Figures 10 (a) - (c) show the resulting applied forces to generate linear velocities. For all the evaluations,  $M_\theta = 3 \text{ kg.m}^2$  and  $D_\theta = 6 \text{ N.m.s/rad}$ . Figure 10 (a) shows the applied force for  $M_x = 50 \text{ kg}$  and  $D_x = 50 \text{ Ns/m}$  and the mean absolute applied force is 15.56 N. Figure 10 (b) shows the applied force for  $M_x = 25 \text{ kg}$  and  $D_x = 25 \text{ Ns/m}$  and the mean absolute applied force is 10.91 N. Figure 10 (c) shows the applied force for  $M_x = 10 \text{ kg}$  and  $D_x = 10 \text{ Ns/m}$  and the mean absolute applied force is 5.81 N. It can be noticed that as the desired dynamics parameters are reduced the applied intentional forces also reduces, which is excellent for power assist. Also, the task completion time is reduced for low mass and damping as shown in Fig. 10. However, oscillations are observed at low values of mass and damping especially when the arms are fully extended.



**Figure 9.** This figure shows the predefined path given to a user to evaluate the high level control. The user moves from start to pt. A, B, C, and returns to start.

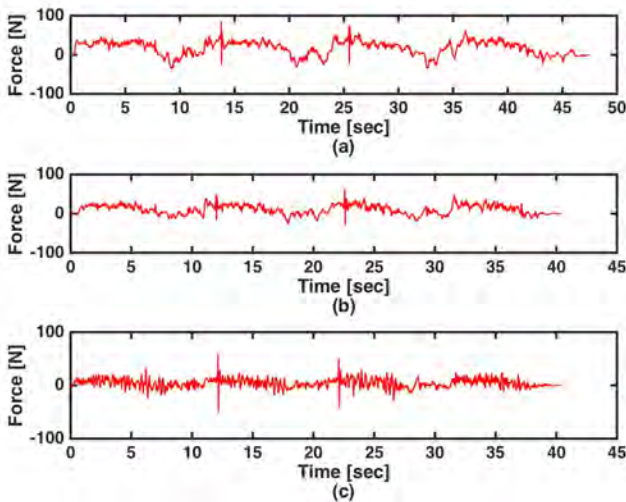


**Figure 10.** The above figures show the applied forces to generate linear velocities for different desired dynamic parameters in the x-axis. The parameters for rotational motion are held constant. (a)  $M_x = 50 \text{ kg}$  and  $D_x = 50 \text{ Ns/m}$  (b)  $M_x = 25 \text{ kg}$  and  $D_x = 25 \text{ Ns/m}$  (c)  $M_x = 10 \text{ kg}$  and  $D_x = 10 \text{ Ns/m}$ .

## 5. Conclusions

This paper presented the hardware components and control approach of a robotic attendant wheelchair with the objective of providing power assist while maintaining excellent maneuverability. An electric powered wheelchair was used as the mobile base and installed with electronic hardware to handle the proposed high level control that addressed attendant-wheelchair physical interaction. The control approach was based on desired dynamics, which emulates the behavior of a manual pushed wheelchair. The initial evaluation results showed that less applied forces were required to complete the given task as the dynamics parameters were reduced. However, oscillations were observed. Future works will focus on further power assist and maneuverability evaluations and addressing the instability of the system during attendant wheelchair physical interaction

## References

- [1] O. Chuy et al. Slip mitigation of an electric powered wheelchair. In *International Conference of Robotics and Automation*, 2014.
- [2] O. Chuy, Y. Hirata, and K. Kosuge. A new control approach for a robotic walking support system in adapting user characteristics. *IEEE Transactions on Systems, Man, and Cybernetics*, 36:725–733, 2006.
- [3] S. Dubowsky et al. Pamm a robotic aid to the elderly for mobility assistance and monitoring: A helping-hand for the elderly. In *Proc. IEEE Int. Conf. Robot. Autom.*, pages 570–576, 2000.
- [4] W. Hongwu et al. Stability analysis of electrical powered wheelchair-mounted robotic assisted transfer device. *Journal of Rehabilitation Research and Development*, 51(5):761–774, 2014.
- [5] H. Yu, M. Spenko, and S. Dubowsky. An adaptive shared control system for an intelligent mobility aid for the elderly. *Journal of Autonomous Robot*, 15:53–66, 2003.

# Development and Testing of Robotic Inspection Tools for the Hanford High-Level Waste Double Shell Tanks

Michael DiBono, Anthony Abrahao, Dwayne McDaniel, Yew Teck Tan

Florida International University Applied Research Center  
10555 W Flagler Street  
Miami, FL 33174

mdibono@fiu.edu, aabrahao@fiu.edu, mcdaniel@fiu.edu, yetan@fiu.edu

## ABSTRACT

Florida International University (FIU) is in the process of developing inspection tools capable of inspecting the tank floors of double shell tanks through two main entry points, the air supply lines and air refractory channels. Two types of tools are being developed as a result: a pneumatic pipe crawler and a miniature rover. The air supply lines consist of an inspection path of approximately 100 feet of piping from grade, down through one of the drop legs and then lateral to the center bottom of the secondary tank containment. The route consists of pipes with varying diameters of 3 and 4 inches, reducers, and several elbows. The pneumatic crawler is being developed in an effort to properly inspect these lines. Resembling that of an inchworm in both motion and appearance and utilizing a modular design, it uses pneumatic actuators to emulate the contractions of peristaltic movements. The air refractory channels are located at the bottom of the tanks with channels as small as 2.5x1.5 inches and multiple 30° turns. The miniature rover is a remote controlled 4-wheeled vehicle utilizing skid steering through 4 micro DC motors designed for the inspection of these channels. There are no embedded electronics except for the camera in order to make the tool suitable for highly radioactive environments. It is designed to magnetically attach to the bottom of the primary tank (top of the air refractory channels) in order to avoid the debris that lines the bottom of the channels. Engineering scale testing of both systems is presented, with slight modifications being made based off of these tests. In order to test the pneumatic crawler, 100 feet of piping with the same lengths, dimensions, and fittings as the air supply line of the double shell tank (DST) named AY-102 was used. Testing for the crawler yielded satisfactory results, showing that the crawler was able to successfully navigate the air supply line. In regard to the testing of the miniature rover, brick pavers were used for the testbed to provide more realistic coefficients of friction between the tether and the channel. The rover proved to be able to overcome these frictional forces, although further modifications need to be made in order to ensure a consistent pull force.

## Keywords

AY-102, leak detection, inspection tools, crawler, rover, robotics

## 1. INTRODUCTION

In August of 2012, traces of waste were found in the annulus of the radioactive waste storing AY-102 double-shell tank at the DOE Hanford site. This prompted the need for the development of inspection tools capable of identifying both the cause and location of the leak. The three possible points of entry for inspection in the tank are noted by Figure 1:

- 1.) The refractory air slots through the annulus
- 2.) The leak detection piping
- 3.) The ventilation header piping

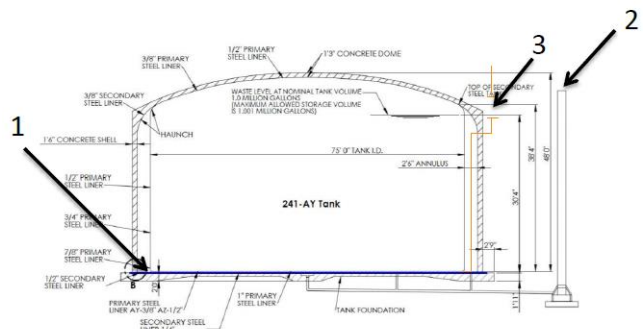


Figure 1. Inspection entry points of the AY-102 double-shell tank

Florida International University is developing inspection tools that are capable of accessing the tank's secondary containment, with the primary goal of providing live visual feedback. A magnetic miniature rover was developed for the inspection of the refractory air slots, and a pneumatic pipe crawler was developed for the inspection of the ventilation header piping.

## 2. RELATED WORKS

Multiple inspection devices have been developed for the visual inspection of small diameter pipeline structures, such as the MICROTUB [1], MRINSPECT [2], and Explorer [3]. These devices are primarily used for visual inspection [4] and nondestructive evaluation [5] of urban gas pipelines. Other applications of the more compact designs are intended for inspection of power plants [6]. These in-pipe inspection tools are not specifically designed for deployment in air refractory channels, as the material that makes up the channels must not be subjected to pressures greater than 200 psi. In addition to this limitation, the dimensions of the refractory air channels restrict the size of the device to a miniature size. The device must also be radiation hardened and equipped with a fail-safe tether.

## 3. PNEUMATIC PIPE CRAWLER

The pneumatic pipe crawler is an inspection tool capable of providing live video feedback while traveling through the air supply line leading to the central plenum of a typical DST at Hanford. For AY-102 specifically, the proposed inspection path is approximately 30.5 m from grade, down through one of the drop legs, and then lateral to the center bottom of the tank secondary containment. The tool must also travel through several reducers and elbows, with diameters ranging from 7.62 to 10.16 cm (Figure 2).

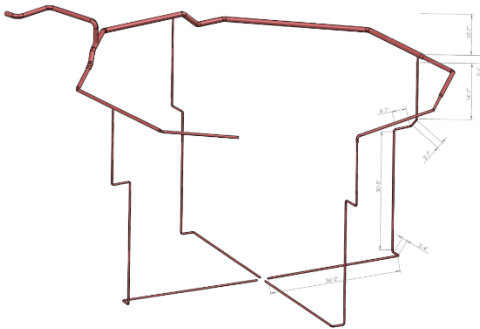


Figure 2. AY-102 air supply lines

Other requirements include:

- 1.) Tolerate elevated temperatures (76.6°C)
- 2.) Tolerate moderate radiation levels (85 rad/hr)
- 3.) Provide a means for removal in the event of a malfunction

The current design resembles that of a worm with a modular design, composed of interchangeable cylindrical modules connected with flexible links (Figure 3). The basic design is composed of five modules: a.) the front camera, b.) the front and back grippers, c.) the two middle expansion modules. The crawler also utilizes a control box, a tether, and an instrumentation module (currently being designed). The expansion modules use compact nonrotating tie rod air cylinders to propel the crawler forward during the peristaltic movements of expansion and contraction. Grip strength is vital as without sufficient grip strength, the tool would be incapable of travel as it wouldn't be able to grip the sides of the pipes.

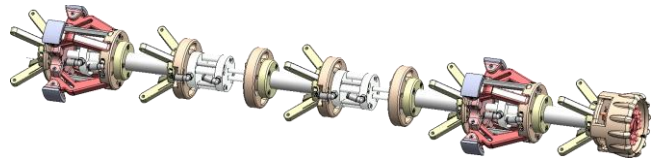


Figure 3. FIU's pneumatic pipe crawler

A full scale mockup of the ventilation system for AY-102 was manufactured, with the primary difference being that FIU's version lays horizontal (Figure 4). This design makes it more difficult for the crawler as it wouldn't be assisted by gravity for the vertical segments. The crawler was able to successfully traverse the test bed, with the pull force of the crawler being approximately 178 N and the average recorded drag force around 22.2 N (peaking at 35.6 N).

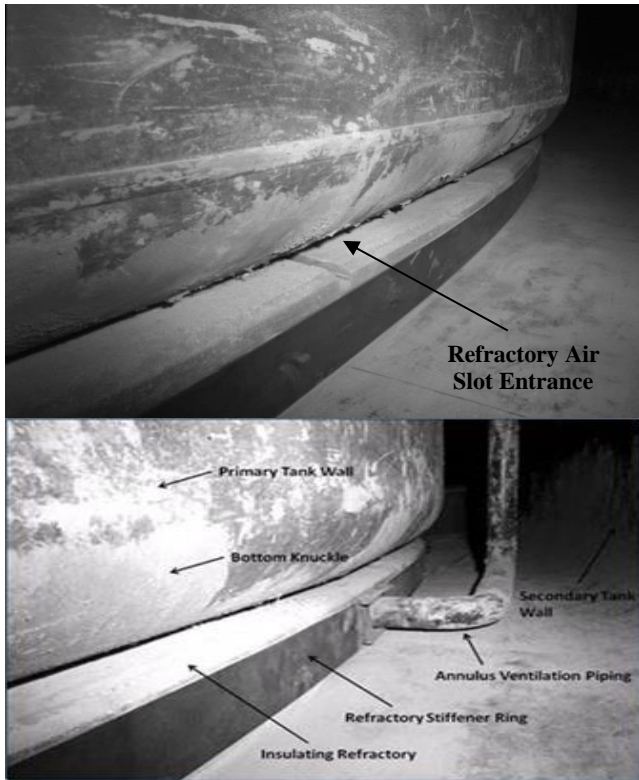


Figure 4. Preliminary tether pull and drag testing

The path forward for the development of the pneumatic crawler includes a) finalizing the instrumentation module design, b) continuing validation of the device in full scale tests, c) continuing the modification of the design as needed, d) developing a cable management system, and e) integrating various non-destructive sensors.

## 4. MAGNETIC MINIATURE ROVER

FIU is developing a miniature rover that will access the primary tank floor of DSTs at Hanford through the annulus and refractory air slots (Figure 5), providing visual feedback of their condition. With widths ranging from as small as 2.54 cm to as large as 7.62 cm, the configuration of the air slots are maze-like, with four 90° turns needed to reach the center of the tank (Figure 6). AY-102 has the most difficult inspection path due to the layout of the refractory cooling channels, as pictured; the other DSTs contain channels with much larger angles in contrast to the 90° turns of AY-102.



**Figure 5. Primary tank and refractory air slot**

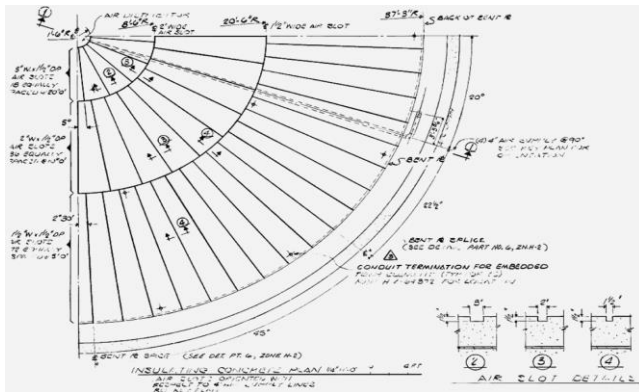


**Figure 6. The AY-102 refractory air slot configuration**

Through collaboration with site engineers, FIU has gathered information for the design specifications of the inspection tool, including annulus and refractory air slot geometry and maximum temperature/radiation limits for the device. Videos of the tank bottoms of other tank configurations (AW-101, AZ-102, and SY-103) from inspections done by an articulated robot ten years ago were viewed, providing FIU with a general idea of the conditions to be encountered along with the condition of the tank bottom surface. The video provided FIU with a better understanding of the refractory pad's low shear strength, along with how quickly debris builds up when the tool comes into contact with the walls of the air slots (Figure 7). The tool is designed to magnetically attach to the bottom of the primary tank (top of the air refractory channels) in order to avoid the debris that lines the bottom of the channels.



**Figure 7. Screenshots from video of refractory air slots showing debris**

A variety of prototypes were developed to take on this challenge, with the majority of the parts for the prototypes being designed in a 3D modeling software and 3D printed on site. With each prototype came a series of improvements, ranging from the strengthening of the wheels to reduce the effects of cyclic stress to the reduction of the overall size of the unit in order to be able to traverse the angles experienced in the channels (Figure 8). One of the design restrictions set by Hanford was the requirement of the unit to be tethered (in case of failure so as to have a way to retrieve the unit). This restriction was used to the advantage of the tool, as it was dual-purposed to also provide power. This voided the need to have the majority of integrated circuitry on the tool, thus making the tool more likely to survive the radioactive environment. A cable management system is also necessary for the storing/supplying of the tether, in order to ensure a tangle free deployment. A first prototype was developed with a stepper motor as the primary driving force and a timing belt used to adjust the gear ration of the system (Figure 9).

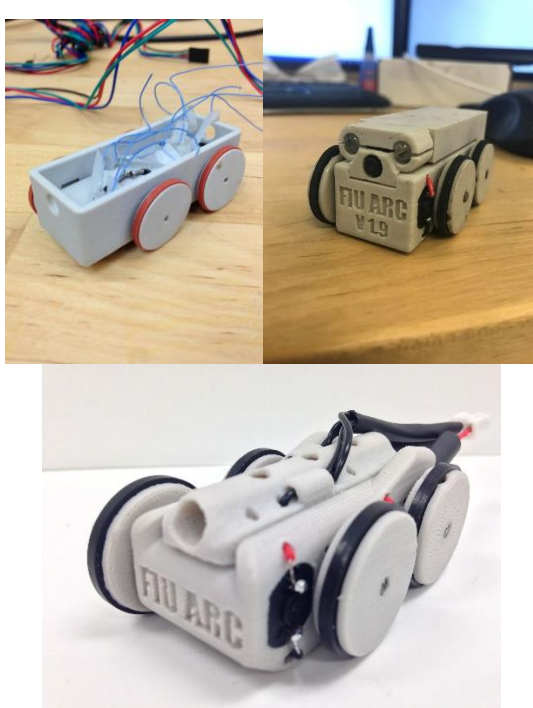


**Figure 8. Evolution of the tool, with the most recent version on the upper right**

Testing was done regarding the pull-force of the tool, with the conclusion of the tool pulling with approximately 5.3 N of force. The pull-force of the tool is important due to the tether that it must pull. A strong pull force is necessary to overcome the frictional forces created by the turns within the channels. Bench scale testing proved that the tool was capable of overcoming these frictional forces. A transparent test bed was also made in order to see the tool in action, proving that the geometry of the tool was fit for travel within the air refractory channels.

Future endeavors for the tool include the development of a deployment robot, as the entrance to the refractory air slots is unreachable by humans (approximately 80 feet underground with traces of radiation). There is also motivation for the integration of other sensors, including temperature and radiation sensors. A full-scale mockup will also be developed to more effectively test the inspection tools.

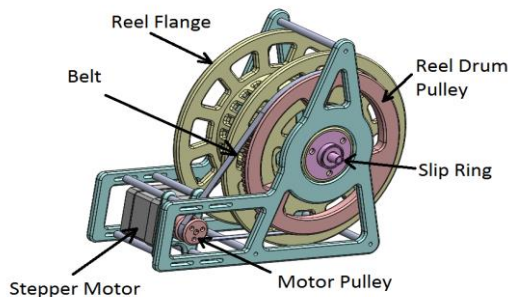


**Figure 9. Cable management system**

## 5. CONCLUSION

In this paper we presented the various inspection tools in development by Florida International University for the inspection of the double-shell tanks in Hanford. A pneumatic pipe crawler designed to carry out the inspection of the ventilation header piping of the DSTs was created with the goal of providing real time video feedback. A functional prototype was successfully manufactured and tested. Based off of the results the crawler has great potential to accomplish the proposed inspection. As the project progresses, non-destructive sensors will be added, along with the finalizing of the instrumentation module and more full-scale testing performed. A magnetic miniature inspection tool was designed for the inspection of the refractory air channels of the DSTs at Hanford. Lab-scale mock up tests identified various areas for improvement, including geometry of the inspection tool and wheel strength. A cable management system was also developed to make sure there is no tether entanglement during operation. Future work includes the development of a deployment robot to assist with the deployment of the inspection tools, as well as integration of environmental sensors for inspection purposes. A full-scale mockup facility is currently being developed to further test the readiness of the inspection tools before the final field deployment.

## 6. REFERENCES

- [1] Gambao, E. M. Hernando, and A. Brunete. Multiconfigurable inspection robots for low diameter canalizations. in 22<sup>nd</sup> International Symposium on Automation and Robotics in Construction ISARC, Ferrara Italy. 2005.
- [2] Roh, S.-g. and H.R. Choi, Differential-drive-in-pipe robot for moving inside urban gas pipelines. Robotics, IEEE Transactions on, 2005. 21(1): p. 1-17.
- [3] Schempf, H., et al., Visual and nondestructive evaluation inspection of live gas mains using the Explorer™ family of pipe robots. Journal of Field Robotics, 2010. 17(3): p. 217-249.
- [4] Dertien, E., S. Stramigioli, and K. Pulles. Development of an inspection robot for small diameter gas distribution mains. in Robotics and Automation (ICRA), 2011 IEEE International Conference on. 2011. IEEE.
- [5] Hirose, S., et al. Design of in-pipe inspection vehicles for 25, 50, 150 pipes. in Robotics and Automation, 1999. Proceedings. 1999 IEEE International Conference on. 1999. IEEE.
- [6] Caprari, G., et al., Highly compact robots for inspection of power plants. Journal of Field Robotics, 2012. 29(1): p. 47-68.

# FARA: Framing Assembly Robotic Arm System for Construction Sites

Francisco Lopez, Carlos Reaño, Alexander Rosenqvist, Melissa Morris, Sabri Tosunoglu

Department of Mechanical and Materials Engineering  
Florida International University  
Miami, Florida 33174

flope076@fiu.edu, crean001@fiu.edu, arose006@fiu.edu, mmorr009@fiu.edu, tosun@fiu.edu

## ABSTRACT

The project aims to develop a manipulator type construction robot empowered with necessary sensors and software so that it can be controlled via manual control to survey the environment, conduct assembly work and avoid obstacles in the work site. An adaptation of Lynxmotion's AL5D servo robotic arm is used to 3D-print a scaled model, and the motion of the robot is studied. Assembly of a 3D-printed model representation of a precast frame construction site is also presented. The manual control of the arm is fully achieved using an Xbox controller, coded with inverse kinematics. Further implementation of IR sensors mounted near the tool tip proves successful to detect obstacles. Additionally, a Microsoft Kinect motion sensor is utilized to provide surveying by using its RGB-D camera, and detecting workers on site to increase safety features. The findings indicate the feasibility of a full-scale Framing Assembly Robot Arm (FARA), as it would potentially reduce in-site casualties and lower the cost of labor.

## Keywords

Construction Robots, Robotic Framework Construction, Framing Assembly Robotic Arm, FARA.

## 1. INTRODUCTION

Since the use of machinery in construction, we have been able to build larger structures and longer roads. Safety at the site, however, has been an area that needed more thorough work. Even with rigorous code and safety checks, workers still suffer injuries and even death. In the year 2015 alone over 900 casualties occurred in construction sites all over the US, with the "Fatal Four" being falls, getting struck by objects, electrocution, and getting caught in between [13]. A solution to keep these numbers low is to look for answers in robotics and automation, while also adding the necessary safety precautions.

Currently there are few simple robotic systems being used to aid in construction, such as the cement 3D printer or the

pavement laying machine aided by sensors, to name a few [14]. This project aims to prove the feasibility of a 6-DOF robotic arm in the construction of a single story, simply supported structures made of pre-fabricated parts as well as to test collision avoidance. The robot will essentially become a Framing Assembly Robotic Arm (FARA), which is manually controlled and able to sense its environment. To achieve the goal, FARA will have the task of assembling a 3D-printed model of the single story frame consisting of a base representing the foundation, three types of columns and the beams.

For better safety features (and future automation) to be further achieved, IR sensors and RGB-D cameras are also implemented to the prototype and testing. The safety of a full scale model is tested with the IR cameras mounted onto the arm itself, while surveying of the site happens with the use of Microsoft's Kinect [12]. The latter can potentially aid in the future plans for full automation of FARA, via shape recognition and mapping. This paper is only concerned with the manual control tasks, collision avoidance, and testing out of the surveying capabilities of the Kinect's RGB-D cameras.

## 2. LITERATURE SURVEY

After a review of automation and robotics in construction publications, it was concluded that although prefabricated or precast pieces already exist in the industry, robots and automated systems for assembly in terms of framing structure mounting is lacking [1]. This is the first attempt at using a 6-DOF robot for construction purposes. Further research into other currently available products in the market, such as brick-laying robots or the cement 3D printers, only have 2 to 3 DOF, limiting their versatility [4]. Other limitations affect these products, for example the "concrete printing" process has material properties to take into account, and can only be useful for smaller paths [7]. As far as bricklaying robots, their task specific capabilities are in fact quite remarkable; however, must be assembled to be

fed by conveyors [8]. Australian bricklayer SAM is a notable example of robotics in construction [14]. Robots such as SAM and other material printers are currently paving the way for automation in construction.

### 3. DESIGN GOALS

Proving that the manual control of the FARA prototype has the necessary safety features to work in the real world requires testing for good user interface, obstacle avoidance and surveying. The buttons on the controller should easily control FARA's movements with fluid and accurate displacements and rotations. The incorporation of IR sensors to the robotic arm will work in conjunction with a Microsoft Kinect V2 for surveying the site by detecting personnel, thus increasing the safety of operations. When the IR sensors detect obstacles, the X-box 360 controller will vibrate, to inform the user. The Kinect's detection of personal would inform the user when and where to move FARA, externally from a surveying tower. The estimated a total budget of \$250 dollars including all servos, linkage, sensors, controller and additional parts.

### 4. PARTS

#### 4.1 ALD5 and SCC-32U Servo Controller

The AL5D is commercially available as a 5-DOF robotic arm by Robotshop/Lynxmotion Inc. This robot, operates by means of a servo controller, SSC-32U [3]. The linkage is primarily integrated by laser-cut steel plates/brackets, metal fasteners, ball bearings, plastic pieces, etc. An additional servo motor was added to improve its mobility to 6 DOF. After trial and error, it was noted that keeping the four links between the base and tool tip coplanar while only rotating the base and the tool allowed for better manipulation for assembling the model. The coplanar adjustment also made it easier for calculations and coding using inverse kinematics [9], [10]. The total weight of 9 lbs and maximum reach of 30 in is envisioned for the scaled first prototype.



Figure 1. Lynxmotion Robotic Arm AL5D (5 DOF) with SSC-32U Servo Controller

#### 4.2 Xbox 360 Controller

For better user interface, a code was implemented to manually control FARA with the controller using inverse kinematics. Figure 1 provides the schematics of the Xbox 360 controller, and Table 1 lists each button's functionality.

Table 1. Button Assignments to Link and Tooltip Movements

Servo No.	Link Description	Button	Movement Description
0	Base Rotation	Left Bumper	Rotates Base CCW
		Right Bumper	Rotates Base CW
1	Link 1	Left Stick	Inverse Kinematics for X & Y axis movement for the position of servo 3
2	Link 2		
3	Link 3	Right Stick	Inverse Kinematics for X & Y axis movement for the position of the gripper
4	Link 4		
5	Wrist	X Button	Rotates Wrist CCW
		Y Button	Rotates Wrist CW
6	Gripper	A Button	Closes Gripper
		B Button	Opens Gripper

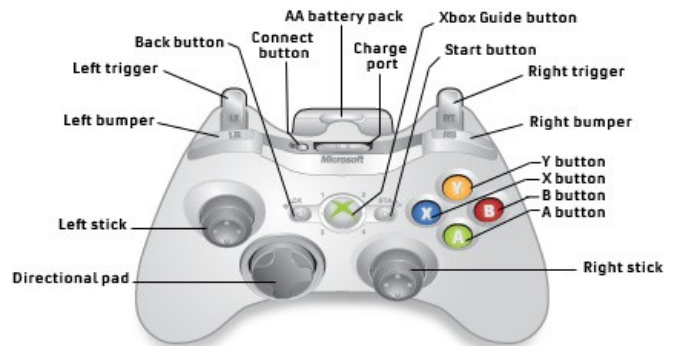


Figure 2. Xbox 360 Controller Map

#### 4.3 Sensors

##### 4.3.1 Sharp GP2Y0A41SK0F IR Sensors

These optical infrared sensors of 4 ~ 30 cm range with analog output are suitable for obstacle avoidance of the FARA, and are attached laterally to the tooltip and at 30 degrees to further increase its sensing field.

The mount was designed and 3D printed for the purpose of incrementing the field of vision of the sensors for better

obstacle detection. Figure 3 shows the customized bracket that is commercially available.



**Figure 3. Sharp GP2Y0A41SK0F IR Sensors and Mounting Modification**

#### 4.3.2 Microsoft Kinect V2

This multifunctional RGB-D camera is used to assist in the mapping of the construction site model, and surveying. Extensive research has proved the effectiveness of RGB-D cameras to not only detect people but also give out information of location in a plane [5].

Future functions to be implemented for full automation of FARA include shape recognition and tracking capabilities [6]. Due to time constraints, testing is only conducted on surveying of the site to detect personnel as FARA is controlled and as it assembles the model.



**Figure 4. Microsoft Kinect V2**

#### 4.4 Arduino UNO with Shield USB Host

The Arduino Uno will be used to program and control the movement of the robot. A USB host shield will also be stacked onto the Arduino to connect the Xbox controller.

Instead of using the servo controller to control the servos, the Arduino will be used since it provides the means to input the Xbox controller via USB, as well as the IR sensor via analog pins, and output the servos via digital pins within the same board.



**Figure 5. Arduino UNO with USB Host Shield and Servo Controller**

#### 4.5 Program and ROS

The Arduino software implements inverse kinematics for the manual control of the arm, basing it on the position of the base. The program also integrates the IR data acquired from the Arduino Board, and the Robot Servo Library for Arduino to control the servos. A Microsoft Kinect interface, i.e. Kinect Studio, integrates recognition of workers on site.

#### 4.6 Model of Prefabricated Structural Frame

For the purpose of representing FARA's feasibility in the real world, the 3D model was designed to resemble a prefabricated structural single-story framing system. The 3D Printer Selected was a Makerbot 1, and the printing setup was 70% infill and 2 shells for Columns and Beams, 15% (to save filament) infill and 3 shells for the base. Figure 6 depicts the 3D-printed individual parts of the model to be assembled by the Robotic arm.



**Figure 6. 3D-Printed Columns and Beams**

The base that is shown in Figure 7 represents the cleared construction area with the square bores as part of the isolated footings where the columns are to be placed.

The bores have supports as four-sided pyramids truncated at the top part, which are reciprocally the same shape as the column lower columns holes to facilitate the beam-footing coupling. All the girders (beams) are equal prismatic T-shapes, so all the columns have same longitudinal and transverse spacing between each other. The columns are square prisms with respective cut-off orifice at the supports where the girders are placed.

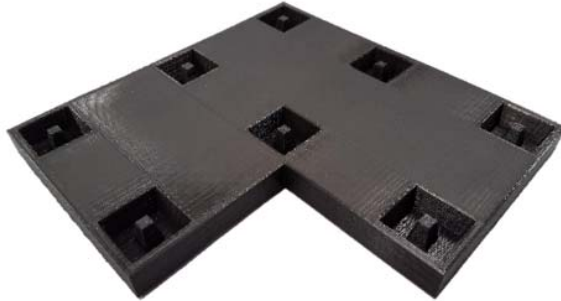


Figure 7. 3D-Printed Base

Furthermore, the columns feature the type and amount of orifices to bear the respective beams according to their location in the framing system; hence, the corner columns have two orifices (for a transverse and a longitudinal girder), the side columns have three orifices (for two longitudinal and one transverse girder), and a center column (two longitudinal girders, and two transverse girders) structural supports are such that the columns are sheathed on the base, and the girders re similarly placed on the column supports.

Although the structural model is statically indeterminate, in the actual construction site the structure is stiffened to any desired rigidity by welding or bolting the supports that are already mounted. This structural system can be described as two mutually double-spanned frames and single spanned frames interconnected perpendicularly by beams as Figure 8 illustrates.



Figure 8. 3D-Printed Structural System

## 5. FUTURE PLANS

Fully automating FARA to assemble the model is possible by implementing more complex code to the Kinect's RGB-D camera sensory response. Mapping the entire worksite while providing surveying is feasible and not farfetched [2]. Adding the positioning capabilities due to mapping, the Kinect would essentially let FARA know where each hole is located, also where to retrieve each piece. With shape recognition, FARA can also be told to pick up the columns first, then the beams, placing them in the most optimal order and correct orientation; i.e. primary tasks for automated structural framework installation.

## 6. CONCLUSIONS

The Xbox controller is very sensitive and susceptible to sudden movements when utilizing the joystick, as such, it is not the most desirable controller for a full-scale project. Although it proved useful for the first prototype, a better controller will definitely need to be considered for the actual application. Although the success of manual controls largely depends on the experience and dexterity of the user, the IR sensors proved beneficial in alerting when near an obstacle.

Further design calculations for the full-scale system must also be developed, keeping in mind materials to be handled; however, the basis of surveying using the manual control is shown to be feasible. With the automation part undergoing development, it was concluded that as a full-scale product, FARA has the potential to be cost effective and safe as a long-term investment for construction firms. Ultimately, the model and testing scenario can also serve as a study model for future experiments that would contribute to the field of automation and use of robotics in construction.

## 7. ACKNOWLEDGMENTS

The authors wish to extend their thanks to Dr. Nipesh Pradhananga for providing the team his support, advice and guidance on automation in construction, and for supplying the team with the prototype materials needed to complete this project. Secondly, the authors extend their thanks to the Robotics and Automation Laboratory and the Department of Mechanical and Materials Engineering for providing access and use of the resources in the labs. Finally, our appreciation is extended to Sudip Subedi, Armando Carrasquillo and the rest of the IAARC team at FIU Miami for their continued support.

## 8. REFERENCES

- [1] C. Balaguer and M. Abderrahim. (2008, October 10). Robotics and Automation in Construction. (1st ed.) [Online] Available: <https://www.intechopen.com>
- [2] E. Lachat, H Macher, T. Landes, and P. Grussenmeyer, "Assessment and Calibration of a RGB-D Camera (Kinect v2 Sensor) Towards a Potential Use for Close-Range 3D Modeling" Remote Sens., vol. 7, no. 10, pp. 13070-13097, Oct. 2015.

- [3] F. Pehlivan and A. E. Dinc. "Laboratory experiences and 3D measurements with AL5A robot arm." M.S. Thesis, Dept. Mech. Eng., Politecnico di Milano, Milan, Italy, 2011.
- [4] G. Pritschow, M. Dalacker, J. Kurz, M. Gaenssleb and J. Hallera, "Application Specific Realisation of a Mobile Robot for On-Site Construction of Masonry" Automation and Robotics in Construction XI, pp. 95-107, May, 1995.
- [5] J. Han, L. Shao, D. Xu, and J. Shotton, (2013, Oct.). Enhanced Computer Vision with Microsoft Kinect Sensor: A review. IEEE Trans. Cybernetics. [Online]. 43(5), pp. 1318-1334. Available: [ieeexplore.ieee.org/](http://ieeexplore.ieee.org/)
- [6] P. Fankhauser, M. Bloesch, D. Rodriguez, R. Kaestner, M. Hutter, and R. Siegwart, (2015, Apr.) Kinect v2 for mobile robot navigation: Evaluation and modeling. Presented at Advanced Robotics (ICAR) 2015 International Conference. [Online]. Available: <http://ieeexplore.ieee.org/xpl/mostRecentIssue.jsp?punumber=7101394>
- [7] S. Lim, R. Buswell, T. Le, R. Wackrow, S. Austin, A. Gibb and T. Thorpe, "Development of a viable concrete printing process," in the 28th ISARC, Seoul, Korea, 2011, pp. 665-670.
- [8] S. Yu, B. Ryu, S. Lim, C. Kim, M. Khan and C. Han, (2009, Feb.) "Feasibility verification of brick-laying robot using manipulation trajectory and the laying pattern optimization." Automation in Construction. [Online]. 18(5), pp. 644-655. Available: <http://www.sciencedirect.com/science/article/pii/S0926580509000028>
- [9] H. Asada. (2005, August). Introduction to Robotics: Ch.4 Planar Kinematics. MIT Open Courseware. [Online]. Available: <https://ocw.mit.edu/courses/mechanical-engineering/2-12-introduction-to-robotics-fall-2005/lecture-notes/chapter4.pdf>
- [10] R. Hessmer. (2009, October). Kinematics for Lynxmotion Robot Arm. Hessmer Org. [Online]. Available: <http://www.hessmer.org/uploads/RobotArm/Inverse%2520Kinematics%2520for%2520Robot%2520Arm.pdf>
- [11] Handbook of Industrial Robotics, 2nd ed., Robotic Industries Assoc., Ann Arbor, MI, 1999, pp. 1167-1183.
- [12] W. Choi, C. Pantofaru and S. Savarese, "Detecting and tracking people using an RGB-D camera via multiple detector fusion," in Proc. IEEE ICCV, 2011, pp. 1514-1519.
- [13] OSHA, Census of Fatal Occupational Injuries Summary, 2015, USDOL, Washington, DC, Dec. 16, 2016.
- [14] O. M. Auskelyte, "On site robotic construction," M. S. thesis, ETSAB, UPC BarcelonaTech, Barcelona, Spain, 2016.

# Humanoid Bipedal Platform Design

Ricardo Olazo, Gilbert Soles, Angel Mendoza, Rodrigo Arredondo, Sabri Tosunoglu

Department of Mechanical and Materials Engineering  
Florida International University  
Miami, Florida 33174

rolaz002@fiu.edu, amend146@fiu.edu, gsole004@fiu.edu, rarre001@fiu.edu, tosun@fiu.edu

## ABSTRACT

Pediatric rehabilitation is a field of medicine which can be fraught with challenges specific to children. Physical therapy focused on the rehabilitation of gross motor skills, can be complicated further if a patient exhibits signs of physical or cognitive developmental issues. Therapy can also be limited by the inability to improve or provide continuity of care for patients in between sessions. Currently, the Humanoid Rehabilitation Project, an open source project started by FIU Mechanical Engineering students, aims at mitigating these issues through the use of a robotic platform.

In support of this ongoing open source project, a pair of humanoid robotic legs have been developed and introduced as an independent, modular unit which can be incorporated with the upper body robotic platforms being developed by the Humanoid Rehabilitation Project. As primary design objectives, the leg unit is designed to be functionally independent, produce anatomically accurate movement, and resemble the human form. As a secondary objective, the team explores different locking mechanisms so that the robotic leg unit can be readily incorporated into any robotic platform which requires humanoid legs.

## Keywords

Robotics, Humanoid Legs, Bipedal Platform, Microcontrollers, Servo Motors.

## 1. Introduction

Humanoid bipedal systems have many applications in the field of robotics, such as robotic assisted gait training. There is also an increasing need, in some cases, for these units to be modular in design. This allows for both easy part replacement and maintenance while reducing design time for a total robotic system by allowing several robotic platforms to be easily integrated or built upon. Several options exist on the market which already satisfy these specifications, but these readily incorporated units are either, very powerful and expensive, or lack robustness and functionality.

The Humanoid Rehabilitation Project required a unit where cost was minimized, but where functionality was retained to a higher degree than currently available at the desired price range. This design effort addressed this problem by prudently trading performance, where possible, for cost savings while the operational

needs of the leg unit were still met. Beyond this specific application, other mid-level functionality, scalable humanoid legs might have applications in various other robotic systems such as educational tools and control testing systems.

## 2. Motivation and Benefits

The primary motivation for this work, as previously stated, is to support the Humanoid Rehabilitation Project in the development of its robotic platform. Currently, The Humanoid Rehabilitation Project is being developed at FIU as a robotic platform intended as an assistive therapy tool in order to reach children with social or emotional developmental issues who have difficulty engaging or are not responsive to traditional forms of physical therapy. By utilizing a robot to demonstrate an exercise or motion to a socially or emotionally impaired child, the human interaction element can be minimized during the course of treatment. In this way, emotional or mental stress can be notably reduced for the child patient and the learning process may be improved. Last, the robot platform aims to allow parents and care takers to provide further care for a child in their home in between sessions.

Therefore, this design effort must complement these overarching goals. Achieving a useful, visual model of gait is the most critical functionality required. The humanoid leg unit being developed will be able to produce this result while being modular to the completed robotic platform and independently controlled. Furthermore, some "universal" leg units which can be readily incorporated into a robot design exist currently. While this approach was considered as a replacement for the need to create a new robot platform, distinct solution, costs and functionality were preventative in the selection of models currently available. Therefore, minimizing costs while achieving only the necessary degree of functionality is a significant motivator.

With true independence, a secondary benefit may be realized. The design developed here may be adopted for use in other robotic systems. The combination of a scalable 3D printable structural design and an emphasis on independent control may make this leg unit compatible with a number of different robotic systems or new custom designs.

### 3. Literature Review

#### 3.1 Trossen Robotics MX-106T

Trossen Robotics is a company that creates robotic kits ranging widely in cost and functional capability. While a good portion of the products available are focused on introductory education, the company also has some more complex and powerful packages as well. One such kit is the Custom MX-106T 6 DOF Humanoid Robot Leg Kit Set. This kit includes aluminum structure, high power servos, and full sensor feedback capabilities. Overall, the unit is very capable though it has a price of over \$6000 and does not come with a control solution integrated.



**Figure 1** - 6 DOF humanoid leg, the MX-106T DYNAMIXEL & MX-64T DYNAMIXEL from Robotis [2]

#### 3.2 EZRobot

EZRobot is another company which creates robotics kits focused on teaching and education. They also have several kits for more advanced users which focus on creating custom robots from standard inter-linking pieces. A Humanoid 2 Servo-motor Foot and Ankle is currently available from their site which can be attached with other proprietary snap fit components to create a humanoid leg. This approach is significantly more cost effective though functionality and scalability are sacrificed



**Figure 2** - EZRobot's legs. These extension cubes allow easy connections [3].

### 4. Design Criteria

The reason behind the chosen design of the legs is to remain autonomous and provide 5 degree of freedom movement for each leg while remaining unaffected by factors such as changes in its scalability. The functionality of the legs should be precise enough to be able to walk while keeping the hip straight. Doing so, the humanoid will be able to walk once an upper robotic platform is attached; assuming the body is symmetrical enough in respect to its center of mass. Although the balancing of the center of mass will be shifted once the body is placed on the hip, this center of mass will remain in the center of the two-dimensional plane that concerns the hip.

The structure of the humanoid legs is capable of being scalable to a maximum size provided by the torque of the servo and the ratio of length between the parts that make up the legs. As the scaling factor for the legs is increased, the bigger the resulting change in the center of mass will be. A maximum size can be attained by further experimenting with the prototype.

Once this size is known, it is important not to exceed it since surpassing the maximum allowable size will require a re-design of the leg's mechanical components. A minimum allowable size is also introduced and is directly related to the size of the hardware used.

So far, the servo motors are the only hardware components that have been added to the design. In the next design iteration, a gyroscope sensor will be added in order to provide a better balance for the 5 DOF leg system and allow for shifting of the center of mass accordingly during training sessions.

The components are made to be 3D printed using PLA as the material. This allows for cheaper manufacturing while the material remains strong enough to hold a desired load. The maximum weight that the humanoid can hold is still unknown but it is estimated that the servo will stall and malfunction before the PLA breaks due to maximum torque output of the chosen servo being 11 N-cm.

### 5. Conceptual Design and Components

Figure 3 represents the current CAD design developed for a single leg. As shown in the figure, the leg features 5 degrees of freedom of movement, as well as a casing that keeps the servos out of reach for safety and security purposes. The casing also yields a more aesthetically pleasing, clean design, which has been one of the goals in this work.

Servos 1 and 2 are contained in the foot and offer a 2 degrees of freedom for the ankle. Servo 3 is responsible for producing the 1 degree of freedom knee motion. Servos 4 and 5 make up the rudimentary hip motions with 2 additional degrees of freedom. Overall, each leg is designed to have 5 degrees of freedom. Figure 3 shows the location of servos to drive each of the 5 joints.

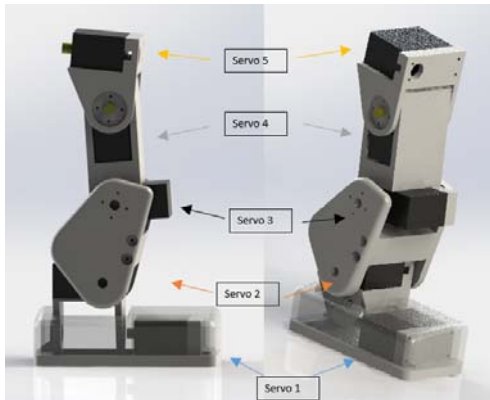


**Figure 3** - Design of the leg. Figure 3 provides the location of the servos needed to create the 5 DOF movement

The leg design also features room inside its components to separate the wires from the servos. This will provide safety to the user, as well as keeping the wires safe from pinching as the servos move.

The hip has been designed as a two-piece assembly that is attached to servo 5 on both legs. The hip also features holes to facilitate wiring, and 4 screws that allow for a torso to be connected on top. With the hip and legs assembled, servo 5 is able to create a rotational movement for the legs normal to the hip. This is essential for the platform to maintain balance throughout its motion. With the inclusion of the hip, the legs provide a total of 10 DOF for various possible movements. The Servos operate at up to 6V and can operate at maximum current of 0.900A.



**Figure 4** - Printed legs

## 5.1 Material

Since the legs are 3D printed, the material can be chosen by the user. PLA was the material selected for all the components in the platform. PLA is a thermoplastic that can be easily molded when heated and returns to a sturdy solid once it cools off. The reason why PLA was chosen instead of ABS was because of its lower cost while being able to withstand a large amount of stress without breaking [6].

## 5.2 Microcontrollers

The Arduino Mega serves as the microcontroller that provides function to the legs. With its ability to control several servos simultaneously, the mega is the best choice when considering a light and powerful microcontroller. Additionally, since Arduino is an open source platform, the price for Arduino clones is much lower than other microcontrollers.



**Figure 5** - Arduino Mega 2560 [5]

Additionally, an Arduino Nano could also be used to fully control the legs. However, it was decided to continue using the Arduino Mega since it accommodates enough pins and processing power to control any added components such as the upper body robotic platform.

## 5.3 Servo Driver

The PCA9685 by Adafruit provides a voltage of 5V to up to 16 servos. This component is necessary in running all the servos in unison since the power provided by the Arduino is not enough to power more than two simultaneously. Furthermore, the device is a product meant to operate with the Raspberry Pi. By adding a library and modifying the open source code, the group has successfully integrated the driver with the Arduino Mega.



**Figure 6** - PCA9685 by Adafruit

## 5.4 Servos

The Servo chosen for the leg mechanism is the MG996r TowerPro Servo. This servo provides a high torque of 11 N-cm at 6V, have a total weight of 55g, and cost \$6. A total of ten servos are used in the robotic legs platform. With the aid of the servo driver, all servos run simultaneously without affecting their performance.



Figure 7 - TowerPro's MG996r Servo Motor [16]

## 5.5 Battery

For this project, selecting a power source capable of providing enough power to move all servos through the PCA9685 was of most importance. With that in mind, it has been decided to leave the decision to the consumer. As of now, a power adaptor is used to power the PCA9685 which subsequently limits the working range of the robot legs. This power supply is plugged in directly into the PCA 9685 and converts the power from the outlet into a voltage of 5V and 10 Amps current. If the user requires to increase the working range of the robot, a battery pack or other independent power supply has to be used.

## 5.6 Additional Components

Other components have also been found that will help in the development of this platform. Electrical wires have been purchased to extend the wiring of the servos for an easier connection as well as allowing for better placement of the microcontroller and power source

## 6. Cost Analysis

An estimation can be made with the expenses of the components that are incorporated into the final design. Currently, the total cost of the project is shown on the table below:

Table 1 – Cost estimate of components

Component	No.	Price (each)	Total Price
Servo	10	\$5.99	\$60.00
Filament	1 Roll	\$22.00	\$22.00
Arduino	1	\$13.98	\$13.98
Electrical Wiring	1	\$12.00	\$12.00
Screws (pack of 100)	1	\$10.09	\$10.09
	Total $\Sigma$		\$118.07

Although the legs are an open source creation, it is our belief that the platform is designed for individual personal use and not for mass production. Therefore, manufacturing costs will vary depending on the access to a 3D printer capable of printing the legs. The following table shows an estimation using a small commercial 3D printer. Due to the size and capabilities of the 3D printer used, the time taken to print the components was extensive. Taking this into consideration, a manufacturing cost of \$6 an hour is assumed for the cost analysis.

Table 2 - Manufacturing time and cost

Component	No. of Pieces	Printing Time (hrs)	Total Time (hrs)	Cost
Hip	1	6.8	6.8	\$40.80
Hip - Front Section	1	3.1	3.1	\$18.60
Hip - Servo Support	2	2.2	4.4	\$26.40
Hip - Servo Support Front Section	2	1.2	2.4	\$14.40
Leg	2	3.7	7.4	\$44.40
Calf	2	1.9	3.8	\$22.80
Calf - Side Section	2	1.7	3.4	\$20.40
Ankle	2	1.8	3.6	\$21.60
Sole	2	4	8	\$48.00
Foot	2	6.8	13.6	\$81.60
Foot - Servo Support	2	0.8	1.6	\$9.60
Bearing Holder	12	0.3	3.6	\$21.60
	Total $\Sigma$		61.7	\$370.20

## 7. Assembly and Calibration

One of the main concepts behind this design was to create a platform that will be easy to assemble, while remaining completely functional and saving time and material while printing. This was achieved by creating small parts that assemble around the servos. A total of 7 parts per leg are assembled together with the use of a few screws.

Before assembling the platform, Servos 1, 2, 4, and 5 have to be positioned in their 90 degree position, while Servo 3 has to be positioned at 0 degrees. This will allow the full range of motion of the servos, including servo 3, the knee, which is only required to move from 0 to 90 degrees.

## 8. Prototype and Experimentation

During the prototyping phase, the individual legs have been programmed to move. These programs are very basic and produce movement with coordination between all the joints in the leg. Programming will likely prove to be the bulk of the experimentation phase as the task is quite tedious.

The next objective will be to control both legs in unison once rigidly connected. After this is achieved, the possibility of incorporating a gyroscopic sensor to maintain equilibrium under different loading conditions will be explored though is not of primary concern as these legs are first and foremost being designed to demonstrate movement with assistance from the operator for balance.



**Figure 8** - Final Design of the legs with "mock" hip

## 9. Execution

As predicted, the programming of the legs to mimic walking was simple but time consuming. The trial and error approach to servo control is effective. The code is written directly into the Arduino IDE, tokenized and written to the controller, executed, then adjusted through numerous iterations. Since the servos move based on position, sending the servo from position A to position B will make it rapidly move. To slow this process down, a variable was created that would vary per loop making the increments bigger or smaller depending on whether a faster or slower movement was required. Furthermore, the delay between the movements of each individual servo played a major role. By setting the delay to 3 milliseconds, the servos' movements became more fluid.

In order to streamline the process, each individual servo motion was fine-tuned systematically, Servo 5 down to Servo 1. Initially, a static walking motion, or walking where the robot is never completely in a "free fall" forward as with a natural gait, was programmed as it was the simpler task. From there, the programming

shifted to focusing on balancing the humanoid on one foot, while the other was raised in the air, with bent knee, to the highest position of the dynamic gait desired. Once achieved, the task became playing with the timing of extending the raised, bent knee and beginning the mirrored movement of the other leg. Ultimately, a fairly realistic gait was achieved through iterative adjustment.



**Figure 9** - The first 3D print of the unit. Functional testing was performed here

As of the finalization of this report, improvements are still required to the coding aspect of the platform. In order to maintain a sustained, unassisted walking motion, logic improvements are necessary for maintaining balance consistently is sometimes problematic. Mainly, the leg unit will occasionally fail to maintain balance and tip over. Improvements with the gyroscopic sensor integration will correct this issue. However, when supported externally, the walking motion is reliable. Overall, the platform's intended design is sufficient for the applications of Humanoid Rehabilitation Project, though the code needs to be adjusted to account for the changed weight distribution.

## 10. Discussion and Future Work

From a manufacturing and structural perspective, this project has accomplished the goals laid out and surpassed our expectations. An easily scalable bipedal platform with structural strength, displaying the necessary degrees of freedom, with adequate servo power capacity, and including independent control and power supply was created within the targeted price point. In total it is estimated that reproducing the unit would cost approximately \$121.07 depending on the cost and availability of rapid prototyping and manufacturing equipment. However, a singular challenge still remains and should be the focus of future work. The single greatest limitation of this platform, in its current state, is the complexity of the coding process. Producing even the most simplistic movements is a time consuming, manual coding process done within Arduino IDE.

Research into publications presenting much more complex humanoid robot projects revealed this to be a common issue in the development of almost all of these humanoid systems. One paper, in particular stated, “Generation of motion for humanoid robots is quite different from that of standard robots because of the large numbers of joints, coupling between joints, redundancies, and people’s expectations that humanoid robots move like humans” [4].

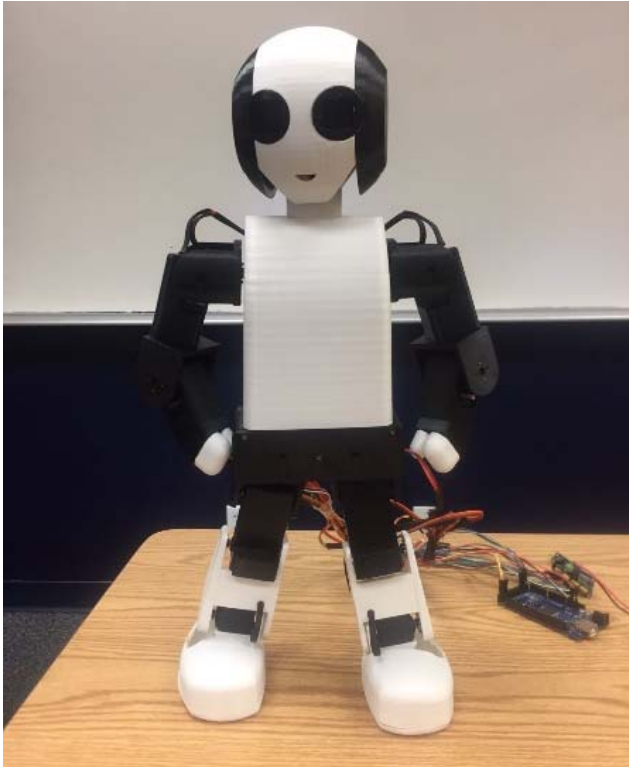


**Figure 10** - An example of the full humanoid robot constructed by using the bipedal legs developed in this work

The paper goes on to note the difficulties which come with a manual coding approach and states that a common solution is to spend time developing “a special motion creator with a rich graphical user interface that enables programmers to tackle these problems in an interactive manner” [4] or, as is the subject of the paper itself, develop alternative programming approaches like motion capture technologies to record human movements and translate them to servo outputs in order to program movement.

Ultimately, the primary and secondary objectives of this design effort were achieved in that, the leg unit is functionally independent, produces roughly anatomically accurate movement, and resembles the human form in proportion.

Additionally, modularity allows for it to be readily incorporated into any robotic platform which requires humanoid legs. However, the development or incorporation of a higher level function generating program is still necessary to simplify the use and application of this independent device.

Therefore, it is proposed for current and future contributors working on the Humanoid Rehabilitation Project to mainly focus on the development of such control and programming techniques.

## 11. REFERENCES

- [1] Shigley’s Mechanical Engineering Design, Richard G. Budynas, and J. Keith Nisbett, 10th edition, McGraw-Hill, Inc., New York, 2015.
- [2] Custom MX-106T 6 DOF Humanoid Robot Leg Kit Set. Trossen Robotics [trossenrobotics.com/p/custom-ex-106-6-DOF-Humanoid-Robot-Leg.aspx](http://trossenrobotics.com/p/custom-ex-106-6-DOF-Humanoid-Robot-Leg.aspx). Accessed 27 Feb 2017.
- [3] EZ-Robot Extension Cubes. Stemfinity [stemfinity.com/EZ-Robot-Extension-Cubes-3](http://stemfinity.com/EZ-Robot-Extension-Cubes-3) Accessed 27 Feb 2017.
- [4] Ude, Aleš, Atkeson, Christopher, Riley, Marcia, Programming Full-Body Movements for Humanoid Robots by Observation. Elsevier, 47(2-3), 2004.
- [5] “Arduino - ArduinoBoardMega.” Arduino - ArduinoBoardMega. N.p., 08 Apr. 2015. Web. November 22, 2016.
- [6] Chilson, Luke “The Difference Between ABS and PLA for 3D Printing” Protoparadigm, [protoparadigm.com/news-updates/the-difference-between-abs-and-pla-for-3d-printing](http://protoparadigm.com/news-updates/the-difference-between-abs-and-pla-for-3d-printing). Accessed January 30, 2017.

# The Humanoid Rehabilitation Project

Ricardo Olazo, Gilbert Soles, Angel Mendoza, Jean-Carlo Drada, Sabri Tosunoglu, Melissa Morris

Department of Mechanical and Materials Engineering  
Florida International University  
Miami, Florida 33174

rolaz002@fiu.edu, amend146@fiu.edu, gsole004@fiu.edu, jdrad002@fiu.edu, tosun@fiu.edu, mmorr009@fiu.edu

## ABSTRACT

Pediatric rehabilitation is a field of medicine which can be fraught with challenges specific to children. Physical therapy, concerned with rehabilitation of gross motor skills, can be complicated further by a range of physical or social developmental issues. Therapy can also be limited by the inability to maximize continuity of care for patients in between sessions. Mitigating these issues through the creation of a robotic platform is the primary focus of the Humanoid Rehabilitation Project. In particular, the robot will be capable of alleviating these issues by 1) serving as a customizable and engaging visual model which can demonstrate a particular rehabilitation exercise or movement and 2) by behaving as a surrogate between the therapist and the child or the parents and the child. By acting as both a visual model and a surrogate for interaction, discomfort and social pressure felt by the child during a therapy session with adults can be reduced while a useful technique or exercise can be introduced and taught more effectively. In order to accomplish these objectives, the Humanoid Rehabilitation Project developed a unique, replicable robot named HCTeR, short for Humanoid Companion Technology for Rehabilitation, composed of a 3D printed, FDM structure, widely available off-the-shelf electronic components, and relying on the Arduino family of microcontrollers.

## Keywords

Robotics, Humanoid Legs, Bipedal Platform, Rehabilitation, Microcontroller, Servo Motors, Physical Therapy.

## 1. INTRODUCTION

### 1.1 Problem Statement

Physical therapy is a rehabilitative form of physical medicine which involves the strengthening and development of gross motor functions in individuals with impairment caused by disease, injury, or cognitive disabilities [1]. Physical therapy can be a difficult process for anyone. Whether a person is attempting to regain a function or learn a new one, the amount of lasting, desirable improvement can be greatly affected by how receptive a patient is to the required therapy. Pediatric rehabilitation brings with it new issues. However, when the patient is a child with other developmental issues, teaching and guiding a successful round of therapy can become a much more robust problem [2]. Specifically, the spectrum of autism disorders, among others, causes pediatric patients to experience debilitating stress or complete closure to

interaction in social settings. This can often make physical therapy much more difficult if not impossible.

### 1.2 Motivation

This robot is being designed initially as a tool to reach children with social or emotional developmental issues who have trouble or are not responsive to traditional forms of physical therapy. It is intended to be an aid tool for physical therapists and parents caring for these developmentally impaired children. By utilizing a robot to demonstrate an exercise or motion to a socially or emotionally handicapped child, the human interaction element can be minimized. In this way, emotional or mental stress can be reduced for the child patient and the learning process may be improved. Because the functionality sought lies in bridging the communication gap with impaired children, a design focus must be placed on creating a robot which is aesthetically pleasing and visually captivating to these children. In addition, the robot, which will mirror the proportions and stature of the patient, may also be used by the child and parents at home to improve the continuity of therapy in between sessions in addition to its therapist surrogate function.

Currently, an open source project called the Poppy Project has sought to develop a database of accessible information for creation of robots. In particular, a robot created to study the biomechanics of biped motion with a focus on how morphology can affect cognition is being used as a point of reference [3]. Because of the costs associated with the Poppy Project and other similar humanoid robotic platforms at thousands of dollars per robot, another significant motivation for this design is producing a unit at a lower price point.

### 1.3 Literature Survey

#### 1.3.1 *Humanoid Robots*

As robots become increasingly present in society, the importance of understanding their origins is magnified. Humanoid robots were first used in research for the purpose of modeling how the human body rudimentary functions. Eventually, these robots gained certain characteristics such as motion and problem solving skills limited by their programming. By utilizing different kinds of mechatronic systems, humanoid robots can be designed to perform tasks that would otherwise seem limited to humans. Motors and servos can produce a flexible output in terms of speed, power, and precision that would be limited only by the characteristics of the components. As technology progresses, so do the abilities of these robots. According to Smashing Robotics, the advancement of A.I.

technologies will allow humanoid robotic systems to display “intelligence...surpass[ing] human intelligence by 2030.” These robots are becoming less restricted to laboratory environments and are slowly growing into a part of society whether it is assisting humans, performing surveillance and other military functions, in prosthetic applications, and many other areas of study. Generally, the cost to produce almost any humanoid robot makes it inaccessible for many, as costs can reach \$5000 for a unit [4].

### 1.3.2 *Pediatric Rehabilitation*

Rehabilitation for children differs from adults in a few ways. One is that pending their age, they may be learning an activity or motor skill for the first time. This means that they don't already know how to perform a function and that they may not be motivated to learn since they've gotten along fine without that functionality thus far. Children also have different body proportions (all children do, but some conditions such as Down syndrome can exaggerate the differences), so you can't just take adult items and do a simple scale. Children also tend to be visual learners, have shorter attention spans and may be shy or avoid adults, particularly strangers. Developmental delays such as autism, which is a condition more prevalent and understood today than ever before, result in children having even greater tendencies towards these behaviors.

Doctors often recommend physical therapy (PT) for children who suffer from certain injuries or who have motor problems associated with certain other conditions. PT might be needed any time a problem with movement limits someone's daily activities. Whether the disability is physical, an illness, or a disease, physical therapists work with the kids in order to decrease pain or to discourage undesired tendencies to help children return to their (or gain) daily activities. To accomplish this, therapists perform different exercises that focus on helping children regain strength and range of motion while at the same time showing families how to prevent future injuries [2].

### 1.3.3 *Poppy Project*

The Poppy Project is an open-source platform for the creation, use and sharing of interactive 3D printed robots. It gathered an interdisciplinary community of beginners and experts, scientists, educators, developers and artists. They all share a vision: robots are powerful tools for learning and creativity and collaborate to improve the project. They develop new robotic behaviors, create pedagogical content, design artistic performances, improve the software or even create new robots [3].

The Poppy project evolved through a community that developed an easy to build and customizable robot that is promoted as an open-source project. In this way, anyone can use it and further develop its hardware as well as its software. A forum has been established to make all this information accessible to the public. Since Poppy is an open source platform, all sources of the Poppy Project (software and hardware) are available.

### 1.3.4 *Ottobot*

The Ottobot is another open source project tasked to interact with kids to improve their social engagement issues. This robot is a small toy that interacts with the environment as well as other Ottobots. While a much smaller project than Poppy, Ottobot shows how 3D printing can be leveraged to create affordable robots which produce a positive social impact. Because this small robot appeals to children through movement, dance, and sound, it is inclusively designed to encourage social interactions and emotional engagement in youth with autism and other special needs. It is intended to be a surrogate for practice with emotional expression or communication. This robot also features a control app on

smartphones that changes its functions very easily without having to restart its coding process. This makes this toy-like robot a much more versatile tool for social engagement [5].

## 2. PROJECT FORMULATION

In general, this project was developed as a platform for implementing robotics to supplement pediatric physical rehabilitation with an emphasis on reaching socially or cognitively impaired patients. Physical therapy involves the strengthening and development of gross motor functions and is often a very burdensome and difficult process which can be further complicated by emotional or learning disabilities. Initially, this application of technology addresses issues regarding interfacing therapy with socially less-responsive children and it will also allow for improved continuity of care. This, however, is not to be taken as a limiting condition for application and use. Because of the open source nature of the work, it can be expanded to possibly include new, more accessible programming tools or increased functionality such as remote control by a therapist, allowing for a more flexible “telemedicine” approach to physical therapy which could reduce the cost of care.

### 2.1 Objectives

The motive of this design is to contribute to society by improving the relationship between a therapist and the child that is undergoing treatment. By creating a robot that serves as an inexpensive surrogate and mediator during pediatric rehabilitation, the team hopes to help patients by providing a new treatment tool and improve results when compared to or used in addition to tools that have been used in the past.

Two main functions that have been selected as design objectives for this robot. The first function of the humanoid robot will be to be capable of serving as a visual model that children may observe and learn from through mimicry. In this way, it will become possible for a therapist to demonstrate a certain movement or exercise to a child through the robot. The second function chosen was for the robot to serve as a social intermediary between the physical therapist and the child patient. Among children who have cognitive disabilities, a major issue in providing any medical treatment often arises from the child's resistance to social interaction with a provider. By allowing for the introduction of interesting stimuli (i.e. lights and sound) and downplaying the human element of receiving physical therapy, the Humanoid Rehabilitation Project will aid in bridging this gap. This combination of functions and priorities will allow a therapist the possibility of more easily demonstrating to a child, how to perform certain activities or exercises.

A secondary yet significant benefit can also be yielded from the Humanoid Rehabilitation Project effort. Because the nature of the project is modular and open source, the project can also be used to improve continuity of treatment. The platform, in concept, may be used and practiced with at home by the child with parental supervision or with therapist supervision via a telemedicine functionality which could be incorporated at a later time. By creating a robot which places an emphasis on hands-on interaction for the patient, the child will interact through different exercises as well as learn through modeling from the robot.

### 2.2 Design Specification

With the intention of creating a more accessible robotic platform, one of our goals is to reduce the overall price while keeping the quality of our final project in comparison to similar humanoid

platforms. With the Poppy Project being the most similar humanoid robot surveyed and using that unit's cost as a reference, we hope to reduce the price by at least 50% while maintaining a unit capable of still performing the required functions. In order to accomplish this, a competitive price analysis was performed concluding that the servo motors are the most expensive component in most humanoid robotic devices. For this reason, servo selection became paramount. Replacing the more expensive units with cheaper servos that are still capable of achieving the required degree of performance may provide a means of reducing the final price of construction significantly. In an attempt to lower the final cost further, the team agreed on including component sourcing information rather than providing any components via the Humanoid Rehabilitation Project itself, unlike other open source projects which may profit from selling components. Therefore, all 3D printable components will be accessible and ready to print using a suggested 3D printer, filament, and a listing of trusted distributors for other critical off-the-shelf components.

### 2.3 Addressing Global Design

Maintaining positive global awareness is a key aspect of any ethical design procedure. Evaluating the resulting consequences and implications a project may have on different people is paramount for producing an end design that accomplishes the task. Accessibility and inclusiveness are cornerstones of solutions that work.

In this design procedure, the target audience is pediatric physical therapy patients with varying disabilities, their families, and the pediatric physical therapists who treat them. This group requires that many careful considerations be made to maintain a high degree of sensitivity. In order to create a solution which is highly accessible and inclusive, three primary factors are being considered in the design which will allow this goal to be achieved.

First, designing with the intent to produce a product with the lowest possible cost will allow this technology to be available to people coming from a wide range of socioeconomic backgrounds. Patients in countries with lower standards of living will be more likely to benefit from this technology with lowered cost. By placing an emphasis on informed component selection for things like microcontrollers and servos, and relying on 3D printing for the bulk of the manufacturing requirements, it will be possible to create a functioning humanoid robot at a lower price point than previously available.

Another major consideration will be focused around continuity of care. Physical therapy typically occurs at a dedicated location such as a clinic or office, or in another appropriate setting such as a home visit. Both of these scenarios involve a physical therapist's direct contact with a patient in order to produce the desired results. However, conducting the optimum number of these face-to-face sessions may be limited by insurance coverage, local therapist availability, or other cost prohibiting factors. By implementing this robotic tool, a family may be able to increase the frequency of therapy without increasing the associated costs of more clinic visits and more hours with a therapist. As a limited surrogate, the robot will allow a family to take more ownership of the therapy process and fill the treatment gaps.

The final consideration being made regards how individual, unique cases may be addressed. By leaving our design process completely transparent and open source, this robot can be modified and customized by someone closer to a particular case in order to produce the optimum amount of benefit. For example, the programming could be altered to allow the robot to interact in a different language or exhibit disproportionate strength in one limb

versus another in order to better approximate the individual patient. Also, because the robot structure will be entirely 3D printable, it will be possible to adjust the physical dimensions and scale of the model in order to create a high degree of similitude between the patient and robot. However the model or program is modified, flexibility is key in order to reach the greatest number of patients.

### 2.4 Constraints and Other Considerations

In this project, the biggest limiting factor was time. This was a very complex design, and the programming took the longest portion of the design process. However, since this is an open source project, this limiting factor for functionality is mainly based on what an end user's individual programming knowledge allows. Through the development of one rudimentary programmed procedure, the platform's functions may begin to be understood and improved upon by end users and any continuing design efforts.

## 3. DESIGN ALTERNATIVES

In order to improve the quality of our final project, we decided to divide our design process into two stages. The first stage consisted of developing a prototype to provide a reference point regarding maintaining the most accessible budget and allowing for some initial testing and analysis to be performed. The prototype used economical, but less capable servos, and had a 3D printable structure with an emphasis on reducing total filament usage. A kinematic analysis was performed using the prototype to determine the range of possible motion and to ensure anatomically realistic movements. Finally, testing of possible additional features such as Bluetooth remote control, MP3 playback, eye emotion simulation, and wi-fi connectivity could also be performed.

The second stage involved creating a new platform which modified and improved the original prototype. It was of a larger size, but retained the same degrees of motion. This way, the prototype more closely models a child and can be more capable in general. For this stage, we focused on the programming and hardware capabilities. By keeping all the functional features, but implementing more effective servos and incorporating other components directly aimed at appealing to a child, the design provides a better model for the patient undergoing treatment.

### 3.1 Design Alternate 1

The first step in implementing this prototype was the components selection. Since only a small scale of the prototype was to be designed for this stage, the use of economical servos was justified. This small scale prototype serves as a learning guide into how the different limbs attached to the humanoid brought movement. Based on these dimensions of the chosen components, a humanoid was designed with 3D printable limbs to simulate the optimal movement of the joints.

At this prototyping point, and because of its design intent in being appealing to children, the group decided to name the humanoid robotic platform HCTeR, pronounced Hector. HCTeR is short for Humanoid Companion Technology for Rehabilitation.

#### 3.1.1 Components

##### 3.1.1.1 Arduino Mega

The Mega 2560 is a microcontroller board based on the ATmega2560. It has 54 digital input/output pins (of which 15 can be used as PWM outputs), 16 analog inputs, 4 UARTs (hardware serial ports), a 16 MHz crystal oscillator, a USB connection, a

power jack, an ICSP header, and a reset button [6]. Also, the Arduino Mega is capable of controlling several servos simultaneously as well as many other components. In addition, there are many forums and websites full of useful information of how to use the Arduino that will help us during the project design. Lastly, since Arduino is an open source platform, the price of the Arduino is relatively low compare to other microcontrollers. For all these features, the Arduino Mega was chosen as the microcontroller.

### 3.1.1.2 SG90 Servo Motor

To pick the correct servo motor for this prototype stage, power was not a deciding factor. Since this prototype was only going to be a small scale design, we turned to the economical aspect of the servos. This is why the SG90 servo motor was chosen.

This servo provided us with an operating voltage of 5V, an operating speed of 0.1s per 60 degrees, and a stall torque of 1.8 Kg\*cm, all of this while having a total weight of 9g. This servo is very limiting in that it has only one input and, unlike other more expensive servos, does not provide feedback [7].

### 3.1.2 CAD Model

This design features a humanoid torso, as well as the arms with five servos that provide one degree of freedom each. This is the structural design of prototype HCTeR. This design is 54cm tall, and has a length of 15.25 cm shoulder to shoulder. This prototype also featured stationary eyes to give us an idea of what the final design would have. Stage two will feature eye components that, once programmed, will simulate emotion through different facial expressions, making the robot appealing, accessible, and unthreatening.



Figure 1. First Prototype of HCTeR

## 3.2 Design Alternate 2

After careful consideration, the group decided that the new design had to be done from scratch introducing only the design ideas that the group wanted to reuse. With this in mind, it was decided to

remove one degree of freedom in the arm; the servo omitted from this design created a rotational motion of the arm which the group believed would complicate the design in this stage. This motion can still be added to future prototypes.

Another consideration was the redesign of the legs. The legs did not work as expected. However, a successful analysis of the degrees of freedom provided by the legs was what the group hoped to achieve in the first prototype. For this design the legs will remain at ten degrees of freedom.

### 3.2.1 Components

Because of the many alterations between stage one and two, some of the components were changed. Design two featured an increased height and weight which meant that stronger servo motors, as well as a higher current output, was needed. The Arduino Mega remained as the chosen microcontroller. This microcontroller successfully controlled the new servo motors. However, a different power supply was used to power these since the Arduino is only capable of powering up to two servos at a time. Also, this design featured the ability to add new components such as Bluetooth and wi-fi connectivity shields for Arduino.

An additional servo was introduced in the hip to create a rotational movement on a plane parallel to the floor. This facilitates walking and allows a turning movement of the torso for different therapy exercises. The complete design features 18 degree of freedom of movement, including the neck movement.

#### 3.2.1.1 MG996r Servo Motor

For the final design, it was fundamental to increase the total functionality of the servo motors, since the design was of a much larger scale. TowerPro's MG996r servo motor possesses a torque of 11 Kg\*cm at 6 V, a stall torque of 15 Kg N\*cm, and a total weight of 55g. [8]

#### 3.2.1.2 LCD Display Module

The eye components consist of two LCD display modules. These are 3.3V, 0.96 inch screens that will work as a display for each eye as shown in the figure below. The LCD display module is of utmost importance since it helps display HCTeR's emotions through its eyes. For cases where a child might not understand emotions as well, the expressions shown by HCTeR can be altered to prevent frightening children.

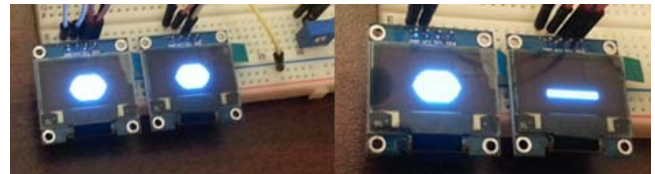


Figure 2. Eye expressions. This figure displays two of the many possible emotions that can be coded into the display

### 3.2.2 CAD Model

The CAD model of the final design features a bigger and friendlier looking platform. Although this model borrows greatly from its previous stage, the group decided that changing the total degrees of freedom of the previous design to 18 (5 in each leg, 3 in each arm, 1 on the hip, and 1 on the neck) will still allow for all the essential movements. This design also has LCD screens as eyes, and careful placing of wiring and servos to prevent harmful situations. This design is shown in Figure 3.



Figure 3. HCTeR stage 2

### 3.3 Integration of Global Design Elements

For the final stage of the prototype, a plethora of considerations was made. First of all, the entire design is a solution to target a social and ethical dilemma. Even though this has the potential to improve lives, certain considerations still need to be made. Because of this, it is critical to follow a code ethics.

By making the prototype a 3D printable platform, it is hoped that it will be more accessible to the target audience. 3D printing, as time progresses, is becoming more accessible as it lowers the cost that goes into the production of these parts. It even creates a DIY environment where someone with sufficient technical background can set this up for a small cost when compared to other humanoid robotic platforms that are commercially available.

### 3.4 Feasibility Assessment

As shown in both CAD models, the parts designed can easily be 3D printed. Each part takes roughly between 5 to 8 hours to print, and is designed for easy assembly. As mentioned in the previous section, the availability of 3D printing, an increasingly available technology, and HCTeR's other components, allows for the

feasibility of this design. Furthermore, by looking at the price of each individual component, a better understanding of the expenses that went into this project was analyzed. For the complete analysis of the total cost, see Section 6.5.

Finally, at this point in the design effort, with the physical structural design and component selection completed, it was decided that the programming effort would be limited to producing walking as the primary focus. As an alternative, crawling, which is a valid physical therapy exercise in pediatrics [9], may be explored.

## 4. ENGINEERING DESIGN ANALYSIS

### 4.1 Overview

From an engineering standpoint, HCTeR is designed to allow for some key kinematic goals to be met, maintaining a high degree of strength, and reduce costs as much as possible. Several simulation analyses are performed to ensure that these goals are met.

From a kinematic perspective, it was necessary for HCTeR's joints to have nearly the same degrees of freedom that the corresponding real human joints have. This allows for a reasonable range of movement in the robot's primary limbs that might be needed for child rehabilitation. Actuator performance and selection would prove to limit function rather than being limited by geometric parameters within this context.

Strength of design was important as well. Besides holding its own weight, HCTeR is designed with a factor of safety in mind which will prevent damage from normal wear and some harsher interactions with children. HCTeR is not designed to withstand severe impacts, but will be resilient within the context of rehabilitating a child under adult supervision.

Another major design focus was the widespread implementation of 3D printing as the primary method of manufacture. This, along with prudent research into components, made reducing the cost simpler. These were the major factors and considerations in the overall engineering design effort.

### 4.2 Kinematic Analysis and Animation

Because the goal of HCTeR is to reproduce a movement, teach, and encourage pediatric physical therapy patients, it is of utmost importance that the design process includes the proper limb motion.

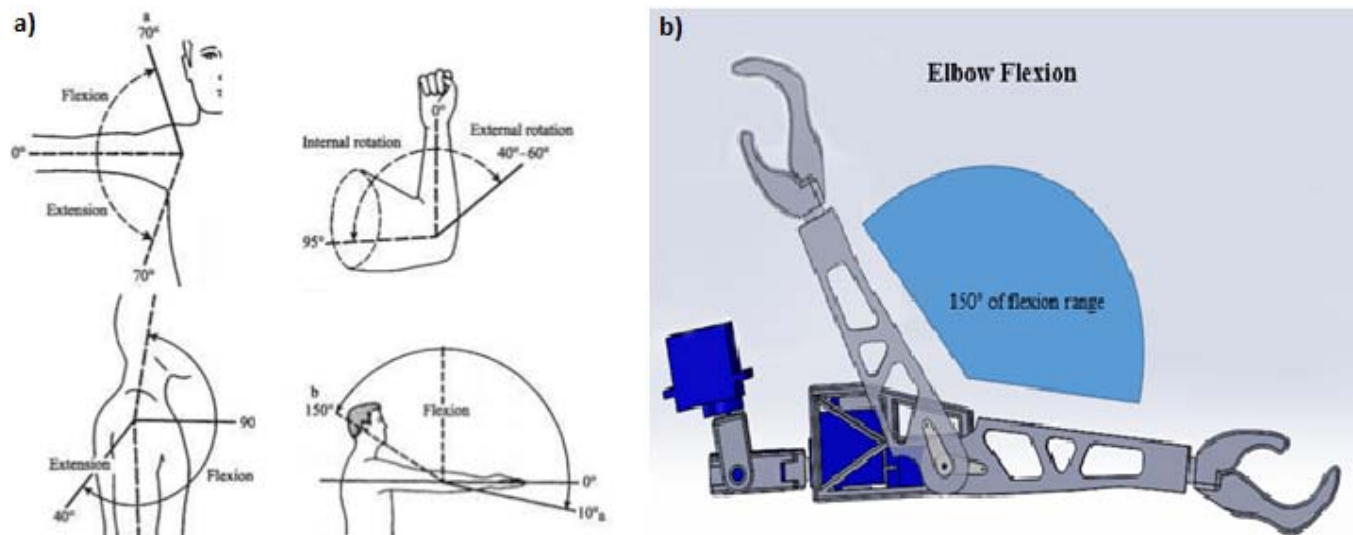


Figure 4. (a) Human Arm Kinematics. (b) HCTeR Prototype Elbow Flexion

By limiting the servo range of operation to that of an actual human child, HCTeR can be used to serve as a model for the child. Figure 4 (a) provides a geometric visualization of the range of the joints in a human arm compared to Figure 4 (b) which displays HCTeR's arm's range of motion for the first stage prototype design. As shown, the average human elbow has a range of motion of 150 degrees, stage 2 also provides this range of motion. However, stage 2 limited the internal and external arm rotation shown in Figure (a). This was a result of the choice to remove a degree of freedom in the elbow allowing more room for wiring in addition to reducing cost and simplifying the design wherever possible.

The programming, however, will be the ultimate control for the kinematics of the elbow and other joints. Likewise, the range of motions of each major joint of the human body (i.e ankle, knee, hips, elbow, shoulder, and neck) were analyzed to determine angular ranges of motion [10]. In general, the major movements were modeled with both the same degrees of freedom and angular ranges of a typical human body.

Because, the team decided to focus on reproducing human walking, ensuring that the set of joints comprising the legs were anatomically accurate with regard to both degrees of freedom and angular range was most important. From a chart by the Department of Social and Health Services, the following movements were recreated accurately:

**Table 1. Summary of Joint Movements Available on HCTeR**

Joint	Movement
Hip	Flexion, Adduction, Abduction, Backward Extension
Knee	Flexion
Shoulder	Abduction, Adduction, Flexion, Extension
Elbow	Flexion
Ankle	Inversion, Eversion, Flexion, Extension
Back	Extension, Flexion, Lateral Flexion
Neck	Rotation

### 4.3 Material Selection

In FDM, or fused deposit material, 3D printing, the most common materials are ABS and PLA. Both of these materials are known as thermoplastics, meaning that they can be easily molded when they are heated and can return to being a sturdy solid once they have cooled off. Based on research, it was determined that ABS is the stronger material. From the stress analysis, however, PLA was found to be strong enough to be able to withstand the more modest loads HCTeR will most likely encounter. In addition to this analysis, the group decided to use PLA for its added benefit of exhibiting lower warping when being printed [11]. Also, to make HCTeR more resilient, the group suggest that the printing be done with a 20% fill density.

### 4.4 Component Design

HCTeR's assembly process was documented and explained in an instruction manual allowing even someone with minimal experience with robotics to purchase and assemble all the components easily. Along with instructions for use and descriptions of the components, the instruction manual contains exploded views,

wiring diagrams and schematic representations of all the components. For example, below is the exploded view of stage 2 design of HCTeR's right arm as for improved clarity.

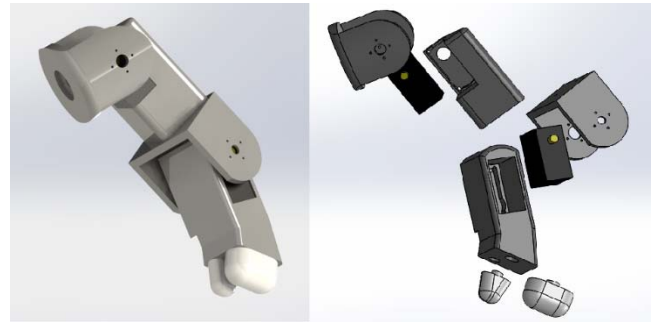


**Figure 5. Exploded view of HCTeR stage 2 arm design**

There is an important note to make regarding the engineering logic used in selecting the components described in Section 3. In the literature survey initially performed, one of the major issues identified with existing platforms is overall cost. The cost of many of these platforms is driven up significantly by the incorporation of proprietary microcontroller systems and very high capacity servos. As a solution to this, the Humanoid Rehabilitation Project prudently sacrificed performance and the benefits of proprietary controllers in order to reduce cost (i.e. less powerful servos and the ability to use software available for proprietary controllers which make control and programming simpler) in the hopes that the work carried on after the publishing of this paper will allow for these factors to be mitigated and adapted to the Arduino family of controllers.

### 4.5 Design Overview

Stage one of the prototype served as a learning curve for producing the version of HCTeR which is able to meet all the kinematic requirements. This prototype features a smaller scale that works best to model and gauge more accurately what stage two will be capable of. By creating the first prototype, a better analysis of the degrees of motion of each limb was achieved.

Stage two features a similar design, though structural improvements were made to ease manufacturability and improve function. A significant modification to this version is that the ability to perform forearm pronation and supination [10] were eliminated. This decision simplified the design, reduced cost, and did not significantly affect the ability of the robot to be programmed to perform the primary therapeutic function of focus. Finally, in this iteration of HCTeR, the use of a Bluetooth and wi-fi connectivity shields were finally ruled out as development of appropriate software was deemed outside the scope of this primary objective. However, because of the use of the Arduino family of controllers, future inclusion of these capabilities and the accompanying programming efforts is possible and will likely increase the effectiveness of the tool.

## 5. PROTOTYPE CONSTRUCTION

For HCTeR's prototype construction, the build was subdivided into segments. These segments were apportioned into smaller, electromechanical systems (i.e. individual arms, individual legs provided by Florida International University's 2017 Spring EML 4840 Robot Design course, Team F, isolated head unit, etc.). This approach allowed for a simplification of the testing and programming phase by isolating systems which could be developed

concurrently. The software programming proved the most difficult aspect of development as the desired functions are extensive and complex. Prototyping proved invaluable in providing the groundwork for understanding of how to best utilize the 3D printer, revealing several physical design weaknesses, and in producing the majority of the programming to be used in the final design.

### 5.1 Description of Prototype

HCTeR is a simplistic humanoid robot whose function is as a tool for improving physical therapy. Fundamentally, the most critical aspect of the robot's function is its ability to replicate a movement which has a sufficient degree of anatomic accuracy. The other fundamental design challenge is to make the unit sufficiently distinct from the human form, to reduce the risk of social intimidation, while still making the robot appealing and physically relatable to a pediatric patient. Therefore, the initial build of HCTeR focused on these factors. A single, simple exoskeleton was used to produce the human-like shape and proportions of the central structure of the robot. The hollowed-out exoskeleton allows for material cost to be minimized while maintaining sufficient structural strength. Simulations of several loading conditions were performed in SolidWorks as part of the prototyping process as well as some rudimentary physical testing. The design philosophy behind the central exoskeleton extends to the HCTeR's simple legs and arms as well. Functionally, the limbs house the servos and wiring while allowing for the full range of movement. In order to fulfill the requirement to be engaging and appealing, visual graphics are incorporated in two LCD screen "eyes" as a principal feature of stage 2 HCTeR. HCTeR stage 1 stands about 43cm tall and 15cm wide in the prototype state assembly, while stage 2 will be modifiable to be the size of the patient.

### 5.2 Prototype Design

Each part is designed to connect at the servo motor, facilitating the assembly of the limbs. The servo motor serves as the joint between these parts. Bearings were introduced into the opposite side of the servos to create a near frictionless movement and support at the joints. In order to further facilitate the assembly, these joints were designed to be supported by eight screws. By carefully testing the model, the group was content with the chosen design of prototype HCTeR.

### 5.3 Parts List

#### 5.3.1 Legs

Leg units incorporated into HCTeR are discussed in further detail in another work [12].

Each leg feature four servos providing a total of four degrees of freedom for each leg and are connected to a fifth servo at the hip which will allow for a total of ten degrees of freedom once the unit is assembled. The functionality of the legs should be precise enough to be able to walk while keeping the core, or center of mass, upright. Since the body is completely symmetrical, the center of mass is located closer to the hip which will help maintain the equilibrium required for walking and standing. The hip designed features an additional servo that will create the rotational movement of the torso parallel to the floor [12].



Figure 6. Leg design

This prototype leg unit also features a hidden chamber underneath the casing of the legs that will conceal the servos under the "toes", as well as the wires passing through the leg structure all the way to the core of the platform.

#### 5.3.2 Head

Though the head doesn't perform any critical movements, it still has a major role in the development of the final design for this platform. The head is the most important aesthetic aspect of the robot when built to appeal to children since this is where the focus of the child will likely be when approaching this platform for the first time. An important consideration when examining a child's motor abilities is considering the increased unbalance caused by the larger proportional size of their heads to the rest of the body when compared with an adults. The platform will attempt to simulate this issue in order to create the same difficulties when standing up or performing other gross motor functions. For the prototype being built in stage 2, further improvements for this component must continue to be considered to include an LCD display, speakers, and other light sources.

#### 5.3.3 Torso

The torso was built to be completely symmetrical while allowing for the placement of the head and arms. The torso shares the center of mass with the hip, so that the platform will be able to maintain balance while moving. To do this, shifting the center of mass around depending on the movement is essential in order to remain upright. Crucially, the center of mass will be determined by the placement of the battery and microcontroller as the most significant sources of mass within the torso. These two are attached inside the torso to create a larger center of mass in the mid region of the robot. A significant change which occurs in the torso between prototype and the second iteration is the enclosure of the structure by a shell. This will protect sensitive electronics and also reduce the risk to children of electrocution or stuck fingers.

#### 5.3.4 Arms

A major change here between the first iteration and second is the removal of a servo and the internal and external rotation [10] functionality to reduce cost and simplify the design. After analyzing the size of the design compared to the servo, the group made the decision that this rotational movement is not essential. Further designs may improve this motion by adding smaller more costly servos. Two further considerable changes are the simplification of the hand in order to produce a less intimidating

form and the enclosure of the skeletal frame in order to improve safety.

### 5.4 Construction

As mentioned before, a significant driver behind this design of HCTeR was simplifying the assembly as much as possible. This was done by creating the parts to fit the joints, servos, as smoothly as possible. The servos are then connected to the microcontroller and to the battery, the latter is only if required. Each limb has screw holes that create a support by attaching each part to a joint. The micro controller is then attached inside of the torso to allow the prototype to freely move around. If a battery is required, this battery is also attached inside of the torso.

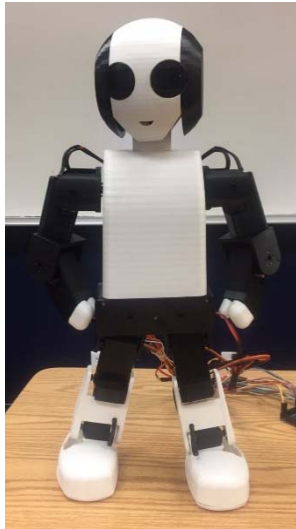


Figure 7. Final Design of HCTeR

## 6. DESIGN CONSIDERATIONS

### 6.1 Health and Safety

Ensuring that the solution created does not produce any unintended or harmful secondary effects is critical, especially for a platform intended for use with disabled children. IEC/NP 80601-2-78 is a document aimed at providing safety standards specific to “medical robots for rehabilitation.” This standard is under development by the International Organization for Standardization (ISO) as of 2015 but is not yet published or available as of the publication of this report. Therefore, in order to guarantee the high degree of safety required, ISO 13482:2014, an international standard defining safety requirements for personal care robots, will be followed with prudence instead. It is important to note that this standard explicitly states that it does not apply to several classes of robots which include “robots as medical devices.” However, the standard goes on to say that “the safety principles established in this International Standard can be useful for [robots as medical devices]” and is, therefore, a relevant reference publication to the project [14].

### 6.2 Assembly and Disassembly

Assembly of HCTeR is intended to be a straight-forward, accessible process. Structurally, HCTeR will require off-the-shelf components which will be fastened to a 3D printed structure via hardware specified in components. Electrically, all the components are housed in the enclosed torso.

### 6.3 Manufacturability

From a manufacturing standpoint, the bulk of the process relies on the increasingly available technology of 3D FDM printing. Costs of purchasing units capable of creating all of HCTeR’s structure have plummeted within the past few years, with printers available for as little as \$300 [15]. Furthermore, shops with these capabilities which charge hourly rates for printing are becoming increasingly common and produce high quality projects. Electromechanical off-the-shelf components will be specified which are widely available and which are cost effective.

### 6.4 Maintenance of the System

HCTeR will require no special maintenance. Because the structure is almost entirely plastic and all mechanical actuators are small and electric, lubrication will not be required. Basic sanitation may be required as the device may be in contact with multiple children. In addition, in the case of a significant break or failure, the robot is modular and replacement parts can be easily obtained and integrated into the unit. If the user has access to a 3D printer, the broken part can be downloaded and reprinted. If the broken part is at the component level, these components can also be purchased from many major retailers.

### 6.5 Economic Impact

After having completed the construction of the finalized version of HCTeR, a cost estimate is provided for replication of the device. In Table 2, we find the components, cost of filament, etc. that have been chosen for the final prototype of HCTeR. Immediately, the group realizes that a modest reduction in the total price can be achieved by changing the servos in the joints that do not require a large amount of torque, such as the neck, to a smaller, more economical servo, such as the SG90. Other components, such as the Arduino Mega, can be changed to comparable open source components. In the case of the above mentioned, the Arduino Mega is valued at \$45, while the Funduino Mega is valued at \$14.75. In the case of these microcontrollers, the schematics and functionality are the same. As a main objective of the project, reducing the economic impact of producing and utilizing this tool is paramount to ensuring the degree of accessibility desired.

Table 2. Component Cost Estimate

Component	Number of Parts	Price
Funduino Mega	1	\$14.75
LCD	2	\$10.88
Sound Module	1	\$8.36
Servo	18	\$107.82
Filament	2	\$44.00
Wiring	50ft	\$12.00
Wire Protector	1	\$7.97
Ball Bearings	40	\$16.65
Gyroscope	1	\$3.00
Battery	1	\$39.99
	Σ	\$265.42

Furthermore, Table 3 breaks down the total manufacture cost, if one is required, of the design. Considering this design as open source, the availability allows for the need of a manufacturer to be

unnecessary to anyone with access to a 3D printer ignoring labor costs. It is important to note that this analysis was performed with a manufacturing cost of \$6 per hour. Costs estimates based on this is provided in Table 3.

It is important to note that the printing not only depends on the size, its shape is also of utmost importance. For some parts, a “raft” support is needed underneath the part that will increase the overall printing time. The fill density also plays a major role in the total printing time. If the components of HCTeR had been printed in a bigger 3D printer, such as the ones used by manufacturers, the total amount of printing time could total half of our current printing time.

**Table 3. Manufacturing Hours and Cost**

Component	Number of Parts	Printing Time (hrs)	Cost
Head	1	13.2	\$79.20
Head - Left Side	2	6	\$72.00
Neck	1	5.2	\$31.20
Chest	1	21.6	\$129.60
Chest - Back Part	1	15.1	\$90.60
Shoulder - Servo Support	2	1.3	\$15.60
Shoulder	2	3.5	\$42.00
Arm - Upper Section	2	2.6	\$31.20
Elbow	2	2.5	\$30.00
Forearm	2	4.2	\$50.40
Finger	2	0.7	\$8.40
Thumb	2	0.3	\$3.60
Hip	1	6.8	\$40.80
Hip - Front section	1	3.1	\$18.60
Hip - Servo Support	2	2.2	\$26.40
Hip - Servo Support Front Section	2	1.2	\$14.40
Leg	2	3.7	\$44.40
Calf	2	1.9	\$22.80
Calf - Side Section	2	1.7	\$20.40
Ankle	2	1.8	\$21.60
Sole	2	4	\$48.00
Foot	2	6.8	\$81.60
Foot - Servo Support	2	0.8	\$9.60
Bearing Holder	12	0.3	\$21.60
Totals $\Sigma$			\$954.00

## 7. DESIGN EXPERIENCE

Overall, the design experience was impacted tremendously by a number of factors. The most defining and difficult of these factors was framing the original problem. The initial idea of using a humanoid robot to improve the quality of physical therapy for children with cognitive disabilities was presented to us by PhD candidate Melissa Morris. However, the prompt was still a fairly open concept. Isolating a significant issue within this medical context which could be addressed with a mechanical solution became the primary effort.

Because of the complexity of the kinematics of the human body, creating a robust humanoid model is incredibly challenging. This first consideration presented a limitation which was accounted for by sacrificing robustness of the model for ease of design, construction, and implementation. Sacrificing robust functionality also directly led to lowered costs of production. Therefore, it was natural for the design effort to focus on the less complex gross motor skills which concern physical therapists rather than fine motor skills which are trained by occupational therapists. This allowed for the solution to focus on issues within the context of physical therapy alone.

Defining the social problem to be addressed became the second area of interest. Research conducted into the field of pediatric rehabilitation yielded a common and pronounced problem of a related nature. According to Autism Speaks, “individuals with autism have a great deal of difficulty with social interactions” which is compounded by the fact that “children with autism frequently have challenges with motor skills such as sitting, walking, running or jumping.” The need for physical therapy is increased with these conditions while the delivery of treatment is also made more difficult by the fact that these children are less likely to behave favorably around therapists. The issue then can then be summarized as a learning barrier which exists between the two. This set of challenges characterizes the need for a solution. Therefore, the design solution needed to be a teaching tool which could help bridge the social gap between physical therapists and patients. By utilizing a humanoid robot whose physical design allowed it to perform the required movements and exercises, but which also had design elements intended to capture a child’s attention, the robot could serve as a teaching model that causes less stress or discomfort than interacting with another human might induce.

Finally, because of time constraints and the interest in creating a modular platform solution, the robot needed to be designed with “room” to be capable of performing other functions which may not be explored or defined in this iteration of implementation. In essence, the project selected some simple functions, such as sitting or walking, to explore as a “default” configuration and created a robotic structure which could be programed to perform differently or modified to include different components.

### 7.1 Contemporary Issues

During the duration of the design experience, it was desired to create a solution to a problem within the context of society and our world today. Centers for Disease Control and Prevention (CDC) has released a study confirming “1 in 68 children (1 in 42 boys and 1 in 189 girls) as having autism spectrum disorder (ASD)” [16]. In the 1970’s, the CDC reported rates closer to “1 in 2,000 children” as having been diagnosed with autism. There is much debate in the media today about whether these rates are increasing dramatically or if the increases are caused by the fact that the definition of autism has been broadened recently. Regardless of the causes for the

increase in cases, the simple fact that more of these patients are being treated has exacerbated the problem faced by many areas of the medical community: interacting and treating patients who are socially unresponsive or behave atypically.

## 7.2 Life-Long Learning Experience

As a team, the project led to a thorough and complete design process which mimics the design environment of industry. For all the members of this team, this was the first complete design process carried out with such robustness and to completion of a unique solution.

As individuals, each member gained invaluable insight into the complexity of completing a full design. The members learned the importance of defining the problem well and the steps taken to create a solution to the identified problem while maintaining focus and keeping the design feasible and within the scope of necessity.

## 8. CONCLUSION

The Humanoid Rehabilitation Project sought to create a modular, robotic platform which could be used as a teaching tool that also mediated between physical therapists and patients. In particular, the design efforts were focused on bridging a treatment gap which often exists between children who have certain cognitive disabilities, and the therapists who are treating them. Children with these conditions can be generally less-responsive to adult strangers such as physical therapists or can become stressed by interacting with others.

In an effort to alleviate this issue, HCTeR is an appealing, accessible, and unimposing robot who can be programmed to demonstrate a gross motor skill, such as walking, while downplaying the human interaction element of therapy which impedes progress otherwise.

HCTeR is physically designed to be functional and inexpensive. Through the rigorous design process, a default configuration of components and structural design was established for HCTeR which will allow him to perform his core functions at a minimum cost. However, because of the open source and modular nature of the project, individual applications and constructions of HCTeR are still possible to vary functionality.

Within the physical configuration of HCTeR, functions can be created to serve a widely variety of needs. Through the use of coding, a program may be produced to allow HCTeR to perform any range of movement allowed by the physical configuration. However, the most significant existing limitation of this platform remains the programming process and, thus, a higher level software solution which takes advantage of an interactive user interface or other input device such as motion capture needs to be explored in order to maximize the potential of HCTeR. Because the default physical configuration is based on a real child, a good approximation of the kinematics of nearly any gross motor skill can be recreated through the application of the code.

## 8.1 Future Work

HCTeR, as a central design tenant, was created to be improved over time by the future teams and end users themselves. This modular nature is seen in many facets of HCTeR. For example, the default configuration, which incorporates the most basic components needed to perform a function such as walking without aid, can be modified or replaced as needed to improve functionality.

The addition of a gyroscope sensor which will provide a sense of balance at the hip may allow for a function such as walking without assistance or running to be accomplished. Additionally, HCTeR's

code can be edited to produce different similar humanoid joints movement. The current configuration of components and coding also concern a limited number of gross motor skills. With further development, a broader selection of motor-skills and therapy options will be possible. A source for a downloadable library and most importantly, a higher level programming solution, is a crucial aspect in the furtherance of this project, as the foundation of this project is expanding accessibility for the users.

Another future functionality to be added concerns enabling control over long distance. wi-fi compatibility will allow therapists to issue commands or modify HCTeR's coding remotely. A telemedicine functionality could greatly reduce costs of use and increase availability as well.

## 9. ACKNOWLEDGMENTS

Our thanks are extended to the Robotics and Automation Laboratory located in the Department of Mechanical Engineering at Florida International University in Miami for providing access to the lab and to Rodrigo Arredondo for helping with ideas for the programming.

## 10. REFERENCES

- [1] "About PT/PTA Careers," American Physical Therapy Association. Web. 26 November 2016. <http://www.apta.org/AboutPTs/>.
- [2] "Physical Therapy," Kids Health, June 2014, [kidshealth.org/en/parents/phys-therapy.html](http://kidshealth.org/en/parents/phys-therapy.html).
- [3] Poppy Project. Poppy documentation version 1.0, 2016, [docs.poppy-project.org/en/getting-started/](http://docs.poppy-project.org/en/getting-started/). Accessed 12 Oct. 2016.
- [4] "Thirteen Advanced Humanoid Robots for Sale Today." Smashing Robotics, 16 Apr. 2016, [smashingrobotics.com/thirteen-advanced-humanoid-robots-for-sale-today](http://smashingrobotics.com/thirteen-advanced-humanoid-robots-for-sale-today).
- [5] Otto DIY. Otto, 2016 [otto.strikingly.com](http://otto.strikingly.com). Accessed 12 October 2016.
- [6] "Arduino - ArduinoBoardMega". Arduino - ArduinoBoardMega. N.p., 08 Apr. 2015. Web. 22 Nov. 2016.
- [7] "TowerPro Servos." TowerPro Servos. N.p., 18 Sept. 2012. Web. 22 Nov. 2016.
- [8] Servodatabase, [servodatabase.com/servo/towerpro/mg996r](http://servodatabase.com/servo/towerpro/mg996r). Accessed 30 January 2017.
- [9] "Encouraging Crawling in Babies" North Shore Pediatric Therapy. Web. Accessed 15 March. 2017. <http://nspt4kids.com/physical-therapy/encouraging-crawling-in-babies/>.
- [10] "Range of Joint Motion Evaluation Chart" Washington State Department of Social & Health Services. Web. Accessed 8 Feb. 2017. <https://www.dshs.wa.gov/sites/default/files/FSA/forms/pdf/13-585a.pdf>.
- [11] Chilson, Luke "The Difference between ABS and PLA for 3D Printing" Protoparadigm, [protoparadigm.com/news-updates/the-difference-between-abs-and-pla-for-3d-printing](http://protoparadigm.com/news-updates/the-difference-between-abs-and-pla-for-3d-printing). Accessed 30 January 2017.
- [12] Humanoid Bipedal Platform Design, R. Olazo, A. Mendoza, G. Soles, M. Morris, S. Tosunoglu, Proceedings of the 30th Florida Conference on Recent Advances in Robotics, FCRAR 2017, Boca Raton, Florida, May 11-12, 2017.
- [13] IEC/CD 80601-2-78 Medical electrical equipment, 3 Mar. 2017.

- [14] "ISO 13482:2014(en) Robots and Robotic Devices — Safety Requirements for Personal Care Robots."  
<https://www.iso.org>. ISO, n.d. Web. 25 Oct. 2016.
- [15] "3D Printing Filament and Materials." 3DPrint360. N.p., 19 June 2016. Web. 22 Nov. 2016.

- [16] "Autism Press Release" Center for Disease Control and Prevention. Web. Accessed 15 March. 2017  
<https://www.cdc.gov/media/releases/2014/p0327-autism-spectrum-disorder.html>.

# Trust, Satisfaction and Frustration Measurements During Human-Robot Interaction

Moaed A. Abd, Iker Gonzalez, Mehrdad Nojournian, and Erik D. Engeberg

Department of Ocean & Mechanical Engineering and Department of Computer & Electrical Engineering and Computer Science  
College of Engineering and Computer Science.

Florida Atlantic University

777 Glades Rd, Bldg. 36; Room 178

Boca Raton, FL , 33431

(mabd2015, ikergonzalez2014, mnojournian, eengeberg) @fau.edu

## ABSTRACT

Since the beginning of human race, we have always sought ways to develop bonds and create meaningful relationships with others. In these interactions, there are several parameters that determine how strong the bond is. These parameters include among many others, the trust towards the other person. Humanlike robots have been created with basic human to human interaction rules. Trust is a significant factor for the interaction with the robot, if a human trusts a robot, certainly the outcome from the interaction would be different from the case when a human does not trust a robot. For a human to be able to interact with the robot without any concern, trust must be developed between human and robot. In this paper, we introduce a starting point for quantifying Human-Robot interactions in which we measure the level of trust, satisfaction, and frustration. Due to the different interaction modes during the collaborative task, the human trust towards the robot varied due to interaction and experiences. Results based on feedback from 10 persons, when they interacted with a Baxter robot in a real time collaborative task showed the trust, frustration and satisfaction levels changed depending on the Baxter robot operation modes. The most significant delivery mode is the dropping mode in which the trust, frustration and satisfaction levels are significantly different in comparison with other delivery modes.

The results are based on feedback from 10 persons, when they interact with Baxter robot in a real time.

## Keywords

Human-Robot Interaction (HRI), Trust, Satisfaction, Frustration, and Baxter Robot.

## 1. INTRODUCTION

Trust is an essential aspect of human lives. It defines in some sense who we are and how we interact with each other daily. It can be placed in almost anyone or anything and ranges for the trust in the workspace as well as the trust we put in our friends and family. It is hard to trust something or someone but even harder to regain trust [1] [2] [3]. For instance, when we drive a car, we believe we will reach our destination safely mostly because we trust that our car is not going to break. But what happens when for some reason the car

stops working in the middle of the road? The trust we placed on it is suddenly lost. This happens in human-human interaction too, and probably on a larger scale [4] [5] [6].

From a social science perspective, trust is the willingness of a person to become vulnerable to the actions of another person irrespective of the ability to control those actions [7]. However, in the computer science community, trust is defined as a personal expectation that a player has regarding the future behavior of another party, i.e., a personal quantity measured to help the players in their future dyadic encounters [8].

In modern life and future life robot will play an important role, due to many applications of robot ranging from performing simple task like delivering object to disabled people [9], doing complex tasks like doing a surgery [10], doing military task [11] or even doing search and rescue in hazardous locations [12], it is important to study the HRI behavior and make models for different parameters like trust. As the robot developed and become more significant for our lives the demand for such model become essential to make it possible to change the trust mode of a certain human when interacting with robot especially in complex tasks. Many researchers address the trust issue for HRI [13] [14] [15].

According to recent findings by researchers at Chapman University [16], Americans expressed the highest levels of fear about man-made disasters followed by fears about technology such as artificial intelligence and robots. These interesting discoveries highlight the necessity and urgency of conducting research to better understand the notion of trust from human reasoning perspective [17], and consequently, to construct computational models of trust [18] to be incorporated into the controller of the robotic systems that interact with humans.

In this paper, we introduce a starting point for understanding human-robot interaction during a collaborative task in which we measure human trust, satisfaction, and frustration of the robotic assistant. In this study, human trust measurements were periodically measured during a collaborative human-robot object sorting task where a Baxter robot performed different delivery modes and speeds.

Section 2 describes the methodology used to build our experiment. Section 3 is the experimental setup, robotic operation mode and the basic steps. All the results are presented in section 4, also a brief discussion of all the results mentioned in section 4 with conclusions in section 5.

## 2. METHODOLOGY

In this experiment, a task for robotic home assistance to provide support to people in a daily task were explored. Specifically, the task of passing a bottle of water was examined. We design our experiment based on changing the operation modes of Baxter robot (table 1) in delivering the objects, to examine three different factors trust, satisfaction and frustration. 10 participants were recruited as explain (table 2). All the participants were of average age ranged from 20 to 40 years old. All participants gave informed consent in accordance with the approved IRB protocol.

In our experiment, we used robot operating system (ROS) to establish a communication, control Baxter robot and to record all the necessary information that is essential for our experiment. All the recorded data was synchronized with each other and have the same time stamp.

## 3. EXPERIMENT SETUP

The purpose of this experiment is to accomplish some collaborative tasks through interactions with a robotic hand. In this experiment, users will conduct set of rounds of passive interactions with the robotic hand where each round consists of three (3) deliveries of water bottles. At the end of each case (three deliveries), the subject answered a five-choice question with respect to their level of trust/satisfaction/frustration

### 3.1 Baxter Robot Operation Modes

Baxter Robot (Rethink Robotics, Inc.) [19] was used in this experiment; the robot was pre-programmed to pick objects in our case bottles of water and deliver them to the test subject. The user was asked to give a feedback rating their feeling trust, satisfaction and frustration after each case (three deliveries).

In the design of our experiment, five different operation mode for Baxter robot were programmed. The first mode is the success mode, in this mode, Baxter robot successfully delivered the object to a human with medium speed and in a suitable location for a human to take the object easy without much effort. In the second mode, the only factor was changed is the speed of delivery, Baxter delivered objects with a very slow speed to the same position from mode 1. Mode 3 was the successful object placement, except with a high delivery speed. Mode 4 is kind of the most significant mode as the results will show, which is the dropping mode. The operation speed medium and Baxter robot was programmed to ‘accidentally’ drop the object before delivering it.

The fifth and final mode is the wrong location mode. Here, the speed of robot was medium, but the Baxter robot delivered the objects to the wrong location far away from a human, necessitating that the human must stand up from his or her location and make effort to take the object from the robot. Table 1 shows Baxter robot operation modes.

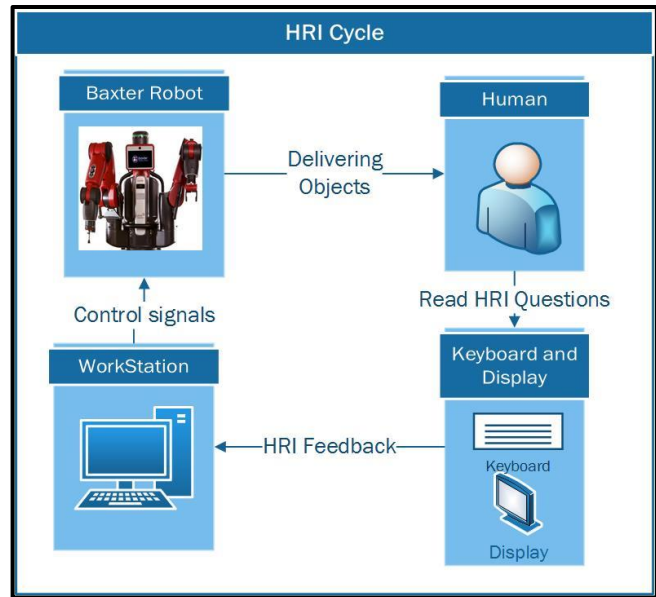


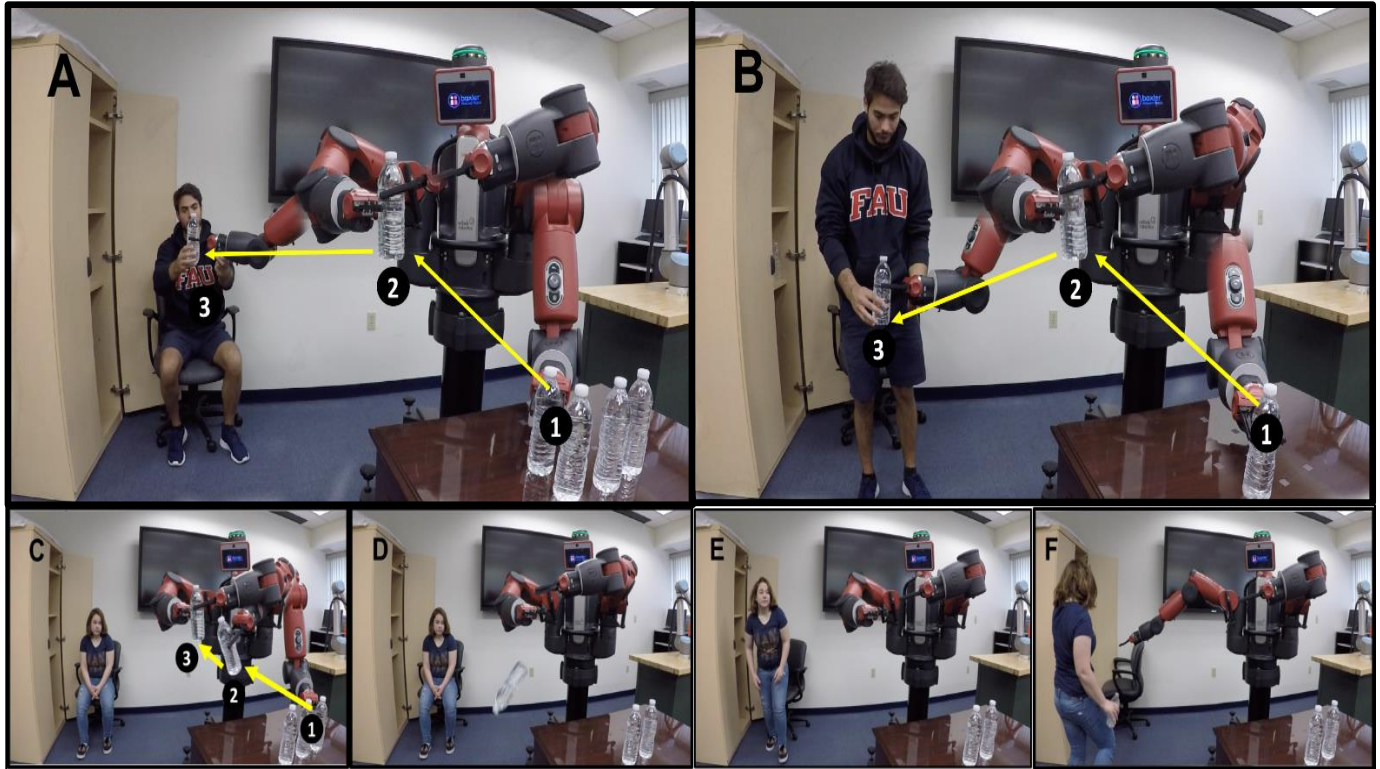
Figure 1. HRI Experiment Setup

Table 1. Baxter Robot Operation Modes

Operational Mode	Robot Operation Mode	Robot Arm Speed
1	Successful placement, medium speed	0.3 m/s
2	Successful placement, slow speed	0.1 m/s
3	Successful placement, high speed	0.7 m/s
4	Bottle Dropped	0.3 m/s
5	Bottle Delivered to the Wrong Location	0.3 m/s

### 3.2 Object Delivery Cases

In this research, the sequence of 12 different delivery cases each with three bottle deliveries per case were followed by each of the ten test subjects (Table 2). The cases represent different operation modes (table 1) for delivering object to a human. A human was asked to control Baxter’s parallel gripper to take the bottle and place it on a shelf. Photo sequences of HRI is shown in Figure 2, which illustrates the different operation modes and the way the human interacted with Baxter.



**Figure 2. Photo sequence of the Baxter Robot operation modes, (A). Successful placement, (B). Bottle Delivered to Wrong Location, (C, D, E, and F). Bottle Dropped**

The nonparametric Mann-Whitney U test (Wilcoxon Rank Sum Test) was used to statistically analyze the data. It is a null hypothesis that data in x-axis and y-axis are samples from a continuous distribution with equal medians, against the alternative that they are not. Both tests are a non-parametric test for equality of population median of two independent samples.

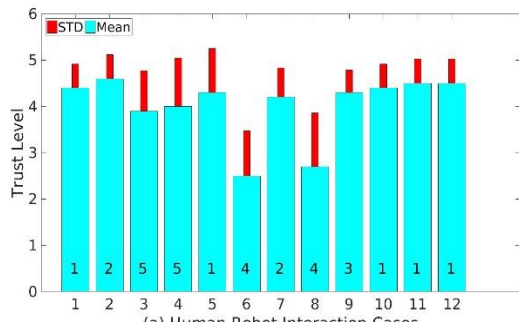
**Table 2. Cases Sequences**

Interaction Case	Number of deliveries	Baxter Robot Delivery Mode
1	3	1
2	3	2
3	3	5
4	3	5
5	3	1
6	3	4
7	3	2
8	3	4
9	3	3
10	3	1
11	3	1
12	3	1

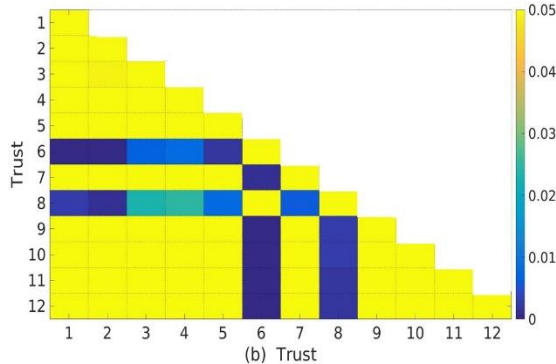
## 4. RESULTS AND DISCUSSION

During the experiment, Baxter performed the tasks in all the different modes that were carefully selected to accomplish and receive an honest feedback from the subjects and allow us to analyze the data in an efficient manner. This set of tasks helped measure the levels of trust, satisfaction, and frustration from the subject towards the robot. Once all the data was collected, the data was plotted with a series of bar graphs showing the mean and standard deviation to understand the significance of the values acquired. Also, a set of comparisons were made by statistically testing the frustration, satisfaction, and trust levels to see the relation that these parameters may play in the experiment.

The mean and standard deviation show a clear comparison for Trust from the subjects towards Baxter Figure (3.a). Also, by using The Mann-Whitney U test, Trust-Trust allows us to understand how each case differs from each other. Figure (3.b) shows the statistical analysis of trust data. Depending on the robot operation mode human trust changed. The most significant change in trust level happened in the dropping mode (mode 4). The trust level declined in case 6 and case 8 which are the cases when robot operation mode was mode 4 dropping mode. The wrong location mode (mode 5) also affected the trust level in comparison with mode 1,2 and 3. Also as shown in Figure 3.b that Case 7 is significantly different in comparison with case 6 and 8 because the trust level sharply rose from case 6 to case 7 then sharply declined between case 7 and 8 Figure 3.a.

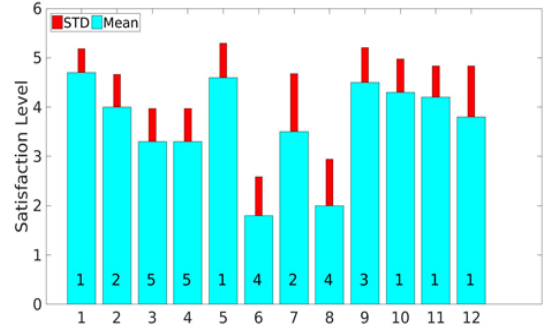


(a) Human Robot Interaction Cases

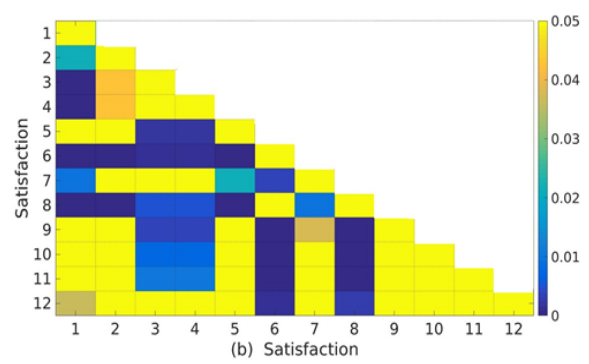


(b) Trust

**Figure 3. Trust Level, (a). Mean and Standard Deviation, and (b). Mann-Whitney U test**



(a) Human Robot Interaction Cases



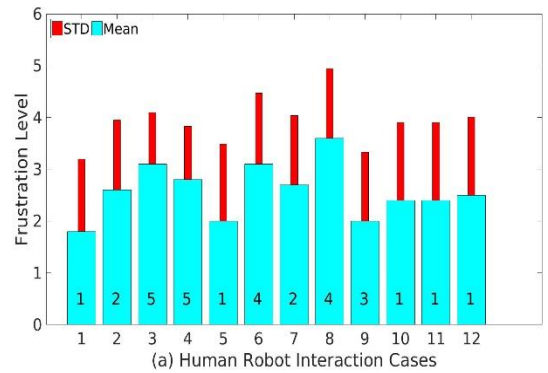
(b) Satisfaction

**Figure 4. Satisfaction Level, (a). Mean and Standard Deviation, and (b). Mann-Whitney U test**

Also, depending on the Baxter robot operation modes, the satisfaction level changed. The speed of the robot affected the satisfaction level as in case 2 (Figure 4.a). The wrong location mode (mode 5) had satisfaction levels lower than in mode 1 the successful mode. Case 6 and 8 which represents the dropping mode have the lowest satisfaction level. The statistical analysis is shown in Figure 4.b demonstrating the statistical differences between any two cases. The blue blocks indicate that the intersection cases are statistically different, such as case 6 or case 8 with the rest of the cases. The satisfaction level of cases 3 and 4 is also significantly different than the rest of the cases except for case 7 and 12.

The mean and standard deviation is shown for frustration as shown in Figure 5.a. The frustration level for all cases is close to each other but still is the highest for case 6 and 8 which represent the dropping mode. The statistical analysis for frustration level is shown in Figure 5.b, which shows that the frustration level for case 1 is completely different from case 8, 6, 3, and 4.

Also, case 8 (dropping) and case 3 (the wrong location) modes are different from case 9, the fast delivery mode.



(a) Human Robot Interaction Cases

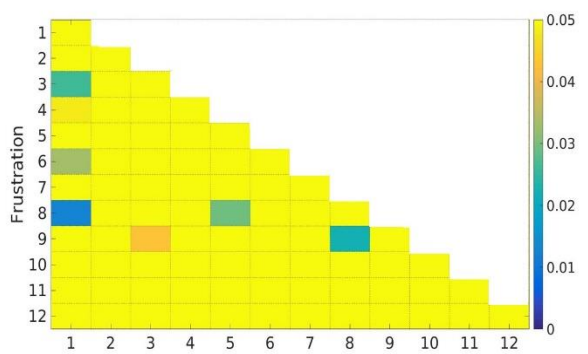


**Figure 5. Frustration Level, (a). Mean and Standard Deviation, (b). Mann-Whitney U test**

## 5. CONCLUSION

As the robot become more and more involved in our environment, the demand for human trust of robots is more important than ever. Humans must trust autonomous systems to improve interaction. This work focused on the interaction with a robot in daily life tasks like passing a common objects to people. This task is representative of how a robot assistant could help disabled or elderly persons with their daily routines. Different Baxter robot operation modes were tested throughout this research. HRI feedback was measured for trust, satisfaction and frustration levels after interaction with Baxter robot. The feedback was altered based on the operation mode of the robot in delivering the objects to a human. It turns out that the human trust, satisfaction and frustration levels depends on the interaction mode with Baxter robot, whether Baxter moving slowly, quickly, or delivering the objects successfully.

## 6. ACKNOWLEDGMENTS

The authors would like to thank the Division of Research at Florida Atlantic University for their support

## 7. REFERENCES

- [1] Stephanie M. Merritt and Daniel R. Ilgen, "Not All Trust Is Created Equal: Dispositional and History-Based Trust in Human-Automation Interactions," *Human Factors: The Journal of the Human Factors and Ergonomics Society*, 2008.
- [2] Kristin E. Oleson, D.R. Billings, Jesseie Y.C. Chen Tracy Sanders, "A Model of Human-Robot Trust Theoretical Model Development," in *Proceedings of the Human Factors and Ergonomics Society Annual Meeting*, 2011.
- [3] L. J., Doll, B. B., van 't Wout, M., Frank, M. J. and Sanfey, A. G Chang, "Seeing is believing: Trustworthiness as a dynamic belief," *Cognitive Psychology.*, no. 61, pp. 87–105, 2010.
- [4] M. J. Mataric and H. I. Christensen A. M. Okamura, "Medical and Health-Care Robotics," in *IEEE Robotics & Automation Magazine*, pp. 26-37, 2010.
- [5] Schaefer KE, Chen JY, Hancock PA Billings DR, "Human-robot interaction," in *Proceedings of the seventh annual ACM/IEEE international conference on Human-Robot*, 2012.
- [6] Kristin E Schaefer, Jessie YC Chen, and Peter A Hancock Deborah R Billings, "Human-robot interaction: developing trust in robots," in *In Proceedings of the seventh annual ACM/IEEE international conference on Human-RobotInteraction*, 2012, pp. 109–110.
- [7] Roger C Mayer, James H Davis, and F David Schoorman. An integrative model of organizational trust. *Academy of Management Review*, 20(3): 709–734, 1995.
- [8] Lik Mui, Mojdeh Mohtashemi, and Ari Halberstadt. Notions of reputation in multi-agents systems: a review. In *1st ACM International Joint Conference on Autonomous Agents and Multiagent Systems*, AAMAS'02, pages 280–287, 2002.
- [9] S. Woods, C. Kaouri, M. L. Walters, Kheng Lee Koay and I. Werry K. Dautenhahn, "What is a robot companion - friend, assistant or butler?," in *IEEE/RSJ International Conference on Intelligent Robots and Systems*, 2005, pp. 1192-1197.
- [10] Lee J. D. and See K. A, "Trust in Automation: Designing for Appropriate Reliance," *Human Factors: The Journal of the Human Factors and Ergonomics Society*, 2004.
- [11] Billings DR, Schaefer KE, Chen JYC, Visser EJD, Parasuraman R Hancock PA, "A Meta-Analysis of Factors Affecting Trust in Human-Robot Interaction. ," *Human Factors*, pp. 517–527, 2011.
- [12] Murphy RR, "Human-robot interaction in rescue robotics," in *IEEE Transactions on Systems, Man, and Cybernetics, Part C (Applications and Reviews)* , pp. 138–153, 2004.
- [13] C. D. and Breazeal, C Kidd, "Effect of a robot on user perception. ," in *In Proceedings of the IEEE/RSJ International Conference on Intelligent Robots and Systems* (pp. 3559–3564). Sendai, Japan: IEEE., 2004.
- [14] V. and Nass, C Groom, "Can robots be teammates? Benchmarks in human-robot teams," *Interaction Studies*, no. 8 , pp. 483–500., 2007.
- [15] D. P., Daly, M. and Gunsch, G Biro, "The influence of task load and automation trust on deception detection," *Group Decision and Negotiation*, no. 13, pp. 173–189, 2004.
- [16] <http://www.chapman.edu/wilkinson/research-centers/babbie-center/survey-american-fears.aspx>
- [17] Mehrdad Nojournian. Trust, influence and reputation management based on human reasoning. In *4th AAAI Workshop on Incentives and Trust in E-Communities*, WIT-EC'15, pages 21–24, 2015.
- [18] Mehrdad Nojournian and Timothy C. Lethbridge. A new approach for the trust calculation in social networks. In *E-business and Telecommunication Networks: 3rd International Conference on E-Business*, Best Papers, volume 9 of CCIS, pages 64–77. Springer, 2008.
- [19] Rethink Robotics. Collaborative Robotics Applications and Industries: Rethink Robotics. [Online]. <http://www.rethinkrobotics.com/applications>

# Impacts of Soft Robotic Actuator Geometry on End Effector Force and Displacement

Moaed A. Abd, Craig Ades, Mohammad Shuqir, Mohammed Holdar, Mostapha Al-Saidi,

Nicholas Lopez and Erik D. Engeberg

Ocean & Mechanical Engineering Department

College of Engineering and Computer Science.

Florida Atlantic University.

[mabd2015@fau.edu](mailto:mabd2015@fau.edu), [caedes@my.fau.edu](mailto:caedes@my.fau.edu), [mshuqir2016@fau.edu](mailto:mshuqir2016@fau.edu), [mholdar2016@fau.edu](mailto:mholdar2016@fau.edu), [malsaidi2015@fau.edu](mailto:malsaidi2015@fau.edu),  
[nlopez2015@fau.edu](mailto:nlopez2015@fau.edu), [eengeberg@fau.edu](mailto:eengeberg@fau.edu)

## ABSTRACT

Soft Pneumatic Actuators (SPA's) received a great interest in the recent years, due to their flexibility and inherent safety with everyday users. SPA's are primarily composed of easily deformable non-rigid materials such as fluids, gels, and elastomers. This study focuses on how varying taper angle parameter ( $\theta$ ) impacts the performance of the soft robotic actuator, specifically, the width of the SPA decreased toward the tip with a trapezoidal footprint. The study includes 7 models with taper angle  $\theta$  varying from  $0^\circ$  to  $6^\circ$  with  $1^\circ$  increments, all other geometric parameters were constant. The actuators were tested with frequencies from 1 to 6 rad/s, then the actuators were tested at the frequency of 0.5 rad/s to obtain the maximum force. It was found that highest force applied by the tip of the soft actuator occurs with taper angle of  $2^\circ$ , whereas the maximum displacement of the tip of the actuator was achieved with a taper angle of  $6^\circ$ .

## Keywords

*Soft actuator, Soft Robot, Pneumatic actuator.*

## 1. INTRODUCTION

Recent developments in robotic technology have shifted from rigid mechanisms based on gears-bearings-motors to a softer biologically inspired actuator [1]. One prime advantage of soft robotics is the ability to interact with soft and delicate objects.

Conventional robots are designed to do manufacturing tasks like the ones used in the food and automotive industries. They are less safe to interact with a human being or any biological system due to its rigidity. Conventional robots have difficulty manipulating delicate objects without harming them. This issue can be mitigated by using soft actuators [2], [3].

The developing field of soft robotics holds great potential for bringing robots into all aspects our daily lives, especially areas previously prohibitive for rigid robots. Soft actuators are becoming an essential part of the robotics community, the reason is that it provides a solution for many challenges that conventional robotics faces [4], for instance, uncertainty about the orientation and the shape of the objects that the robot intended to move [5].

Soft robotics can gently interact with the surrounding environment which makes it more reliable to deal with any delicate objects [6],[7]. SPAs function via pressurized fluid flow through a common channel that inflates flexible chambers to achieve bending motion. The angular speed of bending of a structure actuated by a pneumatic depends upon: i) the rate of inflation, ii) the geometry of the internal channels and exterior walls, and iii) the properties of the structure [16]. Pneumatic actuation was used, since pressurized air has four advantages: i) it provides rapid inflation of the pneumatic structure; ii) it is easily controlled and measured; iii) it is almost universally available; iv) it is light in weight; v) it can be discarded after use by venting to the atmosphere [16].

Several prior applications of soft robotics includes wearable robotics [8], medical robots [9], and micromanipulation [10]. Soft robotics application in the medical field, for example, Harvard Biodesign Lab is using soft robotics to help patients who have had heart failure [11]. For manipulating small and delicate items, soft grippers and control systems have been made for pick and place tasks with high-speed precision for handling fresh eggs. Mimicry of swimming underwater biological system seen in nature have been demonstrated by the Jennifish in the BioRobotics Lab at FAU [12], among applications demonstrated by other researchers such as robotic octopuses and peristaltic robots [13], [14], [15].

Since soft robotics is an emerging field, there is a need to study different parameters and its effects on the applied force, end effector position and velocity. In this paper, the design, fabrication, and evaluation of seven soft actuators will be described. The taper angle  $\theta$  was the only geometric parameter that was varied among the seven actuators to determine the impact that a narrowing, trapezoidal form factor had upon actuator force and displacement.

## 2. METHODOLOGY

The purpose of this study is to investigate the impact that soft actuator taper angle has upon the force and displacement of the actuator. When changing the taper angle, the actuator size changes and the chamber size narrows along the length of the actuator so it is expected that the performance will change.

Seven SPAs, each with a different taper angle ranging from  $0^\circ$  to  $6^\circ$  in  $1^\circ$  increments were designed in this paper, while the other parameters were constant.

## 2.1 Designing the actuators

SolidWorks 2015 was used to modify the molds to create actuators conceptualized in [17]. For consistency among the seven actuators designed in this paper, an inlet nozzle was added to the main design to make sure that the inlet fluid had the same connection (Figure 1). Three different mold parts were designed to manufacture the actuator. The Bottom part is used to make the cavity of chambers; the top part is used to separate the chambers and the base part was used to unify the top and bottom of the actuator. Mold parts for ( $\theta = 3^\circ$ ) are shown in Figure 1.

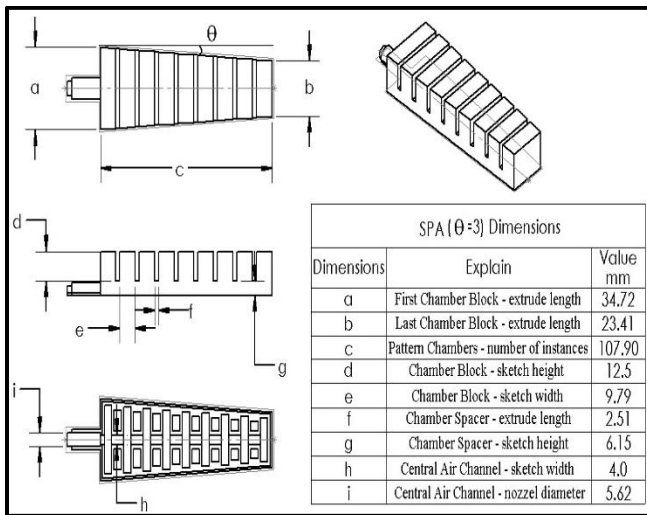


Figure 1. Soft Actuator Dimensions for  $\theta = 3^\circ$ .

## 2.2 3D Printing Molds

The SolidWorks models for the molds were 3D printed. Ultimaker3 (Ultimaker, Netherlands) was used to print all the molds using PLA. The mold for SPA with taper angle  $\theta=30$  is shown in Figure 2.

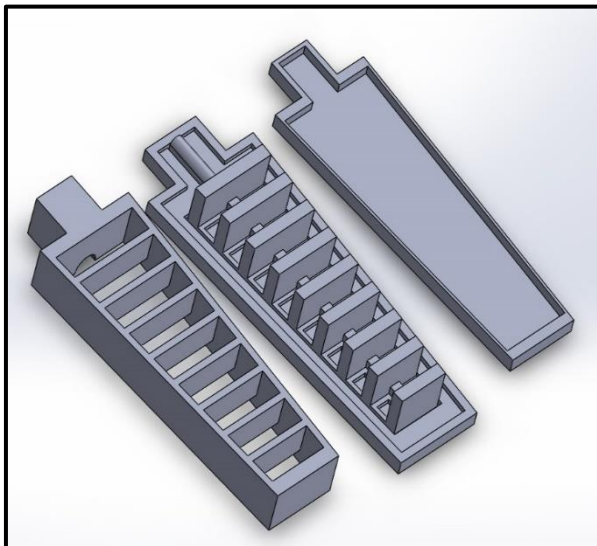


Figure 2. SolidWorks Design mold for  $\theta = 30^\circ$ .

## 2.3 Molds Fabrication

After finishing the 3D printing, the top and bottom parts were put together to hold the Ecoflex 00-30 (Smooth-On, Inc. Macungie, PA, USA). Ecoflex 00-30 has a Young's modulus  $\sim 0.1$  Mpa, and a Shore hardness of 30, and is the material that was used in fabrication the soft actuators. Hot glue was applied to bind the top and bottom molds together to keep the material from leaking. Before pouring the Ecoflex 00-30, Easy Release (Smooth-On, Inc. Macungie, PA, USA) was used to ease removing the actuator from the mold. Figure 3 Shows the fabricated soft actuators.

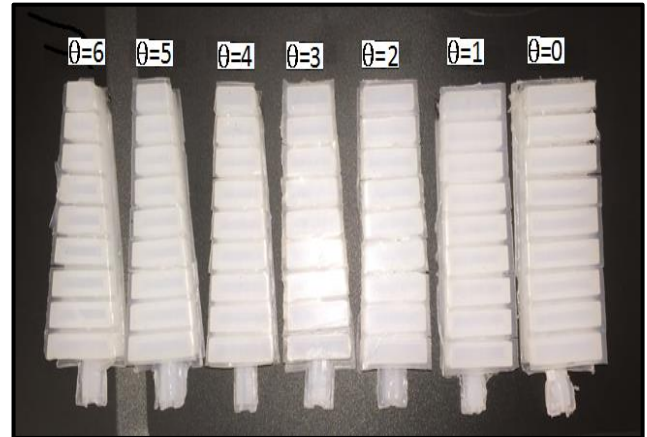


Figure 3. Fabricated Soft Actuators.

## 3. EXPERIMENT SETUP AND DATA ACQUISITION

### 3.1 Testing Station

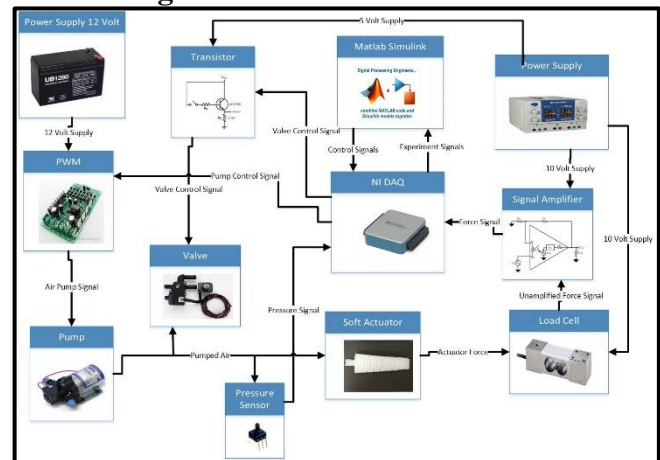


Figure 4. Hardware configuration of Testing station

The testing station (Figure 4) consists of a mount for the actuator, a 1kg load cell (LSP-1 from Transducer Techniques) to record the applied force at the tip of the actuator, a 6V generic air pump to inflate the actuator, a 12V 2-way solenoid valve to direct air flow, a 0-15psi pressure sensor from Honeywell to measure pump pressure, a motor driver (Syren 50A) to drive the air pump and a National Instruments DAQ to integrate all components into the computer for control from Matlab/Simulink.

### 3.2 Controller

The controller was designed using Simulink (Figure 5). It is an open loop controller that uses a sine wave input to control the on/off for the air pump, the open/close of the solenoid valve, and to measure the pressure of the air pump and the force applied to the load cell by the actuator. Whenever the sine wave is positive the valve is closed and the pump is simultaneously turned on to inflate the actuator.

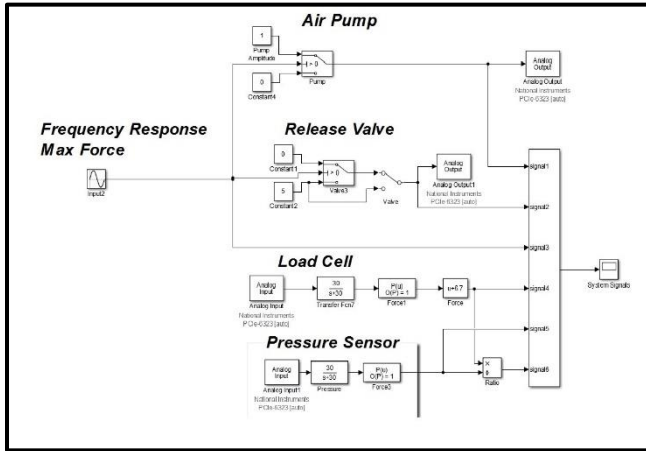


Figure 5. Matlab Simulink controller

Conversely, negative sine wave signals cause the pump to turn off and the valve to open, deflating the actuator. This illustrates the method of inflation/deflation that causes the actuator to apply force to the load cell.

### 3.3 Calibration

Once the system was assembled the load cell needed to be calibrated. This was achieved by incrementally placing known mass onto the load cell and recording the corresponding output voltage from the load cell. Microsoft Excel provided a linear equation relating the voltage to the applied load with a correlation coefficient of 1.

### 3.4 Force Measurement Procedure

To gather the data for the experiment the actuator was inflated/deflated twenty times at six different frequencies ranging from 1 to 6 rad/s incremented by 1 rad/s. First, the inflation tube was inserted into the actuator and a zip-tie used to secure it in place. The tip of the actuator was then aligned to a mark on the load cell. The power was turned on and the battery plugged in. Finally, the actuators were tested at a lower frequency of 0.5 rad/sec to find the maximum applied load. For each frequency, the actuator was run for 20 cycles.

### 3.5 Motion Tracking

The actuator was then rotated to enable unconstrained motion and a black dot was marked on the tip. A GoPro HERO 5 was used to record the motion of the actuator when it was inflated to its unrestricted maximum flexion range and then deflated. Care was taken to ensure that the motion of the actuator was planar, in the field of view of the camera. KINOVEA was used to track the planar motion of the black mark on the tips of the actuators. The x-y planar displacement was output to an excel spreadsheet. Figure 6 shows a photo sequence of the actuator during motion.

### 3.6 Analysis

Upon completion of gathering all the data, analyses were performed to obtain plots of force vs. time, force/pressure vs. time, force vs. pressure, the paths of the tips of the actuators, and the mean and standard deviation of the maximum forces for each frequency. Also, a 1-way ANOVA was performed to test the impact that actuation frequency had upon the force generated.

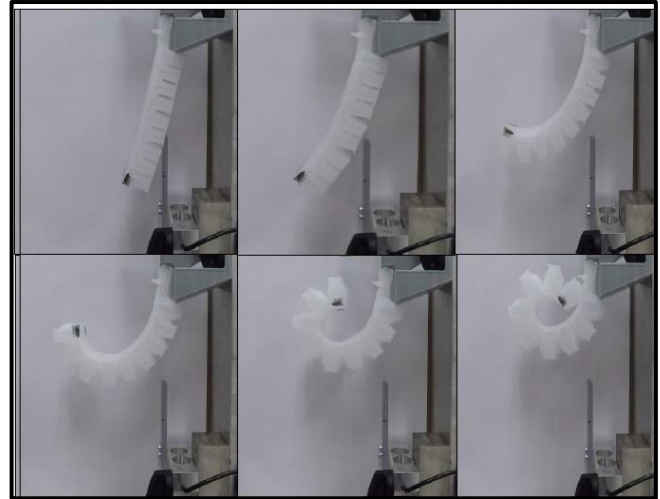


Figure 6. KINOVEA Photo Sequences

## 4. RESULTS AND DISCUSSION

Figure 7, shows the Force with respect to time for an actuator with taper angle  $0^\circ$ , for all seven frequencies respectively.

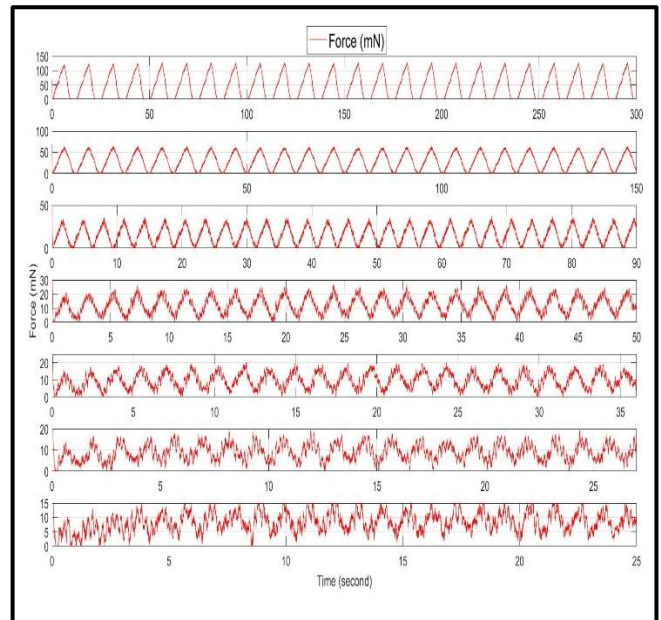
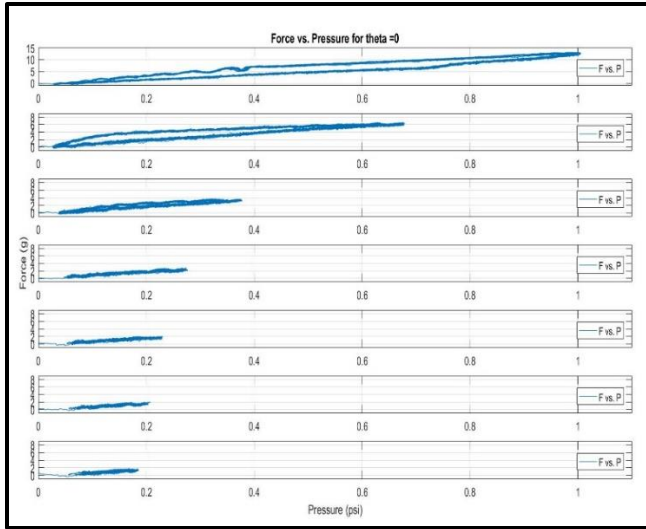


Figure 7. Force for a soft actuator with taper angle  $0^\circ$ .

The graph shows that the maximum force occurs when the frequency is minimum (0.5 rad/s), in general as the frequency increased the force applied by the soft actuator decreased. This behavior was observed for all the soft actuators with different taper angles.



**Figure 8. Hysteresis of the soft actuator with taper angle  $0^\circ$  for all frequencies.**

Figure 8 shows a hysteresis loop; the energy losses are maximum when the frequency is minimum.

As the frequency increase the energy losses decreases, the reason is when the frequency is the minimum the actuation time is longer in comparison to a higher frequency, which means the energy provided to the system is higher.

The input energy to the system is the pressurised air, while the output is the force applied by the soft actuator. Figure 9 represents the Ratio of force over pressure, Force and Pump signal for all the actuators at maximum frequency (0.5 rad/s). When the pump turns on, the actuators started to inflate causing the actuator to apply the force at their tips. As the pressure built up in the actuators, the force increased gradually and reaches its maximum value. Then the pump signal turned off, causing the actuators to deflate, the sudden decrease in actuator pressure causes a high force to pressure ratio in some of the actuators, which explains the spikes of the ratio after the pump signal turns off.

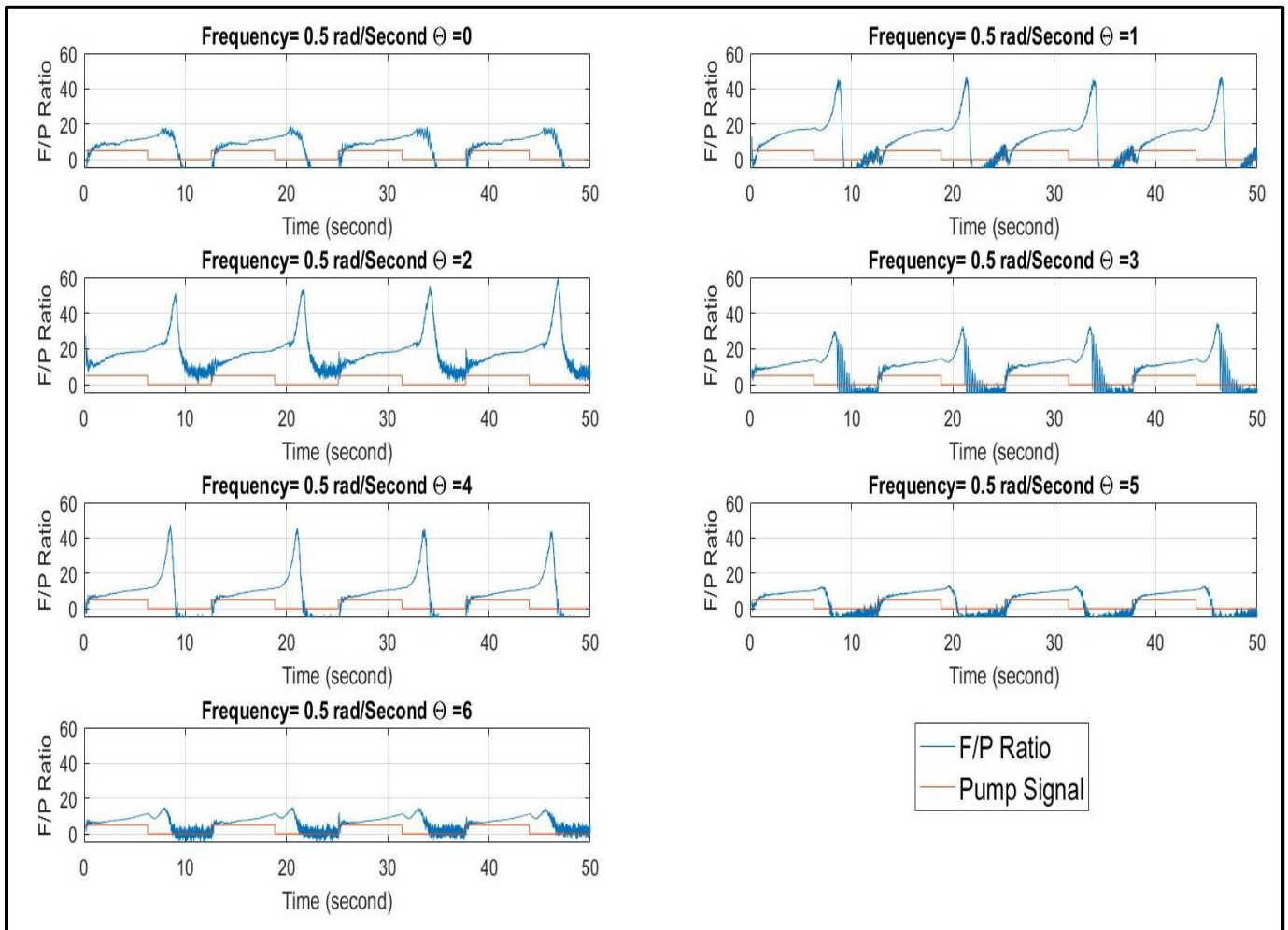


**Figure 9. Force, Ratio of Force over Pressure and Pump signal for the tested actuators over maximum frequency (0.5 rad/s)**

Figure 10 shows the displacement of the soft actuator's tips during inflation in the x-y plane with frequency 0.5 rad/s. The displacement increases as the taper angle increased, with a maximum displacement produced by the actuator with a taper angle 6°.

Figure 11 shows a comparison of Mean and standard deviation for maximum forces for all the soft actuators over different frequencies. In general, the mean of maximum force is at the lowest frequency as discussed previously for all actuators. The figure also shows how the mean Force changes when changing the taper angle. It can be noticed from the figure that the soft actuator with taper angle 2° has the best performance, as it has the largest mean maximum force over all the frequencies.

One-way analysis of variance (ANOVA1) was used to statistically analyze the mean of maximum force with different frequencies to find any correlation between the two of them for each soft actuator. The result of ANOVA1 shows that the actuation frequency significantly impacted the maximum force generated ( $p < 0.05$ ).

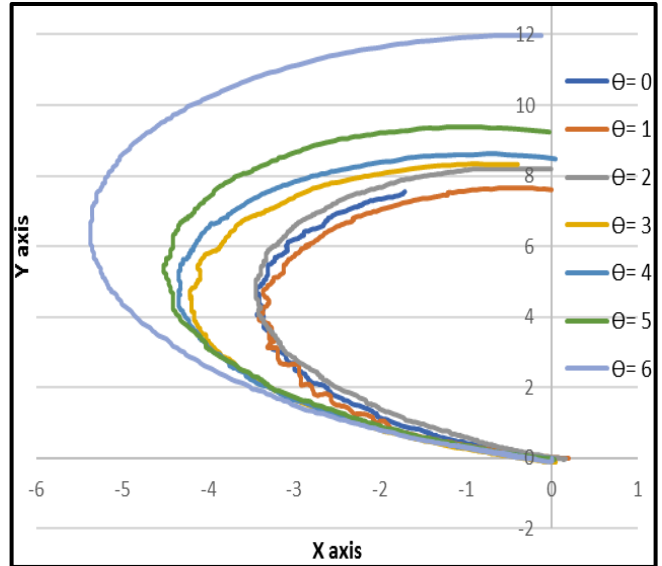


Figure 10. Displacement of the tip of the soft actuators

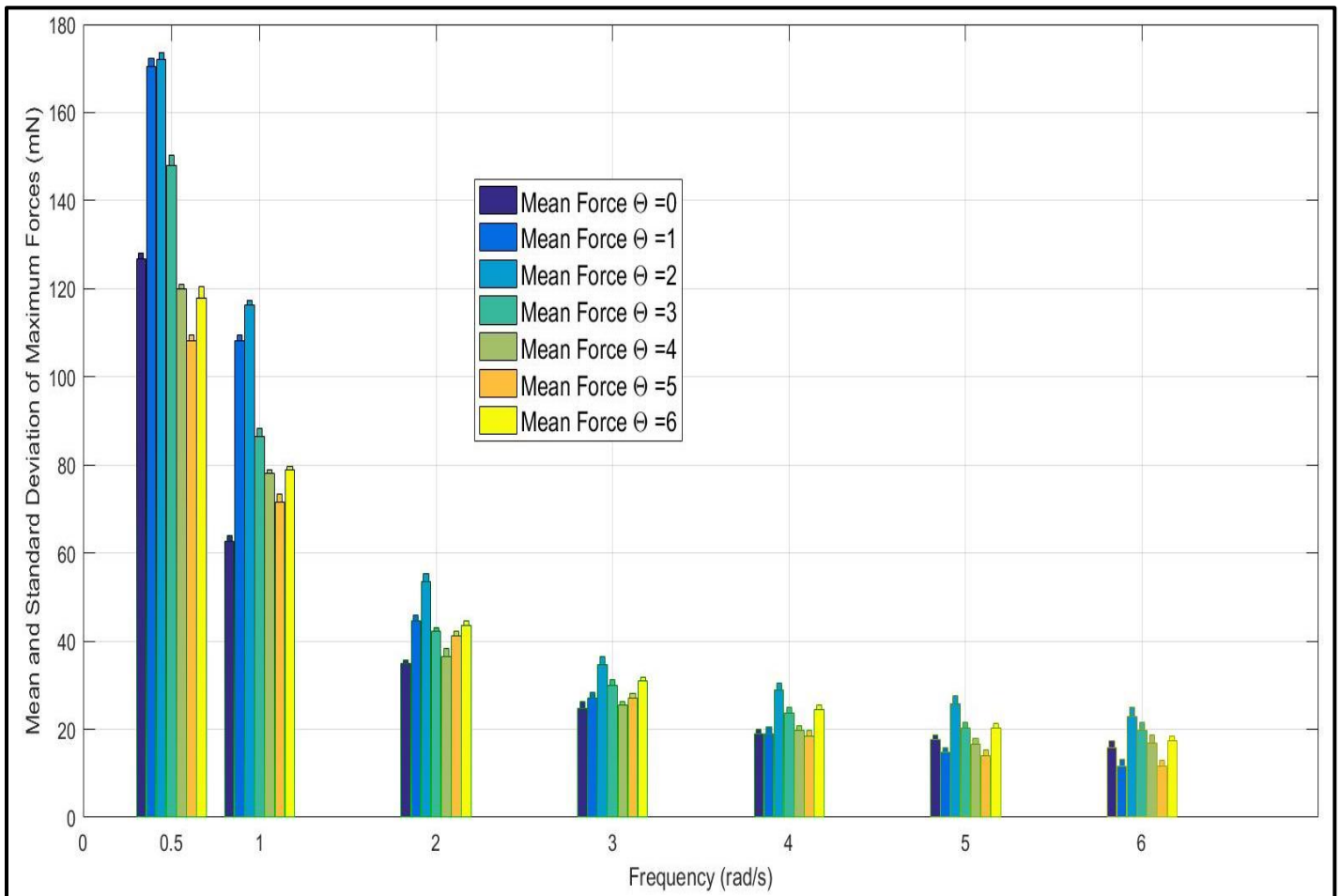


Figure 11. Standard deviation and mean of maximum forces for all the actuators at different frequencies

## 5. CONCLUSION

Seven different soft pneumatic actuators were designed and evaluated in this paper. It has been shown in this study that changing the taper angle of the soft actuators affect the performance of the actuators in different ways. In our case, the force output by the actuator with a taper angle of  $2^\circ$  produced the largest force, whereas the actuator with a taper angle of  $6^\circ$  produced the most displacement in unconstrained tests. Also, it was noted that the actuation frequency significantly impacted the applied force with all seven actuators.

## 6. REFERENCES

- [1] N. Tsagarakis and Darwin G. Caldwell. (2000). Improved Modelling and Assessment of pneumatic Muscle Actuators. IEEE International Conference on Robotics and Automation. 3641-3646.
- [2] Homberg B, Katzschmann RK, Dogar M, Rus D. (2015). Haptic identification of objects using a modular soft robotic gripper. IEEE/RSJ International Conference on Intelligent Robots and Systems (IROS).
- [3] E. Brown, N. Rodenberg, J. Amend, A. Mozeika, E. Steltz, M. R. Zakin, H. Lipson, and H. M. Jaeger. (2010). Universal robotic gripper based on the jamming of granular material. Proceedings of the National Academy of Sciences, vol. 107, no. 44, pp. 18 809–18 814.
- [4] Haddadin, S., Albu-Schaffer, A. and Hirzinger, G. (2009). Requirements for Safe Robots: Measurements, Analysis and New Insights. The International Journal of Robotics Research, 28: 1507-1527.
- [5] Doulergi, Z. and Fasoulas, J. (2003). Grasping control of rolling manipulations with deformable fingertips. Mechatronics, IEEE/ASME Transactions on, 8(2), 283-286.
- [6] R. K. Katzschmann, A. D. Marchese, and D. Rus. (2015). Autonomous object manipulation using a soft planar grasping manipulator. Soft Robot., vol. 2, no. 4, pp. 155–164.
- [7] K. C. Galloway et al. (2016). Soft robotic grippers for biological sampling on deep reefs,” Soft Robot., vol. 3, no. 1, pp. 23–33.
- [8] P. Polygerinos, Z. Wang, K. C. Galloway, R. Wood, and C. J. Walsh. (2014). Soft robotic glove for combined assistance and at-home rehabilitation. Robot. Auton. Syst., vol. 73, pp. 135–143.
- [9] T. Noritsugu and T. Tanaka. (2002). Application of rubber artificial muscle manipulator as a rehabilitation robot. IEEE/ASME Trans. on Mechatronics, vol. 2, no. 4, pp. 259–267.
- [10] Ilievski, F., Mazzeo, A. D., Shepherd, R. F., Chen, X. and Whitesides, G. M. (2011). Soft Robotics for Chemists. Angew. Chem., 123: 1930–1935. doi: 10.1002/ange.201006464.
- [11] Soft Robotics. Harvard Biodesign. 2015. Accessed 10.29.2016. <http://biodesign.seas.harvard.edu/soft-robotics>
- [12] Jennifer Frame, Oscar Curet and Erik D. Engeberg. (2016) Free-Swimming Soft Robotic Jellyfish. The 29th Florida Conference on Recent Advances in Robotics (FCRAR).
- [13] Kim, S., Laschi, C. and Trimmer, B. (2013). Soft robotics: a bioinspired evolution in robotics. Trends in biotechnology, vol. 31, no. 5, pp. 287-294.
- [14] C. Laschi, M. Cianchetti, B. Mazzolai, L. Margheri, M. Follador, and P. Dario. (2012). Soft robot arm inspired by the octopus. Adv. Robot., vol. 26, pp. 709–727.
- [15] Chen, F. J., Dirven, S., Xu, W. L., and Li, X. N. (2014). Soft actuator mimicking human esophageal peristalsis for a swallowing robot. Mechatronics, IEEE/ASME Transactions on, 19(4), 1300-1308.
- [16] Bobak Mosadegh , Panagiotis Polygerinos , Christoph Keplinger , Sophia Wennstedt , Robert F. Shepherd , Unmukt Gupta , Jongmin Shim , Katia Bertoldi , Conor J. Walsh , and George M. Whitesides. (2014). Pneumatic Networks for Soft Robotics that Actuate Rapidly. Advanced Functional Material, 24, 2163–2170.
- [17] Soft Robotics Toolkit. Accessed 03.01.2017. <http://softroboticstoolkit.com/book/pneunets-design>.

# Information Theory to Optimize Plans for Intelligent Robotic Arm Search of Known Objects

Roger Ballard  
Zubin Kadva  
Zongqiao Liu

Timothy Atkinson  
Zemeng Wang  
Rajaa Rahil

Taher Patanwala  
Chimiao Wang  
Marius C. Silaghi

School of Computing  
Florida Institute of Technology

## ABSTRACT

We propose an approach based on information theory and probabilistic models to plan optimized search processes of known objects by intelligent eye in hand robotic arms. Searching and reaching for a known object (a tool) in one's office is an operation that humans perform frequently in their daily activities. Intelligent robotic arms also encounter this problem in the various applications in which they are expected to serve.

The problem suffers from uncertainties coming from the lack of information about the position of the object, from noisy sensors, imperfect models of the target object, imperfect models of the environment, and from approximations in computations. The use of information theoretic and probabilistic models helps us to mitigate at least a few of these challenges, approaching optimality for this important task.

## Author Keywords

Eye-in-arm, Search, Information Theory

## INTRODUCTION

Robotic arms are traditionally used as automates that follow predefined trajectories, but recently they are combined with sensors to provide more intelligent functions such as abilities to open doors and grasp unknown objects. Here we address a seemingly more mundane problem of locating a known object in a partially known and bounded environment. In our problem we assume that the robotic arm has a single camera positioned in the arm. The problem is in fact challenging if we consider the need to optimize the number of movements, speed of localization, and certainty of result [5]. The lack of stereo vision can be compensated by taking pictures from multiple positions of the end effector, an additional challenge that adds up to the aforementioned problems.

Among motivating applications we list manufacturing lines, tool search by robotic arms on autonomous vehicles or in space, and medical robotic arms trying to find the right place to perform a blood drawing.

One of the commonly used approaches to path planning is based on search in the configuration space, where the arm is avoiding collision with elements in the environment, as well

as with itself. In this work the problem of path planning including collision with other objects and among its own segments, is assumed to be solved in a different module, not discussed here. In our own experiments, path planning is performed in the robot driver. Here we are concerned about the planning of a sequence of movements that maximizes the certainty of the localization of the searched object in a minimal number of image captures.

The environment, with potential positions of the object, can be segmented in partly overlapping areas, each of them being a possible view from the camera in the hand of the robot. The search proceeds by selecting the views to acquire and analyze next. The order is given by a heuristic for maximizing the information about the location of the searched object. The information concerning what is known is maintained in a belief map. With each picture, the belief changes and the next picture point of view is planned such as to increase this information. After covering some of the background and related work in the next section, we continue by describing formally the problem and the proposed heuristics. We end with discussions and conclusions.

## BACKGROUND

Planning problems have been addressed by robotics research for multiple decades. An important evolution of this research area consisted in the adoption of probabilistic models to represent in a scientific way the uncertainty existing in most real problems.

The source of uncertainty is constituted jointly by ignorance (e.g., concerning exact position of objects, luminosity and shape) and by the high computational complexity of known algorithms to access and process data. The ignorance is manifested not only in the lack of data but also in the incomplete modeling of physical phenomena, or in the approximations selected for modeling them.

Several other approaches had been proposed to address uncertainty, including default logic, fudge factors and fuzzy logic, but the community has largely concentrated on probabilistic approaches, which are accepted as being better scientifically founded among alternatives.

Probabilistic models generally use "statements" as ontological commitments (nature of reality) and probabilities as "epistemological" commitments (possible states of knowledge),

interpretable as “degrees of belief” or as “frequency”, potentially describing objective properties of the world. The basic objects/statements are represented using random variables. States of the world correspond to assignments of values to these random variables.

The use of probabilistic models does not automatically reduce errors from uncertainty in reasoning except in as much as the probabilistic models do address that particular uncertainty. For example, most probabilistic models still make significant approximations concerning the actual relations (or absence of relation) between facts. Another common approximation is in discretizing time and space, and studies have addressed the convergence of these approximation towards their continuous counterparts [1]. Probabilities can be modeled and learned with technologies such as artificial neural networks and Bayesian networks.

### Bayesian Nets

One of the most influential techniques for creating probabilistic models of phenomena is the Bayesian Network. The Bayesian Networks are graphical probabilistic models where statements (random variables) are depicted with nodes and conditional dependence relations between these concepts are displayed with directed arcs. The strength of Bayesian Networks come from the fact that not all dependence relations have to be depicted, since some of them can be inferred from others. In general, a random variable does not need to be linked to a second variable if they are independent given variables on already specified paths between them. The illustration in Figure 1 shows a simplified belief network for detecting known objects based on signals from camera interpreted as shape, color, and texture [9], in the presence of various orientations and lighting conditions:

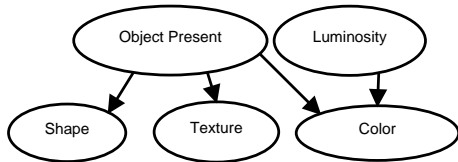


Figure 1. Sketch Belief Network showing potential conditional dependence assumptions between variables involved in the detection of an Object, without showing conditional probability tables.

For planning problems in environments with uncertainty in sensors or actions outcome, an alternative to continuous re-planning is to build *contingent plans* or *policies*. A policy is a mapping from each belief state of the agent into a plan to be executed in that state.

Addressing the robotic eye-in-arm search problems with Partially Observable Markov Decision Processes (POMDPs) has been first suggested in [8]. A POMDP  $(\Sigma, A, T, R, \Omega, O, \gamma)$  is described by a set  $\Sigma$  of states, a set  $A$  of actions, a set  $T$  of conditional transition probabilities between states (given performed actions), a reward function  $R : \Sigma \times A \rightarrow \mathbb{R}$ , a set  $\Omega$  of possible observations, a set  $O$  of conditional observation probabilities and a discount factor  $\gamma$ . Several algorithms were proposed for efficiently solving POMDPs, such as value iteration, policy iteration, point-based value iteration [3, 2, 4]. With POMDPs the goal is to maximize the expected utility,



Figure 2. Sample Search Problem: (a) Space and (b) Object

defined as the scalar (dot) product between belief (vector of probabilities for each state) and the utility of the corresponding states.

### Information Theory and Decision Trees

In this work we propose to address the problem using a different approach, namely information theoretical decision tree learning (ID3) [6]. Decision trees are a technology largely used for learning and classifying one concept. A decision tree consists of a tree data structure where each node represents a question and each branch is a possible answer to that question. Leaves stand for answers to the classification problem represented by the tree.

It is assumed that a user classifying a sample traverses the tree from its root towards one leaf, at each node asking the corresponding question represented by it, and once its answer is obtained, following on the corresponding branch. The leaf reached in this way tells the classification result for the given sample.

### ID3

The question of building decision trees that minimize the number of questions needed for classifying one sample has been heavily researched in the past. It has to be noticed that the number of possible decision trees is exponential and their enumeration is generally out of question. A heuristic commonly proposed for building such trees given available training data is based on information theory. The idea is to ask a question that reduces the expected entropy of the data in a training sample.

---

### Algorithm 1: Pseudocode for Object Search

---

```

1 procedure ObjectSearch() do
2   b = Init_Belief();
3   for (; ; ) do
4     if Object identified and reached, or space exhausted
5       then
6         return(b);
7     q = Best_Next_Viewpoint(b);
8     capture_image(q);
9     Update_Belief(b,q);
  
```

---

### THE ROBOTIC ARM EYE IN HAND SEARCH PROBLEM

A robotic arm controls an area within which it searches for a known object. For example, the area in our experiments is depicted in Figure 2.a and the searched object is shown in Figure 2.b. The algorithm used in [9] for this problem has similarities with the approach proposed here and a pseudocode for it that is reusable here is given in Algorithm 1.

The problem is formally represented as a lattice  $x_{i,j}$  of possible positions for the object (assumed to lay on a flat table). The object can occupy a set of several neighboring elements of the lattice, function of its position and orientation. The object may also not be present in the environment. The ratio of the lattice is given by the desired resolution of the detection. Experiments in this work use a pixel-level representation while some of the previous approaches were aiming at resolutions as rough as 10 cm [9, 7].

Originally the probability distribution of the position of the object is uniform across the lattice. The lattice can be analyzed from any point out of a set of points of observation, each of them covering a different quadrilateral's intersection with a subset in the lattice (function of the orientation, height, and location of the camera). At each step, one of the possible points of observation is selected such as to maximize the expected amount of information gathered about the position of the object. This solution is related to ID3.

We assume that, given uncertainties, capturing the object from immediate positions (1cm) corresponds to fully localizing it. Given that binary search is known to efficiently scan an organized data set, it can be expected that an efficient search will start by taking remote snapshots from higher altitude and converge towards close-up captures.

Note that if the camera would allow for zooming, then the same snapshot could theoretically be taken from multiple positions. However, our camera does not have zooming capabilities, and we will not simulate them by magnifying image areas, as this is assumed to yield lower quality detection.

### SOLUTION BASED ON ID3

We note that the problem can be modeled as a learning/classification problem where we are trying to detect the position of the searched object by asking repeated questions. Each snapshot taking can be seen as such a question. A relevant algorithm that tries to minimize the number of asked questions is ID3, where each step minimizes the entropy.

#### Adapted ID3

The idea is to measure the entropy of each belief distribution  $b_t(s)$  representing the knowledge at a given time  $t$  about the possible exhaustive and mutually exclusive states  $s$  using Shannon's formula  $H(b_t) = \sum_s -b_t(s) \log_2 b_t(s)$ .

The informational gain expected from a given question  $q$  at time  $t$  can be computed as the difference between the entropy before asking the question and the expected entropy after asking the question. The belief at time  $t$  is denoted  $b_t$  and each of the possible beliefs obtainable after learning the answer  $i$  if question  $q$  is posed at this moment, is denoted  $b_{t+1}^{q,i}$ . Assuming each answer  $i$  is expected to question  $q$  with a probability  $p(b_t, q, i)$ , as it can be computed from the belief  $b_t$ , the expected information gain from question  $q$  is:

$$G_{q,t} = H(b_t) - \sum_i p(b_t, q, i) H(b_{t+1}^{q,i})$$

Therefore, the question that the ID3 heuristic recommends to be asked at moment  $t$  is:

$$q(t) = \operatorname{argmax}_q \left( H(b_t) - \sum_i p(b_t, q, i) H(b_{t+1}^{q,i}) \right)$$

In common learning problems, the classification outcome (belief  $b_t$ ) is given by some set of samples in a training set that are matching questions asked so far, and is represented via counts of *positive* and *negative* training samples. Such a decision tree is first built once with large training sets of samples and later reused to classify new incoming samples.

In this research, we do not pre-compute and store such trees due to their sheer size given the number of possible questions. Rather, we recompute the tree on the fly by predicting  $p(b_t, q, i)$  using  $b_t$ .

The aforementioned general procedure being proposed is summarized in the generic pseudocode of Algorithm 2.

---

#### Algorithm 2: Generic Pseudocode for Information Theoretical Search

---

```

1 procedure Init_Belief() do
2   b = lattice representing the whole search space, each
   node being the probability of the object center (or its
   parts) being in the corresponding area;
3   return b;
4 procedure Best_Next_Viewpoint(b) do
5   V = set of  $N$  views sampled with chosen distribution
   across possible views;
6   B = evaluate(V,b); // e.g., set of views with expected
   belief maps and information gain;
7   v = best of B;
8   for (;) do
9     if (timeout) then
10      return (v,B(v),H(B(v)));
11      V = resample  $N$  views based on B;
12      B = evaluate(V,b); // e.g., based on expected
   information gain;
13      v = best of B;

```

---

#### Belief Updates

Each snapshot taking function updates the belief. The effect of the analysis of the snapshot capture at position and orientation  $(p, o)$  which observes the set of states (subset of the lattice with possible positions) given by a function  $View(p, o)$  is a belief function update  $\omega(j)$ , with the properties that

$$\omega(j) : View(p, o) \rightarrow [0, 1]$$

and that

$$\sum_{j \in View(p, o)} \omega(j) \leq 1$$

If the belief before the snapshot is  $b'$ , the belief update is a function  $u$ :

$$b = u(b', \omega)$$

One of the possible ways to integrate the new observation is incremental update:

$$b_\gamma(j) = \begin{cases} \gamma\omega(j) + (1 - \gamma)b'(j) & \text{if } j \in \text{View}(p, o) \\ \frac{1 - \sum_{j \in \text{View}(p, o)} (b_\gamma(j))}{\sum_{j \notin \text{View}(p, o)} b'(j)} * b'(j) & \text{otherwise} \end{cases} \quad (1)$$

In the above approach, a learning factor  $\gamma$  is used for updating the belief about recently observed areas, modeling the classification error probability, and this factor can decrease in time as the snapshots are taken zooming closer to the search area. The belief about areas not observed in this round is updated by normalization to make the total belief integrate to 1, which is done by multiplying it with the factor  $\frac{1 - \sum_{j \in \text{View}(p, o)} (b_\gamma(j))}{\sum_{j \notin \text{View}(p, o)} b'(j)}$ .

#### Aggregated History

An alternative approach is to gather all the features from images captures so far and to use a single classifier (e.g. ANN) to generate a posterior probability for each location. A third approach is to keep the classification given by the snapshot taken from the position from which the area has the largest projection in the image. The approach taken in one of the experiments is to multiply the new object detection probability with the previous belief and with an observation probability modeling the uncertainty of the image analysis.

#### The next question

In a given state of the search, we can evaluate the next question to ask by enumerating a subset of the candidate questions (positions and orientations). For each candidate question, there are two possible outcomes:

- object found with probability limited by the zoom level (size of the corresponding area in snapshot)
- object not found

The probability of each of these outcomes happening is based on the current probability mass assigned to the corresponding region. Therefore the utility of each question can be computed as the expected utility along the aforementioned branches.

#### Stochastic Search of Questions

The set of positions and orientations considered for the next snapshot is explored using a stochastic search method. A set of  $P$  capture positions are distributed throughout the workspace. For example, one can use a density that is higher in the height of the last snapshot than at other heights. At each position, a number of  $O$  orientations towards the searched surface are considered.

The information gain is estimated for each of these points. During a set of  $k$  rounds repeating the above procedure, the positions are redistributed into 3D cubic cells centered at previous points, proportionally with the information gain found

at that position. The size of the cells halves with each round. The orientations at each new point are similarly sampled in rectangles centered in previous directions at the previous point, and distributed proportionally with the corresponding information gains.

#### Computational Considerations

A trade-off exists between the number of positions  $P$  and orientations  $O$  to consider at each round and the number of states  $s$  (surface resolution) where belief of object presence is evaluated. Potential ways to alleviate this complexity is to start with a lower resolution and to increase it with each snapshot being taken, as a function of the height of the snapshot, such that the maximum resolution is obtained when the height is at the minimum accepted value.

#### Look-ahead

Just as with decision trees, the algorithm needs not be limited to evaluating only the next question at a time. Instead, just as with decision trees, game playing, and POMDP solvers, policies consisting in sequences of multiple actions can be evaluated before deciding the next questions. As with general look-ahead techniques, cheap evaluations/predictions at a given search state can make a good trade-off with deeper look-ahead steps (see Algorithm 3).

---

#### Algorithm 3: Look-ahead in evaluation

---

```

1 procedure evaluate( $V$ :view,  $b$ : belief) do
2   for  $q$  in  $V$  do
3     for  $i$  as outcome of snapshot  $q$  do
4        $b'_{q,i} = \text{update}(b, q, i)$ ;
5       if (not deepest level) then
6          $(q', b'_{q,i}, H') = \text{Best\_Next\_Viewpoint}(b'_{q,i})$ ;
7        $H = \text{aggregate\_expected\_gain}(q)$  over all  $i$ ;
8   return maximum ( $q, b, H$ );
```

---



---

#### Algorithm 4: Pseudocode for Greedy Hierarchical Search

---

```

1 procedure Init_Belief() do
2    $b =$  an empty tree with root representing whole search
   space and an empty ordered queue with the leaves of
   the tree;
3   return  $b$ ;
4 procedure Best_Next_Viewpoint( $b$ ) do
5   for ( $::$ ) do
6      $v =$  most likely node in  $b$ ;
7     if ( $v$  is known and not minimal) then
8       split  $v$  in overlapping views;
9       insert splits in  $b$ ;
10  return  $v$ ;
```

---

## DISCUSSION

A solution that was not based on a lattice but on a dynamically expanding belief tree enforcing a hierarchical search

was proposed in [9] and is described in Algorithm 4. Its main drawbacks with respect to the lattice approach used here and in the POMDP model [7] is that views location cannot be flexibly optimized in case objects are detected in border areas, or are so well identified that multiple levels of splitting can be jumped at once.

#### View Ordering Heuristics

The ID3 approach is an alternative to the common approach to action planning which is based on decision theory associating a reward with various states. There the state has to describe knowledge [7]. Alternative heuristics to the ID3 are possible, such as where each action (snapshot taking) is expected to add extra information, and the reward is defined as:

- the mode of the belief function  $b(s)$ ,
- the variance of the obtained belief function  $b(s)$ .

There can also be alternative ways of sampling the search space for candidate next questions. Instead of the described version of stochastic search, one can use:

- a kind of beam search where predefined transitions are tried and only the  $N$  most promising ones are extended further.
- simulated annealing transitions from each out of the set of  $N$  positions.

## IMPLEMENTATIONS AND EXPERIMENTS

Two implementations are detailed together with their evaluation: baseline and optimized search.

### Baseline

The baseline algorithm makes the assumption that in a blind search (with no extra information), all optimal algorithms become equal and it is only after a detection that the search heuristic makes a difference. It further posits that the location of the object may be gleaned from the image directly.

#### Algorithm Initialization

The Bayesian Network model of the object and its colors described in Figure 3 is first trained from a set of sample images. A sequence of viewing angles is built where each next view is selected to maximize marginal information gain assuming lack of object detection with previous views.

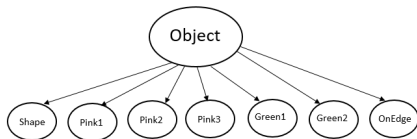


Figure 3. Baseline belief network.

#### Image processing

After each snapshot is taken, this method calculates both where the object could be located in the image and the probability that the object is indeed present.

First the image is scanned for all red and green pixels based on the Hue and Saturation from HSV. These pixels are set in

a red and green binary image. Contours are found and their size is estimated based on their minimal enclosing rectangle. Rectangles with too small of an area for the respective color are pruned. One more sensor is added, an 'onEdge' detection, which evaluates the statement, "Is this blob on the edge of the captured picture?". It is calculated by projecting the corners of the rectangle back onto the image and seeing if any of them falls off the image. We call each rotated rectangle with properties like color and onEdge, blobs.

An attempt is then made to pair multiple blobs together forming Red-Green-Red chains or Green-Green chains referred to as *detections*. In order for red to combine to a green, the two colors must be next to each other and match orientation (orientation can be flipped by 180 degrees as detections cannot tell front from back). Green-green is allowed based on the assumption that there was an undetected red. Unlike red-green pairings, green-green pairings must have a space between them. Not only must the orientation of the green blobs match each other, but the space is treated as an invisible rectangle whose orientation must also match. The one exception to matching orientation is when an object is 'onEdge', in which case we ignore that object's orientation (for example detecting the edge of a square will look like a triangle in the image, and the resulting blob will have an orientation radically off from where it really is at). If a matching only occurs due to the 'onEdge' flag, then that object is considered to not have the proper 'shape'.

This could theoretically lead to a detection of Green-Green or Red-Green-Red-Green-Red-Green (or longer)—these detections are broken down so that each detection has no more than two greens and no more than three reds following the rules noted above. Each of these detections then have their location estimated based on the camera and its position.

Next, if the robot's position is not optimal for estimating the object's location; a new image needs to be taken from a better position. In order to place the new image in the queue, the algorithm calculates the object occurrence probability based on the Bayesian network.

The Bayesian network responds to the blobs that were trained together. If there is only one green, then it is green1, two greens will result in green1 and green2. The first red detected will be red1, the second will be red2 and the third red3. The one exception is if detection links the blobs with the pattern green-red-green and instead the evidence will be green1, red2, green2 as the red2 represents the middle red of the tube.

#### Object Localization

To simplify the detection of the object location, the robot's camera is oriented along the robot's waist such that an  $x$  offset in the image can be directly attributed to a shift of the waist in the robot's configuration space.

The procedure is shown in Algorithm 5. This algorithm scores matches by their probability and can deal with objects not located on the table. However, it has a several weaknesses. Its biggest problem is that its initial search success depends on serendipity. Due to the involved computational

---

**Algorithm 5:** Detailed Baseline

---

```
1 procedure Init_Belief() do
2    $b =$  a set of potential view angles with initial weight of
   .5;
3    $img = \text{null}$ ;
4 procedure Best_Next_Viewpoint(b) do
5   while ( $b \neq \emptyset$ ) do
6      $c =$  first item in queue send  $c$  to the robot;
7     if ( $img \neq \text{null}$ ) then
8        $blobs = \text{processImage}(img)$ ;
9        $dets = \text{processBlobs}(blobs)$ ;
10      score all detections;
11      add all detections to  $b$  based on object
      occurrence probability;
12    return image from last command  $c$  to robot;
```

---

complexity, the selected initial sequence may not be optimal. For example, in a first version, it took 48 moves to search the space in a worse case where the object is in the very last location and there are no purposeful distraction objects (obviously every false match object will take an extra move). A slight improvement to the used approximation, and the search could be reduced to 23 moves for a worse case scenario.

### Optimized Implementation

In this approach, significantly more effort was put into the planning portion of the algorithm than the computer vision portion of the algorithm. In order to simplify the computer vision task, the vision problem was reduced from “find the given object on the table” to “find a pink blob on the table.” By finding the location of the three pink blobs on the object, the exact location and orientation of the object can be determined.

### Representing Belief States

For this problem, the  $1m \times 1m$  table being searched was discretized into  $1cm \times 1cm$  regions, resulting in a  $100 \times 100$  region grid. A belief state is simply a probability distribution of the location of the target pink blob over this grid. An example initial belief state is shown in Figure 4

### Evaluating Belief States

In order to be able to evaluate potential actions for planning, we need to be able to evaluate the utility of their resulting belief states. We experimentally compare two methods for evaluating a belief state: entropy and weighted standard deviation.

For the entropy measure, the entropy of a belief state is defined to be the entropy of the probability distribution:

$$H(B) = \sum_{n=1}^{|B|} -B[n] \log_2 B[n] \quad (2)$$

Where  $|B|$  is the number of regions in the belief state, and  $B[n]$  is the belief that the target is in region  $n$ . From a decision theoretic perspective it can be considered that the utility

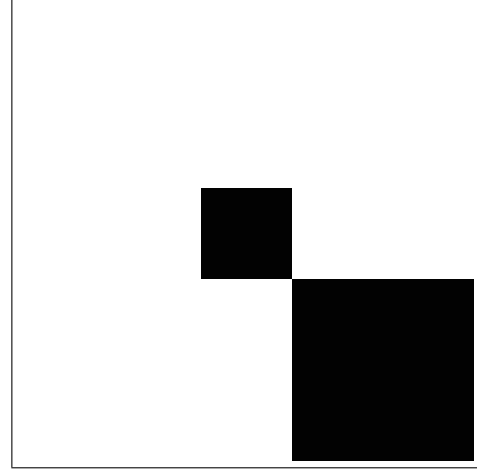


Figure 4. Initial belief state, where black regions have 0 probability and white regions have the maximum probability over the distribution.

of the belief state is simply taken to be the negative of its entropy:

$$U(B) = -H(B) \quad (3)$$

For the weighted standard deviation measure, the weighted standard deviation of a distribution with locations associated with the domain of the distribution is defined as follows:

$$center(B) = \sum_{n=1}^{|B|} B[n] loc[n] \quad (4)$$

$$variance(B) = \sum_{n=1}^{|B|} d(loc[n], center(B))^2 \quad (5)$$

$$stdev(B) = \sqrt{variance(B)} \quad (6)$$

Where  $|B|$  is the number of regions in the belief state,  $B(n)$  is the belief that the target is in region  $n$ ,  $loc[n]$  is the location of region  $n$ , and  $d$  is the distance metric used. The utility of the belief state is simply taken to be the negative of its weighted standard deviation:

$$U(B) = -stdev(B) \quad (7)$$

The motivation for the weighted standard deviation measure is the fact that the entropy measure does not take into account the spatial information of the belief state. Due to this limitation, using the entropy measure (without look-ahead) can lead to plans that leave unexplored regions interleaved with explored regions, potentially leading to a greater overall number of steps required to find the target.

### Updating Beliefs

The current belief state can be maintained at all times and can be updated using Bayesian inference. Given a prior belief state  $B$  and a piece of evidence  $E$ , the following two rules are sufficient to produce a new belief state  $B'$ , such that:

$$\forall n \in \{1..N\} : B'(n) = B(n|E) \quad (8)$$

---

**Algorithm 6:** Pseudocode for Action Space Exploration
 

---

```

1 mostPromising = a new empty list of regions;
2 insert a region representing t*he whole configuration space into mostPromising;
3 for (int depth = 0; depth < search_depth; depth++) do
4   for (int dim =0; dim < dimensionality; dim++) do
5     newMostPromising = a new empty list of regions;
6     split each box into mostPromising into three sub-boxes, splitting on the dimension dim;
7     insert each sub-box into newMostPromising;
8     remove any invalid configurations from newMostPromising;
9     //Some configuration space coordinates are invalid in the workspace;
10    filter newMostPromising to the beam_width boxes with the highest utility;
11    replace mostPromising with newMostPromising;
12 return best element of mostPromising;

```

---

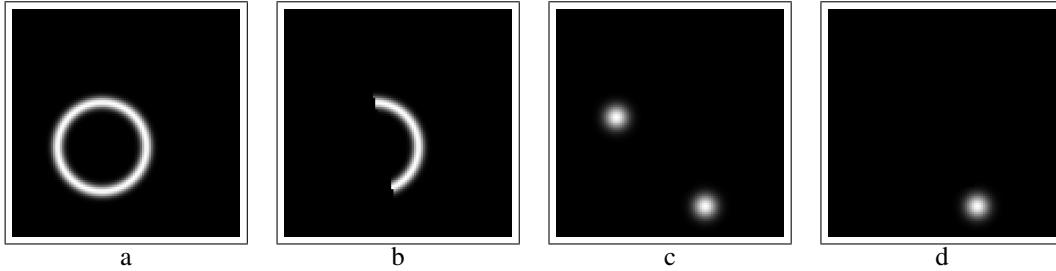


Figure 5. a) Initial belief state for finding the second point. This takes the form of a ring centered on the first point b) The effect of using already-taken photographs to update the belief state for the second point before even beginning the search c) Initial belief state for finding the third point. This takes the form of two radial Gaussians based on the found location of the first two points d) The effect of using already-taken photographs to update the belief state for the third point before even beginning the search

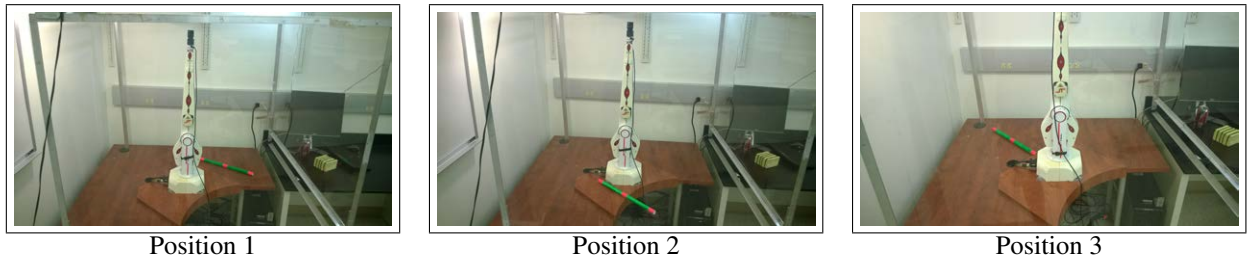


Figure 6. Location of the target object in three position.

- **Target not Detected in Image:** If the target is not detected in the image, then the update rule is given as follows:

$$B'[n] = \begin{cases} \alpha * B[n] * false\_neg\_prob & \text{if } visible(n, c) \\ \alpha * B[n] & \text{otherwise} \end{cases} \quad (9)$$

Where  $c$  is the configuration of the robot arm that the image was taken from, and  $visible(n, c)$  is true iff region  $n$  is visible in configuration  $c$ . A normalization factor,  $\alpha$ , is also employed.

- **Target Detected in Image:** If the target is detected in the image, then the update rule is given as follows:

$$B'[n] = \alpha * B[n] * ((1 - false\_positive\_prob) * kernel(d(loc[n], detect\_loc))) + false\_positive\_prob \quad (10)$$

Where  $detect\_loc$  is the location of the detection mapped to the table, and  $kernel$  is the kernel function representing the uncertainty in the camera. (In this implementation, the kernel was a Gaussian distribution with  $\sigma$  proportional to the distance of the camera from the target and the distance in the image of the target from the center of the image, to model increasing uncertainty at further distances and increasing uncertainty around the edges of the image.)

#### Evaluating Actions

The expected utility of an action (an image taken in a certain configuration) can be naturally defined in terms of the utility of the potential belief states it could result in:

$$U(a, B) = \sum_{loc=1}^{|B|} B(loc)U(resultant\_belief(B, a, loc)) \quad (11)$$

Where  $a$  is the action taken,  $loc$  is the true location of the target,  $B$  is the prior belief state, and  $resultant\_belief$  is defined according to the update rules in the Updating Beliefs section.

However, this direct calculation is prohibitively expensive. Instead, we estimate the utility of an action by sampling several locations from the prior belief distribution and averaging the resultant utilities for each sample.

#### Exploring the Action Space

We can treat our configuration space as an  $n$ -dimensional box, and explore the space by repeatedly dividing the space into sub-boxes. We define the utility of a box in the configuration space to be the maximum utility of any point inside that box. Making the observation that the utility function is locally smooth in the configuration space, we can approximate the utility of a box by evaluating the utility of the center of that box. As we are subdividing, we can take the most promising boxes at any depth (those with the highest approximated utility) and expand them further. We can repeat this process until we have subdivided the boxes into several suitably small volumes, thus selectively exploring the search space. This is outlined more formally in Algorithm 6.

#### Finding a Point

We can find a single point by repeatedly determining the best next action to take, taking it, and updating our belief with the evidence we get. In order to determine when to stop and declare the point found, a threshold value on the utility of our belief state is used. For the entropy measure, this threshold is 5 bits. For the weighted standard deviation measure, this threshold is 2.5cm. In general, taking pictures with successful detection at 1cm distance from the object important features can also be considered an acceptable termination condition.

#### Finding the Object

Given the above algorithm for finding a single point, we can apply this algorithm to find the object's position and orientation. For the first point, we initialize the belief state uniformly randomly, except for certain invalid regions, such as not on the table or inside the base of the robot, as shown in Figure 4.<sup>1</sup> For the second point, since we know the radius of the object and the position of the first point, we initialize the belief state to be a ring of that radius around the first found point, as shown in Figure 5.a. For the third point, since we know the radius of the object and the position of the first two points, we initialize the belief state to be two Gaussian distributions, as shown in Figure 5.c. After initializing the belief states for the second and third points, we can update our belief by factoring in the evidence already gathered. The effect of using this technique is shown in Figures 5.b and 5.d.

## EXPERIMENTAL RESULTS

The three detailed algorithm instances (baseline, optimized with standard deviation heuristic, and optimized with entropy heuristic) were run with the target object in three locations. The results are in Figures 7, 8, and 9. The two optimized heuristics do significantly improve over the baseline version.

<sup>1</sup>Although some of the points may be in these invalid regions, it is guaranteed that not all of the points will be in these regions.

## CONCLUSIONS

In this work we have proposed a new framework and algorithms for planning robotic Eye-in-Arm search of known objects. Our framework is inspired from the artificial intelligence theory of learning based on decision trees. As such, each snapshot-taking operation in the search process corresponds to a question being asked in the decision tree, while the possible positions of the searched object correspond to the possible samples classified by the decision tree. As a further parallel to decision trees, we test search heuristics based on entropy, as inspired from the information theoretical ID3 learning algorithm.

The main difference between our search framework and decision tree learning is that we build the relevant tree branches dynamically for each classification, rather than pre-building it once for all (except for the version keeping one likely branch in the baseline technique). This is due to the size of the tree which would be difficult to store. Another difference is in the fact that we do not use training data but rather compute expected outcomes based on current robot beliefs, represented by a probability distribution of the object location. Considered questions (i.e., snapshot positions) are sampled out of the total set of possible questions using stochastic search or dichotomous beam search. Actions can be selected based on comparing candidate plans composed of sequences of multiple look-ahead steps and evaluating the expected beliefs. This is a process also reminiscent of POMDP policy evaluations.

Experimental evaluations are performed using an ST-12 robotic arm with a camera mounted in its end-effector, and three algorithm versions. A baseline version with a simple search whose intelligence mainly lies in the computer vision part is compared against two heuristics for the robotic arm next-question selection: namely based on entropy, and based on standard deviation. For the described experiments, the two intelligent search processes performed comparatively well, and much better than the technique focusing on computer vision. The intelligent search heuristics are expected to excel in different problem sub-domains, and the identification of these domains is planned for future work, as well as the exploration of several mentioned optimizations.

## REFERENCES

1. Pratik Chaudhari, Sertac Karaman, David Hsu, and Emilio Frazzoli. 2013. Sampling-based algorithms for continuous-time POMDPs. In *2013 American Control Conference*. IEEE, 4604–4610.
2. H. Kurniawati, David Hsu, and Wee Sun Lee. 2008. SARSOP: Efficient point-based POMDP planning by approximating optimally reachable belief spaces. *Robotics: Science and Systems 2008 (2008)*.
3. Joelle Pineau, Geoff Gordon, and Sebastian Thrun. 2003. *Point-Based Value Iteration: An Anytime Algorithm for POMDPs*. Technical Report. Proc. of IJCAI, Mexico.
4. Pascal Poupart, Kee-Eung Kim, and Dongho Kim. 2011. Closing the gap: Improved bounds on optimal POMDP solutions. In *ICAPS*.

Test	StdDev			Entropy			Baseline
	Find 1st	Find 2nd	Find 3rd	Find 1st	Find 2nd	Find 3rd	
1	2	1	1	4	1	1	28
2	4	0	1	3	1	2	
3	2	1	1	3	1	1	
4	2	1	1	3	1	1	
5	2	1	1	3	1	1	
6	5	1	1	3	1	1	
7	2	1	1	3	1	1	
8	4	0	1	4	1	1	
9	2	1	1	2	1	1	
10	4	1	0	4	1	1	
Average	2.9	0.8	0.9	3.2	1	1.1	28
Cumulative	4.6			5.3			

Figure 7. Position 1

Test	StdDev			Entropy			Baseline
	Find 1st	Find 2nd	Find 3rd	Find 1st	Find 2nd	Find 3rd	
1	9	1	1	2	1	2	49
2	3	3	1	4	2	1	
3	10	1	1	6	1	1	
4	7	2	8	4	2	1	
5	5	2	1	7	0	1	
6	7	2	6	4	1	1	
7	7	3	2	5	1	1	
8	6	2	2	7	2	2	
9	4	2	2	3	2	1	
10	8	1	2	6	1	1	
Average	6.6	1.9	2.6	4.8	1.3	1.2	49
Cumulative	11.1			7.3			

Figure 8. Position 2

Test	StdDev			Entropy			Baseline
	Find 1st	Find 2nd	Find 3rd	Find 1st	Find 2nd	Find 3rd	
1	5	1	1	2	1	4	9
2	4	1	1	4	1	1	
3	4	1	1	3	1	1	
4	4	1	1	3	1	2	
5	4	1	1	3	1	1	
6	5	1	4	3	8	3	
7	4	1	1	4	1	1	
8	5	1	0	2	1	1	
9	4	1	1	4	1	1	
10	4	1	0	2	1	1	
Average	4.3	1	1.1	3	1.7	1.6	9
Cumulative	6.4			6.3			

Figure 9. Position 3

5. Jan Rosell, Raúl Suárez, Carlos Rosales, and Alexander Pérez. 2011. Autonomous motion planning of a hand-arm robotic system based on captured human-like hand postures. *Autonomous Robots* 31, 1 (2011), 87.
6. Stuart Russell and Peter Norvig. 2013. *Artificial Intelligence — A Modern Approach*.
7. Marius C. Silaghi and Jixing Zheng. 2017. POMDPs for Robotic Arm Search and Reach to Known Objects. In *ArXiv: 1704.07942*.
8. Srinivasa Venkatesh and Marius C. Silaghi. 2015. Planning One Eye-in-Arm Robot for Object Localization. In *Proceedings of FCRAR 2015*.
9. Srinivasa Venkatesh and Marius C. Silaghi. 2016. Optimizing Eye-in-Arm Robot for Localization of Known Objects. In *Proceedings of FCRAR 2016*.

# Internship Training in Robotics Lab: Exploring Robotics through hands-on experience

Gauthier Sellin, Pierre Laroche

Robotics & Spatial Systems Laboratory  
Florida Institute of Technology  
Melbourne, Florida 32901  
gsellin@my.fit.edu, pierrel@fit.edu

## ABSTRACT

This article presents the future work for an internship in the Robotics and Spatial Systems Laboratory (RASSL). This work is different from robotics lessons because it is a practical work. It enables one to put knowledge into practice and learn robots by experience. It enables one to discover very interesting robotics applications. This internship enables the study of different robots: from the Nao robot to mechanism design and applications by way of mobile robots like PantherBot and IGV. Each robot has special features, consequently new knowledge in many fields will be acquired.

**Keywords:** internship, robotics lab, humanoid robot, mobile robot, mechanism

## 1. Introduction

### 1.1 RASSL

The Robotics and Spatial Systems Laboratory (RASSL) is dedicated to the development of robotic mechanical systems that generate spatial (i.e. 3-dimensional) motion and force transmission [1]. The lab seeks to advance the design methodologies for these challenging systems as well as techniques for their utilization in industrial and consumer applications. The vision of RASSL is to be the world leader in the research and development of novel 3-dimensional robotic mechanical systems. The mission of RASSL is to educate engineers in cutting-edge research and development of 3-dimensional robotic mechanical systems by conducting research, building & testing prototypes, and publishing the findings.

### 1.2 Internship purpose

The goal of the internship is to study different robots: a humanoid robot, mobile robots and a mechanism. Hands-on learning during an internship provides real-world experience [2].

Studied robots will be:

- Nao, a humanoid robot, by using Choregraphe, a programming tool for basic instructions and then Python language in order to program the robot.
- PantherBot, a general purpose mobile robot platform for autonomous navigation and teleoperation.
- Intelligent Ground Vehicle (IGV), an autonomous robot.
- SCUD Linkage, a S-C-U Dual Four-Bar Linkage.

## 2. Nao Robot

### 2.1 Nao Robot Overview

Nao is an autonomous, programmable humanoid robot developed by Aldebaran Robotics, a French robotics company [3]. This company is among the worldwide leaders in human robotics. They developed several humanoid robots including Nao, Romeo and then Pepper in collaboration with Softbank, a Japanese company. These robots have several goals: Nao is for programming, teaching and research; whereas Romeo is designed to explore and further research into assisting elderly people and those who are losing their autonomy [4]; and Pepper is designed to be a life companion and for customer relations.



Figure 1. Nao

Aldebaran Robotics began to develop Nao robot in 2004 with Project Nao. There have been several upgrades to the robot platform: for example the 2011 Nao Next Gen and the 2014 Nao Evolution. Currently it's the 5th version. The different Nao

platforms evolved from 14 to 25 degrees of freedom. A specific robot was created for the Robocup competition with 21 degrees of freedom. Nao robots are used in many academic institutions worldwide for research and teaching. According to Aldebaran Robotics, about 10.000 robots are in use around the world.

Nao has 7 senses for natural interaction [5]:

- **Moving:** 25 degrees of freedom and a humanoid shape that enable him to move and adapt to the world around him. His inertial unit enables him to maintain his balance and to know whether he is standing up or lying down.
- **Feeling:** The numerous sensors in his head, hands and feet, as well as his sonars, enable him to perceive his environment and get his bearings.
- **Hearing and speaking:** With his 4 directional microphones (for voice recognition and sound localization) and loudspeakers (for multilingual text-to-speech synthesis), Nao interacts with humans in a completely natural manner, by listening and speaking.
- **Seeing:** Nao is equipped with two cameras that film his environment in high resolution, helping him to recognize shapes and objects.
- **Connecting:** To access the Internet autonomously, Nao is able to use a range of different connection modes (WiFi, Ethernet).
- **Thinking:** We can't really talk about "Artificial Intelligence" with Nao, but the robots are already able to reproduce human behavior.

Nao is piloted by a Linux-based operating system called NAOqi OS. This OS powers the robot's multimedia system. There is also a graphical programming tool called Choregraphe, which is easy to use.

## 2.2 The use of Nao

### 2.2.1 Choregraphe

First Nao has to be connected with Choregraphe. The interface is very clear (See Figure 2).

In the upper part, there is a toolbar with many functions: create, open or save a project; connect or disconnect the robot; start or stop the motion; set the volume of Nao's speakers; activate or deactivate the animation mode; set on or off the stiffness of all joints of the robot; indicate the level of the battery.

On the left side, there is a box library panel which includes all the elementary boxes you need to create your first behaviors. Those boxes are ordered by their category of action (motion, LEDs, etc) or their function in the diagram (flow control, templates of boxes, etc).

In the middle, there is the flow diagram panel. This is the place to compose Nao's behaviors. In the box path, there are the different levels of the Flow diagram. Boxes from the box library panel can be added and then the boxes need to be connected with the input and output borders located on the right and on the left side.

On the right side, there is the robot view which displays the current position of the joints of the robot.

More advanced panels can be found in the "View" Menu.

### 2.2.2 Basic operations

After creating a project, a behavior can be created in order to make Nao talk, walk, dance, etc. Creating a behavior is easy, simply add desired boxes to the flow diagram panel. All basic operations are listed in the box library panel. This section is divided into several categories: Audio, Behavior, Communication, Data Edit, Flow Control, LEDs, Math, Motions, Sensing, System, Templates, Trackers, Vision, World Representation.

There is also a Pose library panel with basic poses: StandZero, StandInit and Stand. It enables to easily access standard key positions to create a behavior.

### 2.2.3 Python programming

In the previous part, all boxes are easy to use because the code is already written. However there are "script boxes" (See Figure 3) which enable to code in Python our functions. Any Python module can be imported and any Python function can be used as in any Python script.

## 2.3 Proposed Plan for Nao Robot

Firstly Choregraphe will be used to try all functionalities of this software in order to find out all Nao's abilities. Secondly once Nao's abilities are known, Python scripts will be written to program Nao. It will enable the creation of new postures. Creating a choreography could be a good way to teach to use the robot. Programming Nao in order to walk in the lab, to go around the lab would be interesting. Programming Nao to be able to detect the person in front of him among lab members using vision algorithms would be interesting too. Finally the objective is to write lessons or activities in order to discover and to use Nao, Choregraphe and Python programming.

## 3. PantherBot

### 3.1 PantherBot Overview

The PantherBot (See Figure 4) consists of the PowerBot mobile robot base, manufactured by MobileRobotics, Inc.TM, and a 6-DOF robotic arm, manufactured by Schunk Intec [8]. The PantherBot base has the ability to autonomously map terrain, plot coordinates, as well as perform miscellaneous functions at a certain location after a full map is acquired by using the MobilEyesTM, and Mapper3 TM software in conjunction with its on-board sonar sensors and laser range finder. The software can also stream live footage from the PantherBot's two cameras mounted on board, one on the PantherBot's base and one adjacent to the parallel gripper on the robotic arm to monitor the arm's movements remotely over 802.11b WiFi. To give the PantherBot the ability to map out a building, it must be able to gain access to doors and be able to travel between floors. To do that, two tools were designed to perform two basic tasks - one to push buttons and one to open doors. The tools were designed such that they would be tailored to the hardware of the F. W. Olin Engineering Complex at Florida Institute of Technology for ensured repeatability.

### 3.2 Proposed Plan for PantherBot

The objective is to do some activities using PantherBot in order to learn basic operations of this robot and important parameters: plan resolution for narrow spaces with obstacles, rotational speed of the robot, etc. Mapper-3 will be used in order to create or edit a map,

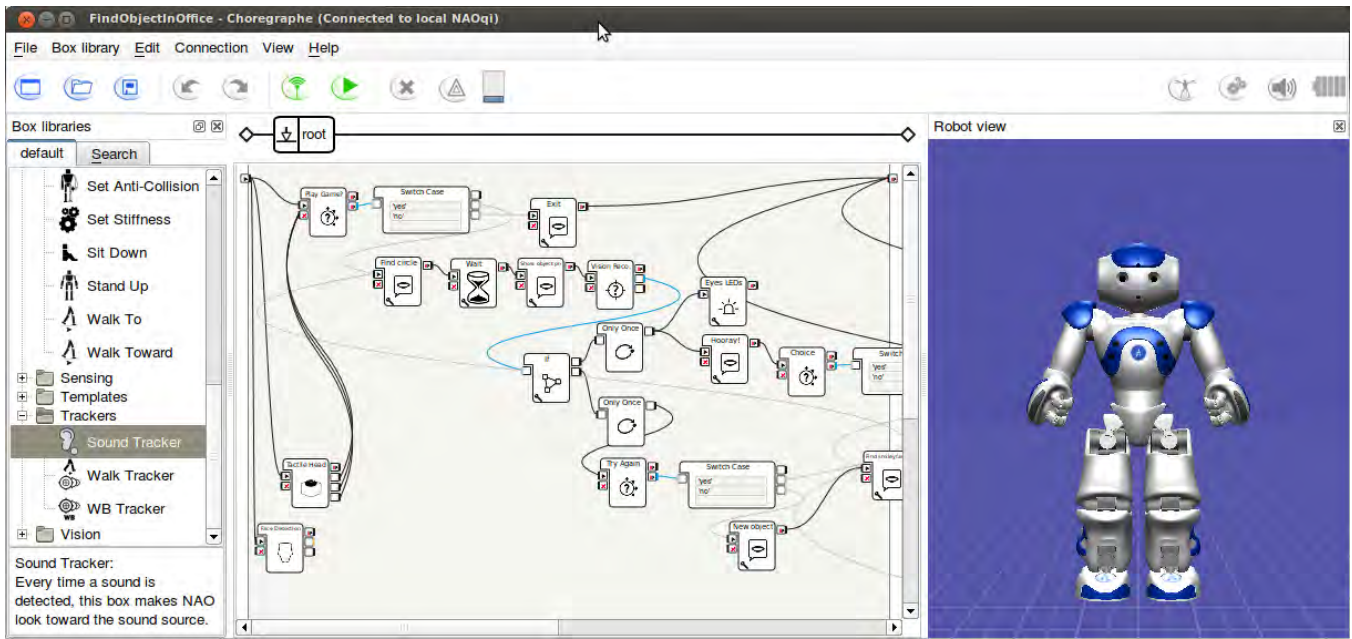


Figure 2. Choregraphe interface [6]

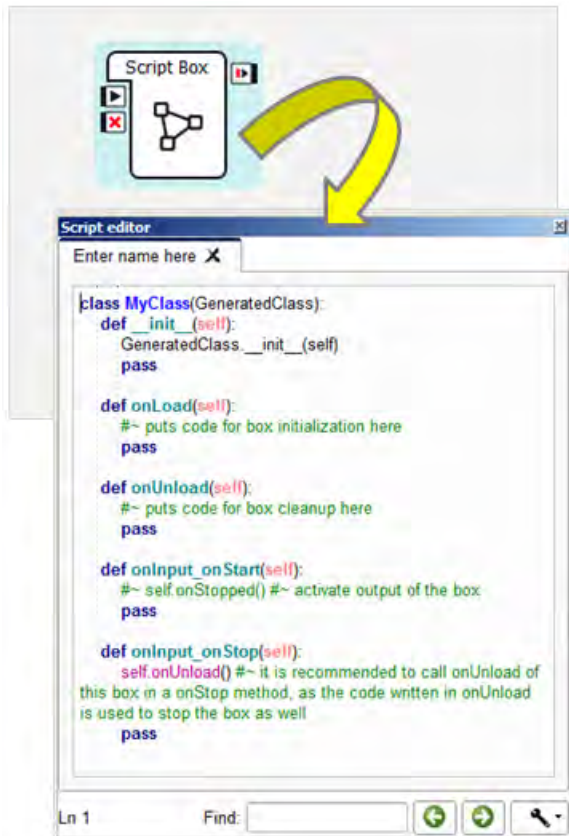


Figure 3. Python programming [7]

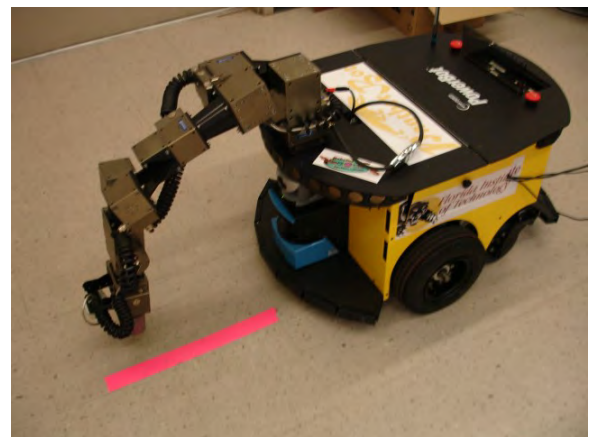


Figure 4. PantherBot with Schunk Robotic Arm [8]

for example a map of the lab building. The robot arm will be used too.

These experiments will enable to understand software and parameters of this robot.

## 4. Intelligent Ground Vehicle

### 4.1 IGV Overview

The Intelligent Ground Vehicle (IGV) (See Figure 5) project began as a senior design project of which the goal was to create an autonomously navigated vehicle to be entered into the Intelligent Ground Vehicle Competition (IGVC), which is an engineering challenge that the main goal is to design a robot with artificial intelligence to autonomously navigate through a course full of obstacles such as barrels, pot holes, and sand traps [9]. The robot is equipped with a SICK LMS291-S05 laser range finder (LiDAR), a digital compass, two servo drives with encoder feedback, and a 24V

(DC) supply for up to 2 hours of autonomous operation. Instead of building a mobile robot that runs on a specific field, right now this project is being modified in order to be more generally functional so that at the end of this project the IGV should be able to navigate through outdoor environments to a designated destination with a given GPS waypoint coordinate only.



Figure 5. Intelligent Ground Vehicle

## 4.2 Proposed Plan for IGV

With the Intelligent Ground Vehicle, the objective is to understand how the system works. The IGV, made by students, is a combination of hardware (motors, servo drives, etc) and software (ROS). Using the IGV will enable to have more knowledge in this field.

## 5. SCUD Linkage

### 5.1 SCUD Linkage Overview

The S-C-U Dual Four-Bar Linkage (See Figure 6), or SCUD Linkage, is a biologically inspired design for articulating the leg in a mechanical walking machine or for manipulating an end effector along a rigid, planar surface [10]. It is difficult to use closed linkages to deal with certain industrial tasks. It is very difficult for planar linkages to generate the desired complex spatial trajectories created by the serial chain robots. A motivation of this research is to design a better and more reasonable linkage mechanism for spatial surface tasks. Due to the features of these specified tasks, the mechanism designed should have the following characteristics:

- Be able to generate general spatial motions with a targeted and efficient approach.

- Perform spatial surface tasks with better repeatability and stability than traditional serial chain robots.
- Be simple to manufacture while being more cost effective than serial chain robots.

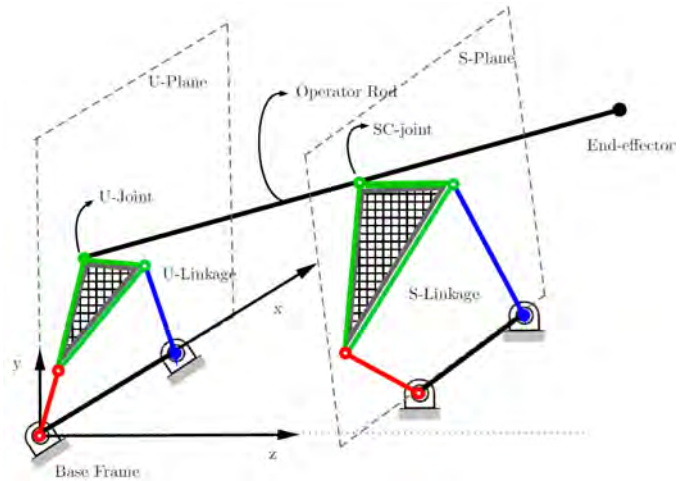


Figure 6. An example SCUD Linkage [10]

To generate fixed spatial curves and surfaces, the novel mechanism should have multiple degrees of freedom and at the same time, make it targeted and efficient for finite fixed curves or surfaces, the degrees of freedom should be reduced to two. To have better repeatability and stability, the novel mechanism should be a classification of spatial closed linkages to utilize their mechanical properties. Returning to the locomotive source of inspiration, a series of SCUD Linkages could be used to generate the motion of a hexapod walking machine.

### 5.2 Proposed Plan for SCUD Linkage

The biological inspired mechanism has known industrial uses as a single entity. When they are combined together, the SCUD Linkages can form a walking machine (See Figure 7) as the original inspiration intended. Six SCUD Linkages can be combined to form a walking gait hexapod machine. This walking gait hexapod features a low center of gravity, versatility over adverse terrain, and six degrees of freedom to move in a variety of gaits.

The objective is to produce such a prototype walking machine. 3D printers and other additive manufacturing technologies will be utilized to manufacture the piece parts. This work will enable to build a real mechanism.

## 6. Conclusion

The study of these robots will establish new teaching platforms in humanoid robotics, mobile robotics and mechanisms. Hands-on experience is the best way for learning. This internship enables the learning of other projects too, for example the use of a robot arm.

All work made during this internship will be very useful for future works. Learning through hands-on experience will be an advantage for future studies.

## 7. Acknowledgments

I would like to thank Dr Pierre Larochelle for accepting me for an internship in his lab in Florida Institute of Technology and all lab members for their help.

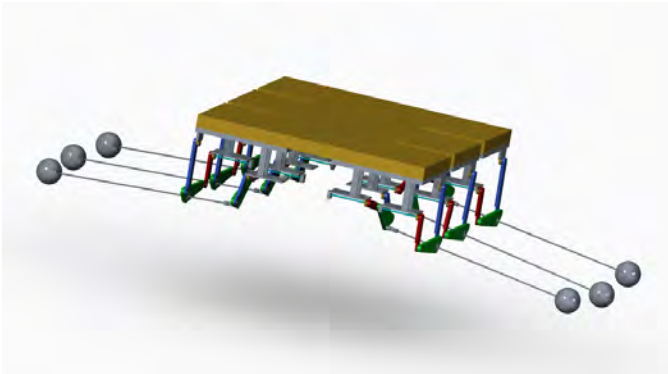


Figure 7. An example SCUD Linkage [10]

## References

- [1] Robotics & Spatial Systems Laboratory - Home. <http://research.fit.edu/rassl/index.php>. Accessed: 2017-04-20.
- [2] Penn State News: 'Hands-on learning: Internship provides real-world experience'. <http://news.psu.edu/story/280427/2013/06/28/hands-learning-internship-provides-real-world-experience>. Accessed: 2017-04-21.
- [3] Nao (robot). [https://en.wikipedia.org/wiki/Nao\\_\(robot\)](https://en.wikipedia.org/wiki/Nao_(robot)). Accessed: 2017-04-18.
- [4] SoftBank Robotics : What is the ROMEO project? <https://www.ald.softbankrobotics.com/en/cool-robots/romeo>. Accessed: 2017-04-18.
- [5] SoftBank Robotics : Find out more about NAO. <https://www.ald.softbankrobotics.com/en/cool-robots/nao/find-out-more-about-nao>. Accessed: 2017-04-18.
- [6] Computer Science, Multimedia Computing. <http://www-users.cs.umn.edu/~karen/dreu/#/house1>. Accessed: 2017-04-21.
- [7] Nao Software documentation: Script box. [http://doc.aldebaran.com/1-14/software/choregraphe/objects/script\\_box.html#choregraphe-reference-box-type-script](http://doc.aldebaran.com/1-14/software/choregraphe/objects/script_box.html#choregraphe-reference-box-type-script). Accessed: 2017-04-21.
- [8] Lok-Wah Jameson Tai, William Rae, Justin Nunn, and Pierre Larochelle. Design and implementation of building navigational tools for the pantherbot mobile robot. *2009 Florida Conference on Recent Advances in Robotics, FCRAR 2009*.
- [9] Jihang Li, Pierre Larochelle, and Shashank Bishnoi. Intelligent ground vehicle. *Proceedings of the 29th Florida Conference on Recent Advances in Robotics, FCRAR 2016, Miami, Florida, May 12-13, 2016*.
- [10] Sida Du, Ismayuzri Ishak, Jesse Nyffenegger, Jihang Li, Mark Moffett, Xiaoyang Mao, and Zachary Rubinfeld. Scud linkage. *The 2016 ASME Student Mechanism and Robot Design Competition Report*.

# Kinematic Modeling and Control Algorithm for Non-holonomic Mobile Manipulator and Testing on WMRA system.

Lei Wu, Redwan Alqasemi and Rajiv Dubey

**Abstract**—In this paper, we will explore combining the manipulation of a robotic arm and the mobility of a mobile platform, both in theory and in hardware implementation. First, the kinematic equations of the 7-DoF redundant robotic arm and the 2-DoF non-holonomic mobile platform will be introduced. Second, we will derive the Jacobian equations of the robotic arm and the mobile platform. The two Jacobian equations will be combined into one so we can accomplish the end-effector guided control without the consideration of controlling the mobile platform separately. Finally, we will implement and test these algorithms both on the simulated and physical Wheelchair-Mounted Robotic Arm (WMRA) system. Comparison and analysis of the results will be presented, and future improvements will be discussed.

**Index Terms**—Jacobians, Kinematics, Mobile manipulator, Non-holonomic system, Redundant robotic arm, Wheelchair Mounted Robotic Arm system(WMRAs).

## I. INTRODUCTION

The 9-DoF wheelchair-mounted robotic arm (WMRA) system consists of a 2-DoF non-holonomic mobile platform and a 7-DoF redundant robotic arm, see Fig. 1. Applications for this system can be used in assistant wheelchairs for disabilities, industrial mobile manipulators and warehouse storage robots. Unfortunately, most WMRA have had limited commercial success due to poor usability. It is often difficult to accomplish many of the Activities of Daily Living (ADL) tasks with the WMRA currently on the market due to their physical and control limitations and its control independence of the wheelchairs' control system.



Fig. 1. Wheelchair-mounted robotic arm system.

Seraji uses the combined Jacobian matrices to solve a simple on-line approach for motion control of holonomic mobile robots [1]. Lim and Seraji presented a real-time system which controls the 7-DoF robotic arm and 1-DoF mobile platform [2]. White evaluated the dynamic redundancy resolution in a non-holonomic wheeled mobile manipulator [3]. Chen presented an adaptive sliding mode backstepping control for the mobile manipulator with non-holonomic constraints [4].

In this paper, we are going to introduce the WMRA system which has the uniqueness in using the universal two wheel driven non-holonomic mobile platform instead of using the omni-directional mobile platform, which has a difficulty overcoming the drifting problem. The uniqueness is the integrated control algorithm of the two systems. We will present how to model the mobile platform in which the arm mounting position is offsetting both in X, Y and Z directions. The combination with the 7-DoF redundant robotic arm will be introduced.

It is desired to fulfill the need of such integrated systems to be used for many ADL tasks, such as opening a spring-loaded door autonomously and go through it, interactively exchange objects with a companion on the move, avoid obstacles by going around them while maneuvering objects, conveniently handle food and beverage between the fridge, Microwave oven, stove, etc. without the need to switch between the wheelchair controller and the robotic arm controller, and avoid singularities in a small working environment, such as an office, where wheelchair motion can be slightly utilized to maneuver objects while avoiding singularities (similar to a person sitting on an office chair and handling objects around him by moving his/her arm while slightly moving the chair to get closer to an object that is otherwise unreachable).

## II. KINEMATIC MODELING OF MOBILE MANIPULATORS

### A. Kinematics of 7-DoF Redundant Robotic Arm

The robotic arm at hand consists of seven revolute joints of which the rotation axes of every two immediate joints intersect. Fig. 2 shows a Solid Works drawing of the new robotic manipulator that was designed and built at the University of South Florida [5]. For that manipulator, frame assignment for each link is shown in Fig. 3, and the D-H parameters are highlighted.

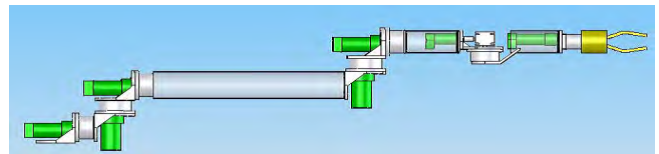


Fig. 2. Solid Works Model of the New 7-DoF Robotic Arm Built at USF.

1) *The Homogeneous Transformation Matrices:* The aim of the forward kinematics is to solve the transformation equations for the end-effector's Cartesian position and orientation or velocities when the joint angles and velocities are

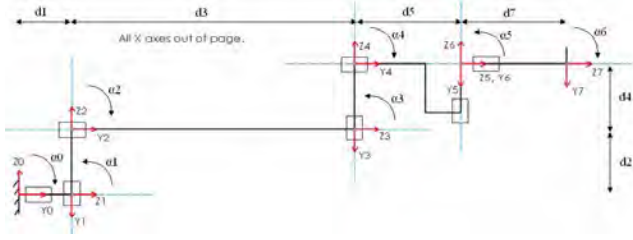


Fig. 3. Frame Assignments and Dimensions of the 7-DoF Robotic Arm.

TABLE I

THE D-H PARAMETERS OF THE 7-DOF ROBOTIC ARM.

$i$	$\alpha_{i-1}$	$a_{i-1}$	$d_i$	$\theta_i$
1	-90	0	$d_1$	$\theta_1$
2	90	0	$d_2$	$\theta_2$
3	-90	0	$d_3$	$\theta_3$
4	90	0	$d_4$	$\theta_4$
5	-90	0	$d_5$	$\theta_5$
6	90	0	$d_6$	$\theta_6$
7	-90	0	$d_7$	$\theta_7$

given. Homogeneous transformation matrices that transform the motion from one coordinate frame reference to the other can be easily obtained from the D-H parameters using the conventional equations [6] that relate every two consecutive frames to each other as follows:

$${}^{i+1}T_i = \begin{bmatrix} C\theta_i & -S\theta_i & 0 & a_{i-1} \\ S\theta_i \cdot C\alpha_{i-1} & C\theta_i \cdot C\alpha_{i-1} & -S\alpha_{i-1} & -S\alpha_{i-1} \cdot d_i \\ S\theta_i \cdot S\alpha_{i-1} & C\theta_i \cdot S\alpha_{i-1} & C\alpha_{i-1} & C\alpha_{i-1} \cdot d_i \\ 0 & 0 & 0 & 1 \end{bmatrix} \quad (1)$$

Where  $S$  is sine, and  $C$  is cosine of the angle. Propagating these matrices from one frame to the other gives us the forward kinematics of the robotic arm that describes the end-effector's frame based on the base frame as follows:

$${}^{Armbase}_{End-effector}T = {}^A_E T = {}^0_1 T \cdot {}^1_2 T \cdot {}^2_3 T \cdot {}^3_4 T \cdot {}^4_5 T \cdot {}^5_6 T \cdot {}^6_7 T \quad (2)$$

2) *The Jacobian Matrices:* We can compute the manipulator Jacobian matrix by simply doing some manipulation of Transformation matrix  ${}^A_E T$ . Detailed steps please reference Orin and Schrader's efficient computation of the Jacobian matrix for robot manipulator [7].

$$\dot{X}_E^{w.r.t.A} = J_E \cdot \dot{q}_A \quad (3)$$

Where  $J_E$  is the Jacobian matrix that relates the 7 joint angular velocities to the end-effector's Cartesian velocities based on the arm base frame. At any time step, knowing the joint velocities and joint angles allows us to translate directly to the end-effector's Cartesian velocities using the Jacobian matrix.  $\dot{X}_E^{w.r.t.A}$  is the velocities of end-effector in Cartesian space with respect to arm base frame.

### B. Kinematics of 2-DoF Mobile Platform

If the controllable DoF is less than the total DoF in the workspace, then the platform is said to be non-holonomic [8]. Examples of non-holonomic platforms are cars, power wheelchairs and other mobile platforms that can, at any

given moment, move in two dimensions out of the three planar dimensions. The wheelchair used in this work is an "Action Ranger X Storm Series" power wheelchair. This wheelchair accomplishes its non-holonomic motion using a differential drive that carries two independently-driven wheels in the back of the power wheelchair. The front of the wheelchair has two passive castors that are placed to support the wheelchair's motion. This makes the wheelchair a 2-DoF system that moves in plane [9].

Three important points of interest were assigned on and around this wheelchair, and coordinate frames were assigned on these three points. These three frames are the wheelchair's coordinate frame assigned at the center of the driving wheels' axle, the ground frame assigned at an arbitrary location on the ground floor, and another frame called frame "A" assigned at the point where the 7-DoF robotic arm will be mounted. Fig. 4 shows two-dimensional top and side views of the SolidWorks model of the wheelchair with the key dimensions and the frame assignments.

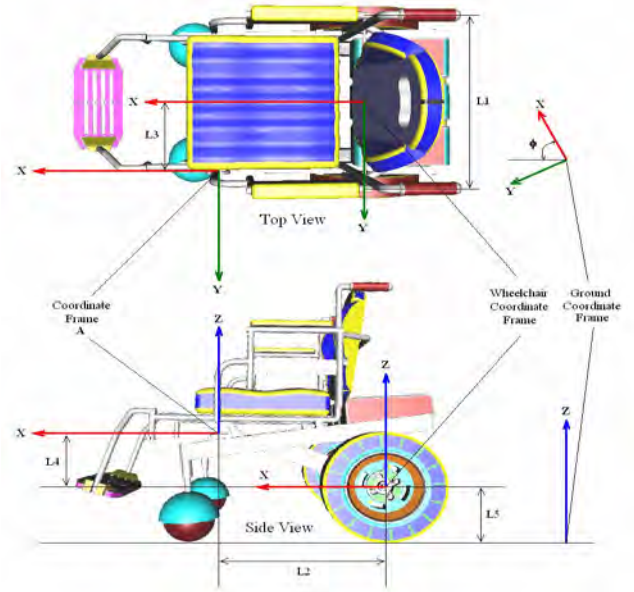


Fig. 4. Mobile platform coordinate frames and dimensions of interest.

Where  $L_1$  is the distance between the centers of the two driving wheels along the differential drive axle,  $L_2$   $L_3$   $L_4$  are the offset distances from the center of the differential drive to the center of frame "A" along the wheelchair's X-axis, Y-axis and Z-axis respectively. And the  $L_5$  is the offset distance from the center of the differential drive to the center of the ground frame along the wheelchair's Z-axis, which is the same as the wheelchair's driving wheels' radius.

1) *The Homogeneous Transformation Matrices:* To transform the wheelchair's coordinate frame during motion, we assume that the initial position and orientation of the frame is known, and we need to find the new position and orientation for the next time step. Let the initial coordinate frame of the wheelchair be " $W_0$ " and the next coordinate frame after moving one step is " $W_1$ " as shown in Fig. 5.

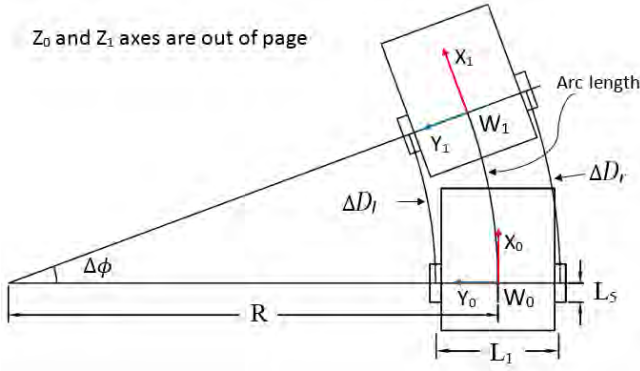


Fig. 5. Transformation of mobile platform frames.

$$\text{Arc length} = \frac{\Delta D_l + \Delta D_r}{2} \quad (4)$$

$$\Delta \phi = \frac{\Delta D_r - \Delta D_l}{L_1} \quad (5)$$

$$R = \frac{\text{Arc length}}{\Delta \phi} \quad (6)$$

Where  $\Delta D_l = L_5 \cdot d\theta_l$ ,  $\Delta D_r = L_5 \cdot d\theta_r$ .  $L_5$  is the radius of the wheel.  $d\theta_l$  and  $d\theta_r$  are the rotational changes during this time loop which can be obtained from the motor encoders. So the transformation from the known coordinate “ $W_0$ ” to the next time step “ $W_1$ ” would be:

$${}_{W_1}T_{W_0} = \begin{bmatrix} C\Delta\phi & -S\Delta\phi & 0 & R \cdot S\Delta\phi \\ S\Delta\phi & C\Delta\phi & 0 & R - R \cdot C\Delta\phi \\ 0 & 0 & 1 & 0 \\ 0 & 0 & 0 & 1 \end{bmatrix} \quad (7)$$

For the purpose of the robotic arm to be mounted on the wheelchair, one more transformation is required between the wheelchair’s coordinate frame and the robotic arm base coordinate frame where it attaches to the wheelchair.

$${}_{A}T_{W_1} = \begin{bmatrix} 1 & 0 & 0 & L_2 \\ 0 & 1 & 0 & L_3 \\ 0 & 0 & 1 & L_4 \\ 0 & 0 & 0 & 1 \end{bmatrix} \quad (8)$$

If we assume that the initial coordinate frame of the wheelchair “ $W_0$ ” was a result of previous transformation from the origin “ $G$ ” as illustrated in Fig. 4, the resulting homogeneous transformation from the ground frame “ $G$ ” to the wheelchair’s initial frame “ $W_0$ ” can be expressed as:

$${}_{W_0}T_G = \begin{bmatrix} C\phi & -S\phi & 0 & P_{0x} \\ S\phi & C\phi & 0 & P_{0y} \\ 0 & 0 & 1 & L_5 \\ 0 & 0 & 0 & 1 \end{bmatrix} \quad (9)$$

Where  $\phi$  is the resultant turning angle from all previous steps added together. The origin of  $W_0$  coordinate indicated by  $P_{0x}$  and  $P_{0y}$  are the resultant positions from all previous steps added together in global X and Y axes respectively .

Multiplying (9) (7) and (8) together results in the relation between the ground coordinate frame “ $G$ ” and the final coordinate frame of the wheelchair “ $A$ ” as follows:

$${}^G T_A = {}^G T_{W_0} \cdot {}_{W_0} T_{W_1} \cdot {}_{W_1} T_A \quad (10)$$

2) *The General Jacobian Matrices:* We can compute the mobile base Jacobian by using velocity propagation approach. For detailed steps please reference Alqasemi’s maximizing manipulation capabilities of persons with disabilities [10].

$$V_A = J_{whA} \cdot \dot{q}_{wh}, \text{ or} \quad (11)$$

$$\begin{bmatrix} \dot{x}_A \\ \dot{y}_A \\ \dot{\phi}_A \end{bmatrix} = \frac{L_5}{2} \begin{bmatrix} C\phi + \frac{2}{L_1}(L_2S\phi + L_3C\phi) & C\phi - \frac{2}{L_1}(L_2S\phi + L_3C\phi) \\ S\phi - \frac{2}{L_1}(L_2C\phi - L_3S\phi) & S\phi + \frac{2}{L_1}(L_2C\phi - L_3S\phi) \\ -\frac{2}{L_1} & \frac{2}{L_1} \end{bmatrix} \begin{bmatrix} \dot{\theta}_l \\ \dot{\theta}_r \end{bmatrix} \quad (12)$$

Where  $J_{whA}$  is the Jacobian matrix that relates the wheels’ angular velocities to the arm base or arm mounting place Cartesian velocities with respect to the global frame “ $G$ ”.

The above equation will be used with the numerical methods to produce the motion commanded by the user in Cartesian coordinates after calculating the wheels’ velocities required to realize the commanded motion. And it is a universal Jacobian matrix that can be used in any 2-DoF non-holonomic mobile system. For example, some platforms’ arm mounting place has no offset in X-axis; therefore, we just need simply let  $L_2 = 0$ .

### C. Kinematics of Integrated Mobile Manipulator

#### 1) The Homogeneous Transformation Matrices:

$${}^G T_E = {}^G T_A \cdot {}_A T_E \quad (13)$$

Matrix  ${}^G T_E$  represents the  $4 \times 4$  homogeneous transformation between the ground and the end-effector’s frame in terms of the WMRA joint space.

2) *The Jacobian Matrices:* In order to combine the motion of the arm with the motion of the wheelchair, it is important to modify the Jacobian matrix of wheelchair to include all six Cartesian velocities in space. So the (12) should be rewritten as:

$$V_A^{6D} = J_{whA}^{6D} \cdot \dot{q}_{wh}, \text{ or} \quad (14)$$

$$\begin{bmatrix} \dot{x} \\ \dot{y} \\ \dot{z} \\ \omega_x \\ \omega_y \\ \omega_z \end{bmatrix}_A = \frac{L_5}{2} \begin{bmatrix} C\phi + \frac{2}{L_1}(L_2S\phi + L_3C\phi) & C\phi - \frac{2}{L_1}(L_2S\phi + L_3C\phi) \\ S\phi - \frac{2}{L_1}(L_2C\phi - L_3S\phi) & S\phi + \frac{2}{L_1}(L_2C\phi - L_3S\phi) \\ 0 & 0 \\ 0 & 0 \\ -\frac{2}{L_1} & \frac{2}{L_1} \end{bmatrix} \begin{bmatrix} \dot{\theta}_l \\ \dot{\theta}_r \end{bmatrix} \quad (15)$$

Note that the Jacobian equation in (15) relates the wheels’ velocity vector to the Cartesian task space at the robotic arm base frame, and what we need is the equivalent relationship defined at the end-effector’s frame. This will be done to the wheelchair’s motion by introducing a new Jacobian as follows:

$$J_A^E = \begin{bmatrix} I_2 & [0] & -(P_{Ex} \cdot S\phi + P_{Ey} \cdot C\phi) \\ [0] & & P_{Ex} \cdot C\phi - P_{Ey} \cdot S\phi \\ & & I_4 \end{bmatrix} \quad (16)$$

Where  $P_{E_x}$  and  $P_{E_y}$  are the x-y coordinates of the end-effector based on the arm base frame which can be obtained from the transformation matrix  ${}^A_E T$ .

It is important to keep all the Jacobian matrices with respect to the global coordinate ‘‘G’’, so the Jacobian matrix in the (20) should be rewritten as:

$$J_E^G = {}^G_A R_{6 \times 6} \cdot J_E, \text{ or} \quad (17)$$

$$J_E^G = \begin{bmatrix} {}^G_A R & [0] \\ [0] & {}^G_A R \end{bmatrix} \cdot J_E \quad (18)$$

Where the  ${}^G_A R$  is the  $3 \times 3$  rotation matrix which can be obtained from  ${}^G_A T$ .

Now the Jacobian equations are augmented separately and ready for combination.

$$\dot{X}_E^{w.r.tG} = J_E^G \cdot \dot{q}_A + J_A^E \cdot J_{whA}^{6D} \cdot \dot{q}_{wh}, \text{ or} \quad (19)$$

$$\begin{bmatrix} \dot{X} \\ \dot{Y} \\ \dot{Z} \\ \omega_x \\ \omega_y \\ \omega_z \end{bmatrix}_E = \begin{bmatrix} J_E^G & J_A^E \cdot J_{whA}^{6D} \end{bmatrix}_{6 \times 9} \cdot \begin{bmatrix} \dot{\theta}_1 \\ \dot{\theta}_2 \\ \dot{\theta}_3 \\ \dot{\theta}_4 \\ \dot{\theta}_5 \\ \dot{\theta}_6 \\ \dot{\theta}_7 \\ \dot{\theta}_l \\ \dot{\theta}_r \end{bmatrix}_{9 \times 1}, \text{ or} \quad (20)$$

$$\dot{X}_E^{w.r.tG} = J_G^E \cdot \dot{q} \quad (21)$$

where  $J_G^E = \begin{bmatrix} J_E^G & J_A^E \cdot J_{whA}^{6D} \end{bmatrix}$ , which is the final combined Jacobian matrix that relates all the 9 joint angular velocities to the end-effector’s Cartesian velocities based on the global frame ‘‘G’’.

### III. HARDWARE IMPLEMENTATION

#### A. Hardware design

For the mobile platform, we modified a universal motor powered wheelchair. The arm mounting system was added to the left side of the wheelchair, and the controller box was added to the back side of the wheelchair. The two motors of the wheelchair were modified with two 1000 pulses/revolution incremental encoders, see Fig.6. We chose

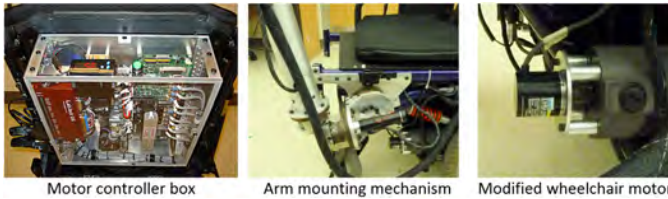


Fig. 6. Important hardware parts.

the Galil DMC-41x3 series motor controller to drive these two wheels, which allows for 4-axis 750W drives, since each motor of the wheelchair has a typical power consumption of 350W. The control board interfaces to a PC with Ethernet

10/100BASE-T which supports TCP/IP or UDP for communication. For the robotic arm, which has 7 servo motor driven joints, each motor was equipped with incremental encoder. The controller is Galil DMC-21x3 series, which allows 8-axis 500W drives in total. The controller board interfaces to a PC with Ethernet 10Base-T which supports TCP/IP or UDP for communication.

#### B. Software structure

The communication between Matlab program and the Galil controller board was designed to use Matlab socket(TCP/IP). All algorithms were programmed in the Matlab environment, where the output of the program is the velocity vector of the 9 joints which are sent to the Galil board at each loop. The input of this program is a vector of the current joint angles read from the Galil motor controller at each loop in encoder counts. Fig.7 shows a flowchart of the algorithm to help with understanding how these equations and variables are used in the actual program.

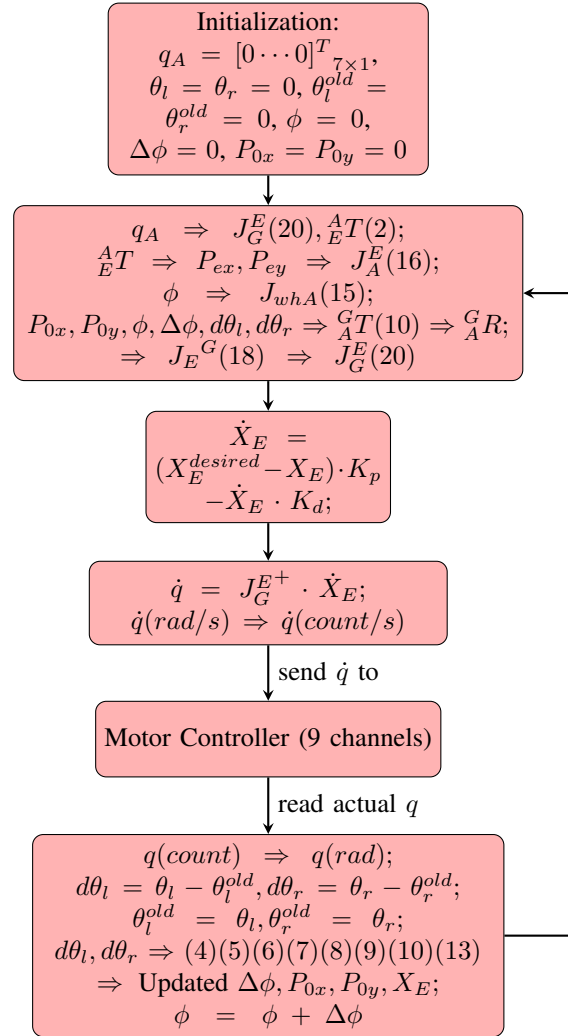


Fig. 7. Control flow diagram.

#### IV. EXPERIMENT AND RESULTS

We designed two tests to verify this algorithm. The first one is commanding the end-effector to follow a straight path at a certain speed. The second one is commanding the end-effector to follow a sinusoidal trajectory.

In the first test, the desired end-effector's trajectory was generated as a linear trajectory as follows:

$$X_E^{desired} = \begin{bmatrix} 90t \\ 0 \\ 0 \\ 0 \\ 0 \\ 0 \end{bmatrix} + X_E^{Initial}$$

where  $X_E^{Initial}$  is the initial position(in mm) and orientation(in rad) of the end-effector.

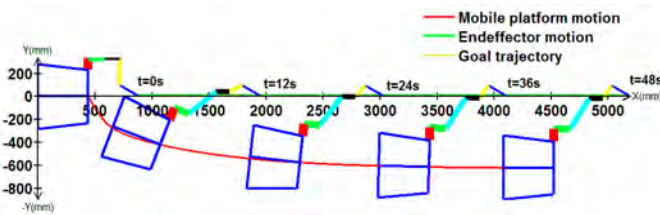


Fig. 8. Following the straight trajectory.

The end-effector's trajectory for the second test was generated as a sinusoidal trajectory as follows:

$$X_E^{desired} = \begin{bmatrix} 90 \cdot t \\ 1000 \cdot \sin(0.1 \cdot t) \\ 0 \\ 0 \\ 0 \\ 0 \end{bmatrix} + X_E^{Initial}$$

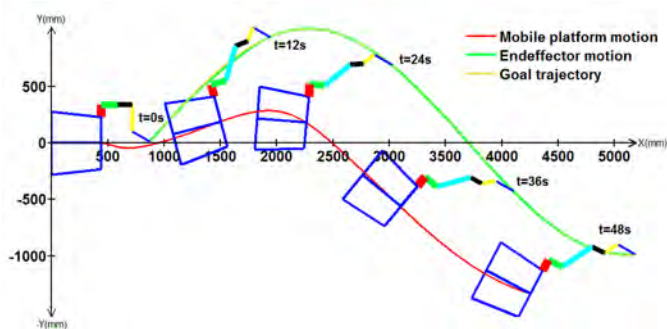


Fig. 9. Following the sinusoidal trajectory.

Fig. 8 and Fig. 9 present the real-time plotting of the operation of the mobile manipulator. The collected data from the 9 encoders based on the feedback from the controller board in real-time(around 100Hz) were used in Matlab algorithm to generate the motion of the physical hardware, as presented in Fig. 8 and Fig. 9. Then the data was sent to the forward kinematic equations to get the Cartesian positions

and orientations of each joint (for detailed steps please see Fig. 7).

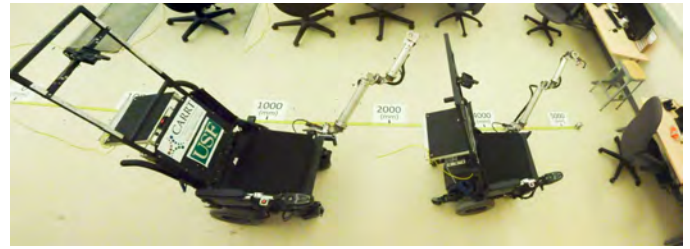


Fig. 10. Panorama picture of test 1 (Top view).

Fig. 10 shows a panoramic view of the test setup from the top view of the first test. We can see a tape measure in the image, which plays the role of the end-effector's trajectory. The landmarks(0mm, 1000mm,....,5000mm) in the picture represent the ticks of the trajectory. This setup will help with verifying that the Matlab algorithm is correctly plotting the position of the mobile robot in the real world.

#### V. CONCLUSIONS

In this paper, we presented a generalized mobile manipulator system which includes a 2-DoF non-holonomic mobile platform and a 7-DoF redundant robotic manipulator. The arm mounting position is offsetting from the center of the driving shaft in X,Y and Z axes. So, the kinematic and Jacobian equations derived here are universal form that can be applied to any situation of non-holonomic mobile platforms. We first introduced the kinematic and Jacobian equations of the manipulator and the mobile platform independently, then we adjusted the Jacobian equation of the robotic arm so that the motion of the end-effector will be relative to global frame. Finally, the two Jacobian equations were combined into one; by this way, the end-effector of the mobile manipulator can be easily navigated by the trajectory generated in the global frame. In the hardware testing, the control diagram was introduced in order to give detailed programming steps so that people can easily repeat this experiment. We verified this algorithm on the Wheelchair mounted robotic arm system(WMRAs) built at USF. From the two experiments, we can see that the mobile manipulator can be used to follow the user commanded trajectories. The kinematics modeling is valid and the control algorithm is correct. This algorithm is applicable for any end-effector based application. For example, surface processing (sanding, coating removal, or painting) of large systems such as aircraft or ships.

#### VI. FUTURE WORK

Since the mobile platform trajectory is undefined and unknown when the program is running, this may not be desirable for operating in a constrained space. Thus, we are going to introduce a safety motion band for the mobile platform in order to limit the mobile platform moving from the outside of a specific area(safety band) while keeping the end-effector following its own trajectory. The differences between

assigning a specific trajectory for the mobile platform and the safety band concept are as follows:

- Generating the trajectory for mobile platform may not be necessary, since the mobile platform usually has its own safety working range. We can free the motion of the mobile platform as long as it remains in its safety working range.
- Freeing the mobile platform motion instead of keeping specific trajectory will produce more redundancy(usually 2-DoF) for the whole system, so we can use this extra redundancy to optimize algorithms, such as maximizing manipulability of the robotic arm on the mobile manipulator or avoiding the joint limits.

#### REFERENCES

- [1] H. Seraji, "A unified approach to motion control of mobile manipulators," *The International Journal of Robotics Research*, vol. 17, no. 2, pp. 107–118, 1998.
- [2] D. Lim and H. Seraji, "Configuration control of a mobile dexterous robot: Real-time implementation and experimentation," *The International Journal of Robotics Research*, vol. 16, no. 5, pp. 601–618, 1997.
- [3] G. White, R. Bhatt, C. P. Tang, and V. Krovi, "Experimental evaluation of dynamic redundancy resolution in a nonholonomic wheeled mobile manipulator," *IEEE/ASME Transactions on*, vol. 14, pp. 349–357, June 2009.
- [4] N. Chen, F. Song, G. Li, X. Sun, and C. Ai, "An adaptive sliding mode backstepping control for the mobile manipulator with nonholonomic constraints," *Communications in Nonlinear Science and Numerical Simulation*, vol. 18, no. 10, pp. 2885 – 2899, 2013.
- [5] K. Edwards, R. Alqasemi, and R. Dubey, "Design, construction and testing of a wheelchair-mounted robotic arm," in *Robotics and Automation, 2006. ICRA 2006. Proceedings 2006 IEEE International Conference on*, pp. 3165–3170, May 2006.
- [6] J. Craig, *Introduction to robotics: mechanics and control*, vol. 3. Addison- Wesley Publishing, 2003.
- [7] D. E. Orin and W. W. Schrader, "Efficient computation of the jacobian for robot manipulators," *The International Journal of Robotics Research*, vol. 3, no. 4, pp. 66–75, 1984.
- [8] O. Krupkov and P. Voln, "Eulerlagrange and hamilton equations for non-holonomic systems in field theory," *Journal of Physics A: Mathematical and General*, vol. 38, no. 40, p. 8715, 2005.
- [9] E. Papadopoulos and J. Poulakakis, "Planning and model-based control for mobile manipulators," in *Intelligent Robots and Systems, 2000. (IROS 2000). Proceedings. 2000 IEEE/RSJ International Conference on*, vol. 3, pp. 1810–1815 vol.3, 2000.
- [10] R. M. Alqasemi, *Maximizing manipulation capabilities of persons with disabilities using a smart 9-degree-of-freedom wheelchair-mounted robotic arm system*. PhD thesis, University of South Florida, 2007.

# Laser Curve Tracing for Robotic Arms

Timothy K. Findling, Marius C. Silaghi

Florida Institute of Technology  
Computer Science  
150 W University Blvd  
Melbourne, FL 32901

tfindling2014@my.fit.edu, msilaghi@fit.edu

## ABSTRACT

Applications such like soldering require robotic arms to follow the soldering line as present on a surface. We assume here that the surface to be soldered is remote from the robotic arm, that the soldering is performed via a laser beam, and that the line to be followed can be an irregular curve that may self-intersect (e.g. a crack in the material).

We describe research conducted using a robotic arm pointing a laser for tracing a remote line on a smooth surface. The trace is converted to a one pixel width skeleton line generated from images using a hit-and miss algorithm. The robotic arm guides the laser dot along a series of target positions based on a set of processed line segments. A camera is used to validate and correct the movement of the robotic laser arm by measuring position accuracy. Considered methods are compared based on various proposed metrics quantifying the areas traversed redundantly and the areas missed.

### Keywords

Robotic Arm, laser, camera, skeletonize, templates, line segments

## 1 INTRODUCTION

Automating a welding process and maintaining a good welding quality requires the alignment of the torch along a welding seam. A robotic arm that guides the welding torch must be able to accurately follow a welding seam and compensate for tolerances in the machinery and local distortions in materials.

We address the problem of automating the control of a robotic laser arm that is tasked with soldering a crack on

a material posted at a certain distance from the arm. The robot is supposed to solder the crack using a laser beam directed at the crack. The laser has to be moved along the crack to produce a good welding. The robot detects the crack using a camera. It processes the image and directs its laser beam based on the visual parameters estimated using its camera and the estimations of the point where the beam intersects the surface.

Many complex challenges can occur in this setting, such as surface irregularities and heat based fumes that can blur vision. The surface may also suffer deformations due to heat. In this research we assume a simpler case where all these additional complications are already solved and we just have to ensure that the torch is correctly directed and following the crack. One has to minimize the number of defects consisting of the laser abandoning the line and welding already correct areas of the surface, or skipping some segments of the crack. A couple of algorithms are investigated and their efficiency is measured by comparing the areas welded without need, and the total length of skipped segments.

In the next section we describe the related work and background concerning robotic soldering and visual line processing and tracing algorithms. In Section 3 we describe the addressed problem formally. The techniques investigated in this research are introduced in Section 4. After describing data collection and precision experiments with a laser robotic arm, we conclude with an analysis of the obtained quality and potential future work.

## 2 BACKGROUND

Robotics can be classified into two categories, servo and non-servo robots. Servo robots operate in a closed loop

controlled environment and non-servo robots operate in an open loop controlled environment. Robots that operate in an open loop controlled environment have discrete check points and are rigid in their preprogrammed operations. These robots cannot adapt to changes in their environment. Robots that operate in a closed loop environment are much more flexible to changes in their environment and find their applications in computer numerical control (CNC) of milling machines, painting, assembling, bio-medical, remote controlled mobile, inspecting and welding [2, 1]. Industrial applications further expand into laser mapping, distance measuring and target tracking, as well as laser cutting.

A laser visual sensing system for welding with robotic arms was described in [3]. Difficulties in laser tracking welding seams arise from variations in the depth of the seam and deviations in the surface reflectivity. The study in [3] includes research of a Missing-Point algorithm that interpolates a path where target points are missing. Laser spot detection is further described in [4], and a comprehensive historical review of robotics applied to welding with vision based seam identification is provided in [5].

### 3 DETAIL PROBLEM DESCRIPTION

We address the problem of soldering a line on a remote surface using a laser beam. Algorithms are proposed and evaluated for achieving this task. This research evaluates a low end robotic laser arm’s execution of algorithms for soldering cracks on a surface. In evaluation experiments, the laser dot traces benchmark cases comprised of various types and shapes of skeletonized lines. Images of hand drawn lines are captured to a repository, and they are further processed to produce these templates. Templates are comprised of skeleton lines, which are further divided into line segments. Every  $n$ -th pixel on a line segment is declared a target position. The robotic arm must traverse these target positions in sequence and meet their coordinate positions within an accuracy  $\mathcal{D}$ . Moving the laser dot to each target position in sequence, effectively reproduces the skeleton line.

A camera system provides position feedback to the controlling software by capturing the current position of the laser dot. The feedback is used to create new position commands which are issued to the robot in order to minimize tracking errors. As the robot moves the laser dot towards the target positions, pixel coordinates of the laser dots are recorded and superimposed onto a trajectory record.

The tracking error is calculated by overlaying the trajectory of the laser dots onto the template. The area of the surface between the two lines is computed. A greater area expressed in pixels indicates a larger tracking error. The percentage of pixels missed along a skeleton line is also provided.

Formally we define the problem as follows:

**Definition 1** *Given a surface  $S$ , a band of maximum width  $d$  drawn on the surface, and a laser positioned in the arm of a robot located at point  $O$ , with dot of diameter  $D$ , the problem is to define a plan and a control scheme for the robot handling the laser such that the laser dot traverses the band with a minimum number of interruptions, such that the laser dot covers the whole band but covers a minimum area outside of the band.*

## 4 TECHNIQUES

The software developed for this research is comprised of three major components:

- the Arduino micro-controller embedded software (sketch),
- the image processing software, and
- the control software.

The sketch configures the Digital IO and the six Pulse Width Modulated (PWM) output signals for the servo motors. The sketch also enables communications via the USB port between the control software and the micro-controller. When the control software issues a position command, the micro-controller processes the commands and returns the current positions of the servo motors.

**Skeleton-based Jumping** The algorithm we report here for this problem is called Skeleton-based jumping. Figure 1 shows the top level diagram of the command processing. Namely, each image is loaded and a set of filters is applied on it to skeletonize the crack line that has to be soldered. The skeletonized line is then processed into a path with a start and an end position. Further, in a loop, a control algorithms focuses the laser dot within a given distance from various positions selected along the skeletonized line being followed.

Figure 3 shows in more detail the steps applying the filters to the images. It can be observed that line thinning is interleaved with smoothing. A tree is built with the obtained skeleton at the end of this processing. The root node of the tree includes the list of pixels from the starting point to the first intersection. Each subsequent

node contains the list of pixels from the parent node's intersection to the next sequential intersection or end point. A simplified example is shown in Figure 2.

## 4.1 Control Software

---

### Algorithm 1 Control Software

---

Given Laser Position  $L$  and Target Position  $T$

```

while Target Available do
  if  $L.X < T.X$  and  $|L.X - T.X| > \mathcal{D}$  then
    X Motor +=  $2us$ 
  else if  $L.X > T.X$  and  $|L.X - T.X| > \mathcal{D}$  then
    X Motor -=  $2us$ 
  end if
  if  $L.Y < T.Y$  and  $|L.Y - T.Y| > \mathcal{D}$  then
    Z Motor +=  $2us$ 
  else if  $L.Y > T.Y$  and  $|L.Y - T.Y| > \mathcal{D}$  then
    Z Motor -=  $2us$ 
  end if
  if  $|L.X - T.X| \leq \mathcal{D}$  and  $|L.Y - T.Y| \leq \mathcal{D}$  then
    Target Met
    Increment Target
  end if
end while

```

---

Any PID motion controller can be used to trace a recorded line. In our case we settled for the Algorithm 1 as an example of controller to calibrate our metric, but other controllers can be used in the future. The control software issues position commands to the micro-controller to traverse the line based on the predetermined target positions. The target positions are visited in the order as determined by the target list algorithms. Camera feedback and position information obtained from the micro-controller corrects the robotic arm to place the laser dot onto each target position within  $\mathcal{D}$  pixel accuracy. On the tested robotic arm, the relative position commands may be as small as half a degree, incrementally steering the laser dot to its target.

## 4.2 Image Processing Software

An image is captured by the camera of a curved line forming a loop. The image is first converted into a B&W image. During this conversion image noise and variations in the background are removed. A hit-and-miss algorithm [6] is looped on the pixels of the line to minimize the line thickness. The algorithm uses several 3x3 transforms shown in Figure 4, which are applied to the B&W line to reduce the line to one pixel width while maintaining a continuity of the line. This process is completed

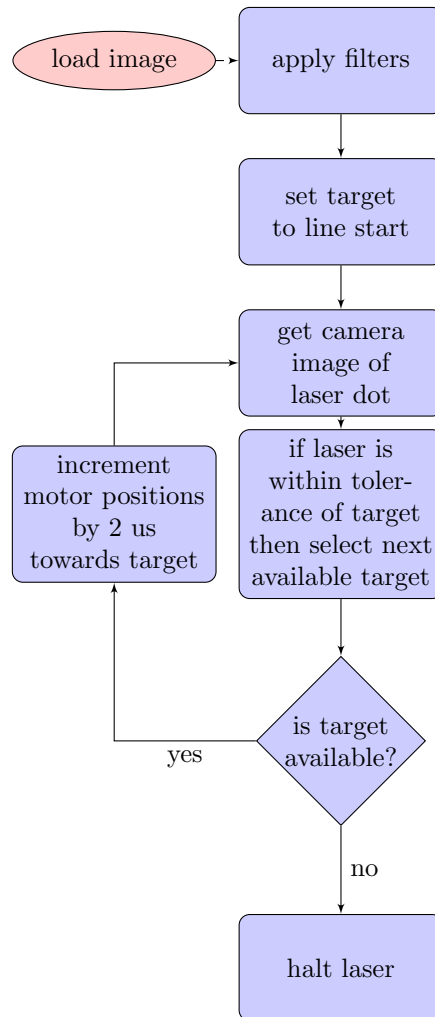


Figure 1: Control Software

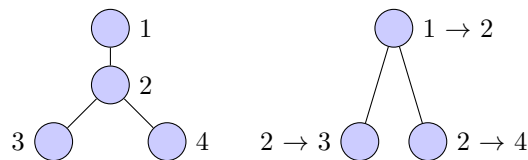


Figure 2: Example Line (Left) and Generated Tree (Right)

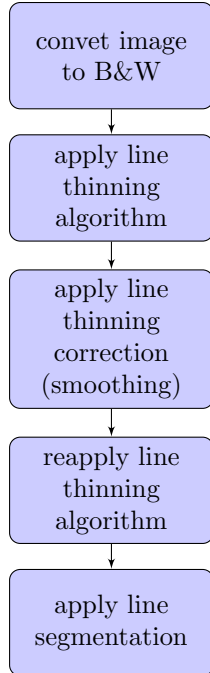


Figure 3: Filters

by looking for black pixels that match the operators and corresponding 90 degree variants of Figure 4. Each black pixel of the line is tested as the center point of the operator. The pixel is converted to white if a match is found. End points and intersections are located during the last iteration of the algorithm. An intersection is defined as a point with three or more neighbors.

A smoothing operator is applied to the skeleton line to reduce the number of neighboring intersections. This process further matches pixels to specific operator cases, where a pixel is either shifted or removed. The line thinning algorithm is called a second time after the smothering operator in order to relabel the intersections. Once a template is created, a list of line segments are determined.

Each line segment is further divided into target positions. For this research every  $n$ -th pixel is used as a target position, where  $n$  is a function of the distance between the laser and the remote surface. Every  $n$ -th pixel of the line is declared a target point that the laser dot must meet before moving on to the next target point. Feedback from the camera and the micro-controller ensures that the laser dot meets the target within  $\mathcal{D}$  pixel accuracy.

---

### Algorithm 2 Line Thinning (Hit-and-miss Transform)

---

Given structuring pairs  $B_1, \dots, B_8$  from Figure 3  
**while** Image  $X$  not converged **do**  
      $X \oplus B_1 \oplus B_2 \oplus \dots \oplus B_8$   
**end while**  
 Mark pixels with 3 or more neighbors as intersections  
 Mark pixels with 1 neighbor as end points

---

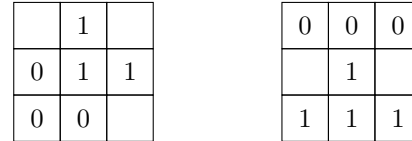


Figure 4: Structured pairs  $B_1$  and  $B_2$  including their 90°, 180°, and 270° rotations  $B_3$ - $B_8$

## 5 TARGET LIST ALGORITHMS

The following algorithms are used to develop the list of targets for the robot to follow when tracing the curve. The target list is developed after application of the filters and the curve is skeletonized.

### 5.1 Long Path Algorithm

---

#### Algorithm 3 Long Path

---

- 1: Set starting point as current pixel  $P$
- 2: Start new line segment
- 3: **while** Unvisited neighboring pixels  $> 1$  **do**
- 4: Add  $P$  to line segment
- 5: **if**  $P$  equals intersection **then**
- 6: Start New Line Segment
- 7: Count pixels to next intersection or end point in both available paths
- 8: Increment  $P$  in direction of larger count
- 9: **else**
- 10: Increment  $P$  to neighboring pixel.
- 11: **end if**
- 12: **end while**
- 13: Add end point to line segment

---

The long path algorithm builds a series of line segments for the robot to use as a target list. The algorithm is ideal for situations where the curve contains minimum intersections and where it is not desired to allow the laser to retrace a portion of the curve already visited. The algorithm begins in Line 1 and 2 by setting the starting point

of the line to  $P$  and creating a new line segment. A while loop is started in Line 3 where the loop continues while an unvisited neighboring pixel is available. The first part of the loop at Line 4 adds  $P$  to the newest created line segment. The  $P$  value is checked in Lines 5 – 7 to detect if  $P$  is an intersection. If  $P$  is an intersection then a new line segment is created. The intersection would signify that there are two available paths to select the next neighboring pixel from. The count of pixels in both paths are counted from the intersection to the next intersection or end point. The path with the largest count is selected to be taken and  $P$  is incremented in the direction of the larger count during Line 8. If  $P$  was not detected to be an intersection during Line 5 then  $P$  is incremented to the only unvisited neighboring pixel available. The loop will exit when no more neighboring pixels are available. At that time,  $P$  would be equal to the end point and would be added to the final line segment in Line 13.

## 5.2 Tree Search Algorithm

---

### Algorithm 4 DFS with Backtracking Algorithm

---

```

1: if isNull(Node.Left) and isNull(Node.Right) then
2:   Add Node.lineSegment to target list
3:   while Node.Parent.Left.Last not equals Node.Last
   or isNull(Node.Parent) do
4:     Add Node.lineSegment in reverse to target list
5:     Node equals Node.Parent
6:     if Node.Parent.Left.Last not equals Node.Last
       then
7:       Add Node.lineSegment in reverse to target list
8:     end if
9:   end while
10:  if isNull(Node.Parent) or Node.Parent.Left.Last
    equals Node.Last then
11:    return;
12:  end if
13: end if
14: if not isNull(Node.Left) then
15:   Add Node.lineSegment to target list
16:   DFS(Node.Left)
17: end if
18: if not isNull(Node.Right) then
19:   Add Node.left.lineSegment to target list in reverse
20:   DFS(Node.Right)
21: end if

```

---

The tree search algorithm is ideal for situations where every portion of the line is desired to be traced regardless of the laser retracing a portion of the line already visited.

The algorithm builds a tree of line segments and traverses the line segments based on a modified depth first search algorithm.

Line 1 of the algorithm checks if the current node does not contain a left and right branch. The pixels of the line segment are then added to the target list during Line 2. Lines 3 through 10 are implemented to reverse the trace when the trace has followed a right branch down to an end point.

Line 14 of the algorithm checks if the left branch of the current node exists. The pixels in the line segment are then added to the target list in Line 15. The tree search algorithm is then called recursively with the left branch of the current node in Line 16.

Line 18 of the algorithm checks if the right branch of the current node exists. The pixels in the line segment are then added in reverse to the target list in Line 19. This will reverse the trace when the trace follows a left branch down to an end point. The tree search algorithm is then called recursively with the right branch of the current node in Line 20.

## 5.3 Adhoc Neighbor Algorithm

---

### Algorithm 5 Ad-Hoc Neighbor

---

```

Set starting point as current pixel  $P$ 
while Unvisited neighboring pixels  $\geq 1$  or intersection
Stack  $> 0$  do
  if Unvisited neighboring pixel is available then
    if  $P$  is an intersection then
      Add  $P$  to the intersection stack
      Increment  $P$  towards pixel with the shortest
      path to next intersection or end point
    else
      Increment  $P$  to unvisited neighboring pixel.
    end if
  else if Neighboring pixel is on top of intersection
  stack then
    Increment  $P$  to intersection
    Remove  $P$  from stack and longer treat  $P$  as an
    intersection
  else
    Reverse  $P$  to previous visited pixel.
  end if
end while

```

---

The Adhoc Neighbor algorithm is similar to the tree algorithm. Every portion of the line is desired to be traced regardless of the laser retracing a portion of the line already visited. In this implementation the algorithm does

not precompute the target list but instead computes the list as the trace is occurring. The algorithm follows the trace of the line by incrementing the target to the next neighboring pixel. When an intersection is encountered the algorithm stores the location in a stack. The algorithm selects the first direction available at the intersection and continues forward until an end point is found. While the intersection array contains values, the trace will reverse towards the first value on the stack. Once the intersection is reached again, the value is removed from the stack. The trace will halt once no values are remaining on the stack.

## 6 EXPERIMENTS

For this research the robotic laser arm was positioned 32 inches away from a whiteboard as seen in Figure 5. The camera was mounted next to the robotic laser arm separately. A small repository of images was created. The images are comprised of a set of hand drawn lines which vary in complexity and size. Figure 6 displays the original line images used in the experiment. The robotic laser arm is directed by the control software to trace the skeleton line. For this research the accuracy of the trace was set to  $\mathcal{D} = 0.4$  mm (which has to be calibrated based on the camera resolution, lenses, and distance to the traced line). Feedback from the camera is recorded to file and then the position points are superimposed onto the skeleton line.

The range of position commands that can be issued to the Arduino micro-controller is between 600 – 2400 usec, which translates into 0.1 degree movement per 1 usec.

Although position commands can be giving as small as 0.1 degrees or in 1 usec increments, the servo motors cannot easily respond to such a small command. The servo motors must overcome friction and resistance of movement by the wires in order to move. In this experiment the position commands are given in 2 usec increments.

## 7 ANALYSIS

The following section is a summary of the results of the laser trace. Data was collected after each movement of the robotic arm. The data was analyzed by comparing the error between the laser trace and the skeletonized line. Additionally the percent of the line traced is also presented.

### 7.1 Error between Trace and Line

The results of the three algorithms are shown in Table 1. The error is calculated by measuring the area in pixels be-



Figure 5: Experimental Setup

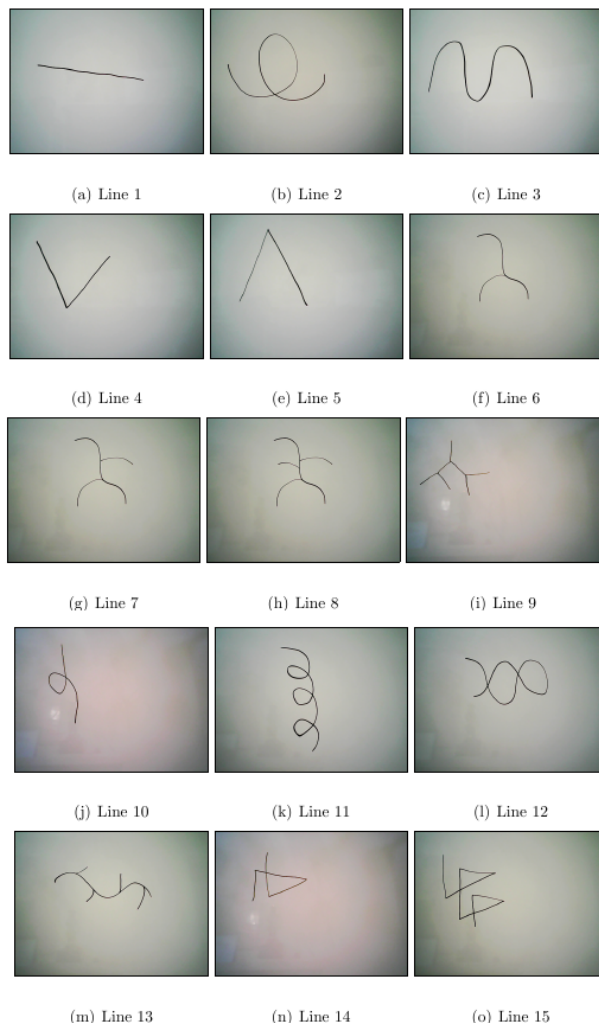


Figure 6: Original Lines

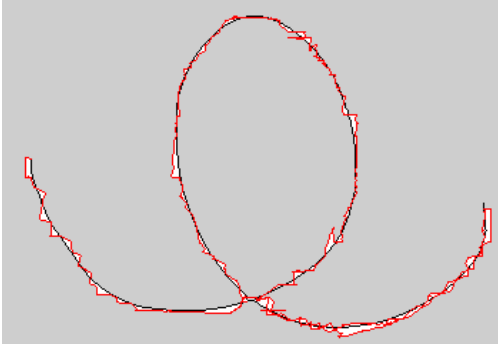


Figure 7: Laser trace of Line

Table 1: Error Between Lines - Results

Line	Pixels in Line	Longest Path	Tree Search	Ad Hoc
1	353	324	619	691
2	844	2124	2104	3141
3	807	803	1843	2634
4	394	592	1299	1643
5	491	533	1036	1487
6	427	330	1692	1405
7	533	364	2192	1809
8	601	313	2601	1973
9	419	72	1674	1674
10	439	661	959	959
11	815	1683	3134	2864
12	789	1913	2570	3178
13	548	1094	1695	2325
14	532	1138	1143	1800
15	926	801	3107	3048

tween the laser trace and the skeletonized line. A portion of the line may have not been traced due to the selected algorithm. The error in these cases are only calculated on the traced portion. A portion of the line may require the laser to retrace the section. The data points during the line retrace are included in the error calculations.

A sample image of the laser trace in Figure 7 show the traced line in red. The skeletonized line is show in black. The area outside the two lines is shown in gray and the area between the lines are shown in white. The area between the lines is calculated by counting the number of white pixels in the images.

### 7.1.1 Long Path Algorithm

The longest path algorithm selects the longest path available when detecting an intersection. The algorithm is the only method tested that does not have any backup capabilities. These properties allow the algorithm to complete its trace quicker than the other methods. With the laser in motion a smaller amount of time, the trace produces a smaller amount of errors.

### 7.1.2 Tree Search Algorithm

The tree search algorithm makes an attempt to trace the full line. The 0.5 mm diameter measurement is slightly larger than the tolerance allowed for the laser trace. It can be seen that no line contained a 100% trace under the 0.5 mm diameter laser. This could be potentially due to the laser tracing the line at the maximum tolerance away from the target position. The percentage increases to nearly 100% in all lines when the laser diameter is increased to 1.0 mm.

The tree search algorithm increases the number of retraces proportionally to the number of intersections. It could be seen in traces with a high number of intersections, such as line 15 (9 intersections), that the laser has a high trace percentage for the 0.5 mm laser.

### 7.1.3 Adhoc Neighbor Algorithm

The Adhoc Neighbor algorithm traces the line without predetermining the target list order. The trace is guided with only the knowledge of the length of the line segments. The trace always selects the shortest path available when at an intersection. The purpose of selecting the shortest path is to attempt to first cover line segments that form due to imperfections in the skeletonization process. This method significantly reduces retracing when the imperfection appears closer to the start of the line. The trace should not require retracing significant portions of the line to return to these imperfections.

## 7.2 Percentage of Line Traced

The laser in this experiment was allowed a tolerance of 4 mm from the target location. The target location is set on the edge of the original line due to the way the line thinning algorithm skeletonized the line. As a result the laser trace has not covered the entire width of the original line. The target list also did not add every pixel as a target. The target list has missed sections of the line with sudden changes in slope. Varying diameters of laser size were analyzed on each laser trace. For these experiments a laser diameter of 0.5 mm and 1.0 mm

Table 2: Long Path - Percent of Line Traced

Line	Pixels in Line	Untraced Pixels .5 mm	% Traced .5 mm	Untraced Pixels 1.0 mm	% Traced 1.0 mm
1	353	65	81.6 %	0	100.0 %
2	844	186	78.0 %	4	99.5 %
3	807	141	82.5 %	6	99.3 %
4	394	109	72.3 %	13	96.7 %
5	491	103	79.0 %	5	99.0 %
6	427	143	66.5 %	108	74.7 %
7	533	359	32.7 %	294	44.8 %
8	601	448	25.5 %	373	37.9 %
9	419	316	24.6 %	304	27.5 %
10	439	212	51.7 %	149	66.1 %
11	815	274	66.4 %	155	81.0 %
12	789	160	79.7 %	5	99.4 %
13	548	260	52.6 %	153	72.1 %
14	532	195	63.4 %	66	87.6 %
15	926	621	32.9 %	545	41.1 %

were compared. Data collected during backtracking was counted when calculating the percent of the line covered.

### 7.2.1 Long Path Algorithm

The longest path algorithm allows the trace to neglect portions of the line. The lines that contain side branches with insignificant length are shown to have the highest percentages. These traces can be seen in Lines 1 - 5. In other cases where the line contained side branches with significant length are shown to have the lowest percentages. The algorithm does not allow for backtracking and therefore the percentages do not benefit from the possibility of the laser getting a second chance to trace the line.

### 7.2.2 Tree Search Algorithm

The tree search algorithm makes an attempt to trace the full line. The 0.5 mm diameter measurement is slightly larger than the tolerance allowed for the laser trace. It can be seen that no line contained a 100% trace under the 0.5 mm diameter laser. This could be potentially due to the laser tracing the line at the maximum tolerance away from the target position. The percentage increases to nearly 100% in all lines when the laser diameter is increased to 1.0 mm.

The tree search algorithm increases the number of retraces proportionally to the number of intersections. It could be seen in traces with a high number of intersec-

Table 3: Tree Search - Percent of Line Traced

Line	Pixels in Line	Untraced Pixels .5 mm	Percent Traced .5 mm	Untraced Pixels 1.0 mm	Percent Traced 1.0 mm
1	353	63	82.2 %	4	98.9 %
2	844	185	78.1 %	1	99.9 %
3	807	148	81.7 %	1	99.9 %
4	394	40	89.9 %	1	99.8 %
5	491	63	87.2 %	1	99.8 %
6	427	72	83.1 %	1	99.8 %
7	533	101	81.1 %	3	99.4 %
8	601	52	91.4 %	0	100.0 %
9	419	50	88.1 %	5	98.8 %
10	439	55	87.5 %	1	99.8 %
11	815	70	91.4 %	0	100.0 %
12	789	126	84.0 %	0	100.0 %
13	548	54	90.2 %	3	99.5 %
14	532	146	72.6 %	6	98.9 %
15	926	77	91.7 %	0	100.0 %

tions, such as line 15 (9 intersections), that the laser has a high trace percentage for the 0.5 mm laser.

### 7.2.3 Adhoc Neighbor Algorithm

The adhoc neighbor algorithm guides the laser trace through all pixels in the line. The algorithm shows similar percentages to the tree search algorithm. The error in the trace is most likely also attributable to the time the laser is tracing at the maximum tolerance allowed. The percent similarly increases to 100% when the laser diameter is increased to 1.0 mm.

Each retraced pixel gives the laser another opportunity to cover a portion of the missed line in the first trace pass. The adhoc neighbor algorithm selects the smaller of two line segments when encountering an intersection. This reduces the amount of pixels retraced in some lines in comparison to the tree search method. This has the potential to cause the percent traced to drop in comparison to the tree search algorithm.

## 8 CONCLUSION

For this research we used a low cost robotic laser arm comprised of six servo motors which are controlled by an Arduino micro-controller. The micro-controller converts the position commands into pulse width modulated signals which provide for 0.1 degrees or 1 microsecond position commands.

Table 4: Adhoc Search - Percent of Line Traced

Line	Pixels in Line	Untraced Pixels .5 mm	% Traced .5 mm	Untraced Pixels 1.0 mm	% Traced 1.0 mm
1	353	60	83.0 %	0	100.0 %
2	844	107	87.3 %	0	100.0 %
3	807	144	82.2 %	4	99.5 %
4	394	100	74.6 %	1	99.8 %
5	491	97	80.2 %	0	100.0 %
6	427	100	76.6 %	1	99.8 %
7	533	74	86.1 %	0	100.0 %
8	601	69	88.5 %	3	99.5 %
9	419	52	87.6 %	1	99.8 %
10	439	94	78.6 %	5	98.9 %
11	815	105	87.1 %	5	99.4 %
12	789	157	80.1 %	3	99.6 %
13	548	96	82.5 %	2	99.6 %
14	532	103	80.6 %	4	99.3 %
15	926	163	82.4 %	4	99.6 %

The operational speed of the robotic arm is limited as it has to process commands serially. The steps include issuing position commands, obtaining position data from the micro-controller, and obtaining and processing images from the camera.

A repository of images was created to test the procedure. The skeletonizing algorithm followed by the line segmentation algorithm successfully provided for position commands. These benchmarks can be executed at any time producing repeatable results, and will be made publicly available. The system provides for a high degree of flexibility.

Our research shows that the robotic arm successfully traced the benchmark lines with limited error. Some of the errors were caused by “stickiness” of the low-end physical system, but may be reduced on higher-end arms. The motor would randomly fail to move the appropriate distance when a position command is issued. Subsequent position commands caught the motor back up and caused the laser to slip from the target positions. The average change in angle between the laser trace and the original trace remained similar between the different algorithms. This implies the different algorithms did not impact the change in angles but were dependent on the accuracy of the motors. This error could be significantly reduced by moving the laser and camera closer to the surface, or introducing extra-delays for feedback and correction. This would improve the accuracy of the servo motor position commands.

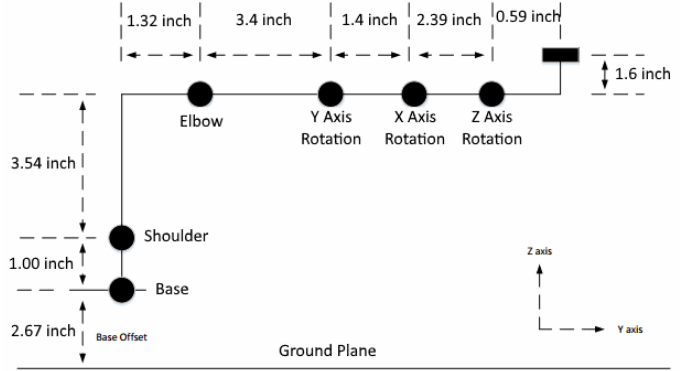


Figure 8: Block Diagram

The effect of choosing the longest path between intersections to be traced maintains the original shape of some of the lines. The trace loses accuracy when the line contains self intersections or significant branching. However, the algorithm prevents the laser from retracing portions of the line already visited.

The tree search and adhoc neighbor search both showed similar results when tracing the lines. The tree search precomputed the target list. This allows the operator to estimate the percent of the line remaining to be traced while the laser is in motion. In contrast, the adhoc neighbor search does not contain knowledge of the remaining amount of untraced pixels.

The width of the laser played a role in the percent of the lines traced. The 0.5 mm wide laser did not succeed in tracing 100% of any of the lines. The error could be reduced for the 0.5 mm laser by moving the robotic arm closer to the line or by improving the accuracy of the servo motor positions. This would allow the tolerance between the laser and target to be reduced. The 1.0 mm wide laser was able to trace 100% or near 100% of the line in the majority of the lines. The exception cases would be where the longest path algorithm ignored a portion of the line. The few pixels missed in the traces with near 100% during the 1.0 mm wide laser traces could be improved upon by increasing the number of target points. This would allow the laser to better react to changes of slope in the lines.

## DESCRIPTION OF THE ROBOTIC ARM

The robotic laser arm is controlled by positioning software running on a PC using visual feedback provided by

a single camera. The robotic arm is comprised of six servo motors controlling position and orientation of the endpoint, where a 5 mW laser (650 nm) is mounted. An Arduino micro-controller generates six pulse-width modulated (PWM) signals to position the servo motors. The servo motors can rotate 0 to 180 degrees, which corresponds to 600 - 2400 usec, respectively. The servo motors are physical centered at 90 degrees (1500 usec) at power of the robot.

The Arduino micro-controller receives position commands from the PC, which are converted to PWM signals to position the servo motors. Communication between the PC and the micro-controller is established using a universal serial bus (USB). Whenever a command is sent from the PC to the micro-controller, the micro-controller executes the command, and returns the current servo motor positions. The laser state can be set to either on or off; and can also be set to blink at some periodic rate.

The analog joysticks are used to manually position the robotic arm. While manually positioning the robotic arm, the USB port to the Arduino micro-controller must be disconnected since PC positioning commands override analog commands. This feature is highly instrumental when manually bore sighting the system. The robotic arm should be adjusted such that traveling along the X-axis and the Z-axis does not generate significant cross-talk. The Y-axis is aligned orthogonal (depth) to the target range and the servo motors should remain centered or 90 degrees +/- a small offset.

Figure 8 shows the physical dimensions of the robotic arm. Each position and orientation servo motor is set to 90 degrees (1500 usec). While maintaining orthogonality to the range, the robotic arm can travel a maximum distance of 43.254 cm along the x-axis and 23.127 cm above its horizontal plane (z-axis). Moving below the horizon-

tal plane is limited by the distance to the ground plane which is approximately 15 cm.

## REFERENCES

- [1] Yinshui He, Yanling Xu, Yuxi Chen, Huabin Chen, and Shanben Chen. Weld seam profile detection and feature point extraction for multi-pass route planning based on visual attention model. *Robotics and Computer-Integrated Manufacturing*, 37:251–261, 2016.
- [2] M.S Hussin, Daut Firdaus, and Jufriadi A. Shahril. Robotics application in arc welding a review on current progress. *Int. J. of Mechanical Computational and Manufacturing Research*, 2(1):1–5, 2013.
- [3] Hong Luo and Xiaoqi Chen. Laser visual sensing for seam tracking in robotic arc welding of titanium alloys. *The International Journal of Advanced Manufacturing Technology*, 26(9-10):1012–1017, 2005.
- [4] Štefan TOTH Matej MEŠKO. Laser spot detection. *Journal of Information, Control and Management Systems*, 11(1), 2013.
- [5] Hairol Shah, Marizan Sulaiman, Ahmad Shukor, Muhammed Jamaluddin, and Mohd Rashid. A review paper on vision based identification, detection and tracking of weld seams path in welding robot environment. *Modern Applied Science*, 10(2):1913–1952, 2016.
- [6] Milan Sonka, Vaclav Hlavac, and Roger Boyle. *Image Processing, Analysis, and Machine Vision*. Thomson-Engineering, 2007.

# Manufacturing Engineering Program Overview

Daniel J. Cox<sup>(1)</sup>

Georgia Southern University  
P.O Box 7991  
Statesboro, Georgia

dcox@georgiasouthern.edu

## ABSTRACT

A program in manufacturing engineering is being established at Georgia Southern University leading to the Bachelor of Science in Manufacturing Engineering degree. The four-year program is currently in its second year with the sophomore cohort concluding their second year. Aspects of the program are described regarding the goal of hands-on experiences in a manufacturing engineering curriculum with significant laboratory and industry-relevant experiences in the program. An overview of the curriculum is provided. The progress to date of the developments of laboratories associated with the courses in the manufacturing engineering curriculum are also discussed in this paper. Several laboratories have been resourced with new equipment acquisitions over the past two years of implementation of the program with additional future acquisitions planned. Many experiments and laboratory exercises in practical aspects of manufacturing can make use of common sets of state-of-the-art, industrial-grade, manufacturing equipment. The equipment includes traditional machine tools, CNC machine tools, other subtractive materials processing equipment, additive manufacturing machines, material handling, robotics and automation, and additional physical equipment. These hardware resources must also be compatible and integrated with software and computing resources including computer-aided design tools, programmable logic controllers, automation software, manufacturing execution systems software, and additional software resources as the courses of the manufacturing engineering curriculum come on-line.

## Keywords

Manufacturing Engineering, Robotics and Automation.

## 1. INTRODUCTION

A newly formed undergraduate manufacturing engineering program requires significant resources to train the modern manufacturing engineer. A new program, in its second year, leverages over forty years of manufacturing and industrial technology programs with the requirements and demands of an engineering program and an increasingly sophisticated manufacturing environment. The four pillars [1] of manufacturing knowledge: materials and manufacturing processes; product tooling and assembly engineering; manufacturing systems and operations; and manufacturing competitiveness provides a framework of educating the next generation manufacturing engineers. Manufacturing engineering at the undergraduate level is

often a track or concentration being shared with either mechanical or industrial engineering. In this new program, currently in the second year of existence, the emphasis and degree is solely focused on manufacturing engineering.

Purposes for the new manufacturing engineering program, now with sophomores, are primarily for workforce development, but also include economic development, attracting industry to the region, job creation, and solve industry challenges through applied research and development. The aim is to prepare the manufacturing engineering workforce to be more prepared to hit the ground running, with less supplementary training required of the employers in the faced-paced manufacturing environment.

Like the other engineering programs at the institution, there is a strong emphasis on co-op opportunities and working with industry. This includes hands-on projects with industry driven requirements, and applied research and development opportunities at both the undergraduate and graduate levels. The focus of this paper though, is on the development of the hands-on laboratories of the manufacturing engineering program. Resources for undergraduate research projects are readily available through the realization of the hands-on laboratories for manufacturing engineering. Thus the well-known benefits of student experiential learning that enable students to interact with professionals, gain professional contacts, and gain confidence and experience are realized.

## 2. CURRICULUM

The strategy with the curriculum is to integrate the hands-on Manufacturing Engineering (MfgE) courses from the onset through the senior year [2]. The degree program results in the bachelor's degree in manufacturing engineering. The program has just completed its second year. There are an abundance on hands-on laboratory experiences creating authentic learning of industry practices. Much of the core engineering requirements are accomplished in the first two years while, as the students' progress through their program of study, they increasingly engage in the MfgE courses and hands-on laboratories. Three thrust areas of the program are supported by authentic industrial grade laboratories. The three thrust areas are: Materials and Processes, Plant Floor Operations, and Advanced Manufacturing.

Materials and Processes

- Traditional Machining and Materials Science
- CNC Machining and Processes
- Additive Manufacturing

#### Plant Floor Operations

- Statistical Process Control
- Lean Manufacturing
- PLCs, Sensors, and Actuators

#### Advanced Manufacturing

- Robotics and Automation
- Automated Inspection Systems
- Manufacturing Execution Systems

The general distribution of the curriculum is outlined below (credits).

#### Basic (61)

- Math (11): Calculus 1&2, Statistics
- Science (12): Physics 1&2, Chemistry
- English (6): Composition 1&2
- General Education (29)
- Economics (3)

#### General Engineering, Lower Division (10)

- ENGR 1133 Engineering Graphics
- MENG 1310 Manufacturing Process Lab
- MENG 2139 Numerical Methods
- ENGR 2131 Circuits

#### Manufacturing Engineering, Lower Div. (18)

- MFGE 2531 Material Science for Manufacturing
- MFGE 2142 Fundamentals Engineering Mechanics
- MFGE 2533 Manufacturing Process 2
- MFGE 2534 Applied Computing in Manufacturing
- MFGE 2239 Mfg Engineering Modeling & Analysis
- MFGE 2421 Intro to Additive Manufacturing

#### Manufacturing Engineering, Upper Div. (31)

- MFGE 3131 Design for Manufacturing
- MFGE 3541 Energy Science
- MFGE 3421 Industrial Controls
- MFGE 3531 Advanced Material Processing
- MFGE 3132 Quality and SPC
- MFGE 3337 Hydraulics and Electromechanical Sys
- MFGE 3423 Facilities Design
- MFGE 4533 Robotics & Automation
- MFGE 4135 Lean Manufacturing
- MFGE 4614 Professional Leadership
- MFGE 4321/22 Senior Capstone 1&2

#### Manufacturing Engineering, Elective Areas (9)

- SAP
- Lean Manufacturing
- Robotics & Automation
- Materials Processing
- Occupational Health and Safety

### 3. Laboratories

A hands-on approach to instruction using state-of-the-art manufacturing equipment is accomplished with physical resources that can be used in a variety of laboratory sections that are used in courses in manufacturing engineering. Many experiments and laboratory exercises in practical aspects of manufacturing can make use of common sets of state-of-the-art, industrial grade manufacturing equipment. The laboratories described below are currently housed in a newly renovated building. The equipment of the laboratories includes traditional machine tools, Computer Numerical Control (CNC) machine tools, other subtractive materials processing equipment, additive manufacturing, material

handling, robotics and automation, and additional physical equipment. These hardware resources must also be compatible and integrated with software and computing resources including computer-aided design tools, PLCs (Programmable Logic Controllers), automation software, MES (Manufacturing Execution Systems) software, and additional software resources.

The development of the laboratories described below has been driven by the design of the curriculum, observation of other manufacturing-related programs, and the existing resources held-over from the former technology program. The new manufacturing engineering program has three thrust areas. The first is materials and processes which includes traditional machining, materials science, CNC machining and processes, and additive manufacturing. The second thrust area is plant floor operations and includes statistical process control, lean manufacturing, PLCs, sensors, and actuators. An additional advanced manufacturing thrust includes robotics and automation, automated inspection systems, and MES. These three thrust areas are correlated to the four pillars of manufacturing knowledge in the following sections.

Most of the laboratories described below support the manufacturing engineering specific curriculum and courses that begin in the freshman year and continue throughout the curriculum. Laboratory and experiment resources must also consist of replicate stations to provide adequate hands-on access for all students in a new and growing manufacturing engineering program. The program is currently in the second year with freshman and sophomore manufacturing engineering student majors. Replications of the various types of physical manufacturing systems contribute to increased student throughput while also keeping the hands-on student group sizes to a minimum, with the goal of a maximum of three to four students per laboratory exercise when hardware resources are used.

Manufacturing in plants and factories has seen dramatic changes over most recent decades compared to the traditional view of manufacturing as a dirty, monotonous, work environment of decades past. Although much of the public perception of manufacturing remains in past misconception, an increased awareness of manufacturing as a profession is driven by a rapid increase and greater awareness of advances in modern manufacturing. A new generation of manufacturing engineers need to be well-trained in areas of computer-based design tools, software and machine programming, CNC machinery, additive manufacturing, plant floor software, automation equipment, and robotics. The laboratories in this section are in various stages of development and will be continuously updated and improved as the new manufacturing engineering program advances and matures.

#### 3.1 Advanced Manufacturing: CNC and Material Processing

The choice of using a single vendor for machine tools is made to keep the maintenance and operational costs of the systems lower than otherwise if multiple vendors are used. By in-large this strategy is used in many other cases regarding equipment selections. It is also important for students to be exposed to, and trained in machinery typical of the industrial environment. Figure 1 partially shows the Advanced Manufacturing Laboratory (AML) - CNC Machining and Materials Processing Laboratory. This laboratory is fairly well developed thus far. Shown in Figure 1 are two CNC mini-milling machines, two CNC lathes, and a 5-axis milling machine. Not shown are industrial grade waterjet, plasma cutter, surface grinder, and band saws. Upcoming acquisitions for

this laboratory include Electrical Discharge Machining (EDM) machines and other materials processing equipment. This laboratory is primarily used by students taking courses in manufacturing processes, computing in manufacturing, quality and SPC, and capstone design. This laboratory supports training in all of the four pillars of manufacturing knowledge: materials and manufacturing processes; product tooling and assembly engineering; manufacturing systems and operations; and manufacturing competitiveness.



**Figure 1. CNC Machining and Materials Processing Laboratory**

The students are trained in engineering graphics and 3D modeling before an applied computing in manufacturing engineering course. The applied computing in manufacturing engineering course trains the students in fundamentals of CNC programming focusing on G and M code programming. An advanced CNC programming course further develops the students' skills in this area. The students are required to learn the programming language of machine tools before using any automatic program generation software tools later in the curriculum. An associated laboratory consisting of multiple small CNC benchtop tools (see Figure 2) is used to train the students in machine programming well in advance of using the industrial grade machine tools shown in Figure 1. The laboratory shown in Figure 2 provides a relatively safe environment for beginning level CNC programming with the benchtop machines running the same software but requiring much less power to produce small, non-ferrous components. This approach is safe both for the students and the more powerful industrial grade equipment shown in Figure 1. The laboratory shown in Figure 2 is primarily used by sophomore students taking introductory computing in manufacturing.



**Figure 2. Machine tool programming laboratory benchtop machine tools**

Also existing in the machine tool programming laboratory are machine tool simulators. Thus the students learn the requisite programming skills on small, much relatively safe hardware and industrial simulators before any exposure to the much more powerful industry-grade machine tools. Note that all three types of machine tool systems run the same software. The industrial grade machine tools shown in Figure 1 are also used to support senior capstone and undergraduate research.

### **3.2 Advanced Manufacturing: Additive Manufacturing**

Although additive manufacturing has been in existence for many years, it is showing strong gains in use due to advancement in new materials and continuously improving price/performance of the new generation of machines. The ability to rapid prototype as a design tool, the capability to engineer new materials, and quantification certainty in base material content are some of the many reasons why the modern manufacturing engineer must be well versed in this technology that will continue to gain wide acceptance. Courses in introduction to additive manufacturing and advanced additive manufacturing studio directly make use of the AML - Additive Manufacturing Laboratory shown in Figure 3. Senior capstone and undergraduate research will also be supported by this laboratory. This laboratory is fairly well developed thus far. The laboratory consists of a variety of primarily polymer 3D printers at this stage. The polymer printers include four low-cost 3D printers, seven modern industrial grade additive manufacturing machines, and a high fidelity state-of the art industrial grade additive manufacturing machine. Also included are wax and resin printers and a 3D scanner. A metal 3D additive manufacturing machine is under procurement as are additional types of 3D printers and scanners. In addition to the additive manufacturing courses, this laboratory is used for courses in quality and SPC as well as capstone design. This laboratory supports three of the four pillars of manufacturing knowledge: materials and manufacturing

processes, manufacturing systems, and manufacturing competitiveness.



**Figure 3. AML – Additive Manufacturing Laboratory**

### **3.3 Advanced Manufacturing: Robotics and Automation**

A Flexible Manufacturing System (FMS) consists of both hardware and software aspects of the material handling system and six robotics and automation stations of the initial installation. The system is capable of production-like scenarios to highlight hands-on learning experience for the students. The six robotized stations are a machining station, a laser engraving station, a machine vision inspection station, a coordinate measurement station, and two robotic assembly stations, one is a single-arm robot, another featuring a dual-arm robot. Four of the six stations described consist of dockable robot carts that can be separated from the FMS for rapid changeover and standalone use in a laboratory instruction. Quick-connect fixtures allow the robots to then be redeployed back into the FMS. Two more stations are intended for the near-term expansion of the FMS. However, the material handling system and software allow for reconfiguration and expansion for more stations. This will be especially useful when the advanced manufacturing laboratories including the FMS move to new spaces.

The FMS is designed to be used across a variety of courses in the manufacturing engineering curriculum to provide hands-on, industry-relevant training for the students. The system is intended to support hands-on experiential learning in courses including industrial robotics and automation; automation and CIM; PLCs, industrial controls and networking; design for manufacturability, assembly, and sustainability; quality and SPC; applied computing in manufacturing engineering; pneumatic, hydraulic and electro-mechanical systems; plant floor software and MES; systems safety in manufacturing; and senior capstone design. Additional graduate-level and undergraduate technical electives are likely to materialize as the program grows.

The students in the program are currently completing the second year of the four-year degree in manufacturing engineering. The FMS installation is positioned for upcoming junior and senior courses. The RFP was posted in 1Q17 with the award committed in

2Q17. The project is scheduled for completion in 3Q17 and fully functional in the 4Q17.

### **3.4 Other Laboratories**

Manufacturing engineers need an understanding of engineering fundamentals. Calculus, calculus-based physics, and chemistry as in most engineering programs form the basis for courses in fundamentals of engineering mechanics that include statics, dynamics, and strength of materials. Other laboratories in the thermo-fluid and energy sciences exist in the mechanical engineering program to support the manufacturing engineering program and are listed:

- Engineering Mechanics
- Traditional Materials Processing
- PLCs, Industrial Controls, and Networking
- Hydraulics, Pneumatics, and Electromechanical Systems

## **4. SUMMARY**

A summary of the curriculum in a new manufacturing engineering program has been presented. The program is currently in its second year with rising juniors. The inaugural class is scheduled to graduate in spring semester 2019. Laboratory equipment was also discussed. The most recent enhancements to the traditional mechanical technology program that has been enhanced to manufacturing engineering program are CNC lathes, CNC mini-mills a five-axis CNC mill, a waterjet cutter, a TIG welder, a surface grinder, a band saw, and sanding table for the CNC Machining and Material Processing Laboratory. EDM machines are also in the process of acquisition for this laboratory. A high-end polymer additive manufacturing machine, midrange additive manufacturing machines, and wax printer have been acquired to expand the Additive Manufacturing Laboratory. An additional polyjet additive manufacturing machine and metal additive manufacturing machine are under acquisition for this laboratory. A coordinate measuring machine and universal testers add to other laboratories and use in the program. Procurement of an industry-grade Flexible Manufacturing System (FMS) consisting of a material handling system, industrial robots, a Manufacturing Execution System (MES), integrated with processing and inspection tools at stations within the system for the Robotics and Automation Laboratory is underway. These resources provide hands-on, authentic, industrial grade experiences for the manufacturing engineering students.

## **ACKNOWLEDGMENTS**

The author would like to acknowledge the support and commitment of Georgia Southern University to the Manufacturing Engineering Program. The author also gratefully acknowledges colleagues, faculty, and staff of Georgia Southern University.

## **REFERENCES**

- [1] [www.sme.org/fourpillars/](http://www.sme.org/fourpillars/)
- [2] [ceit.georgiasouthern.edu/manufacturing-engineering/](http://ceit.georgiasouthern.edu/manufacturing-engineering/)

# On the Measurement of the Coefficient of Friction of Walking Surfaces

Oren Masory

Department of Ocean and Mechanical Engineering  
Florida Atlantic University  
Boca Raton, FL 33431

masoryo@fau.edu

## ABSTRACT

Tribometers, or slip meters, are devices used to measure the Coefficient of Friction (COF) between a walking surfaces and a standard material (Neolite). These measurements are being used to determine whether or not the tested surface is slip resistance that presents minimum risk for users. All tribometers have a “foot” (pad), made of standard material, which make the contact with the examined surface. Commercial tribometers are different from each other in many ways: different size and shape feet, different contact pressure between the foot and the surface and groove or non-grooved feet. The purpose of this study is to determine whether or not these differences affecting the reading of the Coefficient of Friction.

## I. INTRODUCTION

The need for accurate and repeatable measurement of walking surfaces' COF is rooted in the large expenses associated with Slip and Fall accidents. These accidents are the leading cause of workers' compensation and claims and medical costs associated with them is approximately \$70 billion annually [1]. A report by The Bureau of Labor Statistics [2] states “Together, falls, slips, or trips accounted for 35 percent of the injuries and illnesses to heavy and tractor-trailer truck drivers in 2014.” In [3] it is reported “falls on the same level is the second highest category of compensable loss and cost \$6.7 billion, according to the 2006 Liberty Mutual Workplace Safety Index. There are numerous reports on the subject but one that demonstrate the severity of this problem is given in a report of a study performed by the National Floor Safety Institute (NFSI) that found that more than 3 million food service employees and over 1 million guests are injured annually as a result of restaurant Slips and Falls accidents. These injuries are increasing at a rate of about 10% annually [4]

The importance of COF measurements is reflected by the numerous of standards, safety codes, technical reports, brochures and technical papers published in the last 50 years. Topics such as: measurement methods and devices, performance of different

tribometers, measurement of COF of different materials, shoe's sole design, the effect of contamination on COF, floor treatment, Slip and Fall biomechanics and others were covered in many publications. Some references will be given in the following as related to the discussed topic.

The slipperiness of a surface depends on many factors including: material, presence of moisture or contaminants, slope and cross slope, surface texture, wear, surface finish and the all affecting the Coefficient of Friction (COF) between the sliding surfaces. Therefore, the measurement of COF, which is the dominant factor effecting slipperiness, is commonly used to qualify a walking surface as a safe one.

The COF is defined by the ratio of the shear force that acts tangent to the contact surfaces and the normal force between the two bodies. Thus, in order to find out the value of the COF both forces have to be measured while the bodies are impending motion for the Static COF or in motion for Dynamic COF. In cases of Slip and Fall accidents the static COF is of interest since it represents the maximum available friction. Once slip occurs, the value of the COF assumes its dynamic value which is lower than the static one. Thus, the static COF represents a threshold between slipping and non-slipping conditions.

In order to determine the value of the COF, both the shear and the normal forces have to be measured. A simple test, called “pull test”, by which the coefficient of friction force (COF), on any surface, can measured, shown in Figure 1. A foot, made of the material being tested is attached to block of weight  $W$ . The block is placed on a horizontal surface being tested, and a pulling force,  $F$ , is applied to the block. The pulling force increased to the point that block starts to move (impending motion). At that point the friction force assumes its maximum value and the Static COF is given by the ratio the maximum pulling force and the normal, which in this simple case equals to the weight  $W$ . Once the weight is in motion the value of the pulling force drops and this value can be used to determine the dynamic coefficient of friction (DCOF). Thus, the static COF is given by:

$$\mu_s = \frac{F_{max}}{N} \quad (1)$$

This relationship, was established by C. A. Coulomb in 1781 who extensively study dry friction occurring between the contacting surfaces in the absence of a lubricating fluid. This principle is used, directly or indirectly by all tribometers.

When it comes down to the actual contact between the surfaces, commercial tribometers differ one from the other by the size and shape of the foot being use as well as the normal force applied during the test. A partial list of commercial tribometers is given in Table 1 [5, 6].

**Table 1: Details on some commercial tribometers.**

Device	Foot Shape	Foot contact area[mm <sup>2</sup> ]	Load [N]	Pressure [kPa]
50# Hand pull ASTM C-1028	76mm Square	5776	222.4	38.5
BOT-3000	9mm diameter circle	63.617	N/A	-
English XL	33mm diameter circle	855.2	N/A	-
Brungraber Mark II	76 mm Square	5776	44.482	7.701
Brungraber Mark IIB	76 cm Square (grooved)	4645	44.482	9.576
Sigler pendulum	38mcm square	1444	N/A	-
HPS	N/A	380	2.7	71
PAST	N/A	5800	9	9
PFT	N/A	280	112	400
AFPV	N/A	1600	360	225
Tortus	N/A	60	02	30
PSC 2000	N/A	250	24	100
GMG 100	N/A	1170	93	80
Shuster	N/A	2600	40	15
BPST	N/A	220	22	100
VIT	N/A	790	37	47
PSM	N/A	500	200	400

Eq. 1 and the details in Table 1, raises few questions:

- 1) Is there a need for a minimum contact force, or pressure, in order to insure a “good” contact between the surfaces so that the mrasurements will yield reliable value for the COF?
- 2) Is there a minimum contact area between the surfaces which will insure a correct reading of the COF?
- 3) Is the shape of the contact area affecting the value of the COF?

- 4) Is a pattern engraved on the foot, such as the grooves in shoe’s sole, affecting the measured value of the COF?

A limited set of experiments were conducted in attempt to answer the above questions. Although ASTM C-108 standard was withdrawn, it was used in performing these experiments since the reason for the withdrawal is not due to technical deficiencies but “**This standard is being withdrawn without replacement due to its limited use by industry**”. All measurement was taken using TCNA standard tile that was tested in an official ASTM interlaboratory Study.

## II. THE EFFECT OF GROOVED FOOT ON THE VALUE OF THE COF

All research related to the effect of patterns engraved into the foot material, such grooves, are related to tracking capabilities of shoe’s sole. In [7, 8] tests were performed with pads that had grooves in 0°, 45° and 90° to the direction of the test.

It was concluded that “For groove directions, the difference between 0° and 45° was not statistically significant. The COF values of these two conditions were, however, significantly higher than that of the 90° condition”. In [9, 10] the effect of grooves perpendicular to test direction, on the COF where the surface is contaminated. It was concluded that “Tread groove depth is a significant factor affecting the COF at the footwear–floor interface on wet and water–detergent-contaminated floors tested in this study. It was found that the averaged COF gain per tread groove depth increase in millimeters, on either a wet or water–detergent covered floor, ranged from 0.018 to 0.108, depending on the tread groove width, floor, and contaminant”.

From COF measurements point of view the concern is that the use of patterned foot will bias the results. Currently there is one commercial tribometer which uses grooved foot [6]. In [11] two tribometers, Brungraber Mark II and Mark III, were compared. Four different pads were used: 3 flat pad (3” by 3”) made of PVC, Neolite and Nitrile, and one grooved pad (15 evenly spaced grooves, 1 mm width and 3 mm deep, perpendicular to the test direction) made of Neolite. ”A comparison between the flat and grooved Neolite footwear pads shows that the grooved pad had significantly (p<0.05) higher COF readings on the wet surface conditions than those of the flat one on all floors”. Also, “On glycerol-contaminated condition, grooved Neolite footwear pad had also significantly (p<0.05) higher COF reading than that of the flat Neolite pad. But this difference occurred mainly on the quarry tile.”

A series of pull tests according to ASTM C-1028 using TCNA standard tile in dry conditions were performed to further determine the effect of grooved pad on the COF. Three tests were performed using Neolite pads: 1) 3” by 3” square pad with no grooves; 2) 3” by 3” square pad with 6 1/16” wide and 1/16” deep grooves parallel to the pull direction and; 3) 3” by 3” square pad with 6 1/16” wide and 1/16” deep grooves perpendicular to the

pull direction. Each test consisted of 40 pulls 10 in each direction along the axes of the tile. The results of these tests are given in Table 2.

**Table 2: Tests’ results.**

	No Grooves	Parallel Grooves	Perpendicular Grooves
Mean	0.382	0.522	0.570
Variance	0.001826	0.002568	0.003208

The results shown in Table 1 clearly show that the grooved pads affecting the COF reading resulting substantially higher value than in the flat pad case. Also, t-Test verified that there statistically difference between the effects of the parallel and the perpendicular grooves on the COF ( $t_{stat}=4.05$ ,  $t_{critical}=1.99$  and  $P=0.00012$ ).

In another set of tests the COF of 8 different tiles was measured in the same way using a flat and a grooved (parallel to the pull direction) Neolite pads. Each test consisted on 10 pulls along a single direction of the tile. The results are shown in Table 3.

**Table 3: Tests’ results for 8 different tiles.**

Tile	Pad	Mean	Variance
Porcelain (Polished)	Flat	0.548	0.000208
	Grooved	0.818	0.004483
Porcelain (Rough)	Flat	0.654	0.000361
	Grooved	0.813	0.000978
Ceramics - I	Flat	0.447	0.000362
	Grooved	0.628	0.000272
Vinyl	Flat	0.725	0.000245
	Grooved	0.994	0.002110
Granite	Flat	0.615	0.001703
	Grooved	0.914	0.007382
Ceramics (Textured)	Flat	0.461	0.000072
	Grooved	0.893	0.000426
Ceramics - II	Flat	0.405	0.000072
	Grooved	0.607	0.000109
TCNA tile	Flat	0.382	0.001826
	Grooved	0.522	0.002568

The same results are shown in Figure 2 which indicates that the COF’s values obtained using the grooved pad are higher, in all cases, compared with the corresponding results obtained with the flat pad.

### III. THE EFFECT OF FOOT CONTACT AREA ON THE VALUE OF THE COF

A series of pull tests in which two square Neolite pads of  $3in^2$  and  $9in^2$  were performed on TCNA standard tile according to ASTM C-1028. 10 pulls were performed in dry conditions along the same direction with each pad. The contact pressure on the pads was approximately 28[kPa] with deviation of 0.909[kPa] (0.1[psi]). The tests’ and the statistical analysis results are given in Table 4. As shown, the results of the t-Test indicate that within 95% confidence level there is no difference between the COFs. Meaning that the contact area does not affect the value of the COF.

**Table 4: Tests’ results for different contact areas.**

	Contact area [in <sup>2</sup> ]	
	9	3
Contact Pressure [kPa]	28.828	27.918
Mean	0.386	0.387
Variance	0.000106	0.000186
F	0.568	
F <sub>Critical</sub>	0.314	
T	0.123	
T <sub>Critical</sub>	2.100	

In a different experiment two circular Neolite pads were used. This time the contact pressure varied and the coefficient of friction was determined in two ways: 1) The mean of the COF for each pressure (see Table 5); and 2) By linear regression as shown in Figure 3.

**Table 5: Tests’ results with circular pads**

D=1.833[in]			D=1.401[in]		
Normal [lb]	Pull [lb]	COF	Normal [lb]	Pull [lb]	COF
2.538	2.100	0.462	3.400	1.700	0.500
5.006	3.400	0.485	5.869	2.600	0.443
6.506	4.200	0.493	7.369	3.500	0.475
8.975	4.700	0.428	9.838	4.700	0.478
11.981	5.600	0.467	12.838	5.300	0.413
<b>Mean</b>		0.467			0.461
<b>Variance</b>		0.00064			0.001159

**Table 6: Tests' results with circular pads**

Diameter [in]	1.833	1.405
Contact area[sqin]	2.638	1.55
COF	0.467	0.462
Variance	0.00064	0.001159
F	0.552	
F <sub>Critical</sub>	0.156	
T	0.286	
T <sub>Critical</sub>	2.364	
COF (linear regression)	0.4622	0.4452

**IV. THE EFFECT OF LOAD (CONTACT PRESSURE) ON THE VALUE OF THE COF**

As shown in Table 1, the difference in contact pressure vary by two order of magnitude, from 7.7 kPa to 400kPa. The simple Coulomb friction law, expressed in Eq. 1, does not specify the necessary contact pressure to insure a reliable estimation of the COF.

A set of experiments, using a 3 inch square Neolite pad and the same TCNA tile, with different pressures was performed. Each experiment consisted on 20 pulls, 10 in one direction and 10 in the opposite direction. The results are summarized in Table 7.

**Table 7: COF for different pressures.**

	P <sub>1</sub>	P <sub>2</sub>	P <sub>3</sub>	P <sub>4</sub>	P <sub>5</sub>
Pressure [kPa]	7.292	16.413	27.918	46.678	59.864
COF	0.337	0.349	0.383	0.373	0.382
Variance	0.000298	0.000209	0.000225	0.000522	0.000862

A single factor ANOVA test that covers the data obtained in all 5 experiments indicated that the mean value of the COF of these experiments are not the same (F=19.928 and F<sub>Critical</sub>=2.467). Meaning that the contact pressure between the surfaces does effect the value of the COF. The results are also shown in Figure 4.

A single factor ANOVA test that covers the data for the three highest contact pressures (encircled in Figure 4, indicated that their mean values of the COF are the same, meaning that the data for these three cases belong to the same population (F=1.092 and F<sub>Critical</sub>=3.158). It is obvious from Figure 4 that the COF value corresponds to the lowest contact pressure does not belong to the population. A single factor ANOVA test that covers the data for the three highest contact pressures and the lowest one eventually proved it (F=19.148 and F<sub>Critical</sub>=2.724). No convincing explanation were determined for the COF value found for the contact pressure P<sub>2</sub>. In any case, a single factor ANOVA test for the data of the lowest two pressures indicates that they are not of

the same population (F=5.135 and F<sub>Critical</sub>=4.098), as well with the three higher pressures (F=11.014 and F<sub>Critical</sub>=2.724).

**V. THE EFFECT FOOT SHAPE ON THE READING OF THE COF**

The commercial tribometers, shown in table 1, use either square or circular pads. A set of pull tests, using the same TCNA tile, were performed using a square and a circular pads both have the same area of one square inch and made of Neolite. For each pad 20 pull tests were performed 10 in one direction (North) and the other in the opposite direction (South). The results are given in Table 8.

F-test indicate that the variances are the same (F=1.1440 and F<sub>Critical(one tail)</sub>=2.1554). As expected, a corresponding t-Test indicated that the means are not the same (belong to different population with 95% confidence interval t<sub>Stat</sub>=7.678 and t<sub>Critical (two tails)</sub>=2.024). In simple words the mean value of the COF for the square pad is different from the one for the circular pad. Thus, it can be concluded that the shape of the pad does affect the reading of the COF. The same data was analyzed where the pull direction was considered (Circular North v. Square North etc.) statistics analysis results are summarized in Table 9. Again, the results indicate that the foot's shape affecting the COF reading.

**Table 8: Tests' results.**

Direction	Foot's Shape	
	Square	Circle
North	0.259	0.345
	0.287	0.354
	0.278	0.335
	0.297	0.345
	0.306	0.345
	0.306	0.354
	0.268	0.354
	0.287	0.354
	0.268	0.335
	0.297	0.354
South	0.268	0.297
	0.268	0.278
	0.287	0.306
	0.278	0.325
	0.268	0.316
	0.249	0.345
	0.259	0.345
	0.287	0.335
	0.326	0.364
	0.326	0.373
Mean	0.283	0.338
Variance	0.000457	0.000551

**Table 9: Statistical analysis results.**

Direction	North		South	
	Square	Circle	Square	Circle
Mean	0.285	0.281	0.348	0.328
Variance	0.000281	0.000676	0.0000621	0.000897
F	4.526		1.326	
F <sub>Critical</sub>	3.178		3.178	
T <sub>stat</sub>	10.612		3.735	
T <sub>Critical</sub>	2.160		2.101	

## VI. CONCLUSIONS

From the results presented above the following conclusions can be drawn:

- 1) Grooves on the tribometer's foot do affect the COF reading by almost 50%.
- 2) It appears that the contact area between the tribometer's foot and the tested surface does not affect the reading of the COF.
- 3) A minimum contact pressure between the tribometer's foot and the tested area is required. Given the limited results, the value of the minimum pressure cannot be definitely determined. However, contact pressure of 25kPa - 30kPa appears to be adequate.
- 4) The shape of the foot is affecting the reading of the COF but the results obtained by the limited number of tests show a difference of 19.4% (when pull direction is ignored).

One has to bear in mind that the above conclusions were derived from a very limited number of experiments. Additional experiments, preferred in lab environment, are needed for better understanding the effect of the above parameters.

All these issues can be solved if a reference surface can be produced with very high repeatability resulting in the same COF. Thus, it will be expected that all tribometers will measure the same value of COF, eliminating the confusion discussed above.

## VII. REFERENCES

- [1] National Floor Safety Institute, <https://nfsi.org/>
- [2] BLS News Letter USDL 15-2205, November 19, 2015
- [3] Liberty Mutual Research Institute for Safety, Vol. 10, No. 3,
- [4] Slips and Falls Study: Objective Auditing Techniques to Control Slips and Falls in Restaurants, CNA June 2007. Autumn 2007.
- [5] Wen-Ruey Chang, et. al., "The role of friction in the measurement of slipperiness, Part 2: Survey of friction measurement devices", Ergonomics, Vol. 44, Issue 13, 2001.
- [6] Mark IIIB Slip meter Certification tests [http://www.slip-test.com/Slip-Test\\_MarkIIIB\\_F2508\\_Certification.pdf](http://www.slip-test.com/Slip-Test_MarkIIIB_F2508_Certification.pdf)
- [7] Kai Way Li, Chin Jung Chen, "Effects of tread groove orientation and width of the footwear pads on measured friction coefficients", Safety Science, Vol 43, 2005.
- [8] Li Kai Way, CHEN Chin Jung, LIN Ching-Hua, HSU Yao Wen, "Relationship Between Measured Friction Coefficients and Two Tread Groove Design Parameters for Footwear Pads\*", TINGHUA SCIENCE AND TECHNOLOGY ISSN 1007-0214 11/15 pp712-719 Volume 11, Number 6, December 2006.
- [9] Kai Way Lia, Horng Huei Wub, Yu-Chang Linb, "The effect of shoe sole tread groove depth on the friction coefficient with different tread groove widths, floors and contaminants", Applied Ergonomics 37 (2006) 743-748
- [10] Kai Way Li, Chin Jung Chen, "The effect of shoe sole tread groove width on the coefficient of friction with different sole materials, floors, and contaminants", Applied Ergonomics 35 (2004) 499-507
- [11] Kai Way Li\*, Jing Hui Horng, "A Comparison of Friction Measurement Results Using Two Slipmeters", Proc. 2009 IEEE IEEM, pp. 2159-2163

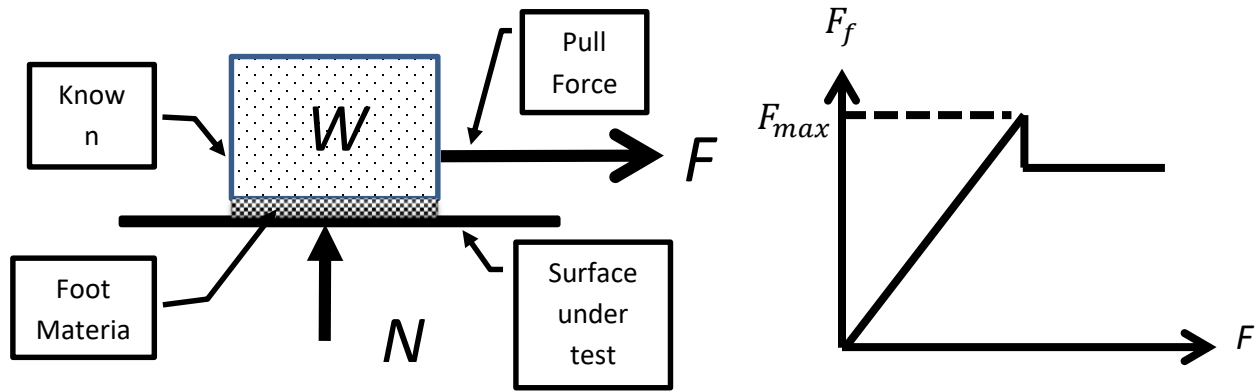


Figure 1: Pull test.

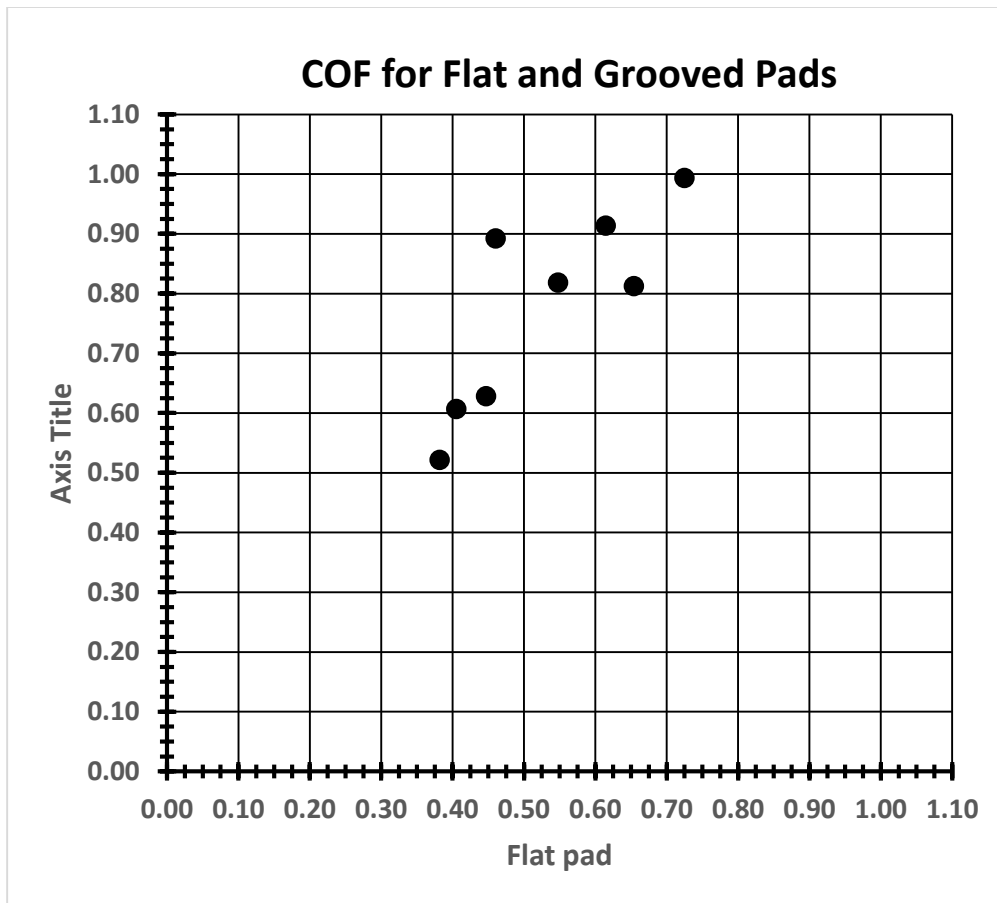


Figure 2: COFs values of flat versus grooved pads.

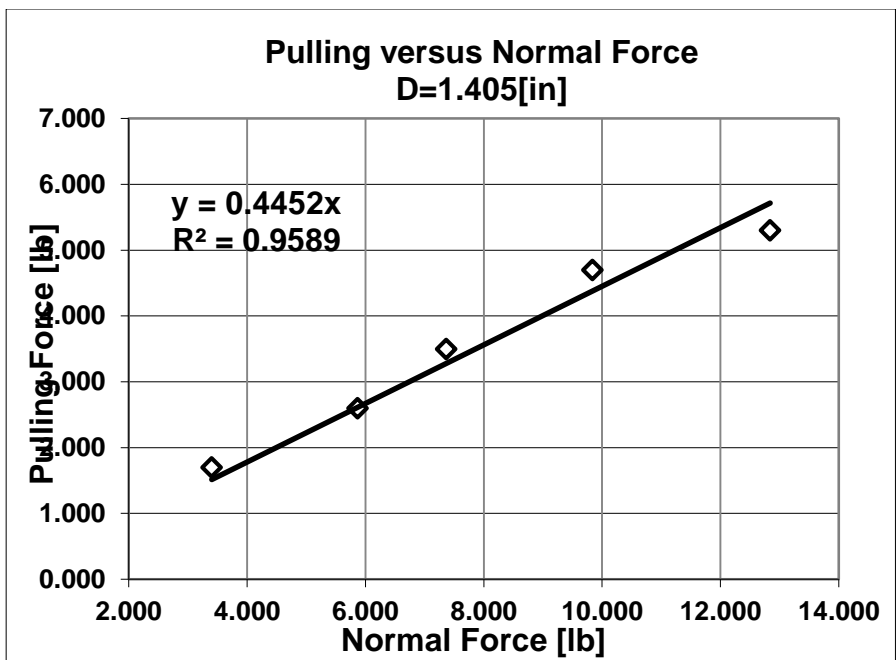
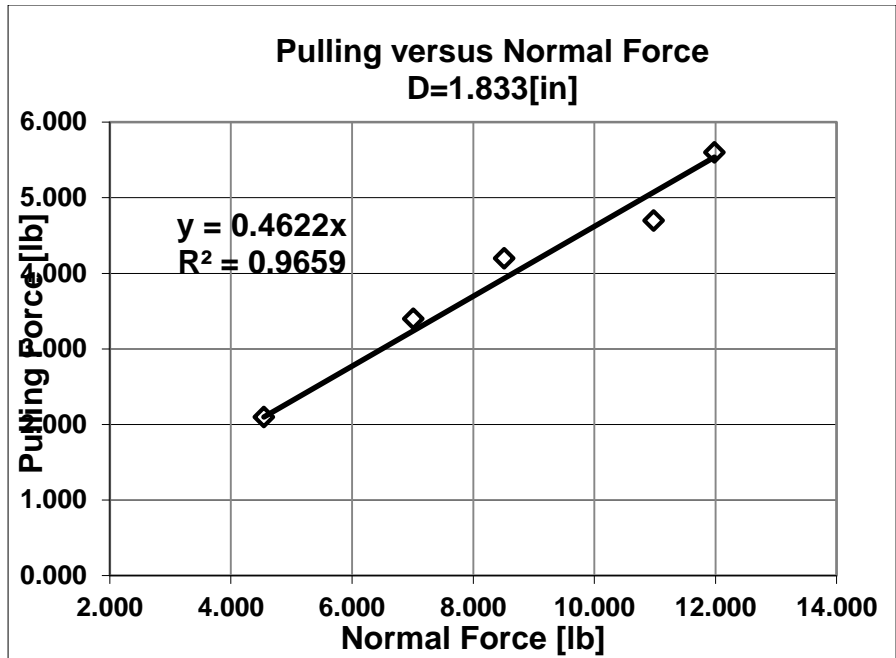


Figure 3: COF by linear regression.

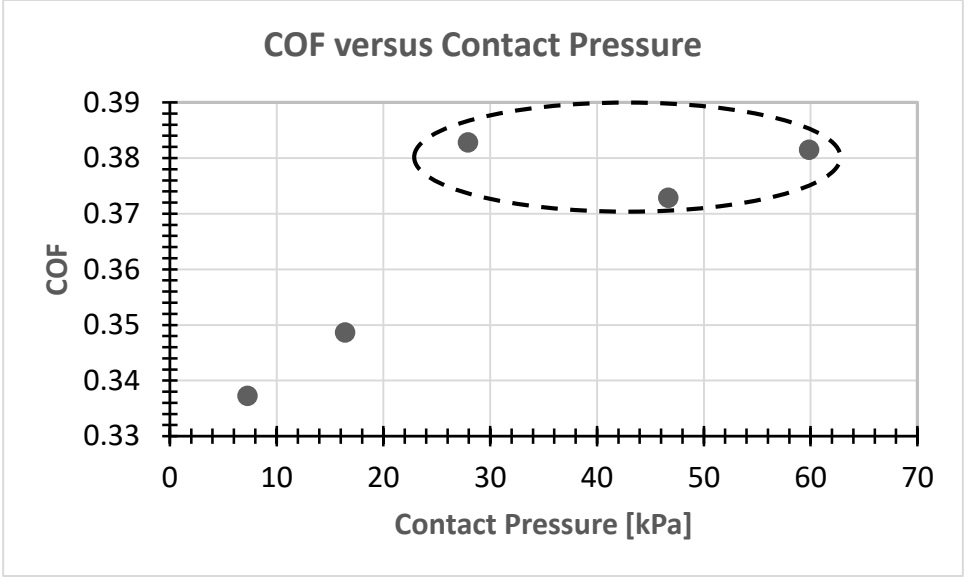


Figure 4: COF values for different contact pressures.

# Miniature Robotic Arm to Manipulate Ophthalmic Lenses

Kassim Kaba, Faris Baksh, Yazeed Almashan, Bader Alsubaei, Austin Bach<sup>1</sup>, Melissa Morris, Sabri Tosunoglu

Department of Mechanical and Materials Engineering  
Florida International University  
Miami, Florida

<sup>1</sup>TYB, Inc.  
Miami Beach, Florida

kkaba001@fiu.edu, yalma011@fiu.edu, fbaks003@fiu.edu, balsu004@fiu.edu,  
austinbach@gmail.com, mmorr009@fiu.edu, tosun@fiu.edu

## ABSTRACT

In this project, a small robotic device intended to replace the human arm during certain eye examinations and procedures was developed. Specifically, it is an attempt to remove tremor and fatigue in the arm of ophthalmologist who traditionally performs these operations manually as well as allow remote control of the lens position. This miniature robot provides physicians with a cost effective and user friendly option that increases precision, accuracy and ergonomics, while reducing risk and fatigue. This paper illustrates how this project achieved these goals. It builds upon previous work done by three of the authors.

## Keywords

Robotic Arm, Ophthalmology, Examination

## 1. INTRODUCTION

### 1.1 Problem Statement

There exist more than one hundred different types of surgeries in medicine and none of them are hundred percent risk free. This means that there is plenty of room for improvement to make operations safer. Certain ophthalmic (eye) surgeries have a noteworthy amount of risk. Due to the inherent human tendency for both the physician operating the equipment and patient attempting to remain still to become fatigued over time, the longer a surgical procedure takes, the riskier it becomes. The sensitive and delicate nature of the eye increases this risk. Currently, many ophthalmologists perform eye exams on patients using a machine called a slit-lamp. Mounted on the patient side of the slit-lamp is a chin rest to allow positioning and stability of the patient's head during the examination. To examine many interior structures of the eye such the retina, the physician is forced to hold an additional lens on the eye of the patient on the other end of the slit-lamp from their position. These lenses are also held in place this way for many laser surgery procedures done with the slit-lamp. It therefore requires the physician to remain in an awkward position to hold the lens steady or make small adjustments for long periods of time. This causes fatigue in the arm of the doctor, which increases

instability and therefore the risk for a laser to hit the incorrect target and possibly damage the eye. The robotic device proposed and implemented in this paper, named the Miniature Robotic Arm (MRA), can eliminate fatigue and thus get closer to a fully safe ophthalmic surgery.

### 1.2 Motivation

Engineers build tools, devices and machines for many reasons such as improving performance, efficiency and more. The project presented here is no different. MRA was intended to reduce the risk of laser eye surgeries, particularly retinal procedures. In doing so, this lens holding robotic arm also can increase the productivity of the physician, the accuracy and reliability of the laser targeting, as well as both the safety and comfort of the patient. Additionally, it helps move innovation one step closer to remotely performing eye examinations and surgery. Ultimately, this is an opportunity to help make people's lives better because it is needed by ophthalmologists and by extension the medical field.

### 1.3 Literature Survey

Many technological advancements have been made in the field of ophthalmology in recent decades. In 2010, the BQ 900 LED was introduced as the first LED slit-lamp in the world. Despite all the advancements made to slit-lamps in over a century since they were introduced, physicians still physically hold external lenses on the patient's eye to view certain optic structures. There does exist steady rests to hold a lens to an eye, but this rest must be manually moved should the physician want to change the lens position to see some other part of the eye or if the patient moves.

Introduced in 1999, the Da Vinci system remains the standard robotic surgery system for cardiac, colorectal, gynecologic, thoracic, urologic, head, and neck surgeries [1]. The U.S. Food & Drug Administration (FDA) continues to approve its use in an increasing range of surgical applications and some are investigated its use in ophthalmic procedures. Along with the Da Vinci robot, there are hundreds smaller robotic devices that help with tasks that require great precision such as the Mako orthopedic surgical system and the Mazor spinal surgery positioning system. These systems

help to illustrate the increasing usefulness and acceptance of specialized surgical robotic systems. Robotic surgery had advantages and disadvantages over traditional manual surgery as outlined in Table 1 below.

**Table 1. Advantages and disadvantages of robotic surgery**

Advantages	Disadvantages
Precision, accuracy, stability	Poor decision making/judgement
Amplified scale of motion	Poor interpretation of qualitative data
Reduced tremor	Expense and maintenance
Multitasking	Availability
Automation	Learning curve
Association of imaging systems	Possibility of malfunction
Teleoperation	Patient trust

Reflecting on previous innovations in robot assisted ophthalmic surgery, it can be seen that the robots were designed and built for either single specific tasks or assisting in technically difficult portions of procedures [2]. In the 1980's the Stereotaxical Microtelemanipulator for Ocular Surgery (SMOS) was invented in France. As one of the first micromanipulators, it allowed four degrees of freedom (DOF). Years later, investigators at Johns Hopkins University developed a steady hand manipulator (SHM) for retinal microsurgery. This device consists of an arm with tilt and roll mechanisms that allowed the instrument to move along with the surgeon [3]. In 2007, an advanced and optimized version of a new SHM for retinal surgery was designed and fabricated. This extended earlier work on cooperative manipulation in microsurgery and focused on performance augmentation [3].

The first robotic ophthalmic surgical device to go to market is expected to be the Preceyes system [4]. This device is intended for performing procedures that require instruments to enter the eye.

A robot intended for both ophthalmic examinations as well as non-invasive laser procedures is under development [5]. This paper describes work that continues the development of one component of that device, the remotely operated lens holder.

## 2. PROTOTYPE CONSTRUCTION

This section describes the design, analysis and construction of the Miniature Robotic Arm prototype. overall building process is discussed.

### 2.1 Description of the Prototype

The MRA prototype can be divided into three major sections. The first section consists of the support, which is the foundation that supports the whole device as its name indicates. It consists of a base structure affixed to the slit-lamp table to which is attached two perpendicular aluminum rods. These rods allow for gross adjustment in height and length to accommodate various patient physiology. In the preliminary design shown below in Figure 1, inner rods are connected to each other and fixed to outer rods

through adjustable handlebars that are tightened and released to obtain the desired position.



**Figure 1. Adjustable cylindrical bars for vertical and horizontal motion**

The second major part of the MRA prototype is the track. This component is connected to the end of the inner horizontal rod of the support. It forms a straight perpendicular track with respect to the horizontal bar allowing gross adjustment closer or further from the eye.. The track is made of two small I-beams to which a flat plate is attached to and thus enables a sliding motion back and forth.

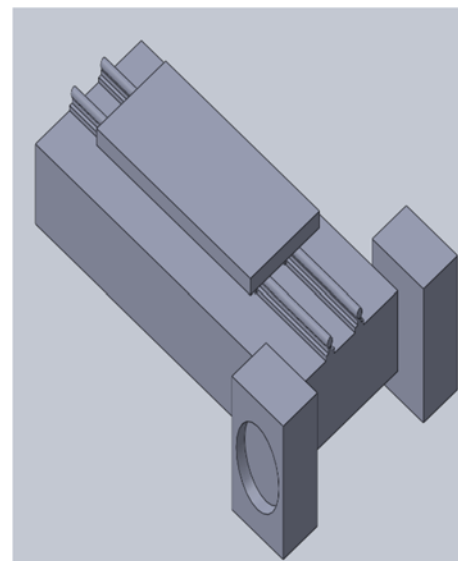


**Figure 2. Lens holder base**

The third major component of the prototype is the lens holder. The preliminary design is shown in Figure 3. This is the piece having

the highest degrees of freedom is the most important part of the system. Inside the lens holder outer bezel, there is an inner bezel held within a track. The inner bezel has screws that can be adjusted to hold any size lens. It also includes a gear to facilitate asymmetric lenses to be rotated parallel to the patient's face when a geared pinion is mounted to a motor to actuate this motion. The outer bezel is mounted by two pins to a bracket. The bezel can rotate about the pins via an actuator to adjust the angle about the horizontal axis in front of the patient's eye. The bracket is able to rotate about the vertical axis in front of the patient's eye via a swiveling base controlled by a third actuator. The lens holder assembly is fixed to the track portion noted above.

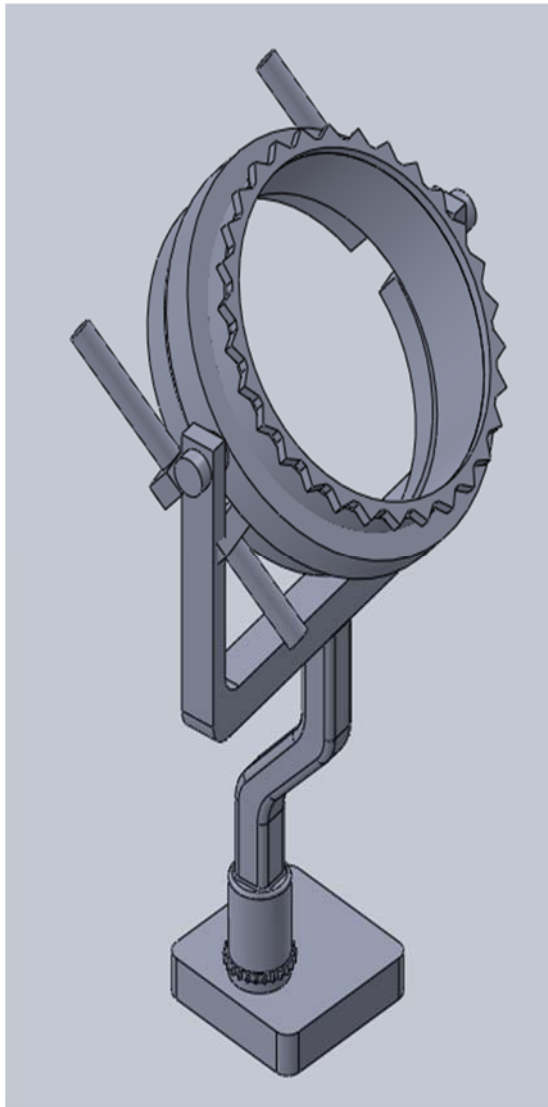


**Figure 3. Proposed lens holder design**

## 2.2 Prototype Design

The complete design with all three parts mentioned above was rendered in SolidWorks. The system model was modified to determine how the physical parts would fit until a final design,

shown in Figures 4 and 5, was produced. Analyses were performed to verify that the design was suitable to hold the lens stable. Appropriate actuators were identified to control the actuated components.



**Figure 4. Front view of assembly of components**



**Figure 5. Isometric view of full assembly**

## 2.3 Parts List

The parts involved in the construction of this project are a combination of different types of materials including: PLA, wood aluminum and other metal.

The parts list includes:

2 aluminum bars

3 small pieces of oak project board

10 screws

3 servo motors

2 small pieces of thick metal wire

Brace corner

Hex nut and hex bolt

Arduino R3 (interchangeably used with Raspberry Pi 3)

Ethernet Shield (for interface use via router or Wi-Fi)

## 2.4 Construction

As expected a project of this complexity required a large amount of trial and error in order to have all the parts come together as one. The building process was performed in two main steps. The first was assembling all of the necessary parts to build the lens holder. The second step was attaching the lens holder to the base support and track to make it a function as one complete usable device. The prototype has been altered many times before having a functional MRA shown.

Many of the lens holder parts were 3D printed. Photos of this process are shown in Figures 6 and 7. The outer bezel was printed in two pieces and glued together so that the inner bezel was secured within a track. The rotational movement was attempted via a servo mounted to the outer bezel with a pinion engaging the geared ring of the inner bezel.

The rotational motion about the pins connecting the bezel to the bracket was achieved by mounting a servo to the bracket and using two thick wires to form linkages from the two arms of a long symmetric servo horn to the ends of two bars designed on the bezel for this purpose.

The vertical rotation was achieved simply by mounting the bracket to a servo horn and mounting the servo base to the base track. The final lens holder portion is shown in Figure 8.

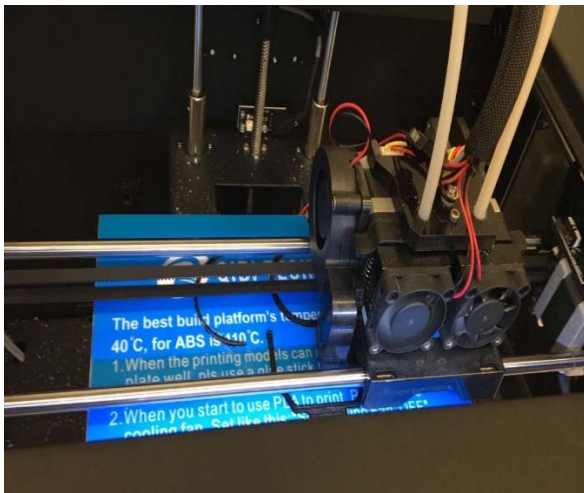


Figure 6. 3D printing of lens holder parts in progress

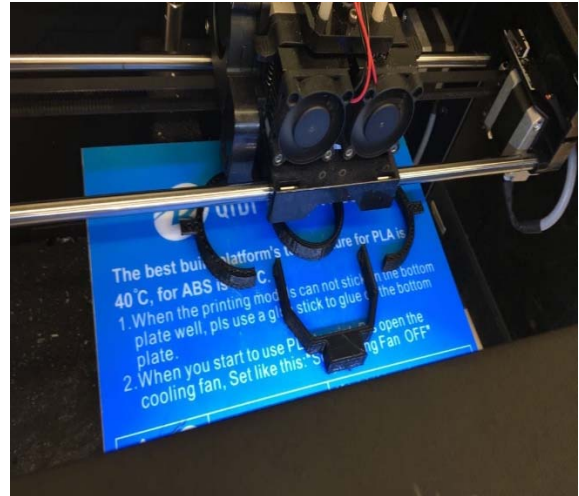


Figure 7. 3D printing of lens holder parts completed

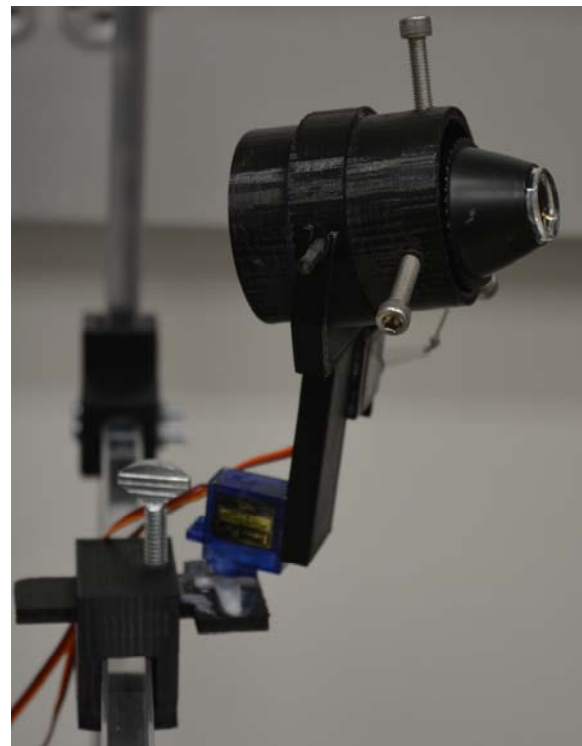


Figure 8. Completed lens holder portion of the MRA

The track portion of the base was also 3D printed. It was assembled by slipping the two parts together.

The base support system was originally constructed in a manner similar to that shown in Figure 1. In order to utilize quick-release levers, bicycle frame was used. The completed base proved to be very stable, but was much too large to comfortably use in front of the patient's face and to fit well between the slit-lamp and chin rest. A second iteration involved redesigning the base and using smaller square hollow extruded aluminum bars. Adjustments to height and length were facilitated by the manufacture of brackets that fit over

the bars and are secured to the desired position by tightening thumb screws. The complete assembly is shown in Figure 9 below.

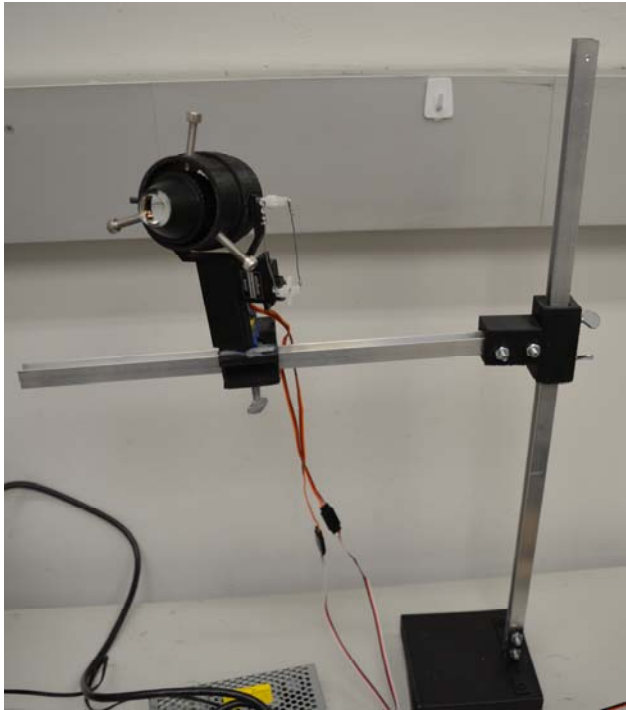


Figure 9. Complete MRA prototype with lens in place

### 3. TESTING AND EVALUATION

As mentioned in section 2, the objective of this project was to create a device that could replace the arm of a physician and allow holding and remote manipulation the lens for long period of times during ophthalmic examinations and laser procedures. By doing so, this would eliminate arm fatigue and tremor while increasing precision and accuracy. To verify the functionality of the prototype, an experiment was done to illustrate through data the improvement that the Miniature Robotic Arm brings.

#### 3.1 Design of the Experiments

The objective of the experiment is to find the difference between a human physically holding a lens weighing less than 5 ounces versus the developed device holding it in place.

The procedure is as follows:

- Assemble on a table a stopwatch and a small lens weighing between 3–5 ounces.
- Using an individuals between the ages of 20-30, record how long each person can hold the lens vertically while keeping his elbow at a 90° angle before feeling any sort of discomfort.
- Record the time that the discomfort started to the point when the person can no longer keep their arm up due to pain and/or tremor.
- Show test result and data in graph and/or table.
- Discuss and evaluate the experimental results.

For this experiment, some assumptions were made. It was assumed that the stress caused by the 3-5 ounces lens on the aluminum bar

would be negligible for the maximum time span of this experiment of two hours.

#### 3.2 Test Results and Data

Using the participation of healthy male of the ages of 22, 23, 25 and 27 respectively, the graph below in Figure 10 represents that discomfort rapidly increased over a three minute period. The graph shown in Figure 11 illustrates what is virtually a negligible stress applied to the lens holder over the same period of time as derived from modeling.

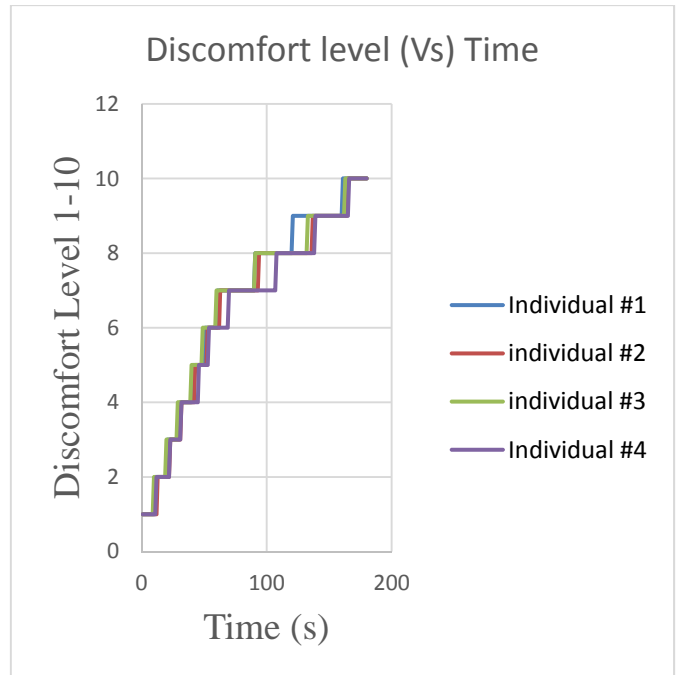


Figure 10. Human discomfort level vs. time

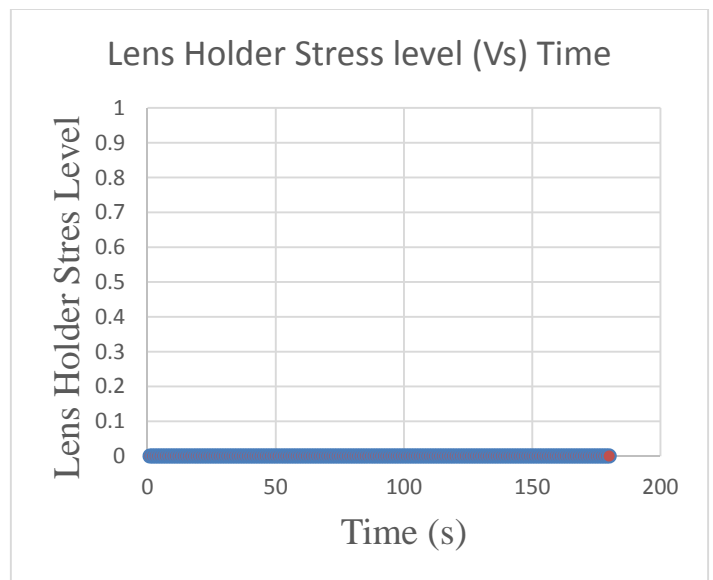


Figure 11. Lens holder stress level vs. time

### 3.3 Evaluation of Experimental Results

It is intuitively obvious that a human arm would get fatigued much more quickly than a physical object which is designed to stand in place holding the specified weight steady. However, the graph helps to visualize how much difference the robot can make even over a short period of time. It is important to note that even though this experiment was performed by young adults, typically an ophthalmologist will spend their career while in their early 30's to late 60's [5]. In other words, if young healthy men holding a lens feel a considerable discomfort after only three minutes in one position, it is fair to conclude that older men will most likely feel unease sooner. Thus, the value of the lens holder is enormous to the ergonomics of ophthalmologists around the world.

### 3.4 Future Work

A few improvements can be made to the design following the experiment. First, the lens holder must be strong enough to hold the heaviest lenses without allowing any instability. Second, the device must be durable enough that it can be used multiple times every day and for long periods of time during each use.

It is also suggested that in future implementations, a strong yet light actuator be used to allow for the rotation of the lens. The SG90 servos that were sufficient for the two other motions did not provide enough torque to rotate the inner bezel. This was due to excess and uneven friction caused from rough surfaces created from the 3D printing process. Close up photos of the final prototype are shown in Figures 12 and 13.



Figure 12. Final prototype lens holder

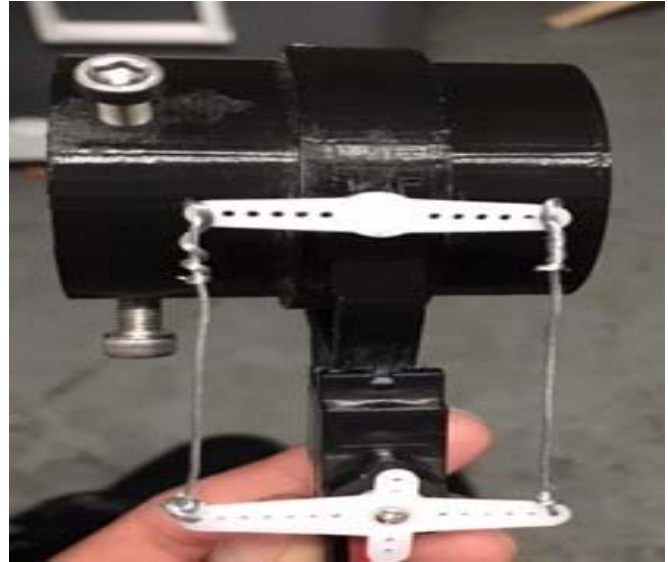


Figure 13. Side view of final prototype

Finally, it is feasible that in the next iteration, the gross adjustments will be actuated to allow for remote adjustment. This was not a goal of the prototype as someone will be able to manually insert a lens and adjust the general position of the lens according to the position of the patient. Actuation could be helpful, however, as it would allow for quick adjustment whether remotely or in-person. Quick adjustments may provide relief for the patient attempting to remain still for long periods of time or allow for the physician to remotely position a patient to more conveniently obtain a view of an area of interest.

## 4. CONCLUSION

Testing and evaluation allows engineers to validate their intuition, expectations, and purpose. It is also an opportunity, for a project to differentiate itself from others by providing solid data and results to back out the product. For this project, the data reveals how useful this machine can be for the productivity of ophthalmologist as well as the safety of patients. Additionally, this was an opportunity to improve a previous design and obtain a better solution as determined from the conclusions drawn from the experiment. The lens holder was integrated into the slit-lamp system developed and the robotic portion was successfully remotely actuated through the web interface.

## 5. ACKNOWLEDGMENTS

The authors extend their thanks to ACM SIGCHI for allowing us to modify templates that they had developed. We also wish to acknowledge and thank Dr. Austin Bach of TYB, Inc. for providing financial support and medical guidance for this project.

## 6. REFERENCES

- [1] Michael MacRae, "The Robo-Doctor will see you now," ASME, 2012.
- [2] John Pitcher, Jason Wilson, Tsu Tsao, Steven Schwartz, and Jean Hubschman, "Robotic eye surgery: Past, present, and future," *Journal of Computer Science & Systems Biology*, 2012.
- [3] Ben Mitchell, John Koo, Iulian Iodachita, Peter Kazanzides, Ankur Kapoor, James Handa, Gregory Hager, and Russell Taylor, "Development and application of a new steady-hand manipulator for retinal surgery," *Proceedings of the IEEE International Conference on Robotics and Automation*, Rome, Italy, pp. 624-629, 2007.
- [4] Melissa Morris, Sabri Tosunoglu, "Teleoperated Ophthalmic Examination Robot," Department of Mechanical and Materials Engineering Florida International University, FCRAR, 2016.
- [5] John B. Pinto, "Issues and opportunities arise for the 55+ ophthalmologist", *Ocular Surgery News U.S. Edition*, July 10, 2011, Extracted from <http://www.healio.com/ophthalmology/practice-management/news/print/ocular-surgery-news/%7B70a6a179-3adc-4ecf-8ac1-3e45f8089ecb%7D/issues-and-opportunities-arise-for-the-55-ophthalmologist>, March 2017.
- [6] R. Douglas, "Robotic surgery in ophthalmology: Reality or fantasy?" *The British Journal of Ophthalmology*, vol. 91, no. 1, 2007.
- [7] Irena Tsui, Angelo Tsirbas, Charles Mango, Steven Schwartz, and Jean Hubschman, "Robotic Surgery in Ophthalmology," Los Angeles, USA: University of California, 2010.
- [8] Jean Thilmany, "Robotic control," ASME, 2013.
- [9] Gabriel I. Barbash, M.D., M.P.H., and Sherry A. Glied, Ph.D., "New Technology and Health Care Costs — The Case of Robot-Assisted Surgery," *The New England Journal of Medicine*, August 19, 2010.

# NASA Swarmathon Search and Rescue

Jose Medina, Andrey Khlapov, Stephanie Forero, Scott Jagolinzer, Sabri Tosunoglu

Department of Mechanical and Materials Engineering  
Florida International University  
Miami, Florida, U.S.A

jmedi089@fiu.edu, akhla001@fiu.edu, sfore009@fiu.edu, sjago001@fiu.edu, tosun@fiu.edu

## ABSTRACT

This paper delineates research results that was carried out on swarm robots with the purpose of searching a large unknown area for specific objects. The robots used in this work operate using ROS or robot operating system. The search algorithm is coded in C++. Different search patterns were tested to see the efficiency of search of each algorithm as well as how the robot deals with errors accumulated in sensors. Search patterns include radial search, inward and outward circular spirals, rectilinear spirals, and grid-style search techniques.

## Keywords

Multi-robot system, swarm robots, UGV, swarm controllers, architecture, search algorithm

## 1. INTRODUCTION

The NASA Swarmathon is a competition to develop cooperative robotics to revolutionize space exploration. These cooperative robots are known as swarmies.



**Figure 1. Swarmies Begin Their Search of a Specific Area**

Swarm robots are considered as a new approach to multi-robot systems. Based on its name, multi-robot systems consist of several amounts of robots that can physically move both alone and as a

group. The main designs of swarm robots come from the behaviors of social insect such as ants. These behaviors are called swarm intelligence.



**Figure 2. Swarmies are Inspired by the Behavior of Ants**

When located in hard to reach environments, a feasible method of searching such areas can be swarm robots. By properly combining the shared intelligence of these robots entire areas can be mapped and searched faster than one could by themselves. The problem then arises in how one can properly search open-ended areas and collect meaningful information. The situation we are presented with is the NASA Swarmathon project. The requirements of the project are left as basic as possible to make the logic applicable to other situations. Assuring that the robots can rapidly search an area and collect object is the primary concern. Concerns that arise because of the first problem are making sure that the robot can avoid other robots and walls, and overcoming the shortcoming of hardware. Sensor reliability is important and must be tested to work well in conjunction with the code. Without a proper meshing of both then information the robots collect, as far as its location, will not have enough certainty to be trusted. Inaccuracies in the actuators may cause the robot to be off its intended location and areas of the importance may be missed throughout its search. For this the other main challenge is overcoming the sensor limitations and making sure the robot's logic can handle these inaccuracies.

The robots we will be using are limited to certain hardware as defined by NASA. This hardware includes 4 motors, three ultrasound sensors in the front of the robot only, a serial arm to grab

object, a camera, and a GPS sensor. We are also provided with a base code which is used to make the robot search. This base code can be altered to increase performance. Actual hardware cannot be modified and will be the final configuration.

## 2. Search Pattern Background

### A. Global Maxima Search

The approach is useful when search region boundaries and target probability are known. The algorithm divides search area into grids and assigns a value of the integral of the probability under the grid to each cell. The algorithm generates trajectory to visit the cells with highest probability and clears the grid-cell once visited. The strategy provides trajectory with multiple overlapping segments due to the shift of global maxima across the search region [1].

### B. Local Maxima Search

This strategy uses the same probability distribution across the grid-cell and clears the cells with maximum values within the local maxima-search results [1]. The trajectory for this search is less overlapping, but the strategy depends on the initial position and robot is tend to stay in the local maxima area.

### C. Radial Search

The algorithm involves a repeated sequence of moving from the center and then making a return. Each new sequence starts with the new heading. The search strategy is greatly improved when outward and inward paths form a loop [2].

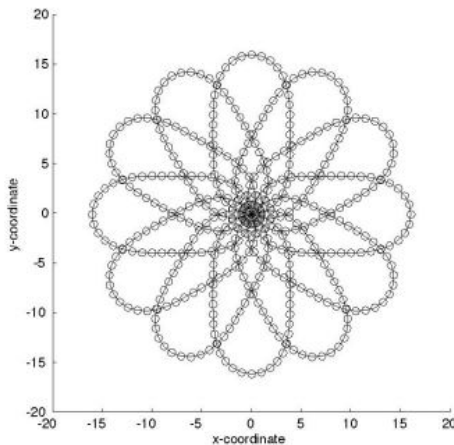


Figure 3. Radial Search

### D. Bees Algorithm

This strategy models the foraging behavior of the colony of bees for the richest and closest food source. The algorithm that was proposed originally was a combination of random search and neighboring search. The goal of the search strategy was to find a single value

which represents the global optimum. A variation of this strategy would be a Distributed Bees Algorithm (DBA), suitable for multiple objects search mission. The objective of this improvement was to attract more robots to the areas with higher target distribution. When robot finds a target, it communicates with other robots and sends target location to the robots in the range [3].

### E. Particle Swarm Optimization, variations and improvements.

PSO is one of the earliest and well-known search algorithms for swarm behavior, provided by Kennedy and Eberhart in 1995 [4]. It provided the inspiration for Robotic Darwinian Particle Swarm Optimization (PDPSO), Extended Particle Swarm Optimizations (EPSO) and many others. PDPSO consist of robots that move collectively in search area and work for optimal solution. Each robot characterized by the performance, position and heading. This strategy allows robots to overcome problems related to obstacle avoidance, robot dynamics, sub-optimal solutions and communication constrains [5]. EPSO algorithm does not use multi-hop connectivity compare to PDPSO and makes each robot to consider information only with robot with fixed radius of communication. This strategy also uses different obstacle avoidance approach.

## 3. Search Pattern Prototypes and Concepts

Since the search starts from initial position in the center of search area, then we propose that a spiral search algorithm to be a reasonable choice. This algorithm is very efficient and in theory provides complete coverage of circular area where radius of the circular area equals half distance of the search arena. In the spiral search algorithm, we have options to use two patterns: inward spiral and outward spiral. The inward spiral pattern first identifies the search region and boundaries and moves forward toward the center. The outward spiral pattern initialized from the center of the search area and expands outwards to cover entire region.

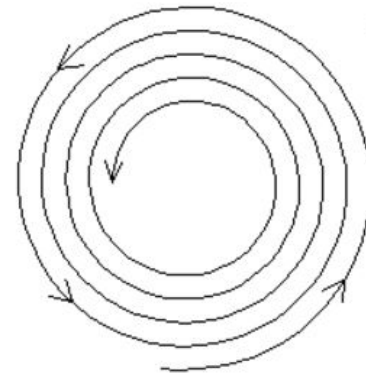
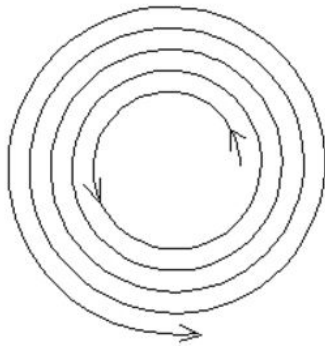


Figure 4. Inward Spiral



**Figure 5. Outward Spiral**

The inward spiral pattern takes much longer search time, but ultimately provides better search results. On the other hand, the outward spiral minimizes the search time, provides greedy search, but at the end the success rate is compromised.

Since it takes time for the Bot to bring the cube back to the collection zone, we propose to use outward spiral pattern. The Bots will collect maximum amount of cubes in the vicinity of collection zone which is also the starting point for the spiral.

The onboard web-camera which is used to find and identify cubes has a very specific parameter. It processes the pixels of the upcoming images left to right, top to bottom. Thus, in terms of the Bots view, the cube in the upper left corner of the screen will be identified first.

Considering this feature, we chose to have a counter-clock rotation for our spiral pattern. By doing so, the Bots will be always collecting the cubes on the “Inner” side of the circular path.

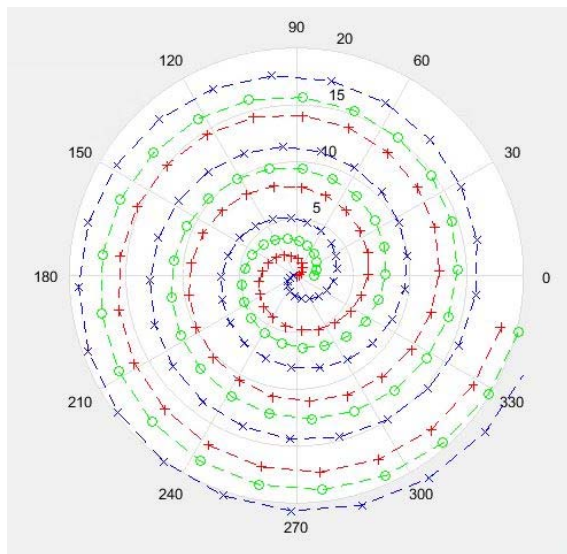


**Figure 6. Counter-clockwise Outward Spiral Path for 3 Robots**

It is important to note that Bots will start their spiral paths not side by side, but rather equidistant from the center point of the search area.

Once the cube is picked up and delivered to the collection zone the Bot can start a new spiral pattern, from the beginning or can resume the spiral where it left off.

As an option, the Bot could be programed in such way that after certain amount of returns to the collection zone it will increase either initial radius of the spiral with respect to time travelled from the center, or increase distance between the spiral turns. This option will help to deliver the Bot to the outer range of the spiral since most of the cubes within the close proximity of the center have been picked up.

Once the Bot reaches the boundary on the outer side of the spiral it will either change the direction to avoid the wall and continue the spiral path or could be programmed to use different algorithm to cover 4 corners of the square arena.

The spiral search is only efficient if there are no errors in navigation. Since our Bot is equipped with the onboard GPS with accuracy of 3-6 feet, we cannot rely on that feature for our spiral path. The only options left for us are encoders on each wheel. The accumulated distance with each turn of the spiral along with slippage of the wheels due to the turn will lead to the error in distance and consequently the path travelled. This might lead to the rapid decrease of the quality of coverage.

The collision avoidance behavior for the Bots should also be taken into consideration. At the beginning of the spiral the Bots will be close to each other. Once one of the Bots will identify and determine the cube, it will become a stationary, possibly blocking the spiral path of the other Bot. The obstacle avoidance algorithm for the bot could be made to assume the robot is a wall and alter its trajectory slightly.

Another possibility for the search pattern is too divide the known search area into different quadrants. Using the onboard compass of the robot, the quadrant assigned to each robot is determined based of what the original trajectory angle is. Once the robot has been assigned a quadrant, it begins snaking outward towards the wall.

This snaking motion will increase in height with each horizontal motion. The move movements will be strict linear movements of 0.5 to 1 meter increments. After each interval, the robot will scan its surrounding search for cubes. The intervals are kept small to minimize any missed cubes due to the limitation of the robot’s camera.

## 4. Logic Structure

There exist multiple ways that this robot can be programmed to perform its desired application. The chosen structure for our robot is with State Machines.

State Machines or the method of using State Machines are defining each task the robot must perform within different cases. The main logic function for this method is the switch case statement.

Certain identifiers that the robot may encounter throughout its operation will prompt it to switch to a different “State” of operation. For our specific application, these prompts to switch to a different state can be obstacle detection, object detection, verification that the object has been collected, drop-off zone detection, and multiple others.

A basic example of the framework state machine logic can be seen in the following image.

## Finite State Machine

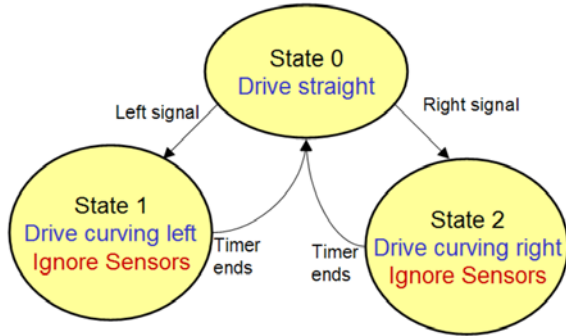


Figure 7. Example of State Machine Logic

The main benefit of programming in terms of state machines is that it allows the robot to continue looping into its function without being locked into that specific function. The robot can exit into a different state at any moment if the correct prompt is presented. The robot is also able to always revert to its original state and determine its following action. New states can also be added to the robot and the redefining of the rest of the code to accommodate this addition is not as strenuous.

## 5. Search Algorithm Testing A Spiral Search

After narrowing down the potential algorithms to two potential patterns we begin the coding and simulation of the search. We begin with the outward spiral search pattern by using the below equations to affect the goalLocation.x and goalLocation.y variables. These equations are placed in the "Transform" stage of the state machines for the robot.

```

goalLocation.theta = currentLocation.theta + (M_PI_2)/12;
goalLocation.x = currentLocation.x + ((0.01 + .03*theta)*
    cos(goalLocation.theta));
goalLocation.y = currentLocation.y + ((0.01 + .03*theta) *
    sin(goalLocation.theta));
theta = theta + (M_PI_2)/12;
  
```

In the above equations, the orientation of the robot, defined by goalLocation.theta, is defined by adding whichever angle one chooses. In order to maintain a tight uniform circle, the angle chosen as what is essentially a step size is 7.5 degree increments. This could be made smaller or larger if one chooses. The rectangular coordinates of the goal location are defined using altered version of the Archimedes spiral equations. The general form of these equations is the following.

$$x_{component} = (a + b\theta)\cos(\theta)$$

$$y_{component} = (a + b\theta)\sin(\theta)$$

The additions of the currentLocation variable to both equations are done in order to make sure that goalLocation coordinates are relative to the actual position of the robot. The more important variables of interest are the "a", "b", and "theta" variables. These variables in tandem control the spacing in between loops of spiral and how tight of a spiral it is. The "theta" variable will have the same step size as the goalLocation.theta variable. Manipulating

those above variables help change the shape of the spiral which will directly influence search time and area coverage.

Initial spiral search patterns were done with larger turning angles in order to avoid slippage of the robot wheels by using only rectilinear movements. The angle increment is responsible for how circular of a spiral one gets. The two angle measures tested for uniform expanding spiral were 45 degree increments and 7.5 degree increments. At the 45-degree increment setting, larger values of "a" and "b" are required in order to get a good balance between search area and time spent searching. An "a" and "b" value of greater than 0.1 is recommended for the 45-degree setting in order to get a good balance between the area covered by each robot and the time it takes it to reach the end of the area. For the 7.5-degree setting, "a" and "b" values less than 0.05 are recommended.

The following is an example of the rectilinear spiral and the circular spiral.

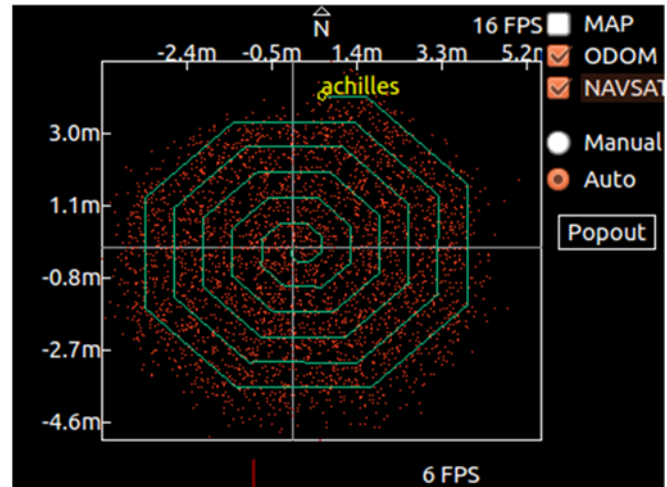


Figure 8. Rectilinear Spiral

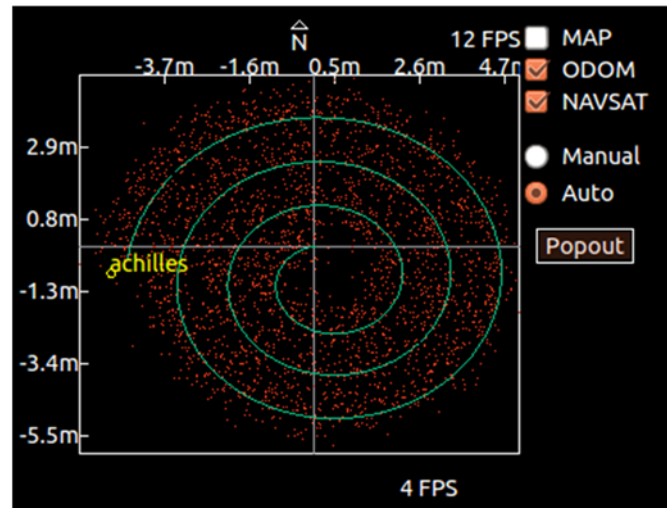
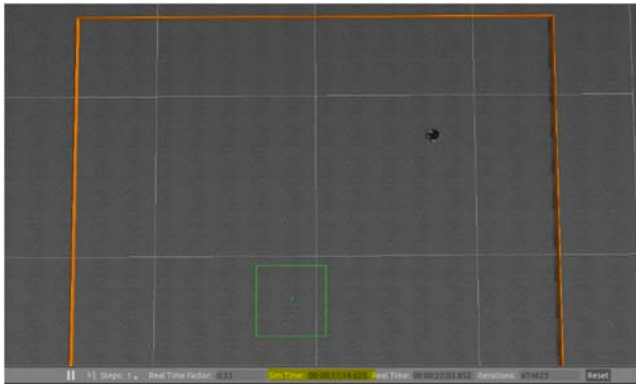


Figure 9. Circular Spiral

In the above examples, values of 0.1 and 0.05 are used, respectively for each spiral type. Each one was tested at the beginning of its range and how much area was covered was compared to the time it took. The rectilinear spiral was tighter at its minimum range, this however can be fixed easily. The circular spiral has good spaces in between its loops, to make it tighter the values can be reduced. Even

taking into account the spacing in between each loop, it takes the robot longer to search in the rectilinear spiral than in the circular spiral. This is because it takes the robot longer to turn to its orientation because it is larger; 45 degree turns compared to 7.5 degree turns. This can also be seen in the following two images.



**Figure 10. Rectilinear Spiral Simulation Time**

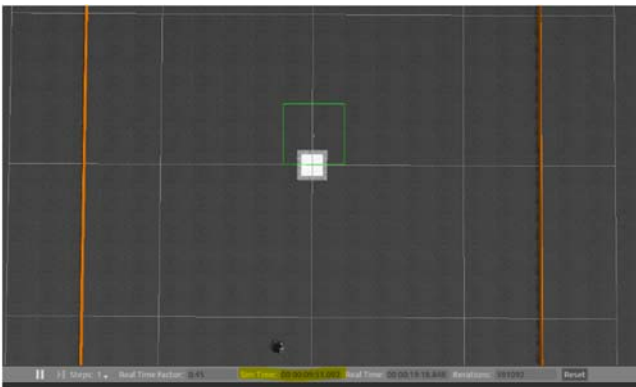


**Figure 11. Circular Spiral Simulation Time**

The time taken by the circular spiral is less than the time taken by the rectilinear spiral and the circular spiral was still able to cover more area than the rectilinear spiral. This however can be remedied significantly for the rectilinear spiral by increase the space in between each loop. This will aid in time used up to search the same amount of area. The time for the rectilinear is still slightly longer than the circular spiral because of the larger turning angle after each increment.

With regards to the space in between the loops, it is most optimal to have a space of 1.5 to 2 meters in between each loop. This is done to accommodate the capabilities of the robot's camera. The camera has a visual area of about 1.5x1.5 meters. With a space in the above specified range, the chances of finding a cube are increased and any cubes not seen by the camera by one robot can be found by one of the other robots that loops adjacent to it. This will help with both time without sacrificing covered area. The rectilinear spiral also has the added benefit of not accumulating as much error in its movements as the circular spiral does. Rough surfaces, such as gravel which has many individual rocks, may pinch wheels and twist the robot slightly and deviate it from its desired destination. This happens more often when the robot attempts to twist as it moves forward as in the case of the circular spiral. So, keeping linear movement and turning separate reduces the buildup of error throughout the search.

The return function for either one of the spiral patterns chosen were the straight shot to the base option. This was chosen over the reset option because of time constraints. The reset option is more secure in returning to the base, however it will take up too much time after multiple collections.

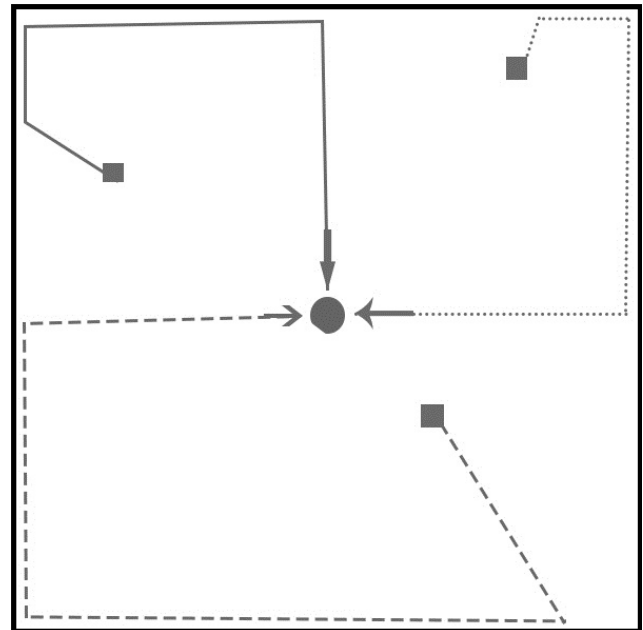


**Figure 12. Return to Base Reset Option**

The straight shot to base option is far more time efficient but depending on how much error has been accumulated throughout the search the robot may miss its destination. In order to correct this, once the robot has reached its assumed goal destination it spins around 90 degree and moves forward, spin another 90 degrees and move forward and continues this pattern. The forward motion is done at varying increments in order prevent the robot from moving in a localized circle. The robot repeats this looking for the markers that indicate the drop off area. In recent testing, the assumed goal location has not been far off from the actual drop off location so this method has worked quickly on each return.

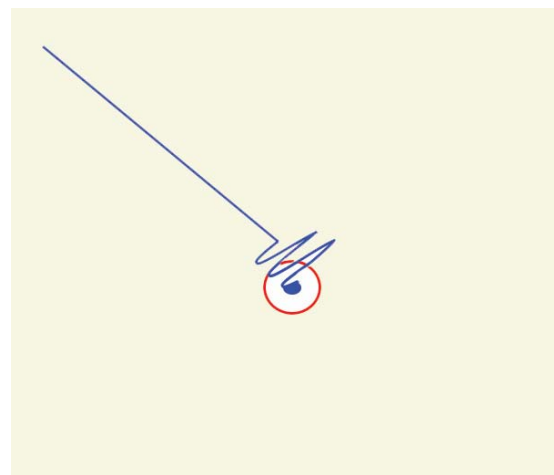


**Figure 13. Return to Base Straight Shot Option**



# Ophthalmic Robot

David Larsson, Daniel Irving, Shehryar Effendi, Joshua Dubin, Austin Bach<sup>1</sup>, Melissa Morris, Sabri Tosunoglu

Department of Mechanical and Materials Engineering  
Florida International University  
Miami, Florida

<sup>1</sup>TYB, Inc.  
Miami Beach, Florida

dlars014@fiu.edu, dirvi004@fiu.edu, seffe001@fiu.edu, jdubi006@fiu.edu, mmorr009@fiu.edu, tosun@fiu.edu

## ABSTRACT

The results of a continuation of the existing novel prototype for robotic eye examination is presented. This work is the next step from the Teleoperated Ophthalmic Examination Robot in implementing a full remote ophthalmic diagnostic and treatment device.

## Keywords

Slit lamp, robotic surgery, remote ophthalmology, telemedicine.

## 1. INTRODUCTION

The Ophthalmic Robot is a motorized slit lamp that allows for remote operation from a computer interface. The project was initiated by ophthalmologist Dr. Austin Bach and the initial prototype was developed by Melissa Morris. This project is a continuation and improvement of Melissa Morris' preliminary work [1]. Figure 1 shows the prototype from the previous work.



Figure 1 – Previous Robotic Slit Lamp Prototype [1]

A slit lamp microscope consists of two components: an illumination system that shines a bright focal light through a slit of variable width or height, and a magnification system that is usually

binocular. Slit lamps allow for close surface examination of the front of the eye and inspection of the interior of the eye with the use of auxiliary lenses [2]. All major instrument manufacturers produce a range of slit lamps, though the basic principles remain the same for whichever model is selected [3]. Slit lamps can have the illumination system either above the magnification system or below. The slit in the illumination system can be adjusted on most slit lamp models. A practitioner should be able to adjust slit width and height while also being able to orient the slit horizontally and vertically. For easy movement of the slit lamp, most have a joystick installed and a locking device to hold it in position [3].

Modern slit lamps allow for photography of the eye, which allows for an accurate and consistent means for eye exam record keeping. Photographic capabilities can also allow for remote examinations where the practitioner does not need to be present with the patient. Traditionally, the most frequently used option for image capture of the anterior segment involves the use of a photographic slit lamp with a beam splitter attached to a 35mm camera back. Conventional 35mm photography requires adjustments to achieve the correct exposure. Recent advances in video cameras, image-capture boards, digital still cameras, and color printers has resulted in a more affordable and easier to use digital imaging where the major advantage of such systems is the ability to generate instantaneous images on a computer monitor [3].

## 2. MOTIVATION

Many people around the world are affected by some degree of visual impairment and seek corrective ophthalmic assistance [1]. Because ophthalmic operations are complex and risky, robotic technology can greatly assist with such procedures. When operating manual devices, physician fatigue becomes a factor as such work produces mental and physical wear. An ophthalmic robot can be controlled and monitored remotely by an ophthalmologist from almost any location with a potentially higher degree of precision. Though the overall cost savings may be questionable, there are some aspects of robotic technology that can provide economic benefits. It could be more cost efficient to develop a robotic slit lamp out of an existing slit lamp rather than designing a robot slit lamp from scratch because many older models are in use throughout the world. By using an established mounted motor retrofit system, an ophthalmologist could select which ever

slit lamp that suits his/her preferences. While the Ophthalmic Robot can be moved, traveling with the robot could potentially be costly [1].

### 3. EVALUATION OF FIRST PROTOTYPE

The previous robot was outfitted with four motor systems to control slit height and width, lens rotation, and slit lamp rotation. The robot was mounted onto a motorized platform allowing for planar movement of the entire structure. The motorized systems are mounted onto an existing slit lamp to allow for a major cost cut and to reduce FDA testing time. Figure 2 displays the four slit lamp adjustment systems and the motorized movement platform.

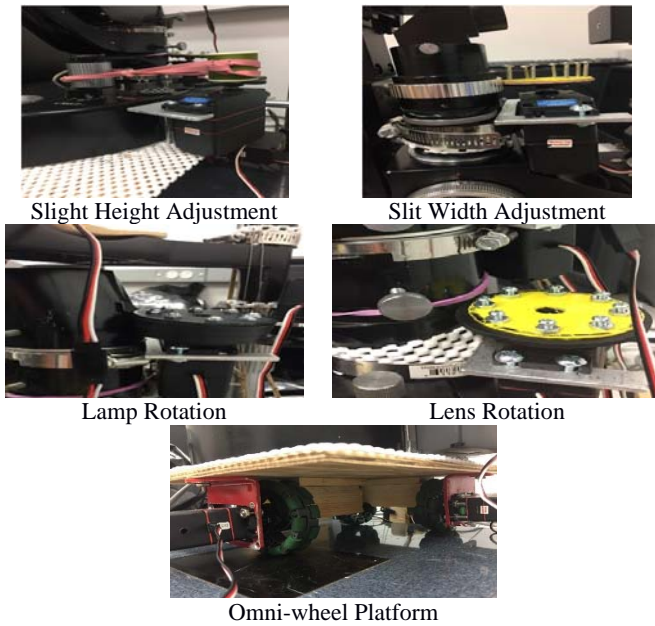


Figure 2 – Previous Prototype Motor Systems

For improvement of the existing prototype, the existing motor systems were evaluated and revamped. There are five main constituents that made up the entire prototype. Firstly, there is a base comprised of four Omni-wheels and two motors that the slit lamp rested on, allowing it to move in the X and Y directions. The other four constituents were small systems composed of a motor and either a friction disk or band, allowing for the alteration of settings of the slit lamp, by rotation of an adjustment knob. The settings that these systems controlled were the slit height, lens rotation, lamp rotation, and slit width.

With all five of these components, there were a few imperfections and deficiencies. Regarding the Omni-wheel base, the system was too convulsive. This was due to a combination of the contour of the wheels, the rotation motors for the wheels, and the existing slit lamp track structure being warped from age and wear. As this instrument is used for eye examinations, smoothness is required.

The system that controlled the slit height was composed of a motor that is affixed to the slit lamp via metal brackets which rotates a spool. Linked rubber bands wrapped around the lamp’s adjustment knob and the driver spool acted as a belt, thus rotating the knob. It

was determined that system was in working order and the slit height knob worked as intended.

The system that controls the slit width was composed of a friction disk that is in tension with the slit width knob. Similar to the knob that adjusts the slit lamp’s height, the light beam width was controlled by a completely circular dial. There was a motor mounted close to the lamp, and as a result a disc, rather than a belt, was intended to rotate the dial by friction. However, a sufficient amount of kinetic friction was not always created in order to adjust the knob consistently and inconsistencies in the knob actuation made the problem more prominent.

The two rotation systems that rotated the microscope and the lamp featured two motors bracketed to the back of the slit lamp. Each used disks to drive rotation of one of the arms. Both disk drives facilitated rotation, however the disks’ friction surfaces degraded rather quickly, creating slippage. The contour at the back of the slit lamp is straight for the microscope rotation system, but the contour slopes for the lamp rotation area. This results in a small amount of contact with the slit lamp, a crucial element in friction drives.

### 4. REVAMPED PROTOTYPE

The previous prototype was redesigned where a new movement platform was implemented and all four of the systems that control the position and settings of the slit lamp were replaced. Although the existing prototype provides a solid working foundation, there was room for improvement. The new designs give the existing prototype a cleaner look and improved performance.

#### 4.1 PROPOSED DESIGNS

Starting with the movement platform, a motorized screw stepper motor stage was developed. The XY stage works by running the stepper motors mounted onto a rail system. The motors used are Haydon 28000 Series 11 Stepper Motor Linear Actuators, shown in Figure 3.



Figure 3 – Stepper Motor Linear Actuator

The slit lamp rested on top of a moving platform and the platform rests on top of eight 0.5in ball bearings. The ball bearings rolled as the motor applies a force on the motor and the adjacent motor slides along the rail. The key focal points of this design were that the weight of the slit lamp rests on the bottom platform, the screw stepper motors allow for a smooth and controlled movement, and the railing system keeps the moving platform in place and moving only in the X and Y directions. Figure 4 shows the SolidWorks model of the XY stage design.

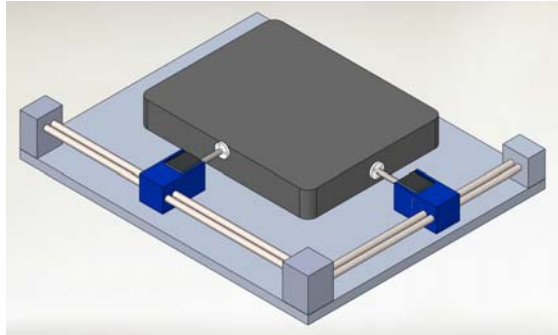


Figure 4 – Proposed XY Stage Design (SolidWorks)

For the four mounted motor systems, the previous motors used on the first prototype was replaced with identical Turnigy Servo motors, shown in Figure 5. The Turnigy servo motors provide ample torque and allow for a variety of mounting options.



Figure 5 – Turnigy Servo Motor

For the two rear-mounted arm rotation systems, gear drives were used to rotate the microscope and illumination system. Gear drives were selected because they do not require a pre-load that a friction drive requires. This results in easier mounting and a higher degree of precision. Circular gear racks were attached to the slit lamp itself and pinions will be attached to the motors. The pinions were the driving forces behind the rotational motion. Figure 6 displays the designs, modeled in SolidWorks, for the illumination system rotation and the lens rotation.

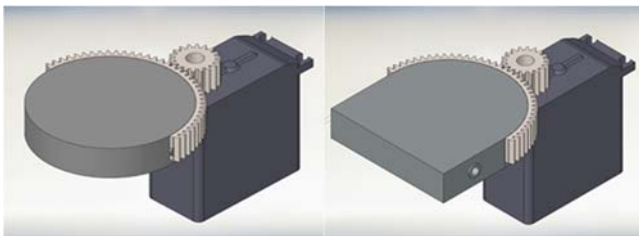


Figure 6 – Lamp Rotation (Right) and Lens Rotation (Left)

For the slit height adjustment, it was decided to keep the belt concept, but improve the belt system. The existing prototype's rubber band setup performed at a satisfactory level, therefore no major change was needed. In the new design, a different belt was used and a pulley was 3D printed for this system. For the slit width adjustment, it was decided to replace the existing friction drive with a belt drive. Similar to the slit height adjustment, a pulley was

manufactured for the system. A gear drive was the ideal option, but difficulty in mounting the gear onto the knob was the main deterrent. Figure 7 shows the SolidWorks models of both systems.

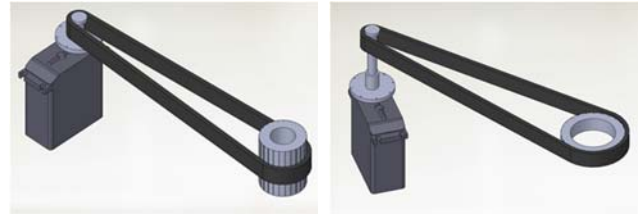


Figure 7 – Slit Height (Left) and Slit Width (Right) Designs

## 4.2 ENGINEERING DESIGN

Stress tests and several structural analyses of the XY stage were conducted to ensure that the stage is capable of safely holding the weight of the slit lamp, withstanding the reaction force of the motors, and that movement occurs. For the gear drives used for the rotation systems, calculations were performed to determine if the selected gears experience any interference.

### 4.2.1 Slit Lamp XY Stage Static Friction

The maximum thrust force that the stepper motors can produce onto the slit lamp platform is 25lbs. The static friction force of the slit lamp and platform must be less than 25lbs for the system to move from rest. The force needed to keep the system in motion is less than the static friction force.

$$F_{motor} > \mu_{static} W_{system}$$

The maximum weight of the slit lamp and its components is 30lbs and the maximum possible weight of the slit lamp platform and ball bearings is 10lbs. The friction coefficient noted is between the stainless-steel ball bearings and the surface of the bottom platform. For a maximum possible system weight of 40lbs and a worst-case scenario friction coefficient of 0.6, the motor needs to provide a force of at least 24lbs to get the system to move. Steps can be taken to reduce the friction coefficient such as using a lower coefficient of friction material combination and by using lubricant. Table 1 displays friction coefficients for possible base material combinations for dry and clean environments.

Table 1. Friction Coefficients for Material Combinations

Material Combination		Static Coefficient of Friction
Stainless Steel	Aluminum	0.45
Stainless Steel	Wood	0.2 – 0.6
Stainless Steel	Plastic	0.25 – 0.4

### 4.2.2 Motor Reaction Force and Rod Design

While the maximum force that the motor can exert onto the slit lamp platform is 25lbs, the rods supporting the motor and mount had to withstand the reaction force that the motor applies on the platform. If the rods could not hold the reaction force, the platform would not move. A stress analysis was conducted by taking a distributed 25lb load on the middle on the longer rod where 14in of the 15in rod is exposed. The distributed load was 1.375in located at

the middle of the rod, as a worst-case scenario as shown in Figure 8.

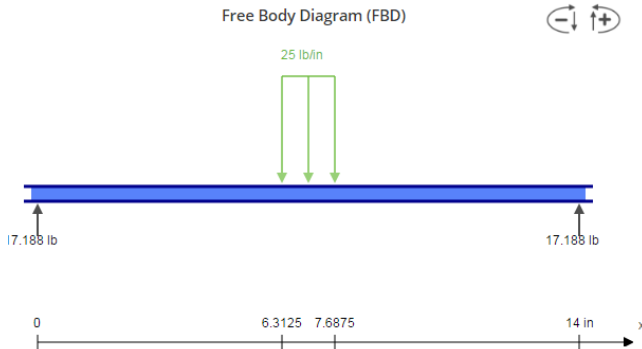


**Figure 8 – Free Body Diagram of Reaction Force on Rod**

Shear force and bending moment diagrams were created to perform a Von Mises failure analysis. The minimum diameter required to hold the motor reaction force was calculated for stainless-steel, steel, and aluminum with an arbitrary factor of safety of 1.25. Once a rod diameter of 5/16in was decided, the factor of safety and maximum rod deflection were calculated. Table 3 displays the results of these calculations.

**Table 2. Rod Design Analysis Results**

Material	Yield Strength	Minimum Diameter	Factor of Safety
Aluminum	13.8 kpsi	0.482 in	0.361
Stainless Steel	72.8 kpsi	0.271 in	1.91
Steel	50.0 kpsi	0.308 in	1.31

Though the 25lb motor reaction force was a worst-case situation, it is important to use rods that withstand this scenario. Aluminum does not perform well under the 25lb reaction load as it fails and undergoes a large deflection of 0.420in, therefore it should not receive consideration for the rod material. Stainless steel and regular steel work fine, but still undergo deflection. Though both stainless and regular steel both work as the rod material, stainless steel was the recommended material.

#### 4.2.3 Gear System Interference

The smallest number of teeth were calculated for both the driver pinion and the circular gear rack. If the selected gears have a tooth count smaller than the smallest allowable amount, interference occurs. Interference occurs when the contact of portions of tooth profiles are not conjugate [4]. A spur gear set of 24 diametral pitch and 20° pressure angle was selected. The circular gear rack had a pitch diameter of 3in with 72 teeth and the pinion had a pitch diameter of 1.25in with 30 teeth. The following equations were used to calculate smallest allowable tooth sizes where  $m$  is the tooth ratio of the gear and pinion. Both the selected pinion and gear satisfy this interference criteria.

$$N_p = \frac{2k}{(1 + 2m)\sin^2\phi} \left( m + \sqrt{m^2 + (1 + 2m)\sin^2\phi} \right) = 7.5T$$

$$N_G = \frac{N_p^2 \sin^2\phi - 4k^2}{4k - 2N_p \sin^2\phi} = 33.5T$$

#### 4.2.4 Stress on Platform and Rod Towers

The slit lamp platform for the XY stage of the Ophthalmic Robot was used to transport the slit lamp in both the X and Y directions. It was powered by the stepper motors referenced earlier in the report. This 10in by 8in platform was supported by eight steel balls 0.5in in diameter. SolidWorks Simulation determined that the platform was able to sufficiently support the weight of the slit lamp without the platform buckling. To take into account cost efficiency and weight of the base, different alternatives for which to build the base were examined. These alternatives included ABS plastic, aluminum, and oak wood. For the simulation, a 25lb distributed load in the shape of the slit lamp’s bottom platform acted on top of the platform. The platform rests on the eight stainless steel ball bearings noted above. It was intended, that as the slit lamp is resting on the platform or while in use, that weight is evenly distributed across that designated area. The maximum stress acting on the platform during the simulation was noted as approximately 13.4psi. This with a very low amount of stress produced high factors of safety. The weight of the slit lamp produced a compression force on the platform, which resulted in a low possibility of failure. It was determined that the platform could be made out of all three considered materials. Figure 9 displays the stress distribution acting on the platform. The stainless-steel ball bearings support the load.

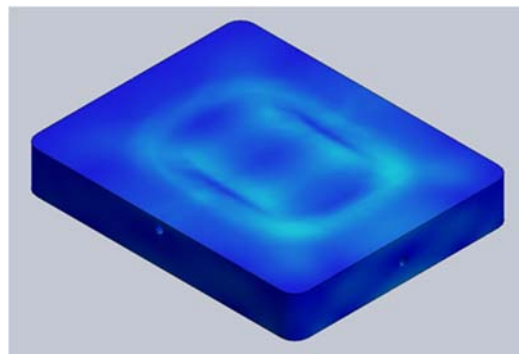


**Figure 9 – Slit Lamp Platform Stress Distribution**

A static study was conducted in SolidWorks Simulation to test the structural integrity of the brackets that supported the rods above the table. The bottom of the brackets were fixed to emulate it being attached to the bottom platform. The reaction forces from the free body diagram at the end of each support was used in the bracket static study. The result of the simulation indicated that the maximum stress was 296.7psi. The maximum stresses occurred inside the holes where the rods act on it and at the bottom corner of the bracket. Figure 10 displays the stress distribution on each rod bracket tower. This result indicates that the brackets can be made out of most materials with the primary options being aluminum, ABS plastic, and wood.

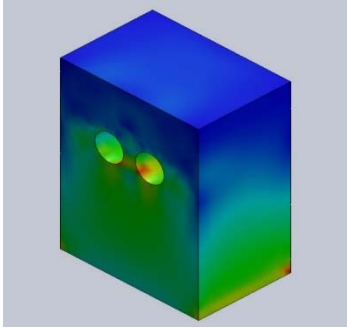


**Figure 10 – Stress Distribution on the Rod Brackets**

### 4.3 PROTOTYPE CONSTRUCTION

For the XY stage, the slit lamp sat atop a moving wooden platform that rolled on eight stainless steel ball bearings. As the platform was pushed by the linear stepper motors, the ball bearings rolled, allowing for ease of movement. The platform was capable of moving in both lateral directions. The linear stepper motor lead screw nuts were glued to the outside of the drilled holes in the sides of the moving platform. The stepper motors rested inside of 3D printed mounts that slid along steel rods. The rods were supported by wooden rod bracket towers at the ends of the bottom platform where everything rested. Each motor mount was meant to slide as the other motor was in motion. Figure 11 shows the constructed XY stage.

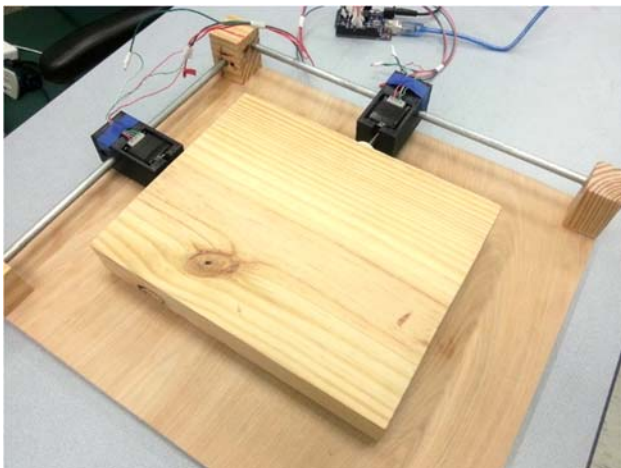


**Figure 11 – XY Stage Assembly**

Once the design phase was completed, the prototyping process was carried out. Due to cost constraints, a decision was made to make the XY stage out of wood. Wood is a cheap alternative to machined aluminum and can withstand many possible structural stresses that may act on it. Many other components of the Ophthalmic Robot were 3D printed with PLA thermoplastic. The other components that could not be 3D printed were bought. Such components include the motor mount rods, stainless steel ball bearings, the drive belts, and all motors used.

Construction of the slit lamp motor systems became an assembly operation once the pulleys, gears, and mounts were 3D printed. For the slit height and slit width motor systems, the servo motors were

attached to the sides of the slit lamp using a combination of metal brackets and hose clamps. The pulleys were attached to the servo motors and the belts were cut to size out of the friction tape. The friction tape was then tensioned and connected together to create the belt drives. Figure 12 shows the revamped slit height motor system and Figure 13 shows the revamped slit width motor system.



**Figure 12 – Revamped Slit Height Motor System**

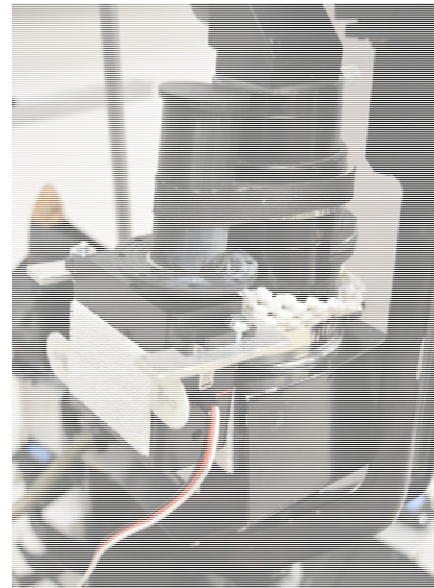


**Figure 13 – Revamped Slit Width Motor System**

For the microscope and lamp rotation motors, a lower motor mount was first attached to the back bottom of the slit lamp. The magnification system rotation motor was attached to the mount with 3mm double-sided tape. The circular gear racks were glued to the slit lamp and the pinion gears were attached to the servo motor output shafts. Care was taken to ensure that the gear meshed with the circular gear rack. For the illumination system rotation motor, two 3D printed brackets were used to connect it to the magnification system rotation motor underneath it. The upper motor was inverted and the gear was meshed with the circular gear

rack. Figure 14 shows the revamped lens rotation system and lamp rotation system.

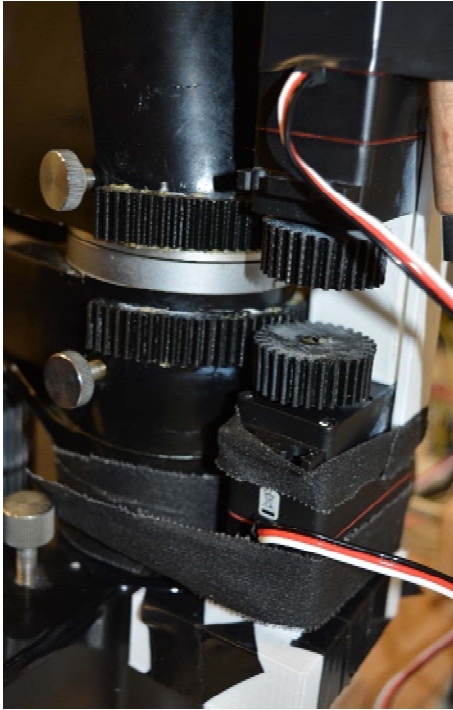


**Figure 14 – Revamped Lens Rotation and Lamp Rotation**

The servo motors were all connected to an Adafruit servo shield that had an external source powering the motors. The stepper motors were connected to stepper drivers on a breadboard with an external 12V power source powering the motors. The servo shield and the stepper motors were connected to a BeagleBone Black that was used as the primary controller. The same software used for the first prototype was used in the controller with updates made to accommodate the stepper motor and XY stage. Figure 15 shows the completed setup of the Ophthalmic Robot and the computer interface.

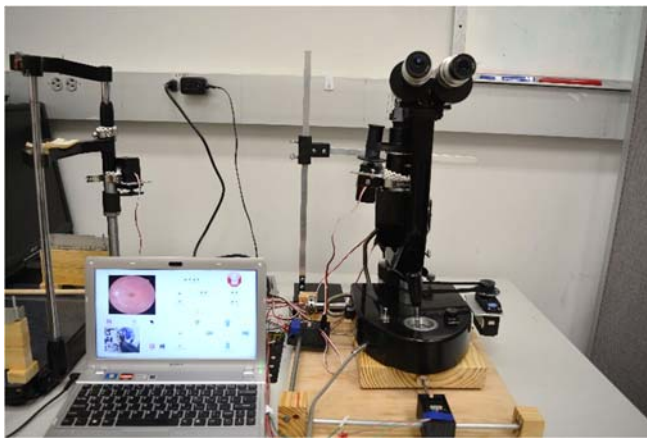


**Figure 15 – Ophthalmic Robot and Computer Interface**

## 5. RESULTS

After assembling the XY stage and mounting the servo motors, the design was tested by running the motors and seeing if the platform moves as intended. After checking the movement of the motor mounts of the XY stage, it was necessary to remove a rod from each railing to give the mounts free movement. The holes of the rod towers did not line up perfectly due to manufacturing constraints, so having two parallel rods for each direction was not feasible. Once the motor mounts could move freely, the motors were run to test the movement of the platform. The platform was able to move in the two directions, both horizontally and vertically. When given the required 12V power source, the motors were able to provide movement to the platform with the slit lamp on top of it at a slow pace of approximately 1mm/s. Despite this slow pace, there are a few advantages. The slit lamp is a delicate instrument that would require a slow acceleration and slow deceleration to be able to move without tipping over. The slow pace also allows the doctor controlling it to accurately position the slit lamp without having to worry about overshooting the intended position.

The slit lamp adjustment systems were each tested to see if they rotated their assigned knob or position. For the slit height and slit width adjustment systems, the friction belts in each system rotate the knobs as intended. They both work at varying motor rotation speeds and in small increments. For the lens rotation system and illumination rotation system, both motors were tested to see if both entities rotate as designed. Both systems rotate smoothly due to the gear pinions and circular gear racks being in mesh and having good contact to provide smooth rotation. Some work can be done in the future to improve the rear servo mounting brackets, however, as they have a tendency to move away from the slit lamp in some instances. Friction tape would ideally also be replaced by custom-sized rubber or silicone belts as the tape must be adjusted and replaced frequently.

Due to the nature of this project, the testing done was more on a trial and error basis. This is because the motors can be controlled to go at any speed within their capabilities. The performance of the motor systems heavily relies on the programming. The main testing that was done was checking if the motor systems run properly through the computer interface and contact between the motor systems and the slit lamp was adequate.

## 6. ACKNOWLEDGMENTS

David Larsson, Daniel Irving, Shehryar Effendi, and Joshua Dubin would like to thank Ph.D. candidate Melissa Morris and Dr. Sabri Tosunoglu for providing support and guidance throughout the duration of this project. They would also like to thank Lars-Erik Larsson for his much appreciated assistance in the construction of the XY stage movement platform. Finally, the authors extend their thanks to Dr. Austin Bach of TYB, Inc. for providing financial support for the first iteration of this project.

## 7. REFERENCES

- [1] Melissa Morris, Sabri Tosunoglu, "Teleoperated Ophthalmic Examination Robot," Florida International University, Miami, FL, May 2016.
- [2] College of Optometrists Associates, "Slit Lamps," College of Optometrists [Online], United Kingdom, 2016. Available: [http://www.collegeoptometrists.org/en/college/museyeum/online\\_exhibitions/optical\\_instruments/slit\\_lamps.cfm](http://www.collegeoptometrists.org/en/college/museyeum/online_exhibitions/optical_instruments/slit_lamps.cfm)

[3] Jane Veys, John Meyler, Ian Davies, "Slit-lamp Examination," Johnson and Johnson Vision Care Institute [Online], 2016. Available: [https://www.jnjvisioncare.co.uk/sites/default/files/public/uk/tvci/eclp\\_chapter\\_2.pdf](https://www.jnjvisioncare.co.uk/sites/default/files/public/uk/tvci/eclp_chapter_2.pdf)

[4] Richard G. Budynas, J. Keith Nisbett, "Shigley's Mechanical Engineering Design Tenth Edition," McGraw-Hill Education, New York, NY, 2015.

# Optical Subsystem for CubeSat Missions

Pradeep Shinde, Carlos Obella, Ibrahim Tansel, Sabri Tosunoglu

Department of Mechanical and Materials Engineering  
Florida International University  
Miami, Florida 33174

pshinde@fiu.edu, cobel001@fiu.edu, tanseli@fiu.edu, tosun@fiu.edu

## ABSTRACT

The CubeSat program has facilitated space access for students for over a decade through the innovative design of versatile, and inexpensive research platforms. However, what started as an initiative for academic institutions to be able to data gathering platforms that can be cheaply and rather quickly assembled and launched, has now revolutionized the way even more established agencies look at orbital and space exploration. The mission type determines the payload and capabilities a CubeSat must have. Standard size of a 1U CubeSat is 10 cm x 10 cm x 10 cm. Due to the small dimensions of the pico-satellite, new innovative subsystem designs must be used to accomplish similar mission parameters that larger platforms perform with ease. This paper presents the design and optimization of a payload originally designed for ROARSAT, a larger 3U satellite of dimensions 10 cm x 10 cm x 30 cm developed at Florida International University. This is accomplished by arranging a set of achromatic lenses with a determined focal length to shrink the overall size of the system, while at the same time providing greater magnification of the imaged object.

## Keywords

CubeSat; Optical System; Lens; Focal length; Magnification

## NOMENCLATURE

$f$	Focal Length, $mm$
$BFL$	Back Focal Length, $mm$
$d_i$	Image Distance, $mm$
$d_o$	Object Distance, $mm$
$h_i$	Image Height, $mm$
$h_o$	Object Height, $mm$
$d$	Lens Separation, $mm$
$M$	Magnification Factor
$S$	Sensor Area, $mm^2$
$n$	Number of Pixels
$A$	Aspect Ratio

## 1. INTRODUCTION

The CubeSat standard has spurred the development of small spacecraft missions along with recent advances in technology miniaturization. Consequently, the space industry that mainly produced large, sophisticated aircraft developed by a large team of engineers, has started to change and opt for smaller platforms

radically [1]. This has opened opportunities for small commercial and academic institutions to develop spacecraft and its missions. Most of the CubeSat missions focus on earth imaging, but other applications such as attitude calibration, proximity monitoring, star tracking [2], and exo-planet tracking [3] have also been presented.

Most CubeSat designs use two types of optical systems. Refractive systems use a single lens or a combination of lenses to achieve the desired resolution and magnification [4]. Reflective optical systems use a combination of mirrors for the same effect. Both types of optical systems have their advantages. In one hand, refractive optical systems have lower tolerances when it comes to the alignment of the optical elements. In the other hand, reflective systems tend to be more compact [5].

The proposed design is an optimization of a single lens optical subsystem developed by the ROARSAT team. ROARSAT is a 3U pico-satellite developed by fellow members of the Near Earth Explorer (NEE) student club at Florida International University (FIU). The ROARSAT team entered the 2016 FUNSAT competition sponsored by NASA and organized by the Florida Space Grant Consortium (FSGC) where they placed first runners up [12].

This paper is organized as follows: NEESAT's mission is elaborated in section 3. In this section, relevant values such as desired resolution, and object distance are determined. Section 4 discusses the parameters for the design and optimization of the optical system, a detailed account of the manufacturing of the design, and finally a description of validation techniques used to test the optical system. In section 5 offers a discussion of cost and weight estimates for the system. This section is followed by sections 6, 7 and 8 which includes a conclusion, acknowledgments, and references respectively.

## 2. PROBLEM STATEMENT

NEESAT's mission is designed to be carried out from a low earth orbit (LEO). From this LEO NEESAT is to photograph the earth's surface and the atmosphere to gather various types of data. This data includes determination of ocean levels, and animal migration patterns; meteorological studies such as cloud formations, and tropical storm tracking; and finally, detection of hazards to human life caused by various natural phenomena. To accomplish this mission, NEESAT's payload includes various off the shelf commercial components as well as a custom optical design. Off the shelf items include a complementary metal-oxide-semiconductor (CMOS) sensor with a through the lens (TTL) camera for which

optics were modified to accommodate the new optical design. A plan to incorporate a thermal camera and an HD camera is also being considered but has not yet been implemented. The TTL camera must capture an area of 25 km x 25 km from 600km above the surface of the earth, and the other cameras should also have similar capabilities.

### 3. OPTICAL SYSTEM DESIGN

#### 3.1 Single Lens System

The system developed by the ROARSAT team could focus on to an area with an  $h_o$  of 25km, and because they had a ¼ inch format sensor, they decided to use an image height ( $h_i$ ) of 6.35mm. The  $d_o$  of 600km is determined by the LEO that the satellite will assume. All the parameters for the design of this system are predetermined except for  $d_i$  and  $f$ . These are critical values because they determine whether the system will fit inside the confined space provided by the 3U platform. To determine these parameters, following calculations were made.

Using the magnification equation

$$M = \frac{-h_i}{h_o} = \frac{d_i}{d_o} \quad (1)$$

Notice that the negative sign means that the image will be inverted. Solving for  $d_i$  we get

$$d_i = \frac{-h_i d_o}{h_o} \quad (2)$$

From the lens equation, we can say that

$$\frac{1}{f} = \frac{1}{d_o} + \frac{1}{d_i} \quad (3)$$

Since  $d_o \gg d_i$  we can say that  $d_i = f$ . Therefore, the focal length of the system is 152.4 mm.

The system was designed in SolidWorks the assembly can be seen in Figure 1. It features a 159.1 mm long carbon fiber tube with an outer diameter of 35mm and an inner diameter of 30mm. It also has a 5mm by 6.7mm fitting for the lens. This design could fit inside a 3U satellite but not a 1U. Therefore, optimization of the system was necessary.

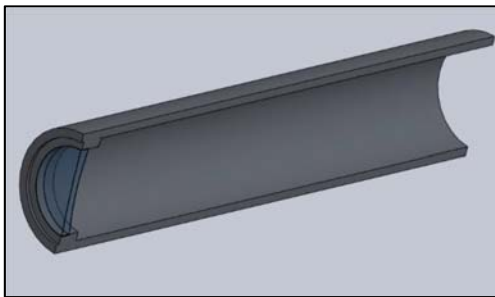


Figure 1. ROARSAT Optical Design

#### 3.2 Single Lens System Simulation

A simulation was run for this system to verify this data. The software used was WinLens3D. This is a free software developed by Qioptiq [6]. It is very easy to use and has a vast library of materials each with their respective properties.

The lens chosen for this system was an Edmund achromatic doublet that was modeled from the manufacturer specifications but slightly modified to have a 152.4mm focal length for simulation purposes

[7]. Its diameter is 25mm and maximum aperture is 24mm. Lens parameters can be seen in Figure 2.



Figure 2. Lens Parameters for Simulation of ROARSAT Optical System

The results for this simulation can be verified in the paraxial system table as seen in Figure 3.

Object side: data vet	First surf	Image side: data vet	LAST surf
Object distance		Infinity	Image distance
Eff. f = FF		-152.386	Eff. f = FF'
Front Focus: F		-151.157	Rear Focus: F'
F-Plane 1: F		1.241	F-Plane 2: F'
Nodal Point: N = FF		1.241	Nodal Point: N' = F'f
Entrance Pupil		0.000	Exit Pupil
Fret - Last surf		7.900	Fret - image surf
Object height			Image height
Lagrange invariant		0.500	

Figure 3. Paraxial System Values for ROARSAT system simulation

#### 3.3 Compound Optical System

It is to be noted that ¼ inch is not really  $h_i$  nor is it the size of the sensor. This measurement is a generalized parameter to categorize certain types of sensors. To calculate the new  $h_i$  the number of pixels, the image size and the pixel size need to be considered. The maximum image size that the sensor can produce is 640 \* 480 pixels, it means that the sensor has a total of 307200 pixels, and an aspect ratio of 4:3. Each pixel has an area of  $5.6\mu m * 5.6\mu m$  so this means that the total sensor area is  $9.634mm^2$  [8]. The exact height of the sensor can be obtained by using the following formula:

$$h_i = \sqrt{\frac{S}{A}} \quad (4)$$

This is acceptable  $BFL$  for the 1U satellite. But the  $BFL$  is not the only parameter that needs to be improved by adding another lens we can further reduce the spherical and chromatic aberrations [10]. That is the main reason why it was decided to build a system with compound achromatic doublets.

To determine the focal lengths of the individual lenses the following formula was used.

$$BFL = \frac{f_2(d-f_1)}{d-(f_1 f_2)} \quad (5)$$

Since the  $BFL$  is known, but  $f_1$  and  $f_2$  are not. This calculation was done iteratively in excel. Table 1. shows the results. The values for  $f_1$  and  $f_2$  that were used are for commercially available 25mm achromatic doublets. It is also to be noted that to save space  $d$  was kept at a minimum of 1mm.

Table 1. Optimal Lens Choices for a Compound

Optimal choices for compound optical system														
di1	do1	f1	M1	d	imput	di2	do2	f2	imput	M2	Mt	ho	imput	hi
150	6.00E+08	150	-2.5E-07	1	59.83936	149	100	0.40161	-1.004E-07	2.50E+07	-2.51			
175	6.00E+08	175	-2.9E-07	1	63.50365	174	100	0.36496	-1.064E-07	2.50E+07	-2.6612			
300	6.00E+08	300	-5E-07	1	63.11346	299	80	0.21108	-1.055E-07	2.50E+07	-2.6385			

The closest choice for this system is one with lenses of  $f_1$  of 175mm and  $f_2$  of 100mm. Figure 4 shows a Solidworks design of the system that was analyzed. It features an optical tube with an outside diameter (OD) of 35mm and an inside diameter (ID) of 30mm. To mount the lenses short sections of a 30mm OD and 25mm ID are cut to the edge thickness dimensions and fitted into the tube. To assemble the system tubes, the tubes must be cut in half then the lens can be mounted. The system then can be sealed by a clamp. The material is carbon fiber to make the design as light as possible.



Figure 4. Section View of Compound Lens System

### 3.4 Compound Lens System Simulation

A simulation was run on WinLens3D with the same parameters as for the ROARSAT but with different lenses. The results of this simulations are concordant with the theoretical calculations. Figure 5a and Figure 5b depict the lenses chosen for the simulation and their respective effective focal lengths (EFL).

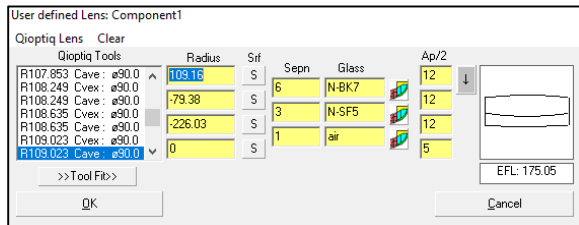


Figure 5a. Lens 1 Parameters



Figure 5b. Lens 2 Parameters

A paraxial graph for the simulated system is shown in Figure 6. The paraxial values for such simulation can be seen in Figure 7.

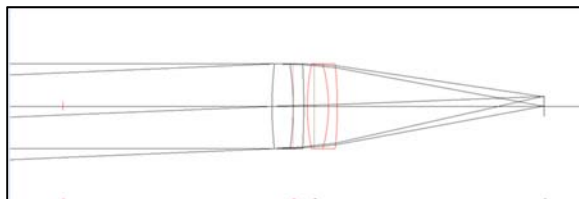


Figure 6. Compound Optical System Paraxial Simulation

Object side: data vet FIRST surf	Image side: data vet LAST surf	
Object distance	Infinity	Image distance
f1 = FF	65.223	f1 = FP
Front Focus: F	59.270	Rear Focus: F'
F Plane 1: F	5.953	F Plane 2: F'
Nodal Point: N = F'F	5.953	Nodal Point: N' = F1
Entrance Pupil	0.000	Exit Pupil
First - Last surf	16.500	First - image surf
Object height	---	Image height
Lagrange Invariant	0.500	

Figure 7. Compound Optical System Paraxial Values

### 3.5 Triple Compounding

To optimize the system, several options were considered. A triple compounding system was proposed.

The main advantage of adding a lens and having a triple compounding system is the added lens power. The additional lens can refract the light further and can create different focus. Therefore, shortening the  $BFL$  while also increasing the maximum possible magnification. This also allows for the system to focus on a smaller area.

Another advantage of adding a lens is the added versatility of the system. This system could potentially be re-focused by rearranging the distances between the lenses.

Lastly, the addition of another lens further reduces the effects of achromatic aberration.

To determine the  $BFL$  of a system of more than one lens the lens equation must be applied to each optical element of the system [9]. These calculations must be iterated using elements of different  $f$ . It was calculated before that an optimal  $BFL$  of 64.5 mm is desired to have  $h_o$  of 25 km. Therefore, only combinations of lenses of this type are to be considered. Calculations were conducted as seen below:

1. The first lens equation is the following:

$$\frac{1}{f_1} = \frac{1}{d_{o1}} + \frac{1}{d_{i1}} \quad (6)$$

Here  $f_1 = 175\text{mm}$ ,  $d_{o1} = \infty$ . Since the object is assumed to be located at infinity, then  $d_{i1} = f_1 = 175\text{mm}$ .

2. The second lens equation is the following:

$$\frac{1}{f_2} = \frac{1}{d_{o2}} + \frac{1}{d_{i2}} \quad (7)$$

Here  $f_2 = -100\text{mm}$ ,  $d_{o2} = d - d_{i1}$ , where  $d = 1\text{mm}$  and is the distance between the first and second lenses. Therefore,  $d_{o2} = -174\text{mm}$ . Solving for  $d_{i2}$ ,  $d_{i2} = -235.1\text{mm}$  it is negative; therefore the image here is upside down and real.

3. The third lens equation is the following:

$$\frac{1}{f_3} = \frac{1}{d_{o3}} + \frac{1}{d_{i3}} \quad (8)$$

Here  $f_3 = 50\text{mm}$ ,  $d_{o3} = d - d_{i2} = 1\text{mm} + (-235.1)\text{mm} = 236.1\text{mm}$ , solving for  $d_{i3}$ ,  $d_{i3} = 63.43\text{mm}$ .

The total magnification ( $M_t$ ) can be calculated in the same manner by applying the magnification equation for each optical component. The product of  $M_1$ ,  $M_2$ , and  $M_3$  gives the total magnification. For this system,  $M_t = -1.06 \times 10^{-6}$  this is an improvement of 36.3% compared to the single lens optical system.

**Table 2. Optimal Lens Choices for a Compound**

$d_{i1}$ (mm)	175.0
$d_{o1}$ (mm)	6.00E+08
$f_1$ (mm)	175.0
$d_{i2}$ (mm)	-235.1
$d_{o2}$ (mm)	-174.0
$f_2$ (mm)	-100.0
$d_{i3}$ (mm)	63.43
$d_{o3}$ (mm)	236.1
$h_i$ (mm)	-2.647
$M_t$	-1.06E-7

The overall length of the system is 80.5mm this is a 47.2 % decrease in the overall length of the system compared to the one used for the ROARSAT. Also by adding the two lenses, the magnification has been improved by 36.3%. This means that this system will be able to zoom in and focus on an area with a height of 10.6 km. This system was chosen because of the great performance characteristics and the fact that this system can fit inside the 1U platform.

The design of this system as seen in Figure 8 features a fiberglass tube with an inner diameter of 25mm, and an outer diameter of 26mm it features three 1mm x1mm and one 1mm x2mm 41 inserts to fix the lenses in place. It also has the back sealed with a small opening that is the size of the desired image. This is done so that no unwanted light can be captured by the sensor.

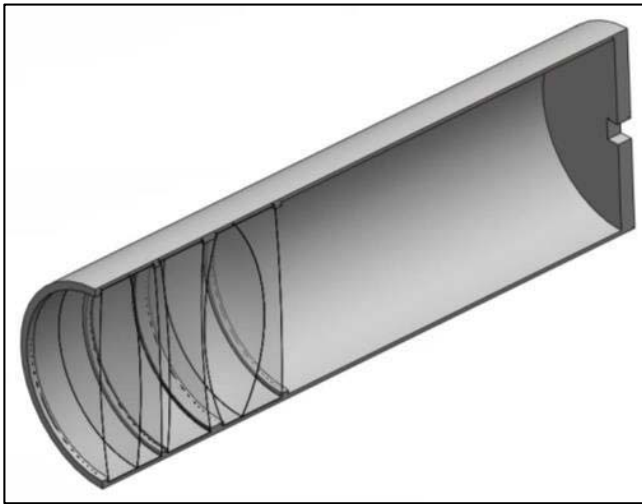


**Figure 8. Section View of Triple Compound Optical System**

The material used for this system is fiberglass this was picked because it is a cheap light-weight option that can protect the lenses. The interior of the tube is coated with a special anti-reflective paint that reduces the effects of stray light within the tube, therefore improving image quality.

### 3.6 Triple Compounding System Simulation

A simulation was run again on WinLens3D Basic to have a basis of comparison to the theoretical values. The three lenses with the predetermined  $f$  values were modeled within the software and arranged according to the design. Figure 9a, Figure 9b, and Figure 9c show the parameters of each lens that were modeled after commercially available lenses. Figure 10 and Figure 11 show the

paraxial graph of the system and the paraxial values of the system respectively.

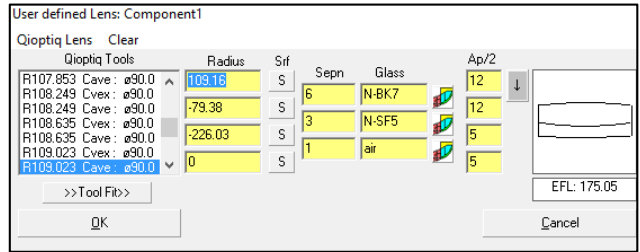


**Figure 9a. Lens 1 Parameters**

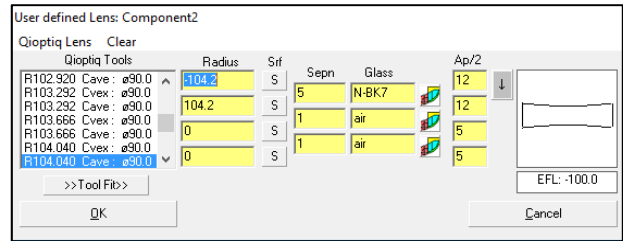


**Figure 9b. Lens 2 Parameters**

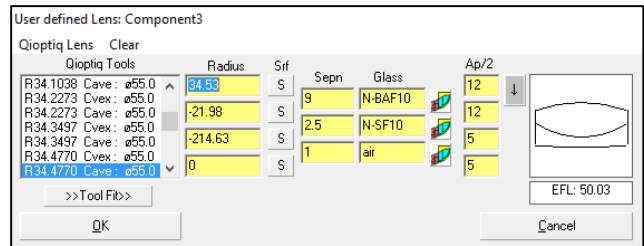


**Figure 9c. Lens 3 Parameters**

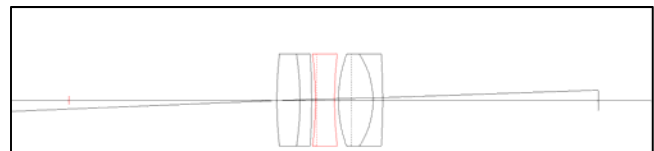


**Figure 10. Triple Compounding Paraxial Simulation**

Object side: data vet FIRST surf	Image side: data vet LAST surf	
Object distance	Infinity	Image distance
f1 = F1'	44.304	f = F1'
Front Focus: F	54.066	Rear Focus: F'
P Plane 1: P	10.229	P Plane 2: P'
Nodal Point: N = F1'	10.229	Nodal Point: N' = F1'
Entrance pupil	0.000	Exit pupil
Fast - Last surf	27.500	Fast - image surf
Object height	---	Image height
Image height	---	Magnification

**Figure 11. Triple Compounding Simulation Paraxial Values**

## 4. CONSTRUCTION AND TESTING

### 4.1 Triple Compounding Construction

The optical system was manufactured manually because refractive systems have lower tolerances when it comes to lens alignment. The manufacturing process included several steps. First, a polyurethane cylindrical mold of a diameter of 25 mm and a length of 100mm was formed by sanding. Then two layers of fiberglass cloth were wrapped around the mold, bonded and hardened with a mixture of fiberglass resin, resin hardener, and acetone. Once the fiberglass was hardened the mold was removed, and all the surfaces

of the optical tube were sanded to have a smooth finish. Then the tube was cut into its designed dimensions with a bandsaw. Another cut was made longitudinally to fit the lenses. The lens fittings were molded from excess material and bonded to the inner surface of the tube using an aerospace certified epoxy compound. Then the whole tube was painted with a light absorbing optical coating. This coating is manufactured by Albrecht and was highly recommended by experienced telescope manufacturer Gerd Neumann Jr [11]. Finally, the lenses were fitted, and the tube was closed and clamped with two light-weight aluminum clamps.



Figure 12. Final Optical System Assembly

## 4.2 Testing

The system was tested to validate the theoretical and simulation values of the design. Since it would be unfeasible to take an image of 25 km from 600 km away at the earth's surface, the test setup was scaled down. Instead, a 25 cm object height was to be photographed from 6 m.

To accomplish this, the TTL camera was fixed behind the optical tube and was plugged into a Beagle Bone Black (BBB). The BBB was operated by a program developed by the author (Dr. Pradeep Shinde) that prompted the camera to shoot a picture every 10s.

The result of this test gave an image height of 25 cm as designed. Due to the low quality of the camera, the image quality is not optimal; therefore, a higher quality camera is proposed for future testing.



Figure 13. Optical System Setup

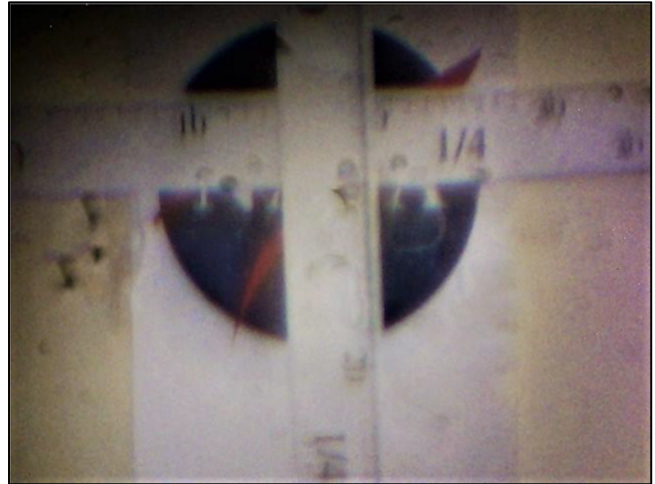


Figure 14. Optical System Test Image

The overall size of the system not only assures that it will fit in the satellite, but it is imperative to the overall quality of the image that is to be processed by the camera. As it was found in testing a slight deviation on the placement of the camera behind the tube would have significant deterioration of image quality. Therefore, it is imperative that the camera is placed right at the focal plane of the system.

## 5. DISCUSSION

It is important to notice that all previous calculations were made assuming the lenses are thin. However, the achromatic lenses are rather thick because they combine two different lenses. The thin lens estimation can be used for the first two lenses but the third lens has a thickness of 13.5mm; thus, the assumption is no longer valid. This is demonstrated with a simulation made with WinLens3D Basic. The paraxial results for this simulation are shown in Fig. 11. It clearly shows that the image distance is measured from the last surface, or be it the surface closest to the sensor, but this is not the BFL of the system. The BFL should be measured from the last lenses principal plane [10]. For a thin lens these would be one and the same, but for the 50mm focal length, the principal plane is located 9.351mm from the last surface. Therefore, the sensor can be located at a shorter distance from the last surface making the entire system smaller.

The total cost of the optical system was of \$275.25 the price of the camera was not included because it was provided by the NEE club at FIU. Because a very light composite material was used for the optical tube, the total weight of the system was reduced to 67.4g as it can be seen Table 3.

Table 3. Cost and Weight Estimate

Component	Weight	Length	Diameter	Cost
175mm <i>f</i> AD Lens	15 g	9.0 mm	25 mm	\$89
-100mm <i>f</i> Lens	8g	6.4 mm	25 mm	\$39
50mm <i>f</i> AD Lens	15.9g	11.5mm	25mm	\$89
2 x Aluminum Clamp	19g	N/A	30mm	\$7.66
Optical Paint	N/A	N/A	N/A	\$21.11
Optical Tube	9.5g	80.5mm	30mm	\$29.48
Total	67.4g			\$275.25

## 6. CONCLUSION

A small light weight cost effective optical system has been designed, manufactured and tested. The system can focus on to an area of at least 25km. The overall size of the system was reduced from the ROARSAT design by 47.2% without sacrificing functionality. This was accomplished by compounding 3 lenses, two biconvex achromatic doublets, and one biconcave lens. The combined lens power not only reduced the size of the system but also increased its magnification by 36.3%.

The system was manufactured and tested with satisfactory results. The overall fiberglass optical tube though very lightweight will have to be further tested for its integrity under critical conditions.

A vibration test is also recommended in the future to verify that the alignment of the lenses does not become compromised during launching. Furthermore, several image quality tests must be conducted to assure maximum performance of the system.

## 7. ACKNOWLEDGMENTS

The development of NEESAT comes as a direct result of the work of the ROARSAT team. Therefore, the authors acknowledge the support guidance of the members of this team and recognize their achievements as first runners up for the FUNSAT 2014-16 competition organized by NASA's Florida Space Grant Consortium (FSGC). The authors also acknowledge the immense support provided by the Department of Mechanical and Materials Engineering (MME) at Florida International University (FIU). The authors finally wish to extend their gratitude toward members of the Near Earth Explorer (NEE) Student Club at FIU for helping with the development of the NEESAT optical system and for continuing its testing and optimization.

## 8. REFERENCES

- [1] Poghosyan, A., & Golkar, A. (2017). CubeSat Evolution: Analyzing CubeSat capabilities for conducting science missions. *Progress in Aerospace Sciences*, 59-83. Retrieved March 26, 2017, from <https://www.journals.elsevier.com/progress-in-aerospace-sciences>.
- [2] Kuuste, H., Eenmaa, T., Allik, V., Agu, A., Vendt, R., Ansko, I., Noorma, M. (2014). Imaging System for nanosatellite proximity operations. *Proceedings of the Estonian Academy of Sciences*, 63(2), 250-257. Retrieved March 26, 2017, from [www.eap.ee/proceedings](http://www.eap.ee/proceedings).
- [3] Viscio, M. A., Viola, N., Corpino, S., Stesina, F., Fineschi, S., Fumentì, F., & Circi, C. (2014). Interplanetary CubeSats system for space wather evaluations and technology demonstrations. *Acta Astronautica*, 104(2), 516-525. Retrieved April 26, 2017, from <http://www.sciencedirect.com.ezproxy.fiu.edu/science/article/pii/S0094576514002045>
- [4] Nakamura, Y., Funase, R., Nagai, M., Enokuchi, A., Nojiri, Y., Funane, T., . . . Nakasuka, S. (2010). Extensible Boom-Based Optical System for Nano-Scale Remote Sensing Satellite "PRISM". 19th Annual AIAA/USU Conference on Small Satellites. Retrieved April 26, 2017.
- [5] Champagne, J. A., Hansen, S. M., Newswander, T. T., & Utah State University Research Foundation Space Dynamics Laboratory. (2016). CubeSat Image Resolution Capabilities with Deployable Optics and Current Imaging technology. 28th Annual AIAA/USU Conference on Small Satellites. Retrieved April 26, 2017.
- [6] Qioptic. (n.d.). WinLens3D Basic [Computer software]. Retrieved January 5, 2017, from <http://www.winlens.de/index.php?id=23>
- [7] Edmund Optics Inc. (n.d.). 25mm Dia. x 150mm FL, MgF2 Coated, Achromatic Doublet Lens. Retrieved January 05, 2017, from <https://www.edmundoptics.com/optics/optical-lenses/achromatic-lenses/25mm-dia.-x-150mm-fl-mgfsb2sub-coated-achromatic-doublet-lens/>
- [8] Adafruit Industries. (n.d.). TTL Serial JPEG Camera with NTSC Video. Retrieved February 06, 2017, from <https://www.adafruit.com/product/397>
- [9] DiMarzio, C. A. (2008, October 8). Compound Lens Example. Retrieved November 10, 2016, from <http://www.ece.neu.edu/courses/eceu646/2008fa/twolens.pdf>
- [10] Edmund Optics Inc. (n.d.). Chromatic and Monochromatic Optical Aberrations. Retrieved November 25, 2016, from <https://www.edmundoptics.com/resources/application-notes/optics/chromatic-and-monochromatic-optical-aberrations/>
- [11] Gerd Neumann, Jr. (n.d.). Deep-black optical paint. Retrieved March 15, 2017, from <http://www.gerdneumann.net/english/instrument-building-parts-teile-fuer-den-fernrohrbau/totmatte-schwarze-optikfarbe-deep-black-optical-paint.html>
- [12] Hernandez, S., Phillippe, C., Salas, W., Shinde, P., Tansel, I., & Tosunoglu, S. (2016). RoarSAT Pico-Satellite. *Proceedings of the 29th Florida Conference on Recent Advances in Robotics, FCRAR 2016*, 271-277. Retrieved May 3, 2017, from <http://www.eng.fiu.edu/mme/robotics/elib/2016FCRAR/FCRAR2016-16-Hernandez-RoarSAT-PicoSatellite.pdf>

# Path-Planning of Miniature Rovers for Inspection of the Hanford High-Level Waste Double Shell Tanks

Sebastián A. Zanlongo, Leonardo Bobadilla, Yew Teck Tan

Florida International University  
11200 SW 8th St  
Miami, FL 33199

szan1001@fiu.edu, bobadilla@cs.fiu.edu, yetan@fiu.edu

## ABSTRACT

The Manhattan Project generated large amount of liquid nuclear waste. This waste is currently stored in million-gallon, double-shell tanks in Hanford. Over the course of 50 years, it is expected that the condition of the tanks would have deteriorated, and one of the tanks has already been found to have leaked. Currently, inspection of the tanks is limited to a visual inspection of the outer perimeter of the tanks using a pole-mounted camera or large wall-climbing robot. In this paper, we propose a methodology whereby a small inspection robot can efficiently navigate a series of small refractory slots located at the bottom of the tanks.

## Keywords

robot, robotics, path-planning, path planning, radiation, deactivation and decommissioning, D&D, sampling

## 1. INTRODUCTION

During WWII's Manhattan Project, large amounts of nuclear waste were generated. Much of this was in liquid form, and stored in large, double-shelled tanks located at the Hanford Site, WA (Figure 2). Over the course of many years, it is expected that the condition of these tanks would have deteriorated. However, inspection of the tanks has been very limited. This is primarily due to the construction of these tanks, where the only way to meaningfully gather data is via visual inspection with a pole-mounted camera, or camera mounted on a wall-climbing robot [1], [2]. As these methods are unable to fully inspect the bottom of the tank, we propose augmenting this inspection to incorporate navigating a small tethered robot (Figure 1) [3] through the series of 2.5in x 1in refractory slots (Figure 1, Figure 3) sandwiched between the bottom of the double shells.

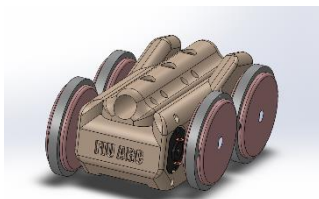


Figure 1: Mini-Rover Robot

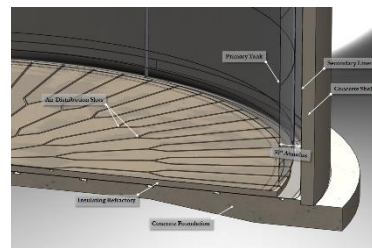


Figure 2: Tank Cutaway

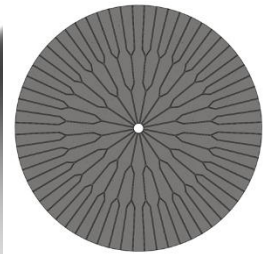


Figure 3: Slot Representation

## 1.1 Refractory Slots

The refractory slots follow a radial, forked structure. Initially, 16 slots radiate outwards from the center. These split into 32 slots, followed by 64 slots at the end. Apart from the large network formed by the refractory slots, note that there are 26 tanks to inspect.

## 1.2 Robot

The robot is represented as a point robot, present along one of the vertices or edges of the refractory slot graph. The robot has the following attributes:

- Position  $(x, y)$
- Tether length
- Visit queue representing the locations to visit, in the order in which to visit
- Planned path to take to satisfy visit queue

Here, we present a path-planning algorithm with the goal of reducing the time needed for the robot to survey the tank bottom. The remainder of this paper is organized as follows: in Section 2, we review the related literature. In Section 3, the problem is stated, and the solution explained in Section 4. Simulation results are shown in Section 5, and the conclusion presented in Section 6.

## 2. RELATED WORK and PROBLEM STATEMENT

Traditional radiation mapping solutions often assume a 2-dimensional planar environment with little or no restrictions on the direction of movement [4], [5], [6]. Being limited to a series of

refractory slots incurs a much higher movement cost, and makes common strategies such as “lawnmower” (zig-zag) movement impractical. Moreover, many of the existing approaches neglect the presence of a tether which constrains the way in which the robot can move. A tether not only limits the distance a robot can travel overall, but may also force the robot to return to “reel in” some of the deployed tether so that it can reuse that tether to reach other locations.

### 3. PROBLEM STATEMENT

Given a robot, a graph representation  $G$  of the refractory slots, and a set of locations  $S$  at which we would like to sample, how can we visit these locations in such a way that we can satisfy the robot’s constraints, and simultaneously minimize the distance travelled, thereby reducing the sampling time?

### 4. METHODOLOGY

Our approach is organized as follows: the refractory slot graph representation is discretized such that it reflects the level of resolution desired by operators. Next, sampling locations are selected using either a randomized approach, or an approximate cellular decomposition. Finally, we design a tour that visits each of the desired sampling locations.

#### 4.1 Graph Discretization

The system of refractory slots is represented as a graph. Locations where the slots fork, or intersect the outer perimeter between the primary tank and secondary liner are represented as vertices  $V$ . The refractory slots themselves are indicated by edges  $E$  joining the vertices.

The starting graph representation  $G$  only has vertices where there is a fork or change in angle. As sampling takes place at vertices, we must introduce new vertices along the edges by discretizing them to the resolution required by an operator. This is done by:

1. Selecting a desired minimum edge length
2. Iteratively divide the edge into smaller edges
3. If remainder is less than length of desired edge, amortize it onto the edges

This method produces edges that are of slightly varying lengths, however the average lengths will closely approximate the desired length, and the process can be computed quickly. An alternative approach would be to simply divide the edges into the desired lengths, and leave the remainder as its own – smaller – edge.

The goal of discretization is to allow the operator to select the granularity with which the robot takes samples (samples are taken at each vertex). So, a finer graph with more vertices would indicate that the robot would also take more frequent samples. This is considered here to examine the effects – if any – on path-planning.

#### 4.2 Sampling Strategies

##### 4.2.1 Random Sampling

The simplest method for sampling the tank is to select a random set  $S$  of sample locations. These locations are selected by first choosing a random location in the 2-dimensional  $\mathbb{R}^2$  environment, and then choosing the vertex in the graph that is closest to that point (“snapping” them into place). To sample these locations, we can visit them in the order in which they are created. Naturally this results in a lengthy completion time as there will be instances where two adjacent sampling locations are visited out-of-sequence.

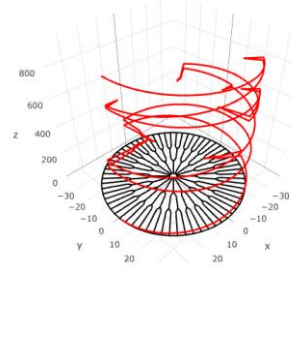


Figure 4: Robot movement over time (isometric view)

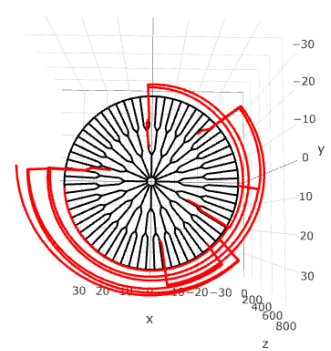


Figure 5: Robot movement over time (overhead view)

##### 4.2.2 Random Sampling with Path Optimization

Given a random sampling technique, we can improve upon it by optimizing the *order* in which the locations are visited. This involves measuring the distances between locations, and selecting the path (or *tour*) that visits each of the locations while minimizing the total distance travelled. One consideration when operating in the refractory slots graph structure is that the graph is not fully connected, nor nearly fully connected. Moreover, travelling between adjacent vertices located in the interior of the tank requires that the robot first return to the perimeter before entering again. This means that a traditional Euclidean distance metric is not suitable. We must instead calculate the length of the path that the robot must take when travelling between the two points. Once this is performed, we can plan a tour that reduces total time.

##### 4.2.3 Grid Sampling with Path Optimization

An alternative to randomly selecting samples is to use an approximate cellular decomposition [7]. This has the benefit of evenly distributing sampling locations regardless of the number of locations selected. Given the grid locations, we then “snap” the locations to the nearest vertex in the graph (as previously described). Next, we again design a tour that reduces total travel distance.

#### 4.3 Path Planning

Provided the set of points to sample, we need to select the *order* in which to visit them. Optimal path planning between multiple locations is a known NP-hard problem as shown in the Travelling Salesman Problem (TSP) [8]. We therefore turn to a heuristic approach. Here, we have selected the nearest neighbor (NN) greedy algorithm. Beginning with the starting location of the robot, we perform Dijkstra’s search [9] to each of the points  $s \in S$  and measure the length of each path. Next, select the point that is closest, and set that as the next location to visit. Using this point, we then repeat the process on the remaining locations  $s \in S$  until finished. On average, this heuristic provides solutions at most 25% longer than the optimal path [10], while remaining fast to compute.

We augment Dijkstra’s algorithm with the constraints that the robot has:

- a limited-length tether
- to travel backwards to exit a slot
- to enter and exit via the same slot, before re-entering an adjacent slot (the robot cannot enter a slot and exit via another due to the space constraint at a fork)

In Figure 5, we show the pseudocode for the modified Dijkstra. The inputs to the algorithm are the adjacency graph  $G$ , **start** and **goal**

```

tethered_dijkstra (G, start, cost, goal, tether, max_length)
01: frontier  $\leftarrow$  PriorityQueue
02: came_from  $\leftarrow$  Dictionary
03: tethers  $\leftarrow$  Dictionary
04: frontier.put(start, 0)
05: came_from[start]  $\leftarrow$  cost
06: cost_so_far  $\leftarrow$  Dictionary
07: tethers[start]  $\leftarrow$  tether
08: while frontier not empty
09:   current  $\leftarrow$  frontier.pop
10:   for neighbor in G[current]
11:     tentative_tether  $\leftarrow$  tethers[current]
12:     if neighbor == previous_position
13:       tentative_tether.pop
14:     else
15:       tentative_tether.append(current)
16:     new_cost  $\leftarrow$  cost_so_far[current] + movement_cost
17:     if (length(tentative_tether) < max_tether_length)
and ((neighbor not in cost_so_far)
or (new_cost < cost_so_far[neighbor]))
or (length(tentative_tether) < length(tethers[neighbor])))
18:       cost_so_far[neighbor]  $\leftarrow$  new_cost
19:       frontier.put(neighbor, new_cost)
20:       came_from[neighbor]  $\leftarrow$  current
21:       tethers[neighbor]  $\leftarrow$  tentative_tether
22: if goal in came_from
23:   path  $\leftarrow$  reconstruct_path(came_from, start, goal)
24:   return path
25: else
26:   return None

```

**Figure 5: Tethered Dijkstra Pseudocode**

locations, **cost** of reaching the current location, the current **tether** occupancy, and the **max length** of the tether. In lines 1 – 7, we initialize a frontier priority queue that contains the vertices to explore in the order provided by a priority heuristic. The *came\_from* dictionary contains the relationships showing how vertices are connected to each other; *cost\_so\_far* indicates the cost to reach each explored vertex, and the tethers dictionary shows the cells occupied by the tether to reach each explored vertex. Each of these is initialized with the starting location of the robot, the tether occupancy, and the cost to reach the current location.

In line 8 and 9, we pop the frontier for unexplored vertices. Line 10 checks each neighbor of a vertex that is currently being expanded. In lines 11 – 15, we keep track of the stack of the *tentative\_tether*, extending or shortening it as the robot moves along. Line 16 considers the cost of reaching the neighbor given the cost already expended, and the additional effort of moving to the next neighbor. In line 17, we check to see if the route under consideration exceeds the maximum tether length. If not, we also check if that neighbor

has not already been explored, or if the route under consideration has a lower movement cost or tether length than the previously examined route. If these conditions are met, save the new route in lines 18 – 21. Finally, we check in line 22 to see if the goal has been reached. If so, we reconstruct the path from the saved neighbors in lines 23 – 24. Otherwise, no valid path exists, and we return None in lines 25 – 26.

The solution here only takes the robot between two locations, **start** and **goal**. To plan a path through all the desired sample locations, the planning process is repeated in a sequential manner where the goal location of the previous search is assigned as the start location for the next search, until all the sample locations have been visited. The corresponding cost and the tether occupancy of the robot are also updated along the searching iterations. Figure 4 shows the movement of a robot throughout the slot network, with the z-axis representing the order of sampling sequence.

## 5. SIMULATION SETUP

The algorithms described in Section 4 were implemented in Python, and tested using multiple scenarios.

These simulations studies consisted of:

- Discretization scales of: 1, 2, 4, 8
- Tether lengths: 200, 300, 400, 800
- Strategies: Random Sampling, Random Sampling with Path Optimization, Grid Sampling with Path Optimization

The discretization scales were selected as they cover the range of edge lengths. At a scale of 1 unit, the smallest edges were unaffected, while the longer edges were discretized; at the 8-unit scale, longer edges were also unaffected.

Tether lengths were chosen so that at 200, the robot had the minimum tether needed to reach every location in the graph. At 300 and 400, the robot would be able to take longer paths before having to return, with 800 providing significantly more play in the tether.

In each of the studies, the robot was tasked with visiting 64 locations. Each of these trials was repeated 40 times, so that the results of the random locations would average out. This gives a total of 1,920 trials.

## 6. RESULTS

In Table 1, we show the distance travelled by the robot with different tether lengths under different strategies. As expected, the grid approach does not change as it always follow the same shortest path across trials. Tether length did not contribute significantly to the total distance travelled, regardless of the strategy. This is likely due to the proximity of the sampling locations, where locations that are far apart require the entire tether to reach, and nearby locations being so close that the tether did not need to be readjusted.

**Table 1**

Distance Travelled (average over scales)			
Tether Length	Random	Random TSP	Grid TSP
200	5731.307951	2070.933453	1829.821503
300	5636.790104	2084.391256	1829.821503
400	5692.83821	2063.240204	1829.821503
800	5703.329017	2099.663685	1829.821503

Next in Table 2, we look at the distance travelled by the robot with different graph discretization scales. As expected, the results

closely mirror the results from Table 1. The discretization resolution should only affect the granularity of sampling, and the results of path-planning should not be affected. This confirms the intuition that granularity of the graph can be tuned as needed depending on how the operator wishes sampling to be performed, and can be modified independently of the path-planning strategy.

**Table 2**

Distance Travelled (average over tethers)			
Scale	Random	Random TSP	Grid TSP
1	6069.814548	2092.21192	1844.3353
2	5819.408242	2062.5826	1992.456128
4	5607.091291	2067.416216	1892.107295
8	5267.9512	2096.017862	1590.387289

Finally, Table 3 shows the distance travelled by the robot under all three strategies, averaged over all trials, scales, and tether lengths. Here, we see that the random TSP solution provides a 63.46% improvement on the completely random approach, while the grid TSP provides a slightly better 67.85% improvement.

**Table 3**

Distance Travelled (average over scales & tethers)		
Random	Random TSP	Grid TSP
5691.066321	2079.55715	1829.821503

## 7. CONCLUSION

In this paper, we have provided a methodology for path-planning for a tethered robot to navigate the series of refractory slots located at the bottom of the Hanford site tanks. We show how Dijkstra's algorithm can be modified to incorporate a tether constraint, and how this search strategy can significantly reduce the distance that the robot travels, and by extension, the amount of time needed for the robot to survey the tank bottom.

In the future, we would like to focus on:

- Using other path-planning strategies such as A\* and Christofides algorithm [11] with the additional tether constraint, and comparing these approaches
- Analyzing how these approaches affect the quality and amount of data gathered by the robot
- Consider additional constraints such as the cost of rounding a sharp corner.
- More analysis of how different tether lengths affect path-planning, especially in edge cases.

## 8. ACKNOWLEDGMENTS

Mr. Zanlongo would like to thank FIU's Applied Research Center (ARC) and the Department of Energy Office of Environmental Management for providing the opportunity to be a DOE Fellow under the Science and Technology Workforce Development Initiative and facilitating research opportunities under the DOE-FIU Cooperative Agreement DE-EM0000598.

## 9. REFERENCES

[1] C. Girardot, J. Engeman, D. Washenfelder, and J. Johnson, "Double-Shell Tank Visual Inspection Changes Resulting from the Tank 241-AY-102 Primary Tank Leak – 14193," *Waste Manag. Conf.*, 2014.

[2] D. Bryson, V. Callahan, M. Ostrom, W. Bryan, and H. Berman, "Life Extension of Aging High Level Waste Tanks," *Pap. HL*, 2002.

[3] R. Sheffield, D. McDaniel, and S. Tosunoglu, "Development of a Prototype Miniature Motorized Inspection Tool for Hanford DOE Site Tank Bottoms," *Florida Conf. Recent Adv. Robot.*, 2015.

[4] C. Cai, B. Carter, M. Srivastava, J. Tsung, J. Vahedi-Faridi, and C. Wiley, "Designing a radiation sensing UAV system," *2016 IEEE Syst. Inf. Eng. Des. Symp. SIEDS 2016*, pp. 165–169, 2016.

[5] J. Towler, B. Krawiec, and K. Kochersberger, "Terrain and Radiation Mapping in Post-Disaster Environments Using an Autonomous Helicopter," *Remote Sens.*, vol. 4, no. 7, pp. 1995–2015, 2012.

[6] P. G. Martin, S. Kwong, N. T. Smith, Y. Yamashiki, O. D. Payton, F. S. Russell-Pavier, J. S. Fardoulis, D. A. Richards, and T. B. Scott, "3D unmanned aerial vehicle radiation mapping for assessing contaminant distribution and mobility," *Int. J. Appl. Earth Obs. Geoinf.*, vol. 52, pp. 12–19, 2016.

[7] H. Choset, "Coverage for robotics—A survey of recent results," *Ann. Math. Artif. Intell.*, pp. 113–126, 2001.

[8] C. H. Papadimitriou, "The Euclidean travelling salesman problem is NP-complete," *Theor. Comput. Sci.*, vol. 4, no. 3, pp. 237–244, 1977.

[9] E. W. Dijkstra, "A note on two problems in connexion with graphs," *Numer. Math.*, vol. 1, no. 1, pp. 269–271, 1959.

[10] D. S. Johnson and L. A. McGeoch, "The traveling salesman problem: A case study in local optimization," *Local search Comb. Optim.*, pp. 215–310, 1997.

[11] N. Christofides, "Worst-Case Analysis of a New Heuristic for the Travelling Salesman Problem," *Rep. 388, Grad. Sch. Ind. Adm. C.*, no. February, 1976.

# Performance Optimization of Swarm Algorithm and Sensor Data for NASA Swarmathon Competition

Juan Aguilar, Ann Blanchard, Adam Sibiski, Jason Soto, Scott Jagolinzer, Sabri Tosunoglu

Department of Mechanical and Materials Engineering  
Florida International University  
10555 W Flagler St  
Miami, FL 33174

jagui080@fiu.edu, ablan115@fiu.edu, asibi003@fiu.edu, jsoto103@fiu.edu, sjago001@fiu.edu, tosun@fiu.edu

## ABSTRACT

This paper contains the methods used by students of Florida International University to optimize an autonomous robotic code to ensure the maximum amount of resource retrieval. Specifically, this paper deals with the ROS operating system and how each of the robot's components can most effectively communicate with each other as well as streamlining communications between robots. The process was carried out by analyzing various portions of the code to obtain marginal increases in performance. This resulted in a faster and more effective overall search and retrieval functioning of the swarm robots.

## Keywords

Swarm Robots, Swarmathon, Robot Operating System, Performance Optimization, Sensor Data, Accuracy, Algorithm.

## I. INTRODUCTION

To make advancements in the field of space exploration using cooperative robotics, the National Aeronautics and Space Administration (NASA) has launched the second annual Swarmathon. It is a competition in which universities nationwide are challenged to use a set of autonomous rovers to explore and collect resources randomly distributed in a large area with possible obstacles. This collaboration allows much quicker resource retrieval rates, ultimately increasing the opportunity for large scale exploration. The competition simulates exploration of an unknown area where humans either cannot reach or cannot survive. It requires each team to develop a unique search algorithm for the rovers to assess the area and collect possible useful resources. For the competition's preliminary stages, teams are allowed three robots to search the area for resources which are represented by April Tags placed on cubes. Because the location of the cubes is unknown, the robots must work together to gather the most possible resources in the least amount of time. Robots are tasked to autonomously scan the area and utilize the onboard camera to detect these tags and a sonar detection systems to detect upcoming obstacles in the robot's path. A claw is then used to pick up the tag and return it to a central collection area in the quickest possible manner.

## 1.1 The Robot

Designed and provided by the Moses Biological Computation Lab at the University of New Mexico, the rovers, or Swarmies, are small robotic vehicles measuring approximately 30 cm x 20 cm x 20 cm. [1] As seen in figure 1 below, they are equipped with claws for the collection of resources. They also include ultrasound distance sensors, a webcam, a WiFi antenna, and a GPS system to allow the robot to navigate, search for the cubes, and locate the base area.



Figure 1. Swarmie 2017 with an Added Claw Feature to Collect the Resources [1]

## 1.2 Robot Operating System

Inspired by the biological conduct of group functioning insects such as ants and termites, swarm robots utilize algorithms that adjust these behaviors into error tolerant, scalable, and flexible robot foraging strategies in varied and complex conditions. [1] Since the robots' hardware cannot be changed, the optimization of resource collection must be carried out through manipulation of the code. The robots rely on the Robot Operating System (ROS) to operate and execute all the independent functions of the

robots. The purpose of the ROS operating system is essentially to compartmentalize the various tasks to be completed by the robots. These tasks are known as packages which control different components of the robot. ROS also allows for the packages to communicate with each other using libraries known as 'topics'. These topics store information that is published to them from packages. Then, a package can subscribe to the topic to receive information from said topic. Each of the robot's functions are separated into their own code but rely on ROS to communicate the information from package to package. For instance, in case one of the robot's sensors detects an obstacle, this is communicated to the mobility package, in charge of the robots' movement, which then uses this information to avoid the obstacle. Editing these packages allows the robot to operate using different logic. The logic used in the packages determines the efficiency at which the robot operates.

### 1.3 Project Overview

Taking advantage of ROS's compartmentalization is key to optimizing the search for resources. Because all tasks are compartmentalized into packages, these packages can function independently of each other. Optimizing ROS and editing the packages, written in C++, can have a beneficial effect on the performance of the search algorithm of the robots. It is important to streamline the exchange of information between packages as well as between robots. This streamlining process is carried out by editing the topics that the packages publish and subscribe to. Ideally, there is a minimum number of topics that should be used by packages in the operating system. Finding a balance between reliability and time efficiency will be key to successfully competing in NASA's Swarmathon competition.

In summary, this work makes the following contributions: (1) optimize the code for a more efficient performance of the robot; (2) locate useful sensor data and compile it into a single location for ease of use; and (3) improve resource retrieval rate by ensuring precise positional awareness, proper object identification, and successful communication.

## II. LITERATURE SURVEY

Autonomous robots can be used to explore a variety of unfamiliar environments. Information can be obtained depending on the functions and components of the robot. These robots are necessary in exploring areas that cannot be accessed by humans, such as caves, deep oceans, and even other planets. NASA



Figure 2. Spirit MER-A Rover

developed two rovers for exploration on Mars. One of the rovers, named Spirit, was launched from Cape Canaveral in 2003. Unfortunately, the rover ceased mobility after entering soft soil. Data was still collected for about a year from the stationary position; however, the rover was determined to be irrecoverable. In 2010, the rover ceased communication and the mission was declared complete. Figure 2 shows the rover being tested inside a lab at NASA.

One month later, NASA launched a second rover which has experienced a much higher level of success. The second rover, named Opportunity, can be found below in Figure 3. The rover has been exploring Mars since January of 2004 and is currently still functioning to share data with scientists and engineers on Earth. The rover has traveled about 24 miles and has proven to be very effective. Although the rover has accomplished much, the use of multiple robots can accelerate the rate of exploration and significantly increase the amount of area covered.

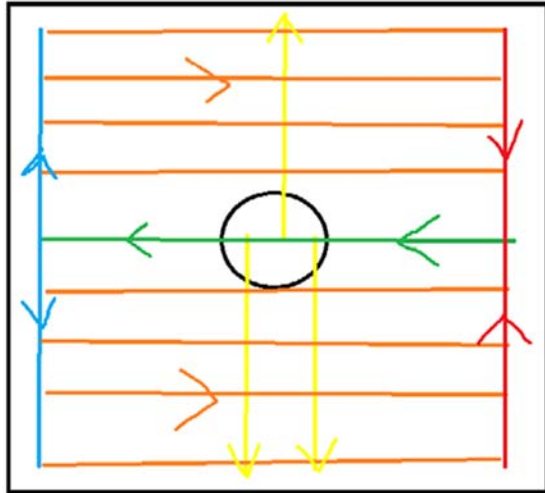


Figure 3. Opportunity MER-B Rover

Swarm robots have proved to be a more efficient and inexpensive alternative to solitary space robots for In-situ resource utilization (ISRU) efforts. For instance, "20 Swarmies can travel and search 42 km of linear distance in 8 hours without recharging which is the distance covered in a marathon and the same distance traveled by the Mars exploration Rover Opportunity in 11 years." [1] This is largely due to the cooperative aspect of their foraging algorithm. Though inexpensive, they are more robust, flexible, and scalable than monolithic robots operating alone. [1]

This project builds on important prior works done by the FIU Panther Swarm Team for the first annual NASA Swarmathon. The first design of the Swarmie included sensors, a camera, a GPS system, and a Wi-Fi antenna to communicate. The robots would scan an area in search of tags which represent a resource or object. After observing a tag, the robot would return then to a central location to virtually deliver the "resource." A search algorithm that relies heavily on the compass and ultrasound data was vital for the robot to keep track of the nest position. To allow the rovers to successfully collect and return the tags, four main mode were implemented. As shown in figure 4, they are broken down as runway (green), position (blue), sweep (orange), and return (red) [2]. "The runway is an east to west path along the x-axis that passes through the nest. The position mode assigns a y-coordinate value to the rover and has the rover either moving north or south to get to the desired y-coordinate. The sweep mode is a west to east path that has the rover looking for tags as it moves back across the arena. The return mode has the rover moving north or

south to return back to the x-axis so that it can go back to the runway mode.” [2] However, the algorithm was not proved to be successful during the physical testing because it made use of the “sonar reading in conjunction with the walls to track and reset the positional data of the rover.” [2]



**Figure 4. Diagram of Search Algorithm used for NASA's Swarmathon Competition 2016 [2]**

The robots used in this competition implement the ROS operating system. This system allows for the compartmentalization of the various tasks the robot must perform. The robots various task, like moving and detecting tags for example, will all have individual codes that are then compiled through ROS and can function independently of each other. To perform all tasks correctly and in a timely manner however, the individual codes, known as packages, must be able to communicate between each other and between the robots. This communication is carried out through a messaging system comprising of topics that can be published to or subscribed to. [6] These topics work as a message board where pertinent information is published for all packages to use. The mobility package, for example, is responsible for the movements and exploration of the robot and depends on the obstacle detection package to alert it of possible obstacles in the robots path. The mobility package then uses this information to take the necessary steps to avoid a collision. For this scenario, the obstacle detection package will detect an obstacle and publish this information to the pertinent topic. The mobility package, who is subscribed to this same topic, notices that there is an obstacle and avoids it. It is in this same manner that all packages communicate to allow the robot to function effectively.

When the code has been compiled and the robot is operational it is important to verify that the code is working in the manner it was designed to. For this, Gazebo is used to simulate the competition. The Gazebo simulator allows the user to simulate both stages of competition with options for 3 robots or 6 as well as variable field sizes. The simulator also has options for changing the distribution of tags dispersed throughout the competition field. These simulations are crucial for understanding how the code will function during competition and how to make adjustments to optimize the robots' functioning. It is also important to experiment with the introduced error in simulation.

The larger the error the more faithful to the real world the simulation will be so experimenting with this variable can be very beneficial for competition. It is also possible to adjust the speed of the simulation. This is a very useful tool because you can increase the number of simulations carried out in each time period. Simulations however are no substitute for a real-life test. These tests will help to finalize the code and ensure that it works as desired.

### III. MOBILITY OPTIMIZATION

The optimization process was carried out with the intent to increase performance without significantly altering the code. Various aspects of the program such as obstacle detection and mobility were critically analyzed to determine the most efficient method in which the swarm robots can explore the unfamiliar environment. [5] Marginal improvements in different algorithms within the program established faster overall functionality which in turn results in a quicker resource retrieval rate.

The search method implemented for the code is a preset pattern in which the swarm robots move in 1 meter increments in the X direction and then after in the Y direction. A representation of this search is shown in Figure 5, which also displays the competition area. This pattern allows for the rovers to quickly return to home base after locating a resource. After each step, the rover completes a 360 degree scan in search of the tags. If one of the tags are located, the robot will collect the tag using a mechanical claw. The swarmie will then return to the home location in one motion which will sum the displacement in the X direction and Y direction to create a single step. There are tradeoffs when designing a search pattern. This structured code will cover the entire area, but unfortunately, a raking pattern will increase the time it takes to complete scanning the area [3].

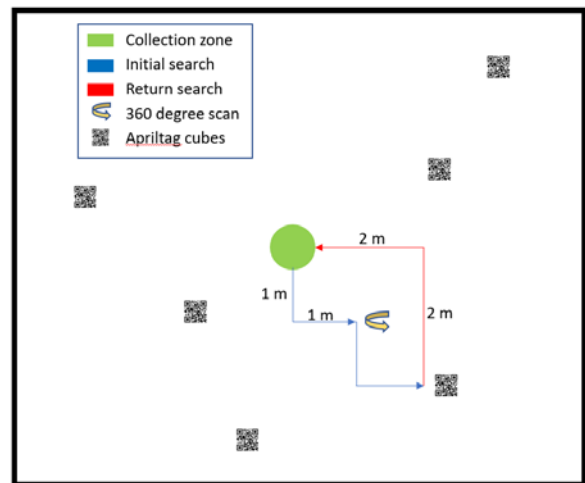


**Figure 5. Diagram of Incremental Search Pattern**

Originally, the code called for the rover to orient itself using local positioning and a compass; however, a preset command proved to be much more effective. When the swarm robot then returns to search again, rather than trying to determine which direction it is facing, it will rotate 180 degrees and then proceed to search. It will follow the same initial path without stopping to scan areas that have already been covered. Once the swarmie reaches an unexplored location, it will then continue to scan and proceed in

1 meter increments until another tag is located. A diagram of the search pattern can be found below.

#### IV. OBJECT DETECTION

Due to the frequent collisions experienced by the swarm robots, it was necessary to focus on improving the robots' response to walls and other swarm robots. The code initially prompted 0.2 radian (~11.45 degree) turning increments when an object was detected by the ultrasound sensors. This turning increment was increased to 1.57 radians (90 degrees) to decrease the time it takes the rover to return to its search for resources or tags. This change within the code is show in Figure 6. Utilizing 90 and 180 degree turns proved to be very effective because they complement the square, stepping motion of the search pattern.

```
void obstacleHandler(const std_msgs::UInt8::ConstPtr& message) {
  if ((!targetDetected || targetCollected) && (message->data > 0)) {
    // obstacle on right side
    if (message->data == 1) {
      // select new heading 0.2 radians to the left → 1.57 radians to the left
      goalLocation.theta = currentLocation.theta + 0.6;
    }
    // obstacle in front or on left side
    else if (message->data == 2) {
      // select new heading 0.2 radians to the right → 1.57 radians to the right
      goalLocation.theta = currentLocation.theta + 0.6;
    }
  }
}
```

Figure 6. Obstacle Avoidance Algorithm Improvement

A goal of proper object identification by distinguishing the difference between robots and walls was not achieved. Due to the sensors being placed on the same axis, the robot is unable to distinguish between objects based on height. To compensate for this, future experimentation and competition could implement modular sensor placement. This would provide the ability to place one or multiple sensors on a higher or lower axis. This would allow for one of the sensors to pass over any rover but not a wall. Distinguishing between a robot and wall is important because the response of a rover may not be the same for both. Optimizing the response based on which object is interfering with the robot's motion could result in a decreased search time. For example, if both swarm robots approach each other and turn 90 degrees to the left and right when facing each other, a large portion of the grid may go unexplored for some time.

#### V. VARIABLE ANALYSIS

The goal of this section was to make the sensor data easy to manipulate and store. To accomplish this, the data must be organized into an array format which updates at regular intervals or continuously. These arrays can then be exported to a text file where they can be saved as a matrix for further analysis. A theoretical array containing the desired raw data is shown in Equation.1 below. Table 1 contains the definitions for the data stored in the array along with information concerning the variables name, location, and how it's generated. After searching the code it was observed that locating the source of the data was much more difficult than observing where it was used. Due to this it is assumed to be easier to extract the sensor data from the current variable locations by publishing the data straight out of the .cpp files.

(R#, T, CC, X, Y,  $\theta$ , S1, S2, S3)

Table 1. Identified Sensor Data

Symbol	Variable	Variable-Name	Variable Location	Variable Generation (and Info)
R	Robot #			
T	Time			
CC	Cube Count	detections[i].pose	mobility.cpp	
X	x-position	currentLocation.x	mobility.cpp	pose.pose.position.x
Y	y-position	currentLocation.y	mobility.cpp	pose.pose.position.y
$\theta$	Angular-position	currentLocation.theta	mobility.cpp	m.getRPY(roll, pitch, yaw) • Yaw is the correct variable • Generated from <u>quaternion</u> data
S1	Left Sonar	sonarLeft->range	obstacle.cpp	
S2	Center Sonar	sonarCenter->range	obstacle.cpp	
S3	Right Sonar	sonarRight->range	obstacle.cpp	

Differing from the Sensor data is the Robot number (R#), a value used to identify data generated by a specific robot. According to previous Swarmathon competitors there does not exist a way to differentiate the robots without pulling the IP address, which is not allowed. Due to this a method is being developed to assign a ranking to each robot which would serve as an identification number. While the communication of the data has not been worked out the logic portion of the code is currently under development. To distinguish the robots each shall generate a random number, save the variable, and proceed publish the result to the message board. All of the robots would be subscribed to this data and receive an array of random variables when the announcing process is completed. The robots would then compare their individual saved values with the list and determine their rankings correspondingly. The robot with the largest number will assign itself the number "1" and subsequently each robot will number itself depending on the "rank" of their number. If two randomly generated numbers are identical the robots will be directed to generate a fresh set of random numbers and begin the comparison process again. This data can theoretically be used for robot specialization and task delegation, however its primary function will be allowing operators and the robots themselves to distinguish individual robot data from the memory matrix.

Table 2. Description of State\_Machine States in Mobility.cpp

Variable Name: stateMachineState	
Variable Value	Meaning
0	Transform <ul style="list-style-type: none"> <li>Mathematically Transform two coordinate points current(x,y) and goal(x,y) into an angle that leads to the goal</li> </ul>
1	Rotate <ul style="list-style-type: none"> <li>Rotate in place until aligned with angle heading towards goal</li> </ul>
2	Skid Steer <ul style="list-style-type: none"> <li>Head towards goal but correct course slightly if beginning to veer off track</li> </ul>
3	Pickup <ul style="list-style-type: none"> <li>Aligns Robot to cube and activates the gripper arm to pick it up</li> </ul>
4	Dropoff <ul style="list-style-type: none"> <li>Heads to Home base and deposits cube at home.</li> </ul>

To obtain sensor data we began by looking into the “mobility.cpp” file as this code can be considered the main program for the swarm robots. After analyzing the code the base behavior of the swarm bots was identified. The robots operate on 5 basic modes called “State\_Machines” where the variables dictate which mode (specified behavior) to follow.

Within this file the usage of multiple desired data points was discovered, these being X-position, y-position, and orientation. The default swarm program uses these variables to direct its movement. By polling its current position (Point A) and setting a goal (point B) the robot determines two points on the coordinate plane. The robot then performs some simple trigonometry to find the angle of the line connecting the two points. By reading its current orientation the robot determines whether it needs to rotate to match its orientation to the direction of the goal. Once the deviation in angles falls below a certain threshold the robot breaks out of the aligning program and enters the driving program where it heads to the destination at a fixed velocity. As long as the angle remains below the threshold the robot will not break into the aligning program, but instead use minor adjustments to maintain on course.

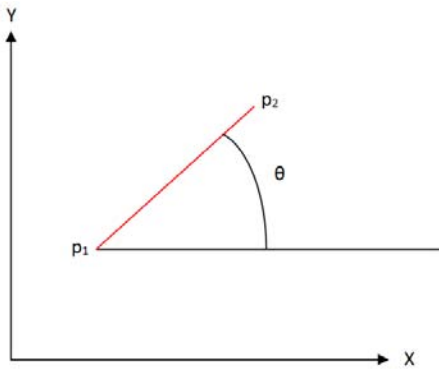


Figure 7. Swarm Bot Alignment Geometry. (Credit David Heffernan)

The next piece of code reviewed was the “Obstacle.cpp” file. The code operates by subscribing to data generated by the sonar sensors, analyzing it, and determining an operating state. By checking which sonar’s are detecting obstacles it specifies one of four obstacle modes as the current state for the robot. Once the correct mode has been determined (See Table 3) the data is published and used by the “mobility.cpp” program. . The format in which data is published follows the format “obstaclePublish.publish(obstacleMode)” while “Obstacle.cpp” operates is that it takes in sonar data then analyzes it to make a decision between four states. It then publishes the corresponding state to be used by other programs. The format in which data is published appears to be as follows.

“obstaclePublish.publish(obstacleMode)”.

To subscribe to the data, “mobility.cpp” first announces

“ros::Subscriber obstacleSubscriber;”

And then later in the code appears to set a variable equal to the subscribed data.

```
“obstacleSubscriber =
mNH.subscribe((publishedName + "/obstacle"), 10,
obstacleHandler);”
```

Table 3. Description of Obstacle Modes in Obstacle.cpp

Variable Name: <u>obstaclemode data</u>	
Variable Value	Meaning
0	No collision
1	Collision on Right Side
2	Collision in front or on Left side
4	Block lifted in front of center ultrasound

“Obstacle.cpp” operates is that it takes in sonar data then analyzes it to make a decision between four states. It then publishes the corresponding state to be used by other programs. The format in which data is published appears to be as follows.

“obstaclePublish.publish(obstacleMode)”.

To subscribe to the data, “mobility.cpp” first announces

“ros::Subscriber obstacleSubscriber;”

And then later in the code appears to set a variable equal to the subscribed data.

```
“obstacleSubscriber =
mNH.subscribe((publishedName + "/obstacle"), 10,
obstacleHandler);”
```

## VI. CONCLUSION

It was necessary to compare various search patterns to determine which would be the most effective. Although the rake covered the entire area, it was important to experiment with a spiral and stepping search pattern to determine which would cover the most area in the shortest period of time. This would allow for the maximum number of theoretical resources retrieved by the autonomous swarm robots.

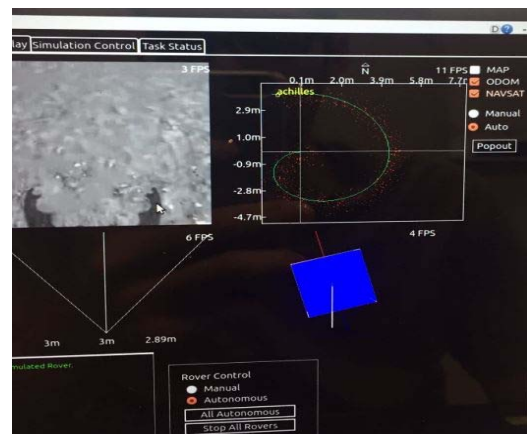


Figure 8. Spiral Search Simulation

The spiral method (shown in figure 8 and 9) proved to be effective in scanning the area; however, it was very difficult to orient the robots. Due to noise and low accuracy GPS tracking, the robots would often misalign themselves making it difficult to return to the goal zone. Using higher quality sensors and hardware could provide much higher performance and programmability.

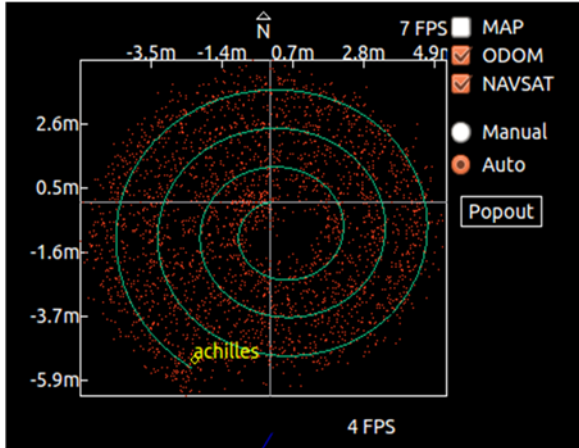


Figure 9. Map Readout of a Spiral Search Simulation

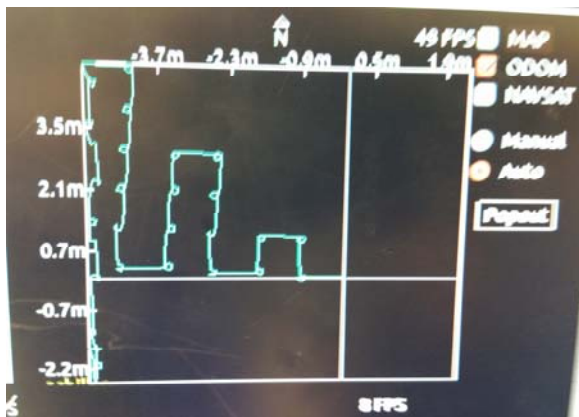


Figure 10. Simulation Result of One of the Zone's Pathing with the Little Circles Representing the 360 Sweep at Each Space

A more structured search method would then be created to eliminate any errors associated with the robots ability to position itself. A chessboard pattern was implemented to allow for the rover to return home after collecting resources by summing the steps it has moved away from home base. The 1 meter increments would allow for the area to be divided up into simple sections for the rovers to explore. After each step, the rover would complete a 360 degree scan and continue searching for resources. Figure 10 displays is an image of the simulated path.

## VII. ACKNOWLEDGMENTS

A special thanks goes to the NASA Kennedy Space Center and all of the volunteers for hosting the Swarmathon competition and inviting Florida International University to participate. The authors also extend their gratitude to the Robotics and Automation Laboratory and the Department of Mechanical and Materials Engineering at Florida International University in Miami, Florida for providing guidance, lab space and equipment for testing.

## VIII. REFERENCES

- [1] National Aeronautics and Space Administration, "Learn more," 17 April 2017. [Online]. Available: <http://nasaswarmathon.com/about/>.
- [2] FIU Panther Swarm Team, "Development of FIU Panther Swarm Algorithm for NASA's Swarmathon Competition," Florida International University, Miami, Florida, 2016.
- [3] Hoff, Nicholas, Robert Wood, and Radhika Nagpal. "Distributed colony-level algorithm switching for robot swarm foraging." *Distributed Autonomous Robotic Systems*: 417-430, 2013.
- [4] Richard, William K., and Stephen M. Majercik. "Swarm-Based Path Creation in Dynamic Environments for Search and Rescue." *Proc. of Genetic and Evolutionary Computation Conference*, Philadelphia, PA, USA. N.p., 11 July 2012. Web. 12 Feb. 2016.
- [5] Shoutao, Li, Lina, Li, Lee, Gordon and Zhang, Hao. "A Hybrid Search Algorithm for Swarm Robots Searching in an Unknown Environment." 11 Nov. 2014. Web. Feb. 2016.
- [6] Stolleis, Karl. "The Ant and the Trap: Evolution of Ant-Inspired Obstacle Avoidance in a Multi-Agent Robotic System." 26 Jun. 2015.

# Prediction of Component Failures of Telepresence Robot with Temporal Data

Jayesh Soni, Nagarajan Prabakar, Jong-Hoon Kim<sup>(1)</sup>

School of Computing and Information Sciences  
Florida International University, Miami, FL 33199

(1) Department of Computer Science, Kent State University, Kent, OH 44242

jsoni@fiu.edu, prabakar@fiu.edu, jkim@cs.kent.edu

## ABSTRACT

With recent advances in computer and sensor technologies in the last few decades, the use of robots for various applications has increased enormously. The reliability of robots depends on the minimization of component failures and downtime. To improve the reliability, periodic monitoring of components and their behavior are essential to inference component fatigue and potential breakdowns.

Since fully autonomous robots are very expensive, telepresence robots are affordable for mass scale deployment and can be controlled by a trained human operator like avatars. To increase the efficiency and to reduce the downtime of telepresence robot service, it is essential to observe the various commands performed on the robot and to analyze the samples of component status over a long period.

We propose an efficient data driven model with a collection of frequent time-stamped data from various components of a telepresence robot and predict potential failure warnings. The collected historical datasets are analyzed to determine an accurate machine learning model for increased failure prediction of components. Analysis of this large collection of data will be performed on a cloud computing platform to alleviate the computational load on telepresence robots. With the incoming temporal data, this machine learning model predicts the component status and probability of failure in real-time.

Potential Applications of the proposed approach also includes detection of component malfunction, estimating the degree of movement of various components for satisfactory level of performance, and migration of workload among multiple telepresence robots in a team work environment.

## Keywords

Telepresence Robot, Machine Learning, Predictive Modeling, Predicting Component Failure

## 1. INTRODUCTION

With recent advances in computer and sensor technologies in the last few decades, the use of robots for various applications have increased enormously. Globally, many research

organizations are concentrating in research and development of various types of robots based on their requirements and applications. Telepresence robotics is one such area of robotics that allows human controllers to remotely operate through a real-time multimedia interface in wireless mode. Remote teleoperation of advanced robotic technologies has great potential in many areas, including applications in education, deep sea exploration [1] explosive mine removal, hazardous environments [2] off-shore projects [3], space explorations [4], etc.

Scheduled maintenance in such robotic system is widely used to ensure that equipment is operating correctly so as to avoid unexpected breakdowns. Such maintenance is often carried out separately for every component, based on its usage or simply on some fixed schedule. However, scheduled maintenance is labor-intensive and ineffective in identifying problems that develop between technician's visits. Unforeseen failures still frequently occur. In contrast, predictive failure techniques help determine the run-time condition of components in order to predict when and what repairs should be performed. The main goal of predictive failure is to prevent unexpected equipment failures.

Predictive failure requires insight into the dynamics of operational components. This can be gained by adding sensors to components for recording and monitoring of signals of interest (such as temperature and voltage). Sensor data log with time stamp information will provide further understanding of a working component. Most of the components are usually operated via software. For example, in case of Telepresence Robot, all device operations, from body movement to usage of battery power, are controlled by various applications. These applications record operation logs. Theoretically, one can trace back how a component was used by analyzing all its associated logs. Mining such rich information can help in detecting potential issues like component failures in advance. A good technique in this area can lower the costs of damage, improve security and reduce the number of unnecessary maintenance service.

## 2. PROPOSED METHODOLOGY

The use of component logs to predict failures poses many challenges and has not yet been fully explored. Since logs are mainly used for debugging purposes, they (i) rarely contain

explicit information for failure prediction; (ii) contain heterogeneous data including symbolic sequence, numeric, time series and categorical variables; and (iii) contain massive amounts of data, posing computational challenges. Before the data can be analyzed, it must be determined how the data can be acquired, what kind of data is accessible, and which format it takes. This data acquisition process is discussed in section 2.1. After the acquisition of data, features need to be extracted from the raw data which is known as feature engineering that involves signal processing, presented in section 2.2. For the feature analysis, the relationship between given input and expected output must be established through data labeling techniques as described in section 2.3. Finally, a set of machine learning (ML) techniques that analyzes the features and predict component failures as outlined in section 2.4. The workflow model for these four phases is shown in Figure 1.

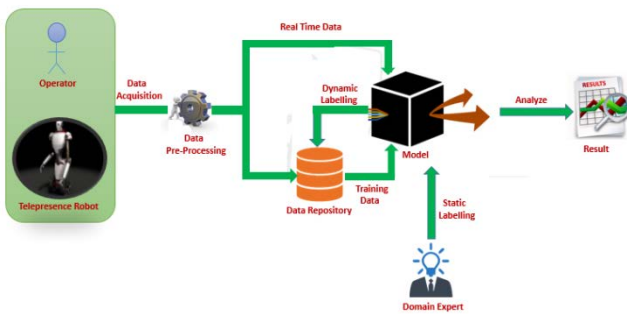


Figure 1. Workflow of the proposed model

## 2.1 Data Acquisition

### 2.1.1 Types of data

The two most important types of data for component failure prediction are sensor data from sensors and event data from log files.

#### Sensor data

In recent years, sensors have become smarter, smaller, easier to implement in existing systems, as well as cheaper and more reliable [5]. A sensor converts physical values into electrical values (voltage, current or resistance). Usually, a sensor measures a mechanical value; for example, the mechanical values of acceleration, pressure, flow, torque or force. With this mechanical value, one can interpret the vibration data, acoustic data, temperature, altitude, etc.

#### Log-files

Events of a system can be recorded to a log file with time-stamp. In this manner, the declaration of an event is very broad. For instance, an event could be component breakdown, replacement, maintenance service, etc. Descriptive log files can be written by humans describing maintenance actions, or any failures or errors detected.

To make use of log data, we first have to interpret the logs, filter out a large amount of noise (i.e. data irrelevant to our goal) and extract predictive features. Next, we have to collect known failure cases for learning/evaluating models. Then, we have to apply machine learning techniques to accurately predict component failures. And finally, we have to choose the best Machine Learning model by choosing appropriate evaluation strategies.

### 2.1.2 Data Acquisition Technique

Data can be collected through either pull-based (polling at periodic intervals) or push-based (when event occurs).

#### Time Interval

Time interval data acquisition system sends the acquired data at periodic time intervals. This type of system is used when communication costs are high. In some cases, it is necessary to have synchronized clocks with the communication partner. They have to determine an interface for how and what data have to be exchanged. Such interfaces can differ, from being very abstract (i.e., all values will be transferred) to very special (transfer a value only when a constraint is fulfilled).

#### Event Driven

The event driven data acquisition technique is a push-based approach. Such systems are also called publisher/subscriber systems [6], because the user of such systems subscribes to a publisher of events. In our case, a subscription is a definition of behavior of the real-world system that the user wants to observe. The data acquisition system publishes the value changes detected (called Event) and sends them to all registered users.

## 2.2 Feature Engineering

For most failure type detection and predictive maintenance applications, the values obtained from the data acquisition system must typically be preprocessed before transforming them into the predictive features for improved accuracy of the machine learning algorithm. The most important processing of the feature engineering for failure detection as shown in Figure 2 with the following stages: i) Signal Processing: The interpretation, generation and transformation of raw unprocessed data, ii) Feature Selection: Selection of the most representative features, and iii) Feature Extraction: Generation of new information by combining features.

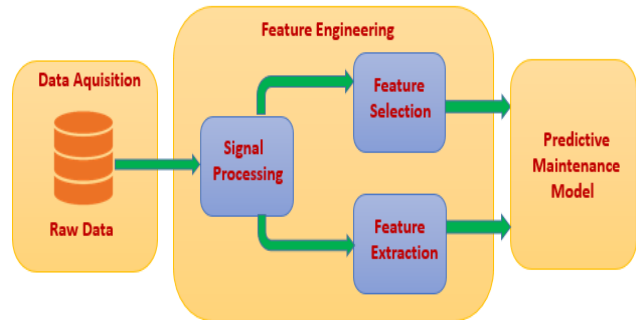


Figure 2. Feature engineering process

### 2.2.1 Signal Processing

A training set is initially extracted from the acquired data set for building the ML models. Since the performance of a classifier is directly influenced by the quality of its training data set, the presence of noise in the training data may affect its performance, decrease its accuracy, and increase its complexity [7].

Two different combinations of the classifiers results are considered. The first is majority voting, in which an example is noisy if the majority of the predictions made by the combined

classifiers is not in accordance to its recorded label. The second considers a consensus of the predictions, by which an example is considered noisy if all classifiers make erroneous classifications for it.

Since there are four classifiers being combined for noise detection, a data item is considered noisy by consensus only if it is misclassified by all four classifiers. Similarly in majority voting, a data item is noisy if at least three classifiers make incorrect predictions for it.

After the noise is identified, the associated data can be processed in the following two ways. The first approach removes noisy data from the training data set. The second approach reclassifies the noisy data with new class labels. The new class will be the one, that will be predicted by most of the noise-detection classifiers.

### 2.2.2 Feature Selection

To select appropriate features, we will use Principal Component Analysis (PCA) which is an orthogonal transformation technique that converts a set of features into a set of linear uncorrelated features, called principal components. The assumption of the PCA is that features with the largest variance have the largest informative content. The samples are centered and rotated in accordance to most relevant features. The outcome of the PCA yields the features with the largest variance that are orthogonal to one another.

### 2.2.3 Feature Extraction

Feature selection picks a subset of the most representative features, whereas feature extraction derives new information from original features. Feature extraction can be a non-linear process, and thus the results are not self-explanatory. An advantage of feature extraction over feature selection is that the features can be reduced to a much greater extent. We will try with different combination of the feature extractions and will check which combination gives the best accuracy.

## 2.3 Data Labelling

For supervised learning, historical data is needed which has to be labeled. Machine learning approaches can create relationships between the input feature vector and the class labels.

ML can distinguish between classification and regression. Classification means that an output variable is discretized to a defined class labels. Regression means that an output variable takes on continuous values. The state-driven data labeling technique is used for classification in component failure prediction.

### State Driven Data Labeling

The state-driven data labeling technique labels the historic data into different states. There are two different types of states in component failure detection:

- Failure type state
- Lifetime state

A component can have one or more failure types. A failure type can also depend on the consequences of other preceding failure (see Figure 3). The lifetime state is usually equally distributed over the lifetime of a component as illustrated in Figure 4.

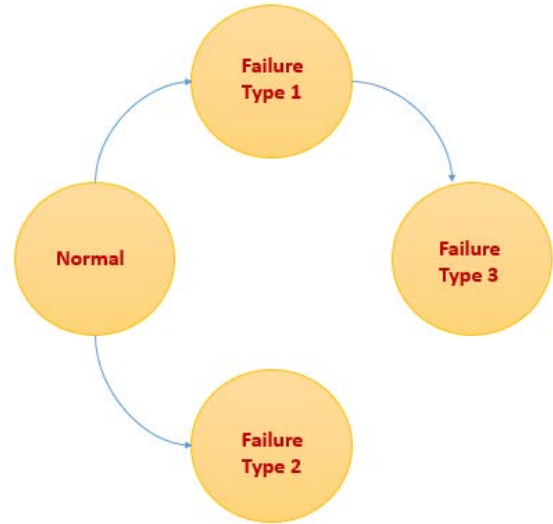


Figure 3. State machine for failure type detection

According to recent literature, the historic data with logged failure types is needed for detecting these different failure types. This implies that every failure type must occur in the historic data, and the more often it occurs, the higher the possibility to eliminate noise factors and achieve a better accuracy. The problem of generating failure type data is costly, and therefore it is not always possible to force the system into a failure situation. Alternatively, many real-world systems are maintained with preventive techniques, where components are replaced after a predefined time, before a failure can occur. It does not matter whether the component is close to failing or not. Failure type detection, without the failure type of historic data, is not easy and not mentioned in the literature. However, it might be useful in analyzing failure types, because some these do not lead to a system crash, but can influence other components and their healthy state.



Figure 4. State machine with equal distributed states

In lifetime-state data labeling for predictive maintenance, it is necessary to categorize the historic data into the lifetime states used. As mentioned above, these states are generally equally distributed over the lifetime of a component. There are two minimum number of states for predictive maintenance (<100% and 100%).

## 2.4 Machine Learning Approaches

In recent years, machine learning has become increasingly important in computer science because data could be collected and stored easily. The collected data is usually so extensive that it

is not practical to analyze the data manually. In such a scenario, the machine learning technique plays a key role.

Another reason for the growing popularity of machine learning is decreasing computational costs. With the evolution of hardware in recent years, the usage of machine learning approaches has become efficient in terms of both cost and time, especially for detecting component failures. Different machine learning algorithm requires different set of parameters that can be learned from the dataset.

We conducted experiments on simulated data with the following three most widely used machine learning algorithms as outlined in Figure 5:

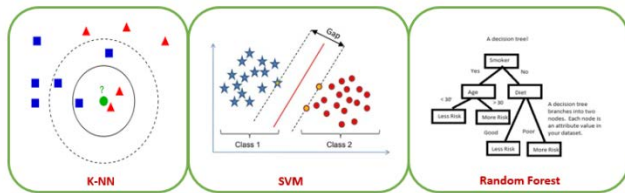


Figure 5. Machine learning models

a) **K-NN** (K-Nearest Neighbor)

In KNN classification [8], the output is a class membership. A new object is classified by a majority vote of its already classified neighbor objects, with the object being assigned to the most common class among its k nearest neighbors.

b) **SVM** (Support Vector Machine)

Support Vector Machines [9] are based on the concept of decision planes that define decision boundaries. A decision plane is one that separates between a set of objects having different class memberships. A new object is classified into the most suitable classes using the decision planes.

c) **Random Forest**

Random forests [10] are ensemble learning method for classification, regression and other tasks, that operate by constructing a multitude of decision trees (classes) at training time and output of a new object is the class that is the most common predicted by the decision trees.

We used a simulated data set with 2207 data points each with 300 features and 23 labels (pre-classified data points) for this experiment. K-Fold [11] cross-validation technique is employed to find the optimal values for parameters for training each of these three ML models. The results of classification of data points are listed below.

Table 1. Experimental results

Machine Learning Model	Accuracy
K-NN	81%
SVM	87%
Random Forrest	85%

Based on the experimental results, SVM performed better than other models.

### 3. CONCLUSION

We proposed a new approach to predict component failures using past data collection with known component failure types. This will identify the necessary preventive actions that will minimize system downtime and cost. We introduced machine learning approach to analyze the data set and to predict the upcoming component failure.

Potential Applications of the proposed approach also includes detection of component malfunction, estimating the degree of movement of various components for satisfactory level of performance, and migration of workload among multiple telepresence robots in a team work environment.

A large collection of component failure types will enhance the quality of analysis. Since it is a tedious process to identify all possible component failure types, a cloud based data analysis from several telepresence robots will be a viable alternative. As the dataset grows extremely very large, designing a distributed machine learning approach would be needed. Such an approach would offer the advantage that large amounts of data could be analyzed in parallel, which results a shorter time to reach a decision.

### 4. REFERENCES

- [1] A. Forrest, B. E. Laval, Lim, D. Williams, A. Trembanis, M. Marinova, R. Shepard, A. Brady, G. Slater, M. Gernhardt, and C. M. Kay, "Performance evaluation of underwater platforms in the context of space exploration", *Planetary and Space Science*. vol.58, no. 4, pp.706-716, 2010.
- [2] L. Parker and J. Drape, "Robotics applications in maintenance and repair", 2nd. ed. vol. 1. Hoboken, NJ, John Wiley and Sons, Inc., 1998.
- [3] C. Heyer, "Human robot interaction and future industrial robotics applications," in Proc. of the *IEEE/RSJ International Conference on Intelligent Robots and Systems*, 2010.
- [4] T. W. Fong, "The human exploration telerobotics project," *Global Space Exploration Conference*, Washington, 2012.
- [5] Chris Van Hoof, Kris Baert, and Ann Witvrouw, "The best materials for tiny, clever sensors," *Science*, vol. 306, no. 5698, pp. 986–987, 2004.
- [6] Patrick Th. Eugster, Pascal A. Felber, Rachid Guerraoui, and Anne-Marie Kermarrec, "The many faces of publish/subscribe," *ACM Computing Surveys (CSUR)*, vol. 35, no. 2, pp. 114–131, 2003.
- [7] X. Zhu, X. Wu, "Class noise vs. Attribute noise: A quantitative study of their impacts," *Artificial Intelligence Review*, vol. 22, no. 3, pp. 177–210, 2004.
- [8] [https://en.wikipedia.org/wiki/Knearest\\_neighbors\\_algorithm](https://en.wikipedia.org/wiki/Knearest_neighbors_algorithm)
- [9] [https://en.wikipedia.org/wiki/Support\\_vector\\_machine](https://en.wikipedia.org/wiki/Support_vector_machine)
- [10] [https://www.stat.berkeley.edu/~breiman/RandomForests/cc\\_home.htm](https://www.stat.berkeley.edu/~breiman/RandomForests/cc_home.htm)
- [11] [https://en.wikipedia.org/wiki/Cross-validation\\_\(statistics\)](https://en.wikipedia.org/wiki/Cross-validation_(statistics))

# Quadcopter with Vertical Landing Payload System

Camilo Torres, Adam Wechsler, Rafael Diaz, Cindy Vargas, Pradeep Shinde, Sabri Tosunoglu

Department of Mechanical and Materials Engineering  
Florida International University  
Miami, Florida 33174

ctorr029@fiu.edu, awech002@fiu.edu, rdiaz060@fiu.edu, cvarg038@fiu.edu, pshin001@fiu.edu, tosun@fiu.edu

## ABSTRACT

The purpose of this research is to propose an alternative method of Vertical Landing Payload through the use of an integrated multicopter system. The quadcopter payload system extends four arms with propellers to stabilize descent. This report aims to address issues in the aerospace industry. The recovery and reuse of expensive equipment lower the cost of space travel. Upright landings allow for stable and soft descents which prevent the equipment from being damaged and allow the reuse of it.

There are two primary reasons for designing a section of a rocket that can land upright. The first reason is that the section can contain a payload that requires a specific orientation upon landing, such as extra-planetary vehicles or people. The second reason is that it can be cost-effective by allowing an expensive component to be recovered undamaged and then reused

## Keywords

Quadcopter, drone, programming, ArduPilot, Arduino, python, vertical landing, rocket, payload, fiberglass, FAA, NASA.

## 1. INTRODUCTION

The NASA Student Launch is a research based, competitive, and experimental exploration project that provides relevant and cost effective research and development. The commitment is to design, build, launch, and fly a payload and vehicle components that support NASA research on high-power rockets to an altitude of 5,280 feet above ground level in a span of 8 months. The challenge of the competition is based on multiple experiment options, and this team decided to participate in the experiment that deals with target identification and landing control.

This competition allows for students to design and manufacture a rocket and promotes a thorough engineering process by which different design report reviews are made and sent to NASA. Teams must successfully complete a Preliminary Design Review (PDR), Critical Design Review (CDR), Flight Readiness Review (FRR), and Launch Readiness Review (LRR) that include safety briefings, and an analysis of vehicle systems, ground support equipment, and flight data.

## 1.1 Literature Survey

The approach is for the section to be a multicopter. There are many types of multicopter configurations, many of which were reviewed for this project. In all standard configurations, the more motors a multicopter has, the more lifting power it will have. The standard quadcopter has four motors on four arms spaced 90 degrees apart. They are the most popular type of multicopter and less complex to design. There are four configurations for the arms: "X" (Figure 1), "+", and "H". The advantage of the "X" and "H" configurations is that a centrally located camera will not capture the propellers. The advantage of the "+" configuration is that manual control is easier.

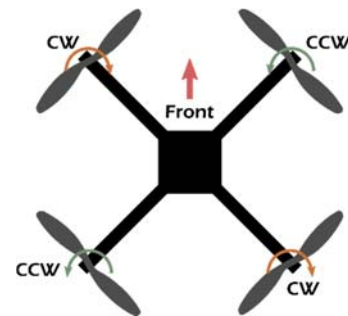


Figure 1. "X" Quadcopter

The flight controller of a UAV is a circuit board that receives sensor data and user commands and sends the appropriate pulse width modulation signals to the motors. Standard flight controller sensors include the accelerometer, gyroscope, barometer, and magnetometer [4]. The accelerometer measures lateral acceleration, while the gyroscope measures rotational acceleration. The barometer measures air pressure, which can be used to determine altitude. The magnetometer acts as a compass. A GPS is another sensor that can be used for long flights and it is used to determine global position.

ArduPilot is an open source unmanned vehicle platform that was initiated in 2007 by members of the DIY Drones community, which has tens of thousands of members [1], [6]. The software, which has been developed by professional engineers and computer scientists, is capable of controlling several types of

multirotor aircraft, traditional helicopters, fixed-wing aircraft, ground rovers, boats and submarines. Earlier versions of ArduPilot were programmed using the Arduino programming language and utilized a companion ArduPilotMega (APM) flight controller. As the project became more involved, the programming was mostly performed in C++ and could be run on multiple hardware platforms.

The ArduPilot flight controller can be controlled from a base station through telemetry utilizing ArduPilot's Mission Planner software. This software allowed the planning, saving and loading of missions utilizing waypoints and automated activation of servos. In 2013, Mission Planner gained the ability to run Python scripts, further extending its functionality. The ArduCopter subproject of ArduPilot is specifically designed for controlling multirotor aircraft.

## 1.2 Project Objectives

The objectives that must be accomplished in for the NASA Student Launch competition are to design, build, launch, and land a payload. The payload will contain a camera that will identify randomly placed targets while it is descending. The payload will also have a recovery system that will allow a controlled descent and will facilitate in an upright landing. The process will require all of the systems on the rocket to perform their tasks correctly. Once the rocket reaches the targeted height of 5,280 feet above ground level, the apogee height, the payload will then disengage from the rocket through black powder combustion. Once the payload is detached from the rocket, a drogue parachute will then be used to reduce the velocity of the payload after which the quadcopter will begin to activate and further decrease the speed at which it is descending

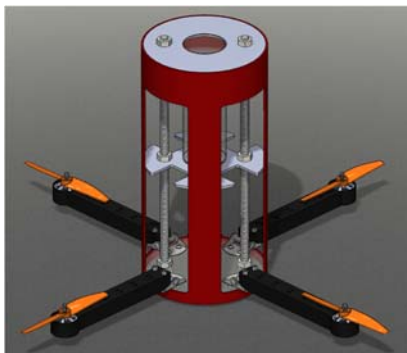


Figure 2. Proposed design

## 2. DESIGN AND ANALYSIS

The structure of the payload had to be designed so that it would withstand the sudden increase in gravitational force during launch. In order to meet this requirement, the lateral face of the cylindrical payload and the circular bulkheads are made of G12 fiberglass connected by two steel threaded rods. The parachute had to be chosen to ensure that the payload would impact the ground with less than 75 ft-lbf of kinetic energy according to NASA's Student Launch safety standards, and a force analysis revealed that the impact would theoretically be 26.3 ft-lbf. The electronics, propellers and battery were chosen to provide enough thrust to maintain stability and ensure an upright landing. A force analysis revealed that at terminal velocity, with a payload weight of 3.7

lbf, a total thrust of 4 lbf would result in the payload achieving zero velocity within 4 seconds and 33 feet.

### 2.1 Structural Design

The payload's structure was designed to ensure easy ejection and maximize internal volume. In order to ensure easy ejection the main body was composed of a cylindrical coupler specifically designed for the rocket that it will be housed in. The circular bulkheads will have the same diameter size as the G12 coupler's inner diameter. With both the exterior of the coupler and the interior of the rocket being smooth surfaces, this ensured that the payload could be ejected without having to overcome significant frictional forces. Furthermore, since the payload's diameter was the same as the interior of the rocket, it prevented the possibility of the payload achieving an oblique angle during ejection and becoming caught.

The cylindrical coupler, while designed for withstanding high gravitational forces during rocket flight, was structurally weakened by cutting out sections. The top and bottom circular faces of the payload were connected by two steel rods in order to reinforce the payload's structure. It also served the purpose of keeping the faces properly aligned with the lateral face.

### 2.2 Force Analysis

During descent, the total vertical forces acting on the payload are weight, force from drag from the parachute, and force from drag from the quadcopter.

$$F_{tot} = -W + F_{dp} + F_{dq} \quad (1)$$

The force from drag is a function of the air density, coefficient of drag, and the square of the velocity.

$$F_{tot} = -W + \frac{1}{2}\rho C_{dp} A_p v^2 + \frac{1}{2}\rho C_{dq} A_q v^2 \quad (2)$$

Terminal velocity occurs when the total force acting on the payload is zero. The weight of the payload is 3.7 lbf. The parachute manufacturer reported a coefficient of drag of 1.1-1.2, and in the interest of not underestimating the descent speed, 1.1 was used. The coefficient of drag for a cylinder moving parallel to flow with the payload's length-to-diameter ratio is 0.83. The resultant terminal velocity is 21.5 ft/s. Figure 3 illustrates the terminal velocity of the payload for a variety of weights. The drag produced by the quadcopter was found to be nearly insignificant compared to that produced by the parachute.

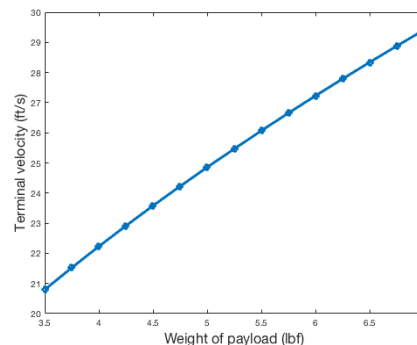
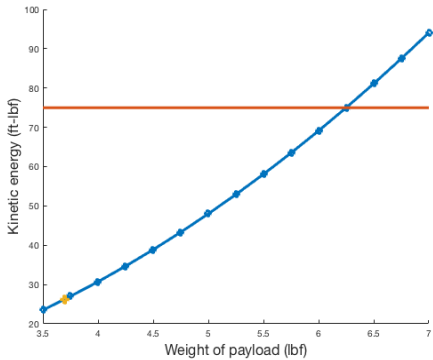


Figure 3. Terminal velocity of the payload as weight increases

If the quadcopter malfunctions and does not provide any thrust, this results in an impact with the ground of 26.3 ft-lbf, which is below the NASA Student Launch maximum of 75 ft-lbf. Figure 10 shows the change in kinetic energy upon impact with the ground as weight increases, with the quadcopter remaining below NASA’s maximum until its weight reaches approximately 6.25 lbf.



**Figure 4. The payload’s kinetic energy upon impact with the ground as the weight increases (yellow point represents the current design)**

When the quadcopter slows the descent speed for upright landing, the total vertical forces acting on the payload now incorporates thrust.

$$F_{tot} = T - W + F_{dp} + F_{dq} \quad (3)$$

When acceleration and velocity are considered as functions of time and incorporated into the formulas for the forces, the equation becomes

$$m \frac{dv}{dt} = T - W + \frac{1}{2} \rho C_{dp} A_p v^2 + \frac{1}{2} \rho C_{dq} A_q v^2 \quad (4)$$

There are two solutions to this differential equation, depending on whether thrust exceeds weight. Although the goal was to design a quadcopter whose thrust exceeded its weight by a factor of 1.5, the “thrust < weight” solution allowed us to determine the impact velocity if adequate thrust could not be obtained. If such was the case, it would then allow us to accurately simulate testing on the landing gear.

When thrust exceeds weight, the equation for velocity as a function of time is

$$v = \sqrt{\frac{\epsilon}{k}} \tan \left( \frac{t \sqrt{kc}}{m} + c_1 \sqrt{kc} \right) \quad (5)$$

Where  $c = T - W$ ,  $k = \frac{1}{2} \rho (C_{dp} A_p + C_{dq} A_q)$ , and  $c_1$  is a constant based on the terminal velocity at  $t = 0$ .

Utilizing this equation with a weight of 3.7 lbf and a thrust of 4 lbf, a velocity of zero was reached in 3.0 seconds. As seen in Figure 5, the time to hover escalates quickly as weight approaches thrust (and in fact, would never hover if the weight equaled or exceeded the thrust). However, the plane representing when thrust exceeds weight by only 0.5 lbf illustrates that if such were the case, hover would still be reached in less than 4 seconds.

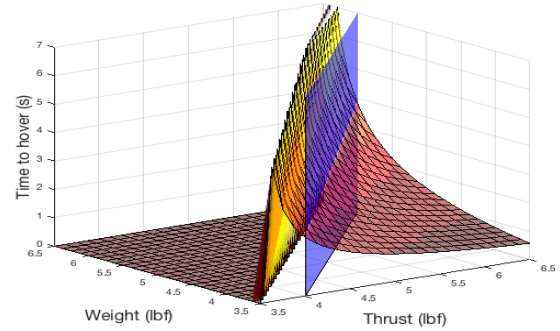


**Figure 5. The time for the quadcopter to hover as determined by thrust and weight**

When velocity is represented as distance as a function of time Eq. 5 becomes

$$x = -\frac{m}{k} \ln \left( \cos \left( \frac{t \sqrt{kc}}{m} + c_1 \sqrt{kc} \right) + c_1 \sqrt{kc} \right) + c_2 \quad (6)$$

The distance,  $x$ , that the payload falls from terminal velocity until reaching hover is found by integrating Eq. 6.

$$\frac{dx}{dt} = \sqrt{\frac{\epsilon}{k}} \tan \left( \frac{t \sqrt{kc}}{m} + c_1 \sqrt{kc} \right) \quad (7)$$

Where  $c_2$  is a constant based on distance  $x = 0$  at  $t = 0$ . Utilizing the above result for a weight of 3.7 lbf, a thrust of 4 lbf, and the previously calculated time to reach hover of 3.0 seconds, the distance to reach hover is 18.4 ft. As seen in Figure 6, the distance to hover escalates quickly as weight approaches thrust (and in fact, would never hover if the weight equaled or exceeded the thrust). However, the plane representing when thrust exceeds weight by only 0.5 lbf illustrates that if such were the case, hover would still be reached in less than 30 feet.

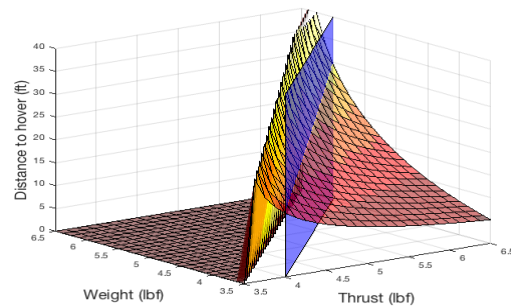


**Figure 6. The distance for the quadcopter to hover as determined by thrust and weight**

When thrust does not exceed weight, the equation for velocity as a function of time is

$$v = \frac{f \cdot \exp(ft/m+fc_2)+f}{2k-2k \cdot \exp(ft/m+fc_2)} \quad (8)$$

Where  $f = \sqrt{-4kc}$  and  $c_2$  is a constant based on the terminal velocity at  $t = 0$ . Utilizing this equation with a weight of 3.7 lbf and a thrust of 3 lbf, terminal velocity approaches 9.5 ft/s, with a velocity of 10.0 ft/s obtained within 2 seconds. Since the thrust exceeds weight in the design, no further analysis is necessary.

### 2.3 Stress Analysis

Since G12 fiberglass was not an available material option for the simulation software, certain material properties had to be input into Solidworks to be able to simulate the how the body would react if it underwent a harsh landing. The most important part of the prototype is the body, without the structural strength of the body, the project falls apart entirely and the requirement of landing upright is no longer met. Cutting sections into the coupler would weaken the structure, various tests were run for this reason. The first number of tests that were run was only done on the G12 coupler alone. Two drop tests were performed; one where the body drops a meter and another where it drops at the terminal velocity, which is 21.5 m/s. below is comparison of both tests.

Figure (7a) shows the stress analysis from a drop of 1 meter. As can be seen from the red marks, the areas that will be most affected are those near the bottom, which reaches a high stress of 21.7 MPa and a minimum of 758 Pa, which is shown by the blue colored portion of the coupler. The maximum displacement experienced is .866 mm. Figure (7b) shows the stress analysis of the coupler when it drops at a velocity of 21.5 m/s. The maximum stressed experienced at impact is 229.6 MP and the minimum is 4.18 kPa. The maximum displacement experienced is 4.62 mm.

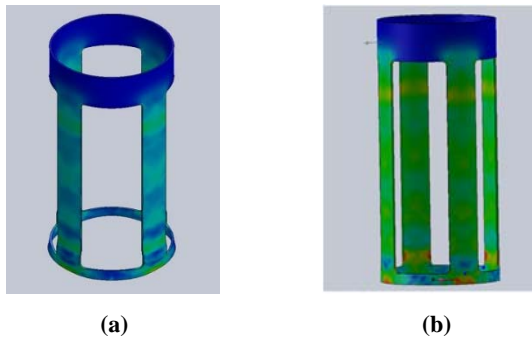


Figure 7. (a) Stress analysis of coupler from a drop of 1 meter and (b) from a velocity of 21.5 m/s

Knowing that the coupler would probably only be able to survive one harsh landing, threaded rods were added to the design so it can absorb most of the impact. Other than the threaded rods that were added to the coupler, a G10 fiberglass bulkhead was added to the top as well as a high impact acrylic bulkhead was added to the bottom. The simulation that was done was a drop test at a velocity equivalent to the terminal velocity. The maximum stress experienced was 1.36 GPa and a minimum stress of 1.63 GPa. The maximum displacement experienced was .087 mm. After viewing the results of the simulations, threaded rods were integrated as part of the final design.

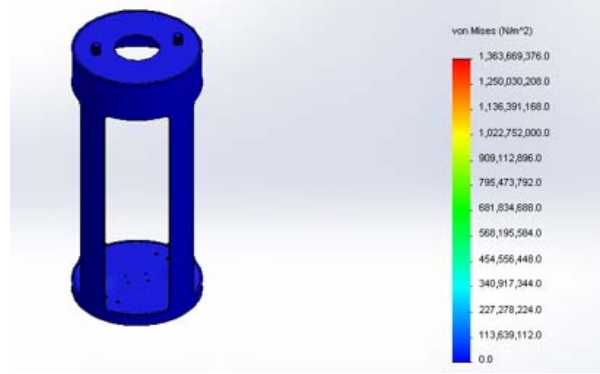


Figure 8. Stress analysis of coupler with threaded rods drop test at terminal velocity

### 2.4 Material Selection

For the lateral face of the payload G12 fiberglass was used. The reason for this was primarily convenience; however the material has several favorable properties. G12 fiberglass is a filament-wound composite that is high-strength, lightweight and machinable. It has a high tensile strength (6000 - 12500 psi) and high compressive strength (20,000 - 37,000 psi). For the lateral face we will be using a G12 coupler that was specifically designed for the rocket, so it should easily withstand the expected g-forces.

For the top face G10 fiberglass was used. G10 is lightweight (0.0686 - 0.0759 lbf/in<sup>3</sup>) and is easily machined. It is also mechanically strong, having yield strength between 9.43 and 10.2 ksi and a tensile strength between 10.2 and 10.9 ksi. For the bottom face, medium to high impact acrylic was selected.

Threaded steel rods were chosen to maintain the position of the G12 lateral face and the top and bottom G-10 faces, as well as provide additional support. The propeller arms were 3D printed.

### 2.5 Component Design/Selection

The initial weight estimation was 3.7 pounds. Motor thrust data tables were referenced to determine motor and propeller size combinations that would result in a total thrust in excess of 4 lbf, or 1 lbf per motor. Harrell tested the DYS Fire 2206 2300kv brushless motor with the following propellers: HQProp 5x4, Gemfan 5x4.5BN, and KingKong 6x4, as seen in Table 4 [3].

Table 1. Motor thrust data table for DYS Fire 2206 2300kv brushless motor

Throttle	HQProp 5x4		Gemfan 5x4.5BN		KingKong 6x4	
	Thrust (lbf)	Current (A)	Thrust (lbf)	Current (A)	Thrust (lbf)	Current (A)
25%	0.25	2.16	0.28	2.27	0.37	2.64
50%	0.73	5.00	0.82	5.47	1.07	6.97
75%	1.43	10.97	1.59	12.25	2.04	16.06
100%	2.23	20.29	2.37	24.78	3.08	29.93

The DYS Fire 2206 2300kv motor is capable of meeting the minimum requirements for all four propellers that were tested. Gemfan 5040 propellers were used, which are comparable to the HQProp 5x4 propellers.

Harrell's test also recorded amperage requirements of up to 29.93 (for the KingKong 6x4 propeller at 100% throttle), so to meet this requirement the Lumenier F390 30A BLHeli electronic speed controllers were used. Harrell utilized a 4s LiPo battery, which is capable of providing 16.8 volts. With four motors drawing a maximum of 120A of current, the current capacity (mAh) and C-rating (hr) had to be chosen to meet this demand, where the maximum current draw is equal to the product of the current and the C-rating [2]. In addition to being able to supply the current for maximum draw, the battery had to be chosen to ensure it would last the entire flight. Assuming the motors begin providing thrust at 5280 feet and a terminal velocity of 21.5 ft/s, the descent would take a maximum of 4.1 minutes. At 75% throttle, which is more throttle than should be necessary to maintain stability, the KingKong 6x4 propellers draw the most current at 16.06 A, which would require a current capacity of 1100 mAh. Based on the maximum current draw and required flight time, a Lumenier 1800 mAh 4s 75C LiPo Battery was selected, which would have a maximum current draw of 135A and a maximum flight time of 6.7 minutes.

The RCTimer ArduFlyer (APM 2.5.2) flight controller was used since it came preinstalled with the ArduPilot open source code, as well as an accelerometer, gyroscope and altimeter. The EMAX Power Distribution Board 0512 5V/12V was chosen due to its small size, number of pads, and 5V and 12V outputs.

## 2.6 Software Selection

Since the quadcopter is required to react to sensors and perform actions that are not standard for hobbyists, open-source was chosen, rather than proprietary, software so that it could be altered. Of the open-source platforms that were researched, the ArduPilot suite of unmanned vehicle platforms had the most useful examples and the largest community. The ArduCopter version 3.2.1 open-source multicopter unmanned aerial vehicle platform was chosen as the platform for this project. While not the most recent version of the platform, it is functional and there are several advantages to using it instead of a more recent version. Version 3.2.1 was the last version to utilize the Arduino programming language. The Arduino IDE is supported on Mac OS and was familiar to the lead programmer. Example code demonstrating the programming of a quadcopter, including a PID controller, was found and understood [5].

Version 3.2.1 runs on the Pixhawk 1 & 2 and ArduPilotMega 1 & 2 flight controllers. Later versions only work on the Pixhawk flight controllers. The Pixhawk flight controllers cost upwards of \$200, while the ArduPilotMega flight controllers cost less than half of that. Considering that testing will involve dropping the quadcopter from a significant height, a catastrophic failure could be very expensive. A disadvantage of utilizing Version 3.2.1 as opposed to more recent versions is that there is more support available for the newer versions than for older versions. Since ArduCopter is an open-source program, this support is in the form of volunteers in an online forum. No official or guaranteed product support is available for any versions.

## 2.7 Design Overview

The final design is pictured in its two configurations: stored (Figure 9). The final design consists of a G12 fiber coupler with windows cut out for arms. The top face is a circular piece of G10 fiberglass and the bottom face is a bulkhead of medium to high impact acrylic. The arms are 3D printed pieces that will be connect with spring hinges. The arms and electronics are mounted to fiberglass decks located in the interior of the payload.

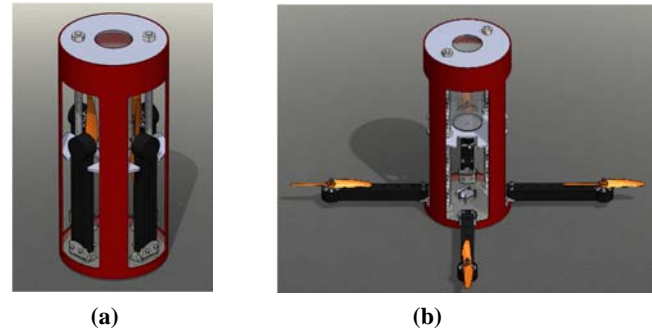


Figure 9. (a) Quadcopter in stored configuration (b) Quadcopter in extended configuration

The circuit diagram for the components that control the arm release and motors is pictured in Figure 10. The flight controller contains a barometer, accelerometer and gyroscope. The ArduPilot software will utilize these sensors to send signals to the electronic speed controls, which in turn adjust the speed of the motors. The flight controller will send a signal to the propeller arm servo according to the altitude and vertical velocity. The flight controller is connected to a receiver so that a transmitter on the ground can activate fail-safes. The telemetry module is necessary for Python script to be interpreted by Mission Planner and send the instructions to the quadcopter. The GPS module allows the quadcopter to be tracked, in accordance with NASA requirements. The power is supplied by a LiPo battery, which is connected to a power distribution board and battery eliminator circuit, which allows the appropriate voltages to be supplied to the different electronic components.

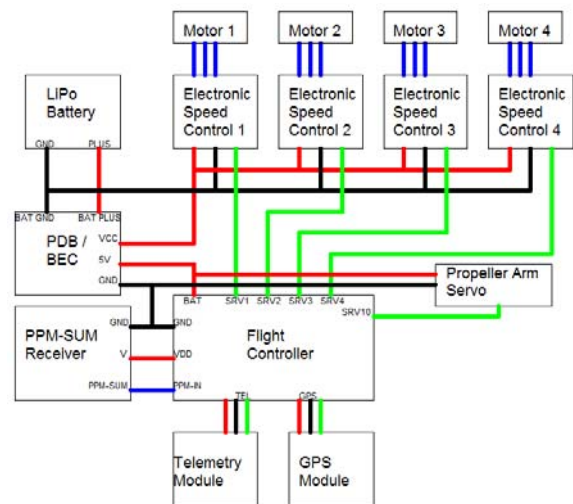


Figure 10. Circuit diagram for the arm servo and motors

The parachute system is separate from the flight control system, in accordance with NASA's safety standards, and the circuit diagram is pictured in Figure 11. The flight computers contain a barometer and an accelerometer. When the flight computer detects a specific altitude during descent, it closes a switch, sending current to ignite a black powder charge which will eject the parachute. In accordance with NASA safety standards, there is a redundant flight computer.

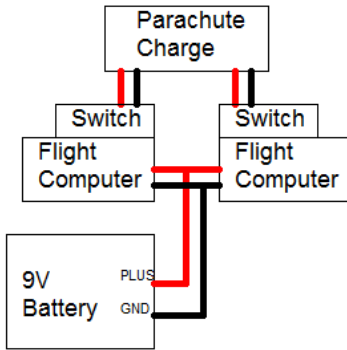


Figure 11. Circuit diagram for the parachute

### 3. PROTOTYPE CONSTRUCTION

#### 3.1 Overview

As the final design was finalized and chosen, and the materials were purchased, the construction of the prototype and design began underway. The parts arrived two weeks after ordering and the machining of the parts took the majority of the time as cutting the couplers needed to be handled carefully and wearing proper attire for safety. The total time it took for machining and assembling the structure of the quadcopter was about 10 days and the team was assembling for one month.

The prototype involved assembling the whole quadcopter and it was divided into three different sections. The first and most arduous section was the programming and working with the flight controls and software. The second section was the machining of all the parts in order to manufacture them to the finalized designs that were selected. The final section was the assembling of all the components which had to be done once testing for the program was working and then further testing with the finalized design could begin. After all of these different prototyping stages was complete is when the team could progress to testing the final prototype and finishing the quadcopter.

#### 3.2 Process

When constructing and machining began, the team focused on machining down and cutting the main parts that were used in the assembly. Cutting of the bulkheads was first as these were the main components inside of the coupler. For the acrylic bulkhead, a dremel was used to reduce the diameter of the bulkhead from 6 inches to 5.2 inches to fit inside of the coupler.

Once it was reduced to the correct size, the next thing was to drill holes for the threaded rods to go through as well as where the spring hinges and the camera are to be mounted. To be precise, 1:1 scale prints of the drawing were made to correctly drill the positions. The following step was to start drilling into the coupler,

to do this and be precise as possible, the diameter of the coupler was traced along where the arm cutouts would be.

Once the outlining of the sections that were going to be cut out were made, the next thing was to figure out how to properly cut into fiberglass with as much precision and minimal damage to the coupler. Also proper attire was necessary for cutting into fiberglass as it is glass and the dust can be very harmful when inhaled or makes contact to the skin. Masks were worn, protective eyewear, and windbreakers with the sleeves rolled out and plastic gloves all in order to prevent the fiberglass dust from making contact with the skin.



Figure 12. Team members cutting coupler

Cutting into the fiberglass began and went about this by drilling small holes all throughout the inside lining of the cutouts and was repeated did for all four sides that were going to be cut out. By performing it this way, the stress that is made when cutting inside the fiberglass was reduced and already drilling into all the sides and not one side at a time. The tool that was most widely used was the dremel and also a thin disked tool which cut through each hole that was previously made and cut through all four cutouts.



Figure 13. Fiberglass coupler after cutting

Once the cutouts were removed, using the dremel drill bit to smoothen the sides was next. What followed next was the cutting of the fiberglass bulkheads which since is fiberglass caution had to be taken when cutting into them. The same procedure used to cut the acrylic bulkheads was used for the fiberglass as a print out of the part to scale was used to drill precisely the holes for the threaded rods and the canister where the parachute would go. The difficulty with cutting of the bulkheads was to align the holes correctly to each other and make sure everything was centered as everything had to have a tight tolerance in order for all the components to fit.

The holes were aligned and fit it into the coupler which held perfectly. So now after the bulkheads were fitted to the coupler, the next thing was to reinforce the coupler with clear nail polish to prevent the fibers from becoming loose and shear as when being cut into, shearing was inevitable.

Also once all the components such as the bulkheads and the threaded rods were inserted and placed to mock the actual assembly and made sure that the propeller arms were adjusted well into the acrylic bulkhead, preparations for the epoxy of the top and bottom bulkheads were taken into account so that they would be fixed. The center bulkheads would be fixed between two locknuts within the threaded rods to secure them in place. The threaded rods were longer than the coupler to allow to longer length in order to have extra than less. The rod was machined down and sanded once it was cut with a saw.

Once all the parts were cut to size and ready to be assembled the components were fit inside of the coupler to test how the parts fit together before using epoxy to settle the components. The components were then assembled and wiring to the motors was added throughout the quadcopter to where the electronics are placed at the top of the quadcopter.



Figure 14. Bottom acrylic bulkhead with propeller arms

With all the components assembled then began the testing of the program and all the components to perform correctly. The main concern with the testing was to make sure that all the systems were working correctly and at the correct moment.



Figure 15. Finished prototype displayed

### 3.3 Prototype Cost Analysis

This project required skill from Mechanical, Electrical and Computer engineering disciplines. As a way to be organized and keep track of the expenses, the project was broken down into two parts: Body and Electronics.

The Body section of the cost analysis includes items such as the coupler, the spring hinges, screws, nuts, bolts, propellers, the steel rods and the acrylic disks.

The electronics section dealt with items such as the motors, flight controller, power distribution boards, wires, altimeter and the power module.

As can be seen below the cost for the prototype to be built was only \$751.87

Table 2. Cost Analysis Breakdown

Body	\$323.38
Electronics	\$428.29
Grand Total	<b>\$751.87</b>

## 4. TESTING AND EVALUATION

### 4.1 Overview

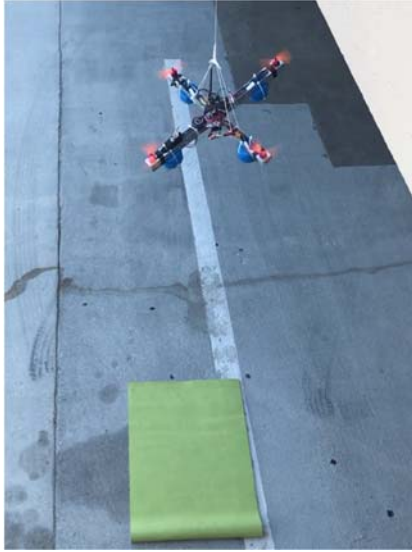
The arm release, stabilization, landing, and vertical landing detection were tested by building a simple quadcopter with similar weight, similar arm length and the required electronic components of the final design (Figure 16). Once these functioned successfully, the electronics would be moved to the final design.



Figure 16. Simple quadcopter used for testing code

### 4.2 Design of Experiments - Description of Experiments view

The simple quadcopter was initially tested utilizing the ArduPilot project's Mission Planner software. This software is a ground station application that simplifies the process of loading the ArduCopter firmware; setting up, configuring and tuning the vehicle; and planning and loading simple autonomous missions. Through the use of telemetry, Mission Planner allows the monitoring of the vehicle during operation. Mission Planner is also capable of running Python scripts through telemetry. During all flight testing, the quadcopter was tethered to a weight or the tether was held by a person.



**Figure 17. Simple quadcopter tethered during land mode testing**

Once the simple quadcopter was assembled, Mission Planner was used to calibrate the radio (Figure 16), accelerometer and compass. The simple quadcopter was then briefly flown to test that it responded to the radio transmissions adjusting throttle, pitch, roll and yaw. Its stability was also observed, but it was determined that unless there were gross stability issues, the stability would be thoroughly tested and refined in the final design.

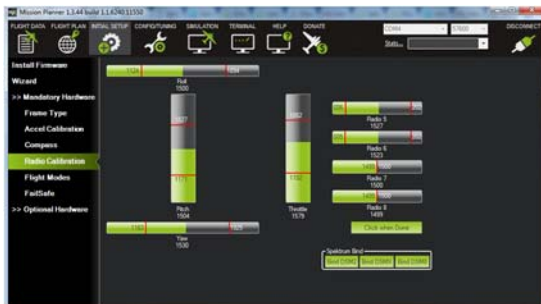


**Figure 18. Radio calibration of quadcopter**

Once the simple quadcopter was observed to respond to the radio transmitter and was sufficiently stable, the Mission Planner software was used to plan a simple Takeoff - Hover - Land sequence in which the quadcopter would takeoff, ascend to an altitude of five feet, hover for three seconds, and land.

### 4.3 Test Results and Data

Figure 19 depicts five trials where the quadcopter was held at a stationary altitude and the altitude read every 0.1 second for ten seconds. The altitude is internally calculated from the measurement of the barometric sensor in the flight controller.

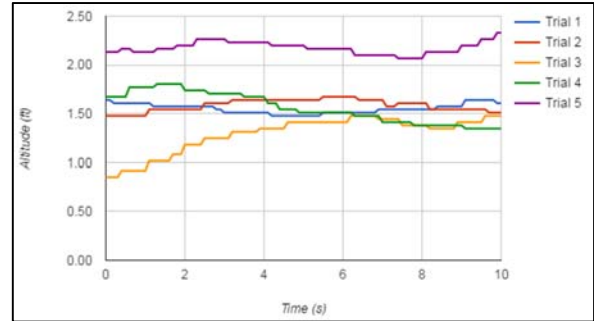


**Figure 19. Altitude reading over time when quadcopter is stationary**

**Table 3. Average and range of altitude readings over ten sec when quad is stationary**

Altitude	Trial 1	Trial 2	Trial 3	Trial 4	Trial 5
Average (ft)	1.55	1.59	1.29	1.56	2.17
Range (ft)	0.16	0.20	0.62	0.46	0.26

### 4.4 Evaluation of Experimental Results

The altitude readings when the simple quadcopter was held stationary were generally consistent within each trial, with a range of no more than 0.62 feet. Between the trials the average altitudes differed by as much as 0.88 feet. Since the altitude readings are going to be used to determine when the arms will be released, which will be at an altitude of a few thousand feet, and when the quadcopter will enter its final landing stage, which will be at an altitude of at least 30 feet, the differences within and between each trial will be inconsequential.

The response of the quadcopter to the Python script was very promising; with the motors appearing to respond correctly and nearly instantaneously to each output that signaled the beginning of a procedure. The accuracy of the vertical velocity could not be tested, but the values would have been based on the tested barometric sensor and an internal clock, and they seemed reasonable. Snippets of the output during the execution of the Python script are shown in Figures 20, 21, 22 and 23.



**Figure 2. Python script output of initial altitude reading and arbitrarily set release altitude**

```

Print statements in the python code will print to this dialog box

Current Altitude: 1.03, Release Altitude: 0.95
Current Altitude: 1.03, Release Altitude: 0.95
Preparing to release arms
3
2
1
Preparing to reset servo
3
2
1
Preparing to arm
3
2
1
Motors Armed!
Entering LAND mode
3
2
1

```

Figure 21. Python script output counting down quadcopter actions for visual confirmation

```

Print statements in the python code will print to this dialog box

Time: 291, Altitude: -0.28, Vertical Speed: -0.05, Throttle: 1188.0, No descent count: 93
Time: 292, Altitude: -0.28, Vertical Speed: -0.05, Throttle: 1188.0, No descent count: 94
Time: 293, Altitude: -0.28, Vertical Speed: -0.05, Throttle: 1188.0, No descent count: 95
Time: 294, Altitude: -0.28, Vertical Speed: -0.05, Throttle: 1188.0, No descent count: 96
Time: 295, Altitude: -0.28, Vertical Speed: -0.05, Throttle: 1188.0, No descent count: 97
Time: 296, Altitude: -0.28, Vertical Speed: -0.05, Throttle: 1188.0, No descent count: 98
Time: 297, Altitude: -0.28, Vertical Speed: -0.05, Throttle: 1188.0, No descent count: 99
Time: 298, Altitude: -0.28, Vertical Speed: -0.05, Throttle: 1188.0, No descent count: 100
No descent detected, disarming
3
2
1

```

Figure 22. Python script output disarming the quadcopter after 100 consecutive, insignificant vertical velocity readings

A separate execution of the Python script bypassing the servo activation, arming and landing was run in order to determine if an upright landing could be detected (Figure 23).

```

Print statements in the python code will print to this dialog box

Time: 97, Altitude: 0.11, Vertical Speed: 0.09, Throttle: 1188.0, No descent count: 97
Time: 98, Altitude: 0.11, Vertical Speed: 0.09, Throttle: 1188.0, No descent count: 98
Time: 99, Altitude: 0.11, Vertical Speed: 0.09, Throttle: 1188.0, No descent count: 99
Time: 100, Altitude: 0.11, Vertical Speed: 0.09, Throttle: 1188.0, No descent count: 100
No descent detected, disarming
3
2
1
Quadcopter disarmed.
Roll angle: -1.74
Pitch angle: 0.33
Upright landing successful!

```

Figure 23. Python script output confirming successful upright landing on the final pitch and roll angle

## 4.5 Discussion

The testing of the barometric sensor was satisfactory, allowing us to utilize the altimeter readings when writing the Python script. The quadcopter responded quickly and accurately to conditions that were based on these sensor readings. The autonomous adjustment of throttle during the Land sequence was unsuccessful, requiring repair of the quadcopter. It has not been resolved at the time of this submission but the outlook is promising. Once completed, the electronics can be moved from the simple quadcopter into the prototype.

The rocket and this project were not completed in time for the NASA Student Launch Flight Readiness Review in early March. This precluded it from participating in the NASA Student Launch on April 8, 2017. A great deal of progress was made, but unexpected and lengthy delays due to the programming of the quadcopter proved insurmountable. The project would definitely have been completed in time had the use of Python script to control the quadcopter been the original approach.

## 5. CONCLUSION

Even though the final design was not tested and compared to the computational models, the simple quadcopter was tested by lowering it from a height using a tether. These tests revealed the accuracy and fluctuations of the flight controller's sensors. The program would be using the barometer to determine the altitude, which in turn would be used to determine when to release the arms and when to begin final descent, and the barometer was determined to be accurate enough for our purposes. The program would be using the accelerometer and gyroscope to determine the pitch and roll of the quadcopter upon landing in order to determine if the quadcopter had landed upright, and they were both determined to be accurate enough.

## 6. REFERENCES

- [1] ArduPilot: About. (2016). Retrieved December 23, 2016, from <http://ardupilot.org/about>
- [2] Hareendran, T. K. (2015, April). The Making of a Radio-Controlled Plane. *Electronics for You*, 3(12).
- [3] Harrell, R. (2015). MQTB - DYS Fire 2206 2300kv. Retrieved February 05, 2017, from <http://www.miniquadtestbench.com/dys-fire-2206-2300kv.html>
- [4] Hobden, A. (2015, June 4). Quadcopters: Sensors. Retrieved December 28, 2016, from <https://hoverbear.org/2015/06/04/quadcopters-sensors/>
- [5] Owenson, Gareth. (2013, August 17). Build Your Own Quadcopter Flight Controller. Retrieved September 20, 2016. <http://blog.owenson.me/build-your-own-quadcopter-flight-controller>
- [6] Raskin, M. (2013, March 28). Drone Makers Get Help From the Open-Source, DIY Crowd. Retrieved December 23, 2016. <https://www.bloomberg.com/news/articles/2013-03-28/drone-makers-get-help-from-the-open-source-diy-crowd>

# Redundant Control Method for Automated Guided Vehicles

Scott Jagolinzer, Sabri Tosunoglu

Department of Mechanical and Materials Engineering  
Florida International University  
10555 W Flagler St  
Miami, Florida 33174

sjago001@fiu.edu, tosun@fiu.edu

## ABSTRACT

The purpose of this research is to explore the current state of automated guided vehicles (AGVs), sensors available for the vehicles to be equipped with, control systems for the vehicles to run on, and wireless technology to connect the whole system together. With a technological push towards increasing automation and maximizing the possible throughput of systems, automated technology needs to improve for trackless and wireless systems such as vehicles that can be used to move loads in a vast array of applications.

The goal of this research is to develop and propose improvements in both vehicle and control system design that allows for improved safety and efficiency. Right now, the main issues are maneuverability of vehicles and control systems being adaptive enough to deal with connection issues between systems. While prolonged connection issues will result in a stoppage of operation of any system that relies on wireless communication, intermittent issues can also cause systems to have an emergency stop. I have looked into ways to offload tasks from the central system and allow the vehicles themselves to have more computational privileges such that they can operate in a semi-independent manner.

The result is a proposed system that remedies or limits negative effects that currently cause issues with trackless vehicles and control systems working with remote systems that communicate via wireless means.

## Keywords

Automated Guided Vehicle, Hybrid Controller, Redundancy, Sensors, Trackless Vehicle.

## 1. INTRODUCTION

Automated guided vehicles began simply as a vehicle following a radio signal emitted from a wire on the ground. This has advanced to the point where we are very close to passenger vehicles being able to drive themselves on a widespread level. Vehicles are used in a wide variety of applications from personal transportation, to carrying payloads, to entertainment purposes. Industrial applications for autonomous trackless vehicles are tough because the vehicles have to be able to operate in a very dynamic and hectic environment that doesn't have the benefit of infrastructure and

ruleset that autonomous vehicles on a road are able to use. The fact that the applications can have the vehicles operating either indoors or outdoors or even moving between the two creates tracking challenges for the system.

Controllers that operate autonomous vehicles must either be contained fully on the vehicle, as with self-driving cars, or can be centrally located and connect wireless to a plurality of vehicles. While trackless vehicles that connect to a wireless control system still need to have on-board computing capability to process the signals they get from the central controller, they are usually tethered to the signal and rely on having a stable connection. There must be ways to improve the balance of computing capability between autonomous systems that rely on a central control system that allow for more forgiving operation in situations where signal interference is possible.

## 2. AUTOMATED GUIDED VEHICLES

Typical AGVs tend to be of a simplistic design and control due to their autonomous nature. Keeping the vehicle and controller simple limits the chance that there is something that can go wrong for these potentially huge machines that are moving around without much human oversight. In general, AGVs consist of platforms that have one or two drive wheels with the rest being free-moving castor wheels to carry weight and provide balance.

### 2.1 Steering

Steering is one of the most important factors in the AGV because the method of steering influences the mobility and control of the platform. There are three major steering schemes used on AGVs.

The most basic steering control is from a differential drive wheel configuration. This is when there are two drive wheels that are parallel to one another and the turning process is created when there is a difference in wheel speeds. This is similar to how a tank steers. It benefits from its design simplicity but is unable to perform more complex movements.

Another steering method is a three-wheel steer drive configuration. There are two castor wheels and the one powered drive wheel that can also spin to control direction. This is the type of steering that is available on most forklifts. This method is more maneuverable than

differential steering and can perform smooth and accurate motions but still isn't the most maneuverable option.

The third option is a two steer-drive wheel configuration. This configuration has two drive wheels that can be rotated and two castor wheels. This steering configuration allows from the vehicle to move in any direction and turn on the spot. Similar to the 2 steer-drive wheel configuration is the Quad wheel configuration. This combines two fully rotatable drive wheels with two castor wheels to give the best range of motion and highest maneuverability [37].

A possible improvement that will be explored is having four drive motors that can all be rotated independently. This has the advantage over the two steer-drive configurations in that all four wheels are driven, allowing for double the available power and can also allow for power efficiency and reliability by disengaging a pair of wheels to drop the power consumption by half or allow for continued operation if a motor for a wheel breaks or a sensor malfunctions. This fault-tolerance system will allow for increased efficiency and reliability.

## 2.2 Vehicle Design

A more robust control system for an AGV requires a more robust vehicle. The design of this vehicle allows for size scalability and maneuverability for a wide array of uses. The vehicle has a very simple design consisting of 3 main parts.

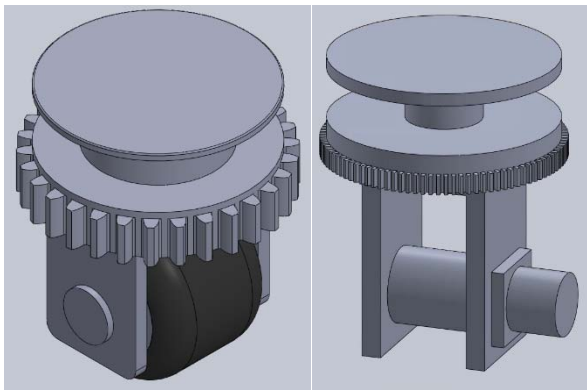


**Figure 1. Wheel mounting bracket showing rotational gear interface and space for linear motor mounting**

First is the wheel and mounting bracket. This consists of the wheel, the bracket that the wheel is mounted to, and the drive motor for the wheel. Since the wheels are meant to spin a full 360 degrees the bracket must be able to easily rotate with respect to the main platform while also being able to stably support the loading of the vehicle. To account for both these needs, the cuff of the bracket has a wide plate on the top and bottom that help distribute the loading for each wheel assembly while also limiting the frictional forces that need to be overcome for rotation of the cuff to be performed. Figure 1 shows an earlier design of the wheel and cuff. As can be seen midway up the bracket, there is a gear built into it. This is for the second motor to interface with to control the wheel orientation. In figure 1 the placement of the drive motor is shown on the outside of the bracket lined up with the axis of the wheel. The bracket can either have one motor mounted to one of the sides, or two motors working in tandem mounted on both sides to amplify the power available to the wheels while keeping the size of the motors in check.

Second is the lower platform. This is the main housing for the vehicle as it is where the wheel brackets link into as well as housing

the required mechanics for the vehicle such as power source (batteries or generator), the motors that control wheel orientation, most of the onboard sensors, and the computer system.

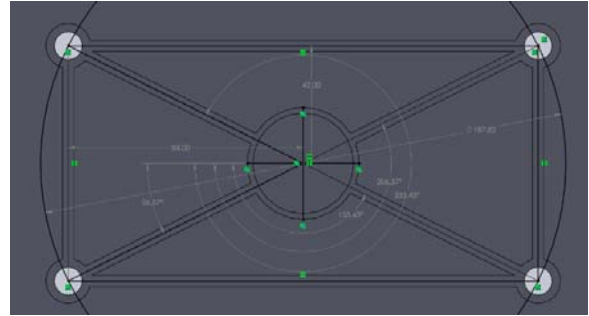
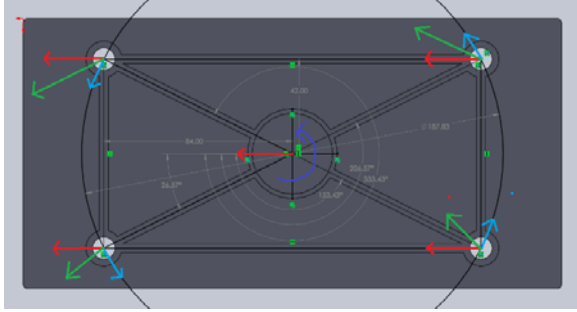


**Figure 2. Underside of platform showing a possible wheel configuration with respect to the center of the vehicle**

To make control of the wheels as simple as possible, they are laid out along a circular pattern with respect to the center of the vehicle. By having the wheels laid out in a circular pattern about the center of the vehicle, it creates an easy reference not only between the central point of the vehicle, where the position will be taken from, but also an easy reference between wheels so that rotational maneuvers have the most evenly distributed output requirements. This layout allows for the required wheel velocities and orientations to be easily calculated getting eight outputs (velocity and orientation of each wheel) from three desired inputs (linear velocity, direction, and vehicle orientation). Knowing only the length and width of the wheelbase, the location of all four wheels can be resolved for the system to properly calculate the required motor outputs to the wheels.

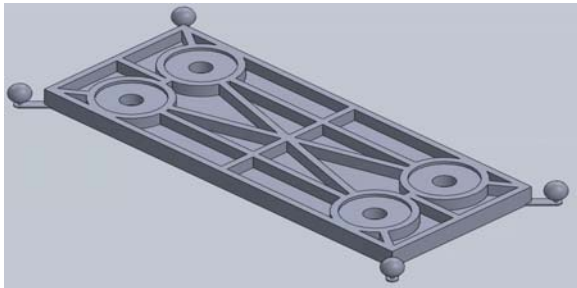
Since each wheel is independently controller that mean each wheel has two motors, one each for linear and rotational velocity outputs. Each wheel system is connected to the main platform via a cuff that is designed to be able to carry the required loadings for the vehicles desired application. The rotational motor is mounted within the platform and interfaces with the wheel system via a gear. The tricky part comes with the mounting location of the drive motor. There are two options, on the platform or directly to the wheel mounting bracket. Mounting from the platform would require a driveshaft that can not only operate at an angle, but be able to compensate for the rotational movements with the vehicle without affecting wheel velocity. Mounting from the wheel bracket gives an easy, direct connection to the wheel but creates an issue with wiring back to the platform to be able to receive power and a signal. Mounting to the wheel bracket was determined to be preferable since slide contacts can be used for the transfer of power and required data.

Figure 3 shows how given a desired linear (red arrow) and rotational (blue arrow) velocity for the vehicle as a whole, it can be broken down to the wheel components which combine for the total output for each wheel (green arrow). Notice how the blue arrows for each wheel are always tangent to the circle that the wheels all lie on. The resultant motion shown is of the vehicle driving in a straight line while its orientation is rotating counter-clockwise.



**Figure 3. Desired linear and rotational velocity depicted in the center result in the wheel outputs (green, with red (linear) and blue (rotational) components)**

Figure 4 shows a design for the lower platform where there are large recessed areas for the wheel bracket to slot into along with ribbing along the platform to reinforce it in areas where forces are expected to be transferred along the body of the vehicle. The positional sensors can also be seen mounted at each of the corners of the vehicle. Having a sensor on each corner allows for an environmental sensor to be able to see at least two of the vehicle sensors at a time assuming no other obstacles possibly blocking the line of sight besides the cargo onboard. Figure 5 shows the same lower platform with the wheels in place. The top of the bracket cuff is flush with the platform ribbing and the built-in gear are exposed below the platform. This allows for the orientation motors to be mounted to the lower platform and have them connect to the wheel brackets via a hole in the floor of the platform.



**Figure 4. Lower platform complete with cutouts for wheel brackets and positional sensors mounted to corners**

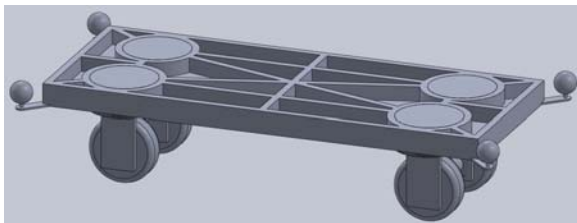


**Figure 5. Lower platform with wheels in place**

Third is the upper platform. The upper platform sits on top the lower platform covering and protecting the mechanical components of the vehicle while also providing the required base to interface with the desired cargo be it pallets, shipping containers, or people. The upper platform can be designed with a specific requirement in mind. Figure 6 shows an upper platform that is designed to hold a 20x8 foot cargo container. The modular design allows for the upper platforms to be interchangeable with the main vehicle allowing for one vehicle to be used with many types of cargo without having to compromise on how the cargo interfaces with the vehicle.

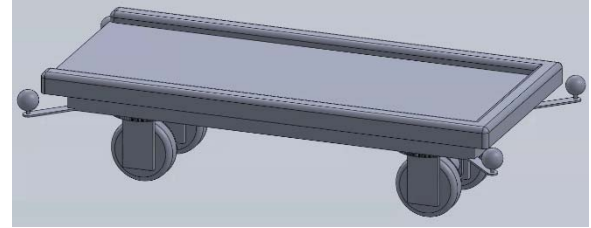


**Figure 6. Complete vehicle with upper platform that is designed to handle large shipping containers**

### 3. SENSORS

#### 3.1 Guidance Methods

There are various methods for guiding the vehicles. These include wired navigation, guide tape, laser target navigation, inertial navigation, natural feature navigation, vision guidance, or geo-guidance.

Wired navigation is simply a wire carrying a radio signal embedded into the path the AGV is to traverse. The AGV has a sensor mounted below it that hovers just off the surface and picks up the signal from the wire, which allows for the vehicle to sense and follow the wire.

Guide tape is similar in principle to the guide wire but the guide tape carries no signal. Instead either a colored or magnetic tape is placed along the desired path and either a vision system or magnetic sensor read and follow the path laid out by the tape. There are advantages and disadvantages to both visible and magnetic tape. Visible tape, while it is cheap to install and make path adjustments, since it needs to be on the surface of the path to be viewed by the AGV, it can be damaged or dirty through daily vehicle and personnel activity. A system that uses a visible guideline for steering control has two ways it handles the guideline to control the steering. The first way, when the vehicle is moving at a slower speed it reacts to the error values of the vehicle with respect to the line. When moving faster, the controller uses the slope of the line to determine the required steering as waiting for error results could cause the vehicle to not be able to react in time at higher speeds. [J. Lee] The magnetic tape allows for it to be embedded into the path and therefore is not exposed to wear. However, having to carve out a channel and cover the buried magnetic tape results in a costlier install and makes it harder to change the path layout.

Laser target navigation uses a rotating laser emitter and sensor in tandem for distance detection that can be used for position tracking. The laser is reflected off reflective tags that are affixed to walls, poles, or other fixed obstacles, each of which corresponds to a known point in the workspace by the system. Therefore, by reflecting off the various reflective tags, the vehicle can triangulate its position and use that knowledge to plan and execute its motion based on the data that is collected and processed in real time. There are two types of laser sensors, modulated and pulsed. Modulated lasers have a larger range and higher accuracy over a pulsed laser with an angular resolution of  $0.006^\circ$ . Pulsed lasers have an angular resolution of  $0.2^\circ$  and must be interpolated by the intensity of the reflection at each data point to reliably get an accurate location. For the system to work the vehicle needs to be in view of at least 3 environmental reflectors to correctly triangulate its position [38].

Inertial navigation uses a gyroscope that can, within an inch, detect the movement of the vehicle. It also uses transponders located in the workspace floor to verify the position of the vehicle. This

system is flexible in that it can be used in a wide range of environments with or without the feedback [39].

Natural feature navigation uses range detecting sensors in conjunction with gyroscopes to read the layout around it and the vehicle triangulates its position using the natural features on the environment. It uses the data of its surrounding to develop the shortest possible distance to its destination since the system doesn't necessarily know the layout of its surroundings [39].

If the natural feature navigation did have full knowledge of its surroundings, then this system would be considered a geo-guidance system as it operates in the same way a laser guidance system works but without the reflective tags.

Vision guidance uses cameras to view their surroundings in a full 3D image and then builds a 3D map of the workspace. It can then match up its live view with that of its 3D map to be able to determine where it is in the workspace. It can also be programmed to recognize certain features such as obstacles or humans as to allow for the vehicle to stop or reroute [19].

### 3.2 Proposed Sensors for Control Method

The sensors that will be used on board and in the environment, will play a large role in the capabilities of the system. While the robustness of the control scheme is the foundation for autonomous control, an equally robust array of sensors is required to feed enough pertinent information that the system can make well informed decisions.

Vision sensors are those that use the visible light spectrum to capture an image for the system to process. Since a computer cannot inherently look at a picture and understand what it is displaying like a human can, the controller needs to be programmed to identify pertinent information from the video feed it is receiving. This can be as simple as recognizing a colored line on the floor and knowing it should follow it to recognizing certain shapes such as walls, other vehicles, or any other obstacles it could come across and knowing how to take evasive action. A vision system is very flexible but requires extensive programming work to get the most out of it [2].

Ultrasonic sensors can typically be used as proximity sensors since it is very easy to time the bounce of the signal and determine the distance of the object reflecting the sound waves. While these sensors would not be used for controlling the vehicle, they are instead used as a fallback safety system to warn and allow for the vehicle to stop if anything unexpected ever enters a predefined workspace of the vehicle. When dealing with large and expensive machinery, especially machinery that is moving autonomously, it is important to have multiple sensing and safety layers [23].

Infrared sensors can be used for tracking of the vehicle and positional sensing. While similar to the vision system, since these sensors only operate on the infrared wavelength, special infrared emitters and reflectors can be placed on the vehicles and in the environment to allow for positional data to be determined since the environmental emitters and sensors will always have a fixed and known location [24].

Radio frequency sensor picks up radio signals that are present. In the history of the

AGV, this sensor has been used to allow the vehicle to read and follow a wire that emits a radio frequency that is embedded into the floor that defines the desired path of the vehicle.

Magnetic sensors pick up on a magnetic field that is present. A magnetic sensor can be used in the same way that the radio sensor was used by reading the signal from a magnetically charged wire that defines a path for the vehicle.

Gyroscopic/force sensors can measure the forces that the AGV is experiencing due to acceleration. This can be used to gauge and control the acceleration and deceleration of the vehicle while also monitoring lateral forces that could be imparted by taking turns with a moderate speed.

Global Positioning Systems are another way to detect the position of the vehicle and is especially useful in an outdoor work environment that is exposed to more variables such as weather and time of day that can affect some of the sensors mentioned above.

All the above sensors can be used together to give an automated vehicle a plethora of instruments that allow for the vehicle to read and navigate its environment [25]. The sensors each have their strengths and weaknesses that must be considered when choosing the right sensors to design a control system around. It is also important to have built in fail safes and redundancies into the system such that control will not be lost should a sensor go down or an environmental condition affect the system. One example is if the lights go out in the workspace and the controller only operated off of vision sensors. This would cause the system to lose all input from the sensors. And while at that point one would hope that the controller is programmed to shut down in that scenario, there is a moment while all these vehicles would be trying to stop that they would be blind and at risk for collision. In this scenario ultrasound and infrared sensors can be used to protect against this situation. Infrared sensors are not impaired by the lack of light and use infrared emitters placed in the environment to determine its position. Ultrasound sensors rely only on sound waves to detect the proximity of objects from it. This could allow for the vehicle to detect any objects that would be in its vicinity and allow for it to maneuver in a way that it would be able to avoid the object although it is not able to 'see' it in the conventional sense.

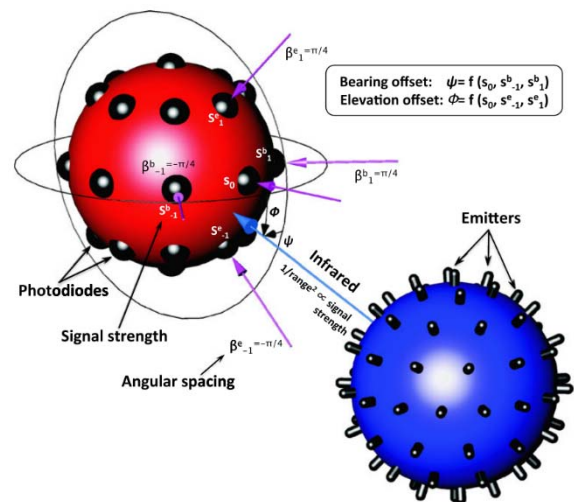


Figure 7. Diagram of 3-D relative positioning sensor for indoor flying robots [14]

The infrared sensor and emitter clusters depicted in figure 7 were developed for use on indoor flying robots [14]. However, the sensor design can be used with an autonomous vehicle control system. The design calls for a spherical array of infrared emitters and sensors.

In the figure below the blue and red spheres depict them respectively, however they are only depicted as two distinct objects to clearly show the interaction between the emitting and sensing portions of two sensors. The actual sensor is a sphere with both the emitters and sensors interspersed between each other. This allows for each vehicle outfitted with the sensor to not only read its environment but to also be able to be sensed by other vehicles and by sensors in the environment that monitor the positions of the vehicles.

When the sensor picks up a signal, it measures the intensity of that signal at each of the sensor nodes. It uses the three strongest signals and then triangulates the direction and uses the signal intensity to determine the distance the object emitting the signal is from the sensing object. This can be done since the geometry of the sensor sphere is known and the decay of the infrared light intensity can be experimentally found and then applied to calculating proximity.

#### **4. CONTROL METHOD**

The proposed control system is to use and build upon elements from previous control systems such that efficiency and reliability are increased.

A hybrid controller will be employed for the system having a main controller monitors all sensors, both environmental and those on each vehicle, and control the fleet of vehicles on a macro level with path planning and task queueing. Each vehicle will also be equipped with a controller able to read from its sensors and perform on board calculations and take independent control of the vehicle when either contact with the main controller is temporarily lost or for a reactionary maneuver that would take too long for the central controller to sense and react to.

The motivation for having multiple control layers for this system is to increase reliability of the system. With these vehicles being trackless, they are not hardwired into the control system and often rely on a Wi-Fi or other close ranged network signal that can fluctuate in coverage or suffer from slowdown when too much information is being transmitted. If control was handled purely from a central system, any network interference would cause an affected vehicle to stop and wait for either the signal to return or for a manual override.

The system will have a wide array of sensors, both onboard the vehicles and in the environment. The primary positioning sensor will be the 3D spherical emitter and sensor arrays. Each vehicle will have of these 3D sensors, on at each corner of the vehicle. This will allow for the sensors in the environment to be able to always have a clear view of at least one of the sensors regardless of vehicle orientation and allow for it to calculate the orientation of the vehicle. These sensors not only allow for the central system to read the position of the vehicles, but also allow the vehicles to read their position in the environment and allow them to read other vehicles that they have line of sight with.

The benefit of each 3D sensor is that it both emits and reads so that the information is always being shared both ways between the various systems. This allows both layers of the control system to independently track position and verify the data between them and allow for them to operate independently should one end fail or lose contact.

A GPS sensor could be used for each of the vehicles if the application has a large outdoor workspace where it would be uneconomical or impractical to cover the whole workspace with positional sensors.

The vehicle themselves are equipped with an accelerometer, load scale, positional and velocity tracking for each of the vehicles wheels, proximity sensors, and cameras.

The goal of the main system level controller is to be the manager of the entire system. It should be able to receive inputs from outside the system, such as user input for desired tasks, and then assign that to an active vehicle in the fleet. In assigning the tasks, the system needs to consider the positions of all the vehicles and their task status. It should assign new tasks as they come in such that it is carried out in the most expedited manner without affecting the flow of the rest of the tasks. The main system also calculates the path that the vehicle needs to take to carry out this task. The path planning is fully calculated before the task is assigned so that after the vehicle is assigned the task from the system, it could complete the task even if its connection with the main system is interrupted. While the task is being completed the two systems share all their sensor data to cross reference for verification and to monitor the progress of the vehicle.

The vehicle level controller is a simpler system that just takes the assigned pathing data and convert that to the required outputs for each of the four wheels. The vehicle controller also monitors onboard sensors that are mostly to monitor the surroundings for possible obstacles that would need to be avoided.

With four independently powered and rotatable wheels there are a lot of factors that go into the outputs for each of the wheels. Since they are not physically synchronized and are capable of being operated at different orientations, the precision of the controller is paramount since loss of wheel control when the vehicle velocity is sufficiently perpendicular to the wheels can cause damage or abrupt stops that could cause the load to be jolted loose. The two data points that are fed into the vehicles system are the desired Cartesian position of the vehicle along with its desired orientation. Each of these can be calculated as separate components of the wheel outputs then combined afterwards to get the independent signals for each wheel. This simplifies the calculations since the component of the wheel output for positional data is the same for each of the wheels. The orientation component of the wheel output is in a direction tangent to a circle that is centered on the middle of the vehicle and passes through each of the wheel's locations. This output is affected by the dimensions of the vehicle so it is very important that those are represented correctly in the system. Each of these components of the wheel output are linearly combined to give the required independent outputs for the wheel velocities and headings.

#### **4.1 Positional Data**

Having the vehicles use 3D relative positioning sensors they do not need to rely on more conventional methods such as GPS or wheel encoders, which each have shortcomings, lack of precision in some environments and error accumulation respectively. The only downside to using the 3D relative positioning sensors (3DRPS) is that you have to make sure that there are enough environmental sensors within line of sight of the vehicle in its workspace. With the vehicles and environmental sensors having a broadcasting and reading sensors, each can determine the location independently and cross reference for accuracy.

Each vehicle would be equipped with a minimum of two sensors in known locations on the vehicle. The environmental sensors are located in known locations within the vehicle workspace.

For the master system to determine the location of a vehicle it requires that one environmental sensor reads two sensors on the

vehicle to resolve the 2 unknowns of location and orientation. If multiple environmental sensors can read the vehicle, then multiple reading can be cross referenced to improve reliability and reduce the possibility of a rogue reading or noise.

The vehicles have two possible methods for determining its location and orientation. The first way to determine its location is by reading its distance from a known location of an environmental sensor plus a compass reading (heading). The second method is to have one of the vehicle sensors read the locations of two environmental sensors.

The above methods for determining the vehicles location are the minimum data points required and more can be used for verification purposes.

### 4.2 System Outputs

The vehicle has a total of eight motors that work together to provide the desired vehicle movement. There are four drive motors (DM), one for each of the drive wheels which are controlled by setting a desired velocity. There are four rotational motors (RM), one for each of the drive wheels that control the angular orientation of each wheel indecently. They are controlled by giving a desired angle.

The vehicle will only need three inputs for the controller to sufficient define the required output. The inputs will be the desired x- y- coordinates of the location and the phi angle, which is the orientation of the platform, not the heading of the vehicle motion. The theta is resolved within the controller by solving the trigonometric relationship between the current vehicle location and the desired vehicle location.

The controller will use the desired values for the inputs, supplied from the main control system, and use a PID controller to determine how each will factor into the two output values for the vehicle motors. Each value will use feedback from sensors for each of the respective inputs to allow for maximum accuracy and responsiveness. Once the framework for the controller is built, the gain values for each input will be optimized to give the best balance between a smooth, yet responsive signal to the output motors. Since the controller can be adapted to vehicle size and environmental needs, the gains for the controller will need to be fine tunes for each application independently.

The velocity and angle for each of the four drive wheels are the result of the desired liner velocity and heading along with the desired platform orientation. Each of these events can be calculated separately then combined linearly to determine the final outputs for each of the wheels.

### 4.3 Vehicle Controller

The system for the trackless vehicles is a two-tiered controller that works in parallel. This consists of a master controller that oversees the entire system, and a local controller that is on board of each vehicle that carries out the plans of the master controller.

The higher-level controller is a system monitor and planner for the entire system. There are multiple facets to this controller.

First, this controller plans tasks and distributes them down to the individual vehicles. This is done by the controller taking a queued task in the system and deciding which vehicle will complete the task. This can be based on proximity or which vehicle was used last or many other parameters. The controller then creates a path for the vehicle from its current location to that where the task needs to be completed. The path is given in terms of x- and y-coordinates and the orientation of the vehicle (phi). These are all given with respect

to time to control the velocity of the vehicle depending on loads such that it can safely stop given the range of its onboard sensors.

Second, the controller monitors all the sensors that are hardwired into its system. These are all the environmental sensors so that the controller can make informed decisions on path planning and current work flow. This can allow the system to read obstructions so that it can plan ahead of time instead of having the vehicle itself sense the obstruction and have to react locally.

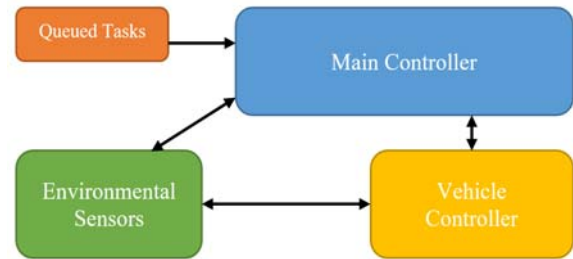


Figure 8. Flowchart for flow between controllers and sensors

Third, the controller receives all the sensor data from each of the vehicles and verifies that data with its own sensor data. Since the positional sensors have a component on both the vehicle and in the environment, the reading from each of the perspectives can be compared since they should ideally be reading the same value. The difference in value is compared to an acceptable tolerance that can trigger a shutdown if the error exceeds it. Since the controller can read the vehicle sensor data, it can make updates to the path should the vehicle encounter a local obstruction that the overall system did not account for when originally planning the path. This allows for the system to adapt in real time using data points from any of the vehicles. While the vehicles do not have to directly connect, the system can use data it receives from one vehicle and apply that information to any other vehicle that the system deems would benefit from the data.

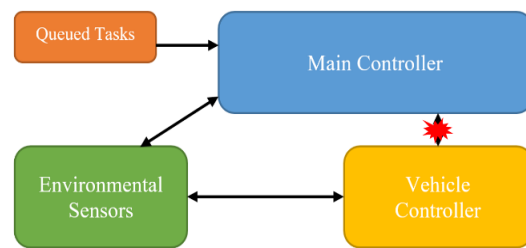


Figure 9. System with connection issues between main controller and vehicle

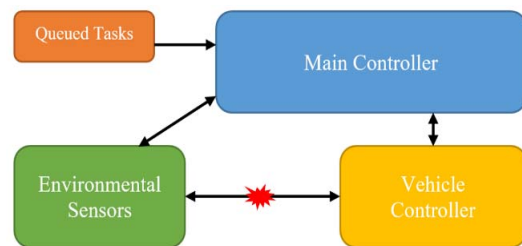


Figure 10. A signal error between the vehicle and environmental sensors

The vehicle controller is fully capable for operating a vehicle independently of the main controller. The only pertinent information the vehicle gets from the main controller is the path to a goal location. Having the vehicle contain a full suite of on-board sensors and processing capabilities allows for the vehicle to navigate the work environment once the path data is supplied to it. This allows for the vehicle to keep running even if the connection is lost with the main system for whatever reason. Once the vehicle reaches its desired goal position, if a connection is still unavailable from the main system, the vehicle will wait. While a major connection issue will cause productivity to stop in some capacity depending on the location of the connection issue, the main benefit on this is that intermittent connection issues will not force emergency stops or lead to vehicles losing control if they relied on the main signal for motor output signals. This can maintain a high uptime barring a major issue with the main controller. With most of the work offloaded and distributed to the vehicles, a vehicle controller issue is minimized to only the affected vehicle and will not impact the performance of any other vehicle in the workspace.

Besides a connection issues between main controller and vehicle, there are other issues that can be overcome by the layout of the system. The positional sensors that are employed for this system are 3D relative positioning sensors (3DRPS). The way these sensors work is that each sensor both emits a signal and reads the signals from other sensors. The 3DRPS are placed in known locations of the environment. This allows the environmental sensors to read the relative position of a vehicle and report that to the main system. This also allows the vehicle sensors to read the relative position of the environmental sensors and calculate their own location. Since the vehicle is having its position read from two sources, this creates a level of redundancy that can be used for verification purposes to increase accuracy, but also to allow for operation to continue if one of the signals is either unable to read or giving bad numbers. This can mainly be used to allow for the system to identify and ignore possible rogue values from the sensors without having the system have to stop. While this can be used to allow for operation to continue if there is a more permanent issue with part of the sensor network, it would be recommended that the vehicle only operate to finish its current task then remove itself from service to be inspected. However, even if a vehicle does have some kind of sensor error, the redundancy and parallel structure of the system allows for the vehicle to finish its task and exit the workspace versus having to perform an emergency stop while loaded in the middle of its work environment.

The main part of the vehicles controller is a PID controller that takes the desired path generated by the main controller, in terms of x- and y-coordinates and a phi angle (vehicles orientation) and calculates the required vehicle outputs in terms of wheel velocities and headings. The controller's feedback uses the sensor data from the 3DRPS to compare the vehicles current location with the desired location described by the intended pathing. The vehicle also contains other on-board sensors that are for local obstacle detection. There are three ways the vehicle controller uses the local obstacle data. If there are no detections or an obstacle is at a distance that is out of the vehicles path envelope, the vehicle will proceed uninterrupted. If the vehicle detects an obstacle that is along the planned path of the vehicle the controller can modify its path to avoid the object. If the vehicle detects an object within a proximity that the vehicle deems is nearing its stopping distance, it will tell the vehicle to stop. There will be a sufficient cushion to the stopping distance that the vehicle will err on the side of safety. The third

condition of having the vehicle stop is only a result of extreme circumstances such as obstacles falling into the vehicle path or a moving obstacle that happens to be moving in the same direction the vehicle is attempting to deviate its path to.

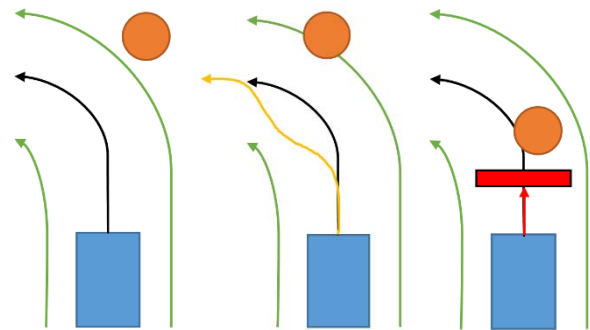


**Figure 10. Obstacle detection and possible courses of action**

The features of the main controller and vehicle controller come together to integrate with a multitude of sensors that allow for improved safety and efficiency over current applications of automated vehicles. This system can be deployed for virtually any application so long as there is enough infrastructure to establish a sufficient network of environmental landmark sensors. The main controller can be calibrated and scaled for any size and application from transportation of shipping crates in a shipping yard, moving raw material in a factory, or controlling a fleet of ride vehicles in an entertainment application.

## 5. REFERENCES

- [1] S. Jagolinzer, S. Tosunoglu, "Trackless Multi-Dimensional Ride Vehicle," 2015 Florida Conference on Recent Advances in Robotics, May 14-15, 2015.
- [2] J. Lee, S. Choi, C. Lee, Y. Lee and K. Lee, "A study for AGV steering control and identification using vision system," Industrial Electronics, 2001. Proceedings. ISIE 2001. IEEE International Symposium on, Pusan, pp. 1575-1578, Vol. 3, 2001.
- [3] YuHon Tee, Y. Tan, BoonYew Teoh, EngBeng Tan and ZhenYang Wong, "A compact design of zero-radius steering autonomous amphibious vehicle with direct differential directional drive - UTAR-AAV," 2010 IEEE Conference on Robotics, Automation and Mechatronics, Singapore, pp. 176-181, 2010.
- [4] X. Ye, Z. Wu and F. Zhao, "Research on a 3 DOF Automated Guided Vehicle based on the improved feedback linearization method," Control Conference (CCC), 2014 33rd Chinese, Nanjing, pp. 184-188, 2014.
- [5] B. Xing, Wen-Jing Gao, K. Battle, T. Marwala and F. V. Nelwamondo, "Can ant algorithms make automated guided vehicle system more intelligent?," Systems Man and Cybernetics (SMC), 2010 IEEE International Conference on, Istanbul, pp. 3226-3234, 2010.
- [6] G. Kaloutsakis, N. Tsurveloudis and P. Spanoudakis, "Design and development of an automated guided vehicle," Industrial Technology, 2003 IEEE International Conference on, pp. 990-993 Vol. 2, 2003.
- [7] Xing Wu, Peihuang Lou, Dunbing Tang and Jun Yu, "An intelligent-optimal predictive controller for path tracking of

- Vision-based Automated Guided Vehicle," *Information and Automation*, 2008. ICIA 2008. International Conference on, Changsha, pp. 844-849, 2008.
- [8] M. P. Fanti, "Event control for deadlock avoidance in automated guided vehicle systems," *Control Conference (ECC)*, 2001 European, Porto, pp. 1217-1222, 2001.
- [9] E. Gebennini, S. Dallari, A. Grassi, G. Perrica, C. Fantuzzi and R. Gamberini, "A simulation based approach for supporting Automated Guided Vehicles (AGVs) systems design," 2008 Winter Simulation Conference, Miami, FL, USA, pp. 2156-2163, 2008.
- [10] M. A. Kermanshahi, M. Rostamian and A. Vosough, "Design, production, and fuzzy control of an automated guided vehicle robot platform with capability of path following," *Control, Instrumentation and Automation (ICCIA)*, 2011 2nd International Conference on, Shiraz, pp. 946-951, 2011.
- [11] D. Xu, Y. I. Liao, Y. j. Pang and N. Sun, "Backstepping control method for the path following for the underactuated surface vehicles," *Control Conference (CCC)*, 2013 32nd Chinese, Xi'an, pp. 4188-4193, 2013.
- [12] Iris F.A. Vis, "Survey of research in the design and control of automated guided vehicle systems," *European Journal of Operational Research*, Volume 170, Issue 3, 1 May 2006, Pages 677-709, 2006.
- [13] Yu, P. Lou, X. Wu, "A Dual-core Real-time Embedded System for Vision-based Automated Guided Vehicle," 2009 IITA International Conference on Control, Automation and Systems Engineering, July 11-12, 2009.
- [14] Roberts, T. Stirling, J. Zufferey, D. Floreano, "3-D relative positioning sensor for indoor flying robots," *Autonomous Robots*, 2012.
- [15] S. Arora, A.K. Raina, A.K. Mittal, "Hybrid Control in Automated Guided Vehicle Systems," 2001 IEEE Intelligent Transportation Systems Conference, August 25-29, 2001.
- [16] R. Grigorevich, "Disaggregation of Control System Synthesis for Mobile Vehicle with Survivability Property," *Middle-East Journal of Scientific Research*, 2013.
- [17] Payton, "An architecture for reflexive autonomous vehicle control," *Proceedings. 1986 IEEE International Conference on Robotics and Automation*, pp. 1838-1845, 1986.
- [18] R. Fenton, G. Melocik and K. Olson, "On the steering of automated vehicles: Theory and experiment," in *IEEE Transactions on Automatic Control*, vol. 21, no. 3, pp. 306-315, Jun 1976.
- [19] M. J. Han, C. Y. Kuo and N. Y. C. Chang, "Vision-based range finder for automated guided vehicle navigation," 2016 IEEE Workshop on Advanced Robotics and its Social Impacts (ARSO), Shanghai, pp. 146-151, 2016.
- [20] Lee, S. Park and H. Son, "Multi-DOFs motion platform based on spherical wheels for unmanned systems," 2016 13th International Conference on Ubiquitous Robots and Ambient Intelligence (URAI), Xi'an, pp. 35-37, 2016.
- [21] K. Koganezawa and H. Yamashita, "Stiffness control of multi-DOF joint," 2009 IEEE/RSJ International Conference on Intelligent Robots and Systems, St. Louis, MO, 2009, pp. 363-370, 2009.
- [22] D. Mahmood, N. Javaid, U. Qasim and Z. A. Khan, "Routing Load of Route Discovery and Route Maintenance in Wireless Reactive Routing Protocols," 2012 Seventh International Conference on Broadband, Wireless Computing, Communication and Applications, Victoria, BC, pp. 511-516, 2012.
- [23] V. Josef, "Trailer backing-up assistant using ultrasound sensors based control units to safely back-up the car with trailer," 2016 17th International Conference on Mechatronics - Mechatronika (ME), Prague, pp. 1-6, 2016.
- [24] S. Nanda, S. Manna, A. K. Sadhu, A. Konar and D. Bhattacharya, "Real-time surface material identification using infrared sensor to control speed of an arduino based car like mobile robot," *Proceedings of the 2015 Third International Conference on Computer, Communication, Control and Information Technology (C3IT)*, Hooghly, pp. 1-6, 2015.
- [25] P. Yuan et al., "AGV System Based on Multi-sensor Information Fusion," 2014 International Symposium on Computer, Consumer and Control, Taichung, pp. 900-905, 2014.
- [26] C. Blum and X. Li, "Swarm Intelligence in Optimization", ALBCOM Research Group, Universitat Politècnica de Catalunya, Barcelona, Spain, School of Computer Science and Information Technology RMIT University, Melbourne, Australia, undated paper.
- [27] C. Cianci, X. Raemy, J. Pugh, and A. Martinoli, "Communication in a Swarm of Miniature Robots: The e-Puck as an Educational Tool for Swarm Robotics", *Swarm-Intelligent Systems Group, École Polytechnique Fédérale de Lausanne, CH-1015 Lausanne, Switzerland*, 2006.
- [28] E. Sahin, S. Girgin, L. Bayındır, and A. Turgut; "Swarm Robotics"; KOVAN Research Laboratory Middle East Technical University, Ankara, Turkey; Team Sequel INRIA Futurs Lille, Villeneuve d'Ascq, France, 2008.
- [29] F. Arvin, K. Samsudin, and A. Ramli; "Development of a Miniature Robot for Swarm Robotic Application"; *International Journal of Computer and Electrical Engineering*, Vol. 1, No. 4, 1793-8163, October, 2009.
- [30] N. Hoff, R. Wood, and R. Nagpal. "Distributed colony-level algorithm switching for robot swarm foraging." *Distributed Autonomous Robotic Systems*, 417-430, 2013.
- [31] Hecker, and M. Moses, *Beyond Pheromones: Evolving Error-Tolerant, Flexible, and Scalable Ant-Inspired Robot Swarms*, 2015.
- [32] L. Parker, "Multiple Mobile Robot System", Springer-Verlag Berlin Heidelberg, Springer Berlin Heidelberg, 2008.
- [33] M. Ling, J. Chen, Z. Li, and D. Zhang. "Relative Localization Method of Multiple Micro Robots Based on Simple Sensors." *Int J Adv Robotic Sy International Journal of Advanced Robotic Systems* (2013): 1. Web. 13 February 2016.
- [34] S. Majercik. "Swarm-Based Path Creation in Dynamic Environments for Search and Rescue." *Proc. of Genetic and Evolutionary Computation Conference*, Philadelphia, PA, USA. N.p., 11 July 2012. Web. 12 February 2016.

- [35] K. Stolleis "The Ant and the Trap: Evolution of Ant-Inspired Obstacle Avoidance in a Multi-Agent Robotic System." 26 June 2015.
- [36] T. Shaneyfelt, M. Joordens, K. Nagothu, J. Prevost, A. Kumar, M. Ghazi, M. Jamshidi, 2008, Control and simulation of robotic swarms in heterogeneous environments, in SMC 2008: Proceedings of 2008 IEEE International Conference on Systems, Man and Cybernetics, IEEE, Piscataway, N.J., pp. 1314-1319, 2008.
- [37] "Automatic Guided Vehicles (AGV) Drive & Steering Options" Transbotics, [www.transbotics.com/learning-center/drive-steering](http://www.transbotics.com/learning-center/drive-steering).
- [38] "Laser Target Navigation" Applied & Integrated Manufacturing Inc. (AIM) <http://www.aimagv.com/laser-target.html>.
- [39] "Ensor-Egemin Navigation System on Robot" Engemin Automation [www.egeminusa.com/automated-guided-vehicles/software/ensor/](http://www.egeminusa.com/automated-guided-vehicles/software/ensor/).

# Remote Controlled Carry-on and Checked Luggage Carrier for High Loads

Ali Qureshi, Mateo Restrepo, Victor Rodriguez, Neha Chawla, Sabri Tosunoglu

Department of Mechanical and Materials Engineering  
Florida International University  
Miami, Florida 33174

aqure010@fiu.edu, mrest031@fiu.edu, vrodr188@fiu.edu, nchaw002@fiu.edu, tosun@fiu.edu

## ABSTRACT

In this paper, we explain the necessity for building a luggage carrier and the manufacturing steps taken to produce a working prototype. The scaled prototype that is developed in this work performs the primary functions of the actual proposed design.

## Keywords

Remote controlled, luggage carrier, carry-on, checked baggage, 100 lb load capacity.

## 1. INTRODUCTION

### 1.1 Problem Statement

Nowadays travelling has become an important part of people's lives. People travel for leisure, vacations or for work and carry luggage during travelling. Passengers with physical limitations and senior citizens find it difficult to carry their luggage around at the airport or at hotels. They need to get special assistance just for this purpose and sometimes waiting for them is inconvenient. Similarly, it is difficult for people travelling alone with babies or toddlers to carry their luggage and simultaneously carry the baby. Since the airports are massive these days, walking between terminals becomes tiresome with the luggage. There are wheeled luggage carriers available in market these days but they need to be pulled across at all times. A system to diversify the carrying capacity will be able to assist customers with transporting checked-in luggage as well would be a great solution.

### 1.2 Motivation

In order to facilitate the ease of traveling and aid travelers, we designed a robot that will carry luggage bags without having to push them around. We created a platform that is remote controlled through a bluetooth connection to an android phone. The platform will carry most commercial luggage bags and will support heavy loads. The robot will have lights all around in order to illuminate the path if the photoresistor detects no light. It will have ultrasonic sensors all around in order to prevent any collision. If the robot detects something ahead of it, it will avoid collision either by stopping at a set distance or by rerouting. The platform will be

available in two different sizes. A large size which will be used by customers before the TSA checkpoint for check-in baggage, and a small size used by customers after the TSA checkpoint for carry-on baggage.

This robot can also be used in many other applications. Every job that requires something to be carried around could use this robot. The platform will be large enough to carry most luggage sizes and could also be used to carry tool boxes. The possible benefits that the user will experience is ease of travel. Another added benefit is that it can carry anything that fits in the platform, and it can be used in the dark because the robot will light up the path.

Our robot can be used as a personal item and can and can also be used instead of renting out the carts that are currently present at airports. The airport luggage cart business has been on a steady decline. According to an article in the *Los Angeles Times*, at "Los Angeles International Airport, cart rentals once provided at least \$2.75 million in annual revenue. Now, the airport is losing nearly \$1 million a year under a deal that obligates it to provide free carts to foreign travelers." [1] By addressing this problem, we hope to turn those finances around by making robotic mechanisms that would significantly decrease the workload for luggage carrying.

### 1.3 Literature Survey

Research was conducted to determine the luggage carriers with integrated robotic system. We found quite a few robotic luggage in the market with robotic systems that use a variety of sensors and automation. One of the carry-on luggage bags was a user controlled motorized carry-on luggage bag on which the user can sit and control the motion using a throttle and steering handle bars. Figure 1 below shows the design of luggage.

Other carry-on luggage bags that were seen within the research were the Cowarobot and the Travelmate Robotics carry-on luggage bags. These bags can be seen in Fig. 2 and Fig. 3 respectively. These two carry-on luggage bags are very similar in design. They use a Bluetooth tracking device to track the user. The Cowarobot luggage bag tracks a bracelet worn by the user, while the Travelmate Robot bag syncs with the user's phone Bluetooth in

order to track. They both use multiple sensors to avoid obstacles that arise when the luggage is following its user.



Figure 1. MODOBAG Motorized Carry-on Luggage Bag [3]

Table 1. Airline Carry-on Regulation Dimensions [2]

Airline	Dimension
United Airlines	9" x 14" x 22"
American Airlines	9" x 14" x 22"
Southwest Airlines	10" x 16" x 24"
Alaska Airlines	10" x 17" x 24"
Delta Airlines	9" x 14" x 22"
JetBlue Airlines	9" x 14" x 22"
Hawaiian Airlines	9" x 14" x 22"
Spirit Airlines	10" x 18" x 22"
Virgin America	10" x 16" x 24"
Allegiant Airlines	9" x 14" x 22"
Horizon Air	10" x 17" x 24"
Frontier Airlines	10" x 16" x 24"
Sun Country	11" x 16" x 24"

Table 1 shows that for most major airlines, the smallest dimensions used for carry-on luggage bag are 9" x 14" x 22". It would be reasonable to take these dimensions as the standard because if the carry-on luggage bag meets these dimensions, the carry-on luggage can be taken on any airline.

## 2. DESIGN CRITERIA

### 2.1 Limits of Weight and Power Calculations

We had in consideration the different applications that the luggage carrier may be designed for. In terms of weight, the carrier was designed to carry up to 100 pounds. For airports, the design will have two different versions, a small one personal up to 100 pounds and a scaled one up to 250 pounds considering the luggage requirements. The difference in load introduces a question for us about the torque required to carry the load.

Power required to move the vehicle in an inclined plane of 5 degrees:

$$Power = (F_{friction} + F_{grade} * Vel) * \frac{1}{eff} \quad (1)$$

$$F_{grade} = 9.81 \left(\frac{m}{s^2}\right) * W_{carrier} * \sin(\alpha) \quad (2)$$

$$F_{friction} = 9.81 \left(\frac{m}{s^2}\right) * W_{carrier} * \mu_{min} \quad (3)$$

$$Where: eff = 0.85, Vel = 10 \left(\frac{km}{h}\right), \mu_{min} = 0.3$$

$$\& W_{carrier} = W_{luggage} + W_{car}$$

Sample calculations:

For a maximum Luggage of 250 pounds and a carrier designed to weights itself 25 pounds the calculations are,

$$W_{carrier} = \frac{250 + 25}{2.22} = 123.87 (kg)$$

$$F_{friction} = 9.81 \left(\frac{m}{s^2}\right) * 123.87 (kg) * 0.3 = 364.56 N$$

$$F_{grade} = 9.81 \left(\frac{m}{s^2}\right) * W_{carrier} * \sin(5) = 105.9 N$$

$$Power = (364.56 (N) + 105(N)) * 10 \left(\frac{km}{h}\right) * \left(\frac{1000 \left(\frac{m}{km}\right)}{3600 \left(\frac{s}{h}\right)}\right) * \frac{1}{0.85} = 1534.51 Watt$$

As previously explained the previous calculations are based on the assumptions that the vehicle will indoors with no significant air resistance force and that the vehicle will move always in a horizontal path. For cases in which these conditions differ the vehicle power consumption will need to be reanalyzed and recalculated. For the case of personal luggage carrier with 100 lb the power needed is 540 (W). This power is to be divided by the number of motors in use.

### 2.2 Size

The luggage carrier was designed to fit most standard airport doors and can be resizable upon request to fit future customers' needs. The vehicle measures 22.69" wide and 24.41" in length, the principal measurements of the design can be seen in Figure 2. Even though the current system exceeds the standard dimensions for personal luggage carriers, the dimensioning was directed to luggage carrier assisters inside airports. So instead of having to look for a car, the passenger is greeted at the airport with one of this vehicle to assist him/her in translating the luggage up to the checking point. For personal luggage, we will design a smaller version to comply with airport standards. The current luggage design has a volumetric capacity of 1897 cubic inches.

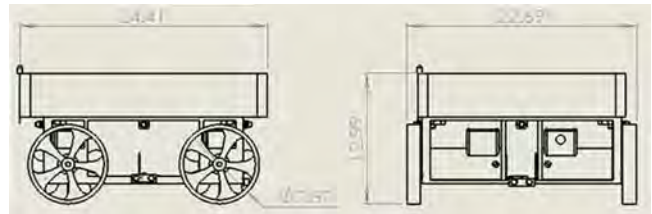
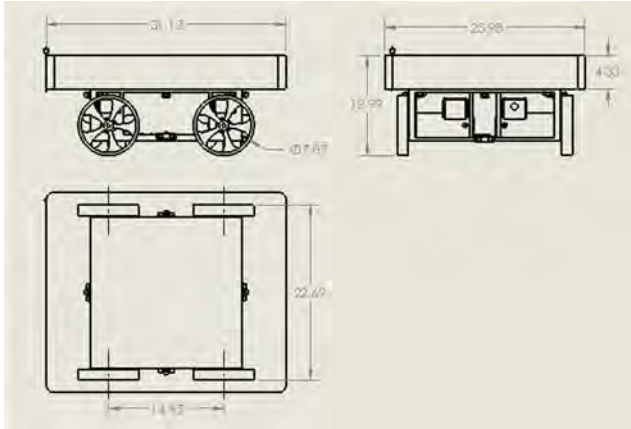


Figure 2. Smaller Platform Conceptual Design Size



**Figure 3. Larger Platform Conceptual Design Size**

The current design will be able to fit even regular house door which are normally less wide than commercial doors. This design will also be useful to handymen and workers that need to carry several tools and want to work more efficiently.

### 2.3 Type of Case

We went for a basic type of box case. The box type of case will avoid objects from falling and the client will be able to organize his/her belongings using the case as a container. We will incorporate for future design modifications compartments to the case in order to assist better the intended market.

### 2.4 Possible Markets

As explained before the carrier can be a useful tool for the following markets:

- Airports
- Warehouses
- Supermarkets
- Moving Companies
- Care

### 2.5 Bluetooth and Override Control

We will control the carrier by Bluetooth. The Arduino microcontroller will have a Bluetooth sensor that will locate the other end of the Bluetooth connection (the user) and will send the location information to the controller. The controller will map its trajectory to the desired destination having in consideration the nearby obstacles. The carrier will have 4 ultrasonic sensors in the 2 plane directions.

We will also connect the microcontroller to a controller android application with an override function to avoid collisions in case the carrier may lose its connection with the Bluetooth device or the trajectory towards the location is full of obstacles and the installed sensors are not capable to input the necessary information to get out of the jam. The override instructions will also assist the design team in the testing and tuning of the robot.

## 3. FINAL CONCEPTUAL DESIGN

The luggage carrier proposed will have either a small platform, shown in Fig. 4, or a large platform, shown in Fig 5, that will carry most commercial luggage. The large platform will be rented out

before checkpoint and are mainly for suitcases. While the smaller ones will be rented out passed checkpoint and are meant for carry-on luggage bags. This way the platforms will not be crossing through security, and doesn't create any safety liabilities. The small platform has a carrying space that measures 24" by 20". While, the large one has a carrying space of 30" by 25". The height of both the holding platform is 3.94". The luggage carrier has four 7.87" diameter wheels which have 5 spokes each. The robot has four ultrasonic sensors, one on each side in order to detect any obstacle. Figures 4 and 5 show the 3D model of the luggage carrier that we made using SolidWorks.

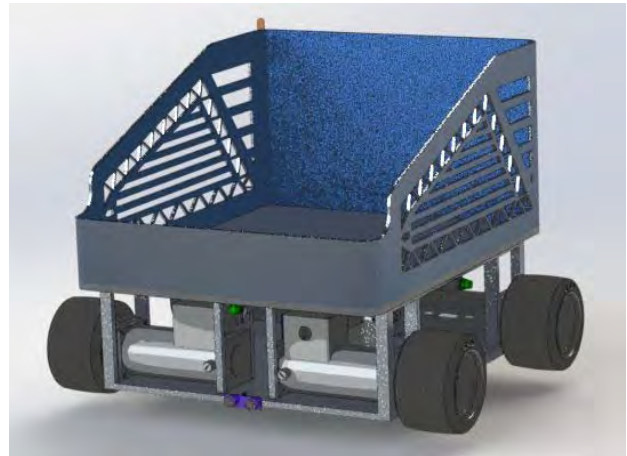
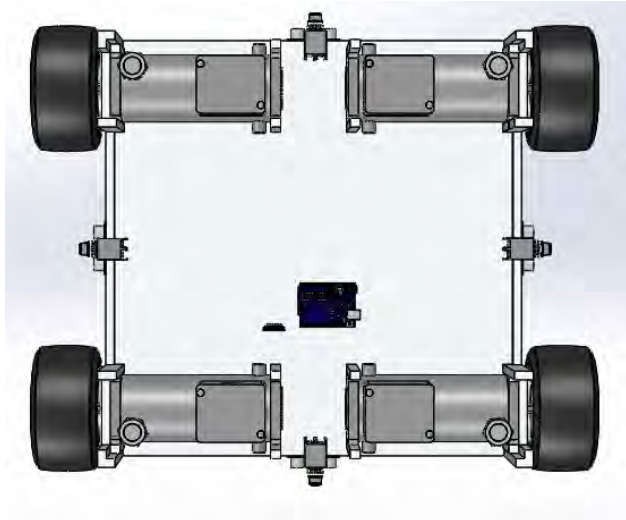


**Figure 4. Smaller Platform Overall View of the Final Design**



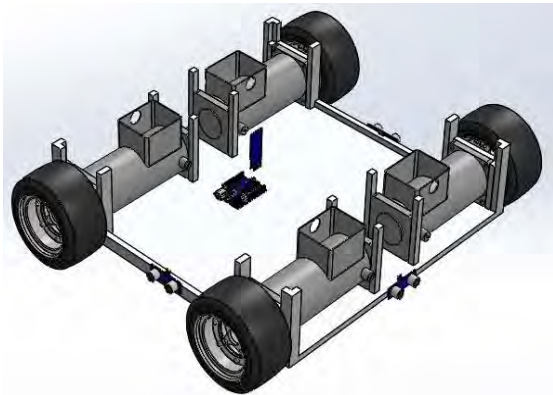
**Figure 2. Larger Platform Overall View of the Final Design**

Figure 6 shows a top down view of the layout of the components. The LED's that will be used to illuminate the ground are shown by the color green. The ultrasonic sensors are shown by the color purple and can be seen on each side of the robot along with the LED's. The microcontroller which is an Arduino UNO is placed in the center and is shown by the color purple. The photo-resistor sensor is shown by the orange color and is located at the top of the platform.



**Figure 6. Top Down View of Components**

To further show the configuration of the motors and the positioning of the ultrasonic sensors with respect to the microcontroller a cut view is shown in Figure 7. This figure shows that the ultrasonic sensors are located on every side of the robot, and that the microcontroller is in the center of the robot.



**Figure 7. 3D View of the Internal Components**

The luggage bags can be placed in the carrier in two ways as shown in the Figures 8 and 9. They show the representation using the larger platform, but the concept of placement is the same for the smaller platform.



**Figure 8. Carrier Loading Style 1**



**Figure 9. Carrier Loading Style 2**

## 4. MODELING

### 4.1 Smaller Platform Simulations

Simulations were conducted on the smaller luggage carrier to simulate the weight of carry-on luggage bags. A 100lb distributed load was placed on the platform. The maximum stress occurring the platform 121 psi. Figure 10 shows the outcome of the simulation.

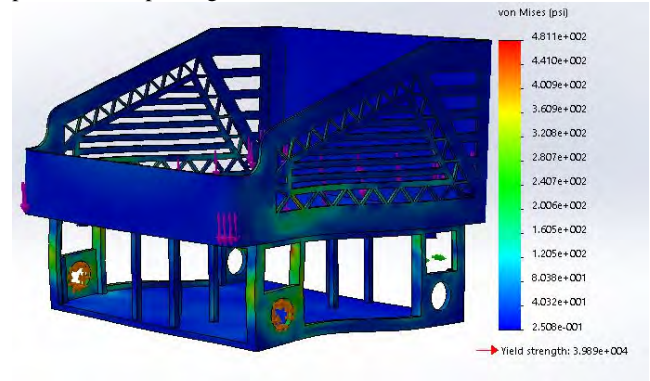


**Figure 10. Maximum Stress on the Smaller Platform**

Figure 11 shows the maximum displacement occurring on the smaller platform. It can be clearly seen that the maximum

displacement occurs in the center of the platform. The maximum displacement occurring is 0.0002963 inch, which is insignificant.

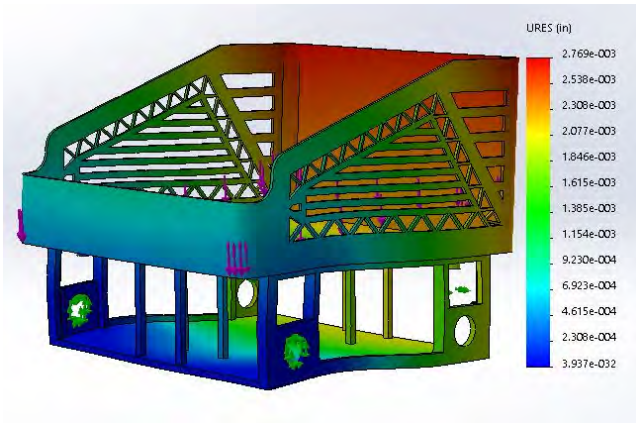


**Figure 11. Smaller Platform Displacement Analysis**

Figure 12 shows the resultant factor of safety from placing the load. The minimum factor of safety was 3.246.

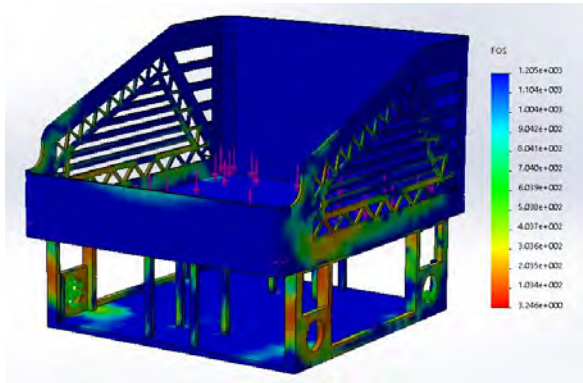


**Figure 12. Smaller Platform Factor of Safety**

## 4.2 Larger Platform Simulations

The larger platform was also simulated with 100lb loading. The maximum stress occurring on the platform according to the simulation is 120.7 psi as shown in the Figure 13.

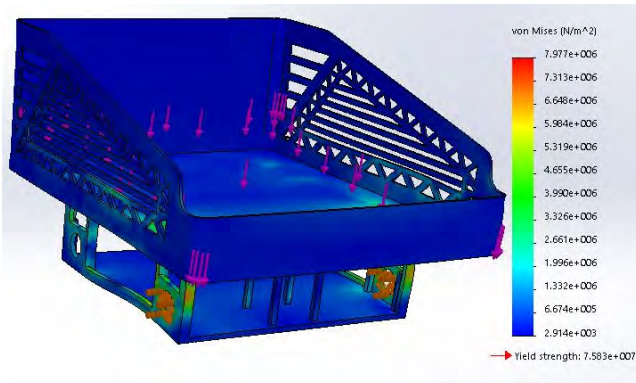


**Figure 13. Larger Platform Stress Analysis**

The maximum deflection occurring on the platform is 0.0002189 in. Similar to the smaller platform, the larger platform's largest deflection occurs towards the center as shown in Figure 14.

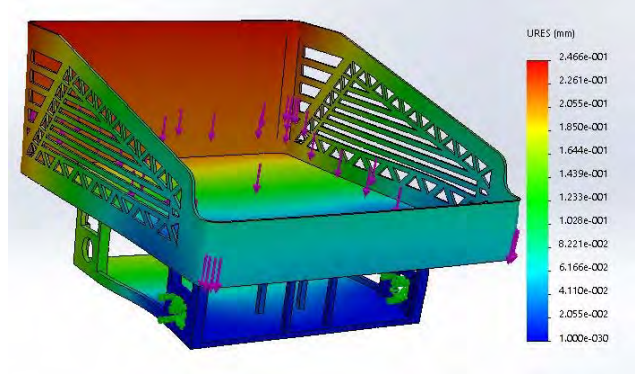


**Figure 14. Larger Platform Deflection Analysis**

The minimum factor of safety occurring on the platform is 3.156 as shown in the Figure 15.

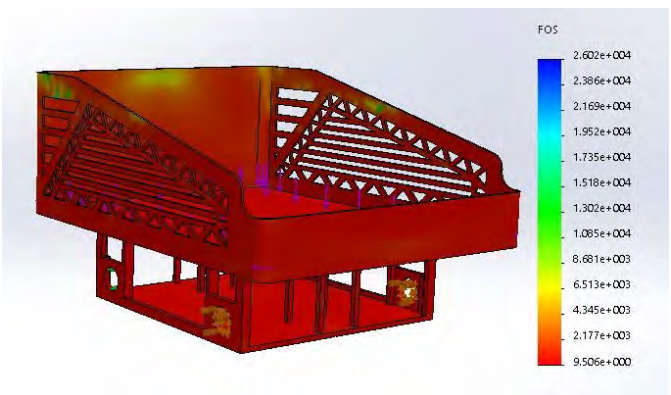


**Figure 15. Larger Platform Factor of Safety**

## 5. CONTROL

### 5.1 Theory and Language

We used C++ language for programming. The code uses a switch case statement for communicating with the user's phone. Within each case an if statement was used for determining whether or not the ultrasound detects an obstacle or not. The following code example shown in section 5.2 is a code developed using this theoretical principle to be used on the small scaled prototype constructed for this project. This code simply makes the platform stop and wait for user command whenever it detects an object.

### 5.2 Sample Code

The code starts opening the Bluetooth library communications and establishing a Bluetooth object as well as defining the variables that will be transmitted through Bluetooth.

```
#include <SoftwareSerial.h>
SoftwareSerial bt(0,1);
#define GO_LEFT 'a'
#define GO_RIGHT 'd'
#define GO_FORWARD 'w'
#define GO_BACK 's'
#define STOP 'x'
```

Variables for the motor driver are created, enA and enB will be the pins that will indicate the velocity of each of the motors, and from in1 to in4 will be the variables that indicate the direction of rotation of the DC motors, in the next code can be seen the assignation of the pins to these variables.

```
//motor one
int enA = 10;
int in1 = 9;
int in2 = 8;
// motor two
int enB = 11;
int in3 = 7;
int in4 = 6;
```

The Arduino UNO that We used for the project is limited to 13 output pins, because of that We use the same trigger pin for each of the ultrasound sensors, each of the sensor though will have an independent echo pin, which is the receiver for each of the cases.

```
#define trigPin 12 // define the trigger pins of your sensors
#define echoPin1 5 // sensor at the front left
#define echoPin2 4 // sensor at the front right
#define echoPin3 3 // sensor at the back
```

In the void setup code We establish the output and input pins, and start the Bluetooth serial port.

```
void setup() {
  Serial.begin(9600); // begin serial communication
  Serial.println("Motor test!");
  pinMode(enA, OUTPUT);
  pinMode(in1, OUTPUT);
  pinMode(in2, OUTPUT);
  pinMode(enB, OUTPUT);
  pinMode(in3, OUTPUT);
  pinMode(in4, OUTPUT);

  bt.begin(9600); //start the bluetooth serial port - send and recieve at
  9600 baud

  pinMode(trigPin, OUTPUT); // set the trig pin to output (Send sound
  waves)
  pinMode(echoPin1, INPUT); // set the echo pin to input (recieve
  sound waves)
  pinMode(echoPin2, INPUT); // set the echo pin to input (recieve
  sound waves)
  pinMode(echoPin3, INPUT); // set the echo pin to input (recieve
  sound waves)
}
```

### Subroutines:

A series of subroutines were programed to stop, move the robot and check the distance on the ultrasound sensors. These subroutines control the rotation direction of the DC motors and the speed, which is an input variable for each of the subroutines to be able to control that velocity in the main code.

```
void allOff(int speed) { //stop the robot
  digitalWrite(in1, speed);
```

```
digitalWrite(in2, speed);
digitalWrite(in3, speed);
digitalWrite(in4, speed);
delay(5);
}

void goForward(int speed) {
  Serial.println ("No obstacle detected. going forward");
  for (int i=0; i <= 2; i++){
    analogWrite(enA, speed);
    digitalWrite(in1, HIGH);
    digitalWrite(in2, LOW);
    analogWrite(enB, speed);
    digitalWrite(in3, HIGH);
    digitalWrite(in4, LOW);
    delay(5); //this delay is the amount of time that is going to be
    applying this operation
  }
}

void goBackward(int speed) {
  Serial.println ("No obstacle detected. going Backward");
  for (int i=0; i <= 2; i++){
    digitalWrite(in1, LOW);
    digitalWrite(in2, HIGH);
    analogWrite(enA, speed);
    digitalWrite(in3, LOW);
    digitalWrite(in4, HIGH);
    analogWrite(enB, speed);
    delay(5);
  }
}

void goRight(int speed) {
  digitalWrite(in1, HIGH);
  digitalWrite(in2, LOW);
  analogWrite(enA, speed);
  digitalWrite(in3, LOW);
  digitalWrite(in4, HIGH);
  analogWrite(enB, speed);
  delay(5);
}

void goLeft(int speed) {
  digitalWrite(in1, LOW);
  digitalWrite(in2, HIGH);
  analogWrite(enA, speed);
  digitalWrite(in3, HIGH);
  digitalWrite(in4, LOW);
  analogWrite(enB, speed);
  delay(5);
}
```

To check the ultrasound sensors we also created two subroutines, one to check the two sensors on the front and the other for the back sensor. Because the sensors are using the same trigger pin one sensor is activated first and then the other. The code returns a value of 1 if an object is detected with less than 25 cm of distance.

```
int checkfront(){
  int result;
  result = 0;
  long duration1, duration2, distance1, distance2; // start the scan
  //////////////////////////////////////
```

```

digitalWrite(trigPin, LOW);
delayMicroseconds(2); // delays are required for a succesful
sensor operation.
digitalWrite(trigPin, HIGH);
delayMicroseconds(10); //this delay is required as well!
digitalWrite(trigPin, LOW);
duration1 = pulseIn(echoPin1, HIGH);
distance1 = (duration1/2) / 29.1;// convert the distance to
centimeters.
////////////////////
delay(10);
////////////////////
digitalWrite(trigPin, LOW);
delayMicroseconds(2); // delays are required for a succesful
sensor operation.
digitalWrite(trigPin, HIGH);
delayMicroseconds(10); //this delay is required as well!
digitalWrite(trigPin, LOW);
duration2 = pulseIn(echoPin2, HIGH);
distance2 = (duration2/2) / 29.1;// convert the distance to
centimeters.
////////////////////
if (distance1 < 25 || distance2 < 25)/*if there's an obstacle 25
centimers, ahead, do the following: */ {
  result = 1;
}
else {
  result = 0;
}
return result;
}

int checkback(){
char result;
result = 0;
long duration3, distance3; // start the scan
////////////////////
digitalWrite(trigPin, LOW);
delayMicroseconds(2); // delays are required for a succesful
sensor operation.
digitalWrite(trigPin, HIGH);
delayMicroseconds(10); //this delay is required as well!
digitalWrite(trigPin, LOW);
duration3 = pulseIn(echoPin3, HIGH);
distance3 = (duration3/2) / 29.1;// convert the distance to
centimeters.
////////////////////
if (distance3 < 25)/*if there's an obstacle 25 centimeters, ahead,
do the following: */ {
  result = 1;
}
else {
  result = 0;
}
return result;
}

```

In the main code of the Arduino the first two lines check if there is Bluetooth connection with other device and stores in the variable 'data' the information sent by the android app from the smartphone, if there is communication then the code will run.

```

if (bt.available()) {
char data = (char)bt.read();

```

A switch selection command was inserted to indicate what action to take by the robot depending on the information sent by the phone, the switch will read the information stored in the variable data and will perform the operation indicated on the phone. For going backwards and forward the code will check first for objects closer than 25 cm, and if no object is close enough the action of forward or backward will take place. The distance of forward and backward motions are controlled by for loops, if the programmer wants to increase the distance in forward or backward motion, the iteration just has to increase the number of loops.

```

switch(data) {
case GO_BACK:
  crash = 0;
  iter = 0;
  while(crash == 0 && iter < 70){
    crash=checkback();
    goBackward(105);
    iter ++;
  }
  iter=0;
  allOff(0);
  break;
case GO_FORWARD:
  crash = 0;
  iter = 0;
  while(crash == 0 && iter < 70){
    crash=checkfront();
    goForward(105);
    iter ++;
  }
  iter=0;
  allOff(0);
  break;
case GO_LEFT:
  for (int i=0; i <= 50; i++){
    goLeft(150);
    delay(20);
  }
  allOff(0);
  break;
case GO_RIGHT:
  for (int i=0; i <= 50; i++){
    goRight(150);
    delay(20);
  }
  allOff(0);
  break;
case STOP:
  allOff(0);
  break;
}
}
}

```

## 6. PROTOTYPE

A small scaled prototype was constructed to develop a running code for the system. The figure below shows the prototype that was created for this project.

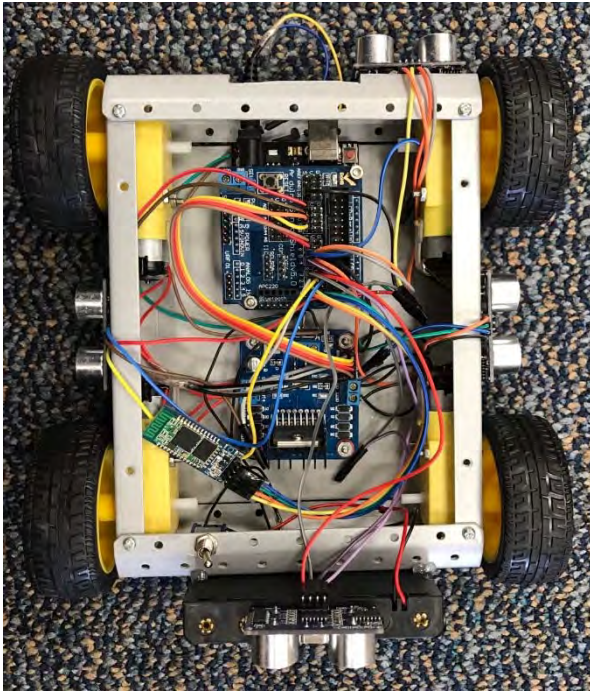


**Figure 16. Prototype Model**

The Arduino controller has a set of 14 digital pins which are used for control. Out of the 14 pins, pins 6 through 11 are used for motor control. Pins 2 through 5 are used for retrieving the unique values of each respective ultrasonic sensor. Pin 12 is used as the trigger pin to allow the ultrasonic sensors to start detecting. Pins 0 and 1 are specific Rx and Tx respectively used to connect the bluetooth device to the Arduino in an interchange manner (i.e. Rx connects to Tx and Tx connects to the bluetooth Rx). The power for the prototype is obtained from a series of 6 1.5V batteries connected to a switch and connected to the power input of the Arduino respectively. The bluetooth controller, the ultrasonic sensors, and the motors are all connected to the power input.

## 7. EXPERIMENTS

An android phone was used to control the prototype. The prototype was made to move in all possible directions. In order to test if the override function will make the robot stop at a safe distance without crashing, we used a person and an object as a barrier.

## 8. RESULTS

The robot was very responsive and achieved a positive outcome. The luggage carrier prototype moved in the desired direction and stopped automatically when it detected something in its path thus avoiding a crash. Initial experimental results, although limited due to time constraints, were judged to be encouraging.

## 9. CONCLUSION

We successfully built the luggage carrier prototype which can be controlled by phone and is capable of moving in all directions and is also able to avoid crashes by detecting the obstacle in the path. For future design we are planning to include machine learning in the robot, and maybe transform it in a personal assistant equipped with voice recognition.

## 10. REFERENCES

- [1] Martín, Hugo. "Idle luggage carts mean lost revenue for airports and cart renters." *Los Angeles Times*. Los Angeles Times, 01 July 2011. Web. 27 Feb. 2017.
- [2] Tsatips. "Can I Bring It On a Plane? TSA Carry-on and Checked Bag Rules." *Airport Security | TSA Travel Tips*. N.p., 04 Jan. 2017. Web. 27 Feb. 2017.
- [3] Hodgkins, Kelly. "Don't walk through the airport, ride on your motorized luggage with Modobag." *Digital Trends*. N.p., 21 July 2016. Web. 27 Feb. 2017.
- [4] "My TSA." *My TSA - Home Airport*. N.p., n.d. Web. 27 Feb. 2017.
- [5] Cowarobot. "COWAROBOT R1: The First and Only Robotic Suitcase." *Indiegogo*. N.p., 26 July 2016. Web. 27 Feb. 2017.
- [6] "Travelmate Robotics." *Company*. N.p., n.d. Web. 27 Feb. 2017.
- [7] "Elegoo UNO Project Super Starter Kit with Tutorial, 5V Relay, UNO R3, Power Supply Module, Servo Motor, 9V Battery with DC, Prototype Expansion Board, ect. for Arduino: Computers & Accessories." *Amazon.com: Elegoo UNO Project Super Starter Kit with Tutorial, 5V Relay, UNO R3, Power Supply Module, Servo Motor, 9V Battery with DC, Prototype Expansion Board, ect. for Arduino: Computers & Accessories*. N.p., n.d. Web. 27 Feb. 2017.
- [8] "Buy Products Online from China Wholesalers at Aliexpress.com." *Buy Products Online from China Wholesalers at Aliexpress.com*. N.p., n.d. Web. 27 Feb. 2017.
- [9] "Arduino UNO Rev3." *Arduino Store USA*. N.p., n.d. Web. 27 Feb. 2017.
- [10] Jazar, Reza N., *Vehicle Dynamics: Theory and application*. Springer, 2017.
- [11] "Design and Manufacturing Laboratory." *Design and Manufacturing Laboratory*. Web. 28 Feb. 2017.

# Road Marking Survey with Mobile Lidar System

Yiming Xu, Patrick J. Neal, Carl D. Crane III

Department of Mechanical and Aerospace Engineering  
University of Florida  
Gainesville, Florida, USA

[yxu@ufl.edu](mailto:yxu@ufl.edu), [neap@ufl.edu](mailto:neap@ufl.edu), [ccrane@ufl.edu](mailto:ccrane@ufl.edu)

## ABSTRACT

In this paper, a mobile lidar system for surveying reflective road markings is presented. Aside from inclusion of typical components in many other mobile lidar systems – compact lidars, integrated global positioning and inertial navigation systems, and onboard computers – the road surveying device is designed to maintain scanning resolution while traveling at normal traffic speeds. Occupancy grids are utilized to register the scanned point cloud data, so that outliers and temporarily obstructing objects could be identified and removed. Details about the system design and the filtering techniques are presented. Surveying results from the preliminary road tests are reported.

## Keywords

Lidar, mobile laser scanning, road marking survey, occupancy grid, point cloud, voxelization.

## 1. INTRODUCTION

Light detection and ranging (lidar) technology is a laser application to remote sensing that provides distance estimation by illuminating objects with pulsed laser beams and measuring the reflected laser pulses. Initially implemented for meteorology [1] and atmospheric studies [2], lidar systems have since been utilized in a broad range of applications in research and industry [3]. The lidar systems could rapidly create dense, three-dimensional (3D) point cloud data and survey the surrounding environment with superior accuracy, precision, and flexibility when compared to conventional measurement methods. Particularly, mobile lidar systems on vehicular platforms (often referred to as mobile laser scanning, or MLS) have received an increasing attention in recent research studies, thanks to advancements in scanning speed and accuracy, as well as the integrated global positioning systems (GPS) and inertial navigation system (INS) that offers real-time localization and orientation information [4]. The mobile lidar systems have become an effective solution for rapid environmental mapping and road inventory surveying. A thorough review of these applications could be found in [4, 5].

This paper presents a mobile lidar system for surveying the reflective markings on road surfaces. The system includes typical components similar to other mobile lidar systems; however, a couple of design choices are made to improve performances. First, the lidar sensor is positioned and oriented to minimize the gap between neighboring scanned points while allowing the vehicle to travel at a reasonable speed in traffic. Additionally, the concept of

occupancy grids is utilized to register the scanned space as either empty (free) or occupied, such that outliers and temporary obstructions could be easily identified by examining the accumulated registrations. The paper is organized as follows: The design of the mobile lidar system is detailed in Section 2. Section 3 discusses the data processing and filtering techniques. Section 4 summarizes the preliminary surveying tests. Section 5 concludes the paper.

## 2. SYSTEM DESIGN

The mobile lidar system consists of a compact lidar sensor, an integrated GPS receiver, a digital inclinometer, and an onboard computer for data processing and storage. Mounted on top of a vehicle platform, the rear-facing lidar collects point cloud data from the road surfaces. Relative distance together with reflectance of the points on the road are obtained. Real-time 3D point clouds are registered in the world reference frame after coordinate transformations. Subsequently, road surface markings are extracted based on their high reflectance.

### 2.1 Lidar Sensor

In this study, the sensor Velodyne PUCK VLP-16 is a compact direct energy detection lidar device as shown in Figure 1. It has a relatively low power consumption (about 8 W) and a small footprint (a cylinder of about 103 mm diameter and 72 mm height). During operation, the laser pulses switch among 16 evenly spaced elevation angles within a  $\pm 15^\circ$  range as they sweep around  $360^\circ$  azimuthally. As illustrated in Figure 2, every laser beam emitted from the center of the lidar could be described using an azimuth angle  $\alpha$  and an elevation angle  $\beta$ . The elevation angle  $\beta$  switches every  $2.3 \mu\text{s}$  during the firing sequence of each set of 16 laser beams, whereas the rotation speed (or rate of change for angle  $\alpha$ ) is adjustable between 5 to 20 rotations per second.



Figure 1. Picture of lidar sensor.

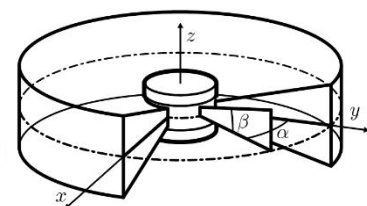


Figure 2. Diagram of lidar scanning field.

Provided that the distance from the scanned object could be inferred based on the amplitude of the returning light, points on the object could be registered with respect to the reference frame that is fixed on the lidar sensor. Data points up to 100 m in range can be detected with measurements of their reflectance.

## 2.2 Scanning Resolution

Since the lidar system is to be mounted onboard a vehicle platform moving in traffic, a reasonable choice would be on the front or the back of the vehicle where the road surfaces are exposed for scanning. Assuming the lidar is mounted on the back without loss of generality, the geometry for the lidar scanning field could be depicted as in Figure 3. As the vehicle traveling forward along the  $x$  axis, the set of 16 laser beams within  $\pm 15^\circ$  separation from the center line (dash-dot line in Figure 3) forms a circular sector, which in turn sweeps along a helix curve. Spacings between the neighboring laser beams could be reduced when they hit the ground, if the lidar is mounted lower in height and/or pitched further down. However, this does not necessarily result in higher scanning resolution because it may also increase the gap between consecutive sweep (full rotation).

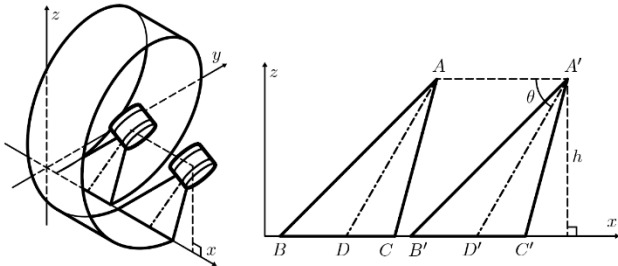


Figure 3. Lidar scanning coverage. Figure 4. Illustration of two consecutive sweeps.

To further investigate the scanning geometry, an approximation is made that all 16 laser beams are fired simultaneously and reach the ground along  $x$  axis on every rotation.<sup>1</sup> The approximated scanning model is illustrated in Figure 4, in which the laser beams make contact to ground along line segment  $BC$  and subsequently  $B'C'$  on the next sweep, while the lidar center travels from point  $A$  to  $A'$ . As a result, the lidar pitch angle  $\theta$  and height  $h$  constitute a minimization problem:

$$\arg \min_{\theta \in [15^\circ, 75^\circ] \subseteq \mathbb{R}, h \in \mathbb{R}^+} h[\cot(\theta - 15^\circ) - \cot(\theta - 13^\circ)],$$

subject to:

$$u_{\max} T_{\text{rot}} \leq h[2 \cot(\theta - 15^\circ) - \cot(\theta + 15^\circ) - \cot(\theta - 13^\circ)],$$

where  $u_{\max}$  denotes the maximum survey speed and  $T_{\text{rot}}$  represents the azimuthal rotation time period.

It is difficult to find the optimal solution analytically. However, the trigonometric functions could be replaced with their estimates at  $\theta = 75^\circ$ , since the expressions in both brackets are monotonically decreasing functions. Subsequently, the minimal value for lidar height  $h$  is obtained based on the maximum surveying speed  $u_{\max}$ .

For example, defining maximum speed  $u_{\max}$  to be 50 mph yields a minimal height  $h$  of around 1.8 m or 6 feet. In simulation, positions of the resulting laser points reaching the ground are illustrated in

<sup>1</sup> The approximation is valid because the time period (55  $\mu$ s) for 16 laser firing sequence is considerably smaller than that of the azimuthal rotation (adjustable between 0.05 to 0.2 s).

Figure 5. Consequently, the scanning sweeps will continuously cover the road surface if the vehicle is moving no faster than the maximum speed. In addition, the lidar may also provide decent measurements on the neighboring lanes when there are no obstructions.

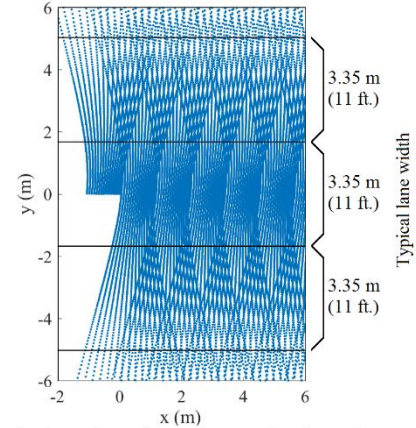


Figure 5. Simulated scanning points on the ground at the maximum surveying speed.

## 3. FILTERING TECHNIQUES

As visually demonstrated by Figure 5, the lidar system can produce a large number of data points (almost 200,000 points per second for this particular model), all of which are stored as a 3D point cloud with an additional variable as reflectance. To reduce data size and computation load, the point cloud data is converted into discrete voxel space where data points are collected in separate cubes. Thus, the geometry of the scanned scene can be represented by voxels that contain one or more data points. Outliers can be readily eliminated by setting a threshold for the number of points in the voxels. Undesired points registered due to temporary obstruction by traffic can be identified by utilizing the concept of occupancy grids to register scanned points.

### 3.1 Occupancy Filter

Application of the occupancy grid concept in lidar scan is proposed in [6], where the scanned scene is categorized as free, occupied, or hidden along the direction of every laser beam and a probabilistic model is derived to facilitate feature detection. A non-parametric solution for occupancy probability estimation is presented in [7] to improve the computation performance.

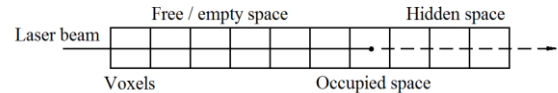


Figure 6. Information about the scanned scene along a single returning laser beam.

The idea behind the filtering technique can be illustrated in Figure 6. As each data point on an object gets registered by the lidar, the corresponding laser beam passes through empty space between the lidar center and the object. The information about the scanned scene suggests that not only is the data point occupied, but the space before the point is empty and the space behind the point is hidden. Therefore, by registering the voxels along the laser ray as empty or occupied and comparing the accumulated registration after multiple

scans, temporary obstructions can be identified by the voxels that are registered as both occupied and empty.

As an example, the lidar system is set stationary in a road and captures point cloud data as two vehicles pass by on neighboring lanes. Figure 7 shows the point cloud from two different time intervals. One depicts the road being empty and the other shows one of the vehicle. As demonstrated in Figure 8, directly voxelizing the accumulated point cloud data gives a 3D scene that contains the traces of both of the pass-by vehicles while the voxels representing the road surface are hidden underneath. Applying the occupancy filter removes the obstruction with little residue.

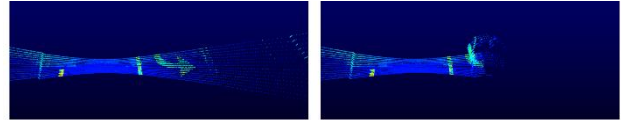


Figure 7. Reflectance point cloud from two stationary scans as traffic blocks view.

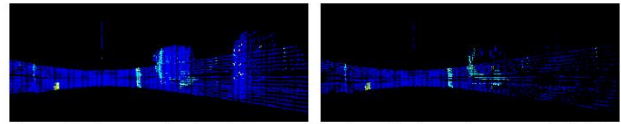


Figure 8. Direct voxelization (left) versus filtering with obstruction removal (right).

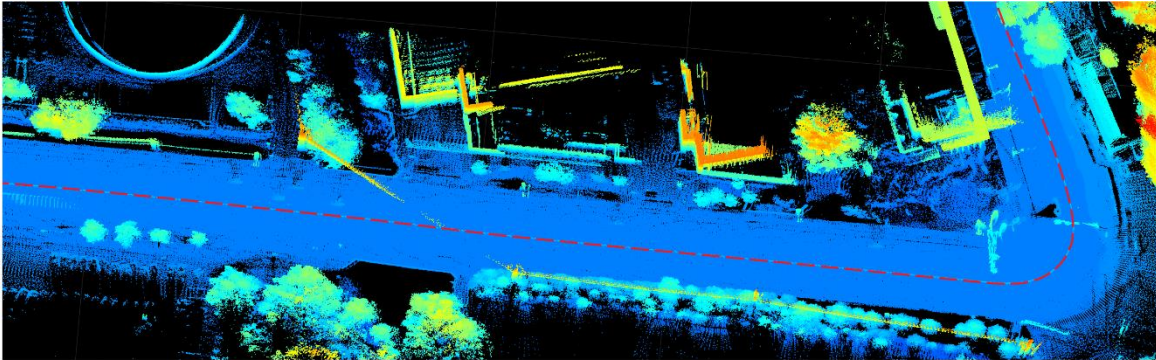


Figure 9. Voxelized lidar scanning result from road survey tests. Color indicates elevation. Vehicle trajectory is illustrated as red dashed lines.

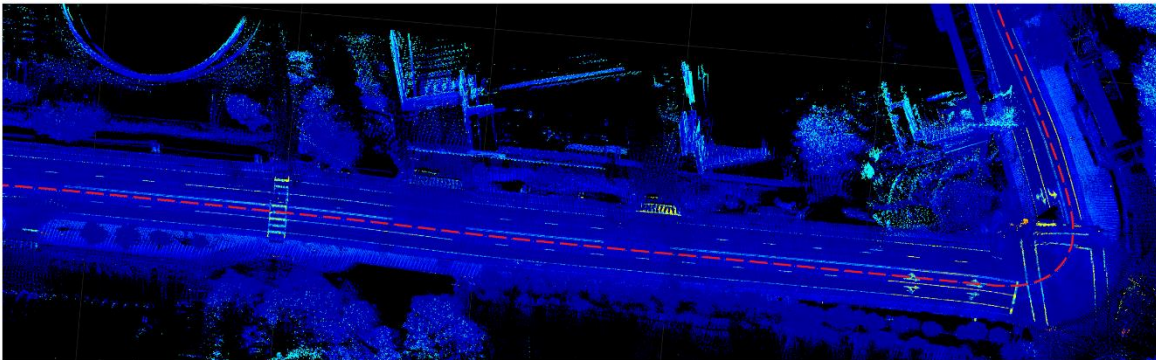


Figure 10. Voxelized lidar scanning result reveals reflective road markings, including solid and broken lines, arrows, and crosswalks. Color represents reflectance.

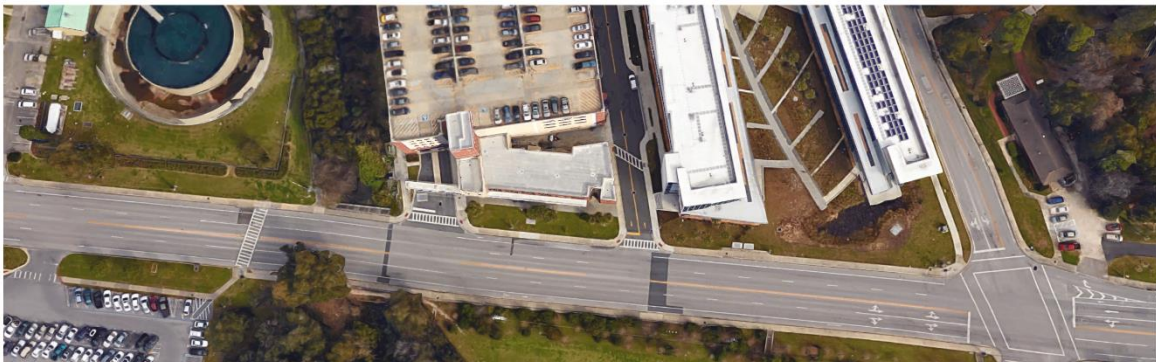


Figure 11. Latest available satellite map from Google. Roadworks have been taken since this picture, especially the crosswalk on left has become perpendicular to road.

## 4. SURVEY TESTS

A series of road survey tests were conducted to validate the design of the mobile lidar system and the filtering techniques. The system is mounted on a vehicle that traverses the campus area in traffic. Voxelized lidar scanning results are shown in Figure 9 and 10, where vehicle trajectory is indicated by red, dashed lines. A satellite map from Google of the same area is provided in Figure 11 for reference. Geometric features of the scene – including trees, buildings, power lines, etc. – can be easily recognized in the elevation map (Figure 9); whereas in the reflectance map (Figure 10), road surface markings, such as the solid and broken lines, arrows, and crosswalks, can be identified and matched with the satellite image.

## 5. CONCLUSION

This paper presents a mobile lidar system for road marking survey. The system design and the filtering techniques are detailed and tested. Results from preliminary road survey tests are satisfactory. Although the system is capable of collecting and registering point cloud data, efficiency and reliability of the data storage and filtering techniques remains to be verified. Future work will also be aimed towards automatic extraction and recognition of road markings.

## REFERENCES

- [1] R. T. B. Jr., "A new lidar for meteorological application," *J. Appl. Meteorol.*, vol. 12, pp. 698-708, Mar. 1973.
- [2] E. D. Hinkley, Ed., *Laser Monitoring of the Atmosphere*. Springer-Verlag, Berlin, 1976.
- [3] P. H. Flamant, "Atmospheric and meteorological Lidar: from pioneers to space applications," *C. R. Physique*, vol. 6, no. 8, pp. 864-875, Oct. 2005.
- [4] K. Williams, M. J. Olsen, G. V. Roe, and C. Glennie, "Synthesis of transportation applications of mobile LIDAR," *Remote Sens.*, vol. 5, no. 9, pp. 4652-4692, Sep. 2013.
- [5] H. Guan, J. Li, S. Cao, and Y. Yu, "Use of mobile LiDAR in road information inventory: a review," *Int. J. Image and Data Fusion*, vol. 7, no. 3, pp. 219-242, May 2016.
- [6] T. C. Yap, C. V. Stewart, and R. J. Radke, "A probabilistic representation of LiDAR range data for efficient 3D object detection," *Proc. CVPR IEEE*, Anchorage, AK, pp. 1-8, 2008.
- [7] C. Deymier, D. Vivet, and T. Chateau, "Non-parametric occupancy map using millions of range data," *IEEE Int. Veh. Sym.*, Gold Coast, QLD, pp. 730-737, 2013.

# Robot Arm Platform for Additive Manufacturing: 3D Lattice Structures

Ismayuzri Ishak, Pierre Larochelle

Robotics & Spatial Systems Laboratory  
Department of Mechanical and Aerospace Engineering  
Florida Institute of Technology, Melbourne, Florida 32901  
iishak2014@my.fit.edu, pierrel@fit.edu

## ABSTRACT

A conventional 3D printer utilizes horizontal plane layerings to produce a 3D printed part. The printing process is based on the slicing of the designed part where it is then 3D printed by depositing a material layer upon layer. A 3D printed part built using 3D lattice structures has a restriction on the minimum size of the struts on the 3D lattice structure design using the FDM process. To overcome this conventional 3D printing method limitation, an industrial robot arm platform is proposed as an additive manufacturing platform. The concept being explored is the integration of existing additive manufacturing process technologies with an industrial robot arm to create a 3D printer with a multi-plane layering capability. The objective is to perform multi-plane toolpath motions that will leverage the increased capability of the robot arm platform compared to conventional gantry-style 3D printers. This approach enables print layering in multiple planes whereas existing conventional 3D printers are restricted to a single toolpath plane (e.g. x-y plane). This integration combines the fused deposition modeling techniques using an extruder head that is typically used in 3D printing and a 6 degree of freedom robot arm. Here, a Motoman SV3X is used as the platform for the robot arm. The integration of the robotic arm and extruder enables multi-plane toolpaths motions to be utilized in the production of 3D lattice structure parts. Using this integrated system, a 3D lattice structure test block with an overhang structure has been 3D printed without using support material. The printing toolpaths are based on the geometric features of the lattice structure.

**Keywords:** 3D printing, Robotic arm, Lattice structure, Multi-plane layering

## 1. INTRODUCTION

Additive manufacturing (AM) is a process of joining materials to make a 3D part [1]. The AM process is usually performed by depositing or curing a material layer upon layer. The material can be in the form of liquid, powder, or filament. AM process is also known as a 3D printing technique. The AM process enables the fabrication of complex geometric structures such as three-dimensional (3D) lattice structures which usually have limitations in fabrication using conventional manufacturing processes.

3D lattice structures enhance the strength to weight ratio of the material [2, 3, 4]. The strength to weight ratio of the material can be improved by increasing the material strength or reducing

the material density [3]. For the application of the same material, reducing the part density is more desirable. With many different AM processes available, the fused deposition modeling process is one of the techniques that can be used to produce 3D lattice structures.

Fused deposition modeling (FDM) is a technique used in 3D printer extruder heads. The FDM process is performed by extruding a material through a nozzle to form an object. A conventional 3D printer using the FDM technique utilizes a horizontal planar layering to deposit the material. The horizontal planar layering process is repeated on different layer heights which enables the 3D printed part to be produced. Some of the typical platforms used in 3D printing utilize a gantry style computer numerical controlled (CNC) machine to move the printer head. One of the constraints with the current process is that the gantry machine limits the motion of the extruder head to only translate in the x, y, and z directions. Because the extruder head cannot rotate, conventional 3D printers are limited to only printing in flat layers. The conventional AM process uses a layer upon layer deposition, the FDM process produces struts to build 3D lattice structures. These lattice structures are limited to a minimum of 2 mm in diameter in order for the part to be usable [5]. To enable a part to be printed in a multi-plane manner, a higher degree of freedom platform is needed to produce the multi-plane motion.

Industrial robotic arms are versatile platforms used in most manufacturing industries. Flexibility in their functions is what allows them to be utilized in so many different applications including welding, painting, assembly, pick and place, product inspection, testing, etc. The industrial robot arm has a freedom of movement based on the number and types of joints that have been connected. The main advantage of industrial robot arms is the relatively high degree of freedom (DoF). Because of this, a serial arm with 6 DoF is capable of performing multi-plane motions in their work environment [6, 7]. A gantry machine style conventional 3D printers that have 3 DoF are only capable of performing planar layering.

In this research, an additive manufacturing process using a robot arm as a motion generating platform is explored. The combination of a 3D printing element utilizing the fused deposition modeling method and a robot arm architecture that has 6 degrees of freedom in its interaction with the work environment allows for the development of multi-plane toolpath strategies. The multi-plane toolpath strategies in 3D printing can be used to produce 3D lattice structures. With the 6 DoF robot arm and the FDM printing

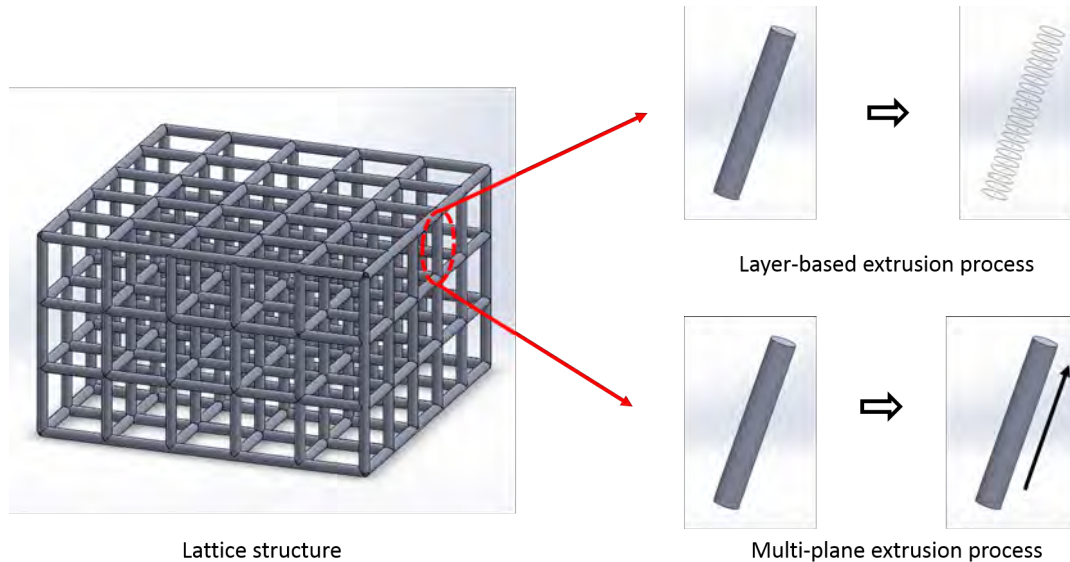


**Figure 1.** Comparison of additive manufacturing processes based on different approaches

process, a strut to be utilized in fabricating a 3D lattice structure can be fabricated directly based on its geometric shapes without the need to be sliced (see Figure 1). Finally, the future work on the robot arm platform in development is discussed.

## 2. LITERATURE REVIEW

A lattice structure is a structure with the combination of a connected network of struts [8]. A lattice structure has advantages through the use of minimum structural material while achieving higher strength capabilities. Regarding 3D printing applications, 3D lattice structure geometries can be achieved with the benefits of 3D printing technologies that allow the production of complex structure geometries.

Gorguluarslan et al. [4] introduced a design and fabrication framework for periodic lattice-based cellular structures in additive manufacturing. The design framework uses a size optimization algorithm to produced an optimum lattice structure design based on the load on the structure. The optimized lattice structure is built with the 3D printer using SLS and FDM processes. However, the 3D lattice structure built by the 3D printer used for the research still uses parallel planar layering techniques to produce the struts of the lattice structure.

A research group from ETH Singapore, ETH Zurich and SIKA Technologies AG received a patent [9] for a method to fabricate a 3D structure. One of the methods used for building a 3D structure uses a movable robot arm. A mesh formwork element is used to build the 3D structure. The robot can produce different mesh formworks with various designs made of filament extruded through the end effector of the robot arm. One of the applications of the project is to implement the robotic platform for fabrication in architecture, art, and design.

## 3. METHODOLOGY

In this section, we provide a general description of the robot arm as a platform for additive manufacturing. To investigate the idea of printing 3D lattice structures, an industrial robot arm was utilized as the platform to perform multi-plane motion and was integrated

with an extruder head typically used in a gantry-style 3D printing process.

### 3.1 Hardware

The robot system used includes a Motoman model SV3X arm driven by a Yasnac XRC SV3X controller. The SV3X has a maximum speed of 7.33 rad/s for the wrist angle, with a maximum reach of 677 mm. The system is setup for filament made of PLA plastic. The robot arm platform for the system is shown in Figure 2. The 3D printer components utilized are a 0.4 mm extended nozzle with an air forced cooling system (see Figure 3).

### 3.2 Software

A personal computer (PC) was implemented as the higher level controller. The PC runs custom software that interfaces with the XRC robot controller as well as the controller board for the extruder. Communication with the robot is accomplished by using the MotoCom SDK libraries. Communication between the PC and the extruder controller is facilitated by an Arduino board flashed with the Repetier Firmware [10]. Having a single program on the PC controlling the whole system allows for the movement and material deposition speeds to be controlled synchronously. The higher level control software was developed using Microsoft Foundation Class (MFC) Library created using Microsoft Visual Studio.

### 3.3 Interfacing Hardware & Software

Communication between hardware and software is crucial in order to successfully 3D print a part. The process involved coordination between the extruder system and the robot arm. The printing process starts by reading toolpaths from a text file. The toolpaths contains information for the printing workspace and extruder parameters. The printing workspace parameters are X, Y, and Z axis coordinates, RX, RY, and RZ axis wrist angles and the motion speed. For the extruder system, it has four parameters: extruder flowrate, amount of extrusion, extruder temperature and cooling fan speed. The printing workspace and the extruder system parameters

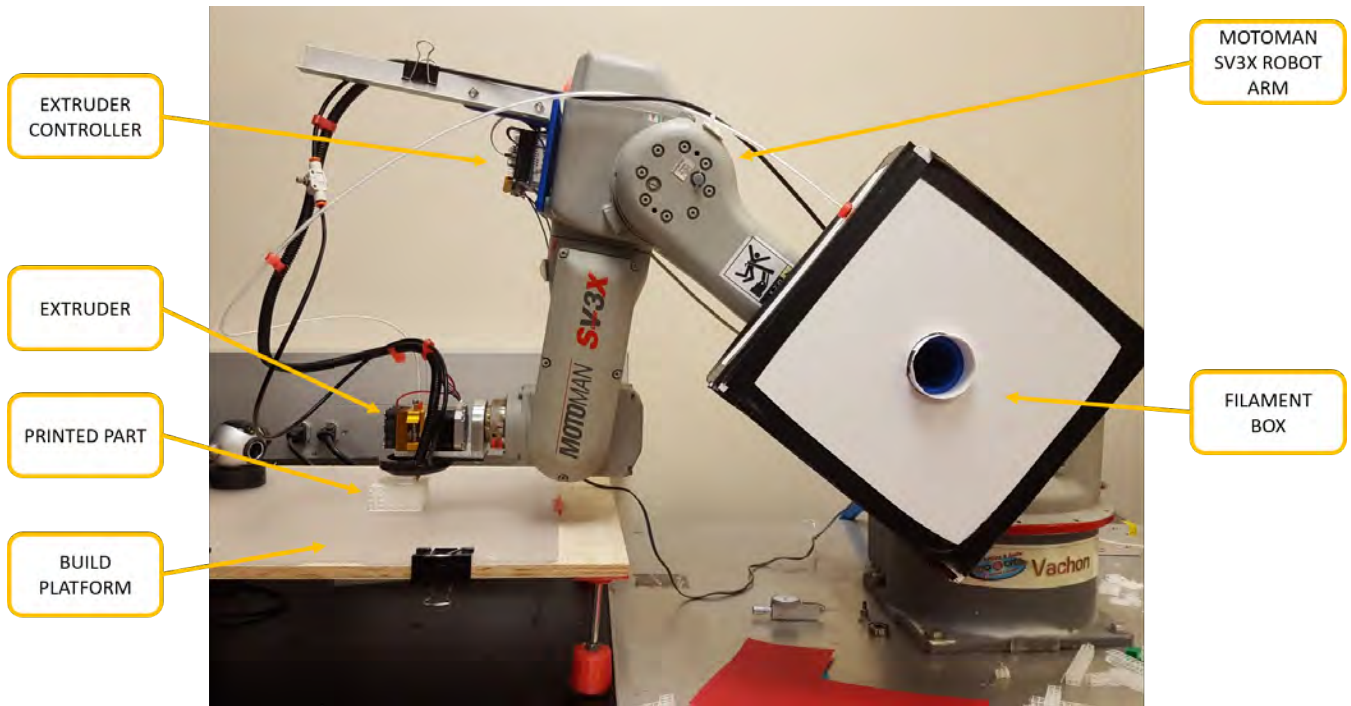


Figure 2. Robot arm platform

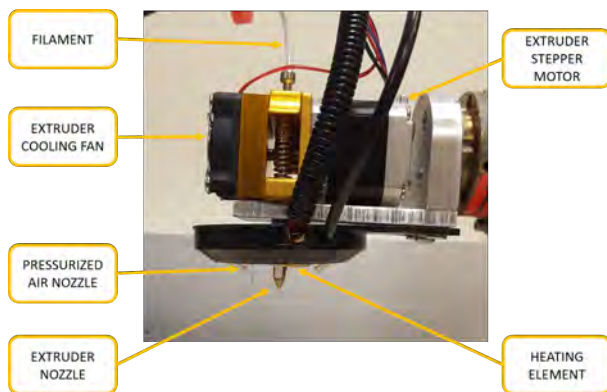


Figure 3. Extruder nozzle with forced air cooling

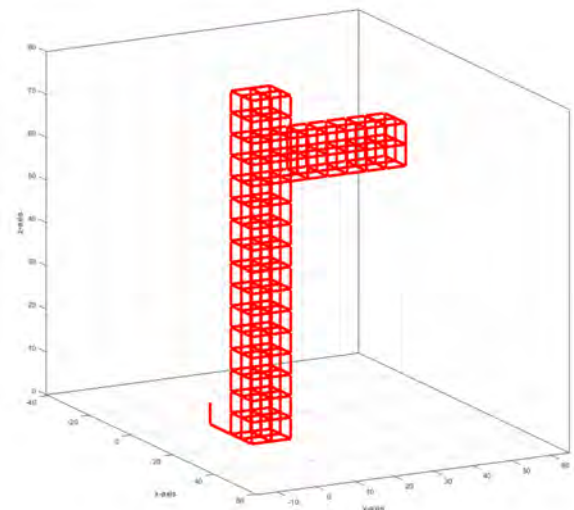


Figure 4. Toolpath simulation

data are sent to the robot controller through the interface program. The communication with the robot arm uses Ethernet protocols and the extruder system uses USB UART protocols.

#### 4. 3D LATTICE STRUCTURES

In order to demonstrate the capability of multi-plane printing to create 3D lattice structures, a 3D lattice structure test block with an overhang structure was printed using the platform. The test block dimensions are 10 mm width  $\times$  10 mm length  $\times$  80 mm height and the overhang structure dimensions are 10 mm width  $\times$  30 mm length  $\times$  10 mm height. The printing toolpath strategy used is based on the geometric features of the 3D lattice structure. A simulation for the toolpath is shown in Figure 4. The horizontal and vertical planes are chosen for the toolpaths layering because they

demonstrate the capability of the robot arm platform to perform multi-plane motions.

The 3D lattice structure test block printing process is shown in Figure 5. The printing process is started by extruding filament in the horizontal x-y plane. The x-y plane printing process is used to produce the 10 mm  $\times$  10 mm  $\times$  80 mm structure. The toolpath of the printing process is based on the strut profile. To create the overhang structure, the extruder head was rotated  $-90^\circ$  about the

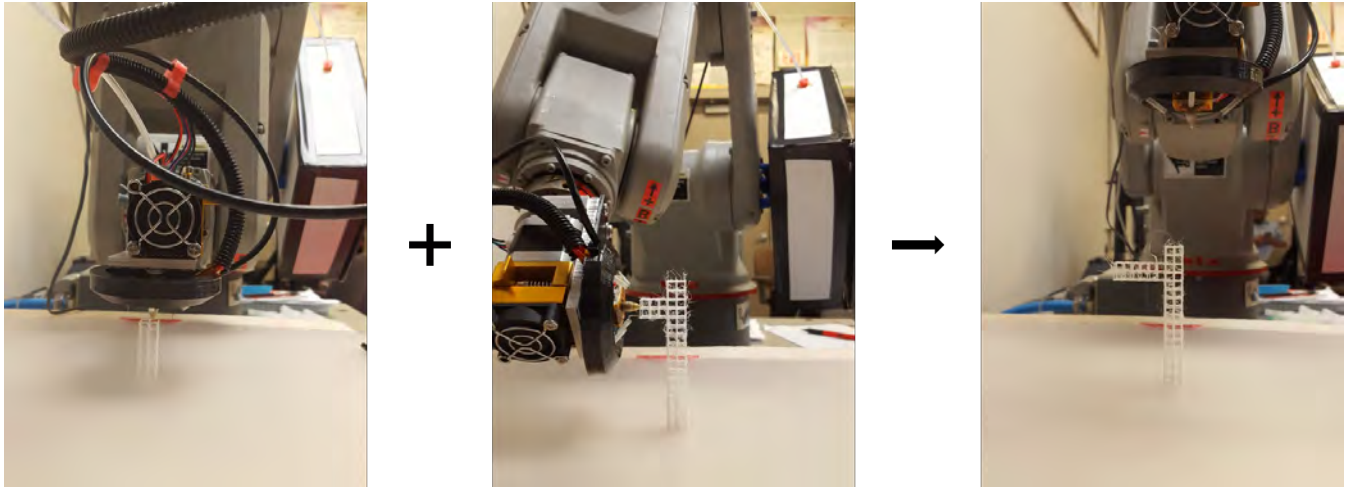


Figure 5. 3D lattice structure printing process

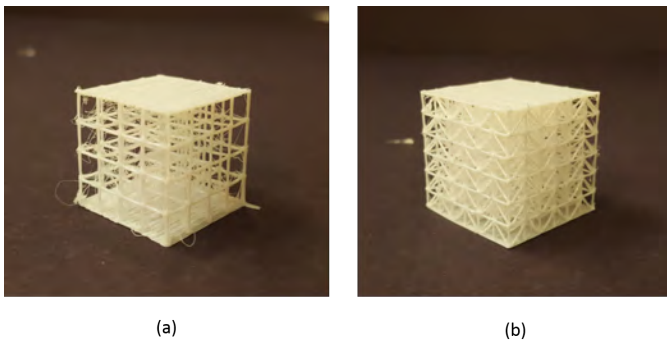


Figure 6. Different 3D lattice structure designs

X axis. The printing process continued on the side of the block in vertical x-z plane. The x-z plane printing process was used to produce the 10 mm × 30 mm × 10 mm structure. The printing speed is set to 1 mm/s in order for the extruded material to solidify with the assistance of forced air cooling from compressed air at the nozzle outlet. The diameter of each strut is  $0.48 \pm 0.02$  mm. The length of the strut is 5 mm.

Different lattice structures could be implemented by utilizing unique 3D lattice structure printing toolpaths. Moreover, 3D lattice structures could be designed based on the number of the struts connected to the nodes. Examples of different 3D lattice structures are shown in Figure 6. The 3D lattice structures with a dimensions of 20 mm width × 20 mm length × 20 mm height are printed using the robotic arm platform.

## 5. FUTURE WORK

The use of the robotic arm platform for additive manufacturing enables a new approach for 3D printing. From horizontal planar layering using a conventional 3D printer to multi-plane layering strategies using a robotic arm platform can be implement in 3D printing. With these new possibilities, new 3D lattice structure designs may be explored. A 3D lattice structure could be designed to provide improved strength to weight ratio. The continued development should focus on testing the 3D lattice structures using standard ASTM methods to determine their mechanical properties.

## 6. CONCLUSIONS

In this article, we presented the integration of a 6 DoF robot arm with an extruder head used in conventional 3D printing systems. 3D lattice structures with overhang structures are able to be printed with the use of multi-plane motion of the printing platform. New material toolpath strategies to design 3D lattice structures can be explored that may lead to improvement in mechanical strength, lowered fabrication time, and reduced filament usage to produce the 3D printed part.

## 7. ACKNOWLEDGMENTS

The authors would like to express their gratitude to Yaskawa Motoman U.S.A for offering the resources for this project.

## 8. REFERENCES

- [1] ISO/ASTM 52900:2015. Standard Terminology for Additive Manufacturing General Principles. i:1–9, 2016.
- [2] Li Yang. Experimental-assisted design development for an octahedral cellular structure using additive manufacturing. *Rapid Prototyping Journal*, 21(2):168–176, 2015.
- [3] J. Bauer, S. Hengsbach, I. Tesari, R. Schwaiger, and O. Kraft. High-strength cellular ceramic composites with 3D microarchitecture. *Proceedings of the National Academy of Sciences*, 111(7):2453–2458, 2014.
- [4] Recep M. Gorgularslan, Umesh N. Gandhi, Raghuram Mandapati, and Seung Kyum Choi. Design and fabrication of periodic lattice-based cellular structures. *Computer-Aided Design and Applications*, 13(1):50–62, 2016.
- [5] SOLIDFILL. Design guidelines for FDM technology. [http://solidfill.com/resource-files/52fa4a1c16869/FDM\\_Design\\_Guidelines.pdf](http://solidfill.com/resource-files/52fa4a1c16869/FDM_Design_Guidelines.pdf), 2017. [Online; accessed 18-April-2017].
- [6] I. B. Ishak, J. Fisher, and P. Larochelle. Robot arm platform for additive manufacturing using multi-plane toolpaths. In *Proceedings of the 2016 ASME International Design Engineering Technical Conferences and Computers and Information in Engineering (IDETC/CIE 2016)*, 2016.
- [7] I. Ishak, J. Fisher, and P. Larochelle. Robot arm platform for additive manufacturing: Multi-plane printing. In *Proceedings*

of the 2016 Florida Conference on Recent Advances in Robotics (FCRAR 2016), 2016.

- [8] M F Ashby. The properties of foams and lattices. *Philosophical transactions. Series A, Mathematical, physical, and engineering sciences*, 364(1838):15–30, 2006.
- [9] N.P. Hack, W.V. Lauer, F.M. Gramazio, M. Kohler, and N. Blank. Method of fabricating a 3-dimensional structure, mesh formwork element for fabricating a 3-dimensional structure, and method of fabricating the same, July 21 2016. US Patent App. 14/916,475.
- [10] Repetier-Firmware. Firmware for arduino based 3d printers. <http://www.repetier.com>, 2011. [Online; accessed 30-March-2015].

# Robotic Face to Simulate Humans Undergoing Eye Surgery

Luis Ramos, Steven Valencia, Shawnak Verma, Karina Zornoza, Melissa Morris, Sabri Tosunoglu

Department of Mechanical and Materials Engineering  
Florida International University  
10555 W Flagler Street  
Miami, Florida 33174

lramo070@fiu.edu, svale049@fiu.edu, sverm005@fiu.edu, kzorn001@fiu.edu, mmorr009@fiu.edu, tosun@fiu.edu

## ABSTRACT

This paper outlines the design and implementation of a facial robot which can perform realistic eye movement to simulate eye surgery conditions. This model also appends to a slit lamp which an ophthalmologist will test. The focal point of the project is the realistic eye movement which will be controlled remotely by the user. The design has been made in such a manner that anyone in the world who has a 3-D printer can access it and replicate the project. Hence, the project incorporates global design elements in it. Moreover, it is made of biodegradable plastic PLA and is environmentally-friendly.

## Keywords

Eye surgery, robotic face, simulation, eye movement, remote control.

## 1. INTRODUCTION

Robotics is a growing field of engineering that has the capability to automate the most difficult processes making them significantly more complex and accurate at the same time. One of the first pioneers of humanoid robotics was Leonardo Da Vinci, who in 1495 created a mechanical armored knight that was able to perform certain body gestures [1]. This science has entered many industries such as car manufacturing, military applications, aerospace, and others. However, there is still an industry that remains relatively untouched by robotics. This is medicine. This industry encompasses many constraints that impedes robotic development. One the biggest constraints is equipment testing. There are certain procedures that cannot simply be performed on humans due to the risk it carries.

This work will be focused on the development of a robotic face that simulates human gestures undergoing eye surgery. The robot will serve as testing platform for ophthalmologist around the world to experiment and test laser equipment. The main points of interest for the robotic face are the precise and realistic movement of the eyeballs and the eyelids. Such movements will be control by the user remotely and applying a code that was developed using experimental data of human eyes. The prototype was made of biodegradable plastic components along with electrical and

mechanical components that puts together a compact design suitable for medical practices.

## 2. LITERATURE SURVEY

The overall intention of robots is to simplify human assignments making them sensible. In other works, robots are used to do work. Nowadays “androids” have become remarkably sophisticated and their primary objectives has shifted from industry uses to services uses. One of the most important aspects of creating a robotic face that imitates human gestures is to be able to have a better understanding of human behaviors when exposed to unfamiliar situations. Robots have become an essential tool for companies, especially in the manufacturing industry where automation plays an important role for efficiency and cost reduction. However, the development of humanoids is relatively new for the medical field due to the implications for testing new equipment. The health care system is ready to accept increased efficiency and cost improvements seen in manufacturing as a result rising health costs and a growing elderly population. Hence, humanoids that replicate human expressions open the door for a bright future for that has captured the attention of world.

### 2.1 Application

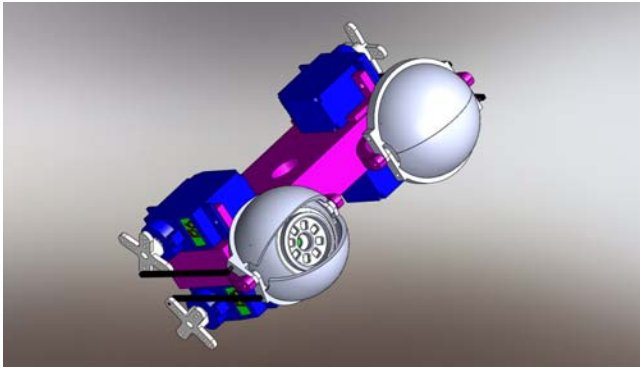
Since this work was focused on human gestures, some level of automation had to be taken into consideration in order to achieve realistic goals. There are four levels of autonomy: human operated, human delegated, human supervised, and fully autonomous.

The technology industry is widely known for the use of robots. However, these machines in most cases do not perform essential tasks. They have been presented to the public as state-of-the-art prototypes that have great potential for the future. Well-known humanoids such as the Toyota Partner Robot and Honda Asimo are perfect examples of these prototypes. Other important applications are seen in space missions with NASA Robonaut and DRL’s Justin Robot which are both tele-operated [2].

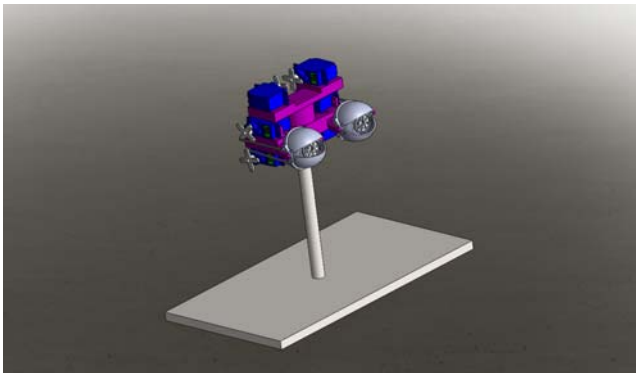
## 3. DESIGN

Figure 1 illustrates only the eyelid mechanism. This first prototype was chosen to use cables as main driver system for the eyes. It is

important to note that for the open-close displacement of the upper and lower lid, a metallic rope would be implemented. This motion can be easily calculated by treating the gesticulation as a four bar mechanism.



**Figure 1. Design of Cable/Tendon System for Eyelid Mechanism**



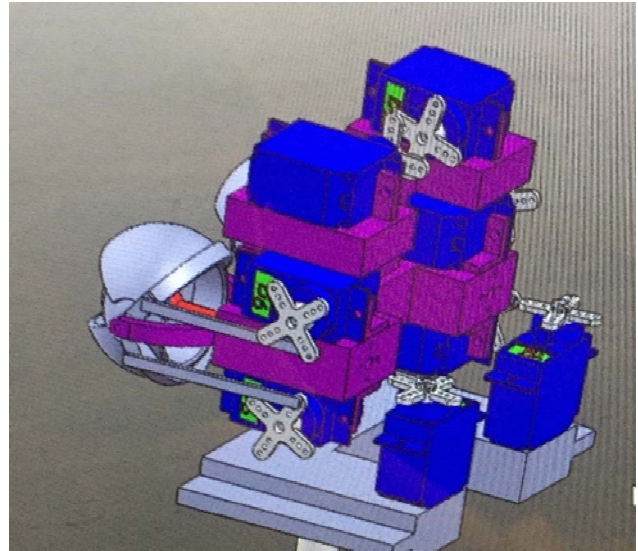
**Figure 2. Design of Cable/Tendon-System for Eyelid and Eye Mechanism**

Figure 2 displays the entire prototype for the cable/tendon system. This 3D model includes the actuation mechanism for the two eyes. Therefore, the eyelids are moved by implementing four single servos, two on each side. These servos connect to the upper and lower lid with a cable or metallic rope that acts as a four bar mechanism. Furthermore, the eyes are connected to the actuation system by using thin steel wire. These wires are a great and inexpensive solution to drive the two degree of freedom needed for the left-right and up-down motion of the eyes. The servos in control of this transfer of motion are located in a separate piece situated on top of the frame. This piece holds two servos. Each servo has the task to move one degree of freedom for each eye. Hence, it is expected to have four different lines connected to one servo at the time.

### 3.1 Structural Design

The proposed design is a unique one because it is made using a 3D printer and therefore is extremely affordable. It is also able to adequately mimic the movements of a normal eye. It can move almost in accordance with the degrees of freedom of a biological eye. The model uses a swashplate mechanism which is used to move the eyeball in different directions. A swashplate is a device used in mechanical engineering to translate the motion of a rotating

shaft into reciprocating motion, or to translate a reciprocating motion into a rotating one. There are strings which pull the eyeballs in every direction and the strings are controlled by servo motors attached at the back of the model.



**Figure 3. Back View of Design with Servo Motor Arrangement**

### 3.2 Material Selection

For the manufacturing of the robotic face, since it is 3D printed, the use of a PLA plastic was used. PLA (Polylactic Acid) has been selected due to its properties. Being strong, durable and malleable. PLA is considered a thermoplastic. This means that this material can be recycled, since it can be heated to its melting point (150-160 degrees Celsius) multiple times without significantly affecting its properties. One disadvantage of this material is that it has relatively low glass transition temperature between 44 and 63 degrees Celsius [7]. This disadvantage makes it unsuitable for high temperature applications.

This prototype has been mainly 3D printed, so materials needed for the manufacture are mostly those needed for the printing phase.

### 3.3 Component Design/Selection

All the components used to build the robotic face were chosen based on their properties including strength, cost, performance and attainability. Components like the servo motors, SG90, were chosen based on their easy programmability and their low cost, while still able to meet the task of generate the movements of the face. In order to operate the motors, a T12ZA controller has been used for the remote control of the mechanism. An Arduino UNO R3 has been utilized to program our servo motors so they generate the appropriate movements to simulate how human eyes move. Common hardware such as screws, springs and hinges allow for easy replacements.

## 4. ANALYSIS

There were two main analysis made for this prototype; motion and acceleration. In order to create a competitive prototype that outperforms other medical robots in the industry, this project focused heavily on the motion and acceleration of all the

operational parts. The reason this was important is because accuracy played a vital role of the final outcome. The movement of the eye, eyelid and other mechanisms have to have a very low error to increase the precision of the laser targeting the retina. In addition, the CAD measurements were made according to average geometry of human anatomy. Other analysis such as structural investigations were made to increase the robustness of the overall design. However, there are not significant external loads anticipated that affect the global performance of the simulation.

#### 4.1 Kinematic Analysis and Animation

Among all robotic mechanism there is one frequently used in the robotic industry: a four bar mechanism. This mechanism was applied to most actuators. The concept gave better understanding of the final position of either the eyelid closure at its two points. The same was implemented for the eye travel, yet, the up-down and left-right was driven by only one actuator for both eyes.

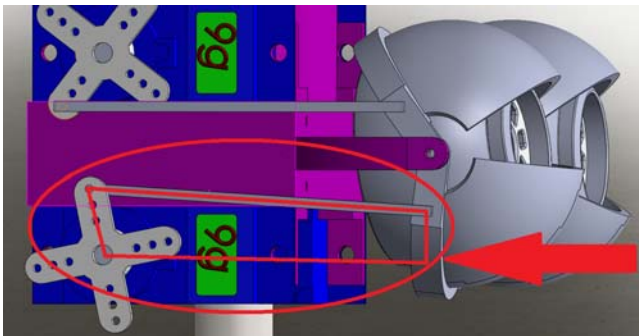


**Figure 4. Four Bar Mechanism Implemented for All Actuators.**

The parameters used for the eyelid closures were based on standard data from the US National Library of Medicine [3]. For this sequence, the eyelid was positioned as a closed eye (90 degrees). A motor was place on each servo running at 200 Hz which seem to be the most realistic human frequency. Table 1 shows part of the data collected from the CAD simulation run for one second.

**Table 1. Eyelid Angular Displacement for 1 Second at 200 Hz**

Frame	Time	Frame1-1
		Angular Displacement (deg) Ref. Coordinate System
1	0.000	-8.9311E+01
2	0.040	-8.9039E+01
3	0.080	-8.8240E+01
4	0.120	-8.6971E+01
5	0.160	-8.5314E+01
6	0.200	-8.3380E+01
7	0.240	-8.1293E+01
8	0.280	-7.9185E+01
9	0.320	-7.7185E+01
10	0.360	-7.5417E+01
11	0.400	-7.3987E+01

12	0.440	-7.2982E+01
13	0.480	-7.2464E+01
14	0.520	-7.2464E+01
15	0.560	-7.2982E+01
16	0.600	-7.3987E+01
17	0.640	-7.5417E+01
18	0.680	-7.7185E+01
19	0.720	-7.9185E+01
20	0.760	-8.1293E+01
21	0.800	-8.3380E+01
22	0.840	-8.5314E+01
23	0.880	-8.6971E+01
24	0.920	-8.8240E+01
25	0.960	-8.9039E+01
26	1.000	-8.9311E+01

#### 5. CONSTRUCTION

Most of this prototype was designed to be 3D printed. The 3DP 1000 printer shown in Figure 5 below was utilized. This industrial printer was facilitated by UTC Aerospace Systems to manufacture the frame, and other components.



**Figure 5. 3DP 1000 Printer**

The first parts to be printed were the pole holder and the frame. The frame houses the eyes and the actuation systems. The pole holder was printed in order to a single piece, but this can also be made of metal which is more rigid. The frame is the largest assembly in the robotic face. It took two and a half hours to print using about \$3 in materials.

The next step in the printing process were the smaller components that make up the eyes. This included the eye lids, swash plates, and eyeballs as well as smaller pieces that hold the servos to the connectors that hold the lids together.

After collecting all the components, both printed and not printed, the assembly part of the process began. A soldering gun, screw drivers, pliers, and many small screws were utilized for the construction.

Four servo motors were needed to control the eye lids, one for each lid. The next step was to add the servos that would control the eyes themselves. The horizontal motion and vertical motion of the eyes are each controlled by two servos. Figure 6 displays the preliminary construction with these eight servos.

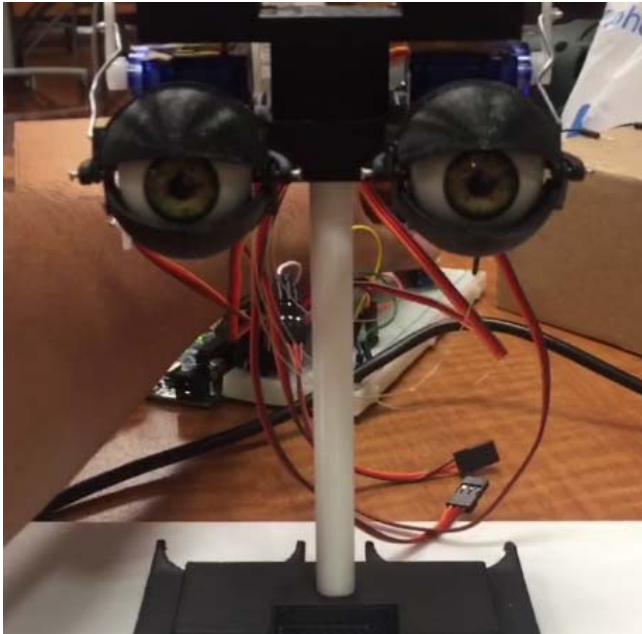


**Figure 6. Beginning Assembly Stage**

To assure that the tension in steel wire cables does not interfere with the other steel wire cables, plastic tubes enclosed them (see Figure 7).

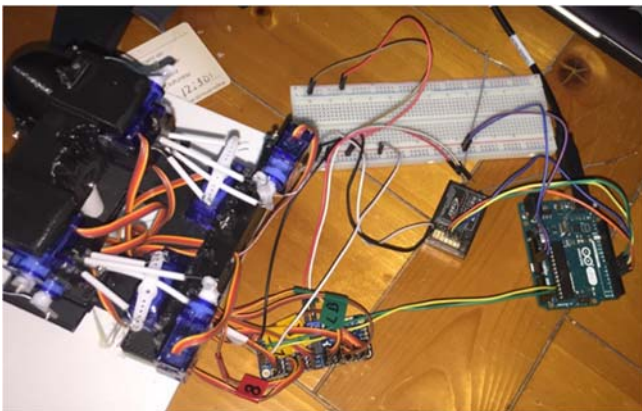


**Figure 7. Configuration of Eight Servos with Tubes Enclosing Steel Wires**

Finally, to make a further aesthetically realistic prototype, a human face mold was added over the prototype as seen in Figure 8 through 10.

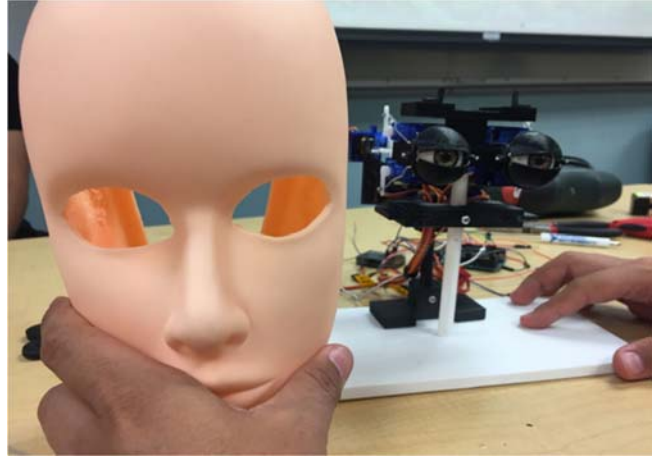


**Figure 8. Mannequin Face to Enclose Prototype**

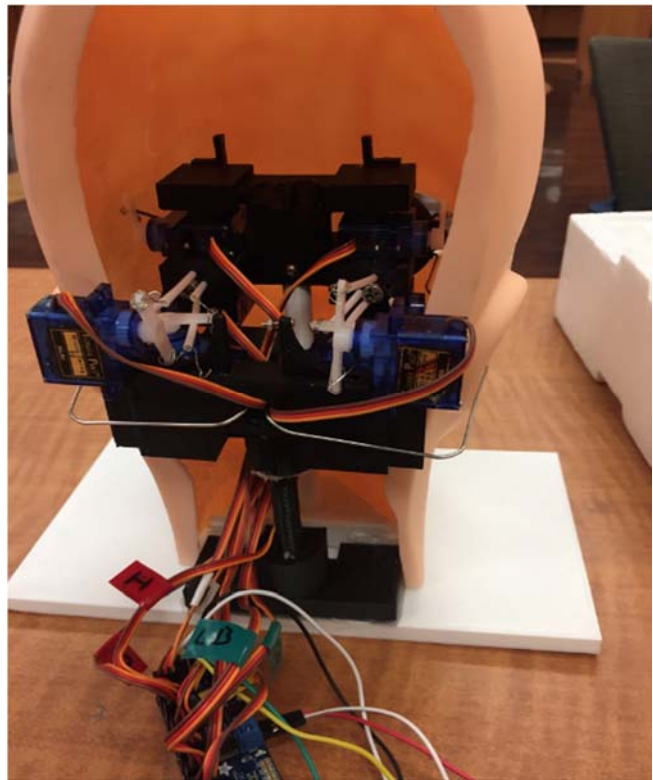


**Figure 9. Mannequin Face Enclosing Prototype**

## **6. TESTING AND EVALUATION**

This section provides an overview of the testing process of the project.

### **6.1 Design of Experiments – Description of Experiments**

The main purpose of this robot is to simulate eye movement. Therefore, it was necessary to test the full movement of these eyes. Several Arduino programs were created to analyze how the servos would generate the movement of the eyes and the eyelids.

One of the important specifications about the SG90 servos is that they do not possess a continual motion configuration. These means that its range of motion is limited. In the case of the SG90 servo, its range of movement is between 0° and 180°. For our testing analysis, the first step was to test the sweep motion of the servos which was done by creating a code to operate the servo utilizing a potentiometer as an analog input. Utilizing a potentiometer allowed us to have more control over the motion and to better understand how the rotation of the gear would move the eyes or the eyelids.



**Figure 10. Completed Prototype**

After testing and analyzing the rotation of the servo motors, another program was created to generate the opened and closed configuration for the eyelids. Since the eyelids play an imperative role in how surgeries are done, if a patient closes an eyelid during the surgery how would the slit lamp react to this or how a trainee doctor would react to this event should be determined.

The next scenario is the case when the eyes move in the horizontal direction. During some eye surgeries or when inspecting the eye before a surgery, a patient may be required to move his eyes left or right so the doctor can look at certain areas of the eyeball better. The vertical motion of the eyes was done to accomplish the same criteria as the horizontal.

The final stage of testing is to integrate all the components together and running a final test on the software. For this final stage a program was created to utilize a RC controller and its receiver to

control the full movement of the mechanism. The whole purpose of these tests is to ensure the hardware and software function correctly, ensure that the software developed control the hardware the right way, and that it meets all the criteria specified in this report.

## 6.2 Test Results and Data

Before even starting to test the software, we needed to ensure our hardware was properly set up and that it could withstand the stresses generated due to the movement of the eyes and eyelids. Figure 11 shows the factor of safety obtained when analyzing the main frame of the hardware utilizing the Von Mises theory. For the SolidWorks simulation, the input is the force transmitted through the shafts (for the eyelids) or the wire (for the eyeballs) due to the torque produced by the servo motors. After running the simulation, the hardware had a factor of safety of 1.3 which means that it is just safe enough to undergo the stress produced by the servos.

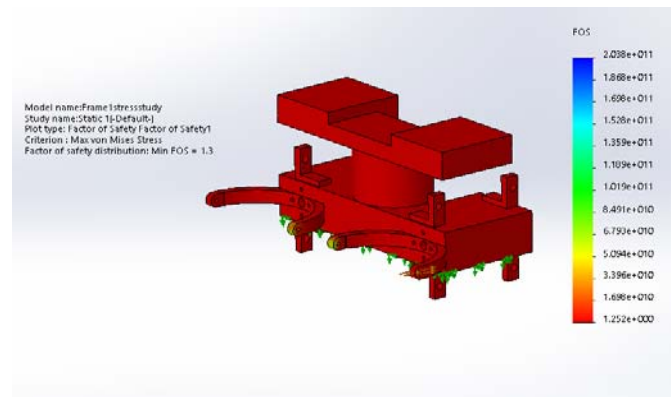


**Figure 11. Factor of Safety Analysis on Solidworks**

After ensuring our main frame was capable of withholding the stresses, an analysis of the four-bar linkage mechanism, which is implemented in the robot to drive motions, was done. This analysis was to predict the range of angles at which the eye will operate and to predict how much the motors would have to be rotated to achieve the desired positions of the eyes. The same theory was applied to study the mechanism utilized to move the eyelids.

## 6.3 Evaluation of Experimental Results

An analysis of the four-bar linkage mechanism to move the eyelids. It was done on MATLAB to make sure the servo motors move only a certain amount of degree to simulate exact eyelid opening and closure. Moreover, the same had to be done for the horizontal and vertical motion of the eyeball. The lengths of every part that aided movement was taken from the SolidWorks assembly and a 2D sketch was made using those lengths. Then the change in those lengths and their orientation was calculated because the movement of the eyes changes everything. Therefore, all the lengths were calculated within the confines of the eyeball movement. These changes in length were then converted into the degrees by which the servo motors must turn to provide precise and realistic movement to the eyeballs.

Despite the calculations, there was a lot of trial and error involved to get the exact numbers. Moreover, the left and right motors were not the same distance apart due to a small degree of human error in

the manufacturing process. Hence, the program for both the motors had to be tweaked slightly to accommodate that difference.

The above process was repeated for the vertical motion of the eyeballs as well.

## 6.4 Improvement of the Design

After doing all the previously mentioned tests, the project began to focus on three major obstacles which hindered the proper functioning of the eyeballs.

The first obstacle was regarding the tension in the fishing line we used to connect the motors with the eyeball. The fishing line lacked the tension required for smooth movement of the eyeball. It would slack during testing of the up and movement of the eyeball. It would climb as expected but as soon as the command to move down was implemented, gravity would take over and the eyeball would free fall as if hinged to nothing. Moreover, it was very difficult to tie the fishing line and without a constrained path, it would take any random shape. The group decided to switch to a small diameter aluminum wire. The aluminum wire was small enough go through tiny holes initially designed for the fishing line, but most importantly the tension in the wire ensured smooth functioning of the eyeball.

The second problem overcome in this project was in using the space behind the frame to mount the servo motors. The initial design led to very tight space in which the fishing line would get entangled with the servo motor cables. It would also compromise the functioning of the eyeballs because of all the entanglement. In addition, it made disassembly a long and arduous task. Rather than design something new, existing 3D printed parts were salvaged to create a new adjustable platform which was installed below the frame. Its height can be adjusted and two motors were installed on that platform which ensured horizontal movement of the eyeball. Another rejected frame was installed vertically behind this platform and the servos attached to this platform took care of the vertical movement of the eyeball. In these platforms, there is also a wire sink where the servo motors' wires go and they don't entangle with the other aluminum wire. Moreover, disassembly became very convenient after these design additions.

The third obstacle was regarding the number of servo motors the design used. The initial design included only two servo motors which controlled the horizontal and vertical movement of the eyeballs. This concept looked promising in the design phase but during testing, it suffered severe problems in synchronicity. The wires moving the farther eyeball would be less tense and would regularly fail in moving their respective eyeballs when compared to their counterparts.

Moreover, when it was decided to use the aluminum wire, the crossing of the wires became obsolete since the aluminum wire did not regain its shape when it was bent. It had to be kept straight and the motors had to be placed parallel to the holes the lines came out from. Therefore, it became imperative that two servo motors be used for each eyeball. It also gave the luxury of testing each eyeball separately.

## 7. CONCLUSION

This project's main goal was to design, analyze, manufacture, and test a robotic face to simulate eye surgery. With the main concern being the robotic eyes, this was the focal point of the project. Much research was done and the information collected was used to create several design alternatives. After deliberation on which alternative was the best concept the best one was chosen. Next, the feasibility and the cost were analyzed.

After these were all formulated and finalized, the manufacturing stage began. Since this is still an early prototype, it is not yet in an optimal state. In the future, the hope is that this will be manufactured with top-of-the-line materials, upgraded electrical components, and improved programming. These will make the look and movement of the robotic face be that much more realistic and precise. If more time is spent on the programming, then more advanced facial expressions will be able to be extracted making the robotic face a more enhanced one.

## 8. ACKNOWLEDGMENTS

The authors extend their thanks to Rodrigo Arredondo for his assistance in the programming of the prototype.

## 9. REFERENCES

- [1] Leonardo Da Vinci Inventions. "Robotic Knight." Leonardo Da Vinci's Invention. N.p., n.d. Web. 25 October 2016.
- [2] O'Sullivan Igoe. "Mechanics of Robotics." Mechanics of Robotics. N.p., n.d. Web. 25 October 2016.
- [3] Eyelid Closure Data, US National Library of Medicine, Robotic Industries Association, 900 Victors Way, P.O. Box 3724, Ann Arbor, Michigan 48106.
- [4] "Animatronic Robotic Eyes." PyroElectro Electronics News Projects Tutorials RSS. N.p., n.d. Web. 25 October 2016.
- [5] Michigan Technology Institute. "Macro-, Micro-, and Nano-sciences." Macro-, Micro-, and Nano-sciences. N.p., n.d. Web. 25 October 2016.

# Robotic Hands to Teach Sign Language

Raheem Maliki, Dalal Alhaidar, Khalid Attallah, Saleh Alsalem, Melissa Morris, Sabri Tosunoglu

Florida International University  
Department of Mechanical Engineering  
Miami, Florida 33174

rmali005@fiu.edu, dalhi001@fiu.edu, salsa029@fiu.edu, katta005@fiu.edu, mmorr009@fiu.edu, tosun@fiu.edu

## ABSTRACT

This paper develops a robotic platform intended for the task of reproducing and teaching sign language. Specifically, realistic arm and finger motions were developed and then produced by the prototype constructed. The device presented can be used as an interactive way to teach sign language, one that is particularly engaging to children, or be a critical component of an automated system to translate spoken language into visual signs in real-time.

## 1. INTRODUCTION

Human beings are innately social and the need to communicate is essential in order to pass on ideas and information. This is done primarily by speech and listening, but unfortunately some people live with disabilities that hinder verbal communication. Individuals who are deaf cannot hear speech, while physical or mental impairments inhibit the production of speech for others. Therefore, sign language was developed as a means of non-verbal real-time communication.

This project looked into the concept of teaching children sign language with the aid of robotic hands. Generally, children have short attention spans and can usually become overstimulated during learning of a subject as broad as sign language.

Furthermore, we live in an age where robotics are becoming a regular part of our daily lives, hence using robotic hands to teach the children will not only improve their enthusiasm towards learning the subject, but will also reduce over-stimulation in classrooms.

American sign language (ASL), the primary form of sign language in the United States traces its origins back to the early 1800s. A Yale graduate by the name of Dr. Thomas Hopkins Gallaudet wished to communicate with his neighbor's deaf daughter. He traveled to France where signing had already been developed and met Laurent Clerc. Clerc later traveled back to the US with Gallaudet and started the first school for deaf in Hartford, Connecticut. In 1864 congress passed a legislation that created the National Deaf-Mute College, the first college of signing, to issue degrees. This university was later renamed Gallaudet University [1].

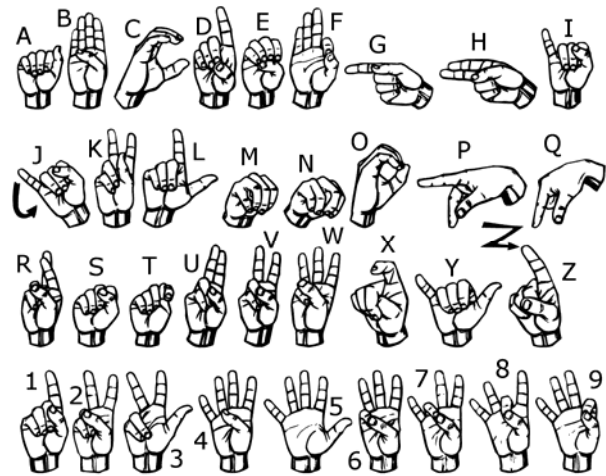


Figure 1. Sign Language Letters [2]

Much like sign language, robotics has a long history. The term robot was coined from "robota", which means servitude. There are different forms of robots available today. These include robots in animal form to full humanoid robots that complete tasks with or without instructions from people. Robots are now an everyday item seen in homes around the world. In general, their purpose is to make leading a life easier for people whether it is an iRobot [3] that aides cleaning the house to the more humanoid robots like the Softbank companion robot shown in Figure 2.



Figure 2. Softbank Robot Companion [4]

## 2. Conceptual design

The primary goal of this project was to find a cost-effective solution to the proposed topic of developing a robot to teach sign language. Since learning sign language is worldwide endeavor, an open source design for the robot was sought as one objective. In addition, the robot was minimally required to have sufficient degrees of freedom and range of motion to enable the performance of sign language.

To help accomplish the project goals with the limited time and resources available during the duration of this project, currently available platforms were investigated. The InMoov robot, an open source design, was used as the base for this project because it met the primary objectives noted above. A complete InMoov robot is shown in Figure 3. Figure 4 shows a closer view of only arm and hand portion.



Figure 3. InMoov Robot [5]

The primary form of production for this project was 3D printing. ABS plastic was used as it was found to be stronger than its PLA counterpart. The arms of the InMoov robot are intended to be printed and mounted on a specially-designed platform for programming.

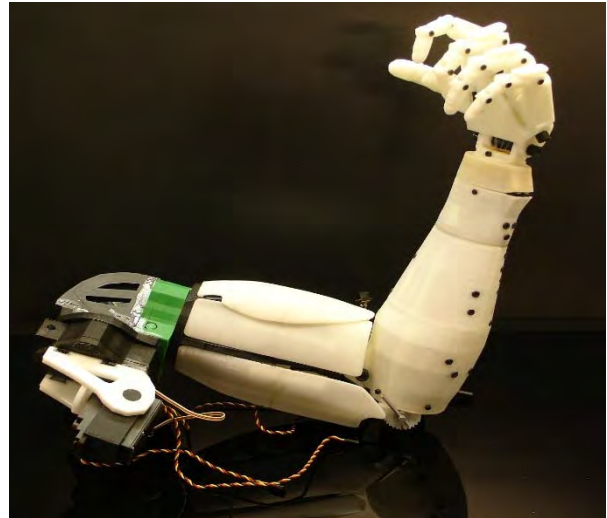


Figure 4. InMoov Robotic Arm [5]

### 2.1 Servo Motors

Three different specifications of servos were used in the robotic arm assemblies. The servos had to be carefully selected to perform the different angles of motion required for different parts of the arms and hands. There were especially differences in the torque requirements to move different parts of the robotic hand that required proper sizing and consideration of actuators. Table 1 summarizes the servos and specifications selected.

Table 1. Servos and Specifications

	HS 805BB	MG996R	HK15298B
Max Torque	24.7 Kg-cm	11 Kg-cm	18 Kg-cm
Speed	0.19 sec/60°	0.19 sec/60°	0.18 sec/60°
Mass	152.0 g	55.0 g	66.0 g

### 2.2 Assembly

My Robot Lab (MRL) was used in the initial assembling and programming of the robot. Several of the robot components had to be put to certain angles before assembling. The instructions for assembling can be found on the InMoov website. [6]

The Raspberry Pi was used to do the initial programming of the robotic arm. The MRL Graphical User Interface (GUI) was installed on the Raspberry Pi and ran using the sequence shown in Figure 5.

```
pi@raspberrypi: ~/mrl
File Edit Tabs Help
pi@raspberrypi:~$ cd mrl
pi@raspberrypi:~/mrl$ java -jar myrobotlab.jar
```

Figure 5. Sequence to Launch MRL

Due to the limited Pulse Width Modulation (PWM) pins available on the Raspberry Pi, an Adafruit PCA9685 with 16 channels was used to interface the Raspberry Pi with all the servos via i2c communication. This servo driver is shown in Figure 6.

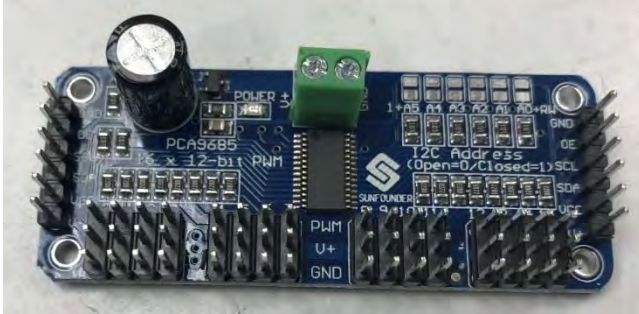


Figure 6. Adafruit PCA9685

Once the MRL is launched in the Raspberry Pi, a window such as the one in Figure 7 is displayed.



Figure 7. MRL GUI

The programming language used for the MRL GUI is Python. Once all the necessary services necessary for servo control are installed on the MRL GUI, the following code is entered in the python window to initiate the servo control GUI:

```
.adaFruit16c =
Runtime.createAndStart("AdaFruit16C", "Adafruit16CServoDriver")
2.raspi =
Runtime.createAndStart("RasPi", "RasPi")
3.adaFruit16c.setController("RasPi", "1", "0x40")
4.lpinky = Runtime.createAndStart("LPinky", "Servo")
5.lring= Runtime.createAndStart("LRing", "Servo")
6.lmid = Runtime.createAndStart("LMid", "Servo")
7.lindex = Runtime.createAndStart("LIndex", "Servo")
8.lthumb = Runtime.createAndStart("LThumb", "Servo")
9.lwrist = Runtime.createAndStart("LWrist", "Servo")
```

```
10.llowerbicep =
Runtime.createAndStart("LLowerBicep", "Servo")
11.lupperbicep =
Runtime.createAndStart("LUpperBicep", "Servo")
12.lshoulderside =
Runtime.createAndStart("lshoulderside", "Servo")
13.lshoulderforward =
Runtime.createAndStart("lshoulderforward", "Servo")
14.lpinky.attach(adaFruit16c,0)
15.lring.attach(adaFruit16c,1)
16.lmid.attach(adaFruit16c,2)
17.lindex.attach(adaFruit16c,3)
18.lthumb.attach(adaFruit16c,4)
19.lwrist.attach(adaFruit16c,5)
20.llowerbicep.attach(adaFruit16c,6)
21.lupperbicep.attach(adaFruit16c,7)
22.lshoulderside.attach(adaFruit16c,9)
23.lshoulderforward.attach(adaFruit16c,8)
```

Each servo on the robotic hand is assigned a pin on the Adafruit PCA9685. Once the servos are plugged into the correct pins, they can be controlled by the GUI.

Once the code is run, a window such as that shown in Figure 8 appears. The servos can be activated by moving the sliders shown in the upper portion of the window.

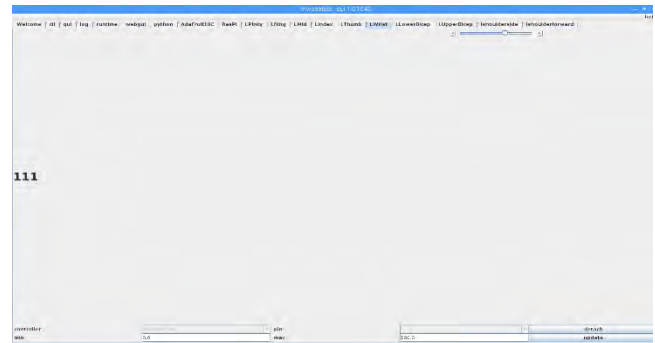
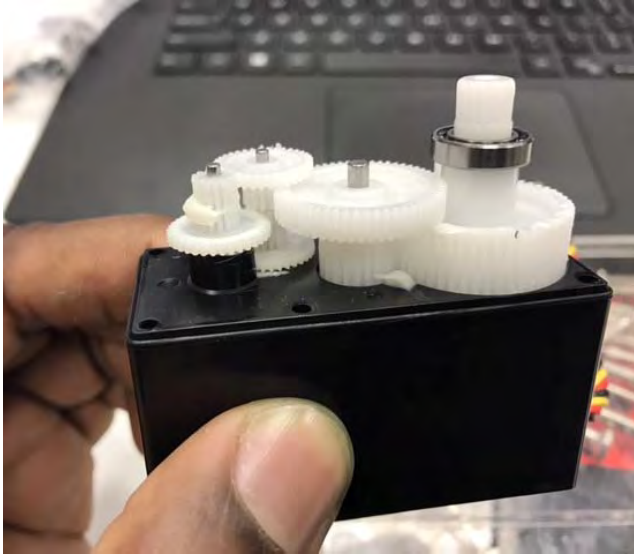


Figure 8. Servo Control GUI on MRL

As noted previously, three different servos were used to control different areas of the arms and hands. The HK15298B servos were used to drive the fingers, the MG996R servos were used to drive the wrist rotations, and the HS805BB servos were used to drive the shoulders and the biceps. Due to the limited angle of motion of the HS805B servos, they were modified to allow continuous rotation. This was accomplished by opening the servos as shown in Figure 9 and cutting the stopper on the gears which limited their range of rotation. Furthermore, the feedback potentiometer in each servo was removed and soldered to an extension cable. Each potentiometer was attached to different joints of the robotic arm where required to obtain proper feedback and control of the servo positions.



**Figure 9. Inside the HS805BB Servo**

The servos were implemented according to guidelines provided by the InMoov open-source documentation. However, modifications were required to accommodate the specific servos used as well as to accommodate other variances in printing, design and the materials used.

Figures 10 – 14 shown depict various parts as they were assembled into the final prototype. Specifically, finger servos, assembly of fingers, forearm attachments to the forearm and the wrist as well as the torso of the robot are displayed in these figures.

Figure 15 shows the completed left arm attached to a moveable base at a proper height proportional to the size of the arm.

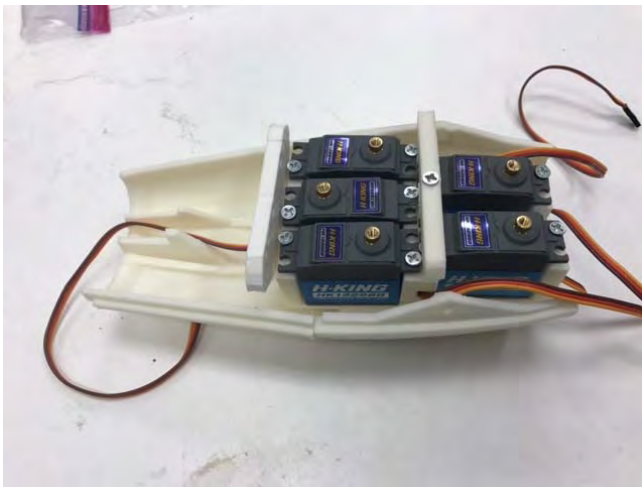


**Figure 10. Finger Servos in the Forearm**

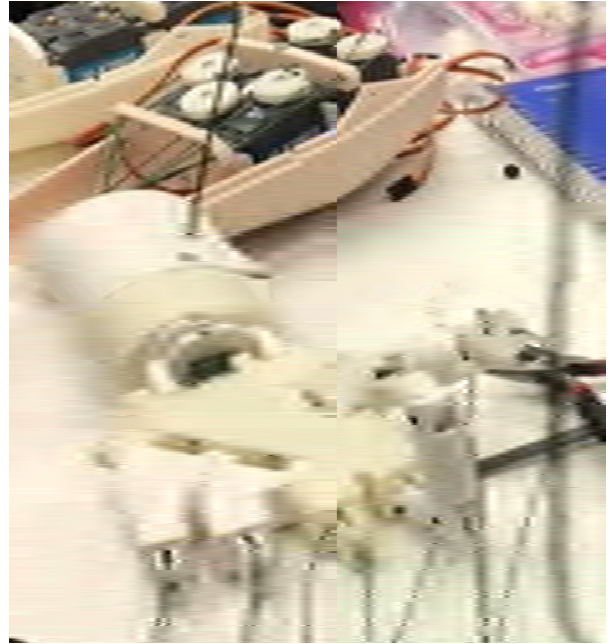


**Figure 11. Assembly of Fingers unto the Wrist**

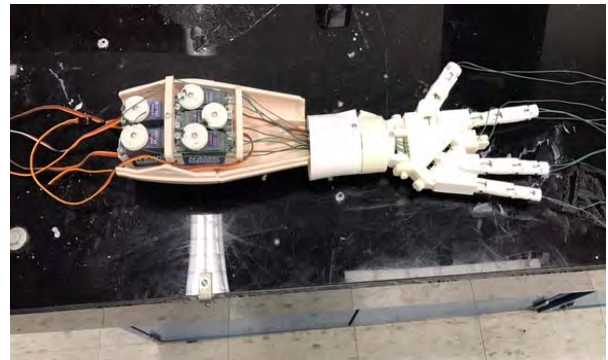


**Figure 12. The Forearm Attached to the Wrist**

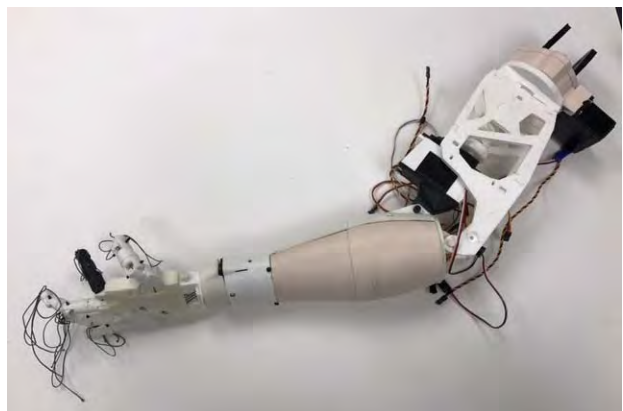


**Figure 13. Forearm Attached to the Bicep**



Figure 14. The Torso of the Robot

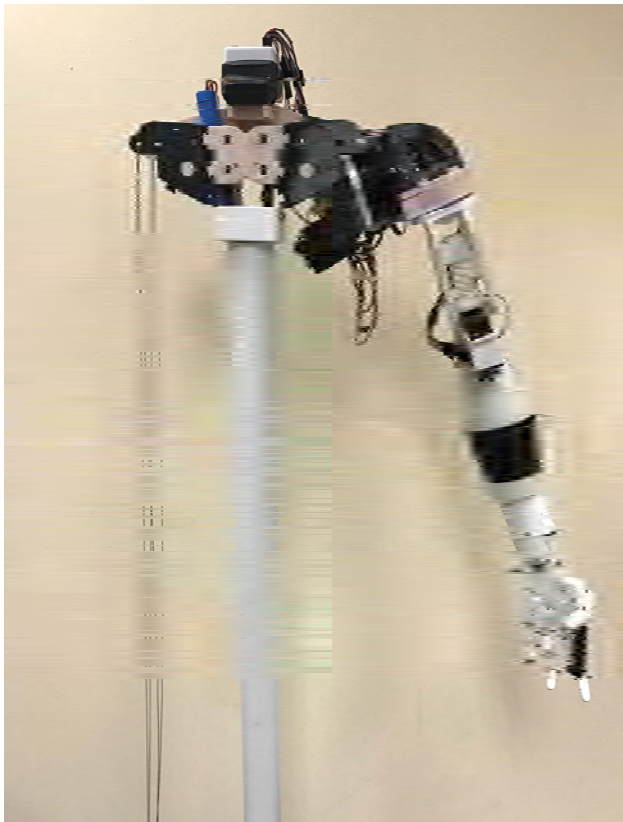


Figure 15. The Left Arm of the Robot

### 3. Programming

Though a Raspberry Pi with MRL was used in the preliminary stages of assembly and testing, a different controller was used in the final system to ease the amount of programming and speed up development and testing.

The EZ-B V4, shown in Figure 16, was used for the final programming of the robotic arm. It is a robotic servo controller that has 24 digital pins in addition to eight analog pins. It features built-in voice command options, speaker and Wi-Fi capabilities allow for integrated web-based remote control.



Figure 16. EZ-B V4 Robotic Controller

The EZ-B runs its own operating system and software that makes programming servos an easy task. The on-board Wi-Fi capabilities makes it possible to control the robot from different devices including PCs, laptops, tablets, and smartphones.

For this project, two specific software functions of the EZ-B are used, namely, the frame creating options and the action creating option. An example of the GUI for these tools is shown in Figures 17 and 18.

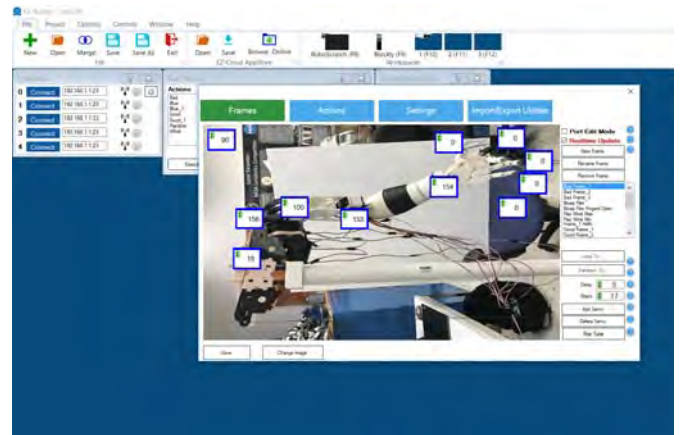
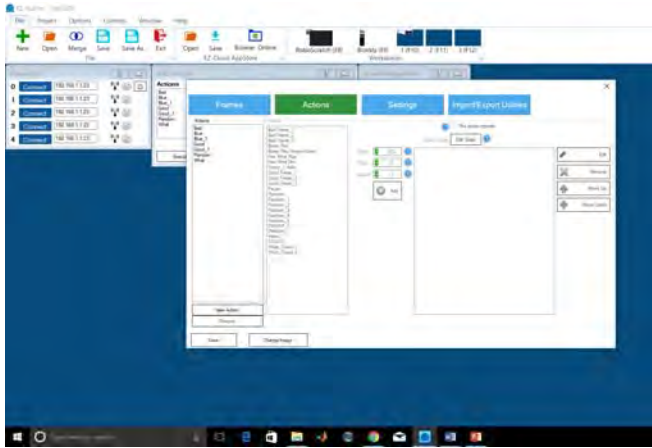


Figure 17. EZ-B Frame Creating Window

In the frame creating window of the EZ-B software, all the attached servos are given specific frames. This then allows intuitive actuation of each servo to obtain the desired joint angles.



**Figure 18. EZ-B action Creating Window**

In the action creating window of the program, several frames can be put together to create specific gestures. This feature is especially helpful as sign language depends upon the use of gestures. This greatly reduced the amount of time spent coding.

## 4. Design Considerations

### 4.1 Health and Safety

Caution must be taken when operating the robotic arms as there are moving parts that form pinch points or collision hazards. To reduce the risk of harming someone, adequate space should be given for the workspace of the robotic arms during operation. Children should be properly supervised when learning sign language from the robotic arms and be kept away at a safe distance. Also, users must make sure that the wheels are properly secured. The wheels of the current prototype do not have brakes and the robot might move slightly while operating, but brakes can be installed and utilized in future versions. The structural components of the robotic arms were printed and assembled in accordance to the regulations for health and safety to reduce problems with this aspect.

### 4.2 Manufacturability

The 3-D parts of the robotic arms used are found on the InMoov project website as mentioned previously. The parts were printed on a 3-D printer. The choice of material used in the printing is something that must be considered in the manufacturability. The major difference during assembling with either PLA or ABS plastic is the method in which the plastic parts are joined together. Acetone, if used properly, can be used to weld ABS together. Acetone melts the ABS plastic and gives the impression of the parts having been printed as one solid piece. If, however, PLA is used, a strong glue is to be used to bind the parts together. ABS plastic was used in the printing as it had a higher strength than its PLA counterpart and due to the ability to combine parts together to form larger components.

A PVC pipe was used as a stand for the robot in conjunction with the mounting platform that was designed for the robotic arms. The other end of the PVC pipe was attached to steel wheel base to ensure ease of transporting the robotic arm while being a sturdy foundation.

## 5. Design Experience

### 5.1 Overview

The objective of the project was to design humanoid robotic arms that could teach sign language to children. The design experience included contemporary issues, standards used, the impact of design in global markets, ethical responsibilities, and life-long learning.

### 5.2 Contemporary Issues

Several issues were encountered when assembling the robot. The primary issue encountered was the accuracy of the parts generated by the 3-D printer that was used. The accuracy of the printer varied from print to print which resulted in difficulties mating the parts. This is evident in the Figures 19 and 20 below.



**Figure 19. Forearm Assembly Misalignment**

The misaligned parts had to be reprinted several times until suitable alignment was achieved. In addition, several of the parts had to be modified to fit the required design criteria.

One of these areas was the wrist. The wrist was modified due to the change in size of the servo utilized from that which was suggested by the InMoov project. The space provided had to be modified to allow for a bigger servo to fit.



**Figure 20. Forearm Assembly Misalignment**

## 6. Future Work

The platform used as the basis of this project was developed from an open source and is available for download. The code generated for making the arms perform sign language were made available to the public. Users may print the parts for the robotic arm, purchase and install the other components, and install the code developed to gain benefit of the platform presented in this paper. It is expected that the robot will encounter some marketing and implementation issues since it is a new idea and can benefit from further programming and development. However, it is expected that eventually people around the globe will get used to the idea of learning sign language by using humanoid robotic arms.

Several improvements can be made in the future to further improve this project. The focus of this phase of the project was assembly of the left arm and hand and making sure they moved properly. In the future, some of the parts can be modified to improve signing. For example, the wrist only rotates in the presented implementation and it does not bend back and forth. Adding another servo for the wrist will greatly improve the degrees of freedom of the arms, which in turn will make signing more accurate and versatile.

## 7. Conclusions

Children with certain disabilities and conditions face communication obstacles. Studies have noted that children can be overstimulated when taught sign language by traditional means. This can be detrimental to their ability to learn sign language. The robot presented in this work was designed and programmed to teach children sign language while overcoming the common obstacle of overstimulation.

The robot's signs need to be correct and precise to avoid teaching a wrong sign or incorrect gestures. The InMoov robot has never been used in such a way before nor has it been fashioned towards such a goal. As such, improvements and future work are needed to make the robot even more versatile.

## 8. Acknowledgments

The authors extend their thanks to the Robotics and Automation Laboratory, Department of Mechanical and Materials Engineering, and Florida International University for providing the opportunity to work on this extraordinary project. The unlimited access provided to the 3D printer in the Robotics and Automation Laboratory made it possible for the authors to build the prototype literally after printing hundreds of parts.

## 9. References

- [1] History of American Sign Language - Start ASL. Retrieved October 11, 2016, from [https://www.start-american-sign-language.com/history-of-american-sign-language\\_html](https://www.start-american-sign-language.com/history-of-american-sign-language_html)
- [2] Sign Language Letters. (2016, March 1). Retrieved October 16, 2016, from <http://www.mnhuntingcalendar.com/sign-language-letters/>
- [3] Roomba Robot Vacuum | iRobot. (n.d.). Retrieved October 16, 2016, from <http://www.irobot.com/For-the-Home/Vacuuming/Roomba.aspx>
- [4] Do you remember Pepper? The Robot in Japan with Emotions. Newdawn. (2016). Retrieved October 17, 2016, from <http://newdawnblog.com/2016/08/11/do-you-remember-pepper/>
- [5] Build yours. (n.d.). Retrieved October 16, 2016, from <http://inmoov.fr/build-yours/>
- [6] InMoov Project, <https://www.inmoov.fr/>.

# Robotic Implementation to Automate a Vertical Farm System

William Marchant, Sabri Tosunoglu

Department of Mechanical and Materials Engineering  
Florida International University  
Miami, Florida 33174

wmarc002@fiu.edu, tosun@fiu.edu

## ABSTRACT

Continued global population growth, increasing loss of cultivated land to urban sprawl, land degradation, and climate change provide a serious threat to our society, particularly how we feed our society, agriculture. Our agricultural production will be expected to produce an ever increasing amount of food with much less arable land. These problems will require us to innovate and continue to advance agricultural technology. One of the recent trends gaining traction is the use of vertical hydroponic indoor farms. Unlike traditional outdoor farms that span hundreds acres, these farms are stacked vertically to maximize limited space and are protected from some of the more dangerous elements of outdoor environments, such as pest, unfavorable weather or seasons. These systems are designed to maximize crop yield and reduce turnover by providing crops the most ideal lighting and environment constantly. This paper proposes implementing a robotic and vision system to plant and harvest crops in a preexisting vertical farm system. We will also propose two algorithms to control the automated procedures. A robotic system would allow a vertical farm to maximize efficiencies to tackle the problems agriculture will face. We will conclude with a discussion on the promising potential of uniting robotics with vertical farms.

## Keywords

Vertical Farm, Automation, Soil-less Farming, Hydroponics

## 1. INTRODUCTION

As of 2015, our current global population is estimated at 7.3 billion people. Population is expected to peak at 10 billion before the end of the 21<sup>st</sup> century with growth rates above 1% per year [1]. As a result, during the next 50 years, demand for food is projected to grow by at least 70%. Over the decades we have experienced significant human migration from rural areas to cities, more than half of the world's population now lives in highly dense urban areas [1]. This great migration to urban areas is expected to accelerate the loss of cultivable land to urban sprawl [2]. These factors in combination with land degradation via soil erosion and salinization, loss of arable land to urban expansion, and climate change creating unfavorable conditions for crops are some of causes threatening agricultural land as a resource [3][4]. As our population continues to grow, we need to innovate agricultural technology in an effort to

maximize our crop efficiencies, in crop yield and turnover. We must also find ways to efficiently use land for production, as space becomes a scarce commodity in urban environments.

One of the proposed solutions is vertical farming. The underlying idea for vertical farming is to increase productivity by extending cultivated area vertically instead of horizontally, in doing so we increase the land efficiency to produce crops [5]. Vertical farming can be implemented both in the large and small scales. Large scale vertical farming involves vertically stacking building sized facilities such as glass houses or controlled environments into high rises. On the smaller scale, there are vertical farming systems, which use the same idea on smaller room size scale, maximizing crop yield by vertically stacking the floor area. Common examples of vertical farming systems include vertical columns [6], conveyer driven stacked growth systems [7], A-frame designs using conveyer driven systems [8], and plant factory approaches seen below [9].



Figure 1. A plant factoring and its use of artificial lighting

Plant factory refers to a plant production facility with a thermally insulated and nearly airtight warehouse-like structure [10]. These warehouses are stacked with multiple culture shelves lit with energy efficient LEDs. Plant factory also use other equipment to optimize the indoor environment, such as air conditioning, air circulation fans, carbon dioxide and nutrient solution supply, and an environmental control unit. Stacking more culture plates will increase crop production efficiency. These plant factory systems were designed to bring agriculture to areas generally not suited for it, such as an urban environment [10]. The enclosed and controlled

environment of these factories offers unique advantages to crops, such as consistent humidity, lighting, and the avoidance of pest.

The aim of this paper is to propose an affordable implementation of a robotic and vision system to work within a vertical farm. The proposal would be applied to an existing small scale vertical farm system with the intention to potentially extending the proposal to larger scale plant factories. A robotic harvesting/planting system would allow for greater efficiency in crop turnover and production. The camera system proposed should also be able to identify when a crop is ready to be harvested or removed based on different factors such as size and color. Finally, the robotic system should allow plant factory to remain enclosed most of the time, keeping crops in the ideal created environment, but still allow for human interaction with crops when necessary.

### 1.1 Related Work

The promise of vertical farming crop efficiency has inspired many variations. However, automated or semi-automated vertical farms remains an underdeveloped field. Current approaches automate certain parts of the vertical farming system. More common approaches involve automating growth plate movement for easy human manipulation and uniform sunlight, while others focus on automating environmental control and crop maintenance. Below we describe two vertical farm systems that served as inspirations for the proposed robotic system.

One of the first examples of semi-automated vertical farm comes out of the Singapore. SkyGreen has created a system using “A-Go-Gro” technology. This technology uses hydraulic water-driven vertical farming system. The rotation system is gravity aided water pulley system, the same water used to power the rotation is recycled and filtered before returning to the plants. The vertical farm uses the A-frame design, roughly 6 meters tall. Each A-frame tower consists of 22 to 26 tiers of growth troughs, rotated around the frame to ensure uniform distribution of sunlight and good airflow. The towers are housed in a protected environment of PVC roofing and netted walls [11].



Figure 2. SkyGreen “A-Go-Gro” vertical farm

The SkyGreen vertical farm has several advantages. One advantage is the vertical farm does not rely on electricity but rather a source of water that also serves the plants. Another advantage is its enclosed structure allows for sunlight but keeps pest out. A couple of disadvantages however do exist within this vertical farm system. The A-frame vertical farm system is large and tall; this would require a large space to contain a modest scale farm. Another drawback is the system is dependent on the weather, using any available sunlight and rain to power its rotation. Its size and dependence on environmental factors limit its potential as a replacement for more traditional methods of farming.



Figure 3. CityCrop automated indoor farming

The CityCrop Automated Indoor Farming system is a mini vertical farm system out of Greece. This system is intended to bring vertical farming to your home or small business. CityCrop aims to make an intelligent farming system that will only require the users to plant and harvest their crops, and let their system take care of the rest. The CityCrop Automated farm is equipped with a climate control system used to control temperature, humidity, lighting, etc. In addition it uses hydroponics to give plants nutrients, LED growth lights, adjustable trays, and even has its own app to control its indoor environment as well as monitor and manage crops. It has two trays with 12 pods for planting each, so a user can plant a maximum of 24 plants. This automated farming specializes on growing leafy green crops such as lettuce. [12].

The City Crop automated indoor farming system offers a couple of advantages to traditional farming methods. One primary advantage is its small dimensions, allowing households and businesses to potentially grow their own fresh crops indoors. Another advantage is the system is not dependent on the user of optimal crop growth, with its automate controlled environment it reduces some of the learning curve required for farming various crops. Despite these advantages, we still do not have a completely automated system. CityCrops system still requires the user to know when to harvest a crop as well as planting new ones. This procedure requires constant

opening and closing of this carefully controlled environment, this disturbance reduces the potential for maximum crop production.

## 2. DESIGN

The proposed robotic implementation is designed for use in the CityCrop Automated Indoor Farm and hence should fit those dimensions. The robotic system will have a camera to identify crops that are ready to be harvested or removed. The camera vision system will be mounted between the robotic manipulator such that it can harvest and remove the identified crops. The robotic manipulator can serve a dual role as a planter as well. In addition, we will propose an algorithm to control the behavior of the camera and robotic manipulator.

### 2.1 Camera Vision System

The camera device proposed for the vision system is an inexpensive commercially available USB camera. The Minoru 3D USB webcam uses two VGA CMOS color sensors with a maximum resolution of 800 x 600 pixels and a maximum frame rate of 30 fps. The cameras are on the same plane at a distance of 6 cm apart. This device has the option to take two individual image from both cameras or one combined stereo image. In either case the left and right camera shutters do not synchronize with a maximum deviation of 16.5ms. The device has a manual focus from 10 cm to infinity and for our purposes it would remain fixed once set [14]. This camera was selected because its features allow us adapt to a variety of crops that may require more visual information before harvest.



Figure 4. Minoru 3D webcam



Figure 5. Minoru 3D Webcam stripped front to remove excess material

#### 2.1.1 Estimating distance with vision system

The camera vision system should serve multiple purposes in terms of identification. In order to harvest or plant crops the system will need to identify a variety of factors such as color, size and location of the targeted crop. One of the main factors the robotic manipulator will need to know is distance from the camera to the crop. In order to successfully harvest a crop, we need to account for the distance perceived by the camera to the crop, then make any adjustments related distance between camera and the robotic manipulator to avoid damaging the crops.

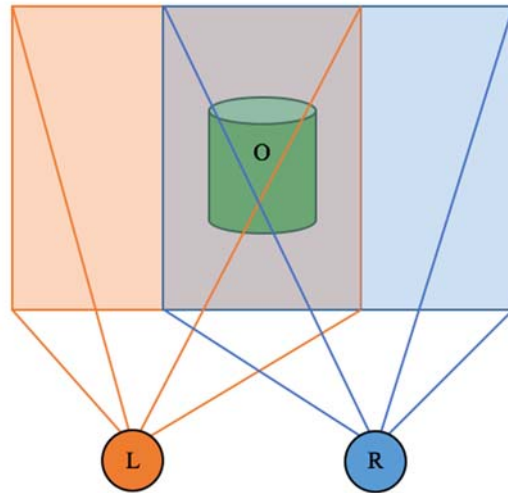


Figure 6. Overlapping image from left camera (L) and right camera (R) on object (O) creating stereovision image

As stated before, the two cameras on the Minoru 3D webcam takes one photo from each camera. These cameras are a certain distance apart, which produces different images of the same object, this is known as a stereovision image. These two images of the same object are at a known but at different point of views, with this information we can analytically estimate the target relative position and distance, and the objects absolute diameter.

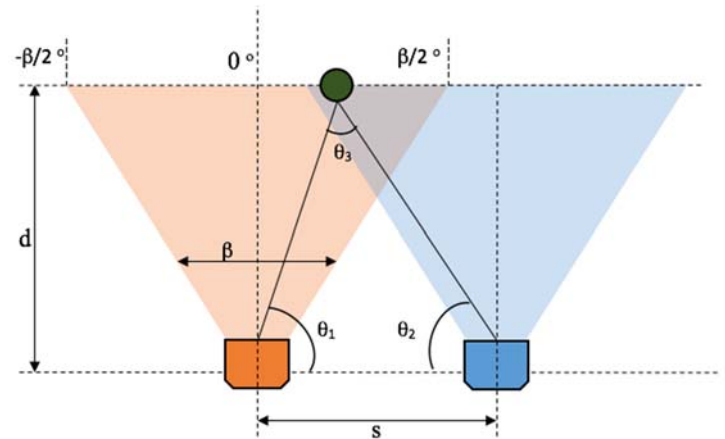


Figure 7. Schematic representation of camera and object with parameters involved in the calculation of the distance estimation

Figure 7 above shows us a diagram representation of the parameters involved in calculation relative distance and position. Where  $s$  is the known distance between the two cameras,  $d$  being the distance between the cameras and object, and  $\beta$  is the horizontal angle of the view of the cameras. Analytically computing  $\theta_1$ ,  $\theta_2$ , and  $\theta_3$ , we can calculate the distance with the equation below.

$$d = \left| \frac{s \cdot \sin\theta_1 \cdot \sin\theta_2}{\sin\theta_3} \right|$$

We should note this equation only allows us an estimation of the distance between cameras and the object. The distance estimation could be greatly improved with more specific camera calibrations beyond what the manufacturer requires.

## 2.2 Robotic Frame

The robotic system frame that we propose be implemented in the automated farm is based on 3D-printer frames. These farm offer great movement through a planar environment. In figure 8 we can see a CAD rendering of the proposed design. Designed to fit in the confined space of the CityCrop Automated farm (~17in x 17in x 34in) [13]. This design will allow our manipulator to vertically up and down with the four rails, useful for avoiding sweeping through crops. The mechanism also allows for movement left, right, forward and backwards to ensure our ability to reach any pod for harvest or planting material. This frame could successfully be powered by a couple motors and a belt driven system, much like found in some modern 3D printers.

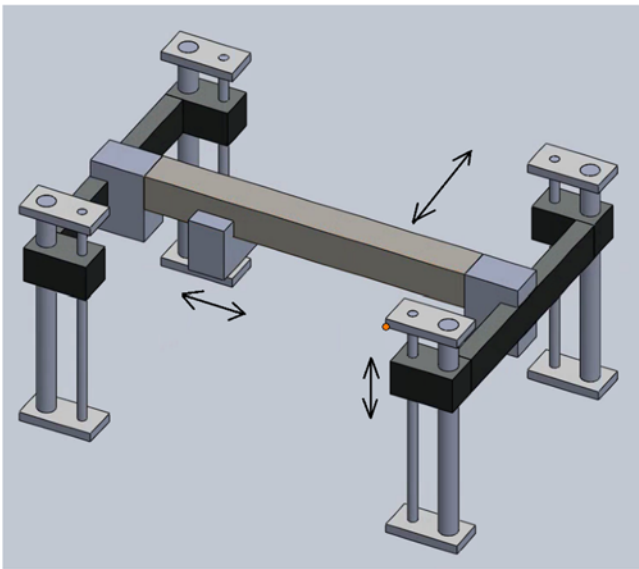


Figure 8. The robotic frame used to move the manipulator around a vertical farm stack

## 2.3 Robotic Manipulator

For the robotic manipulator we propose using a premade gripper and adapting it with our vision system. ROBOTIQ produces 2-finger grippers that could be ideal for our purposes, our manipulator needs to be able to pick up and drop off crops. The 2-finger 85 offer 20 to 235 N of grip force and only adds about 2lbs of weight to our system [14]. The gripper proposed can be seen in figure 9, the left most gripper in the image.

Adaptations to the gripper may be necessary to avoid damaging fragile crops. These could include adding a rubberized gloves or

reducing the closing speed to ensure we don't crush leafy crops. These manipulators claim to be easy to install, and if adapted correctly would be able to work with our proposed frame as well with a traditional robotic arm if designs must change. This manipulator with the proposed vision system attached to it, along with the proposed frame should allow the automated vertical farm to successfully harvest and plant its crops. Adaptations to the gripper to reduce risk of damaging fragile crops.



Figure 9. ROBOTIQ 2-finger grippers

## 3. PLANTING/HARVESTING ALGORITHM

In order to ensure the proposed automated vertical farm plants and harvest procedures work as intended, we will implement a planting and harvesting algorithm. The planting algorithm should allow the robotic implementation to decide to plant a new crop based on factors such as an opening for a crop, stock of planting material, and success of previous harvests. The harvesting algorithm should take into account several factors of the crop, such as size and color, before deciding to harvest. In addition, the harvesting algorithm should work in conjunction with the planting algorithm to decide whether harvesting is the most efficient step considering planting supply. The features included with the CityCrop automated vertical farm, specifically the app, would allow for a fluid communication between the user and algorithm to maximize production.

### 3.1 Harvesting Algorithm

The harvesting algorithm is designed to check all the pods and determine whether to give it a planting flag and whether to harvest or not. The harvesting cycle is originally designed to run every 12 hours, but there would be an option to change how often the cycle is to happen. The robotic system will start from the rest position and check the first pod in the sequence. The vision system will check whether the pod is empty, if the pod is empty the robotic system will virtually tag that pod for planting and move onto the next "unchecked pod". If at this point all pods have been checked it will stop the process and begin the planting algorithm, otherwise it will check the next pod in the sequence.

If the pod is not empty, the system checks the date planted log to see when this pod was planted. Here we have one of our first critical checks, this check involves time, the algorithm checks when current crop was planted. If the crop has not reached a certain amount of time in the farm, determined by previous or standard crop averages, the system will ignore the pod and move onto the next one. If the crop has been in the farm long enough, it will go

through the second check, a color check. If the color of crop is not within an acceptable range from the standard crop, such as a crop that has died, it is removed and the pod is given a virtual warning tag and the system moves onto the next pod. If the crop passes the color check, it moves onto the final check, a size check. If the size of the crop is within harvestable size, from averages or standards, it is harvested and virtually tags the pod to be planted, otherwise it moves onto the next pod.

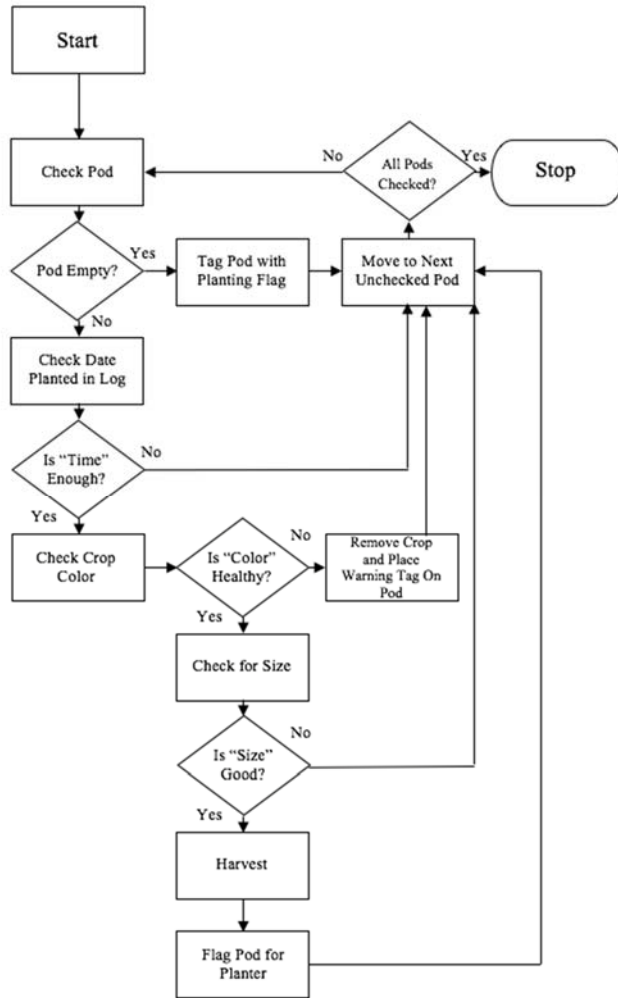


Figure 10. The harvesting algorithm which checks all pods, tagging which pods need to be planted and which could be harvested

### 3.2 Planting Algorithm

The planting algorithm is activated once the harvesting algorithm completes its actions. The planting algorithm works to plant new crops in empty pods and also works to notify the user if there is a pod producing poorly. The algorithm starts by checking if there is any supply to plant new crops. If there is no supply the system is to alert the user via the app and stop the planting process until the supply is refilled. If there is planting supply the algorithm checks for pods that contain the virtual planting flag. If there are no pods with planting flags the algorithm stops and waits for next harvesting cycle. If there is a pod with an identified planting flag, the system

will first grab planting material and move to the flagged pod. Once the robotic system reaches the pod it will search the pod history for any warning flags, if there are consecutive warning flags the system will alert the user of the under producing pod to make sure the pods hydroponic system is in working order. Otherwise the system proceeds to plant the new crop. Once new crop is planted it removes the virtual planting flag and logs the date and time it was planted. Once planted the system will again check for planting flags to close the loop.

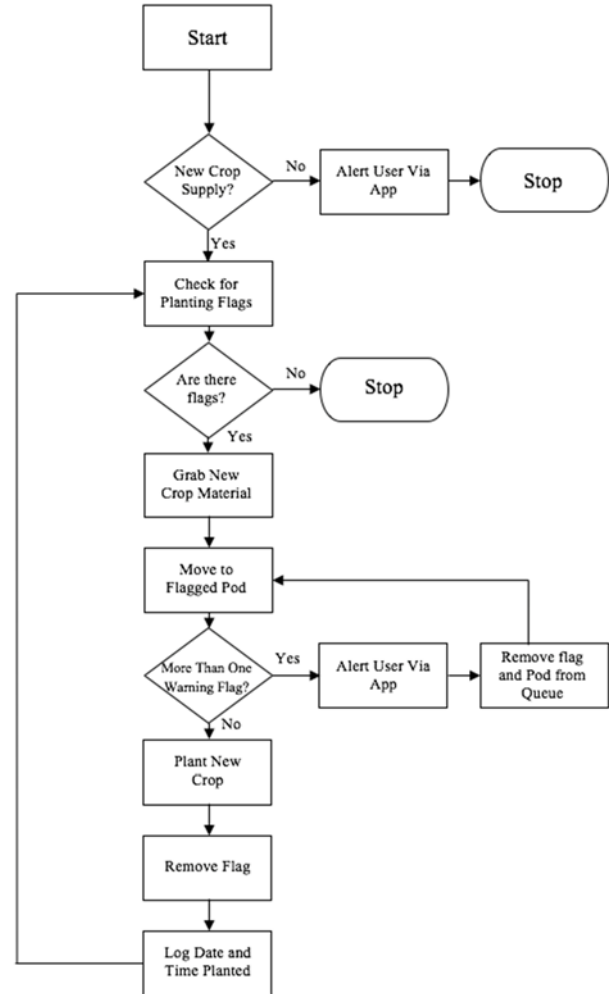


Figure 11. The planting algorithm plants new crops and identifies which pods are not producing properly

### 4. FUTURE WORK

By examining the current landscape and anticipating future trends in both technology and population/environmental needs we proposed further automation of vertical farming systems with the help of robotics. The idea proposed in this paper are just the first steps to what I believe will be a highly invested field. However promising the idea, there still remains work to be done. Future work would include building and testing a small scale of the proposed system. With a built system we could continuously improve upon our own design. In addition, we must improve current vertical farm design to work in conjunction with emerging technologies. Improving vertical farm designs to allow for easy implementation

of technology should improve maximum crop production. Improvement on our own design could come in the form of a better camera or a different form for the vision system, we could also change our robotic manipulator to a more traditional robotic arm form. We want to make this system implementable in the current CityCrop systems as it is an ideal enclosed system, and eventually scale up to larger scale plant factories.

## 5. ACKNOWLEDGMENTS

My thanks are extended to the Robotics and Automation Laboratory and the Department of Mechanical and Materials Engineering at Florida International University for making the resources available to carry out this research project.

## 6. REFERENCES

- [1] Corvalan, C., S. Hales, and A. J. McMichael. 2005. Ecosystems and human well-being: health synthesis. World Health Organization.
- [2] Pandey, B., and K. C. Seto. 2015. Urbanization and agricultural land loss in India: comparing satellite estimates with census data. *J. Environ. Manage.* 148:- 53–66, Land Cover/Land Use Change (LC/LUC) and Environmental Impacts in South Asia.
- [3] Foley, J. A., N. Ramankutty, K. A. Brauman, E. S. Cassidy, J. S. Gerber, M. Johnston, et al. 2011. Solutions for a cultivated planet. *Nature* 478:337–342.
- [4] Lambin, E. F., and P. Meyfroidt. 2011. Global land use change, economic globalization, and the looming land scarcity. *Proc. Natl Acad. Sci. USA* 108:3465–3472.
- [5] Eigenbrod, C., and N. Gruda. 2014. Urban vegetable for food security in cities. A review. *Agron. Sustain. Dev.* 35:483–498.
- [6] Linsley-Noakes, G., L. Wilken, and S. de Villiers. 2006. High density, vertical hydroponics growing system for strawberries. *Acta Hort.* 708:365.
- [7] Mahdavi, S., M. Kafi, R. Naderi, and T. Sadat. 2012. Vertical mobile planting system consistent with the pattern of solar radiation and effects of system on light exposure and growth of Gerbera cut flowers (*Gerbera jamesonii* cv. Antibes), in greenhouse culture. *J. Agric. Technol.* 8:1461–1468.
- [8] Hayden, A. L. 2006. Aeroponic and hydroponic systems for medicinal herb, rhizome, and root crops. *HortScience* 41:536–538.
- [9] Kato, K., R. Yoshida, A. Kikuzaki, T. Hirai, H. Kuroda, K. Hiwasa, Tanase, et al. 2010. Molecular breeding of tomato lines for mass production of miraculin in a plant factory. *J. Agric. Food Chem.* 58:9505–9510.
- [10] Kozai, T, Niu,G, Takagaki, M, 2015, "Plant Factory: An Indoor Vertical Farming System for Efficient Quality Food Production". Academic Press U.S.A.
- [11] "Automated Indoor Farming." CityCrop. N.p., n.d. Web. 1 Apr. 2017. Available at <https://www.citycrop.io/>
- [12] "Vertical Farming: Singapore's Solution to Feed the Local Urban Population." The Permaculture Research Institute. .p., 24 July 2014. Web. 10 Apr. 2017.
- [13] "Adaptive Robot Gripper 2-Finger." Robotiq. N.p., n.d. Web. 15 Apr. 2017. Available at <http://robotiq.com/products/adaptive-robot-gripper/>
- [14] "Minoru3D." Minoru3D — Minoru 3D Webcam. N.p., n.d. Web. 5 Apr. 2017. Available at <http://www.minoru3d.com/>

# Soft Robotic Jellyfish Steering Control

Nick Lopez, Erik D. Engeberg<sup>(1)</sup>

nlopez2015@fau.edu, eengeberg@fau.edu

## ABSTRACT

The exploration and ability to monitor vulnerable sponge and coral ecosystems can benefit from highly maneuverable underwater vehicles able to navigate and hover in cluttered spaces. Using soft materials for robots is safer than conventional robots as it reduces impact forces, allowing preservation these delicate environments.

The research hypothesis was that actuation of tentacles on one side of the jellyfish would impact the direction the robot travels to impart an ability to steer. Different amplitudes and offset pump actuations were visually tested until a consistent method of steering was found. A controlled descent was achieved by partially actuating one half of the robot, reducing its resistance to sinking. This created an angled descent which could be used to control the direction the robot travels.

## Keywords

Soft Robotics, bio-inspired robots, coral reef, ocean monitoring, underwater vehicles

## 1. INTRODUCTION

The exploration and ability to monitor vulnerable sponge and coral ecosystems can benefit from highly maneuverable underwater vehicles able to navigate and hover in cluttered spaces. This propulsion and control technology, however, is poorly developed currently. Conventional robots are rigid, whereas the newer soft robots have the ability to elastically deform adapting to their environment in a non-invasive manner [1]. Using soft material for robots is much safer allowing stress to be distributed over a larger volume as well as increasing contact time reducing impact forces that could damage the robot or its environment [2]. Bio-inspired flexible propulsors have the potential to catalyze novel technology and the development of novel research vessels used in the exploration of these complex environments [3-15]. The cutting edge soft robotic jellyfish (Figure 2) will enable breakthrough research in vulnerable coral and sponge ecosystems.

Currently the soft robotic jellyfish contains two degrees of freedom with the ability to move upward or sideways through a series of tentacle actuations (Fig. 2) or downward through allowing the tentacles to return to their natural position and allowing its negative buoyancy to take effect. The purpose of the research presented in this paper was to develop a process which would enable a steering control in the previously developed soft robotic jellyfish. Through the use of the two impeller pumps which each control one half of the jellyfish's tentacles, it is hypothesized that a combination of offset pump efforts would enable steering control. Developing this steering ability in the soft robotic jellyfish would highly increase its future use in health monitoring of delicate ecosystems.

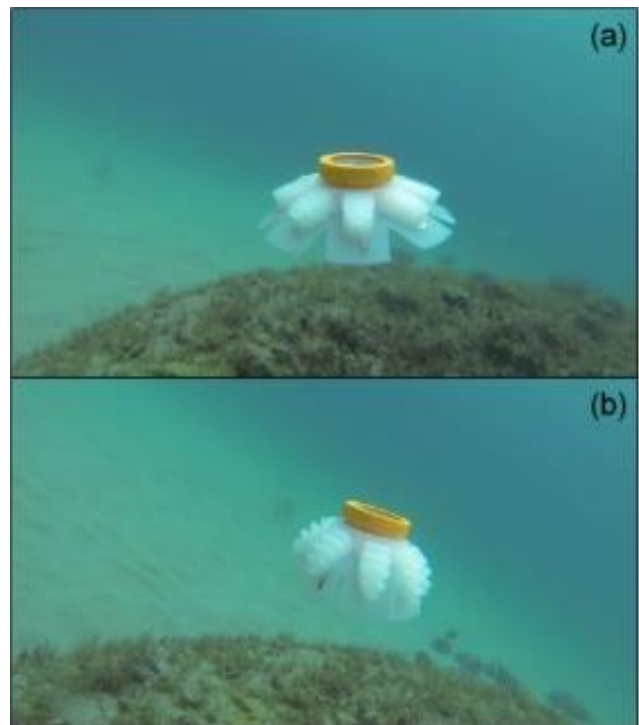


Figure 1: The soft robotic jellyfish during open water testing

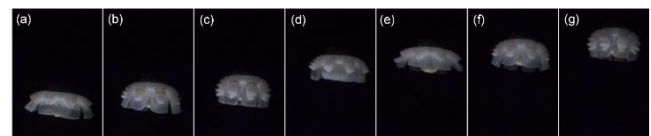


Figure 2: Photo sequence of the soft robotic jellyfish

## 2. METHODOLOGY

To begin, the jellyfish was tested to ensure it was swimming properly in a completely vertical direction to avoid skewed results due to unbalanced swimming. This was achieved by adding small washers to the top of the jellyfish's electronics can using an adhesive to ensure a proper balance as well as buoyancy. Each time the jellyfish was removed from the water, the following testing also included a re-check of the balance and buoyancy, as well as squeezing out any air bubbles that were introduced into the tentacles of the jellyfish, which could affect the trial's performance.

To implement steering control, various combinations of off-set pump actuations were visually tested for steering, two cycles of

each combination can be seen in Fig. 3. All five of these pump effort combinations were also tested at two frequencies, 0.8 Hz and 0.3 Hz. In Fig. 4 the 0.8 Hz timing is shown.

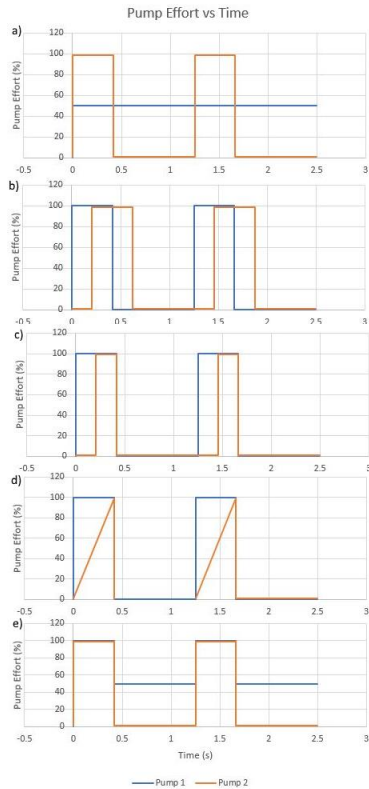


**Figure 3: Variations of off-set pump actuations tested**

These tests were performed in an aquarium tanks measuring 762mm long by 305mm wide by 320mm tall. The objective was to successfully swim from one side to the other lengthwise consistently. During testing, the jellyfish was programmed to perform 10 actuation cycles of each pump effort combination from Fig. 3, at which point another 10 cycles was performed with the pump efforts reversed to ensure the jellyfish was capable of being steered in both directions.

### 3. RESULTS

After testing each of the pump effort combinations at 0.8 Hz, it became visually clear that at 0.8 Hz there was not enough time between actuation cycles to consistently achieve the needed angle which would allow an angled propulsion of the jellyfish. At this point, a 0.3 Hz swimming frequency was introduced, which did allow enough time between actuation cycles to obtain a consistent angle needed for an angled propulsion.

The most consistent steering control was a result of using the pump effort combination seen in Fig. 3e at 0.3 Hz. This form of pump actuation allowed the jellyfish to swim upwards, and when pump 1 remained partially inflated it created an angled descent. This occurred due to there being a decreased resistance to sinking on one half of the tentacles. After sinking at an angle for just over 2 seconds, another actuation cycle would begin which allowed an angled propulsion. This sequence can be seen below in Fig. 4.

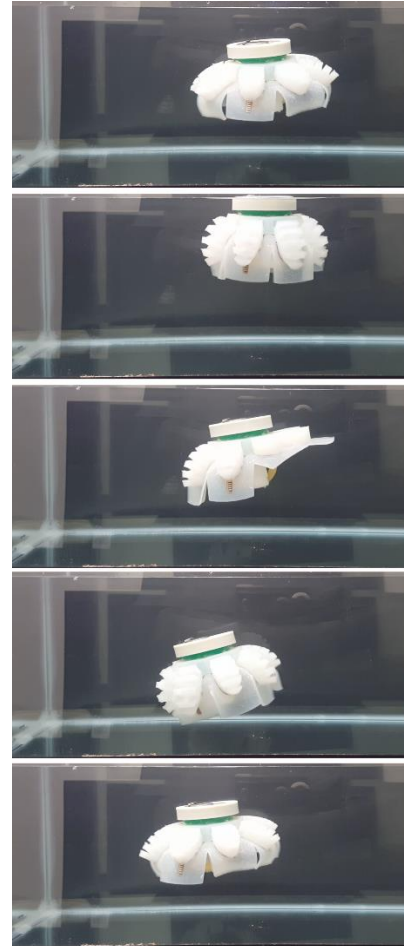


**Figure 4: Angled descent followed by angled propulsion**

## 4. CONCLUSION

In conclusion, it was possible to develop steering control for the soft robotic jellyfish. This was achieved using offset pump actuation cycles which left one half of the jellyfish partially inflated, creating an angled descent followed by an angled propulsion. This development has the potential to vastly increase the usability of the jellyfish during navigation of complex and delicate ecosystems for health monitoring.

## 5. REFERENCES

- [1] C. Majidi, "Soft Robotics: A Perspective—Current Trends and Prospects for the Future," *Soft Robotics*, vol. 1, no. 1, pp. 5-11, 2014.
- [2] S. Kim, C. Laschi and B. Trimmer, "Soft robotics: a bioinspired evolution in robotics," *Trends in Biotechnology*, vol. 31, no. 5, pp. 287-294, 2013.
- [3] P. Panagiotis, S. Lyne, Z. Wang, L. F. Nicolini, B. Mosadegh, G. M. Whitesides and C. J. Walsh, "Towards a Soft Pneumatic Glove for Hand Rehabilitation," in *IEEE/RSJ International Conference on Intelligent Robots and Systems (IROS)*, Tokyo, 2013.

- [4] S. Kim, C. Laschi and B. Trimmer, "Soft robotics: a bioinspired evolution in robotics," *Trends in Biotechnology*, vol. 31, no. 5, pp. 287-294, 2013.
- [5] R. F. Shepherd, F. Ilievski, W. Choi, S. A. Morin, A. A. Stokes, A. D. Mazzeo, X. Chen, M. Wang and G. M. Whitesides, "Multigait soft robot," *Proceedings of the National Academy of Sciences of the United States of America*, vol. 108, no. 51, p. 20400-20403, 2011.
- [6] F. Ilievski, A. D. Mazzeo, R. F. Shepherd, X. Chen and G. M. Whitesides, "Soft Robotics for Chemists," *Angewandte Chemie*, vol. 50, no. 8, pp. 1890-1895, 2011.
- [7] C.-P. Chou and B. Hannaford, "Measurement and Modeling of McKibben Pneumatic Artificial Muscles," *IEEE Transactions on Robotics and Automation*, pp. 90-102, 1996.
- [8] M. T. Tolley and D. Rus, "Design, fabrication and control of soft robots," *Nature*, pp. 467-475, 2015.
- [9] M. Seckin, N. Y. Turan and A. C. Seckin, "Comparison of Production Methods in Soft Robotics," in *2015 International Conference on Advances in Software, Control, and Mechanical Engineering*, Antalya, 2015.
- [10] B. Mosadegh, P. Polygerinos, C. Keplinger, S. Wennstedt, R. F. Shepherd, U. Gupta, J. Shim, K. Bertoldi, C. J. Walsh and G. M. Whitesides, "Pneumatic Networks for Soft Robotics that Actuate Rapidly," *Advanced Functional Materials*, vol. 24, no. 15, pp. 2163-2170, 2014.
- [11] K. Suzumori, S. Endo, T. Kanda, N. Kato and H. Suzuki, "A Bending Pneumatic Rubber Actuator Realizing Soft-bodied Manta Swimming Robot," in *IEEE International Conference on Robotics and Automation*, Roma, Italy, 2007.
- [12] M. Calisti, M. Giorelli, G. Levy, B. Mazzolai, B. Hochner, C. Laschi and P. Dario, "An octopus-bioinspired solution to movement and manipulation for soft robots," *Bioinspiration & Biomimetics*, p. 10, 2011.
- [13] H.-J. Kim, S.-H. Song and S.-H. Ahn, "A turtle-like swimming robot using a smart soft composite (SSC) structure," *Smart Materials and Structures*, p. 11, 2013.
- [14] A. D. Marchese, C. D. Onal and D. Rus, "Autonomous Soft Robotic Fish Capable of Escape Maneuvers Using Fluidic Elastomer Actuators," *Soft Robotics*, pp. 75-87, 2014.
- [15] M. J. McHenry and J. Jed, "The ontogenetic scaling of hydrodynamics and swimming performance in jellyfish (*Aurelia aurita*)," *The Journal of Experimental Biology*, vol. 12, no. 206, pp. 4125-4137, 2003.

# Simple Solder

Jean-Carlo Drada, Jackson Fadely, Kevin Martinez, Rodrigo Arredondo, Sabri Tosunoglu

Department of Mechanical and Materials Engineering  
Florida International University  
10555 West Flagler Street  
Miami, Florida 33174

jdrad002@fiu.edu, jfade004@fiu.edu, kmart126@fiu.edu, rarre001@fiu.edu, tosun@fiu.edu

## ABSTRACT

In this paper, the design and construction of the ‘Simple Solder’ device is presented. The Simple Solder aims to allow users the ability to quickly and effortlessly solder electrical components using a computer numeric controlled (CNC) device. The goal of the design, is to create an inexpensive and user friendly soldering CNC mechanism capable of fusing simple electronic pieces onto a small electrical board.

Most of the CNC soldering systems currently available to the public, are of industrial grade. For the most part, these machines have large footprints but at a high cost. At the time of this writing, there are no economical options or solutions available for home use. Generally, soldering electrical components is done manually with a soldering tool and soldering material. For these reasons, the main objective is to create a low-cost and easy to use CNC system for personal use. By making use of open-source software and easy to manufacture components, the production cost is maintained low and the simplicity and robustness of the Simple Solder high.

An initial 3D model was designed using custom components, which was ultimately abandoned due to time and complexity constraints. Instead, an Anet A8 3D printer, was modified to allow for solder extrusion, manual positioning control, and adaptability for multiple soldering irons. Through the low cost of the printer and the use of a 3D printer mount instead of the extruder, the printer was transformed into the Simple Solder. Utilizing the Repetier Host firmware and software, we were able to calibrate and change movement controls for the printer, as well as send manually generated G-code for movement and solder extrusion. It was found that the G-code editor incorporated with the Repetier Host was an excellent resource, for it automatically comments on its specific G-code functions.

## Keywords

CNC Soldering, 3D printing.

## 1. INTRODUCTION

The motivation in creating the Simple Solder, is to produce a printable 3D CNC style soldering machine. Simple and affordable, the Simple Solder can be used by advanced and beginners alike. Simple modifications to the mounting tool, allow for a variety of soldering tools to be fitted. Once attached, it can then be used to

solder electrical components with high accuracy and precision in a quick manner.

The benefits of creating an affordable CNC style soldering device, is to allow the customer to have all skills, precision, and accuracy needed to solder electrical components autonomously. Simple Solder will be targeted at beginners, hobby enthusiasts, and eventually manufacturing facilities. The secondary objective of the Simple Solder is to completely eliminate the risk of damaging electrical components or boards due to faulty connections or human error. Furthermore, it can also be used by hobby-level enthusiasts who want to replicate PCB’s or electrical designs due to its repeatability and elimination of hand labor. Simple Solder will also teach the user how much material should be used.

## 2. SOLDERING CNCs

The two most common CNC soldering devices that are currently available are Pick-n-Place, and SMD Heat soldering machines. The Pick-and-Place machines work by picking up components that have solder paste applied to them, and then placing those components onto a printed circuit board shown in Figure 1. After all components have been positioned, the board is then placed in an oven which melts the solder paste fixing the components to the board.

Surface Mount Diode works in a similar fashion. Solder paste and flux is first applied to the board, usually with a machine. The components are then placed in position, either manually or with a machine, and a heat gun/torch flows the solder into position. SMD soldering machines are typically very precise, and capable of soldering extremely small components with high precision. However, special care must be taken to not overheat the board or components with this method. Since the torch or heat gun is a localized high temperature source, it may be more difficult to accurately control.

Both types of soldering devices are very large and are typically used for industrial mass production of circuit boards and electronics. Their high price, ranging from \$2,000 to well above \$250,000, may prevent potential consumers from attaining one. Currently, there are no products available that can mimic the Simple Solder’s capabilities at its current size and cost. Without doubt, the system

has the potential to be very profitable and desired by a wide range of consumers.

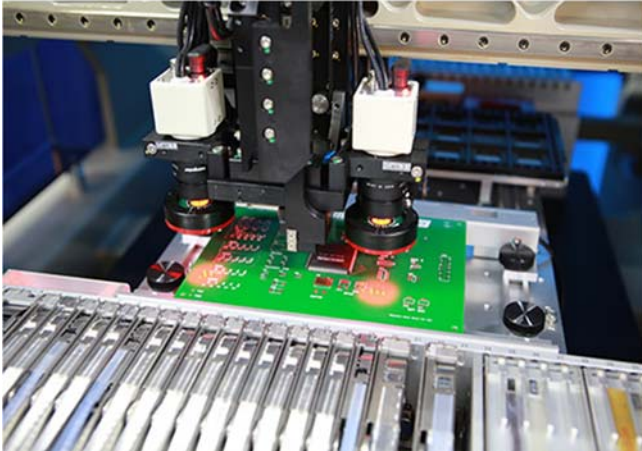


Figure 1. Pick and Place Soldering

## 2.1 Conceptual Design

The main goal of this project, is to create a cheap and easy to use soldering CNC machine. This mechanism, is designed to assist with small and medium component soldering. In order to guarantee repeatability with high precision and accuracy, several components were considered. In the end, the following software and hardware devices are utilized in the prototype.

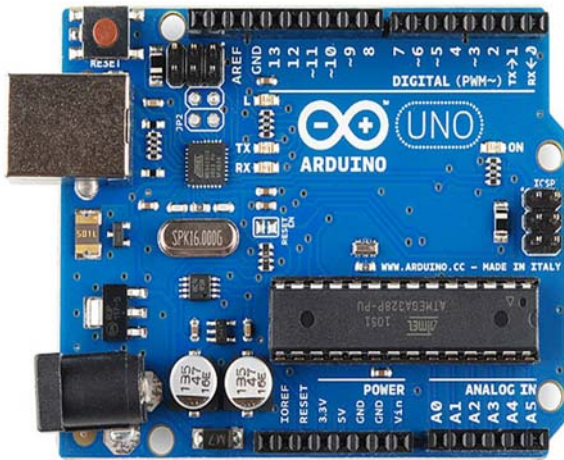


Figure 2. Arduino

Shown in Figure 2, the Arduino, is a micro-sized integrated circuit chip used for the control of electrical devices and mechanisms. It is also an open source software that features thousands of libraries, firmware revisions, use cases, and applications. It is intended for anyone making interactive projects such as the Simple Solder or other. Arduino boards can receive information from several sensors or the user and sends commands to devices such as LED technology or step motors depending on the application. The Arduino language consists of a set of C/C++ functions that can be called from code to execute the actions needed.

The original design called for the use of an Arduino Uno and a motor driver 'hat' to move the solder. A PC power supply would be used to provide 12V power. A number of Arduino-compatible firmware and control programs were considered for this project. Ultimately, LinuxCNC was chosen to control the Simple Solder prototype.



Figure 3. Linux CNC

LinuxCNC is a computer software program used for numerical control of different types of machines. Some of these are milling machines, lathes and plasma cutters, routers, cutting machines, robots and hexapods among others. The software is capable of controlling up to 9 axis or joints of a CNC machine using G-code. G-code, which has many variants, is the common name for the most widely used numerical control programming language. It is used mainly in computer-aided manufacturing to control automated machine tools. LinuxCNC has several specific kinds of usage such as touch screen, and other interactive devices. Currently, it is almost exclusively used on PC. The software makes extensive use of a real time-modified kernel, and supports both stepper-motors as planned to use. Additionally, LinuxCNC uses the model of interactions with hardware. For instance, it reads the current axis position, calculates a new target position/voltage, and then writes that to the hardware before executing the necessary movements.



Figure 4. Stepper Motor

The stepper motor is used in applications requiring about 2000 rpm or less, where high torque is needed at the low end. Typically, a servo motor is used for higher speed applications that are more dynamic and require more acceleration and deceleration. However,

the stepper motor is an electromagnetic device that converts digital pulses into mechanical shaft rotation. Some of the advantages of stepper motors are low cost, high reliability, high torque at low speeds, and their simplicity to control. These are also usually robust and are able to operate in a number of environments. This makes them more than ideal for a home environment where the CNC machines may be exposed to dirt, debris, or run for extended periods of time. The way stepper motors work, consists of a permanent magnetic rotating shaft, called the rotor, and electromagnets on the stationary portion that surrounds the motor, called the stator. Stepper motors have a step angle that determine the angular position of the shaft. Dividing one revolution by the step angle of the motor, gives the number of steps necessary to rotate the shaft to the desired position. The Arduino controls the motor increments by sending electrical pulses to the spindle, allowing for rotation for both clockwise and counter clockwise directions.



**Figure 5. 3D Printer**

A 3D model is created one layer at a time by similar printers to the one shown in Figure 5. This process is called rapid prototyping, or 3D printing. A common procedure of rapid printing, is to first apply a fine material such as PLA or ABS in a 3D inkjet printer. The machine then prints out several layers of powder on a bed creating a fixed object. The design is defined by a 3D STL file, which is the format used by most 3D printers. In addition to solid material pallets, the printer is able to use liquids such as photopolymers.

Nowadays, 3D printers are mainly used in applications that require short lead times but are highly complex. These include not only applications in medicine and architecture, but also in the entertainment industry. Today there are more and more companies that specialize in the printing of 3D models and provide services for businesses and individuals as planned for the Simple Solder. However, the biggest drawback for the regular user, is still the high cost of 3D printing services. Another drawback, the long time it takes to print a 3D model, depending on the complexity and resolution of the model. Furthermore, professional 3D software and 3D model designs are in a high cost range. Alternatively, there are several 3D printers available at a lower cost but at a lower printing resolution.

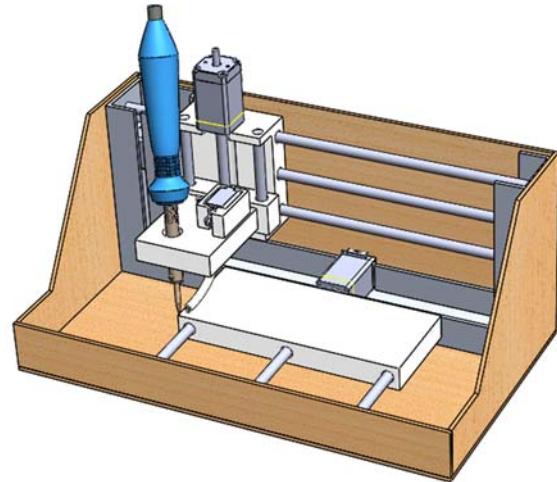


**Figure 6. Initial Conceptual Design of Mill**

The Initial conceptual design uses three Nema-11 stepper motors for the three primary axes. These are used due to their relatively low weight, small size, and medium torque. An additional Nema-8 stepper motor is used for the solder extrusion seen in Figure 7. The working area of the prototype is a rectangular cuboid of 7.5" x 3" x 3", allowing the user to solder relatively large PCB boards, tall components, or allow the use of clamps, hold downs, and other devices.

A fixed y-axis gantry was chosen to minimize end-effector movement, since it would carry the heaviest components of the machine. The bed moves linearly along the y-axis with the PCB board or components that are to be soldered. Ideally, z-axis movements would only take place while the bed, x-axis, and y-axis are all stationary. This reduces play in the tip of the iron and allows for repeatable movements. The end effector, solder extruder motor, extrusion tube, soldering iron, and other features, can be seen in Figure 7.

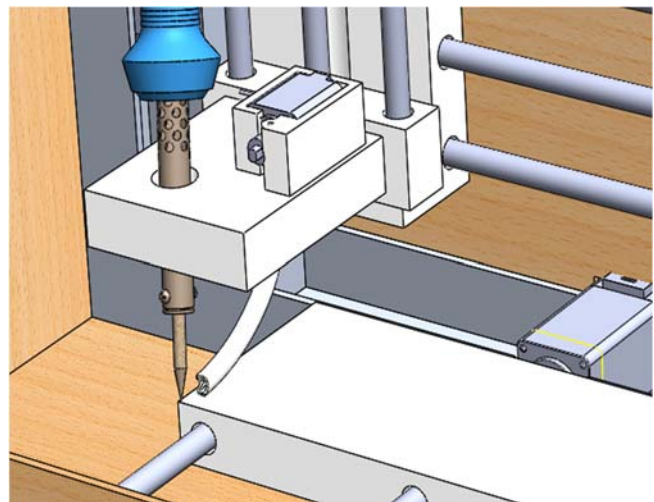


**Figure 7. End Effector Detail**

### 3. PROTOTYPE AND EXPERIMENTAL PROCEDURE

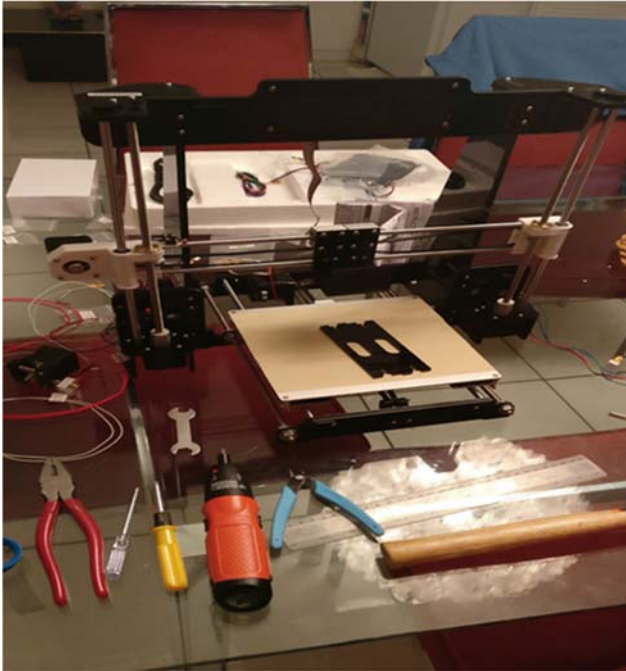


Figure 8. Simple Solder Building Phase

The CNC frame components that were used to hold the entire system together are shown in Figure 8. As stated previously, an Arduino board was used to control the stepper motors of the system. After the frame was created, a soldering tool was attached to the end effector of the system once the Arduino and LinuxCNC integration was complete. A feed system was developed that feeds soldering material to the tip of the solder iron. After all components had been assembled, testing was conducted and adjustments were made as needed.



Figure 9. The Repetier-Host

The Repetier-Host, is a simple to use control and slicing software, which is compatible with most computer boards. The initial purpose of the program is to add and position the STL files on the simulated print bed and slice them altogether. Repetier Host can handle up to 16 extruders with different filament types and colors simultaneously. Through the program, a user can also preview the

end result, including individual filament colors, before printing. After the slicing process is complete, an image will show all extruder movements and support structures as shown in Figure 10.

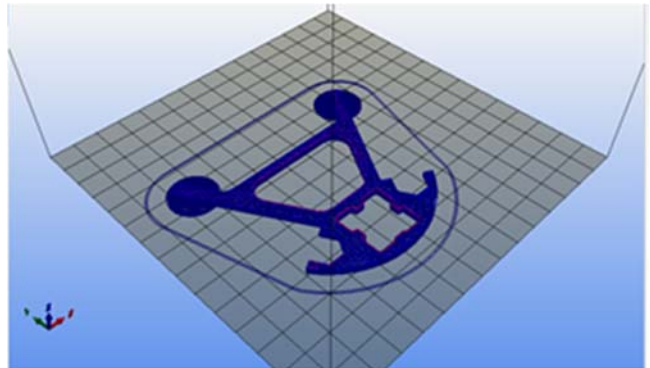


Figure 10. Slicing Example

The efficient use of the build plate can save the user a lot of time. The position and location can be selected manually or using the Repetier Host auto position feature. The software is easy to use, even for beginners, giving the user full control of the simple solder, slicer and printing process if need be. Even biotech companies utilize Repetier Host to print organs. The accessibility and control of the printers from computer platforms such as Windows or Apple products comes in very handy. Not to mention Repetier Host has the ability to run multiple printers simultaneously if applicable.

A small amount of memory is required to run codes of any size, with the new file management. Price calculations can also be recorded to get the production costs before soldering. The previews image shows a feature which allows for fully configurable, high quality rendered images before executing the program. This is essential for exact and easy recognition of solder locations on a board. Last, the Heat Up Wizard measures heating and cooling speeds needed for accurate soldering and specific soldering material amount to be melted.

#### 3.1 Final Design Prototype

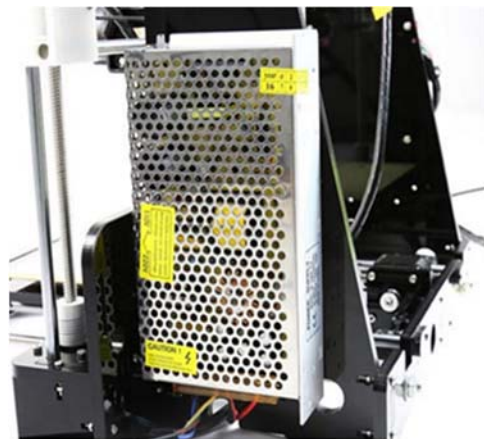
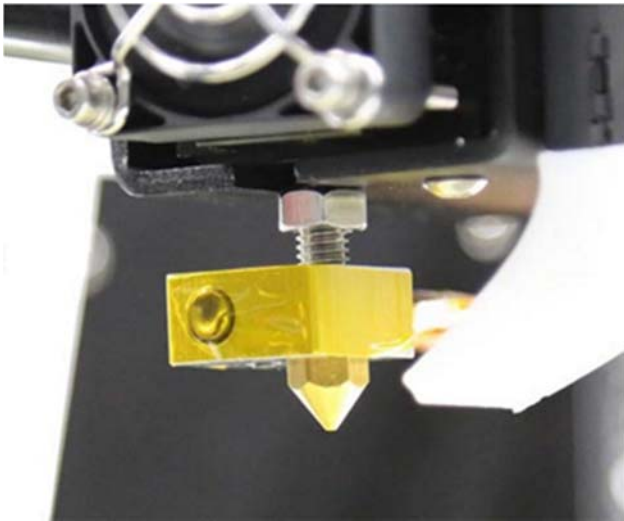


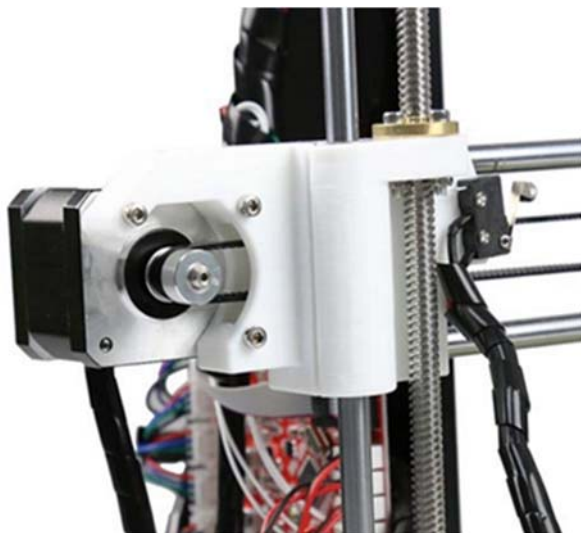
Figure 11. 12-Volt Battery

Figure 11 shows the 12-Volt battery the Simple Solder operates with. However, for the purpose of this project we will be using soldering wire, which is a 1.75 mm Tin Lead Alloy material. Built for high printing precision, stainless steel rail rods, gears, bearings, and connectors allow for the smooth execution of a given task. The system is able to print on a 220 x 220 x 240 millimeters printing volume. The accuracy achieved by the printer in the XY-axis reaches a 0.012mm and a Z-axis 0.004mm standard deviation.



**Figure 12. Soldering Nozzle**

Furthermore, quick release feed gears for faster and effortless filament feeding is shown in Figure 12. This allows for the extrusion of the soldering material through a single 0.4mm diameter nozzle at a printing speed of 100 millimeters per second. Pulleys are made out of metal for improved functionality and performance as shown in Figure 13.



**Figure 13. Servo Motor and Material**

Moreover, the operating system runs on Windows XP, Windows 7, Windows 8, Mac, and Linux. For offline printing, files must be saved as a G-code, OBJ, or STL file on an SD card. For the prototype, the working temperature ranges around 10 - 30 Degree Celsius, and humidity of 20 - 50%.

The prototype is engineered to provide redefined usability, quality, and performance. The Simple Solder is made from a piano-black laser-cut acrylic plate frame with an aluminum base as shown in Figure 14. Additionally, the build your own feel, and the hands on appeal is felt while assembling it. The DIY approach provides a memorable step-by-step learning experience of 3D printers from beginning to end. As long as there is a desire for creativity, this product has a great use. Suitable for a wide range of users, young or old, professional or amateur.

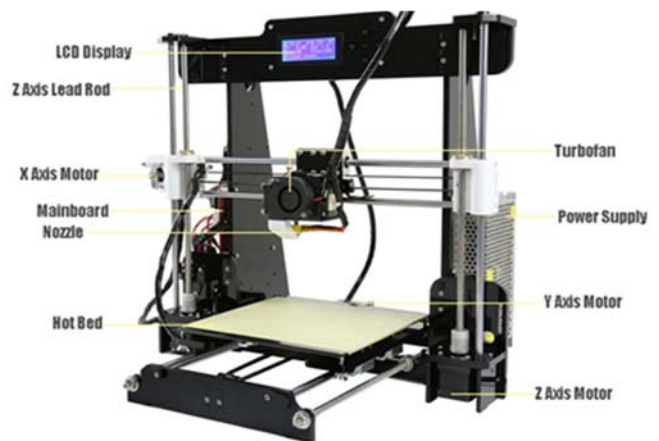


**Figure 14. Anet A8 Desktop 3D printer Prusa i3 DIY Kit**

#### **4. CONCLUSION AND RECOMMENDATIONS**

The original design made use of custom-fabricated components, including the frame, gantry, covers, plates, and build platform. It would have taken up the same footprint as a 13" laptop, but unfortunately would have taken longer than our time and funding constraints allowed. Instead, the approach of modifying a Prusa i3 DIY 3D printer kit to allow for easier assembly and software support was taken. A 3D printed clamp was designed to allow attachment of a soldering iron in place of the extruder nozzle, and the extruder motor was re-used to push solder onto the tip in place of plastic filament.

Repetier-Host is the control interface and firmware selected that the 3D printer platform runs on, allowing for manual G-code entry and editing. This feature allows the user to move the soldering iron tip to the desired position, without having to calibrate stepper motors, steps per revolution, or any other time consuming tuning processes. This saved a lot of time, but reduced the full operational capacity of the Simple Solder since we were limited to producing G-code manually and inputting it. For the next iteration of the prototype, we aim to build the initial design concept and make use of the lessons learned while modifying the 3D printer. Notably, the soldering iron needs to be mounted by the handle if using 3D-

printed parts due to the high heat on the metal shaft. The need for more accurate clamping designs to minimize deflection of the tip of the iron will be further explored.

Another concept that will be applied to the next iteration, is using a regular 3D printing nozzle to extrude soldering material. Since most commercially available soldering material melts around 180-190 degrees Celsius, most modern extruders such as the E3D-V6 should be capable of melting and extruding solder without the need for expensive retrofitting. This would also allow for simple integration and the ability to scale up production using commercially available parts.

Lastly, the modification of the Repetier Host firmware will be prioritized. The focus, is to allow pre-prepared CAD files to be "sliced" like traditional STL models, greatly reducing setup time and effort for the user to prepare their parts for soldering. This should be relatively easy to do since Repetier Host is open source and has clear documentation. Especially taking into consideration the control and movement commands is already completed. In addition, a G-code movement function would be called after moving into position that would lower the soldering iron tip, wait a few seconds, extrude a small length of solder, and then retract the solder and move the tip upwards. The main program would then move the iron tip to the next position and the function would be called again. These can be achieved by changing variables and tuning of the stepper motors, as well as constants like bed size, mm/step, acceleration etc. Conceptually, these are some of the new features the next iteration will include.

## 5. ACKNOWLEDGMENTS

The authors extend their thanks to FIU's Department of Mechanical and Materials Engineering and the Robotics and Automation Lab for providing access to the lab, which expedited the progress of the present work. Partial funding provided by the Department of Mechanical and Materials Engineering for the construction of the prototype is also acknowledged.

## 6. REFERENCES

- [1] Judd, Mike, and Keith Brindley. Soldering in Electronics Assembly. Oxford: Newnes, 1999.
- [2] Craig, John J. Introduction to Robotics: Mechanics and Control. Upper Saddle River, NJ: Pearson Prentice Hall, 2005.
- [3] Janesler Gonzalez, Dan Becker, Sabri Tosunoglu, "Improving Print Time Predictions for Cartesian 3D-Printers," Proceedings of the 29th Florida Conference on Recent Advances in Robotics, FCRAR 2016, pp. 50-55, Miami, Florida, May 12-13, 2016.
- [4] William Billini, Xavier Bercy, Ricardo Charlestin, Sabri Tosunoglu, "Digital Photolithography System with Machine Vision and Motion Control," Proceedings of the 29th Florida Conference on Recent Advances in Robotics, FCRAR 2016, pp. 262-265, Miami, Florida, May 12-13, 2016.

# SkateBot: Bipedal Skating Robot Design

Alexander Piedra, Trevor Solorzano, Kishan Kalpoe, Neha Chawla, Sabri Tosunoglu

Department of Mechanical and Materials Engineering  
Florida International University  
10555 West Flagler Street  
Miami, Florida 33174

apied015@fiu.edu, tsolo013@fiu.edu, kkalp001@fiu.edu, nchaw002@fiu.edu, tosun@fiu.edu

## ABSTRACT

A bipedal skating robot is designed to maneuver effectively while carrying a light payload. Research on current available technology is performed. Multiple designs are evaluated based on a literature survey. Several parameters are used from an existing design, assisting the construction of a prototype. Experiments including self-balancing and leg control are conducted. Faults with the prototype and improvements for future iterations are discussed.

## Keywords

Skate, Balance, Bipedal, Gyro, Servo, Agility, Speed, Logistics.

## 1. INTRODUCTION

### 1.1 Problem Definition

Nowadays, many companies are seeking to automate their logistics. The transportation of goods in warehouses is relying more and more on robots rather than humans. Creating an agile robot that can perform a wide assortment of tasks quickly and efficiently, while still maintaining a small footprint, could prove to be very beneficial for many industries including commercial and military applications. Bipedal robots are capable of many tasks, but lack the speed of wheeled systems. Wheeled robots can quickly maneuver environments, but lack the versatility that bipedal robots can provide. Creating an agile, wheeled bipedal robot can improve the productivity of sectors that require robotic technologies.

### 1.2 Motivation and Benefits

The intent of this project is to create a robot that combines the speed of wheeled robots with the versatility of bipedal robots. Inspiration came from the recently announced "Handle" robot made by Boston Dynamics. Possible uses for this robot include: Handling and transporting loads/objects, assistance in shipping and handling process, application in industrial settings as well as assistance in military settings. The benefits of this robot include: higher energy efficiency, higher mobility, and a smaller footprint compared to traditional legged robots, with a larger range of possible tasks next to wheeled robotic systems.

### 1.3 Literature Survey

Multiple ideas and projects were researched and performed on self-balancing robots which include the robots that balance with actual

legs and knees and robots that balance using the traditional 2 wheeled system.

A major contributor to the main idea of this report is attributed to the Boston Dynamics Handle robot. Much like the other projects that Boston Dynamics spearheads like the Big Dog, the Atlas, and the Cheetah, Handle is made to do heavy lifting while operating in a lifelike form as a human. Incredibly, the Handle is able to lift 100 lbs. vertically and is able to transport it from one location to the next as long as there are no major obstacles or rough terrain.



Figure 1. Boston Dynamics Handle Robot

We found that there are many commercially available robot kits that can balance on two wheels. These proved to be a major source of information for our research.

Research on the controller of choice led to the necessity of integrating a PID controller to keep the robot upright. PID stands for Proportional, Integral and Derivative, which identifies how the controller reads input via the gyroscopic sensors and how it outputs signal to the servo motors. The Arduino Uno is a capable platform

with the ATmega328P microcontroller, which allows for 14 digital input/output pins, 6 of which are capable of PWM output. For the project, this provides us with enough input and output to read all gyroscope and proximity sensors as well as the control of all servos and motors.

The recommended gyroscope is the MPU-6050 six-axis gyro and accelerometer by Motion Tracking Devices. This provides the angular data needed by the microcontroller to balance the robot on two wheels.

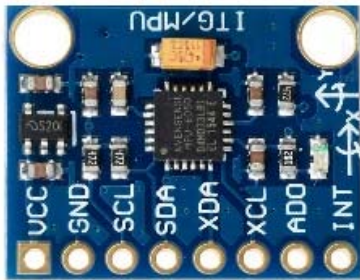


Figure 2. MPU-6050 Six-Axis Gyro+Accelerometer

## 2. DESIGN

The self-balancing robot (dubbed the “SkateBot”) was designed to balance itself, traverse an environment, and carry a small payload. Ideally the robot will move itself and various payloads from one location to another while being remotely controlled by a user. The inspiration for our robot came from the recently announced “Handle” robot from Boston Dynamics. Our design criteria was loosely based on the Handle’s design. For this project, it was deemed unfeasible to create a fully functional wheeled bipedal robot with functioning arms and a full torso. Because of this, it was chosen to design a wheeled bipedal robot consisting of only two individual legs, wheels as feet, and a small representation of a torso. The design is also simplified with minimal degrees of freedom when compared to the Handle robot as to not overcomplicate the project and to reach completion within our target window.

### 2.1 First Conceptual Design

Our initial conceptual design consisted of a self-balancing wheelbase with a movable arm mounted on top of it. The wheelbase would be the balancing platform, independent of the moving arm. This way, balancing the robot would be less intensive, as it would utilize an existing, proven design. This was primarily based on the findings from our literature survey and not as much on the “Handle”, which we initially wanted to base our project on.

The arm on top of the base would perform its tasks, while the base would work on balancing the robot. This is a less involved process, as the arm and balancing platform work almost independently of each other. Shifting the weight of the arm would cause the balancing platform to move forward or backward. In short, this is a very easy and doable design.

The drawback of this design was that the robot would be less agile. This design does not use two independent legs, but a base platform instead. This means that the robot would not be able to go upstairs, for example.

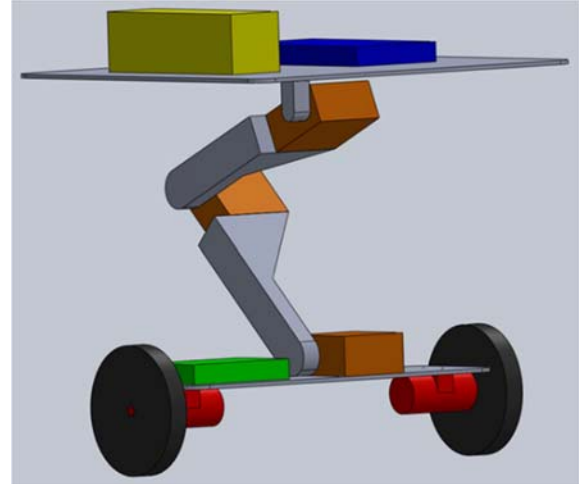


Figure 3. First Concept

### 2.2 Second Conceptual Design

The alternate conceptual design is more akin to the “Handle” that initially inspired our project. It consists of two independent legs with wheels as feet. A platform is mounted on top of those two legs. It does not have a movable arm. In this design, the movement of the legs and the balancing of the robot itself are not as independent from each other as the initial conceptual design. This concept uses roughly the same components as the previous one with additional servos.

This design offers more maneuverability than the initial design. The independent legs allow the robot to climb stairs for example and give it the ability to lean into corners when at high speeds. To conclude, this design is more complex than the initial concept but offers many advantages by two individual legs. Therefore, it is the design of which our first prototype is based on.

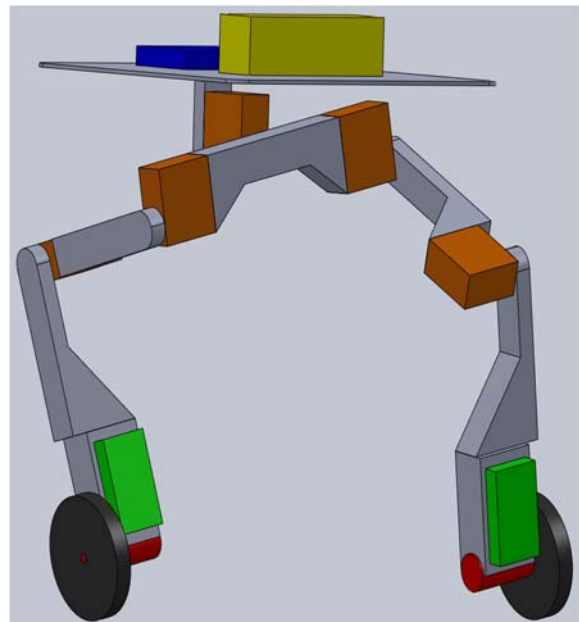
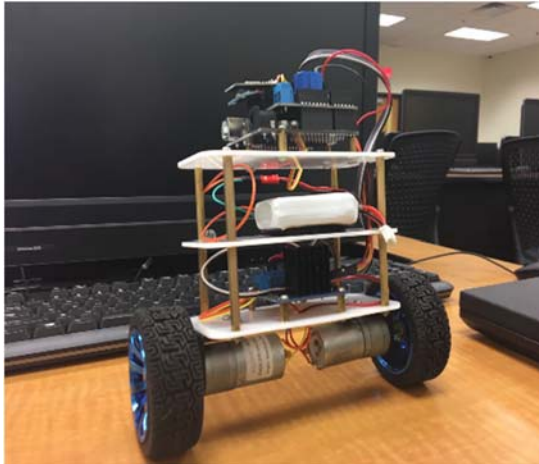


Figure 4. Second Concept with Increased Complexity

### 3. BASE PLATFORM EXPERIMENT

With our limited experience on many of the aspects required for this project, it was first wanted to familiarize ourselves with the balancing aspect of the drone. To do that, a kit was purchased specifically made to showcase the balancing capabilities of two wheeled robots. This also gave the team the opportunity to get familiar with the components required to complete the project. The base platform consisted of a simple balancing base with two wheels and a hard-mounted platform on top of it.



**Figure 5. Base Platform**

After procurement of the base platform, several tasks were completed towards getting the robot to function as intended and understanding how it works. These tasks include properly connecting the components of the system as well as trouble shooting several of the provided components. By analyzing the provided code, it was possible to understand how the robot functions in terms of balancing.

Once the components, programing, and self-balancing aspects were made familiar with, a greater foresight into the creation of the prototype was achieved.

### 4. COMPONENTS

The first purchase made for the construction of the prototype was the SainSmart InstaBots, 2-Wheel Self-Balancing Upright Rover Robot Kit. The kit allowed the team to learn about the balance and coding aspects of the conceptual bipedal wheeled robot design that our team built. A quick list of all components included in the set are listed below:

- SainSmart Arudino Uno (x2)
- SainSmart upright rover sensor shield
- ASLONG geared DC motors JGA25-370-12V-400 RPM
- MPU-6050 6 Axis Gyro Accelerometer Module
- SainSmart L298N Dual H Bridge Stepper Motor Driver Controller
- 2.4 GHz controller
- 2 Wheels

All components that were originally a part of the upright rover kit were dismantled and used to create the conceptual bipedal robot. Additional components were bought to make the conceptual design

possible. The additional items and components that were purchased to construct the prototype concept robot are listed below:

- Futaba S3004 Servos (x4)
- Turnigy TGY-1501MG High torque servo
- Xbox 360 controller
- SenMod Arduino USB Host Shield
- Microsoft Xbox 360 Wireless Receiver for Windows
- SunFounder PCA9685 16 Ch Servo Driver
- Balsa Wood
- Epoxy Glue mix

Components such as servos had to be purchased to allow for motion in the two legs. An Xbox 360 controller was found to be a good interface for controlling the robot. An interface was required to control the robot using the controller. This necessitated the purchase of the USB host shield. The Servo driver was purchased to power all 5 servos. The balsa wood was used to create the legs and the epoxy glue was used to connect the servo motors and dc motors to the balsa wood pieces.

**Table 1. Cost Analysis**

Component	Price per Part	Number of Parts	Total Price
Upright Rover Kit	\$85.99	1	\$85.99
Xbox Controller	\$30.00	1	\$30.00
Servos (Futaba)	\$13.00	4	\$52.00
Servo (Turnigy)	\$12.00	1	\$12.00
SunFounder PCA9685 16 Ch Servo Driver	\$11.99	1	\$11.99
SenMod Arduino USB HOST Shield	\$16.18	1	\$16.18
Microsoft Xbox 360 Wireless Receiver for Windows	\$17.65	1	\$17.65
Balsa Wood	\$10	3	\$30.00
Epoxy Glue Mix	\$9.99	1	\$9.99
Total Price			\$ 265.80

### 5. CONTROL

For the first iteration of the SkateBot prototype, a simple but intuitive control scheme was opted to allow the user ease of use and smooth control of the robot. The initial base platform was controlled by an included remote consisting of two analog sticks as well as an LCD screen. The left analog stick was dedicated to controlling forward and backward motion, while the right analog stick would cause an offset between the motors, inducing a right or left turn. Meanwhile, the LCD would output the angle values recorded by the Gyro/Accelerometer as well as the PID values stemming from the potentiometers.

Although this original controller functioned well for the base platform, it was desired to have more control and allow the user to control the legs of the skate bot. Multiple control schemes were considered, including one where the user would press a button activating a crouching routine. With this, the user could toggle between a crouched and straight leg position. While this control

scheme is very straight forward, it does not allow individual leg control. A two-button configuration was considered with each button toggling its respective leg between a straight and contracted position. While this two-button configuration allows individual control of the legs, it is still rather binary, solely allowing a crouched and un crouched position.

For these reasons, an Xbox controller was ultimately selected as our controller and with a proper configuration will give the user more control of the crouching motion. The action of the Xbox controller's triggers reads a significant number of steps between pressed and depressed. These steps can allow incremental adjustments to the contracting of each leg. Therefore, the legs can be partially contracted when the trigger is only partially pulled. The left trigger will be dedicated to the contracting level of the left leg while the same effect is mirrored with the right trigger and right leg. This should feel natural and be generally intuitive for most users.

Meanwhile, the Xbox controller's analog sticks would function similarly to the initial base platforms analog sticks. Most other gamepad like controllers would have sufficed, but the Xbox controller was already procured. Also, an LCD was chosen not to be used as it was decided it would not significantly improve the users' control experience without a large amount of resources invested into making the screen more worthwhile. To conclude, this control configuration is intuitive, simple and provides an acceptable range of control for the SkateBot.

To continue, several adjustments to the base platforms Arduino code would have to be implemented to adjust to multiple introduced variables. Due to the center of gravity of the system changing while the legs are contracted, the intensity of the compensation required from the motors to keep the system balanced will need to be dynamic. This requires the PID values to adjust proportionally to the height of the system.

The torso section of the robot will also have to adjust and keep the payload and electronic components leveled when the legs are contracting at different levels. Therefore, the servo controlling the torso must adjust to the crouching offset of the two legs. This will be done by obtaining the difference of the contracting levels of the legs while having the torso servo turning accordingly. In addition, other possible control systems were discussed. An example would be having the code contract one leg while turning at higher speeds. This would automatically have the system lean into corners. While this should overall increase the stability of the SkateBot, it was decided to prioritize other features of the robot and simply allow the user to always control the legs of the system.

## 6. PROTOTYPE

As stated previously, the team decided to use the second conceptual design as our prototype. It was built simply using balsa and plywood. This was done to minimize cost and allow for rapid construction of the prototype, as wood is very easy to work with.

The electronics consisted of two Arduino Uno boards. One was dedicated to balancing the robot, so it used the sensor shield. The other was dedicated to servo control and the Xbox 360 controller remote interface, so that one used the USB host shield. 5 servos are used throughout the prototype.

One is for tilting the platform side to side. The other four are split amongst both legs and allow the legs to contract and expand. The motor driver was used to power the two motors that drive the

wheels the robot stands on. Finally, the servo driver was used to control each of the servos.

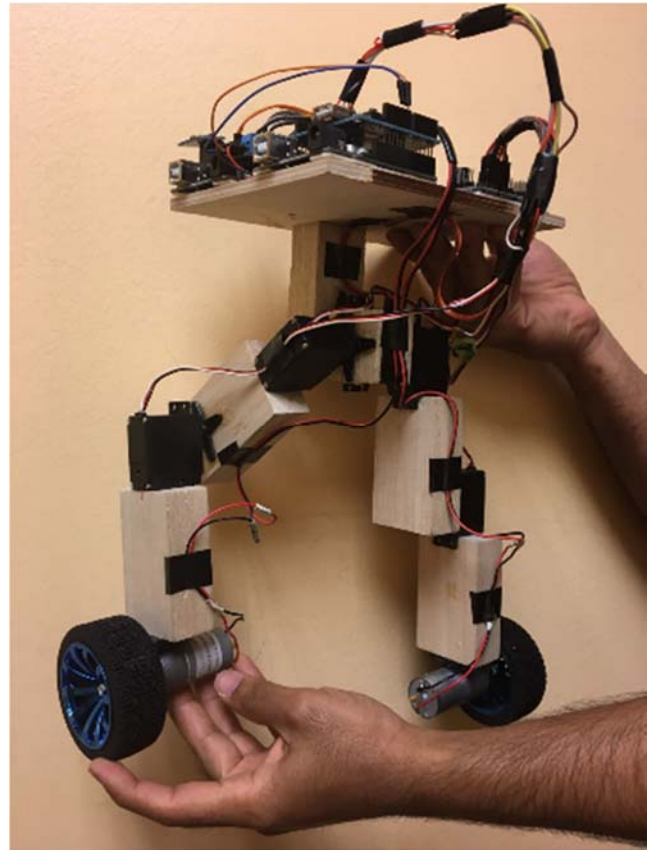


Figure 6: Final Prototype

## 7. EXPERIMENTS

Once the prototype was constructed, testing commenced. The self-balancing capabilities of the prototype were tested. Since the balancing system was now placed on a new platform, issues could arise. However, no issues were expected, as the balancing system was deemed very capable from the base platform experimentation. The servos were also tested to verify their center positions and maximum deflections. The servos had to move freely without binding on anything or pulling the wires too tightly.

## 8. RESULTS

The servo driver made it difficult to program the servos. We therefore decided to power the servos through the servo driver, but send the signals to the servos directly from the Arduino, instead of through the driver.

Power issues were encountered when trying to power the entire system using one battery. The motor driver required to be replaced due to damage stemming from this issue. This led to the use of an 11.1 V lithium polymer battery for powering the DC motors and the two Arduino boards, and another 6 V Nickel Cadmium battery to power the servos.

Additional experiments for remote controlling of the robot, as well as leg control are intended to take place following the addressing of the power issues

## 9. CONCLUSIONS

A prototype of the lower section of a wheeled bipedal robot was constructed, but after testing, issues with the power delivery system made it unable to function. It is still intended to make this prototype functional. Further testing of the power delivery configuration will be performed once the motor driver has been replaced. Following this, additional developments will be made on controlling of the servos. Factors such as quality, coding, and connectivity of the servos will be researched in the hopes of improving their performance. Advancements with the remote control of the SkateBot are also intended.

For future iterations of the SkateBot, there are multiple adjustments to the electrical components and materials used that can be made. Using solely one micro controller rather than two will reduce the power consumption and redundancy of the electrical components. Using plastic and or 3D printed parts, rather than the wood and glue currently used, will increase the strength and durability of the SkateBot. Additional servos could be added to increase the degrees of freedom as well as the dexterity of the system. Once the SkateBot reaches a commendable level of functionality, additions of a torso as well as arms may be explored.

## 10. REFERENCES

- [1] U. (2016, May 12). 2-Wheel Self Balancing Robot by Using Arduino and MPU6050. Retrieved May 02, 2017, from [http://www.instructables.com/id/2-Wheel-Self-Balancing-Robot-by-using-Arduino-and-/,](http://www.instructables.com/id/2-Wheel-Self-Balancing-Robot-by-using-Arduino-and-/) 2016.
- [2] SainSmart InstaBots Upright Rover Kit V2.0 Updated 2-Wheel Self-Balancing Robot Kit. (n.d.). Retrieved February 28, 2017, from [http://www.sainsmart.com/sainsmart-balancing-robot-kit-v2.html,](http://www.sainsmart.com/sainsmart-balancing-robot-kit-v2.html) 2017.
- [3] How do I power my Arduino? (2015, September 18). Retrieved April 20, 2017, from [http://www.modmypi.com/blog/how-do-i-power-my-arduino,](http://www.modmypi.com/blog/how-do-i-power-my-arduino) 2017.
- [4] Glaser, A. (2017, March 01). Roboticists say Boston Dynamic's new nightmare robot is unlike anything ever seen before. Retrieved March 15, 2017, from [https://www.recode.net/2017/3/1/14771330/boston-dynamics-new-nightmare-robot,](https://www.recode.net/2017/3/1/14771330/boston-dynamics-new-nightmare-robot) 2017.

# SkillCourt Autonomous Ball Launcher

Izak Negron, Jose Perdomo, Richard Saco, Adrian Sinanan, Sabri Tosunoglu

Department of Mechanical and Materials Engineering  
Florida International University

10555 West Flagler Street

Miami, Florida 33174

inegr003@fiu.edu, jperd033@fiu.edu, rsaco006@fiu.edu, asina001@fiu.edu, tosun@fiu.edu

## ABSTRACT

SkillCourt is a proposed soccer training system to develop player cognitive and decision making skills using computer-aided technology and automated feedback capabilities. Our goal is to incorporate an autonomous ball delivery system that will track the user and interact with the SkillCourt software; thus, allowing for maximum customization and computer aided training.

Ball delivery systems are already common and widely used in sports such as tennis, football, and baseball. These devices have similar traits in means of function and purpose, but most lack autonomy and diversity in the complexity of delivery. For soccer, there are both advanced and basic machines that are capable of various shots and passes available on the market. On the other hand, these systems do not have automatic and user based capabilities as well as costs that are in reach of a common household or academy.

Our main design concerns will include movement capabilities of the ball delivery mechanism, independent loading and unloading of a ball, user tracking, and automatic delivery integration with the SkillCourt software. The team has delivered a unique prototype with many customizations (i.e. three degrees-of-freedom, micro-controller system, Open Cv tracking, auto loading, and SkillCourt software) of which have been implemented. Lastly, the team will continuously optimize and calibrate the functionality and accuracy of the system. Soccer is a worldwide sport played by nearly every culture and background, an automatic training system will have great potential for both youth and professional levels of global soccer programs.

## Keywords

Autonomous, Open CV, SkillCourt, Three degrees of Freedom, Motor Control, Raspberry Pi, Arduino.

## 1. INTRODUCTION

Ball delivery systems are already widely used for many types of sports across the globe. These devices have similar traits in means of function and purpose, but many lack user interaction capabilities and customizations. The main design has provided movement of various degrees of freedom and a basis for independent loading and unloading of a ball, while player motion tracking and automatic have been provided a strong basis to be accomplished and integrated with the SkillCourt software. The team has worked on a prototype using concepts from commercially available launchers as well as software used to track objects.

Soccer is a worldwide sport played by nearly every culture and background, an automatic training system will have great potential for both youth and professional levels of global soccer programs. By building an automatic ball delivery system with the integration and software capabilities of SkillCourt, we hope to provide a reasonably priced device for all players of the sport.

This launcher has great potential for future work as a working base for developments and improvements can be implemented. Likewise, like any other type of commercial product there must be recognition of similar tools and technologies with similar capabilities. SkillCourt is a new form of soccer training that takes into account the already proven studies of brain growth and soccer drills. This launcher will be integral in the line of products that already exist within SkillCourt. Lastly, the team will continuously improve and calibrate the functionality and accuracy of the various components of the system.

### 1.1 Related Work

Before the launcher can be designed, there must first be understanding of how a ball moves and behaves one launched and through the air. In sports, many characteristics must be considered, for any that incorporate a ball, the aerodynamics of the ball are critical for trajectory prediction and study. Particularly in football, several wind tunnel and computer models have been used to simulate and analyze ball physics. To describe the phenomena associated with footballs traveling in air, the dimensionless value of Reynolds number must be considered. The range of speed varies in the game of football with ranges from 10 mph to 70 mph or 4.5 to 31 meters per second [1].

The industry of ball launching devices is very diverse and ranges across many sports, the biggest consumers being baseball and tennis. Currently there are additional launchers for other sports such as soccer, volleyball, and football though they lack intricacy and do not provide statistics and user feedback. These launchers have capabilities such as speed adjustment, direction and angle customization, and finally unique shots and passes that can be achieved through their respective machines. Some previous works considered are the Sidekick and First Pitch ball launching systems shown in Figure 1. Adjustments for the ball are made through manipulation of tire speeds and angle of the mechanism used to launch the ball [2]. Specifications will include structure of the launcher and its changes in direction. Though numerous are available, prices ranges are usually out of reach for lower levels of sports and amateurs. For the launcher proposed in this report, a launcher that is affordable, provides a wide variety of features, and directly interacts with the user will be sought after.



**Figure 1. SideKick Ball Launcher**

To accomplish the initial goals of this project one must first look into the primary demands of such a device and the possible directions the team can look forward to. The SkillCourt ball launcher delivery device will consist of a two motorized friction wheel assembly that will receive the soccer ball, automatically load, and launch the soccer ball to a specific destination. The uses of motorized wheels will allow accurate ball service with both wet and dry balls. To adjust the trajectory of the soccer ball three degrees-of-freedom will be needed. In other words, the ball launcher will rotate along three axes; this type of motion is described by yaw, roll, and pitch rotation matrix used in aeronautics.

To achieve these motions two assemblies are researched, the Gimbal platform and Stewart platform [3]. These platforms are software-programmable control mechanism that will instruct motion features to the soccer ball. The Gough-Stewart Platform is a parallel robot consisting of six prismatic actuators that are attached in pairs on the base plate and is diagonally connected to three mounting plates displayed in Figure 2 [4]. Trademarked “hexapod” by Geodetic Technology is the term used to describe this 6-jack platform due to its similarity to six legs; this results in a total of six degrees-of-freedom. Other applications of this includes NASA Low impact docking systems and flight simulators.



**Figure 2. Gough-Stewart Platform**

Additionally, the research of William Mendez, Yuniesky Rodriguez, Lee Brady, and Sabri Tosunoglu pertaining to the concept of three degrees-of-freedom rotating platforms with high accuracy has been looked in to, allowing a new method of soccer ball launching that can be achieved. A three degree-of-freedom rotary table mechanism contains three gimbals seen in Figure 3, of which act as swiveled supports that allows the rotation of an object about its own axis, each being structurally designed for perpendicular rotation with regards to one another [5].

As one can imagine with different designs each has its own pros and cons, for example an arrangement of outer gimbals would require further actuators would be needed to move a gimbal setup with a high moment of inertia. Likewise, weight can be arranged to where one actuator can move a gimbal depending of the rotation axis. It is understood that a three-degree axis table will need four tranches, the base, the outer, middle and inner gimbals. To reduce torque in the actuators light weight material should be considered such as plastic.

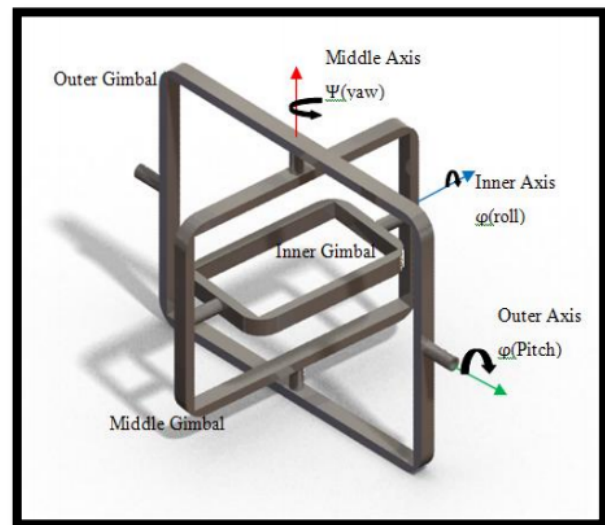


**Figure 3. Gimbal Platform**

Open CV (Open Source Computer Vision Library) is an open source software library that is used in computer vision and learning applications. Open CV supports Windows, Linux, MacOS, and Android operating systems, and interfaces with C, C++, Java, Python, and MATLAB. Additionally, this software library features algorithms used in face recognition, object identification, motion tracking, three-dimensional object plotting, with potential for other subjects [6]. Open CV software brings a range of applications that is useful in the ball launcher player tracking characteristic.

## 2. DESIGN COMPONENTS

### 2.1 3-DOF Platform

For the two degree of freedom platform, the design based on commercial vehicle simulators is made. First, the top platform consists of three legs. One has a universal joint fixed to ground and its rotation about its axis has been removed. This joint will constraint the system to the two degrees of freedom desired. Additionally, the platform has two other legs that consist of a revolute joint, and two spherical joints. The revolute joints

represent the input motors, which will be high torque low speed motors, and the spherical to spherical links consist of end rod joints. This configuration is shown in Figure 4.

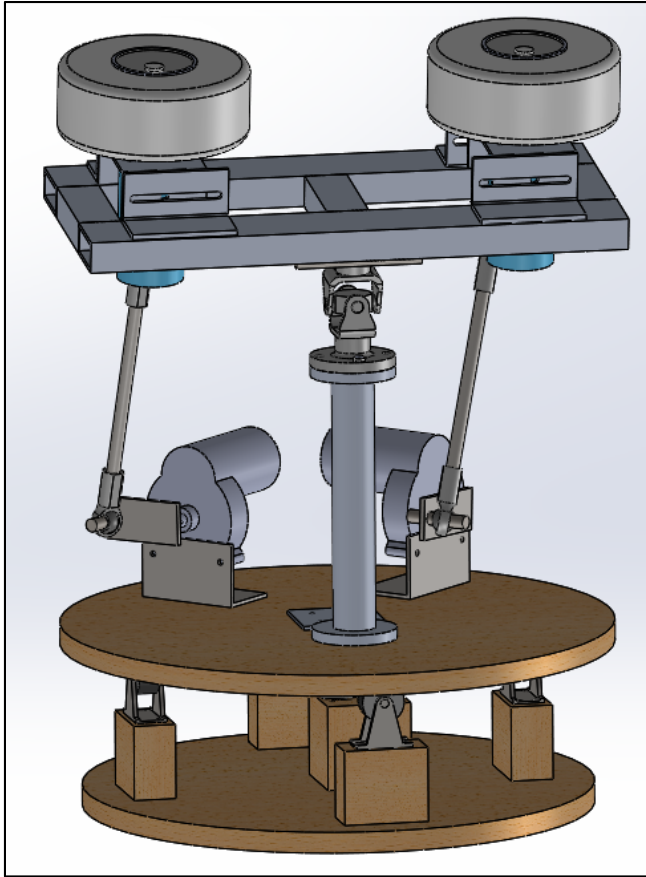


Figure 4. 3-DOF Platform

This platform is of utmost importance as it will provide the ability for shot customization in terms of lobs, driven, curved, and angled shots. The final platform of yaw will allow for slow rotation and player tracking both in reverse in forward motions, the key to the platform will be the motors used to provide these operations, of which will be controlled wirelessly. The yaw platform was supported with a quartet of rigid caster wheels which evenly distributed to vertical load of the platform.

## 2.2 DC Motors

The two flywheels provide the necessary force to launch a ball as it is pushed through them, this function is of dire need to the user's desire to provide different speeds of shots and curves. Curves are assured as one motor can be controlled to rotate faster than one another. The motors used were repurposed from an already existing softball machine, and so were not ideal for soccer ball purposes but still provide a necessary punch. These motors are rated at 90 volts, 3 amps, and 4500 RPM which, through testing, was found to be sufficient for this prototype. Likewise two high torque motors were used to operate the two degree of free of pitch and roll, of which could be stopped to ensure a desired degree. These motors were rated 12 volts, 15 amps, with a torque of 30 Nm and 160 RPM

which was more than enough for the prototype's purposes. For the yaw platform a high torque motor with a maximum speed of 12 RPM and torque of 12Nm was used for player tracking, of which was capable of rotating up to 200lbs of force. All of these motors were controlled individually as will be discussed in the next section.

## 2.3 Motor Control

For the control of all motors in the system, they must both be able to be controlled by the user, but also intake information from another and convert it information to be used in player tracking or shot manipulation. The first motors to be modified by the user will be the flywheels, as the user will tell the launcher what kind of pass or shot they want, thus telling the Raspberry Pi and later the Arduinos to adjust the speed of the flywheels. After a speed has been determined, the angle of the pass or shot must also be changed, Raspberry Pi will also do this by communicating to the Arduinos controlling the two degree of freedom platform which will adjust the pitch and roll of the launcher as a whole. Each of these motions will control the vertical and horizontal angles of the shot respectively as designated by the user. Lastly, the yaw motion of the platform that will both track the user and predict its position will be controlled by the Arduino, but will intake information by the Raspberry Pi of which will compute the other inputs into the equations needed to find ideal future position of the user.

Beginning with the flywheels, the motors must have complete control, this will be done using a combination of N-Channel power mosfets, Pulse Width Modulation, and the Arduino. This circuit can be seen in Figure 5.

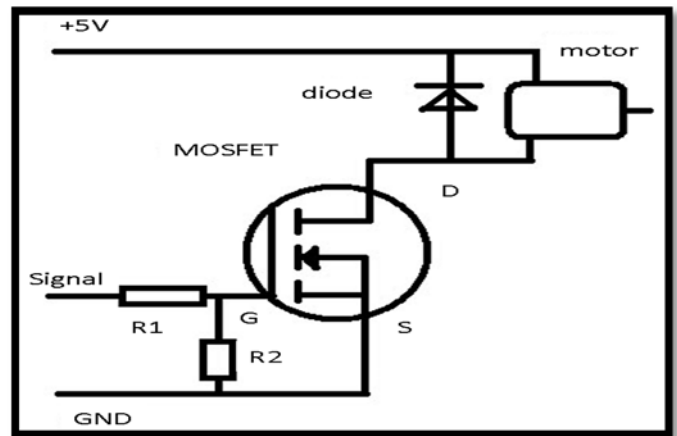


Figure 5. Flywheel Motor Control

This simple yet effective circuit will allow for simultaneous control of the flywheel motors regardless of their high power capabilities, a Schottky Diode is used for protection of the motor from the power source and the N-Channel mosfet acts as a switch [7]. Next the two degree of free platform will be controlled by their own individual motors, of which will be controlled using a Monster Moto Shield Driver, of which will be able to simultaneously control the two motors for speed, braking, and reverse and forward actions. This shield is illustrated in Figure 6.

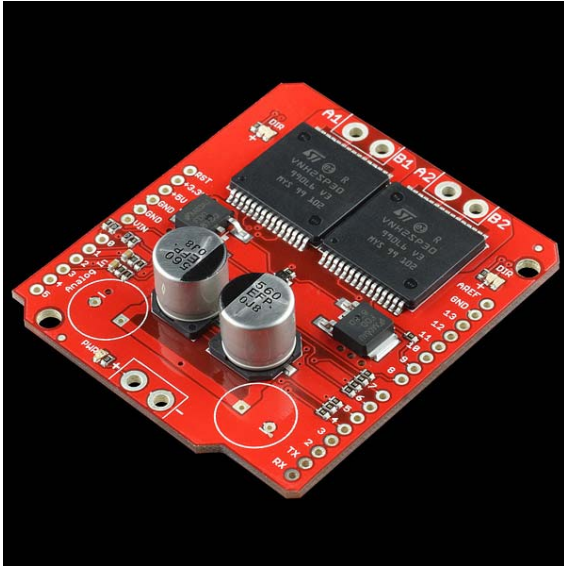


Figure 6. Monster Moto Shield

This shield acts similarly to an H-Bridge, of which can be a collection of mosfets and is used for various types of motor control. The code for the driver could then be used through Arduino to provide a wide range of user inputs and customization abilities.

Finally the yaw platform motor will be intertwined with a Raspberry Pi with serial control, allowing for the Pi to process information and deliver a command to the Arduino. By interacting with the Open Cv capabilities, the Pi will direct the Arduino to move the motor in the desired direction to achieve player tracking, this will be further explain in Player Tracking.

## 2.4 Wireless Control

The prototype and product's main goal is to accomplish the autonomous nature of the launcher, for this to occur there must be components that will allow for wireless control of the five dc motors.

The chosen Wi-Fi module was the ESP8266 of has various traits which aided in the decision with cost and power capabilities being of utmost importance. With the module's ability to quickly be installed and used with an Arduino or any other micro controller, the ESP 8266 could be implemented as simply as Wi-Fi transmitter [8].

The module is shown in Figure 7, and provides ports for use in microcontrollers, of which will be wired to the various Arduinos. Not only is the module compatible to the Arduino and its economically efficient, it is also very powerful for its size and cost as it has a memory of 1MB and data speeds acceptable for our purpose.

Five Wi-Fi transmitters will be used to control the motors with each motor controlled in its own right, with information being fed to a wireless server controlled by a computer and eventually the Raspberry Pi.

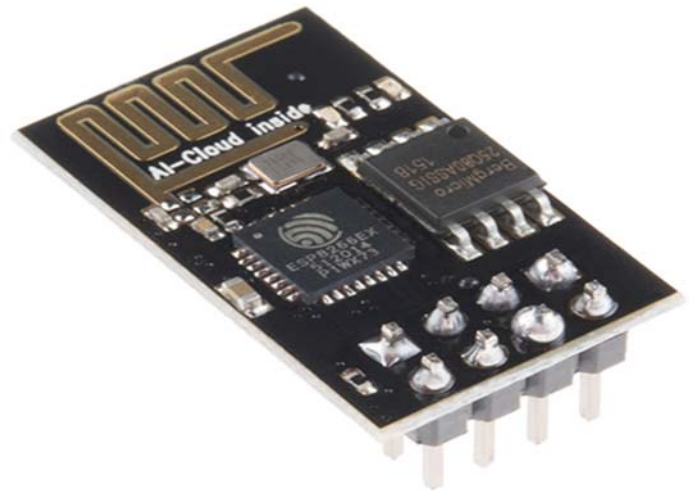


Figure 7. ESP8266 Wi-Fi Transmitter for Arduino

## 2.5 Power Supply

With emphasis on being able to use the ball launcher on a soccer field with little to no hazards to other players on the field, safety is of great concern. This concern has risen the challenge of using portable batteries as the power source for the launcher as well as other electrical components such as the Raspberry Pi and Arduino Uno, all of which will be operated wirelessly.

Primarily, the RPI and Arduino are usually powered by a usb power source from a computer or outlet, consequently a set of alkaline batteries can also be used as a wireless power source solely for the proving of independent power. An adapter employed along with a set of alkaline batteries are used for the processing devices while a much larger and higher capacity battery is used to power the motors.

There are numerous challenges when determining the necessary battery for an application, it is even more difficult when costs, weight, and capacity times are all important variables needed for a product to succeed and function as intended. The typical battery found in many cases is the lead-acid battery due to its relatively inexpensive costs and multi-purpose ability, though it does have drawbacks such as its weight. Other types of batteries include Nickel-Metal Hydride, Nickel Cadmium, Lithium Ion, Lithium Ion Polymer, and Alkaline. Each having their own pros and cons relative to their use. With some having greater energy to weight ratios than others, but with relatively high costs. For the purpose of this project, the lead acid battery will be used to cut costs but also because of its uses. [9]

Portable dc batteries like car batteries are usually rated in with a range of 12-15 v and 40-45 amphs thus proving quite a large energy capacity, though are also fairly heavy. Finding a dc power source for the flywheels motors is a difficult task, this is due to the heavy needs of the motors. Originally the dc motor specifications as previously mentioned are a max of 90 volts and 3 amps. This indicates that the motors can retain a maximum of 270 watts of power, though for this prototype a variable speed will be reached in the range of 40-60 volts and 3 amps, with possible power input of 120-200 volts.

A boost converter can be created by building a circuit consisting of diodes, transistors, a capacitor, and or an inductor, though this would require far more research and experience. By purchasing a readymade device, reliability is greatly increased. Similarly to how voltage will be controlled through the motors, voltage is increased through the boost converter by tracing advantage of the inner resistance of an inductor [10].

Due to the uses of the prototype, the two degree of freedom and yaw motors will only operate for small amounts of time, while the flywheels will run continuously. These requirements essentially translate to three motors requiring doses of power for shorts periods, and the others large amounts of continuous power and draining the batteries quicker. By using a pair of 12v 15amh rechargeable battery, testing and usage of the motors will be used for continuous amounts of time. Figure 8 shows the battery that is used, and another that holds a higher capacity and may be also considered in the future.



Figure 8. Universal Power Group Rechargeable Battery

## 2.6 Player Tracking

Object detection and segmentation is the task that Open CV computer vision is developed for, this field of work is still an open problem that is still being researched today. One of the easiest ways to detect and separate an object from the background is a color based method. With the assumption that the object being tracked is a complete separate and distinguishable color from the background, a successfully object segmentation can occur. For the tracking of the soccer player an assumed color of purple is chosen to differentiate the object from the surroundings. The webcam will be proceed through a binary threshold, provided to use through Open CV function that will allow the thresholding to the color purple. That is to say the video image would be converted to black and white pixels in a separate window, where the white (1) color depicts the finding of purple color in the image and the black (0) pixels depict lack of purple color. This can be seen in Figure 9. Open CV process this by capturing an image and video in an 8-bit, unsigned integer, and BGR format [11].

Figure 9 describes the color array broken down to its Blue, Green, and Red primaries. It is true that the BGR color space, (integer values rages from 0 to 255) can be suitable for color segmentation,

however, the HSV color space is the most suitable color space for image segmentation. The HSV stands for hue, saturation, and value

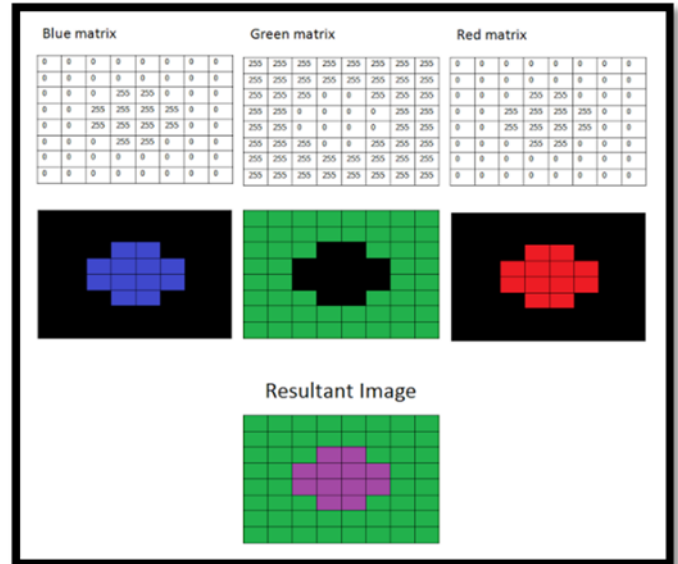


Figure 9. Open CV Color Detection and Building of Matrix

(brightness). Unlike RGB, HSV separates the image intensity, or luma, thus getting better information from the color space thus distinguishably the color from one another easier. Open CV makes the use of HSV simple, thanks to a prebuilt function that converts between RGB and HSV to be implemented. The range for hue, saturation, and value are respectively 0-170, 0-255, and 0-255. The hue represents the color, the amount of the color mixed with white is its saturation, and value is the amount mixed with respect to black. In the development of using the Open CV library to track objects the integer value is determined by using multiple track bars that can slide to the desirable range, described in Table 1 for hue integers. The saturation and value track bar is used to get rid of the white noise the webcam may pick up due to lighting and surface of the object [12].

Table 1. Values of Hue Integers to Threshold Specific Colors

Threshold Specific Color	Values of Hue Integers
Orange	0-22
Yellow	22-38
Green	38-75
Blue	75-130
Violet	130-160
Red	160-179

After thresholding the image binary image may contain numerous imperfections, white isolated object might be visible at random areas on the screen, this may be due to white noise or a small object

with the same color. To get rid of this a morphological opening technique is applied. Morphological image processing is a collection of non-linear operations shape or form of the image. Typically the Morphological technique probes the image with a structuring element that transform a “hit” pixel to the desired color. The structuring element can be thought of as a binary matrix of pixels that restructures the pixel values of 1’s or 0’s. For Open CV color tracking two commonly used morphological operations are erosion and dilation. A square erosion matrix shrinks an image by stripping away layer from the boundary of the regions, eliminating small details. Whereas, dilation, is completely opposite, it adds layers of pixels to the boundary region. Combination of these creates a compound operations opening or closing filters that can eliminate noisy details while not damaging the object of interest. After detecting the object, locating the real world position X and Y coordinates of the object. To describe objects after segmentation, Open CV image moment function is used. Image moment is a weighted average of the pixels intensities use to find the orientation and the centroid of the object. Using the 0th central moments the binary image is equal to the white area of the image in pixels. An example of this method is done by assuming the binary image is less than or equal to 10000 pixels, no object is detected since the expected object will have an area greater than 10000 pixels. This method can only work with 1 of the particular object. Shape detection and tracking using contours. Open Cv contour function allow sequences of points of vertices to create “white patch” polygons. Open CV provides a basis for player that is both accurate and reasonable for the purposes of this launcher and its tracking capabilities. In order to work together with the yaw platform, a program was devised using C++, that was able to control a motor to ensure the target was always in the designated location, providing proof of concept. This is shown in Figure 10.

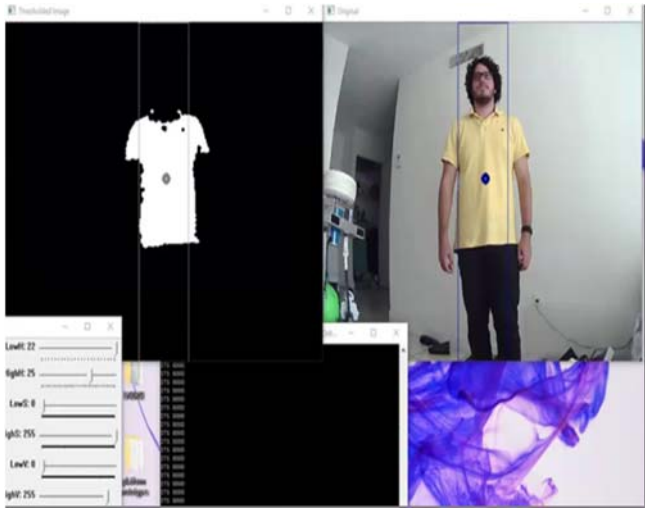


Figure 10. Object Detection, Color Recognition and Motor Movement

### 3. DESIGN ANALYSIS

#### 3.1 Vibration Analysis

For the design of the platform, the only component experiencing hard vibrations directly is the flywheel motor mounts. Therefore, a natural frequency study was done for 10 nodes and evaluated

against the different rotations of each motor. To elaborate more, since the motors bought from JUGS are certified to be balanced, the only vibrations in the system come from the rotational speed of the system. Assuming that only this vibration is transferred to the mount, the resonant frequencies are evaluated. Using SolidWorks Simulations, the natural frequencies of the mount were found; see Figure 11 and Table 2. For the simulation, the weld of the mount was simulated as accurately as possible, the remote load of the motor, and gravity were considered.

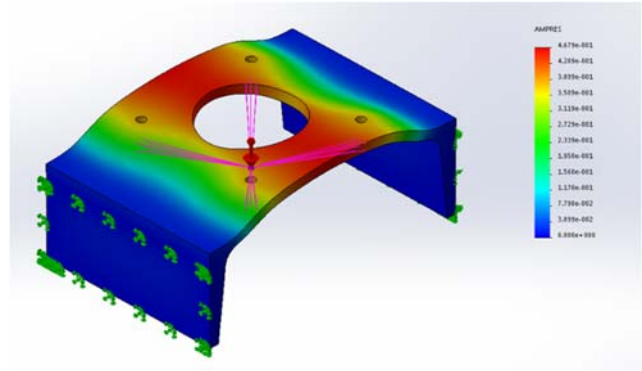


Figure 11. Vibration Analysis via SolidWorks Simulation

The natural frequencies for 10 nodes were obtained and displayed in Table 2. Next, assuming the range of rotational velocities used in the flywheels goes from 1000 to 4000 rpm, the range of vibration frequencies will be equal to 16.67 Hz to 66.67 Hz. Therefore, none of the frequencies inside the range of rpm used will cause resonance in the motor mount.

Table 2. Motor Mount Natural Frequencies

Mode No.	Frequency (Rad/sec)	Frequency (Hertz)	Period (Seconds)
1	3819	607.9	1.65E-03
2	7962	1267.2	7.89E-04
3	9520	1515.1	6.60E-04
4	25486	4056.3	2.47E-04
5	33781	5376.5	1.86E-04
6	39153	6231.4	1.60E-04
7	41883	6665.9	1.50E-04
8	55722	8868.4	1.13E-04
9	57573	9163.1	1.09E-04
10	60328	9601.5	1.04E-04

#### 3.2 Stress Analysis

Since multiple components of the system need to be manufactured to fit the proposed design, some of them turned out to look not strong enough, and stress analysis was done to clear out any doubts

on their designs. First, the motor mounts were tested to hold the motor-wheel assembly weighing 15 lbs (Figure 12).

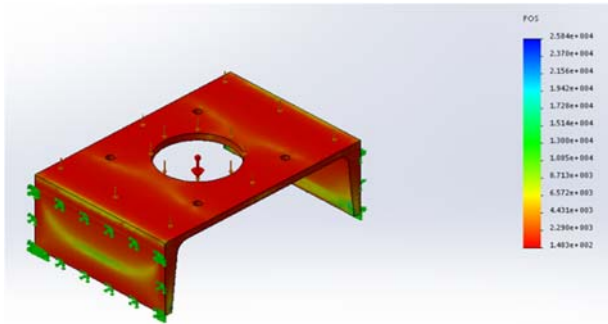


**Figure 12. Motor Mount FOS Stress Analysis**

While the figure color scheme is misleading, thanks to the material selected for the motor mount, the minimum safety factor was 148.3, which is relatively high, but was needed to make sure the vibrations of the motor would not be an issue in the future.

The next component that was tested were the tabs joining the spherical joints to the top platform seen in Figure 13. Initially, the component consisted of a single tab connected to a threaded rod held in place by steel nuts. However, the safety factor of a single tab for an estimated load of 50 lbs, was of 1.6. Therefore, a second tab was added, and the threaded rod was elongated to allow enough clearance for all bolts needed.

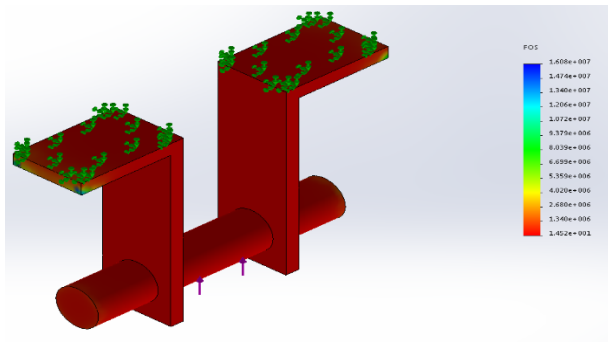


**Figure 13. Tab FOS Stress Analysis**

Adding the second tab in the component increased its safety factor to a minimum of 14.5, which gives an overall safe contingency for one of the least safe items. Similarly, the link connected to the motors in the 2-DOF platform will have a similar structure and therefore, needed to be analyzed (Figure 14).

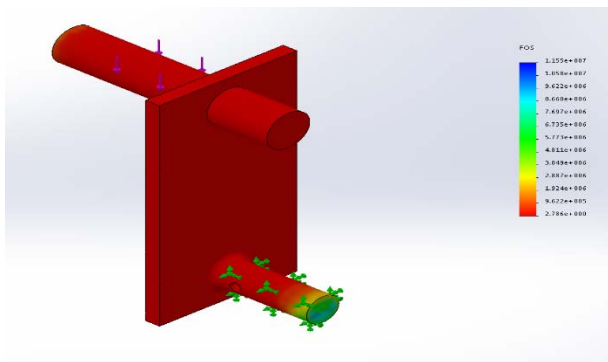


**Figure 14. Motor link FOS Stress Analysis**

Consequently, it was found that the link connected to the motors and spherical joints would have the lowest safety factor with a value of 2.8 seen in Figure 15. However, it is important to note that this component was analyzed under a load of 100 lbs. which is relatively higher than what is expected. The last component that was analyzed using the same method was the bottom platform that is providing the yaw motion. Since the budget is the biggest design constrain, there are multiple components that will be made of wood, including this platform. Therefore, for this component, materials were researched previously and pine was selected as the best available wood for the platform. The data of the material was obtained online, and a custom material was created on SolidWorks to simulate pine wood.

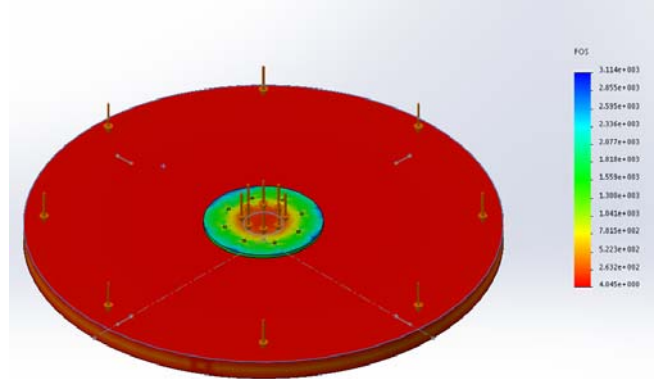


**Figure 15. Wood and Hub Yaw Platform Stress Analysis**

The component was rated under 200 lbs. which is double the maximum amount of weight expected to account for any miscalculations on the overall system design. The minimum safety factor found was of 4. Something that needs to be considered when evaluating this component is that there would be four more supports on it that will be caster wheels to help distribute the load while avoiding any friction on it. Therefore, the component will experience less critical loads through its body as it is seen in its stress analysis.

Overall, all critical components were evaluated depending on its design due to their design needs to fit the prototype that will be done. For the rest of the components that will be purchased, all of them are rated from their manufacturer. Therefore, the team did not see a need to simulate those components. However, the team made sure that the ratings on all components exceeded expectations, as it was mentioned, to account for calculation errors.

## 4. PROTOTYPE APPLICATION

Given the demands of the sponsor and the needs of the SkillCourt training methods, the launcher was destined to be incomplete due to lack of skills in electrical and computer software programming. The end goal of the prototype was to be able to completely control the various customizations of the launcher and constitute them into a realistic soccer drill. This application could only succeed with additional assistance from software engineers who could provide a simplistic yet meaningful application for a user. This possible application was depicted in Figure 16.

Due to the many demands of the launcher, the severe lack for implementation of the wireless and autonomous control are of great potential. The future for the launcher will be directly correlated to the skills of the Electrical and Computer software engineers. These



**Figure 16. Ideal SkillCourt Application Control**

future works will directly ensure that the launcher does achieve safety requirements and complete autonomy through its electrical and computer software capabilities.

## 5. PARTS LIST

**Table 3. Prototype Parts List**

Part	Number of Parts	Part	Number of Parts
Aluminum Rectangular Tubing	1	Arduino Uno	4
Aluminum Rectangular Tubing	1	Raspberry Pi	1
Threaded Steel Links	2	Arduino Monster Moto Shield	1
Steel Ball Joint Ends	4	Rechargeable Battery	2
Steel U-Joint	1	Boost Converter	2
Aluminum Tube	1	N-Mosfet (Flywheels)	2
Steel Disk	1	Diode (Flywheels)	2
Low Carbon Steel Channel	1	Diode (2DOF)	2
Steel link	2	Diode (Yaw)	1
Low Carbon Steel Rectangular Bar	1	Yaw Motion Motor	1
Low Carbon Steel Rod	1	Two DOF Motor	2
Grade 8 Steel Fully Threaded Rod	1	Flywheel Motor	2
Aluminum Disk	2	Rigid Caster Wheels	4
Grade A36 U Channel	1	Term Block (2 positions)	10

## 6. FUTURE WORK

With any product there is always room for improvement, whether it best manufacturing costs or durability of the machine. For this launcher, the areas that can and will be improved in the future include programming, electrical, and material properties. The reason behind most of the components used were of cost and practical use, future work would include using material from a supplier that will come cheaper and just as sufficient or of higher quality with a slightly higher price. Material chosen could also be reclaimed after a substantial duration of use rather than tossed in a landfill.

Work regarding the automated collection and loading of the launcher previously mentioned is still under design and manufacturing considerations, but will become an integral necessity. This component of the SkillCourt ball launcher is a projected within itself, and requires careful safety considerations and automated control, similar to those of the motors. Overall, continuous work will be done for both the launcher and automatic loading which will require assistance from electrical and computer teams.

Likewise, the motors and batteries used may be swapped for those of an eco-friendly nature allowing for recycling of products and being certified for bio friendly uses. Obviously programming is at the core nature of the prototype, future work will include improving upon the processing power and response time of the Arduinos and Raspberry Pi used in this system and finally the SkillCourt application. The launcher relies on all components to successfully run simultaneously in a smooth operation, this will be a key trait that will need to be continuously monitored, compared, with many continuous trials made.

## 7. ACKNOWLEDGMENTS

The authors extend their thanks to SkillCourt LLC and Guðmundur Traustason, who sponsored the project and holds the intellectual property (patents and trademark rights) as the creator of SkillCourt projects. Further thanks are extended to faculty advisor Professor Dr. Sabri Tosunoglu and the Robotics and Automation Laboratory for guidance in platform design and robotic control. Autoronics and Richard Zicarelli are also thanked for their assistance and advice in the manufacturing process of the launcher.

## 8. REFERENCES

- [1] Crass, Scott. Dynamics of a Soccer Ball. Rep. Mathematics, California State University: Long Beach. N.p.: n.p., n.d. 1-18. Web.
- [2] "Sidekick." Sidekick. Keeperstop, 2016. Web. 17 Oct. 2016.
- [3] Gimbal Platform Pic "Super Gyroscope Gimbals (add-on Kit) - From Gyroscope.com." Gyroscope.com. Gyroscope, n.d. Web. 17 Oct. 2016.
- [4] "Motion Base/Stewart Platform - Mark Roberts Motion Control." Mark Roberts Motion Control. MrMoco, 2016. Web. 17 Oct. 2016.
- [5] William Mendez, Yuniesky Rodriguez, Lee Brady, Sabri Tosunoglu. Design of a Three-Axis Rotary Platform. Mechanics and Materials Engineering, Florida International University. Florida Conference on Recent Advances in Robotics, FCRAR 2010, Jacksonville, Florida, May 20-21, 2010.

[6] OpenCV About. Opencv.org. N.p. N.d., Web 20 Oct. 2016.

[7] Kumar, Karan, Mansi Aggarwal, and Pranav Haldar. P.C. Interfaced Speed Control of D.C. Motor. Thesis. College of Engineering Roorkee, 2010. Roorkee: n.p., 2010.

[8] "WiFi Module - ESP8266." WRL-13678 - SparkFun Electronics. N.p., n.d. Web. 16 Mar. 2017.

[9] "Universal Power Group | Stay Powered@." Universal Power Group | Stay Powered@. N.p., n.d. Web. 01 Mar. 2017.

[10] "How Boost Converters Work." Electronic Circuit Projects. N.p., 23 Feb. 2017. Web. 01 Mar. 2017.

[11] Bradski, Gary R., and Adrian Kaehler. Learning OpenCV: computer vision with the OpenCV library. Sebastopol, CA: O'Reilly, 2008.

[12] Fernando, Sermal Ruwantha. "Color Detection & Object Tracking." Color Detection & Object Tracking. N.p., n.d. Web. 12 Mar. 2017.

# SkillCourt Pad Design

Alexander Diaz, Sebastian Maciel, Sabri Tosunoglu, Pradeep Shinde

Department of Mechanical and Materials Engineering  
Florida International University  
10555 West Flagler Street  
Miami, Florida 33174

adiaz357@fiu.edu, smaci009@fiu.edu, tosun@fiu.edu, pshinde@fiu.edu

## ABSTRACT

Even though roughly 50% of the world's population follows soccer, only 4% actively participates in the sport. At this junction is where SkillCourt rises. Creating and providing an interactive and informative athletic training system geared toward professional and amateur levels of soccer play was the goal of SkillCourt. To facilitate the availability of performance data a device was proposed that can quantify a user's physical exertion and play in statistics such as accuracy, force, and speed. In efforts towards accomplishing this task, the execution of creating what will be referred to as the SkillCourt Pad will be explored within this paper.

## KEYWORDS

Skillcourt, Arduino, Potentiometric Sensor, Velocity Sensor, Striking Surface.

## 1. INTRODUCTION

In 2013, soccer reached an estimated fan base of 3.5 billion people. With this size of a following, it is easy to see that soccer is one of, if not the largest and most beloved sport the world over. In 2006, FIFA conducted a global survey, known as the Big Count, aiming to determine the count of soccer players [1]. The survey determined that there were roughly 265 million professional, registered, and unregistered soccer players worldwide.

### 1.1 Problem Statement

This paper describes our endeavor to design an athletic apparatus that caters to the requirements of the many involved and interested in the world of soccer. In this report, the authors describe the methods taken to create a durable apparatus for multiple terrains as well as lightweight to enhance the mobility of the gamepad itself. The focus was given to the addition of velocity, position, and force sensors as features to the SkillCourt Pad. The pads must be able to detect an accurate reading of these three sensors when the sports ball (primarily soccer) impacts the pad. There are also LED lights that will be implemented into the pads as markers to where the user should aim to hit. All these features are to be held inside the pads and protected so that the equipment does not become damaged. The velocity aspect will record the speed of the ball upon impact with the pad. The position attribute will discern which side of the pad is hit by the ball. The force feature will approximate the amount of force the pad is struck with by the projectile. All relevant information will be available to the user of the SkillCourt training system. The purpose of recording all this data is for both amateur and

professional athletes to have feedback of their performance in hopes of aiding with the improvement.

### 1.2 Motivation

The design for the SkillCourt pad is aimed primarily towards soccer. Soccer is the most played sport in the world, with an estimated fan base of 3.5 billion people worldwide. As for here, in the United States, the popularity of soccer has been on the rise since the world cup of 1994 which was hosted by the United States. Thus, the market for soccer equipment is always on the rise. The functionality of the SkillCourt pad would catch the attention of just about any type of soccer player, from beginners to professionals. For the beginners, it could be used as more of a game comparing individual scores, since one way of using the design would be to track how many times the target was hit correctly. Whereas for the professionals, the design is useful for group training or even individual training focusing on improving fundamental soccer skills such as passing, accuracy, power, and reaction time.

Additional motivation for our efforts include expanding upon the original design given to us by the proprietor of SkillCourt LLC., Gudmundur Orn Traustason [2]. To assist us in this endeavor we must follow the patent published on February 2, 2016. The goal of the design is to be able to reach the largest group of individuals possible. Since the differences in terrains and climates are strongly considered in the design as well as durability and mobility, there should not be any problems in reaching different countries that have harsh climate conditions. As well, the SkillCourt pad is planned to be available to both soccer clubs and school systems, with the intention of improving the skill level of soccer players globally.

### 1.3 Literature Survey

#### 1.3.1 Position Sensing

Position sensors are used to measure the distance a body travels from a reference location. Many methodologies for determining position exist, including Potentiometric, Capacitive, Linear Voltage Differential Transformers, Magnetostrictive, Eddy Current, Hall Effect, Fiber-Optic, and Optical [3]. Though many methods exist, few present any reasonable functionality within the SkillCourt Pad ecosystem. The clear majority of the available methods could not work within our requirements. Many methods require properties that a soccer ball does not possess (such as electrical capacitance for capacitive position sensing or a magnetic field for Hall Effect, Eddy Current, or Magnetostrictive position sensing). While other methods simply measure relative

distance variations and would not be applicable to determining the impact position upon a surface.

One promising method is the potentiometric, or resistive-based position sensors, as they work based on applied pressure rather than any electromagnetism phenomenon. Potentiometric Sensors work on the principle of a semi-flexible material deforming, causing a grid of electrodes to make contact providing a coordinate position upon a plane based on an output voltage.

While still maintaining a similar level of accuracy as a resistive touch screen, a series of ultrasound (US) sensors could be used in a method called triangulation. With the use of two or three US sensors, a bit of geometry, and trigonometry, an accurate position within a coordinate system, this would be applied to the striking surface, can be achieved. Finally, a more binary state position sensing can be achieved with the use of force sensors. With the inclusion of multiple force sensors, a comparison of the force readouts of all sensors can provide a general location, left or right, top or bottom, of where the soccer ball made contact.

### 1.3.2 Materials

Due to the nature of the pads use, as well as its sensitive internal electronic components, the general design of the pad incorporates an outer shell of a single material that can house several layers of other materials. These inner materials would primarily function to give incoming projectiles a surface to rebound off with as much energy as possible and to protect internal electronics from all shock received from the strike of a projectile.

Initially, the first choice to act as a casing was wood due to its cost and ease to work with. However, wood would degrade over time and would not do a sufficient job of protecting internals from external elements. Carbon fiber would be the ideal choice. However the process to mold carbon fiber is extremely costly and outside of the realm of our capabilities. The best choice for our purposes was concluded to be aluminum. Aluminum is easy to manipulate, oxidizes only external layers, has good yield stress for our purposes, and quite affordable [4].

Internal materials consist of two acrylic layers, one being Lexan due to its high-stress tolerance and flexibility, and a second layer to support the initial layer of Lexan as well as to sandwich the sensors. To protect the electronics two material types were explored, rubbers and foams. Polysiloxane polymers, or Silicone as it is commonly known, come in several forms such as gels, resins, fluids and elastomers. For the needs of SkillCourt, elastomers, also known as rubber, were researched. Silicone rubber is an inorganic material not comprised of carbon bonds. Instead it uses silicon and oxygen bonds that are stronger and more flexible than the bonds found in organic rubbers. This allows silicone rubbers to have a higher tolerance to changes in temperature, has a longer lifespan than common rubber, and promotes a higher resilience to ozone and ultraviolet environments [5]. Along with this resilience comes the ability to tailor the silicon rubber formula to the needs of the user, such as altering the tear strength, elongation and compression the material will experience, and the temperature ranges it must tolerate. In industry, there are two major types of silicone rubber, Liquid Silicone Rubber (LSR) and High Consistency Rubber (HCR). For the purposes of SkillCourt, HCR was considered due

to its lower cost, broader range of temperature resilience, and better compression set resistance. Due to weight considerations, though, the rubber option is less intriguing and a path towards some form of polyurethane or polystyrene foam was chosen.

### 1.3.3 Velocity Sensors

Velocity sensors are used to calculate how fast an object is moving. Velocimeters are typically defined as a device for measuring speed, as for fluid flow or sound, but there are some that do measure the speed of a moving object. One type of velocimeter that could be of use are laser surface velocimeters. The purpose of the velocity sensor in the design would be to record the velocity of the ball as it meets the pad. Now, the only problem with this meter is that it is a non-contact optical speed sensor measuring velocity and length of moving surfaces, but the meter uses the Doppler Effect phenomenon which is quite helpful for this problem. This leads to another velocity sensor that uses the Doppler Effect HB100 Doppler Speed Sensor [6]. This sensor can record the speed of an object that is coming at it from tens of meters away which is ideal due to the scoring area in soccer generally, being within 25 meters of the goal posts.

## 1.4 Current Benefits

As described in this report, the current SkillCourt Pad is capable of measuring the forces applied by a soccer ball. Improvements were also made in the overall construction of the Pad, being capable of withstanding multiple impacts without falling apart as previously familiar. Implementing all the necessary electronics within the Pad's internal structure aided in the improved portability of the Pad, removing external wires from the system and one less source of failure.

## 2. DESIGN

### 2.1 Dimensions

With portability and modularity being an important aspect of the SkillCourt Pad, the footprint of the design will be a defining specification of this product. For modularity purposes, a regular polygonal shape was desired to aid in a tessellating configuration. With a rectangular design, multiple pads can be used in conjunction with one another to produce a larger training area both outdoors and indoors. At 36" wide by 18" tall (91.5 cm by 45.75 cm) the pad will provide a realistic passing area, as these dimensions were chosen to mimic the average stance of a soccer player expecting a pass. The thickness of the pad will be largely dependent upon the volume requirements of the included electronics, but a goal of less than 3" thick (7.5 cm) is desired.

### 2.2 Materials

Within professional soccer play, an exerted force of 315 lbf (1420 N) upon the soccer ball is not uncommon, as such designing towards sustaining a minimum of these expectant forces is required. As well as designing towards the expectant forces, a desired feature of the SkillCourt Pad will be interactive illuminating forward faces, because of this a material with translucent properties and strength rated to sustain dynamic impacts of 315 lbf (1420 N) is desirable.

As portability and outdoor use are concerns as well, a lightweight chassis that will also sustain the perils of weathering is required. The chassis would also have to endure impact forces

of up to 315 lbf (1420 N), as previously stated above. Achieving this task would come done to either a metal casing or plastic mold. For this design, a choice of aluminum was made, which brings another concern along with it, temperature.

Finally, protecting the electronics from damaging vibrations. Achieving this problem will be the use of a silicone rubber mat or a foam insert to embed the LED's inside, immediately behind the impact surface, and a high impact foam rear housing where most included electronics would be placed.

## 2.3 Electronics

Force sensors, velocity sensors, position sensors, embedded electronics, and a power supply. A fully enclosed product is the goal for the SkillCourt Pad when it comes to the electronics. As discussed above, the force sensors will be required to register a reading, at least, up to 315 lbf (1420 N). Flexible piezoresistive film force sensors will be used to aid in the pads slim thickness as well as provide an accurate readout of the applied forces.

Determining the velocity of an incoming soccer ball will be achieved using a velocity sensor, namely the HB100 Microwave Sensory. Many velocity sensors work around the principle of optical tracking, this approach does not work for the SkillCourt Pad, as the electronics will not be exposed externally. As such, a system that works around the Doppler effect was chosen. The use of the Doppler effect also poses a challenge though, any object approaching the sensor perpendicularly will not be registered. Fortunately, the sensor will be placed parallel with the striking surface, as readings of any object moving perpendicular to the surface, is undesired.

Detecting the location of impact on the striking surface provides increased functionality of the SkillCourt Pad, in the sense that a single pad can simulate multiple striking zones. An example being, in soccer, when players are passing the soccer ball to another player, special attention must be taken as to which foot they are passing to, as this can be the determining factor between a successful goal and a missed pass. Simulating this scenario in the SkillCourt Pad simply requires the designation between a left and right side, emulating a pass to the left or right foot of a teammate. To achieve this level of position detection no additional electronics were required as a comparison between the readouts of the multiple force sensors can dictate a general location, whether that be more force on the left or right side, of where the ball struck the surface. Another use case for position detection was to aid in the calculation of an accurate force reading. With multiple force sensors located in randomly distributed locations, the readings obtained would not be the true force exerted by the soccer ball, due to the force being equally distributed and not being directly applied to an individual force sensor. As such, if an accurate position of impact is known, statistical methods could be applied to calculate an accurate force. This approach would require the use of either a potentiometric position sensor or a triangulation method using sonar sensors.

Other embedded electronics used within the SkillCourt Pad design were an Atmel based microcontroller, led strips, ambient light sensors, and an enclosed power bank. Due to our desire for the SkillCourt Pad to be a training device, a method of

communication between the user and the pad must be available. Accomplishing this task will be a set of led strips behind the striking surface. In this way, the led strips will allow the user to understand whether the pad is expecting a hit and which side (full face, left or right), by lighting in different colors. The ambient light sensor will be used in conjunction with the led strips to vary their brightness in accordance with the surrounding light levels. A microcontroller was chosen as the core electronic to take all the input data available from the force, velocity, position, and ambient light sensors, and produce functional information for the SkillCourt Pad users. Atmel was chosen as the microcontroller manufacturer as the Arduino brand is a global giant and produces cheap, inexpensive hardware available to many. Finally, an internal battery bank was used to supply power to the whole system, allowing for outdoor and indoor use, even if an external power source is unavailable.

## 3. DESIGN ANALYSIS

### 3.1 Component Design

Due to a simplistic design footprint, namely rectangular, all the components are designed with the same 36" x 15" frame while the thickness was adjusted to maintain a Factor of Safety (FoS) above one.

#### 3.1.1 Striking Surface

The proper translation of the experienced impact force is critical for accurate force readings. Achieving this goal meant the use of two different sheets of plastic: acrylic and polycarbonate, and a spacer between the sheets that will be used to focus the applied force towards the force sensors. The exposed surface was chosen to be Lexan, a polycarbonate derivative, due to its capabilities in withstanding high impact forces and the support surface was selected to be Plexiglass, an acrylic derivative, to provide a more rigid backing for the striking surface. Both sheets are designed at a thickness of 0.093".

#### 3.1.2 Vibration Isolation

Due to the high impact forces that are to be expected, vibrations within the pad are inevitable. Dampening the vibrational effects upon the electronics is required for the longevity and accuracy of the electronics [4]. Two sheets of foam are to be used, one for embedding the LED's behind the striking surface, and a second to house the electronics within. As the foam sheets are available in 2" thick sheets, that was the dimensions used in our product.

#### 3.1.3 Housing

Each sheet is independent of the sheets around them. Without a housing, the SkillCourt Pad would have no rigidity. Aluminum was chosen to provide the necessary rigidity as it is both lightweight and durable. The housing was designed in two parts, a front enclosure, and a rear panel. The front enclosure will include a 1" border that will expose the striking surface while also securing the pad within the housing, and the rear panel will be removable to allow ease of access to the internals. The aluminum chosen was a 0.125" thick sheet of 5052-H32 aluminum alloy.

#### 3.1.4 Structural Design

The striking surface will be designed with a spacer between the acrylic and polycarbonate sheets, with the goal of focusing the force of impact upon the force sensors, rather than across the entire support face of the polycarbonate sheet. Behind the

striking surface, the electronics will be housed and protected from vibration damage within the two foam sheets. These four layers will be enclosed by an aluminum sheet housing.

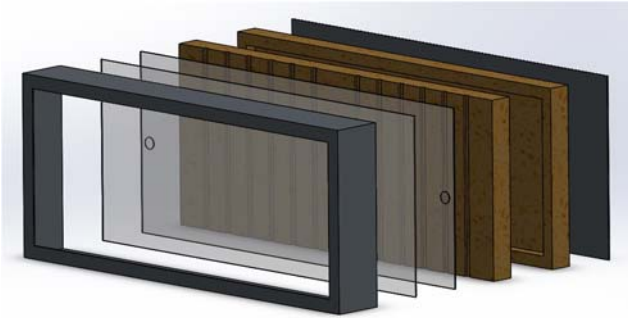


**Figure 1. Internal Components and Design of SkillCourt Pad**

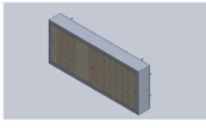
### 3.2 Finite Element Analysis

Validation of our design was provided using SolidWorks and the Simulation add-in. A static simulation was performed upon the Pad with the setup as described in ‘5.1.4 Structural Design’. The contact boundaries are defined as ‘No Penetration’, this allows slippage between surfaces without penetration, for all but one coincident contact surface, the aluminum enclosure and rear panel are defined as ‘Bonded’, no motion of parts relative to each other.

The pad was supported with a fixed geometry across the rear panel, simulating a condition of being mounted on a wall. A force of 1418 N was applied at the center of the striking surface perpendicular to the plane. A standard mesh was applied and the simulation was run, the results obtained were as follows.

Through the process of using the SolidWorks Simulation features, data was obtained pertaining to applied and resultant forces that occurred within the system, the strain that the system underwent, and the deflection observed upon the components of the system.

**Table 1. Loading Conditions for the Support and Applied Forces of the Proposed SkillCourt Pad Design**

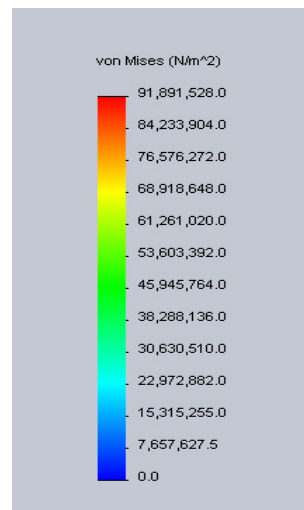
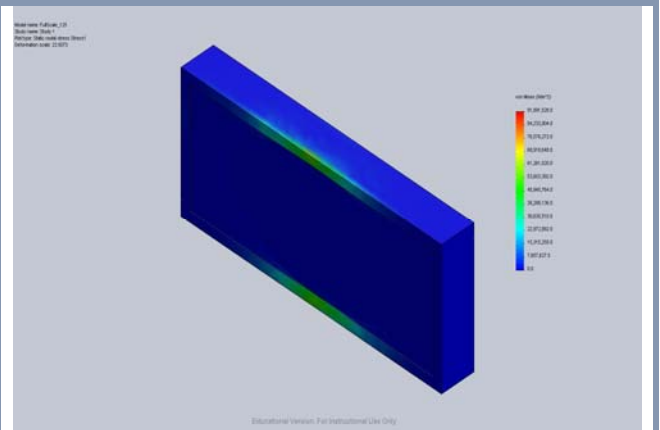
Fixture name	Fixture Image	Fixture Details		
<b>Fixed-1</b>		<b>Entities: 1 face(s)</b> <b>Type: Fixed Geometry</b>		
<b>Resultant Forces</b>				
<b>Components</b>	<b>X</b>	<b>Y</b>	<b>Z</b>	<b>Resultant</b>
<b>Reaction force</b>	-0.178337 mN	0.206292 mN	1418 N	1418 N

Load name	Load Image	Load Details
<b>Force-1</b>		<b>Reference: Face&lt; 1 &gt;</b> <b>Type: Apply force</b> <b>Values: —, 1418, — N</b>

As stated above, representing a professional kick localized towards the center of the striking surface, a force of 1418 N was applied perpendicularly towards the striking surface located at the geometric center of the plane and the rear panel has an applied fixed geometry support structure.

**Table 2. Stress Analysis of the Proposed SkillCourt Pad Design**

Name	Type	Min	Max
Stress1	VON: von Mises Stress	0.0150068 N/m <sup>2</sup> Node: 4991	9.18915e+007 N/m <sup>2</sup> Node: 9819



**FullScale\_125-Study 1-Stress-Stress1**

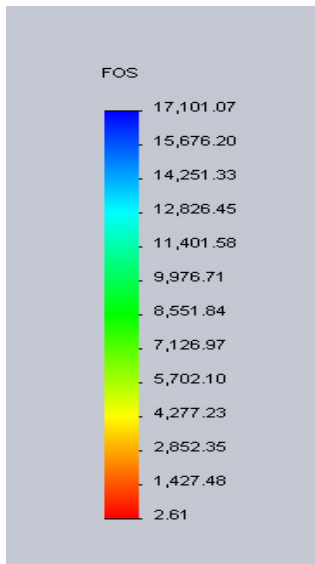
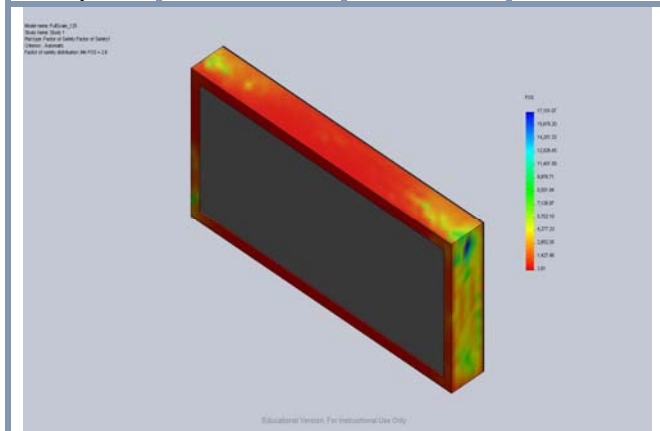
As seen from the data obtained through SolidWorks Report feature, the striking surface has an applied force of 1418 N, and

the rear panel absorbs a resultant force of 1418 N. Slight resultant forces in the x and y directions are likely results of any deformation that will be discussed later in the report.

Stress analysis and a factor of safety calculations are used to validate and expose defects in mechanical design. As such, these two features were gathered from the simulation using Von Mises calculations. Our minimum observed factor of safety was 2.6, well above the necessary 1.0 and within any margin of error.

**Table 3. Factor of Safety of the Proposed SkillCourt Pad Design**

Name	Type	Min	Max
Factor of Safety1	Automatic	2.61178 Node: 9819	17101.1 Node: 7290



**FullScale\_125-Study 1-Factor of Safety-Factor of Safety1**

The deflection of the striking surface is important to take note of, as a deflection too large entails the striking surface contacting with the support surface at an undesired location leading to inaccurate force readings. An observed maximum deflection

across the entire system was 3.92 mm. This metric is not a system critical measurement; it lends itself more to a design criterion. This expected deflection must be considered when choosing the spacers between the striking surface and support surface.

## 4. ELECTRONICS

Ensuring accurate readings from the included force and velocity sensors is a required task in providing a quality product for end users. Accomplishing this task requires calibration of the sensors against known inputs and correlating the outputs from the sensors to the known values. Through this process, signal relationships are created, and desired measurements are possible.

### 4.1 HB100 Velocity Sensor Calibration

Calibration of the HB100 was done through the simplification of the Doppler equation:

$$F_d = 2V * \left(\frac{F_t}{c}\right) * \cos \theta \quad Eq. 1$$

In which,  $F_d$  is the Doppler frequency (the sensor input to the Arduino),  $V$  is the velocity of the target object (the output desired from sensor),  $F_t$  is the transition frequency (10.525 GHz for the HB100 sensor),  $c$  being the speed of light, and  $\theta$  is the angle between the target object and the normal axis of the sensor (assumed to be zero for simplification purposes). Once all conditions and assumptions are substituted into the equation, the velocity of the target object then becomes a function inversely related to the targets reflected Doppler frequency:

$$F_d = kV \quad Eq. 2$$

In this equation, constant  $k$  is found through substitution of all the values and is 19.49 for velocity in kilometers per hour (km/hr) or 31.36 for velocity in miles per hour (mph).

Though simple to implement, this method overlooks the effects of off angled strikes, causing slight inaccuracies in readings. This method also does not take into consideration variation in the supplied transmitted frequency. Due to both variables being set to a constant value, the accuracy of the readings will be hampered, but ultimately still useful for gauging player performance improvement. Possible improvements to this method of calibration would be to implement a method of determining the angle of the incoming target object as well as determining a correction factor for the theoretical relationship through real world testing.

### 4.2 Force Sensor Calibration

Flexiforce force sensors are designed, such that, as the applied force is increased, the resistance decreases causing an increase in signal reading. If comparing output signal to resistance, the outcome is a power relation. This type of relationship is too sporadic in nature, as large changes in resistance are seen at low input forces with very little difference in resistance at high force inputs. For this reason, Flexiforce recommends relating the conductance of their force sensors to the input force, conductance being the inverse of resistance. Through this method, a linear calibration curve can be found and used to relate the force sensor signal to an applied force accurately.

Calculating the calibration curve for the force sensor required placing weights of known values atop a platform, whose

additional weight was taken into consideration by attributing this unknown weight, from the platform, as the zero point. With each additional weight, a change in input signal was observed from the Arduino and correlated to a resistance value of the force sensor using a voltage divider circuit with a 10 kΩ resistor.

B	C	D	E
Force	Output	Resistance	Conductance
0	1	1023000	9.77517E-07
2.5	2	511000	1.95695E-06
5	5	203800	4.90677E-06
10	11	92090.52	1.08589E-05
15	16	63000	1.5873E-05
25	25	39960	2.5025E-05
35			#DIV/0!
45			#DIV/0!
55			#DIV/0!
80			#DIV/0!
105			#DIV/0!
140			#DIV/0!
175			#DIV/0!
220			#DIV/0!
265			#DIV/0!

```

Vout: 0.16
R2: 31000.00
zaw: 31
Vout: 0.15
R2: 32032.26
zaw: 31
Vout: 0.15
R2: 32032.26
zaw: 31
Vout: 0.15
R2: 32032.26
zaw: 31
Vout: 0.16
R2: 31000.00
zaw: 31
Vout: 0.15
R2: 32032.26
zaw: 32
Vout: 0.15
R2: 32032.26
zaw: 31
Vout: 0.15
R2: 32032.26
zaw: 31
Vout: 0.15
R2: 32032.26
zaw: 32

```

Figure 2. Collecting of Input Data from Force Sensor

With the data collected and plotted, a linear trend line can be graphed and the correlation equation is obtained. This correlation equation is then used in the program that runs on the hardware. The equation was found to be:

$$Force \cong 2 \times 10^6 * Conductance - 25 \quad Eq. 3$$

From this equation, the applied force is found with the units of pounds (lbs), to convert to kilograms, a conversion factor of 0.453592 can be multiplied to the found results.

Table 4. Gathered Experimental Data for Force Sensor Calibration

Force (lbs)	Input	Resistance	Conductance
0	1	1023000	9.78E-07
2.5	2	511000	1.96E-06
5	5	203800	4.91E-06
10	11	92091	1.09E-05
15	16	63000	1.59E-05
25	25	39960	2.50E-05
35	32	31000	3.23E-05
45	38	25947	3.85E-05
55	42	23381	4.28E-05
80	50	19480	5.13E-05
105	62	15516	6.44E-05
140	67	14284	7.00E-05
175	77	12299	8.13E-05
220	87	10770	9.28E-05
265	96	9667	1.03E-04

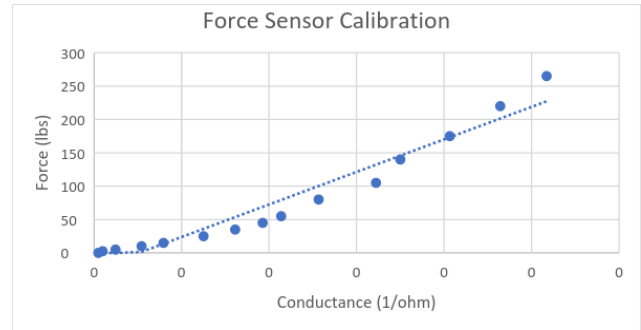


Figure 3. Experimental Force Sensor Calibration Curve

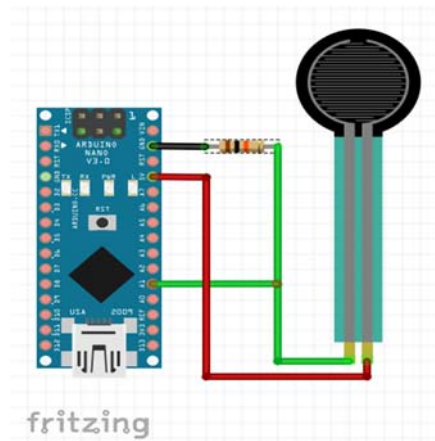


Figure 4. Voltage Divider Circuit Used for Calibration of a Force Sensor

## 5. PART LIST AND COST ANALYSIS

Table 5. Cost Analysis of SkillCourt Pad Prototype

Materials	Cost	Material	Cost	
Plywood	\$7.07	Lexan	\$16.31	
Foam	\$29.54	Plexiglass	\$9.55	
Fasteners	\$0.94	---	---	
			<b>Subtotal</b>	\$63.41
Electronics	Cost	Part	Cost	
Force Sensor	\$39.00	Arduino	\$34.99	
LED Strip	\$26.99	Battery	\$19.53	
Voltage Regulator	\$10.99	Resistors	\$0.55	
Switch	\$2.70	Battery Connector	\$0.60	
			<b>Subtotal</b>	\$135.35
			<b>Total</b>	\$198.76

## 6. FUTURE WORK

Most products are subject to various design and manufacturing improvements, and the SkillCourt Pad is no exception. Areas in which the pad can vastly improve are the material selection and quality as well as the electronics and their housing. There are materials available that are a better choice for the SkillCourt Pad enclosure such as carbon fiber which has a high strength to weight ratio. Carbon fiber also has a very heat tolerance depending on its treatment during manufacturing as well as low thermal expansion.

Similar improvements can be made for electronics. Currently, the foam enclosure is suitable enough to reduce shock to the electronics, however over time either due to mechanical fatigue or thermal deformation the foam would no longer be suitable as a means of dampening and would have to be replaced. To this end, another means of housing the electronics could be implemented such as suspending the electronics in the SkillCourt Pad itself or embedding them in some form of silicone. For example, a brand name Silicone rubber known as Dragon Skin has satisfactory mechanical and thermal properties suitable for acting as an enclosure.

## 7. ACKNOWLEDGMENTS

The authors extend their thanks to SkillCourt LLC and Guðmundur Traustason, who sponsored the project and holds the intellectual property (patents and trademark rights) as the creator of SkillCourt projects.

## 8. REFERENCES

- [1] Kunz, Matthias. "Big Count." FIFA Magazine (2007): pp. 10-15.
- [2] Method and Apparatus for a User-configurable Athletic Training Apparatus, by Traustason, Guðmundur Orn, assignee. (2013 Feb. 18). *Patent Number US20160045800A1* [Online]. Available: <https://www.google.com/patents/US20160045800>
- [3] Jain, Preeti. "Position Sensor: Types of Position Sensor." *Engineers Garage*. 28 Mar. 2013. Web. 16 Oct. 2016.
- [4] Lucas, George F., and David A. Stubbs. *Nontraditional Methods of Sensing Stress, Strain, and Damage in Materials and Structures*. West Conshohocken, PA: ASTM, 1997.
- [5] Jemian, WA, BZ Jang, and JS Chou. *Testing, Simulation, and Interpretation of Materials Impact Characteristics*. Auburn University, Auburn, AL: ASTM, 1986.
- [6] V.C. Nyugen, D.K. Dinh, and V.A. Le, "Length and speed detection using microwave motion sensor", in *ATC*, Hanoi, 2014.

# SkillCourt Pad Design

Alexander Diaz, Sebastian Maciel, Sabri Tosunoglu, Pradeep Shinde

Department of Mechanical and Materials Engineering  
Florida International University  
10555 West Flagler Street  
Miami, Florida 33174

adiaz357@fiu.edu, smaci009@fiu.edu, tosun@fiu.edu, pshinde@fiu.edu

## ABSTRACT

Even though roughly 50% of the world's population follows soccer, only 4% actively participates in the sport. At this junction is where SkillCourt rises. Creating and providing an interactive and informative athletic training system geared toward professional and amateur levels of soccer play was the goal of SkillCourt. To facilitate the availability of performance data a device was proposed that can quantify a user's physical exertion and play in statistics such as accuracy, force, and speed. In efforts towards accomplishing this task, the execution of creating what will be referred to as the SkillCourt Pad will be explored within this paper.

## KEYWORDS

Skillcourt, Arduino, Potentiometric Sensor, Velocity Sensor, Striking Surface.

## 1. INTRODUCTION

In 2013, soccer reached an estimated fan base of 3.5 billion people. With this size of a following, it is easy to see that soccer is one of, if not the largest and most beloved sport the world over. In 2006, FIFA conducted a global survey, known as the Big Count, aiming to determine the count of soccer players [1]. The survey determined that there were roughly 265 million professional, registered, and unregistered soccer players worldwide.

### 1.1 Problem Statement

This paper describes our endeavor to design an athletic apparatus that caters to the requirements of the many involved and interested in the world of soccer. In this report, the authors describe the methods taken to create a durable apparatus for multiple terrains as well as lightweight to enhance the mobility of the gamepad itself. The focus was given to the addition of velocity, position, and force sensors as features to the SkillCourt Pad. The pads must be able to detect an accurate reading of these three sensors when the sports ball (primarily soccer) impacts the pad. There are also LED lights that will be implemented into the pads as markers to where the user should aim to hit. All these features are to be held inside the pads and protected so that the equipment does not become damaged. The velocity aspect will record the speed of the ball upon impact with the pad. The position attribute will discern which side of the pad is hit by the ball. The force feature will approximate the amount of force the pad is struck with by the projectile. All relevant information will be available to the user of the SkillCourt training system. The purpose of recording all this data is for both amateur and

professional athletes to have feedback of their performance in hopes of aiding with the improvement.

### 1.2 Motivation

The design for the SkillCourt pad is aimed primarily towards soccer. Soccer is the most played sport in the world, with an estimated fan base of 3.5 billion people worldwide. As for here, in the United States, the popularity of soccer has been on the rise since the world cup of 1994 which was hosted by the United States. Thus, the market for soccer equipment is always on the rise. The functionality of the SkillCourt pad would catch the attention of just about any type of soccer player, from beginners to professionals. For the beginners, it could be used as more of a game comparing individual scores, since one way of using the design would be to track how many times the target was hit correctly. Whereas for the professionals, the design is useful for group training or even individual training focusing on improving fundamental soccer skills such as passing, accuracy, power, and reaction time.

Additional motivation for our efforts include expanding upon the original design given to us by the proprietor of SkillCourt LLC., Gudmundur Orn Traustason [2]. To assist us in this endeavor we must follow the patent published on February 2, 2016. The goal of the design is to be able to reach the largest group of individuals possible. Since the differences in terrains and climates are strongly considered in the design as well as durability and mobility, there should not be any problems in reaching different countries that have harsh climate conditions. As well, the SkillCourt pad is planned to be available to both soccer clubs and school systems, with the intention of improving the skill level of soccer players globally.

### 1.3 Literature Survey

#### 1.3.1 Position Sensing

Position sensors are used to measure the distance a body travels from a reference location. Many methodologies for determining position exist, including Potentiometric, Capacitive, Linear Voltage Differential Transformers, Magnetostrictive, Eddy Current, Hall Effect, Fiber-Optic, and Optical [3]. Though many methods exist, few present any reasonable functionality within the SkillCourt Pad ecosystem. The clear majority of the available methods could not work within our requirements. Many methods require properties that a soccer ball does not possess (such as electrical capacitance for capacitive position sensing or a magnetic field for Hall Effect, Eddy Current, or Magnetostrictive position sensing). While other methods simply measure relative

distance variations and would not be applicable to determining the impact position upon a surface.

One promising method is the potentiometric, or resistive-based position sensors, as they work based on applied pressure rather than any electromagnetism phenomenon. Potentiometric Sensors work on the principle of a semi-flexible material deforming, causing a grid of electrodes to make contact providing a coordinate position upon a plane based on an output voltage.

While still maintaining a similar level of accuracy as a resistive touch screen, a series of ultrasound (US) sensors could be used in a method called triangulation. With the use of two or three US sensors, a bit of geometry, and trigonometry, an accurate position within a coordinate system, this would be applied to the striking surface, can be achieved. Finally, a more binary state position sensing can be achieved with the use of force sensors. With the inclusion of multiple force sensors, a comparison of the force readouts of all sensors can provide a general location, left or right, top or bottom, of where the soccer ball made contact.

### 1.3.2 Materials

Due to the nature of the pads use, as well as its sensitive internal electronic components, the general design of the pad incorporates an outer shell of a single material that can house several layers of other materials. These inner materials would primarily function to give incoming projectiles a surface to rebound off with as much energy as possible and to protect internal electronics from all shock received from the strike of a projectile.

Initially, the first choice to act as a casing was wood due to its cost and ease to work with. However, wood would degrade over time and would not do a sufficient job of protecting internals from external elements. Carbon fiber would be the ideal choice. However the process to mold carbon fiber is extremely costly and outside of the realm of our capabilities. The best choice for our purposes was concluded to be aluminum. Aluminum is easy to manipulate, oxidizes only external layers, has good yield stress for our purposes, and quite affordable [4].

Internal materials consist of two acrylic layers, one being Lexan due to its high-stress tolerance and flexibility, and a second layer to support the initial layer of Lexan as well as to sandwich the sensors. To protect the electronics two material types were explored, rubbers and foams. Polysiloxane polymers, or Silicone as it is commonly known, come in several forms such as gels, resins, fluids and elastomers. For the needs of SkillCourt, elastomers, also known as rubber, were researched. Silicone rubber is an inorganic material not comprised of carbon bonds. Instead it uses silicon and oxygen bonds that are stronger and more flexible than the bonds found in organic rubbers. This allows silicone rubbers to have a higher tolerance to changes in temperature, has a longer lifespan than common rubber, and promotes a higher resilience to ozone and ultraviolet environments [5]. Along with this resilience comes the ability to tailor the silicon rubber formula to the needs of the user, such as altering the tear strength, elongation and compression the material will experience, and the temperature ranges it must tolerate. In industry, there are two major types of silicone rubber, Liquid Silicone Rubber (LSR) and High Consistency Rubber (HCR). For the purposes of SkillCourt, HCR was considered due

to its lower cost, broader range of temperature resilience, and better compression set resistance. Due to weight considerations, though, the rubber option is less intriguing and a path towards some form of polyurethane or polystyrene foam was chosen.

### 1.3.3 Velocity Sensors

Velocity sensors are used to calculate how fast an object is moving. Velocimeters are typically defined as a device for measuring speed, as for fluid flow or sound, but there are some that do measure the speed of a moving object. One type of velocimeter that could be of use are laser surface velocimeters. The purpose of the velocity sensor in the design would be to record the velocity of the ball as it meets the pad. Now, the only problem with this meter is that it is a non-contact optical speed sensor measuring velocity and length of moving surfaces, but the meter uses the Doppler Effect phenomenon which is quite helpful for this problem. This leads to another velocity sensor that uses the Doppler Effect HB100 Doppler Speed Sensor [6]. This sensor can record the speed of an object that is coming at it from tens of meters away which is ideal due to the scoring area in soccer generally, being within 25 meters of the goal posts.

## 1.4 Current Benefits

As described in this report, the current SkillCourt Pad is capable of measuring the forces applied by a soccer ball. Improvements were also made in the overall construction of the Pad, being capable of withstanding multiple impacts without falling apart as previously familiar. Implementing all the necessary electronics within the Pad's internal structure aided in the improved portability of the Pad, removing external wires from the system and one less source of failure.

## 2. DESIGN

### 2.1 Dimensions

With portability and modularity being an important aspect of the SkillCourt Pad, the footprint of the design will be a defining specification of this product. For modularity purposes, a regular polygonal shape was desired to aid in a tessellating configuration. With a rectangular design, multiple pads can be used in conjunction with one another to produce a larger training area both outdoors and indoors. At 36" wide by 18" tall (91.5 cm by 45.75 cm) the pad will provide a realistic passing area, as these dimensions were chosen to mimic the average stance of a soccer player expecting a pass. The thickness of the pad will be largely dependent upon the volume requirements of the included electronics, but a goal of less than 3" thick (7.5 cm) is desired.

### 2.2 Materials

Within professional soccer play, an exerted force of 315 lbf (1420 N) upon the soccer ball is not uncommon, as such designing towards sustaining a minimum of these expectant forces is required. As well as designing towards the expectant forces, a desired feature of the SkillCourt Pad will be interactive illuminating forward faces, because of this a material with translucent properties and strength rated to sustain dynamic impacts of 315 lbf (1420 N) is desirable.

As portability and outdoor use are concerns as well, a lightweight chassis that will also sustain the perils of weathering is required. The chassis would also have to endure impact forces

of up to 315 lbf (1420 N), as previously stated above. Achieving this task would come done to either a metal casing or plastic mold. For this design, a choice of aluminum was made, which brings another concern along with it, temperature.

Finally, protecting the electronics from damaging vibrations. Achieving this problem will be the use of a silicone rubber mat or a foam insert to embed the LED's inside, immediately behind the impact surface, and a high impact foam rear housing where most included electronics would be placed.

## 2.3 Electronics

Force sensors, velocity sensors, position sensors, embedded electronics, and a power supply. A fully enclosed product is the goal for the SkillCourt Pad when it comes to the electronics. As discussed above, the force sensors will be required to register a reading, at least, up to 315 lbf (1420 N). Flexible piezoresistive film force sensors will be used to aid in the pads slim thickness as well as provide an accurate readout of the applied forces.

Determining the velocity of an incoming soccer ball will be achieved using a velocity sensor, namely the HB100 Microwave Sensory. Many velocity sensors work around the principle of optical tracking, this approach does not work for the SkillCourt Pad, as the electronics will not be exposed externally. As such, a system that works around the Doppler effect was chosen. The use of the Doppler effect also poses a challenge though, any object approaching the sensor perpendicularly will not be registered. Fortunately, the sensor will be placed parallel with the striking surface, as readings of any object moving perpendicular to the surface, is undesired.

Detecting the location of impact on the striking surface provides increased functionality of the SkillCourt Pad, in the sense that a single pad can simulate multiple striking zones. An example being, in soccer, when players are passing the soccer ball to another player, special attention must be taken as to which foot they are passing to, as this can be the determining factor between a successful goal and a missed pass. Simulating this scenario in the SkillCourt Pad simply requires the designation between a left and right side, emulating a pass to the left or right foot of a teammate. To achieve this level of position detection no additional electronics were required as a comparison between the readouts of the multiple force sensors can dictate a general location, whether that be more force on the left or right side, of where the ball struck the surface. Another use case for position detection was to aid in the calculation of an accurate force reading. With multiple force sensors located in randomly distributed locations, the readings obtained would not be the true force exerted by the soccer ball, due to the force being equally distributed and not being directly applied to an individual force sensor. As such, if an accurate position of impact is known, statistical methods could be applied to calculate an accurate force. This approach would require the use of either a potentiometric position sensor or a triangulation method using sonar sensors.

Other embedded electronics used within the SkillCourt Pad design were an Atmel based microcontroller, led strips, ambient light sensors, and an enclosed power bank. Due to our desire for the SkillCourt Pad to be a training device, a method of

communication between the user and the pad must be available. Accomplishing this task will be a set of led strips behind the striking surface. In this way, the led strips will allow the user to understand whether the pad is expecting a hit and which side (full face, left or right), by lighting in different colors. The ambient light sensor will be used in conjunction with the led strips to vary their brightness in accordance with the surrounding light levels. A microcontroller was chosen as the core electronic to take all the input data available from the force, velocity, position, and ambient light sensors, and produce functional information for the SkillCourt Pad users. Atmel was chosen as the microcontroller manufacturer as the Arduino brand is a global giant and produces cheap, inexpensive hardware available to many. Finally, an internal battery bank was used to supply power to the whole system, allowing for outdoor and indoor use, even if an external power source is unavailable.

## 3. DESIGN ANALYSIS

### 3.1 Component Design

Due to a simplistic design footprint, namely rectangular, all the components are designed with the same 36" x 15" frame while the thickness was adjusted to maintain a Factor of Safety (FoS) above one.

#### 3.1.1 Striking Surface

The proper translation of the experienced impact force is critical for accurate force readings. Achieving this goal meant the use of two different sheets of plastic: acrylic and polycarbonate, and a spacer between the sheets that will be used to focus the applied force towards the force sensors. The exposed surface was chosen to be Lexan, a polycarbonate derivative, due to its capabilities in withstanding high impact forces and the support surface was selected to be Plexiglass, an acrylic derivative, to provide a more rigid backing for the striking surface. Both sheets are designed at a thickness of 0.093".

#### 3.1.2 Vibration Isolation

Due to the high impact forces that are to be expected, vibrations within the pad are inevitable. Dampening the vibrational effects upon the electronics is required for the longevity and accuracy of the electronics [4]. Two sheets of foam are to be used, one for embedding the LED's behind the striking surface, and a second to house the electronics within. As the foam sheets are available in 2" thick sheets, that was the dimensions used in our product.

#### 3.1.3 Housing

Each sheet is independent of the sheets around them. Without a housing, the SkillCourt Pad would have no rigidity. Aluminum was chosen to provide the necessary rigidity as it is both lightweight and durable. The housing was designed in two parts, a front enclosure, and a rear panel. The front enclosure will include a 1" border that will expose the striking surface while also securing the pad within the housing, and the rear panel will be removable to allow ease of access to the internals. The aluminum chosen was a 0.125" thick sheet of 5052-H32 aluminum alloy.

#### 3.1.4 Structural Design

The striking surface will be designed with a spacer between the acrylic and polycarbonate sheets, with the goal of focusing the force of impact upon the force sensors, rather than across the entire support face of the polycarbonate sheet. Behind the

striking surface, the electronics will be housed and protected from vibration damage within the two foam sheets. These four layers will be enclosed by an aluminum sheet housing.

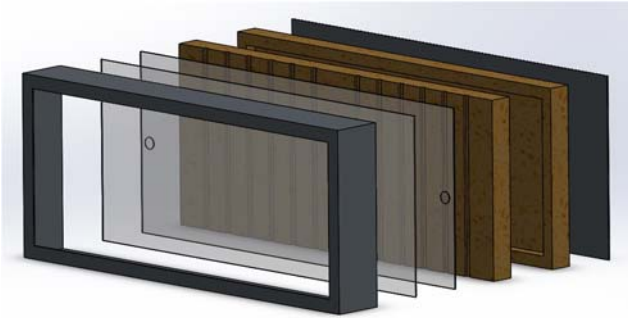


**Figure 1. Internal Components and Design of SkillCourt Pad**

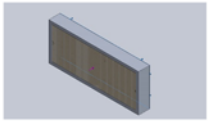
### 3.2 Finite Element Analysis

Validation of our design was provided using SolidWorks and the Simulation add-in. A static simulation was performed upon the Pad with the setup as described in ‘5.1.4 Structural Design’. The contact boundaries are defined as ‘No Penetration’, this allows slippage between surfaces without penetration, for all but one coincident contact surface, the aluminum enclosure and rear panel are defined as ‘Bonded’, no motion of parts relative to each other.

The pad was supported with a fixed geometry across the rear panel, simulating a condition of being mounted on a wall. A force of 1418 N was applied at the center of the striking surface perpendicular to the plane. A standard mesh was applied and the simulation was run, the results obtained were as follows.

Through the process of using the SolidWorks Simulation features, data was obtained pertaining to applied and resultant forces that occurred within the system, the strain that the system underwent, and the deflection observed upon the components of the system.

**Table 1. Loading Conditions for the Support and Applied Forces of the Proposed SkillCourt Pad Design**

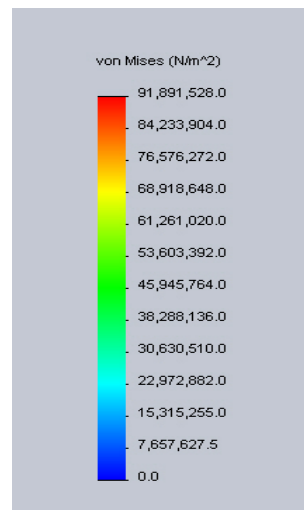
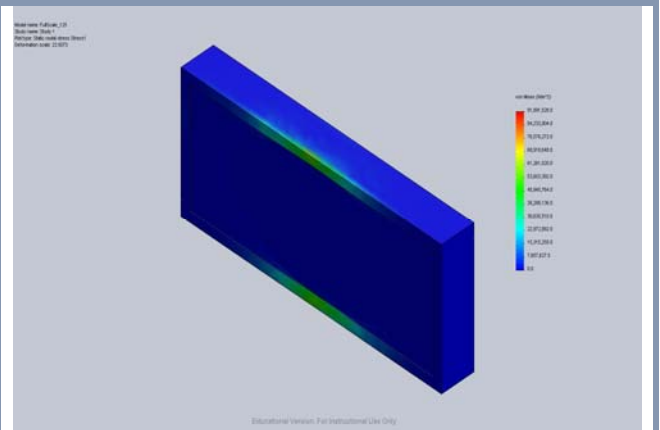
Fixture name	Fixture Image	Fixture Details		
<b>Fixed-1</b>		<b>Entities: 1 face(s)</b> <b>Type: Fixed Geometry</b>		
<b>Resultant Forces</b>				
<b>Components</b>	<b>X</b>	<b>Y</b>	<b>Z</b>	<b>Resultant</b>
<b>Reaction force</b>	-0.178337 mN	0.206292 mN	1418 N	1418 N

Load name	Load Image	Load Details
<b>Force-1</b>		<b>Reference: Face&lt; 1 &gt;</b> <b>Type: Apply force</b> <b>Values: —, 1418, — N</b>

As stated above, representing a professional kick localized towards the center of the striking surface, a force of 1418 N was applied perpendicularly towards the striking surface located at the geometric center of the plane and the rear panel has an applied fixed geometry support structure.

**Table 2. Stress Analysis of the Proposed SkillCourt Pad Design**

Name	Type	Min	Max
Stress1	VON: von Mises Stress	0.0150068 N/m <sup>2</sup> Node: 4991	9.18915e+007 N/m <sup>2</sup> Node: 9819



**FullScale\_125-Study 1-Stress-Stress1**

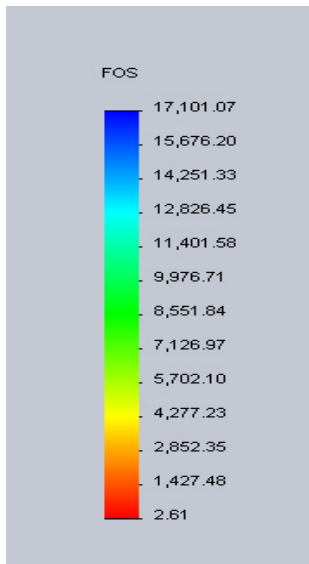
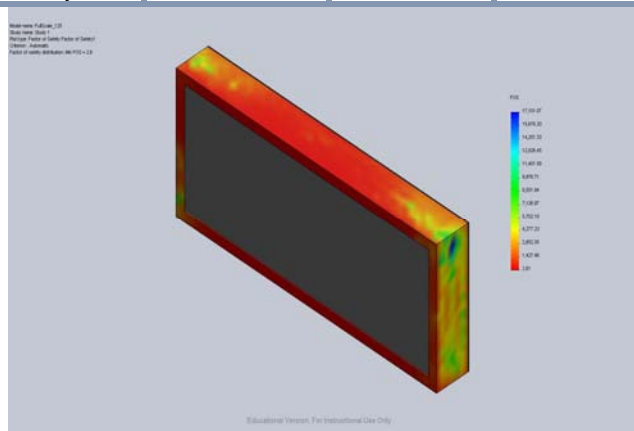
As seen from the data obtained through SolidWorks Report feature, the striking surface has an applied force of 1418 N, and

the rear panel absorbs a resultant force of 1418 N. Slight resultant forces in the x and y directions are likely results of any deformation that will be discussed later in the report.

Stress analysis and a factor of safety calculations are used to validate and expose defects in mechanical design. As such, these two features were gathered from the simulation using Von Mises calculations. Our minimum observed factor of safety was 2.6, well above the necessary 1.0 and within any margin of error.

**Table 3. Factor of Safety of the Proposed SkillCourt Pad Design**

Name	Type	Min	Max
Factor of Safety1	Automatic	2.61178 Node: 9819	17101.1 Node: 7290



**FullScale\_125-Study 1-Factor of Safety-Factor of Safety1**

The deflection of the striking surface is important to take note of, as a deflection too large entails the striking surface contacting with the support surface at an undesired location leading to inaccurate force readings. An observed maximum deflection

across the entire system was 3.92 mm. This metric is not a system critical measurement; it lends itself more to a design criterion. This expected deflection must be considered when choosing the spacers between the striking surface and support surface.

## 4. ELECTRONICS

Ensuring accurate readings from the included force and velocity sensors is a required task in providing a quality product for end users. Accomplishing this task requires calibration of the sensors against known inputs and correlating the outputs from the sensors to the known values. Through this process, signal relationships are created, and desired measurements are possible.

### 4.1 HB100 Velocity Sensor Calibration

Calibration of the HB100 was done through the simplification of the Doppler equation:

$$F_d = 2V * \left(\frac{F_t}{c}\right) * \cos \theta \quad Eq. 1$$

In which,  $F_d$  is the Doppler frequency (the sensor input to the Arduino),  $V$  is the velocity of the target object (the output desired from sensor),  $F_t$  is the transition frequency (10.525 GHz for the HB100 sensor),  $c$  being the speed of light, and  $\theta$  is the angle between the target object and the normal axis of the sensor (assumed to be zero for simplification purposes). Once all conditions and assumptions are substituted into the equation, the velocity of the target object then becomes a function inversely related to the targets reflected Doppler frequency:

$$F_d = kV \quad Eq. 2$$

In this equation, constant  $k$  is found through substitution of all the values and is 19.49 for velocity in kilometers per hour (km/hr) or 31.36 for velocity in miles per hour (mph).

Though simple to implement, this method overlooks the effects of off angled strikes, causing slight inaccuracies in readings. This method also does not take into consideration variation in the supplied transmitted frequency. Due to both variables being set to a constant value, the accuracy of the readings will be hampered, but ultimately still useful for gauging player performance improvement. Possible improvements to this method of calibration would be to implement a method of determining the angle of the incoming target object as well as determining a correction factor for the theoretical relationship through real world testing.

### 4.2 Force Sensor Calibration

Flexiforce force sensors are designed, such that, as the applied force is increased, the resistance decreases causing an increase in signal reading. If comparing output signal to resistance, the outcome is a power relation. This type of relationship is too sporadic in nature, as large changes in resistance are seen at low input forces with very little difference in resistance at high force inputs. For this reason, Flexiforce recommends relating the conductance of their force sensors to the input force, conductance being the inverse of resistance. Through this method, a linear calibration curve can be found and used to relate the force sensor signal to an applied force accurately.

Calculating the calibration curve for the force sensor required placing weights of known values atop a platform, whose

additional weight was taken into consideration by attributing this unknown weight, from the platform, as the zero point. With each additional weight, a change in input signal was observed from the Arduino and correlated to a resistance value of the force sensor using a voltage divider circuit with a 10 kΩ resistor.

B	C	D	E	
Force	Output	Resistance	Conductance	
0	1	1023000	9.77517E-07	Vout: 0.16 R2: 31000.00 zaw: 31
2.5	2	511000	1.95695E-06	Vout: 0.15 R2: 32032.26 zaw: 31
5	5	203800	4.90677E-06	Vout: 0.15 R2: 32032.26 zaw: 31
10	11	92090.52	1.08589E-05	Vout: 0.15 R2: 32032.26 zaw: 31
15	16	63000	1.5873E-05	Vout: 0.15 R2: 32032.26 zaw: 31
25	25	39960	2.5025E-05	Vout: 0.15 R2: 32032.26 zaw: 31
35			#DIV/0!	Vout: 0.16 R2: 31000.00 zaw: 31
45			#DIV/0!	Vout: 0.15 R2: 32032.26 zaw: 32
55			#DIV/0!	Vout: 0.16 R2: 31000.00 zaw: 31
80			#DIV/0!	Vout: 0.15 R2: 32032.26 zaw: 31
105			#DIV/0!	Vout: 0.15 R2: 32032.26 zaw: 31
140			#DIV/0!	Vout: 0.15 R2: 32032.26 zaw: 31
175			#DIV/0!	Vout: 0.15 R2: 32032.26 zaw: 31
220			#DIV/0!	Vout: 0.15 R2: 32032.26 zaw: 31
265			#DIV/0!	Vout: 0.15 R2: 32032.26 zaw: 32

Figure 2. Collecting of Input Data from Force Sensor

With the data collected and plotted, a linear trend line can be graphed and the correlation equation is obtained. This correlation equation is then used in the program that runs on the hardware. The equation was found to be:

$$Force \cong 2x10^6 * Conductance - 25 \quad Eq. 3$$

From this equation, the applied force is found with the units of pounds (lbs), to convert to kilograms, a conversion factor of 0.453592 can be multiplied to the found results.

Table 4. Gathered Experimental Data for Force Sensor Calibration

Force (lbs)	Input	Resistance	Conductance
0	1	1023000	9.78E-07
2.5	2	511000	1.96E-06
5	5	203800	4.91E-06
10	11	92091	1.09E-05
15	16	63000	1.59E-05
25	25	39960	2.50E-05
35	32	31000	3.23E-05
45	38	25947	3.85E-05
55	42	23381	4.28E-05
80	50	19480	5.13E-05
105	62	15516	6.44E-05
140	67	14284	7.00E-05
175	77	12299	8.13E-05
220	87	10770	9.28E-05
265	96	9667	1.03E-04

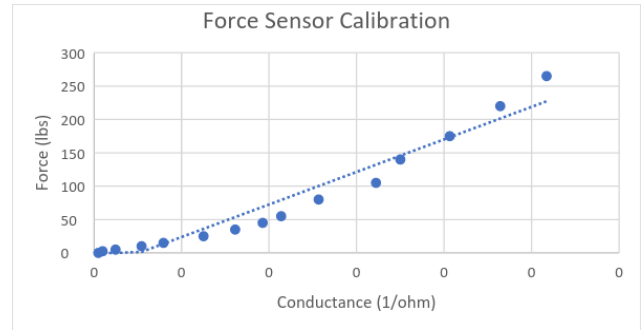


Figure 3. Experimental Force Sensor Calibration Curve

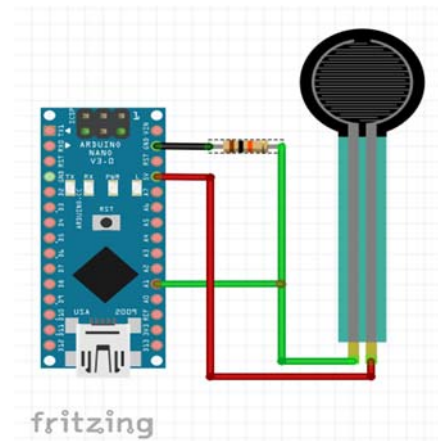


Figure 4. Voltage Divider Circuit Used for Calibration of a Force Sensor

## 5. PART LIST AND COST ANALYSIS

Table 5. Cost Analysis of SkillCourt Pad Prototype

Materials	Cost	Material	Cost
Plywood	\$7.07	Lexan	\$16.31
Foam	\$29.54	Plexiglass	\$9.55
Fasteners	\$0.94	---	---
			<b>Subtotal</b>
			\$63.41
Electronics	Cost	Part	Cost
Force Sensor	\$39.00	Arduino	\$34.99
LED Strip	\$26.99	Battery	\$19.53
Voltage Regulator	\$10.99	Resistors	\$0.55
Switch	\$2.70	Battery Connector	\$0.60
			<b>Subtotal</b>
			\$135.35
			<b>Total</b>
			\$198.76

## 6. FUTURE WORK

Most products are subject to various design and manufacturing improvements, and the SkillCourt Pad is no exception. Areas in which the pad can vastly improve are the material selection and quality as well as the electronics and their housing. There are materials available that are a better choice for the SkillCourt Pad enclosure such as carbon fiber which has a high strength to weight ratio. Carbon fiber also has a very heat tolerance depending on its treatment during manufacturing as well as low thermal expansion.

Similar improvements can be made for electronics. Currently, the foam enclosure is suitable enough to reduce shock to the electronics, however over time either due to mechanical fatigue or thermal deformation the foam would no longer be suitable as a means of dampening and would have to be replaced. To this end, another means of housing the electronics could be implemented such as suspending the electronics in the SkillCourt Pad itself or embedding them in some form of silicone. For example, a brand name Silicone rubber known as Dragon Skin has satisfactory mechanical and thermal properties suitable for acting as an enclosure.

## 7. ACKNOWLEDGMENTS

The authors extend their thanks to SkillCourt LLC and Guðmundur Traustason, who sponsored the project and holds the intellectual property (patents and trademark rights) as the creator of SkillCourt projects.

## 8. REFERENCES

- [1] Kunz, Matthias. "Big Count." FIFA Magazine (2007): pp. 10-15.
- [2] Method and Apparatus for a User-configurable Athletic Training Apparatus, by Traustason, Guðmundur Orn, assignee. (2013 Feb. 18). *Patent Number US20160045800A1* [Online]. Available: <https://www.google.com/patents/US20160045800>
- [3] Jain, Preeti. "Position Sensor: Types of Position Sensor." *Engineers Garage*. 28 Mar. 2013. Web. 16 Oct. 2016.
- [4] Lucas, George F., and David A. Stubbs. *Nontraditional Methods of Sensing Stress, Strain, and Damage in Materials and Structures*. West Conshohocken, PA: ASTM, 1997.
- [5] Jemian, WA, BZ Jang, and JS Chou. *Testing, Simulation, and Interpretation of Materials Impact Characteristics*. Auburn University, Auburn, AL: ASTM, 1986.
- [6] V.C. Nyugen, D.K. Dinh, and V.A. Le, "Length and speed detection using microwave motion sensor", in *ATC*, Hanoi, 2014.

# SkillCourt Autonomous Soccer Ball Reload Mechanism

Jose Perdomo, Adrian Sinanan, Tahsin Asgar, Rodrigo Arredondo, Sabri Tosunoglu

Department of Mechanical and Materials Engineering  
Florida International University  
10555 West Flagler Street  
Miami, Florida 33174

jperd033@fiu.edu, asina001@fiu.edu, tasga001@fiu.edu, rarre001@fiu.edu, tosun@fiu.edu

## ABSTRACT

In this paper, a reload mechanism for the autonomous SkillCourt ball launcher is proposed. SkillCourt is an up and coming soccer-training system used to develop player cognitive and decision-making skills using computer aided technology and automated feedback capabilities. By incorporating an autonomous ball delivery system, the goal is to improve the quality of training sessions. Furthermore, the project aims to improve the overall user experience, and allow multiple users to customize their own routines. This is accomplished by the reload mechanism's capability to track the user in motion, and interact with the SkillCourt software with little human interference.

Ball delivery systems are already common and widely used in sports such as tennis, football, and baseball. These devices have similar traits in means of function and purpose, but most lack autonomy and diversity in the complexity of delivery. For soccer, there are both advanced and basic mechanisms capable of various trick shots and passes currently available on the market. Unfortunately, most of these systems lack of autonomy and user based capabilities require human intervention. Not to mention the increasing costs of such systems may prevent households or academies from acquiring one.

For these reasons, the main objectives are reducing cost, improving motion capabilities of the ball delivery mechanism, independent loading and unloading of a ball, user tracking, and automatic delivery integration with the SkillCourt software. The team built and tested a prototype based on a commercially available system. The system's main features of tracking, auto loading, and SkillCourt software were implemented. Last, the continuous optimization and functionality of the system scrutinized.

## Keywords

Autonomous Ball Launcher, SkillCourt, OpenCV-Player Tracking

## 1. INTRODUCTION

Ball delivery systems are already widely used for many types of sports across the globe. These devices have similar traits in means of function and purpose, but many lack user interaction capabilities and customizations. The main design will address movement

capabilities of the ball delivery mechanism, independent loading and unloading of a ball, player motion tracking, and automatic delivery integration with the SkillCourt software. A prototype using concepts from commercially available launchers, as well as tracking software worked as expected.

## 2. Autonomous Ball Launcher

The industry of ball launching devices is very diverse and ranges across many sports, of which the biggest consumers are baseball and tennis. Currently, there are additional launchers for other sports such as soccer, volleyball, and football, although they lack intricacy and do not provide user feedback. These launchers have capabilities such as speed adjustment, trajectory customization, and a variety of unique shots and passes achieved through their respective systems. Some previous works considered are the Sidekick and First Pitch ball launching systems seen below in Figure 1.



Figure 1. Sidekick Ball Launcher

The user controls the ball's trajectory through the manipulation of the tire's speed and angular position of the mechanism.

Specifications will include structure of the launcher and its positional transition in the course of an operation. Though numerous systems are available, their higher cost limits athletes from affordable options. Consumers would desire a launcher that is affordable, provides a wide variety of features, and directly interacts with the user.

## 2.1 OpenCV- Player Tracking

OpenCV (Open Source Computer Vision Library) is an open source software library that is used in computer vision and learning applications. OpenCV supports Windows, Linux, MacOS, and Android operating systems, and interfaces with C, C++, Java, Python, or MATLAB. Additionally, this software library features algorithms used in face recognition, object identification, motion tracking, and three-dimensional object plotting, with potential for multiple subjects. OpenCV software brings a range of applications that are useful in the ball launcher's player tracking characteristic.

At Florida International University, an Electrical Engineering senior team featured this software in their American Football launcher, to track and estimate the position of a person attempting to catch the football. Their system consisted of two cameras that recorded the player's movements, while the software would track the player and rotate the ball launcher accordingly, seen below in Figure 4. Additionally, to estimate the distance between the ball launcher and the player, the concept of triangulation is used. This method allows for the accurate approximation of an object's distance and relative position using two or more points.



Figure 2. Autonomous Football Throwing Machine

## 2.2 Automatic Loading Machines

Automation for ball launchers does exist, but consists of a two-machine system where the balls are first collected by a loader and delivered to a launcher. These are prevalent in the tennis industry as tennis academies and training facilities use a large number of balls. If a person is to collect them individually, training sessions become interrupted and inefficient. For example, the Tennibot shown in Figure 5 is a patent pending robot that is able to identify tennis balls apart from different objects on the court.

Once identified, the loader will then gather up to seventy tennis balls autonomously, or via remote control. After the collection process is complete, the balls can be loaded back into the launcher using a bucket, net loading system, or manually. This concept can

be applied to soccer training by integrating a similar mechanism that will collect balls provided by the user, and then directly load the balls into the launcher.



Figure 3. Tennibot

## 2.3 Mobility and Tracking

The chief focus of the product is its ability to track a player in motion and accurately launch the ball. The machine is capable of determining the distance and pinpointing a player's position based on their movement while at the same time, delivering an accurate pass. This is possible due to the working range and mobility capabilities of the launcher.

The Launcher is able to rotate in terms of roll, pitch and yaw. For yaw, or oscillating around the vertical axis, the launcher is capable of rotating  $\pm 60$  degrees from its initial position. As for roll and pitch, or rotating along the z-axis and x-axis respectively, the launcher can rotate 45 degrees tilt in either direction. In addition to its maneuverability, the launcher has been fitted with a self-locking mechanism. This allows for five different types of preset soccer strikes and passes for a variance in play.

## 2.4 Reloading

The Ball Collection and reloading of the Ball Launcher is capable of storing up to five size No.5 soccer balls at any given time. This area of storage will then transfer the balls into the shooting segment automatically delivering a ball. The Ball Launcher will then fire a shot every 7 seconds in order to maintain a lively and continuous workout. In addition to a workout, with consumer use in mind, the reloading mechanism would be easily assembled and attached to the main component of the launcher and easily detach as needed.

## 2.5 SkillCourt Integration

SkillCourt is the main software selected to communicate with the ball launcher. SkillCourt provides a user feedback and timing system that encourages the trainer to improve reaction times and practice their skills.

Training drills can be used to integrate the launcher, reloading, and collection systems, with SkillCourt to time and test player's performance. The software allows the user to communicate with the launcher to begin a drill, and the collection device to complete

the drill, while providing various stats such as ball velocity and time of completion.

### 3. Design Components

The flow chart below illustrates the hardware used on the design. As shown on Figure 6, the main components are the Arduino UNO, and a stepper actuator. Other items used are a variety of sensors and LED technology. Once fitted to the frame, these allow for a simple but effective system. Using the Arduino, a continuous reloading process is created.

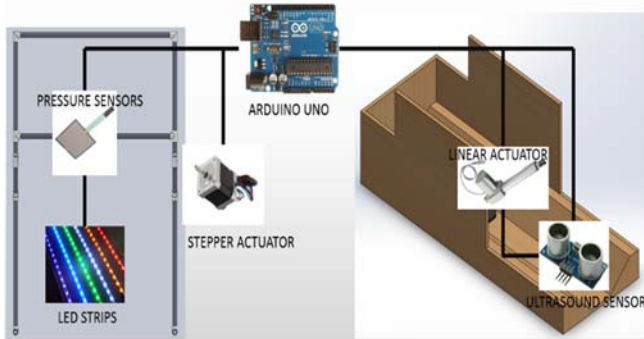


Figure 6. Triangulation Diagram

#### 3.1. OpenCV Motion Tracking System

As previously stated, OpenCV, an open source vision software, will be used for the main tracking and distance measuring algorithms. OpenCV works with several programming languages. Some of these include C, C++, and Python, which are the most common, and user friendly. A recent FIU EE senior team project based on motion tracking and distance measuring used this software. In their project, OpenCV interacts with two webcams to track the movement of a person. Likewise, using an Arduino, a servo motor rotates to aim the ball launcher.

Similarly, the SkillCourt ball launcher employs an Arduino and a single servo to achieve the third degree of freedom (i.e. yaw rotation) needed by the ball launcher. In order to calculate the position of a target, the triangulation method is used. As shown in Figure 7 below, there are two cameras on the same axis, at a fixed distance from each other. Using the angle provided OpenCV draws a line drawn from each camera to the object being tracked, thus creating a triangle from which a distance relative to the launcher is obtained.

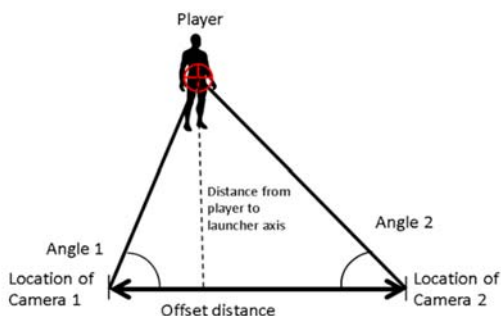


Figure 7. Triangulation Diagram

There is, however, an issue with the triangulation method, in regards to the distance approximation and accuracy range that it can provide. The accuracy of long distance measurements depends highly on the quality of the cameras used. As the object being tracked moves away from the cameras, the depth of field increases and the cameras struggle to focus on the object. Although high-end cameras are more efficient, it increases the cost of the system significantly.

Since the current SkillCourt training system does not utilize an extensive field area, the limit of the tracking device has been set to 20 yards. Therefore, using this distance measuring method is suitable for prototype purposes. As an alternative to using cameras, measuring distance via lasers can be very effective on stationary objects at long distances. However, with moving objects the time of flight of the laser can slow down the distance reading. These lasers provide many benefits but are far more expensive than the two-camera method as Laser distance measuring devices range in the hundredths. Consequently, the motion tracking and distance measuring with OpenCV is a more feasible option.

#### 3.2. Reloading Mechanism

Referring to the images below, Figures 8a and 8b depict the first iteration of the reloading system. In this design, there are two concepts from the SkillCourt ball launcher project adapted to the system. First, the receiving mechanism is composed of a wall curved in the shape of a wave that elevates a ball to a catching net. The ball then drops down to a rail that will hold and guide it to the next-section. Here, the transition of the ball from the loader, to the launcher system is controlled. As the ball rolls into position in the launcher, a piston then pushes it into the mechanism's flywheels propelling the ball to the target.

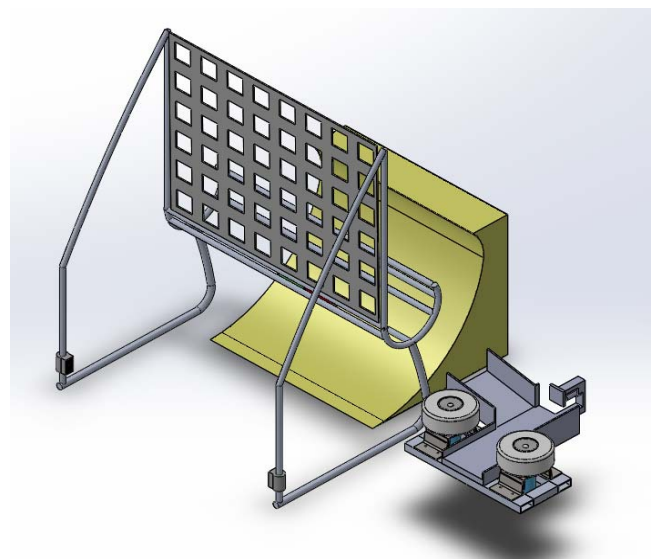
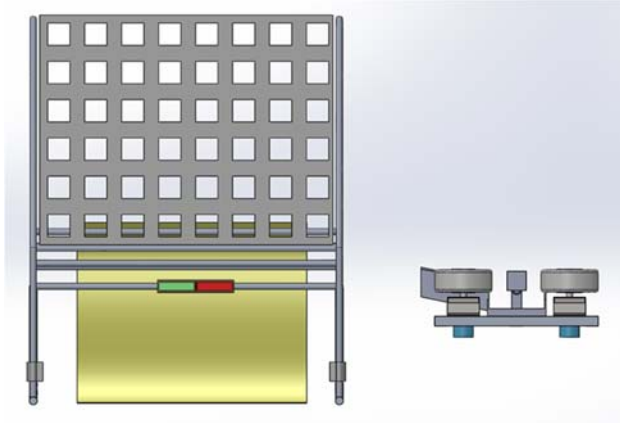


Figure 8a. Conceptual Design of SkillCourt Launcher System.



**Figure 8b.** Conceptual Design of SkillCourt Launcher System.

In addition to the previous systems, there will be sensors controlling and giving feedback to the player. When the ball goes in, an LED display lights up showing the player a green light if the ball properly reaches the rail. Similarly, a red light lights up if the ball does not reach the rail. In addition, there are other sensors and servos controlling the system. One of these is a pressure sensor, which activates an actuator when a ball is in the correct position before propelling it. Aiming to further improve the process and lower the cost of manufacturability, other changes are as follow:

- The connection between the launcher and the ramp was improved
- Actual placement for the linear actuator was changed
- Different sensor locations and orientations were tested in order to ensure optimal ball detection
- Cost efficient materials
- Easy assembly for consumer usage

The reloading mechanism has gone through several trial and error stages in order to position the ball correctly in the launcher. **Figure 9** represents the first iteration of a link between the net and the launcher system. This component is necessary in order to facilitate the ball's transition from the net to the launcher's linear actuator. Without it, the ball could be stuck in the rail, fall off the net, or transition to the wrong position.

If any of above, issues were to present themselves, manual feeding would be required. In order to reduce the load of friction for the ball, the edges of the link were made into curves that would follow the contour of the ball. With portability and consumers in mind, the ramp is also equipped with an interlocking connection in which it would “snap” into place as well as come apart for effortless assembly and transportation. Last, at the far end of the mechanism, there is a series of four circular protrusions, where the sensors that communicate with the loading mechanism are located. In essence, once the ball goes over the sensors, the actuator moves into position for the ball to line up properly into the slot.

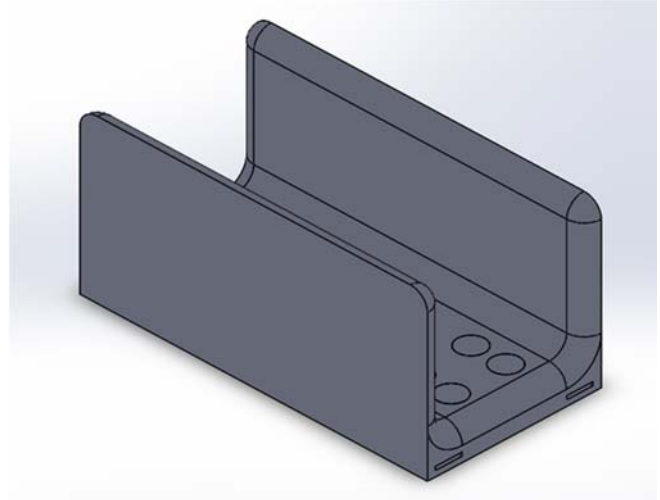


**Figure 9.** First iteration of reloading mechanism.

A simpler design was necessary due to time constraints, and the high cost of materials needed. Not to mention the challenging manufacturability of the component with the tools at our disposal. Considering these issues, a different approach was taken in which the functionality of the original design is implemented on the next iteration. Illustrated in **Figure 10**, in order to further reduce cost and ease manufacturability, the second iteration consists of flexible wood components and plastic.

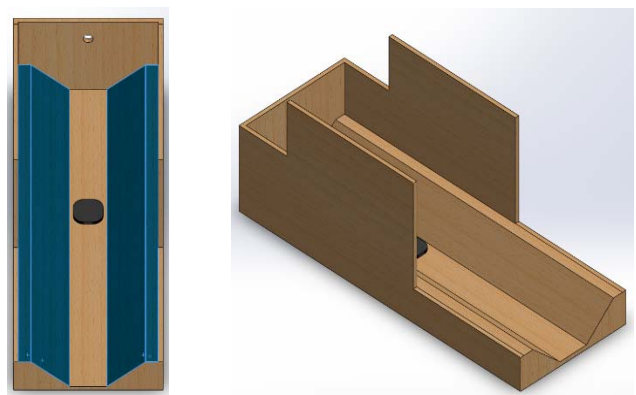


**Figure 10.** Top and Side Views of Reloading Mechanism

As seen in the images above, a single pressure sensor located on the ramp, notifies the launcher when a ball is ready in position before launch. When the ball triggers the pressure sensor, a linear actuator activates. This component is located behind the hole on the vertical wall shown on the image above. As the actuator moves, it pushes the balls into the launcher with a set time delay, feeding the launcher continuously. In order to guaranty the balls move along the path effortlessly, an inclined plane in the launching area is used to provide a path of less resistance for the balls to follow.

### 3.3. SkillCourt Software

Last, all of the aforementioned systems operate with the Skill Court software to establish full integration, in addition to data collection and user feedback. Compartments for the basic box unit and vertical collection system protect the relatively small wireless computers. These compartments are encased in a high impact resistant box, to ensure little to no damage to the computers during training sessions. Likewise, all other electrical components are positioned on various parts of the support stand capable of absorbing the impact force of a soccer ball.

Similarly, for the vertical collection system, the LED light strips can be re-positioned anywhere along the net, along the length of the half cylinder ramp, or along the supporting stand of the system. Next, velocity and acceleration sensors track ball characteristics in the data collection process in order to compare user performance over subsequent training sessions. Similar to the Skill wireless computers, these sensors require to be enclosed or be able to endure high impact forces. Obviously, there are many components that must be considered and be able to sustain any impact that could occur on any soccer field or training facility.

## 4. Integration of Global Design Elements

When discussing designs and their impact on the user and the environment, it is important to consider the components that went into the system and how they could affect people across the world. The materials chosen to construct the ball launcher have a significant effect on cost and environmental concerns. Ideally, cheap products and materials that minimize or eliminate any negative impact on the environment are to be used. Keeping this in mind, cheaper plastics such as PVC or clear extruded acrylic are considered. Eco-friendly plastics and cheaper metals such as aluminum are compared for their stress capabilities and economic uses. Ultimately, designing a launcher that does not produce, or greatly reduces various forms of harmful and toxic emissions is imperative. Likewise, safety concerns for children and adults are also taken into consideration. Furthermore, the mechanism can be easily transportable and will adhere itself to being able to fit in most car trunks or truck beds, as well as movement across a field. Lastly, casings made for the launcher ensure longevity in different types of weather.

Manufacturability of parts is a major influence in costs of the product across the globe. By first using premade products like the Soccer Wave ramp and Soccer Wave Jr nets, the ability to rebound the ball in the opposite direction and vertically while maintaining energy is far simpler rather than designing a new one. For the ball collector, aluminum was abandoned due to its difficulty to manufacture intricate parts thus increasing the production and shipping costs across the world. As previously stated, the main goal of the entire SkillCourt ball launching and collecting system is to make it economically feasible for anyone across the globe, ranging from individual families, to youth academies, and professionals. In addition, user feedback will become available with a wide range of options that will interact with the Skill Court program.

## 4.1. Feasibility Assessment and Future Improvements

When assessing the overall feasibility of this design, one can ensure that it is indeed achievable. Beginning with its manufacturability,

the parts are relatively simple to produce as many other products have used similar components. Along with being easily manufactured, the materials used can be made from low-cost plastics and metals making it light weight and economical. Parts such as the swivel wheels or the smooth tires can be found for a viable and economical price for the system. The amount of moving parts needed in ball launching is limited, as only three degrees of freedom will be required.

Cost and strength of the various parts are of the utmost importance, both affecting one another continuously and dire to the durability of the complete device. For the respective rebounders, their economic costs are strongly considered since the products are directly incorporated as previously described. It is far more likely that the net-based rebounder will be used rather than the plastic encased ramp, as it will be portable, cheaper, and multipurpose. There are drawbacks and positives for both the ramp and net rebounder, but the latter will be chosen as the more likely means of changing direction of the ball while maintaining momentum. Cost considerations of the ramp rebounder will range up to \$200, while the net rebounder is a reasonable \$60-\$100.

To continue, the vertical collection system and net attached to it must be able to withstand the force of an incoming soccer ball up to a range of 70 mph and not tip over, thus ensuring continuous play and little need for reset. Likewise, the material portion of the vertical system must be sturdy enough to not be damaged by an incoming projectile while also ensuring the safety of the software. If the lighting systems and computer compartments will be located on the vertical collection stem or supports, design considerations for the vertical collector will be altered slightly with additional material needed. This system is the wildcard for the structure as metalworking may cost a considerable amount. On the other hand, supplementary materials can be considered for the collector, such as fiberglass for its price and compressive strengths, or other types of plastic that are durable. Prices could range from a cheap \$100 up to \$400, which would be detrimental to the global design of the system.

Finally, the net used will be likely those used for baseball and football practices, these nets are loose and their main goal being to completely stop a ball's momentum. By attaching this type of net system to the vertical collector, balls can continuously be reloaded into the ball launching system. It is likely the net will be locked by a set of wires and lines that will be attached to the vertical collector. There are some stress and vibration concerns that must be considered, as the net must be tied down in several areas, this additional system would cost \$50-200 depending on quality and size.

Similarly, weather conditions that the product will be exposed to may also affect the structural capability of the various components. Wet areas may cause erosion of the metallic components, while windy conditions may tip over the vertical collector. Some additions to consider combating these environments are coverings for the metallic parts like the collector and rebounder, but also stronger ropes and tightening tools.

## 5. Conclusion

The result of the task in regards to the reloading mechanism for the Autonomous Launcher is not only to work together with teammates from very diverse backgrounds and ideals, but also to create a unique design concept that could possibly lead to a change in the

way launchers are used in a variety of sports. The main goals were to develop a simple autonomous reloading mechanism for a launcher that is cost effective for consumers to purchase and manufacturers to make, while portability to take it anywhere for a quick setup were met satisfactorily. The team approached every aspect of those main ideas to develop an effective solution to those problems. However, further research is necessary in regards to maneuverability to achieve a wider range of motion for the launcher to track the user.

## 6. ACKNOWLEDGMENTS

The authors extend their thanks to SkillCourt LLC and Guðmundur Traustason, who sponsored the project and holds the intellectual property (patents and trademark rights) as the creator of SkillCourt projects. The authors also extend their gratitude to the FIU's Department of Mechanical and Materials Engineering and the Robotics and Automation Lab for providing access to the lab, which expedited the progress of the present work. Partial funding provided by the Department of Mechanical and Materials Engineering for the construction of the prototype is also acknowledged.

## 4. REFERENCES

- [1] Crass, Scott. Dynamics of a Soccer Ball. Rep. Mathematics, California State University: Long Beach. N.p.: n.p., n.d. 1-18. 2014, Web.
- [2] "Motion Platform." Simge. Simge Simulations Technologies, 2016. Web. 20 Oct. 2016.
- [3] "Sidekick." Sidekick. Keeperstop, 2016. Web. 17 Oct. 2016.
- [4] Gimbal Platform Pic "Super Gyroscope Gimbals (add-on Kit) - From Gyroscope.com." Gyroscope.com. Gyroscope, n.d. Web. 17 Oct. 2016.
- [5] "Motion Base/Stewart Platform - Mark Roberts Motion Control." Mark Roberts Motion Control. MrMoco, 2016. Web. 17 Oct. 2016.
- [6] William Mendez, Yuniesky Rodriguez, Lee Brady, Sabri Tosunoglu. Design of a Three-Axis Rotary Platform. Mechanics and Materials Engineering, Florida International University. Florida Conference on Recent Advances in Robotics, FCRAR 2010 - Jacksonville, Florida, May 20-21, 2010.
- [7] OpenCV About. Opencv.org. N.p. N.d., Web 20 Oct. 2016
- [8] Oakley, Adam. "Tracking a Ball and Rotating Camera with OpenCV and ..." Hackaday.io. Hackaday, 7 July 2014. Web. 23 Oct. 2016.
- [9] "A.F.T.M FIU Senior Design 2 Team 16" YouTube. N.p., 8 Apr. 2014. Web. 22 Oct. 2016.
- [10] "Tennibot™." Tennibot, LLC. N.p., 2016. Web. 17 Oct. 2016.
- [11] Gibbs, Dan. "Revealed: How Jurgen Klopp's Remarkable Training Methods Could Get Liverpool Firing." Daily Express Football RSS. N.p., 2015. Web. 17 Oct. 2016.
- [12] "Henrik Mkhitarjan vs Footbonaut Machine [HD] - YouTube." N.p., 8 Apr. 2014. Web. 22 Oct. 2016.
- [13] "ASTM International" ASTM American Society for Testing and Materials. N.p, N.d. Web 16 Oct. 2016.
- [14] "ANSI" American National Standards Institute. N.p. N,d.Web 20 Oct. 2016.
- [15] "Home." ISO International Organization for Standardization. N.p., N.d. Web. 20 Oct. 2016.
- [16] "IEEE-SA" Institute of Electrical and Electronics Engineers Standards Association. N.p., N.d. Web. 20 Oct. 2016.
- [17] "NEMA" National Electrical Manufacturers Association. N.p., N.d., Web. 20 Oct. 2016.
- [18] "Skill Court Demo." N.p., 24 Aug. 2016. Web. 22 Oct. 2016.
- [19] "SoccerWave Jr" SoccerWave. Web. 20 Oct. 2016.
- [20] Hibbeler, Russel C. Engineering Mechanics Dynamics . 13th ed. N.p.: Prentice Hall, n.d. Print.
- [21] Wójcicki, Krzysztof. Puciłowski, Kazimierz. Kulesza, Zbigniew. "Mathematical Analysis for a New Tennis Ball Launcher." N.J., N.V, 1995, 110-118
- [22] NASA. NASA, n.d. Web. 03 Mar. 2017.
- [23] "Robotech Shop." Robotech Shop. N.p., n.d. Web. 01 Feb. 2017.
- [24] "Arduino - Introduction." Arduino - Introduction. N.p., n.d. Web. 01 Feb. 2017.
- [25] "New product launch! Introducing Raspberry Pi Model B." Raspberry Pi. N.p., 01 Feb. 2015. Web. 28 Jan. 2017.
- [26] Kumar, Karan, Mansi Aggarwal, and Pranav Haldar. P.C. Interfaced Speed Control of D.C. Motor. Thesis. College of Engineering Roorkee, 2010. Roorkee: n.p., 2010. Print.
- [27] "The Half-Bridge Circuit Revealed ." PowerGuru, 30 Aug. 2012. Web.
- [28] "How To Use MOSFET - Beginner's Tutorial." Oscar Liang. N.p., 17 June 2015. Web. Jan 29. 2017.
- [29] Barkhordarian, Vrej. Power MOSFET Basics. N. p.: International Rectifier, n.d. PDF.
- [30] YouTube. YouTube, 18 July 2014. Web. 22 Jan. 2017.
- [31] "Selecting the right MOSFET." Selecting the right MOSFET - Electronic Products. N.p., n.d. Web. 02 Feb. 2017.
- [32] "How Boost Converters Work." Electronic Circuit Projects. N.p., 23 Feb. 2017. Web. 01 Mar. 2017.
- [33] "1200W DC Boost Converter 10-60V to 12-83V Step-up Driver Power Module Adjustable." EBay. N.p., n.d. Web. 01 Mar. 2017.
- [34] "LATEST." All About Circuits. N.p., n.d. Web. 24 Feb. 2017
- [35] Offerman, Nick . "Three steps to select the right fuse for control circuit protection." Three steps to select the right fuse for control circuit protection | Control Engineering. N.p., n.d. Web. 26 Feb. 2017.
- [36] "Universal Power Group | Stay Powered®." Universal Power Group | Stay Powered®. N.p., n.d. Web. 01 Mar. 2017.

[37] "What's the Best Battery?" Basic to Advanced Battery Information from Battery University. Battery University, 1 Nov. 2017. Web. 01 Mar. 2017.

[38]#699105, Member. "SparkFun Monster Moto Shield." DEV-10182 - SparkFun Electronics. N.p., n.d. Web. 02 Mar. 2017.

[39] "Bring ideas to life with free online Arduino simulator and PCB apps | Autodesk Circuits." Bring ideas to life with free online Arduino simulator and PCB apps | Autodesk Circuits. N.p., n.d. Web. 01 Mar. 2017.

[40] Bradski, Gary R., and Adrian Kaehler. Learning OpenCV: computer vision with the OpenCV library. Sebastopol, CA: O'Reilly, 2008. Print.

[41] Dusan Johnson "Top smart gadgets for soccer/football" Gadgets & Wearables. 5 October 2016. W3eb 25 Nov. 2016.

[42] Jeff Alger "Does a ball machine belong on your pitch?" Success in Soccer Magazine. May 2012. Web 25 Nov. 2016.

# Space Exploration Robot

Hanser Castro, Raheem Maliki, Michael Benitez, Scott Jagolinzer, Sabri Tosunoglu

Department of Mechanical and Materials Engineering  
Florida International University  
Miami, Florida 33174

hcast012@fiu.edu, rmali005@fiu.edu, mbeni022@fiu.edu, sjago001@fiu.edu, tosun@fiu.edu

## ABSTRACT

Robots in space have different functionalities as they are used for different applications including Planetary Surface Exploration (PSE). Robots that are designed and built for PSE are expected to perform activities such as rover, shovel, and search for life. This paper presents a Space Exploration Robot (SER) that will use sensors, motors and a camera in order to operate in space and in autonomous mode. For the purpose of this work, this robot is envisioned to communicate and be controlled by Wi-Fi. The SER is also envisioned to be a robot able to explore unknown territory in space and communicate its findings to the control center nearby or on earth.

## 1. INTRODUCTION

The development of Automation and Robotics (A&R) has had a positive effect on space exploration [1]. The implementation of this technology on space missions has enabled the exploration of areas that are beyond human access. A fast evolution of robotic devices is necessary for the development of complex spacecraft and space exploration missions. Autonomous robots allow the exploration of planetary surfaces and serve as a platform for in space activities. Throughout the years, the evolution of this technology has led to great number of achievements and will continue to be a great contributor to space exploration.

Since 1950s humans have been trying to explore outer space. The capability of going beyond Earth, and exploration of planets, moon, comets, asteroid have been an irresistible attraction for humankind. Space exploration began in the late 1950s early 1960s as a result of the space race between the USSR and USA, sending humans into the Earth orbit and the Moon was the main objective. The development space programs were extremely expensive, scientists used cheap robotic proxies to understand the space environments that astronauts would be operating.

Table 1 shows successful robot missions flown on Earth orbit, the moon, and Mars. Each mission developed systems that include surface rover, robotic hands, and subsurface sampler and drills. These systems helped to understand environmental conditions that exist beyond earth.

The first robotic mobility system successfully operated was a manipulation sampling device also known as a scoop. This device was on board of Surveyor 3 launched on 1967 to the Moon. Following that Luna 16 launched the first planetary robotic-arm mounted drill in 1970, and Luna 17 succeed with the first planetary rover called Lunokhod 1 on 1970.

The new generation of planetary exploration robots has travelled farther into the solar system, its technology and autonomous level is increasing with each mission. Future space missions will require a higher autonomous level on each robot, leading to better robotic explorers and robotic assistants.

**Table 1. Successful Robots on Earth Orbit, Moon, and Mars [2]**

Year	Mission	Country	Target	Rover	Arm	Sampler	Drill
1967	Surveyor 3	USA	Moon			x	
1970/72/76	Luna 16/20/24	USSR	Moon		x	x	x
1970/73	Luna 17/21	USSR	Moon	x			
1975	Viking	USA	Mars		x	x	
1981/2001/08	ISS's Canadarm1/2/Dextre	Canada	Earth orbit		x		
1996	Mars Path Finder	USA	Mars	x			
2003	Hayabusa	Japan	Asteroid			x	
2003	Mars Exploration Rovers	USA	Mars	x	x	x	
2007	ISS's Kibo	Japan	Earth orbit		x		
2008	Phoenix	USA	Mars		x	x	
2011	Mars Science Laboratory	USA	Mars	x	x	x	
2013	Chang'E 3	China	Moon	x			
2004-14	Rosetta	Europe	Comet		x	x	x

## 2. Conceptual design

This project is based on 4WD Hercules mobile robotic platform. This is a closed-loop control system with four powerful gear motors to provide precise control process.



**Figure 1. Hercules platform [3]**

## 2.1 Robot Components

Hercules skeleton is made up of aluminum alloy plate. The platform includes four servo motors, motor controller, and a lithium battery.



Figure 2. Hercules components [3]

Table 2 shows the bill of materials for the assembly. It also shows specifications and material for each part.

Table 2. Hercules Platform Parts List [3]

No.	Part	Material	Quantity (pcs)
1	Bracket-1	L Aluminum extrusion 6061	2
2	Bracket-2	L Aluminum extrusion 6061	2
3	Reducing motor	310 rpm DC6V torque: 70 Kg	2
4	Reducing motor w/ encoder	310 rpm DC6V torque: 27 Kg*cm	2
5	Bracket adapter Plate	Cold rolled plate	4
6	Screws (3*10mm)	Metal	30
7	Nut	Metal	4
8	Motor connector	Metal	4
9	Wheel	Plastic-rubber	4
10	Spring shim	Metal	4
11	Screw (M4*10mm)	metal	4
12	Under-Plate	Tea black Acrylic	1
13	Washer	PA	4
14	Power switch	-	1
15	Hercules dual 15A 6-20V motor controller	-	1
16	Screw (M3*23mm)	Metal	4
17	Acrylic-plate	Transparent acrylic	2
18	Cover-plate	Tea black acrylic	1
19	Cu pillar	Signal stud	4
20	Top-plate	Aluminum	1
21	Screw (3*21mm)	Metal	4

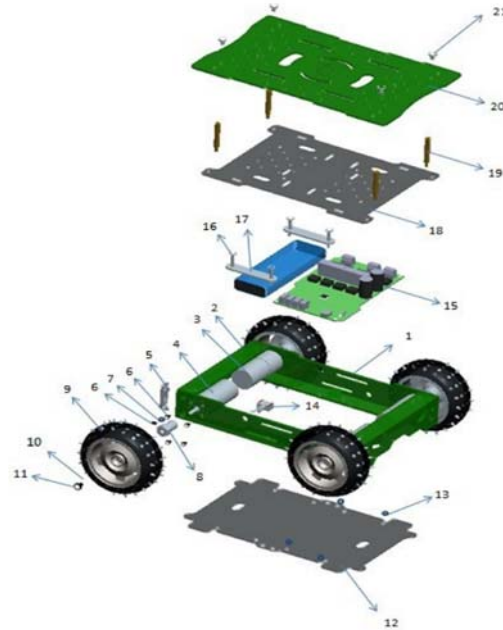


Figure 3. Assembly diagram [3]

## 2.2 Servo Motors

Hercules platform uses four 25GA-370 servo motors.



Figure 4. 25GA-370 motor [3]

The motors are horizontally placed on the output shaft. They work with a nominal voltage of DC 6.0V. Motors have a CCW rotation (CW, from the direction of the shaft).

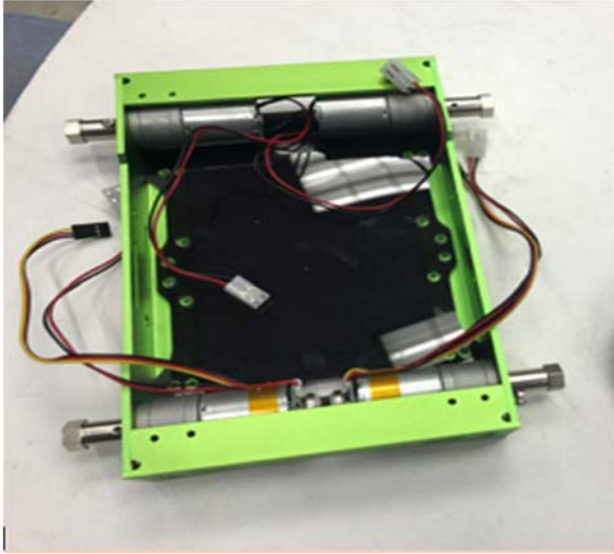


**Figure 5. Servo motors installation**

Full connection diagram was obtained from Seed Studio and it can be seen in Figure 6.

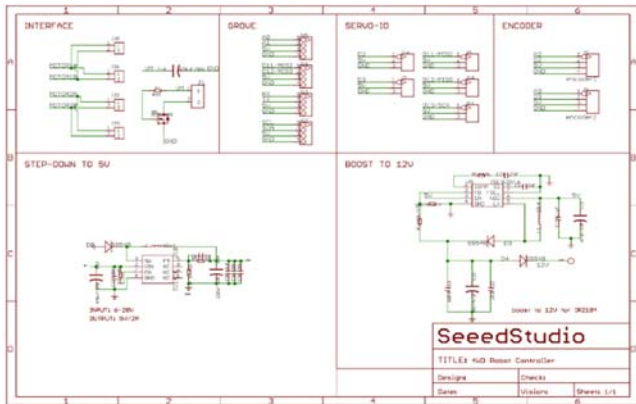


**Figure 6. Servo motor connection diagram [3]**

### 2.3 Motor Controller

Hercules uses a 15A 6-20V Motor Controller. This control board is Arduino compatible and includes a microcontroller processor, motor drive circuit, a charging unit, and two fuse to protect the board from overloading. Figure 7 illustrates the controller used.



**Figure 7. Robot Controller [3]**

Figure 8 shows output wiring connections from servo motors to motor controller.

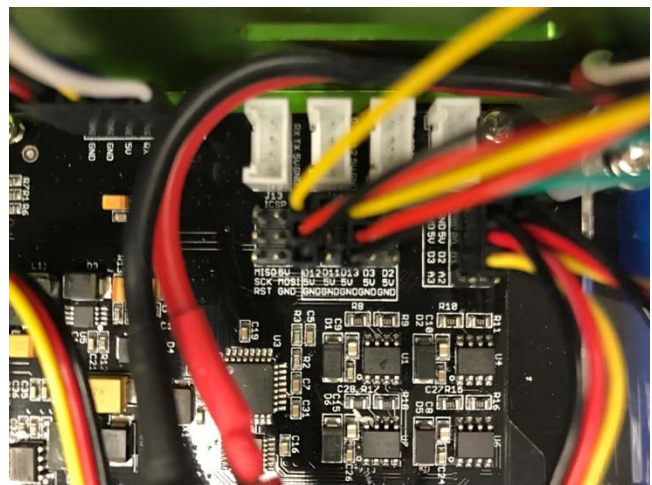


**Figure 8. Output wiring connection**

### Battery

Hercules uses a two cell Lithium Battery with outputs 7.4V storing 2200mAh of charge, since this is a two-cell battery, a special charger is needed.



**Figure 9. Platform battery [3]**

The battery is soldered to a power switch and is located right next to motor controller. Soldering and installation process can be seen in Figure 10 and Figure 11, respectively.

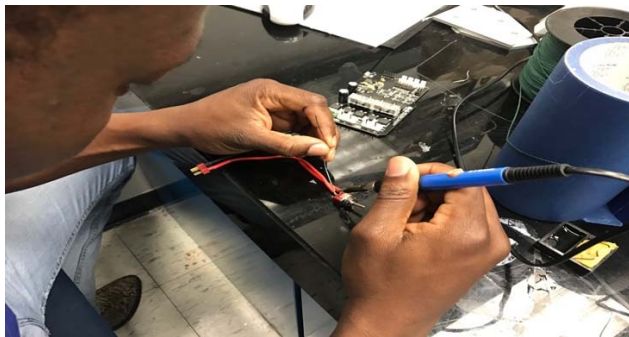


**Figure 10. Switch soldering**

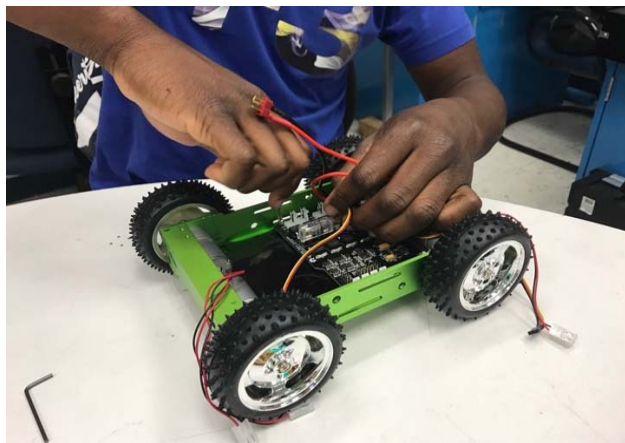


**Figure 11. Battery installation**

## 2.4 Object detection sensor

SER uses five SF-SR02 ultrasonic distance sensors. These sensors have a detection range between 0.79 to 275.6 inches. They have a power indicator LED to tell when the sensor is powered. Sensors work with 5V and 16mA current.



**Figure 12. SF-SR02 Ultrasonic distance sensor [4]**

## 2.5 Camera

Platform will use a DZDL HD mini super small portable camera to record videos. This camera has a video resolution of 1080P, and can be controlled with smartphones or PC. The camera has 90-degree lens view angle, support 32GB Micro SD Card, works with 3000mAh, and has 5-hour battery operating life.



**Figure 13. Mini camera**

## 2.6 Base for Sensors and Camera

A base will be created to mount object detection sensors and camera mentioned before. This base will be first designed in 3D using SolidWorks, and then will be printed in 3D using ABS material.

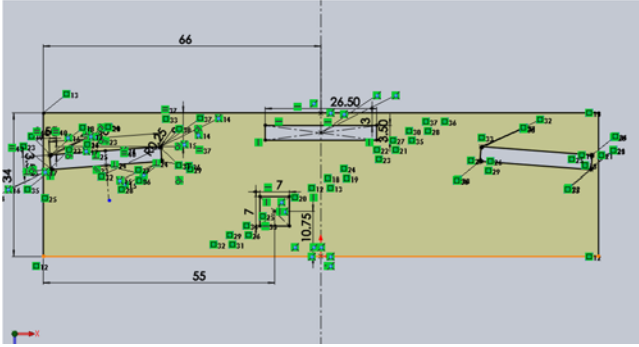


**Figure 14. Solid Works 3D base contraction**

The ABS base must have enough spaces to install five sensors. A sensor on the middle will detect how far an object is from the front of the platform. Sensor on the top right-left will detect objects near front wheels, avoiding collisions against walls. Platform has also two sensors on the side to determine how far objects are. If platform has to make 90 degrees turn, these sensors will turn platform toward farthest object avoiding collision on back wheels.

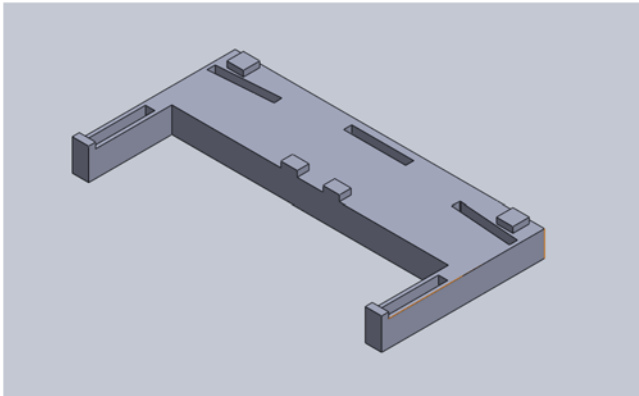


**Figure 15. Solidworks 3D base**

### 3. Programming

For programming, C++ language is used. Since, Arduino boards are being used, the use of C++ is the most reasonable choice. The programming of the Bot is as simple as possible, sensors are used so that the bot continues traveling and exploring forward until an object is detected.

When an object is detected in the front, the bot turns right about ninety degrees and continues forward until it is able to get around that object. There are many if statements that set the conditions on how the robot should travel. Following the program developed, the robot should not get stuck and should be able to traverse until its battery power is low.

### 4. Final Prototype

The prototype that has been created has five ultrasound sensors. Platform itself came with a few pins. The team hardwired another Arduino board to the other to have more pins; so, practically there is no limit on how many accessories that could be placed onto the platform.

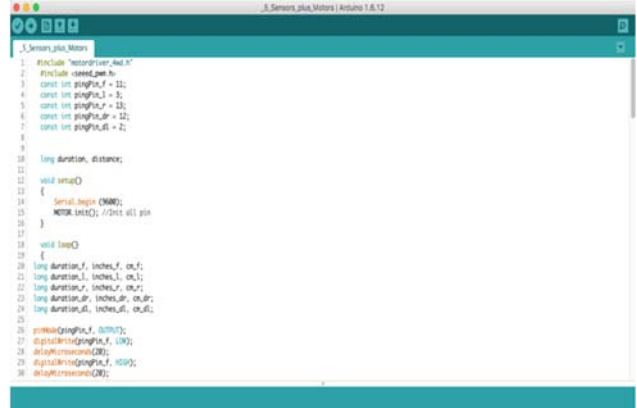


**Figure 16. Sensors programming on Arduino**

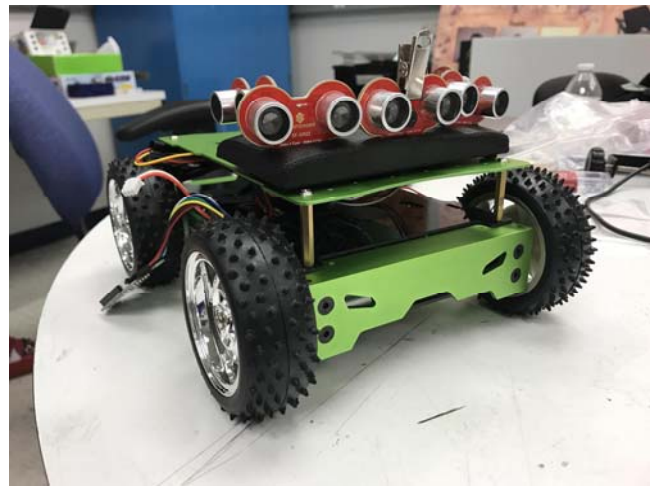


**Figure 17. SER side view**

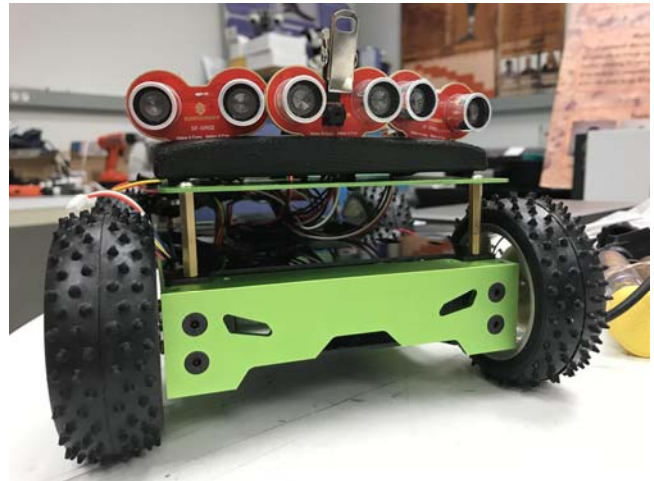


**Figure 18. SER front view**

For the camera that has been installed onto the platform, there is no coding necessary. The team decided on an option to make the camera wirelessly controlled with its own wireless capability.

Since there is wireless onboard, set user can modify the wireless chip to be able to put in more distance between the user and robot.

Having such wireless capability gives more control to the user to be able to look at where the robot is and what is being explored in real time, while capturing the images themselves. A micro-SD slot and card is also installed where the pictures being taken will be stored in, where the user can collect once the robot returns. The camera having its own battery supply ensures further travel and performance of the sensors and motors of the platform.

### 5. Platform testing

SER was tested on both flat and rough terrain. On rough terrain, sensors tend to slide from their original position and tend to fall from their base indicating malfunction in obstacle detection. To solve this problem, a better base must be created, this base must have a better grip of the five sensors to prevent them falling or moving.



**Figure 19. Hard terrain platform testing**

The camera was also tested to make sure the platform meets all expectations. The camera is clipped to the middle sensor. This was a quick solution, but obviously not an ideal solution. Ideally, the camera must be separated from the sensor. In case the sensor has to be replaced, the camera position should not be affected.



**Figure 20. Camera clipped to front sensor**

To use the camera, an application named P2PLiveCam must be downloaded. On this application, the user can connect wirelessly with a phone and can record videos, take snapshots as shown in Figure 21 and 22, or set an alarm to record during set time periods.



**Figure 21. Platform testing**



**Figure 22. Team members Hanser Castro and Raheem Maliki in the Robotics and Automation Laboratory testing P2PLiveCam**

## 6. Conclusions

The Space Exploration Robot (SER) can be a useful asset for the exploration of unknown territories. This platform can be a tool to preserve the lives of astronauts during dangerous space missions. The robot uses multiple motors and sensors to detect objects and avoid obstacles in autonomous mode. The platform also has a camera with HD resolution. This camera can take photos and record videos making it easy to study the terrain before sending humans. The prototype developed for this project is the first attempt to study the behavior of the proposed platform SER. Further study and development of more realistic platforms will undoubtedly be needed before such a platform can perform successfully on other planets.

## 7. Acknowledgments

Our thanks are extended to Florida International University, Department of Mechanical and Materials Engineering, and especially the Robotics and Automation Laboratory for providing the opportunity to work on this extraordinary project.

## 8. References

- [1] W. De Peuter. Development program on space automation and robotics. Symposium "Artificial Intelligence, Robotics and Automation in Space". Toulouse, September 1992.
- [2] Yang, Guang Zhong. Space Robotics & Autonomous Systems: Widening the Horizon of Space Exploration. United Kingdom: UK-RAS, 2016. PDF.
- [3] Team, Seedstudio. "Skeleton Bot - 4WD hercules mobile robotic platform." Seed Wiki. N.p., n.d. Web. 11 Apr. 2017.
- [4] "SunFounder SF-SR02 Ultrasonic Distance Sensor Module Kit Ultrasonic Module HC-SR02." Mazentop Demo. N.p., n.d. Web. 12 Apr. 2017.
- [5] "GZDL HD 1080P Mini Super Small Portable Hidden Spy Camera P2P Wireless WiFi Indoor Internet Video Recorder for Home Cars Bathrooms Kids Remote View." Camera Focused. N.p., n.d. Web. 12 Apr. 2017.
- [6] Y. Tsumaki, M. Yokohama, D. Nenchev. *Intra-Vehicular Free-Flyer System*. Proceedings of the 2003 IEEE/RSJ Intl. Conference on Intelligent Robots and Systems. Las Vegas, Nevada. October 2003.
- [7] P. Putz. *Space robotics in Europe: A survey*. Journal of Robotics and Autonomous Systems 23 (1998) 3-16.
- [8] B. Hannaford, A. Bejczy, P. Buttolo, M. Moreyra, S. Venema. *Mini-Teleoperation Technology for Space Research*. Proceedings of MIMR-95, Sendai Japan, September 1995.

# Vocational Rehabilitation of Individuals with Disabilities Using Virtual Reality

Evren Bozgeyikli, Lal Bozgeyikli, Andoni Aguirrezabal, Redwan Alqasemi, Stephen Sundarrao, Rajiv Dubey

University of South Florida  
4202 E Fowler Ave  
Tampa, FL

evren@mail.usf.edu, gamze@mail.usf.edu, aaguirrezaba@mail.usf.edu, alqasemi@usf.edu, sundarra@usf.edu, dubey@usf.edu

## ABSTRACT

In this paper, a system for vocational training and assessment of individuals with severe disabilities is presented. This system is currently in its iteration phase. The system aims at providing effective vocational training to three groups of individuals with disabilities: autism spectrum disorder (ASD), traumatic brain injury (TBI) and severe mobility impairment, such as spinal cord injury (SCI). System components and training modules are presented in the paper. A user study was performed with 5 individuals with ASD and 1 individual with TBI, with accompanying expert job coaches. User study results and the observations of the job coaches indicate that VR4VR system is promising in providing very effective vocational training to individuals with severe cognitive disabilities. Since training module for physical disabilities is currently under development, it could not be included in the user study.

## Keywords

Vocational rehabilitation, virtual reality, autism spectrum disorder.

## 1. INTRODUCTION

The US Census Bureau reports that 54.4 million of U.S. population has disabilities, of which 64% is severe [2]. 2012 data reveals that employment rate of individuals with disabilities have a ratio of 3:10 as compared to employment rate of individuals without disabilities [3]. Employment is an important aspect of life which provides individuals with economic independence, satisfaction and better quality of life [11, 15]. As unemployed population with disabilities was interviewed, 66% stated that they would prefer getting employed if they had the chance [9].

We believe that easily accessible training would help in improving the employment rate of individuals with disabilities. To take part in improving the chances of individuals with disabilities to gain employment, we proposed a virtual reality system for vocational rehabilitation of individuals with disabilities (VR4VR). Our VR4VR uses several modules on different skills for training and assessment of individuals with disabilities using immersive virtual reality. The long-term goal is to provide a low cost, easily accessible and effective training environment for individuals with disabilities and to help increase their employment rate.

Virtual reality (VR) offers several advantages such as: safe training, customizable scenarios, real time prompts and distractions,

repetitive training, automated data collection for reflection, wide range of modules, real time feedback, system scalability and reduced transportation costs. Of course, these advantages are not to claim that VR offers better training than conventional job training with one to one job coaches. VR can be utilized as an adjunct to conventional job training and create more possibilities for more people in the same amount of time. A training program that utilizes VR first, then one to one complementary training and assessment with a job coach seems suitable for a sophisticated training.

Our VR4VR caters to three disability groups: autism spectrum disorder (ASD), traumatic brain injury (TBI) and severe mobility impairment. The system uses immersive virtual reality to train individuals on transferrable skills with seven training modules of cleaning, loading the back of a truck, money management, shelving, environmental awareness, social skills, and object manipulation with an assistive robot. A user study was performed with five individuals with ASD and one individual with TBI in the presence of accompanying job coaches. The results are promising in terms of effective usage of virtual reality for training individuals with severe disabilities. This paper presents the VR4VR system, training modules and user study results. We also share the observations of the job coaches who are experts in vocational training of individuals with severe disabilities. A previous version of our system can be seen in [1].

## 2. RELATED WORK

Vocational training with virtual reality is an emerging area because of the several advantages it offers over conventional job training. The key works on vocational training using virtual reality technologies are presented in this section.

Tsang and Man worked on vocational training of individuals with schizophrenia using virtual reality environments [13]. Wade et al. developed an adaptive driving training system with immersive virtual reality [14]. Smith et al. proposed a job interview training system for individuals with ASD with immersive virtual reality environments [12].

Some studies concentrated on providing assistive technological devices as a real time vocational assistant to individuals with disabilities. Chang et al. worked on a system that provides employees with handheld assistive palm computers that creates context aware prompts [4]. A follow up study by Chang et al.

provided context aware prompts on a large display to assist individuals with disabilities in vocational tasks [5]. Mechling and Ortega-Hurndon developed a system that provides video based instructions for teaching vocational tasks to individuals with disabilities [8].

As compared to the previous works in the area of vocational rehabilitation using virtual reality, the novelty of our system can be stated as: (1) Several off the shelf components that are incorporated seamlessly, (2) Several vocational skills, (3) Several real time distractions, and (4) Real time tangible interaction in real world and virtual reality.

### 3. VR4VR SYSTEM

The proposed VR4VR system utilizes several hardware components to provide and immersive training with several options. A VR2200 head mounted display (HMD) with 1024x768 resolution was used as the viewing device of the motion tracking system. For motion tracking, an optical system with 12 OptiTrack Flex: V100 cameras was used. For interaction, tangible objects equipped with optical markers that can be tracked real time by the system were used. As an alternative training model, a large 180° curved curtain screen was used as a display device along with input devices such as mouse, haptic device, and touchscreen tablet computer. A server computer with AMD FX-8150 8-Core Processor, 16 GB Memory and AMD FirePro W600 Graphics Card was used to run the software.

In the VR4VR software, there are several immersive virtual environments such as warehouse, outdoor parking lot, grocery store, cash register area, office space and outdoor street. The training is achieved with three levels for each module: tutorial level, training level, distracters level. Distracters are composed of common daily life and work place events that are related to the scenario environments: lightning, announcements, complaining customers, traffic noise and fireworks. Distracters can be in the form of 3D animation, 2D visual, sound or a combination of those. The aim of the distracters is to help individuals with cognitive disabilities overcome their fears or irritations over them. The distracters can be applied automatically or in real time by the job coaches. The system has a remote control system for the job coaches that allows for several actions such as running/stopping simulation, applying distracters, tracking remaining tasks/instances, and reviewing trainee reports.

### 4. TRAINING AND ASSESSMENT MODULES

VR4VR offers seven different modules for vocational training and assessment of the individuals with severe disabilities. The modules are designed to train individuals on transferrable skills of cleaning, loading the back of a truck, money management, shelving, environmental awareness, social skills and object manipulation with an assistive robot. All six modules other than object manipulation with an assistive robot were designed for individuals with cognitive disabilities. The skills for the modules were designed following discussions with the job coaches and the prevalence among employment of individuals with disabilities [10, 7].

Each module has their own three levels: tutorial level, training level and distracters level. Tutorial level aims at teaching the user the task they will be practicing on. Training level allows for the repetition of the learned task without any environmental distractions. Distracters level aims at preparing the users to perform

vocational tasks in the presence of real world distractions. Pictures of shelving, money management and object manipulation with an assistive robot skills can be seen in Figure 1, Figure 2 and Figure 3 respectively.

Each module offers three different subtasks with their own three levels. Training subtasks for each module is presented in Table 1. Object manipulation with an assistive robot module is currently under development. All other modules are finished.

**Table 1. Subtasks offered in each training module of VR4VR system**

Graphics	Top
Cleaning	<ul style="list-style-type: none"> <li>• Vacuum cleaning</li> <li>• Mopping</li> <li>• Litter collection</li> </ul>
Loading the Back of a Truck	<ul style="list-style-type: none"> <li>• Loading identical boxes</li> <li>• Loading labeled boxes</li> <li>• Loading within a short timeframe</li> </ul>
Money Management	<ul style="list-style-type: none"> <li>• Recognizing coins and bills</li> <li>• Counting money</li> <li>• Providing change</li> </ul>
Shelving	<ul style="list-style-type: none"> <li>• Aligning boxes</li> <li>• Orders/deliveries with graphical labels</li> <li>• Orders/deliveries with item codes</li> </ul>
Environmental Awareness	<ul style="list-style-type: none"> <li>• Navigating around stationary objects</li> <li>• Navigating around moving people</li> <li>• Navigating around moving cars</li> </ul>
Social Skills	<ul style="list-style-type: none"> <li>• Basic personal information questions</li> <li>• Intermediate job experience questions</li> <li>• Advanced reasoning questions</li> </ul>
Object Manipulation with Assistive Robot	<ul style="list-style-type: none"> <li>• Robot navigation</li> <li>• Arm control</li> <li>• Object manipulation</li> </ul>



**Figure 1. Training on shelving skills in a virtual warehouse environment with tracked boxes**

### 5. USER STUDY

#### 5.1 Research Question

Our research question is about validating the usage of virtual reality technologies for vocational training of individuals with severe disabilities: “Can immersive virtual reality be used effectively for vocational training and assessment of individuals with severe disabilities?”

## 5.2 Participants

Currently, we are performing user studies to validate our research question. In this paper, we will present results of the users who participated in the user study so far, along with the observations of the job coaches. In total, three job coaches participated in the study. Six participants (five with ASD and one with TBI) participated in the user study. Demographics were as follows: all male, mean age of 24.6, no prior virtual reality experience.

The study was performed under IRB Study #Pro00013008. Subjects were recruited via posters, e-mail announcements, job coaches and clinicaltrials.gov webpage announcements. All participants signed an informed consent form before participating in the study. The users completed six skills of cleaning, loading the back of a truck, money management, shelving, environmental awareness and social skills in two sessions of two hours. Job coaches accompanied the users during all testing sessions. The two sessions were scheduled on different days.



Figure 2. Training on money management skills in a virtual grocery store with a touchscreen computer



Figure 3. Object manipulation with an assistive robot skill in a virtual warehouse environment

## 5.3 Results

To validate the usability of our system by individuals with disabilities, our first measure of success was the successful completion of a level. In VR4VR system, if a user cannot complete a level within five minutes, the level is considered as failed. The percentages of participants who completed levels of the trained skills successfully are presented in Figure 4.

In each level, 4-8 instances of the practiced task are requested. The number of tasks per level is decided by the system randomly within this range during run time. Average time to complete the levels that the user completed successfully was measured. Since the levels

may contain different number of instances, this score was normalized by dividing the time by number of instances per level. The normalized results for average time to complete each level of each skill are presented in Figure 5.

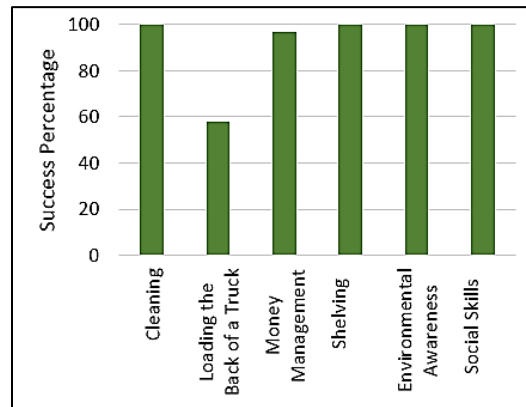


Figure 4. Percentage of participants who completed the levels successfully

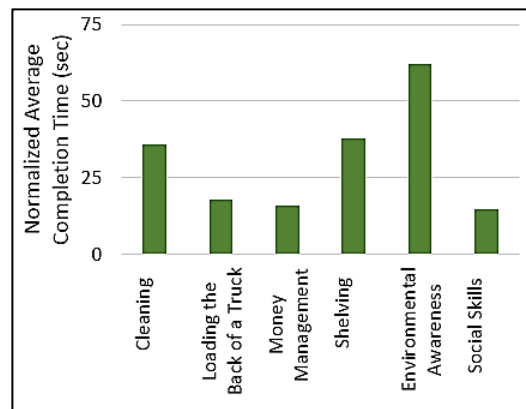


Figure 5. Average completion time results normalized by instances per level

## 6. DISCUSSION

The results indicated that the users with ASD and TBI were able to complete the tasks within the VR4VR system successfully.

All users completed the cleaning, shelving, environmental awareness and social skills successfully. The lowest completion rate was in loading the back of a truck skill, which was criticized by the job coaches to be cognitively too demanding for these special groups. This skill will be updated to include more free space to make it less cognitively demanding for individuals with ASD and TBI. Only one individual with ASD was not able to complete the money management levels successfully, which may be a personal deficiency to be trained on. We perceive successful completion rates as our VR4VR system's being effectively usable by individuals with disabilities.

As average completion times are reviewed, environmental awareness, shelving and cleaning skills are more demanding in time as compared to other three. We believe this is due to the design of these skills in requiring navigation. The time to virtually move from one point to another increases the skill completion times. However, the job coaches stated that requiring navigation is a positive part of

the training which prepares the individuals for real life job environments. So, no update will be made in regards to the navigational requirements.

We did not observe any acceptability issues for HMD, wearable markers and any other controlling device. All participants stated that they would come back again to train with the VR4VR system. The participants with ASD stated positive comments on the enjoyment VR training provided to them, which overlaps with the tech savvy characteristic of this population [6].

The job coaches stated that VR4VR system is promising in providing very effective training and convenient assessment for individuals with ASD and TBI. They observed improvement in participants on the trained skills. The job coaches also noted that the most effective usage of virtual reality training would be first training the individual on VR for a period of time and then training them conventionally with a job coach for a shorter time.

## 7. CONCLUSION AND FUTURE WORK

In this paper, we discussed VR4VR system which provides vocational training and assessment to individuals with severe disabilities of ASD, TBI and severe mobility impairment. The paper presents system properties, training modules, user study results of 5 ASD and 1 TBI individuals and observations of the job coaches during the user studies. User study results, statements of the participants and the job coaches indicate that VR4VR system is promising in providing effective training and convenient assessment to individuals with cognitive disabilities. As future work, we will test the system with more participants and update the system according to results and suggestions of the job coaches. The object manipulation with an assistive robot is currently under development. This module will be completed soon and included in user studies.

## 8. REFERENCES

- [1] Bozgeyikli, L., Bozgeyikli, E., Clevenger, M., Raij, A., Alqasemi, R., Sundarrao, S., & Dubey, R. (2015). VR4VR: vocational rehabilitation of individuals with disabilities in immersive virtual reality environments. In Proceedings of the 8th ACM International Conference on Pervasive Technologies Related to Assistive Environments (PETRA '15). Article 54, 4 pages.
- [2] Brault, M.W. (2012). Americans with disabilities: 2010. US Census Bureau, Census Brief. Retrieved February 11, 2015, from <http://www.census.gov/prod/2012pubs/p70-131.pdf>
- [3] Bureau of Labor Statistics. (2015). Persons with a Disability: Labor Force Characteristics. Retrieved February 11, 2015, from <http://www.bls.gov/news.release/disabl.nr0.ht>
- [4] Chang, Y., Chang, W. C., & Wang, T. (2009). Context-aware prompting to transition autonomously through vocational tasks for individuals with cognitive impairments. In Proceedings of the 11th international ACM SIGACCESS conference on Computers and accessibility (Assets '09), 19-26.
- [5] Chang, Y., Chou, L., Wang, F., & Chen, S. (2013). A Kinect-based vocational task prompting system for individuals with cognitive impairments. *Personal Ubiquitous Comput.*, 17, 2, 351-358.
- [6] Frauenberger, C. (2015). Rethinking autism and technology. *Universal Interactions*, 22(2):57-59.
- [7] JAN. (2016). Job Accommodation Network. Retrieved February 15, 2016, from <http://askjan.org/index.html>
- [8] Mechling L. C., & Ortega-Hurndon, F. (2007). Computer-based video instruction to teach young adults with moderate intellectual disabilities to perform multiple step, job tasks in a generalized setting. *Educ Train Develop Disabil.*, 42:24-37.
- [9] National Council on Disability. (2007). Empowerment for Americans with Disabilities: Breaking Barriers to Careers and Full Employment. Retrieved February 11, 2015, from <http://www.ncd.gov/publications/2007/Oct2007>
- [10] O\*NET. (2016). Resource Center. Retrieved February 15, 2016, from <http://www.onetcenter.org/overview.html>
- [11] Schur, L. (2012). The Difference a Job Makes: The Effects of Employment among People with Disabilities. In *Journal of Economic Issues*, Volume 36, 339-347.
- [12] Smith, M.J., Ginger, E.J., Wright, K., Wright, M.A., Taylor, J.L., Humm, L.B., Olsen, D.E., Bell, M.D., & Fleming, M.F. (2014). Virtual reality job interview training in adults with autism spectrum disorder. *Journal of Autism and Developmental Disorders*, 44 (10):2450-2463.
- [13] Tsang, M. & Man, D. (2013). A virtual reality-based vocational training system (VRVTS) for people with schizophrenia in vocational rehabilitation. In *Schizophrenia Research*, 144(1), 51-6.
- [14] Wade, J., Bian, D., Zhang, L., Swanson, A., Sarkar, M., Warren, Z., & Sarkar, N. (2014). Design of a Virtual Reality Driving Environment to Assess Performance of Teenagers with ASD. In *Universal Access in Human-Computer Interaction Universal Access to Information and Knowledge* (pp. 466-474). Springer.
- [15] Yasuda, S., Wehman, P., Targett, P., Cifu, D., & West, M. (2002). Return to work after spinal cord injury: a review of recent research. In *Neuro Rehabilitation*, 17(3):177-186. J. K. Author, "Title of chapter in the book," in *Title of His Published Book*, xth ed. City of Publisher, Country if not